

MASARYK UNIVERSITY
FACULTY OF SCIENCE

HABILITATION THESIS

VIRION STRUCTURES AND
GENOME RELEASE
MECHANISMS OF PICORNA-
LIKE VIRUSES

PAVEL PLEVKA

BRNO 2019

ABSTRACT

Picornaviruses are the causative agents of human diseases ranging from the common cold to life-threatening encephalitis. In contrast, several dicistroviruses and iflaviruses are economically important pathogens of honeybees causing their decline in North America and Europe. Despite their societal and economic impact, many of these viruses had not been structurally characterized, and there was limited information about their genome delivery. This thesis summarizes X-ray crystallography and cryo-electron microscopy studies of virions of picorna-like viruses and changes in their capsids required for genome release. Picornaviruses have capsids with pseudo T = 3 icosahedral symmetries built from proteins with jellyroll folds. Receptor binding or acidic pH in endosomes trigger the genome release of these viruses. Nevertheless, viruses from the order *Picornavirales* differ in the behavior of their particles before genome release: the capsids of picornaviruses and iflaviruses expand, whereas those of dicistroviruses remain compact. In contrast to previous speculations, our results indicate that particles of picorna-like viruses crack open to release their genomes in microsecond time scales. The speed of the process prevents the genomic RNA from being degraded by ribonucleases. Furthermore, viruses from the order *Picornavirales* differ in the mechanisms that enable delivery of their genomes across cell membranes into the cytoplasm. Whereas picornaviruses and dicistroviruses use VP4 subunits for membrane disruption, virions of iflaviruses probably lack VP4 subunits and employ protruding domains of VP3 subunits or minor capsid proteins attached to the particle surface to penetrate membranes.

ACKNOWLEDGEMENTS

I would like to thank my past supervisors and mentors Jitka Forstová, Alwyn T. Jones, Gerard J. Kleywegt, Richard J. Kuhn, Lars Liljas, Michael G. Rossmann, and Kaspars Tars who introduced me to virology, X-ray crystallography, and cryo-electron microscopy. It was a privilege to share your passion for virus research.

I wish to thank Jaroslav Koča and Vladimír Sklenář for the opportunity to establish the research group at CEITEC. I am grateful to Wolfgang Baumeister and Juergen Plitzko for their support to CEITEC in establishing cryo-EM facility. Many thanks go to Michal Marcolla, Jiří Nantl, Martina Pokorná, Karel Říha, and Richard Štefl for their efforts to maintain productive working environment at CEITEC. I am indebted to my coworkers from CEITEC and Masaryk University administration, in particular to: Roman Badík, Ladislav Čoček, Iveta Häringová, Ludmila Konečná, Barbora Loučková, Veronika Mikitová, Veronika Papoušková, Jana Rosolová, Jana Šilarová, and Zdenka Žampachová for their diligent administrative support.

I would like to thank my collaborators Pavel Kulich, Frank J.M. van Kuppeveld, Michael A. Lindberg, Joachim R. de Miranda, Jiří Nováček, Robert J. Paxton, Antonín Přidal, Lukáš Sukeník, and Robert Vácha for making the research presented in this thesis possible. I wish to thank scientists from CEITEC Cryo-Electron Microscopy and Tomography, Biomolecular Interactions and Crystallization, X-ray Diffraction and Bio-SAXS, and Proteomics core facilities: Michal Babiak, Josef Houser, Tomáš Klumpler, Jana Kosourová, Jaromír Marek, Daniel Němeček, Jiří Nováček, Mirek Peterek, Ondřej Šedo, Michaela Wimmerová, and Zbyněk Zdráhal for their support in collecting and analyzing data.

I wish to thank my colleagues Pavol Bárdy, Roman Baška, Ján Bíňovský, Barbora Břenková, David Buchta, Carina Renate Büttner, Zuzana Cieniková, Alžběta Dikunová, Tibor Füzik, Mária Gondová, Danyil Grybchuk, Miroslav Homola, Dominik Hřebík, Aygul Ishemgulova, Sergei Kalynych, Adam Kujan, Yevgen Levdansky, Markéta Londýnová, Pavol Mikulaj, Yuliia Mironova, Jana Moravcová, Liya Mukhamedova, Edukondalu Mullapudi, Lenka Pálková, Michal Poljak, Michaela Procházková, Dorota Rousová, Charles David Sabin, Anna Sobotková, Radovan Spurný, Hana Šáchová, Marta Šiborová, Karel Škubník, Hoa Khanh Tran Kiem, Zorica Ubiparip, and Lucie Valentová for their hard work, enthusiasm, and friendship.

I am immensely grateful to my parents Dagmar Kolářová and Josef Plevka for their support, appreciation, and respect. Very special thanks and love belong to Zuzana Ringlerová, Adam J. Plevka, and Peter M. Plevka for their patience, inspiration, and countless opportunities for distraction.

LIST OF PAPERS INCLUDED IN THE THESIS

This thesis is based on the following publications, which will be referred to in the text by their Roman numerals:

- I. Kalynych S, Pálková L, **Plevka P**. *The structure of Human Parechovirus-1 reveals an association of the RNA genome with the capsid*. J Virol. 2016; 90(3):1377-86
- II. Sabin C, Füzik T, Škubník K, Pálková L, Lindberg AM, **Plevka P**. *Structure of Aichi virus 1 and its empty particle: clues to kobuvirus genome release mechanism*. J Virol. 2016; 90(23):10800-10810.
- III. Mullanpudi E, Nováček J, Pálková L, Kulich P, Lindberg AM, van Kuppeveld FJ, **Plevka P**. *Structure and genome release mechanism of human cardiovirus Saffold virus-3*. J Virol. 2016; 90(17):7628-39.
- IV. Mullanpudi E, Přidal A, Pálková L, de Miranda JR, **Plevka P**. *Virion structure of Israeli acute bee paralysis virus*. J Virol. 2016; 90(18):8150-9.
- V. Mullanpudi E, Füzik T, Přidal A, **Plevka P**. *Cryo-EM study of genome release of dicistrovirus Israeli acute bee paralysis virus*. J Virol. 2017; 91(4):2060-16.
- VI. Spurny R, Přidal A, Pálková L, Tran Kiem HK, de Miranda JR, **Plevka P**. *Virion structure of black queen cell virus, a common honeybee pathogen*. J Virol. 2017; 91(6):2100-16.
- VII. Kalynych S, Přidal A, Pálková L, Levdansky Y, de Miranda JR, **Plevka P**. *Virion structure of iflavirus slow bee paralysis virus at 2.6Å resolution*. J Virol. 2016; 90(16):7444-55.
- VIII. Kalynych S, Füzik T, Přidal A, de Miranda J, **Plevka P**. *Cryo-EM study of slow bee paralysis virus at low pH reveals iflavirus genome release mechanism*. PNAS. 2017; 114(3):598-603.
- IX. Škubník K, Nováček J, Füzik T, Přidal A, Paxton RJ, **Plevka P**. *Structure of deformed wing virus, a major honey bee pathogen*. PNAS. 2017; 114(12):3210-3215.
- X. Procházková M, Füzik T, Škubník K, Moravcová J, Ubiparip Z, Přidal A, **Plevka P**. *Virion structure and genome delivery mechanism of sacbrood honeybee virus*. PNAS. 2018; 115(30):7759-7764.
- XI. Buchta D, Füzik T, Hřebík D, Levdansky Y, Sukeník L, Mukhamedova L, Moravcová J, Vácha R, **Plevka P**. *Enterovirus particles expel capsid pentamers to enable genome release*. Nat Commun. 2019; 10(1):1138.

The articles have been reproduced in the appendix with permissions from the respective copyright holders.

CONTENTS

| | | |
|----------|---|-----------|
| 1 | Outline of the thesis | 7 |
| 2 | Introduction..... | 8 |
| 2.1 | Human picornaviruses | 8 |
| 2.2 | Honeybee dicistroviruses and iflaviruses..... | 8 |
| 2.3 | Virion structures and replication of picorna-like viruses | 8 |
| 2.4 | Capsid protein naming conventions | 11 |
| 2.5 | Methods for studying virus structures..... | 11 |
| 2.5.1 | X-ray crystallography..... | 11 |
| 2.5.2 | Cryo-electron microscopy | 12 |
| 3 | Results and discussion | 13 |
| 3.1 | Human cardioviruses, parechoviruses, and kobuviruses | 13 |
| 3.1.1 | Virion structure of human parechovirus 1 (paper I)..... | 13 |
| 3.1.2 | Structure and genome release of aichi virus 1 (paper II) | 14 |
| 3.1.3 | Structure and genome release of saffold virus 3 (paper III)..... | 16 |
| 3.2 | Dicistroviruses infecting honeybees | 17 |
| 3.2.1 | Israeli acute bee paralysis virus (paper IV)..... | 17 |
| 3.2.2 | Inclusion of VP4 in dicistrovirus virions (papers IV and V) | 18 |
| 3.2.3 | Genome release of Israeli acute bee virus (paper V) | 19 |
| 3.2.4 | Black queen cell virus (paper VI) | 19 |
| 3.3 | Iflaviruses infecting honeybees..... | 19 |
| 3.3.1 | Virion structure of slow bee paralysis virus (paper VII)..... | 20 |
| 3.3.2 | Genome release of slow bee paralysis virus (paper VIII)..... | 21 |
| 3.3.3 | Structure of deformed wing virus (paper IX)..... | 21 |
| 3.3.4 | Genome delivery of sacbrood virus (paper X) | 22 |
| 3.3.5 | Evolution of iflaviruses (papers VII-X)..... | 23 |
| 3.4 | Genome release mechanism of enteroviruses | 24 |
| 3.4.1 | Capsid cracking enables genome release (paper XI) | 25 |
| 3.4.2 | Dynamics of genome release (paper XI)..... | 26 |
| 3.4.3 | Model of picornavirus genome release (paper XI) | 26 |
| 4 | Summary and future prospects | 28 |
| 5 | References..... | 29 |

1 OUTLINE OF THE THESIS

This thesis is based on eleven research papers published in the years 2016 to 2019 that describe studies of virus infection by X-ray crystallography, cryo-electron microscopy (cryo-EM), and biochemical methods. I contributed to the publications as the corresponding author by conceiving the research questions, designing experiments, measuring and analyzing data, and writing the manuscripts. Reprints of the papers are included in the appendix of the thesis.

The introduction explains my motivation to study human and honeybee viruses from the order *Picornavirales*. It also summarizes aspects of virion architecture, replication cycles, and protein-naming conventions of these viruses. A general description of virus structure determination by X-ray crystallography and cryo-EM is given.

The results presented in this thesis describe the structures of virions of viruses from the order *Picornavirales* and provide information on how the particles release and deliver their genomes into the cell cytoplasm. The combined discussion and results section focuses on identifying the general mechanisms that enable viruses from the order *Picornavirales* to infect cells.

2 INTRODUCTION

2.1 Human picornaviruses

Diseases caused by human picornaviruses range from upper and lower respiratory tract infections, gastroenteritis, hand-foot-and-mouth-disease to life-threatening encephalitis (1, 2). Enteroviruses are responsible for 40% of common cold cases, which result in a yearly cost of tens of billions of US\$ in treatments and lost working hours worldwide (3). Currently, there are no anti-viral drugs approved against picornavirus infections, and the available treatments are only symptomatic. Given the number of serotypes and strains of picornavirus species, it is unlikely that vaccination will ever be practical (4). Previously, the development of anti-picornavirus drugs concentrated predominantly on enteroviruses, which cause the most severe diseases among picornaviruses (5, 6). There is limited information about other picornaviruses, which are also important pathogens, such as cardioviruses, parechoviruses, and kobuviruses (7-9). Structural characterization of the virions and processes of cell entry of these viruses may identify new targets for the development of antiviral compounds.

2.2 Honeybee dicistroviruses and iflaviruses

Honeybees (*Apis mellifera*) are found all over the world and play an essential role in the agricultural industry by providing pollination services for food crops. About 10% of the total economic value of agricultural production depends on insect pollination – in the year 2000 this amounted to \$15 billion in the United States alone (10). In addition, the abundance of insect-pollinated plant species declines in areas with reduced populations of honeybees (11). However, the bees suffer from a combination of factors such as environmental stress, parasites, and pathogens, including numerous viruses that result in colony losses (12, 13). Winter colony mortality has been increasing in North America and Europe over the last few decades, leading to a decline in the number of honeybees. The shortage of honeybees available for pollination may become a serious threat to food security and ecosystem stability. Virus infections are a major threat to the health and productivity of honeybees (13). The viruses that have the greatest impact on honeybees belong to the families *Dicistroviridae* and *Iflaviridae* (12, 14). The spread of bee viruses is accelerated by their transmission by a parasitic mite, *Varroa destructor* (14).

2.3 Virion structures and replication of picorna-like viruses

Virions of the viruses from the order *Picornavirales* have pseudo-T = 3 icosahedral capsids composed of sixty copies of three major capsid proteins (usually named VP1, VP2, VP3) (Fig. 1AB) (5, 15, 16). Most of the viruses also possess minor capsid proteins VP4 attached to

the inner surface of a capsid. The coat proteins VP1, VP2, and VP3 have β -sandwich jellyroll folds, whereas VP4 usually lacks extensive secondary structure elements (Fig. 1B) (5, 15, 17).

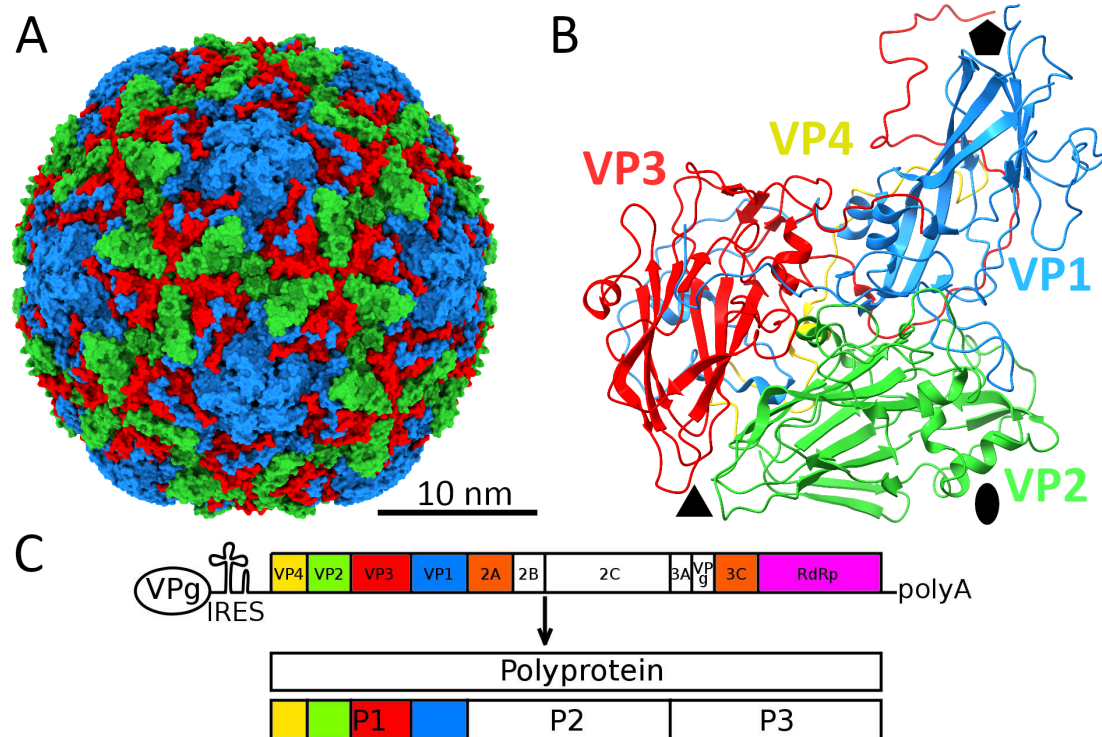


Fig. 1. Virion structure and genome organization of picornaviruses. (A) Capsid structure of human echovirus 18 in surface representation with VP1 subunits shown in blue, VP2 in green, and VP3 in red. The capsid proteins are labeled according to the homology-based convention for picornaviruses. (B) Structure of icosahedral asymmetric unit of human echovirus 18 in cartoon representation. Subunits are colored as in (A) and the VP4 subunit is shown in yellow. The positions of icosahedral symmetry axes are indicated by a pentagon for fivefold, triangle for threefold, and oval for twofold. (C) Diagram of picornavirus RNA genome with 5' end linked to protein VPg, 5' untranslated region containing internal ribosomal entry site, and 3' untranslated region ending with poly-adenine tail. The genome is translated into a single polyprotein. Intermediates of the polyprotein cleavage P1, P2, and P3 are shown. Capsid proteins VP4, VP2, VP3, and VP1 are shown in yellow, green, red, and blue, respectively.

Most picornaviruses that have been studied to date, which predominantly includes enteroviruses, enter cells by receptor-mediated endocytosis (18). The surfaces of enterovirus particles have depressions called “canyons”, which encircle the fivefold axes of icosahedral symmetry of their capsids (15). The canyons are the binding sites of receptors from the immunoglobulin family (19). Receptors with other types of protein fold bind to protrusions at the virion surface (5). Binding to receptors or exposure to acidic pH in endosomes induces the transformation of enterovirus virions to “activated” particles characterized by an increased size relative to the native virions, the formation of pores along twofold axes of symmetry of their capsids, externalization of N-termini of VP1, and the release of VP4 subunits (5, 20-24). The observed pores in enterovirus capsids were never of sufficient size to allow passage of the genome, and additional structural changes to the capsid are required for genome release (20-23, 25-29). Nevertheless, it has been demonstrated that the formation of activated particles is a prerequisite for genome release (5, 21, 28, 30). Small molecule inhibitors that bind into a hydrophobic pocket within the capsid protein VP1 prevent the formation of activated particles and block the genome release of enteroviruses (24, 31). However, the hydrophobic pocket is a specific feature of

enteroviruses and it has not been found in other picornaviruses and picorna-like viruses. The N-terminus of VP1 contains a predicted hydrophobic α -helix, whereas the VP4 of most enteroviruses is myristoylated (32, 33). Both VP1 and VP4 were shown to function in picornavirus genome delivery across membranes (33).

After cell entry, internal ribosomal entry sites initiate the translation of picornavirus genomes into polyproteins, which are cleaved to functional subunits by virus-encoded proteases (Fig. 1C, 2). Picornavirus non-structural proteins 2C and 2BC induce the reorganization of intracellular membranes into “virus replication factory”, compartments for viral RNA synthesis and particle assembly (Fig. 2) (34, 35). The genomes are replicated by virus-encoded RNA-dependent-RNA-polymerases. Newly synthesized enterovirus capsid proteins and genomes accumulate in the vicinity of the virus replication factories. The protomers of capsid proteins assemble into pentamers and empty particles (36). It has not been determined whether the empty particles are precursors of virions, dead end products, or serve as a storage state of the capsid proteins (37, 38). New virions are released after cell disruption due to the cytopathic effect (Fig. 2). However, it has been shown that a sub-population of particles of hepatitis A virus is released from cells in exosomes (39). This may enable the viruses to employ receptor-independent entry pathways and infect additional cell types.

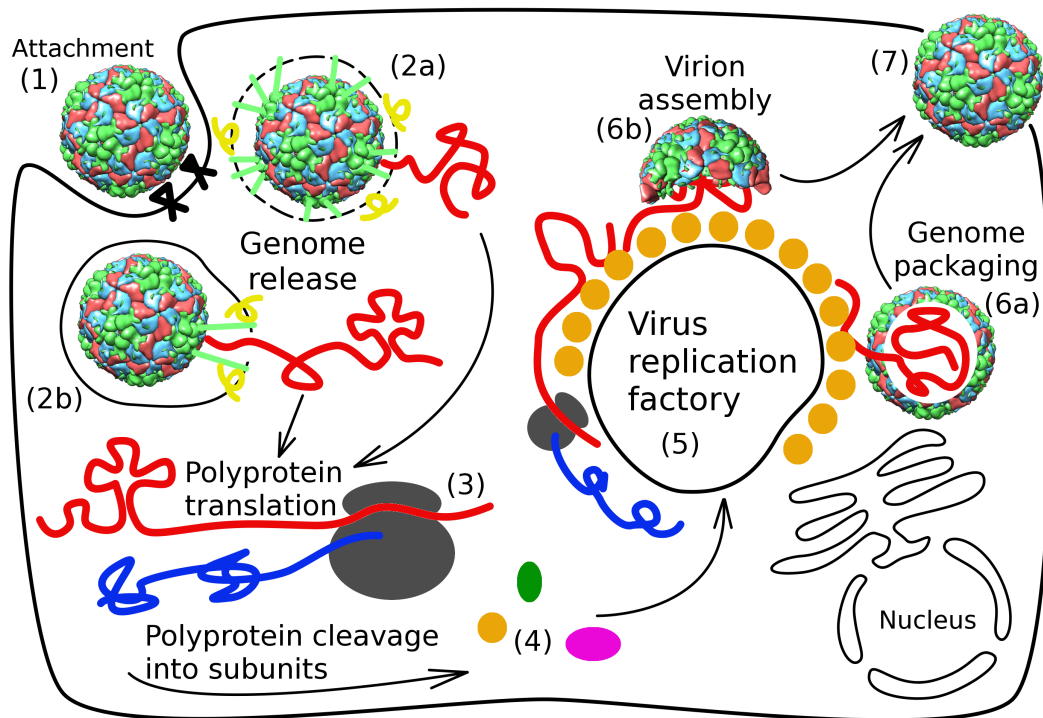


Fig. 2. Replication cycle of picornaviruses. Virus particles attach to receptor and are endocytosed (1). Two mechanisms for the escape of the virus genome from the endosome were proposed: VP4 (yellow) and N-termini of VP1 (green) externalized from particles either induce endosome disruption (2a) or form a transmembrane pore for genome (red ribbon) release (2b). The positive-sense single-stranded RNA genome is translated into polyprotein (blue ribbon) (3), which is cleaved into subunits (4). The translation is initiated by the internal ribosomal entry site in the 5' part of the genome. Viral proteins induce the formation of “virus replication factories” from internal cellular membranes and adapt the cell for the efficient production of virus progeny (5). Virus RNA-dependent-RNA-polymerases are shown as orange circles. Virions form either by the packaging of genomes into pre-formed capsids (6a) or by the assembly of particles around genomes (6b). Progeny virions are released after cell lysis (7).

2.4 Capsid protein naming conventions

There are two alternative conventions for naming the capsid proteins of picorna-like viruses. According to the molecular weight convention, the proteins are named from the largest subunit, VP1, to the smallest, VP4. Application of the molecular weight convention results in different protein orders within the polyprotein for various viruses, making cross-species comparison cumbersome. An alternative approach is to label the capsid proteins according to their positions in the icosahedral asymmetric unit of the virus capsid, which reflects the evolutionary relationships among the proteins of various viruses (Fig. 1) (16). To facilitate the structural comparisons, we use the homology-based convention throughout the thesis. The order of the major capsid proteins in the P1 polyprotein according to the homology-based convention is VP2, VP3, and VP1 (Fig. 1C).

2.5 Methods for studying virus structures

Knowledge of the high-resolution structures of virus particles and their assembly and genome release intermediates has played an important role in our understanding of virus infection. Furthermore, the structures of non-structural proteins and their complexes have helped to explain the processes required for virus replication in infected cells. Because of methodological limitations, most of the structural studies performed to date were limited to *in vitro* analyses of purified macromolecular samples.

2.5.1 X-ray crystallography

A traditional method for determining virus structures to high resolution is X-ray crystallography. This method relies on measuring the relative intensities of spots produced by the diffraction of an X-ray beam on a crystal. The measured intensities are then converted to structure factor amplitudes; however, the phase information is lost during data collection. In the structure determination of viruses, sufficient initial phase information can be obtained from molecular replacement models that are of limited resolution or structurally distinct from the crystallized virus, because the phases can be improved by non-crystallographic symmetry averaging (40-49). Phase extension can be employed to obtain phase information for high-resolution data (15, 43). A bottleneck in a structure determination using X-ray crystallography is the production of a sufficient amount of virus particles to identify crystallization conditions and to obtain crystals that diffract well.

There are specific challenges associated with virus crystallography. Virus crystals diffract weakly because of the large unit cell dimensions. Therefore, intense exposures to the X-ray beam are needed to collect data, and this in turn results in radiation damage to the crystals. Thus, the virus datasets require a careful approach during integration and scaling, and are frequently incomplete. This limited data completeness needs to be taken into account during molecular replacement and model building. The orientation of virus particles, needed for the molecular replacement, is usually determined by rotation or locked rotation functions that take advantage of the icosahedral symmetry of the capsid. Fortunately, the high symmetry of virus particles usually more than compensates for the incomplete data by allowing the non-crystallographic symmetry averaging of corresponding parts of the electron density map. However, current developments in cryo-EM and single-

particle reconstruction techniques enable a faster determination of virus structures with lesser demands on sample concentration, volume, heterogeneity, and purity than those needed for X-ray crystallography.

2.5.2 Cryo-electron microscopy

In the single-particle cryo-EM approach to determine macromolecular structures, a sample is deposited on a grid in a thin layer of aqueous solution and rapidly plunged into liquid ethane (50, 51). This results in the formation of vitreous ice with a structure similar to that of liquid water. Rapid cooling is required to prevent the formation of crystalline ice, which may damage cellular structures (50, 51). The rate of heat transfer limits the thickness of samples vitrified under ambient pressure to a few micrometers. Individual molecules or macromolecular complexes embedded in vitreous ice are photographed using a transmission electron microscope. The images are aligned and averaged to improve the signal to noise ratio of the observed particles. Classification is employed to improve the homogeneity of the images used for reconstruction. Subsequently, the projection images are used to reconstruct the three-dimensional structure of the studied macromolecule (52). Currently, high-resolution structures can only be routinely determined for proteins or macromolecular complexes that can be prepared with high purity and exhibit limited structural heterogeneity. These constraints limit the knowledge that can be gained from the resulting structures, because the complexes may exhibit different conformations *in vivo*. Determining the structures of macromolecular complexes *in situ* without the need to purify them from cells would avoid these experimental limitations. Such structural analyses are becoming practical thanks to improvements in sample preparation, correlative light and electron microscopy, focused ion beam milling, and software for data processing.

Pleomorphic objects, such as cells or irregular virus particles can be studied by cryo-electron tomography. In the cryo-electron tomography approach, samples are imaged from different directions by tilting the stage of the microscope. The resulting tilt series of images is used to calculate the three-dimensional reconstruction of the object (53, 54). For optimal imaging in a transmission electron microscope operated at 200 or 300 kV, samples should be thinner than 200 nm because of the limited penetration of electrons through biological samples (55, 56). Cells have to be thinned by cryo-sectioning or focused ion beam milling before imaging in a transmission electron microscope. The sensitivity of biological objects to an electron beam limits the overall dose that can be used to image one sample, resulting in a low signal to noise ratio in the reconstructed tomograms (56, 57). However, sub-tomogram averaging can be used to resolve the structures of regular components of the tomograms with improved contrast and resolution (58-62).

3 RESULTS AND DISCUSSION

3.1 Human cardioviruses, parechoviruses, and kobuviruses

Structural studies of cardioviruses, parechoviruses, and kobuviruses were motivated by the goal of comparing their virions and genome release mechanisms with those of enteroviruses and enable general aspects of picornavirus infection to be identified. Parechoviruses and kobuviruses differ from enteroviruses by lacking minor capsid proteins VP4 (63, 64). In enterovirus infections, the VP4 subunits are expelled from virions and interfere with endosome membranes to enable genome delivery (5). The polypeptides corresponding to VP4 are not cleaved from the N-termini of VP0 subunits that replace VP2 subunits in the virions of parechoviruses and kobuviruses.

While structures of virions of numerous enteroviruses have been determined, no structures were available for the genera *Parechovirus* and *Kobuvirus*. However, these two genera include viruses that cause enteric and neurological diseases in newborns and immunosuppressed individuals (7-9). We used X-ray crystallography and cryo-EM to determine the virion structures of human parechovirus 1 and kobuvirus aichi virus 1. Cardioviruses differ from enteroviruses by lacking the canyon depressions at the surface of their particles and in the receptor molecules that they utilize for cell entry (65-68). It could be expected that they also differ in some aspects of genome release. The molecular-level description of picornavirus virions and of processes connected to their cell entry not only answers open questions in picornavirus biology, but also identifies new targets for anti-viral therapeutics.

3.1.1 Virion structure of human parechovirus 1 (paper I)

Parechoviruses usually cause mild gastrointestinal diseases in newborns and young children (69-72). Occasionally, parechovirus infections develop into serious illnesses, including pneumonia or encephalitis (73-75). After their discovery (76, 77), parechoviruses were grouped with enteroviruses. Subsequently, the separate genus *Parechovirus* was established due to the differences in their genome sequences to those of enteroviruses (78-80).

We used X-ray crystallography to determine the structure of a virion of human parechovirus 1 to a resolution of 3.1 Å. Unlike the capsids of most picornaviruses, that of parechovirus 1 is formed by three types of subunits: VP0, VP1, and VP3. Interactions among pentamers of capsid protein protomers in human parechovirus 1 are mediated by the N-termini of VP0 subunits, which correspond to the capsid protein VP4 of enteroviruses and the N-terminal part of the capsid protein VP2 of other picornaviruses. A hydrophobic pocket in the VP1 subunit, which can be targeted by capsid-binding antiviral compounds in enteroviruses, is not present in human parechovirus 1.

The virion of human parechovirus 1 contains an electron density corresponding to an RNA hexanucleotide associated with each icosahedral asymmetric unit close to the fivefold symmetry axes of the capsid (Fig. 3). A crystallographic refinement resulted in 94% occupancy of the RNA, showing that the linear single-stranded RNA genome of human parechovirus 1 forms close to sixty unique interactions with the inner surface of the capsid. Overall, the sixty copies of the ordered hexanucleotides represent 5% of the 7,500-nucleotide genome. The RNA did not affect the packing of particles within the crystal, and therefore the diffraction data contains information about the icosahedrally averaged RNA structure. Thus, the observed RNA density corresponds to an averaged nucleotide sequence. The shapes of the electron densities of the individual bases indicate that the first nucleotide is a purine, whereas the following five nucleotides are pyrimidines (Fig. 3B). Each RNA hexanucleotide forms extensive interactions with one VP1 and three VP3 subunits belonging to different protomers from one pentamer. The residues involved in RNA binding are conserved among all parechoviruses, suggesting a putative role of the genome in virion stability or assembly. Therefore, putative small molecules that could disrupt parechovirus RNA-capsid protein interactions may be developed into antiviral inhibitors. Icosahedrally ordered RNA with a similar structure was also observed in virions of human parechovirus 3 and Ljungan virus (81, 82). It was subsequently speculated by Shakeel et al. that the RNA sequences interacting with the capsid may constitute packaging signals (83).

Seitsonen et al. have shown that the receptor-binding site of human parechovirus 1 is located in between the fivefold and threefold symmetry axes of the capsid (84). Our structure of human parechovirus 1 determined that the RGD motif responsible for the integrin recognition is located at the corresponding position, but it is not structured.

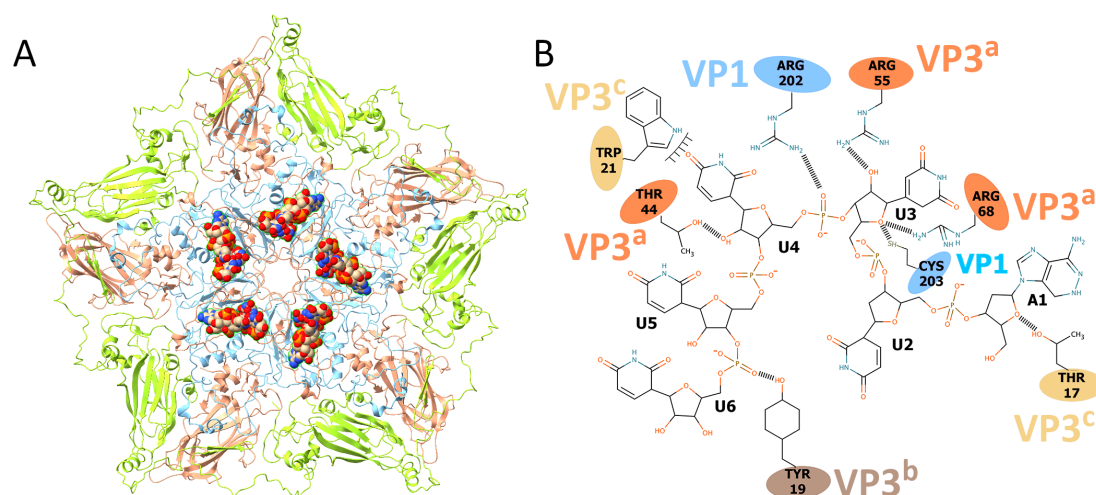


Fig. 3. Interaction of parechovirus genomic RNA with capsid. (A) Location of RNA hexanucleotides, shown as space-filling spheres colored according to element, within a capsid protein pentamer as seen from the inside of the virion. Capsid proteins are shown in cartoon representation with VP1 in blue, VP2 in green, and VP3 in red. (B) Two-dimensional representation of RNA-protein contacts. Hydrophobic interactions and hydrogen bonds are shown. VP3 subunits from different icosahedral asymmetric units are distinguished by the label shades and superscripts A, B, and C.

3.1.2 Structure and genome release of aichi virus 1 (paper II)

Aichi virus 1 is a human pathogen from the genus *Kobuvirus* of the family *Picornaviridae*. In environmental virus screening, aichi virus 1 is detected more frequently and in greater

abundance than other human enteric viruses (85-91). Accordingly, 70-95% of adults worldwide have antibodies against aichi virus 1 (89, 91, 92). Infections of aichi virus 1 are often asymptomatic, but it can cause diarrhea, nausea, vomiting, and fever (85, 91).

Unlike most picornaviruses, but similar to parechoviruses, kobuvirus capsids are composed of three types of subunits: VP0, VP1, and VP3. We determined the structure of the virion of aichi virus 1 to a resolution of 2.1 Å using X-ray crystallography. The structure did not confirm the presence of the previously proposed astrovirus-like protrusions at the surface of the aichi virus 1 virion (85, 93). Instead, the capsid of aichi virus 1 has plateaus around threefold axes, depressions at twofold axes, and protrusions at icosahedral fivefold axes that are encircled by circular depressions that we, according to the enterovirus convention, called canyons. However, the canyon of aichi virus 1 is formed by a distinct part of the capsid proteins and has a different shape to that of enteroviruses. It was pointed out by Zhu et al. that aichi virus 1 capsid includes a polyproline helix formed by the C-terminus of VP1 (94). The polyproline helix is positioned in an area where integrin binding motifs are found in some other picornaviruses (94). Peptides with polyproline sequences derived from that of the C-terminus of VP1 decrease the infectivity of aichi virus 1 to 50%, possibly by blocking attachment of the virus to an as-yet-unknown receptor (94).

Electron micrographs of virions of aichi virus 1 heated to 53°C for 10 minutes contained 95% of empty capsids, which were used to reconstruct the structure of the empty particle to a resolution of 4.2 Å. The empty capsid is expanded by 8 Å in diameter relative to the native virus, and the inner volume of the capsid cavity increases from 4.8×10^6 Å³ to 5.5×10^6 Å³. Major differences between the structures of the native virions and empty particles are in the contacts between the pentamers of capsid protein protomers. In the native virion of aichi virus 1, the inter-pentamer contacts are mediated by strand β2 from the N-terminus of VP0, which interacts with β-strand F from subunit VP3. Strands β1 and β2 of VP0 extend the β-sheet CHEF of VP3. In contrast, in the empty particle, the β1 and β2 strands of VP0 are not formed. Thus, the inter-pentamer interface is reduced from 2,750 to 1,400 Å². Nevertheless, residues 55 to 60 of VP0 became structured in the empty particle of aichi virus 1, indicating that the N-terminal arm of VP0 does not externalize from the empty particle. This is in contrast to the assumption that the N-terminal part of aichi virus 1 VP0 is functionally homologous to the VP4 of other picornaviruses and might play a role in the transport of the virus genome across the endosomal membrane into the host cytoplasm (33).

The empty particles of aichi virus 1 are stable, at least *in vitro*, and do not contain pores that might serve as channels for genome release. Therefore, extensive and probably reversible local re-organization of the capsid of aichi virus 1 is required for its genome release. The mechanism of genome release involving the loss of pentamers of capsid protein protomers, as described for enteroviruses in chapter 3.4, would enable the genome release and externalization of the N-termini of VP0 subunits through openings formed by the removal of pentamers of capsid protein protomers.

In contrast to aichi virus 1, empty particles of parechovirus 1 rapidly dissociate into pentamers after the genome release (81, 95). Major differences between aichi virus 1 and parechovirus 1 are in the inter-pentamer interactions mediated by the N-terminal arms of VP0 subunits. Whereas in aichi virus 1 the strands β1 and β2 extend the β-sheet CHEF of VP3 from the icosahedral asymmetric unit from a neighboring pentamer; in parechovirus 1 the N-terminal arm forms a loop that stretches around the icosahedral twofold axis and the β-

strands extend the β -sheet of the VP3 subunit from the same pentamer. The differences in the positioning of the N-terminal arms of VP0 subunits may influence the stability of the empty capsids, since enteroviruses, which produce stable empty particles after genome release, have the same type of inter-pentamer interaction mediated by the N-terminus of VP2 as that of aichi virus 1 (5, 15, 17).

The N-terminal arm of aichi virus 1 VP1 undergoes structural reorganization upon the formation of the empty particle. Residues 1-30 become disordered, and residues 31-35 refold into a new structure with the last resolved residue pointing toward the particle center. This is in contrast to the previous observation of the activated particle of coxsackievirus A16, in which the N-terminus of VP1 was exposed at the capsid surface (20).

3.1.3 Structure and genome release of saffold virus 3 (paper III)

Saffold virus 3 belongs to the genus *Cardiovirus* from the family *Picornaviridae* (96, 97). It was isolated from the cerebrospinal fluid of a patient with aseptic meningitis (98, 99). To date, more than 11 genotypes of saffold viruses have been identified (100-103). The structures of Mengo virus and Theiler's murine encephalomyelitis virus have shown that cardiovirus particles lack canyons and pocket factors (104, 105). Cardioviruses differ from enteroviruses in the details of their capsid structures and in the receptor molecules they utilize for cell entry.

We determined the structure of a native virion of saffold virus 3 to a resolution of 2.5 Å using X-ray crystallography. In addition, we used cryo-EM to determine an 11-Å-resolution cryo-EM reconstruction of an activated particle of saffold virus 3 that is primed for genome release. The CD loop of the VP3 subunit of saffold virus 3 contains a disulfide bond connecting cysteines separated by just one residue. A similar disulfide bond has also been observed in Mengo virus (104). Disruption of the bond in saffold virus 3 had a minimal effect on the structure of the surface-exposed CD loop, but it increased the stability and decreased the infectivity of the virus. Therefore, compounds specifically disrupting or binding to the disulfide bond may function as inhibitors of cardiovirus infection.

The formation of activated particles of saffold virus 3 can be induced by heating the virions to 42°C for two minutes. In addition to the activated particles, the sample also contained 1% of empty capsids. However, if the virions of saffold virus 3 were left at room temperature for more than five minutes after heating, the sample contained only pentamers of capsid protein protomers. This verifies the previous suggestion that cardiovirus virions disassemble upon or shortly after genome release (106-108). The activated particle of saffold virus 3 is expanded 4% in diameter compared to the virion, and has pores located approximately in the middle between the fivefold and threefold icosahedral symmetry axes. The pores are circular in shape with a diameter of 15 Å. The opening of the pores is enabled by shifts of the VP1 subunits toward the icosahedral fivefold axes and of VP3 subunits toward the threefold axes relative to their positions in the native virus. The changes in subunit positions are possible due to the radial expansion of the capsid. Parts of the VP1 and VP3 subunits forming edges of the pores became flexible, indicating the possibility of additional expansion of the pores.

The activated particles of picornaviruses are not only primed for genome release but also facilitate the transport of the genomes across biological membranes. A difference map calculated by subtracting the electron density map of the activated particle of saffold virus 3

from that of the native virion indicates that VP4 is missing from the activated particles. The last ordered residues of the VP4 in native particles of scaffold virus 3 are located immediately below the pore in the activated particle. The VP4 subunits are thus optimally positioned for release from the activated particles. Besides the release of VP4, the pores may also enable externalization of the N-termini of VP1 subunits.

3.2 Dicistroviruses infecting honeybees

The genomes of dicistroviruses include two open reading frames, which encode polyproteins containing non-structural and capsid-forming subunits, respectively. The family *Dicistroviridae* includes the genera *Aparavirus*, *Cripavirus*, and *Triatovirus*. The structures of cricket paralysis virus and triatoma virus have been structurally characterized previously (109-112). It is assumed that protomers of dicistrovirus capsid proteins assemble into pentamers and then associate with the RNA genome to form immature virions (113-116). The cleavage of VP0 into subunits VP4 and VP3 is required for the formation of the mature infectious virions (111, 112). This is in contrast to most picornaviruses, in which the VP4 proteins are cleaved from the N-termini of VP2 subunits (5). Tate et al. speculated that an Asp-Asp-Phe motif, which is part of the VP1 subunit and conserved among dicistroviruses, is involved in the VP0 cleavage (111, 112, 117-119). The VP4 subunits of dicistroviruses are 51 to 75 residues long (110-112). Whereas virions of cricket paralysis virus contain structured VP4 subunits attached to the inner faces of their capsids (110, 111), virions of triatoma virus contain VP4 subunits but are not attached to the capsids (112).

3.2.1 Israeli acute bee paralysis virus (paper IV)

Israeli acute bee paralysis virus, Kashmir bee virus, and acute bee paralysis virus constitute a group of closely related viruses that are distributed worldwide (120). Israeli acute bee paralysis virus has been linked with colony collapse disorder in the United States (121), whereas acute bee paralysis virus has been associated with similar rapid bee depopulation phenomena in Europe (120, 122).

We determined the virion structure of Israeli acute bee paralysis virus to a resolution of 4.0 Å and the structure of a pentamer of capsid protein protomers at a resolution of 2.7 Å using X-ray crystallography. Israeli acute bee paralysis virus represents the first structurally characterized member of the genus *Aparavirus*. Its virion is spherical, with plateaus around the icosahedral fivefold and threefold axes. There are depressions at the capsid surface around the icosahedral twofold axes similar to those previously identified in triatoma virus (112). In contrast, in cricket paralysis virus, the depressions are partly filled with residues from the C-termini of VP2 subunits (110, 111). Israeli acute bee paralysis virus has major capsid proteins VP1 and VP3 with non-canonical jellyroll β-sandwich folds composed of only seven instead of eight β-strands, as is the rule for capsid proteins of other viruses. β-strand C from VP1 of Israeli acute bee paralysis virus is replaced by a loop and an α-helix (Fig. 4A). β-strand C in VP3 is replaced by an elongated loop that forms the capsid surface (Fig. 4B). Israeli acute bee paralysis virus contains the Asp-Asp-Phe sequence in VP1, formed by residues 186 to 188, located close to the N-terminus of the VP3 subunit and the

C-terminus of subunit VP4 from the neighboring protomer, indicating that it may catalyze the cleavage of VP0.

The most prominent features of the virion of Israeli acute bee paralysis virus are spikes located between the icosahedral fivefold and threefold axes of symmetry that rise 20 Å above the virion surface. The spikes are formed by antiparallel β-strands from the CD loop and C-terminus of VP3 and a C-terminal β-strand of VP1 (Fig. 4).

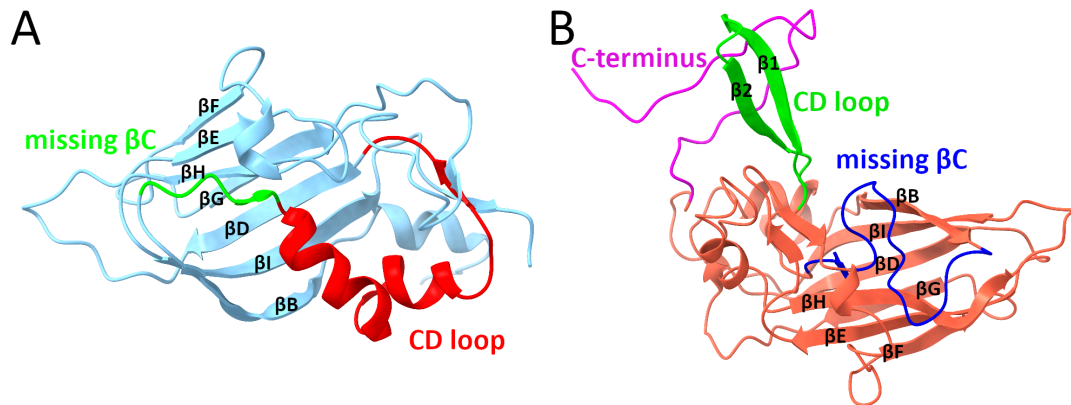


Fig. 4. Structures of subunits VP1 and VP3 of Israeli acute bee paralysis virus. (A) VP1 of Israeli acute bee paralysis virus contains a loop and α-helix highlighted in green and red, respectively, that replace β-strand C. (B) The VP3 subunit of Israeli acute bee paralysis virus lacks β-strand C, which is replaced by the loop highlighted in blue. Strands β1 and β2 in the CD loop, shown in green, and the C-terminus, highlighted in magenta, form the most prominent surface feature of the virion.

3.2.2 Inclusion of VP4 in dicistrovirus virions (papers IV and V)

The relative positioning of the Asp-Asp-Phe motif in Israeli acute bee paralysis virus and the C-terminus of VP4 and N-terminus of VP3 indicates that the formation of pentamers is sufficient to achieve the optimal spatial arrangement of the catalytic center and substrate for the cleavage of the precursor protein VP0. This poses a potential problem during the assembly of infectious particles, because the VP0 may be cleaved and the resulting VP4 subunits may detach from pentamers before their assembly into virions. Virions formed from pentamers lacking VP4 subunits would be non-infectious, because VP4 subunits are required for the delivery of genomes into the cytoplasm. However, there is evidence that dicistroviruses employ a mechanism preventing the incorporation of pentamers which lack VP4 subunits into virions (123). Agirre et al. proposed that pentamers of protomers of capsid proteins of triatoma virus lacking VP4 subunits form dimers of pentamers that cannot be incorporated into virions (123). Analogous particles co-purified with virions of Israeli acute bee paralysis virus. Furthermore, the dimer of pentamers is the building block of one of the crystal forms obtained from the crystallization of virions of Israeli acute bee paralysis virus. Pentamers in this crystal form lacked a resolved density for VP4. It is unlikely to be a coincidence that the capsid proteins of Israeli acute bee paralysis and triatoma viruses, which share only 22% sequence identity, are capable of forming similar dimers of pentamers. Therefore, we support the speculation by Agirre et al. that the formation of dimers of pentamers may be a mechanism that prevents the assembly of aberrant capsids lacking VP4.

3.2.3 Genome release of Israeli acute bee virus (paper V)

Virions of Israeli acute bee paralysis virus can be induced to release their genomes by heating to 63°C. The heated sample contained a mixture of full and empty particles, the structures of which were determined to resolutions of 3.3 Å and 3.9 Å, respectively. The heated genome-containing and empty particles resulting from genome release were not expanded. The structural changes observed in the empty particles of Israeli acute bee paralysis virus relative to native virions include detachment of the VP4 subunits from the inner face of the capsid and partial loss of the structure of the N-terminal arms of the VP2 capsid proteins. There are no pores in the capsids of empty particles of Israeli acute bee paralysis virus that could serve for genome release. Therefore, rearrangement of a unique region of the capsid is probably required for genome release. It was speculated that a partial capsid cracking or disassembly is required for triatoma virus RNA externalization, because there are no obvious pores for RNA egress (123). This is consistent with our current studies of enterovirus genome release, which are discussed in detail in chapter 3.4.

The N-termini of VP1 subunits, which become exposed at the surface of activated particles of enteroviruses, together with VP4 subunits enable the transport of virus genomes into the cell cytoplasm (33, 124, 125). In contrast, the N-termini of VP1 subunits are fully resolved on the inside of full and empty particles of Israeli acute bee paralysis virus primed for genome release. A pore at the base of the canyon, which was shown to be the site of externalization of N-termini of VP1 subunits of coxsackievirus 16 (22, 25), is not formed in the empty particles of Israeli acute bee paralysis virus. Therefore, the mechanism by which Israeli acute bee paralysis virus delivers its genome across the biological membrane is probably distinct from that of enteroviruses.

3.2.4 Black queen cell virus (paper VI)

Black queen cell virus persists chronically and mostly asymptotically in bee colonies through social transmission among adults and through vertical transmission from the queen to her offspring (126-129). At elevated titers, black queen cell virus kills developing queen larvae, whose necrotic remains stain their wax cells black (130, 131). The disease is of concern for the honeybee queen-rearing industry (132, 133). The host range of black queen cell virus includes many *Apis* species, as well as several bumblebees (134).

The structure of the virion of black queen cell virus has been determined to a resolution of 3.4 Å using X-ray crystallography. The native virion of black queen cell virus lacks a resolved density corresponding to 75-residue-long VP4 subunits. Nevertheless, mass spectrometry indicated that the VP4 subunits are present in the crystallized virions, which were infectious. The C-terminus of the VP1 and CD loops of capsid proteins VP1 and VP3 of black queen cell virus form 34 Å-tall finger-like protrusions at the virion surface, which are the largest of the dicistroviruses structurally characterized to date. The homologous finger-like protrusions of triatoma virus were proposed to enable the virus to bind a cell entry receptor (112).

3.3 I flaviruses infecting honeybees

The majority of the iflaviruses identified to date infect insects, and several of those, such as

slow bee paralysis virus, deformed wing virus, and sacbrood virus, are pathogens of honeybees. Prior to our studies, there was limited information about the structures of iflaviruses. A cryo-EM structure of Chinese sacbrood virus had been determined to a resolution of 25 Å, which demonstrated that the particles have a diameter of 30 nm and a smooth surface (135). The genome sequences of iflaviruses provide evidence that their VP4 subunits, which are only about twenty residues long, are cleaved from the N-termini of VP3 (136, 137).

3.3.1 Virion structure of slow bee paralysis virus (paper VII)

Slow bee paralysis virus was discovered in 1974 (138) and was linked to honeybee colony mortality in the United Kingdom in the 1980s (139). Despite its efficient transmission by *Varroa destructor*, it is a rare disease of honeybees (137, 140).

The structure of slow bee paralysis virus was determined from two crystal forms to resolutions of 2.6 Å and 3.4 Å. Unlike in the previously structurally characterized viruses from the order *Picornavirales*, the capsid protein VP3 of slow bee paralysis virus contains a C-terminal extension of residues 267 to 430 that folds into the globular protruding domain positioned at the capsid surface (Fig. 5). The domain consists of a central twisted antiparallel β -sheet formed from strands β 4, β 5, and β 6 surrounded by the fourteen-residue-long α -helix α 1, three-residue-long 3.10 helix, and two shorter β -sheets containing strands β 1 – β 2 and β 3 – β 7. The β -strands are connected by loops that vary in length between six and twenty-three residues.

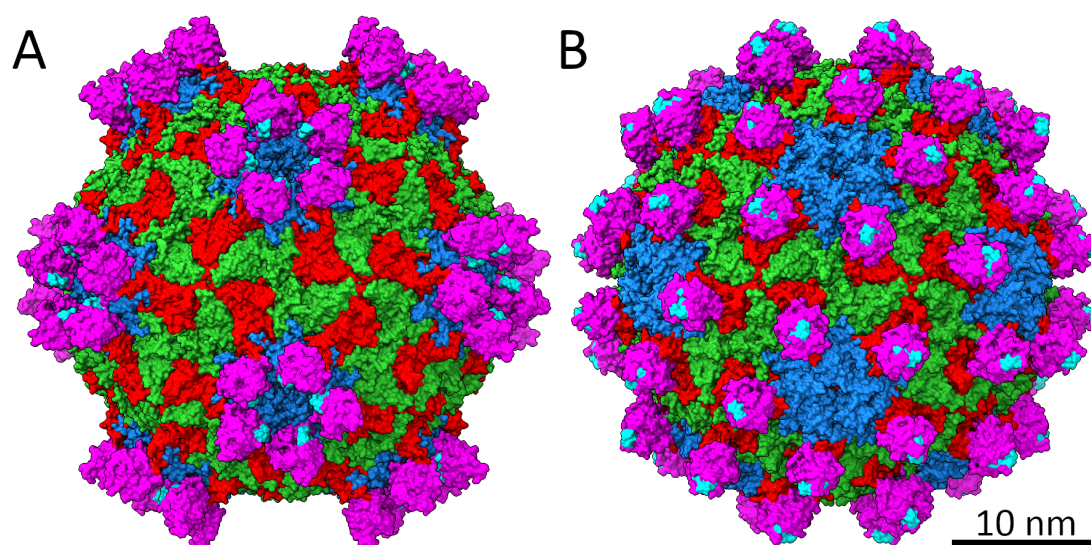


Fig. 5. Virion structures of slow bee paralysis virus highlighting the alternative positioning of protruding domains in crown-like (A) and open (B) conformations. VP1 subunits are shown in blue, VP2 in green, and VP3 in red. The protruding domains of VP3 are highlighted in magenta and the putative active sites in cyan.

The protruding domains of five VP3 subunits form a “crown” at the virion surface around each fivefold axis in one of the crystal forms (Fig. 5A). However, the protruding domains are shifted 36 Å toward the threefold axes in the other crystal form (Fig. 5B). The differences in the positioning of protruding domains were caused by the distinct crystallization conditions that differed in their pH and salt concentrations. Residues Ser284, His283, and Asp300 from the protruding domain are located close to each other in a

characteristic arrangement for a triad catalyzing a hydrolytic reaction (Fig. 6A) (141). This type of active site has been previously identified in proteases, lipases, and esterases (141-143). The distances between the side chains of the putative active site are larger than ideal for catalyzing the hydrolytic reaction (141) but it is possible that the optimal configuration of the active site might be achieved upon binding an as-yet-unknown substrate. The residues constituting the putative active site are conserved among other iflaviruses that have protruding domains (136, 144, 145). The putative active sites face the interior of the crown; however, they constitute the apex of the protruding domain in the crystal form with protruding domains shifted towards threefold axes (Fig. 5). The movements of the protruding domains may be required for efficient substrate cleavage or receptor binding during virus cell entry.

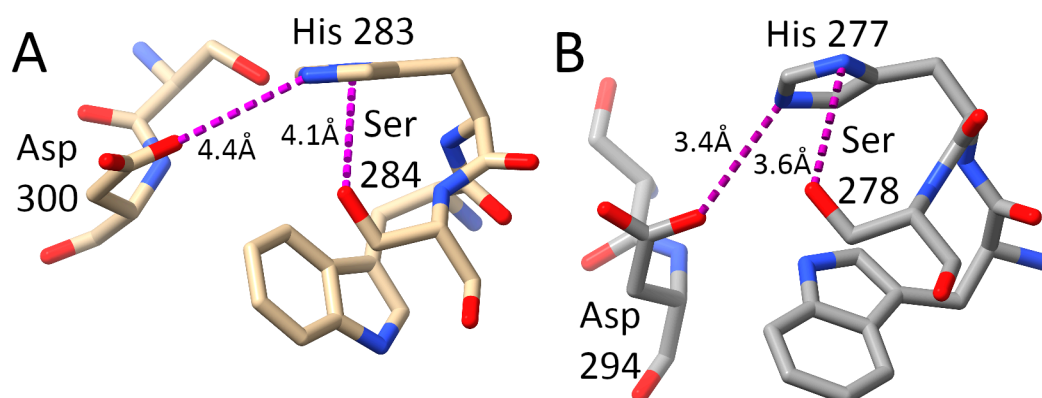


Fig. 6. Structure of putative Asp-His-Ser hydrolase sites in protruding domains of slow bee paralysis virus (A) and deformed wing virus (B). The residues are displayed in stick representation. Distances between the side chains constituting the putative catalytic triad are shown as magenta dashed lines.

3.3.2 Genome release of slow bee paralysis virus (paper VIII)

The exposure of slow bee paralysis virus and other picorna-like viruses to acidic pH 5 induces a release of the RNA genome from the virions (146-148). The induction of genome release under acidic conditions implies that slow bee paralysis virus uses endosomes for cell entry (149). We determined the structures of slow bee paralysis virus before and after genome release to resolutions of 3.3 and 3.4 Å, respectively. The capsids of genome-containing particles of slow bee paralysis virus in acidic pH are not expanded. The egress of genomes from virions of slow bee paralysis virus is associated with a reduction in inter-pentamer contacts mediated by the N-terminal arms of VP2 subunits, which cause an expansion of the empty capsid. However, the comparison of capsid structures before and after the genome release did not provide any clear indication as to how the RNA genome escapes from the particles.

3.3.3 Structure of deformed wing virus (paper IX)

Symptoms of acute infections by deformed wing virus include deformed wings, aggressive behavior, the death of pupae and adult bees, and colony collapse (150, 151). Furthermore, winter colony mortality is strongly correlated with the presence of deformed wing virus (151, 152). The deformed wing virus-induced loss of honeybees has become a serious threat

to the adequate provision of pollination services, threatening food security and ecosystem stability in Europe and Northern America (153).

The virion structures of deformed wing virus were determined to resolutions of 3.1 Å using cryo-EM and 3.8 Å by X-ray crystallography. Similar to that of slow bee paralysis virus, the C-terminal extension of the VP3 subunit of deformed wing virus folds into a globular protruding domain, which contains a putative Asp-His-Ser hydrolase triad. A nucleotide of the RNA genome of deformed wing virus interacts with each of the sixty VP3 subunits within the capsid. The capsid protein residues involved in the RNA binding are conserved among honeybee iflaviruses, suggesting a putative role of the genome in stabilizing the virion or facilitating capsid assembly. Identifying the RNA-binding and putative catalytic sites within the deformed wing virus virion structure enables future analyses of how deformed wing virus and other iflaviruses infect insect cells and also opens up possibilities for the development of antiviral treatments.

The structure of deformed wing virus and its empty particles has been independently determined by Organtini et al. (154). The authors speculated that the open conformation of protruding domains is characteristic for the pro-capsid and native virions, whereas the putative activated particles and empty capsids, which had released their genomes, had the protruding domains in a closed crown conformation. The authors concluded that the genome may escape from particles of deformed wing virus through a channel formed by the protruding domains at a fivefold vertex.

3.3.4 Genome delivery of sacbrood virus (paper X)

Symptoms of the sacbrood virus infection of pupae include the accumulation of ecdysial fluid, cuticle discoloration, and death, resulting in a typical gondola-shaped dry cadaver (155). Although sacbrood virus is lethal for larvae, infected colonies rarely collapse, and thus sacbrood virus poses a limited threat to honeybees (155).

The crystal structure of sacbrood virus has been determined to a resolution of 2.1 Å. In contrast to other viruses from the order *Picornavirales* that have been structurally characterized to date, the virion of sacbrood virus contains sixty copies of a “minor capsid protein” attached at the capsid surface (Fig. 7A). The minor capsid protein is positioned equidistant from the icosahedral twofold, threefold, and fivefold symmetry axes of the capsid (Fig. 7B). The structure of the minor capsid protein could be built for residues 22–47 out of 48. The structured residues form a loop that turns 360° on itself. The minor capsid protein binds to the capsid through an interface with a buried surface area of 1,100 Å² formed by twenty-four residues of VP2, seven residues of VP1, and six residues of VP3. An occupancy refinement showed that minor capsid protein peptides are present in all sixty positions at the virion surface.

The amino acid sequence of the minor capsid protein is located between the C-terminus of VP3 and the N-terminus of VP1 in the polypeptide (Fig. 7C). Mass spectrometry determined the protein cleavage sites that separate the minor capsid protein from VP3 and VP1 to be Ser708 / Arg709 Arg710 and Gln756 / Met757 Asp758, which is in agreement with the previously characterized target sequences for picornavirus-like proteases (156-158). The location of the coding sequence of minor capsid protein within the sacbrood virus genome indicates that it evolved from a C-terminal extension of a major capsid protein VP3 by the introduction of a cleavage site for a virus protease.

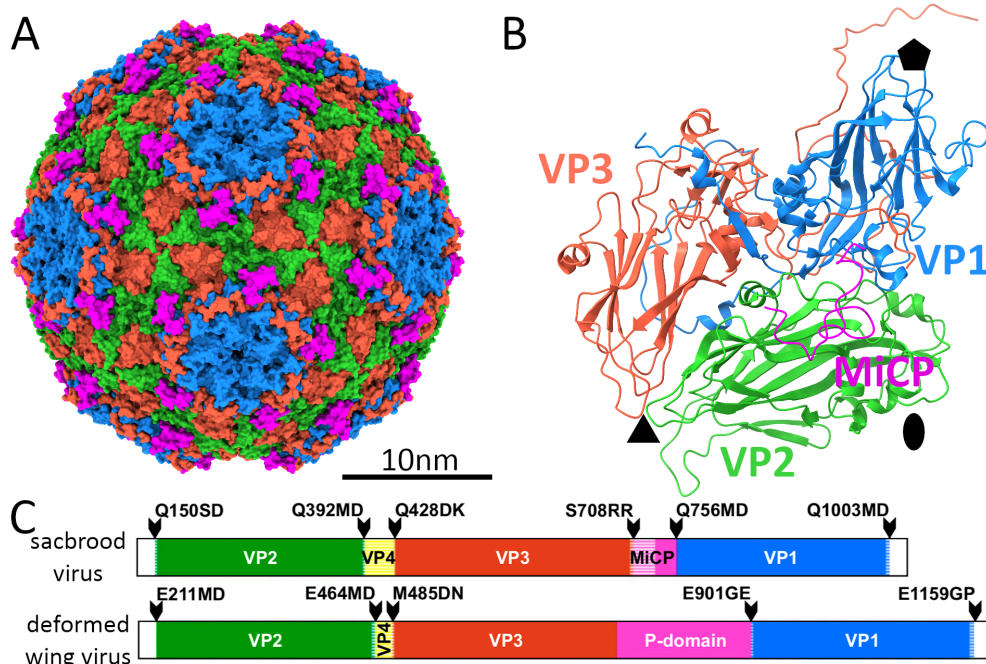


Fig. 7. Virion structure of sacbrood virus and comparison of P1 polyproteins of sacbrood and deformed wing viruses. (A) Capsid structure of sacbrood virus in surface representation with VP1 subunits shown in blue, VP2 in green, VP3 in red, and minor capsid protein in magenta. (B) Structure of icosahedral asymmetric unit of sacbrood virus in cartoon representation. Subunits are colored as in (A). Positions of icosahedral symmetry axes are indicated by a pentagon for fivefold, triangle for threefold, and oval for twofold. (C) Organization of the P1 polyproteins of iflaviruses sacbrood virus and deformed wing virus. Capsid proteins are labeled and colored according to the homology convention for picornaviruses: VP1 in blue, VP2 in green, VP3 in red, and VP4 in yellow. The minor capsid protein of sacbrood virus and protruding domain of deformed wing virus are shown in magenta. Arrowheads indicate the positions of protease cleavage sites, and the target cleavage sequences are shown. Parts of the proteins resolved in experimentally determined structures are shown in bright colors; the parts that are not structured are highlighted with hatching.

The exposure of sacbrood virus to acidic pH, which the virus may encounter during cell entry, induces the formation of pores at threefold and fivefold axes of the capsid that are 7 Å and 12 Å in diameter, respectively. Sacbrood virus encodes a 36-residue-long VP4 subunit; however, the electron density map of the virion does not contain resolved features that could be interpreted as residues of VP4. Furthermore, VP4 was not detected in virions of sacbrood virus by mass spectrometry. The minor capsid protein of sacbrood virus induces liposome disruption *in vitro*, indicating that it may be a functional analog of VP4 and enable the virus genome to escape across the endosome membrane into the cell cytoplasm.

Another function of the minor capsid protein of sacbrood virus may be in receptor binding. The volume at the surface of the sacbrood virus virion occupied by the minor capsid protein is taken up by the EF loop known as the “puff” loop from the VP2 subunit in enteroviruses (15, 17). Residues from the puff of many enteroviruses participate in receptor binding (24), and it is possible that the minor capsid protein has the same function.

3.3.5 Evolution of iflaviruses (papers VII-X)

Structural analyses and a comparison of the genome sequences of iflaviruses indicate that the family contains two groups of viruses distinguished by the presence or absence of protruding domains. There are no structural or sequence similarities between the 48-

residue-long minor capsid protein of sacbrood virus and the 160-residue-long protruding domains of slow bee paralysis virus and deformed wing virus. Nevertheless, the locations of the sequences coding the minor capsid protein and protruding domains in iflavirus genomes show that both of them evolved as C-terminal extensions of VP3 subunits (Fig. 7C). The phylogenetic tree based on a comparison of the sequences of iflavirus P1 polyproteins shows that the protruding domain is probably a filial feature (Fig. 8).

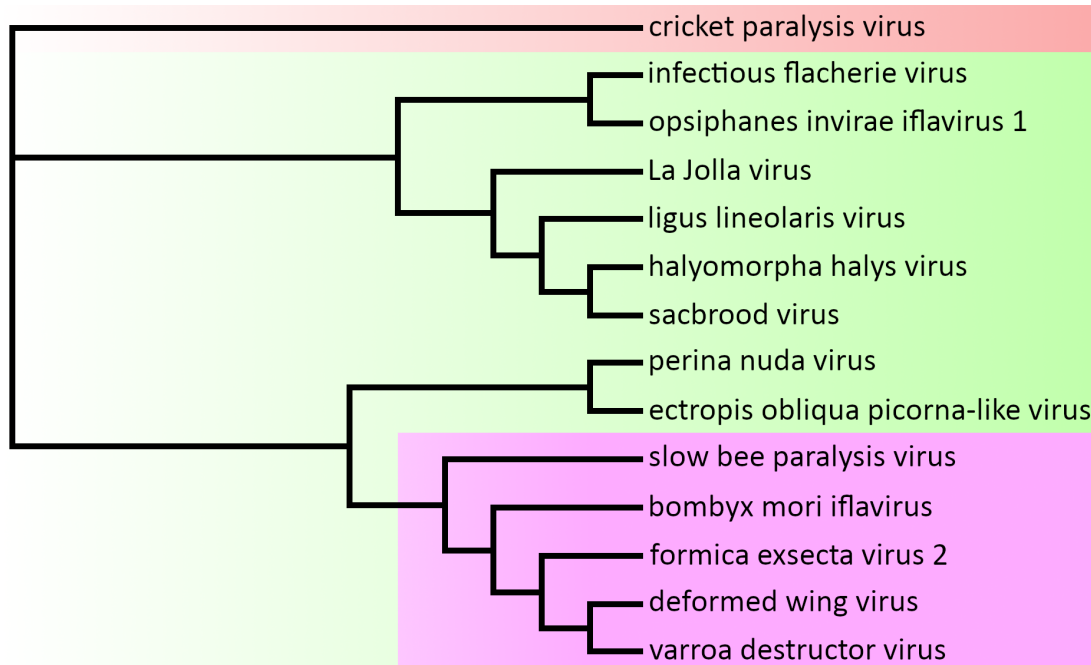


Fig. 8. Cladogram of iflaviruses based on sequences of their capsid proteins. The maximum likelihood tree was constructed from the P1 polyprotein sequences of selected iflaviruses with dicistrovirus cricket paralysis virus as an outgroup. Iflaviruses with protruding domains are highlighted with the magenta background.

3.4 Genome release mechanism of enteroviruses

The interactions of enteroviruses with receptors or exposure to acidic pH in endosomes induce conformational changes of the virions into activated particles characterized by an increased diameter, reduced contacts between the pentamers of capsid protein protomers, the release of VP4 subunits from particles, and externalization of the N-termini of VP1 subunits (5, 20-23, 159). It has been speculated that pores along twofold ($5 \times 10 \text{ \AA}$) and fivefold (diameters of up to 8 \AA) axes of icosahedral symmetry of capsids of activated particles of enteroviruses serve for the release of enterovirus genomes (20-23, 25, 30, 160, 161). However, the capsids of viruses from the families *Reoviridae* and *Totiviridae*, which release single-stranded RNA through pores in their capsids, provide evidence that the pores have to be larger than 15 \AA in diameter (162, 163). Furthermore, enterovirus genomes contain sequences that form double-stranded RNA segments, which fold into three-dimensional structures, such as the internal ribosomal entry site (164). If the double-stranded RNA segments were present in enterovirus particles, the genome release would require either opening pores larger than 40 \AA in diameter, or a mechanism to unwind the double-stranded RNA segments. However, there is no evidence that enterovirus virions contain enzymes with RNA helicase activity (5). The structures of enterovirus particles before and after genome release have been characterized at high resolution (21, 25-29).

However, most of these cryo-EM and X-ray crystallography studies imposed icosahedral symmetry during the structure determination process and were not aimed at identifying the unique sites of RNA exit (21-23, 25, 26, 28). Asymmetric single-particle reconstruction and sub-tomogram averaging studies were used to indicate that RNA exits the poliovirus particle close to a twofold axis (27). However, the uncoating of poliovirus was induced by heating the particles to 56°C, which may have affected the secondary structure of the genome and the nature of its release. The end products of the enterovirus genome release are the empty capsids (22, 23).

3.4.1 Capsid cracking enables genome release (paper XI)

We used cryo-EM to image particles of echovirus 18 exposed to conditions mimicking the acidic environment that the virus encounters in endosomes (5, 20-23). The sample contained particles that were in the process of genome release. The remaining particles were either activated particles or empty capsids. Reference-free two-dimensional class averages show that the particles releasing genomes lack parts of their capsids (Fig. 9A). Asymmetric reconstruction combined with three-dimensional classification identified subpopulations of particles of echovirus 18 that lacked up to three pentamers of capsid protein protomers, which always formed a single compact opening through the capsid (Fig. 9B-D). We call the particles lacking one or several pentamers open particles. Native virions of echovirus 18 that lacked pentamers were not detected.

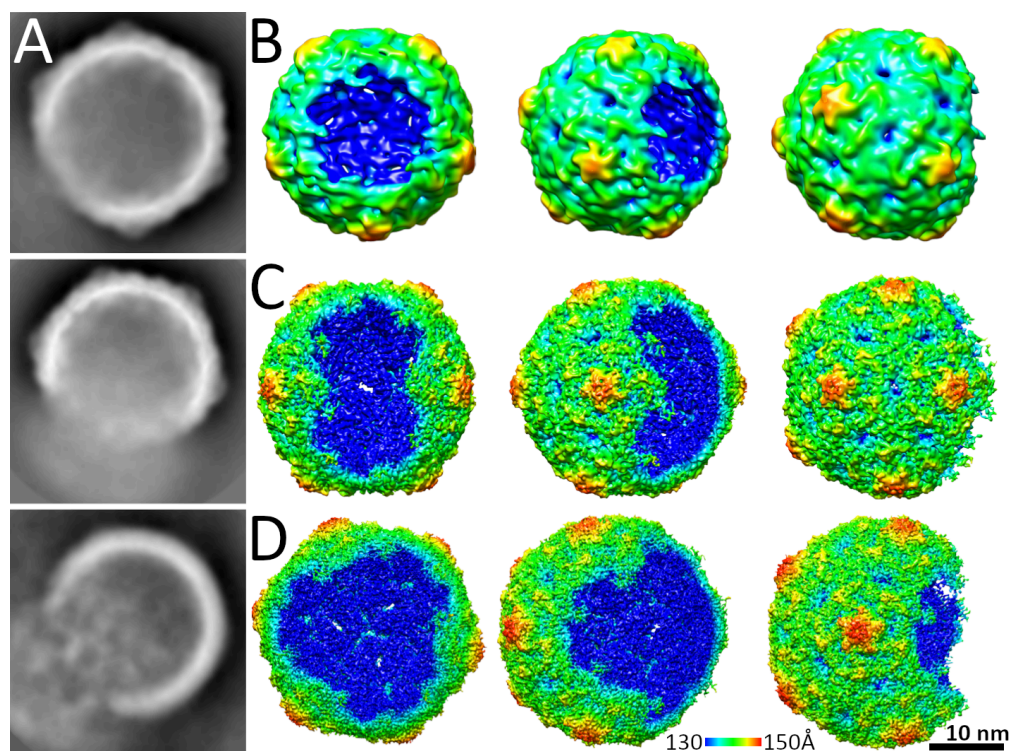


Fig. 9. Structure of open particles of echovirus 18. (A) Reference-free two-dimensional class averages showing particles of echovirus 18 in the process of RNA release lacking parts of their capsids. (B-D) Asymmetric three-dimensional reconstructions of open particles lacking one (B), two (C), and three pentamers (D). The electron density maps are rainbow colored based on the distance of the electron density surface from the particle center.

3.4.2 Dynamics of genome release (paper XI)

The dynamic of genome release after which a pentamer was separated from a capsid was studied using *in silico* simulations. The capsid first cracked open and split into two or a few parts to allow the release of part of the genome (Fig. 10). After capsid rupture the genome pressure decreases, so the parts of the capsid usually do not separate completely and can quickly reassemble. The escaping genome can break off some pentamers, as observed in our cryo-EM experiments. The genome was released after 10^6 simulation steps corresponding to 0.1 microseconds. Correspondingly, free diffusion of the genome from the capsid, calculated using the Stokes-Einstein relation, requires less than one microsecond. The speed of the genome release is likely to protect the genomic RNA from degradation by ribonucleases.

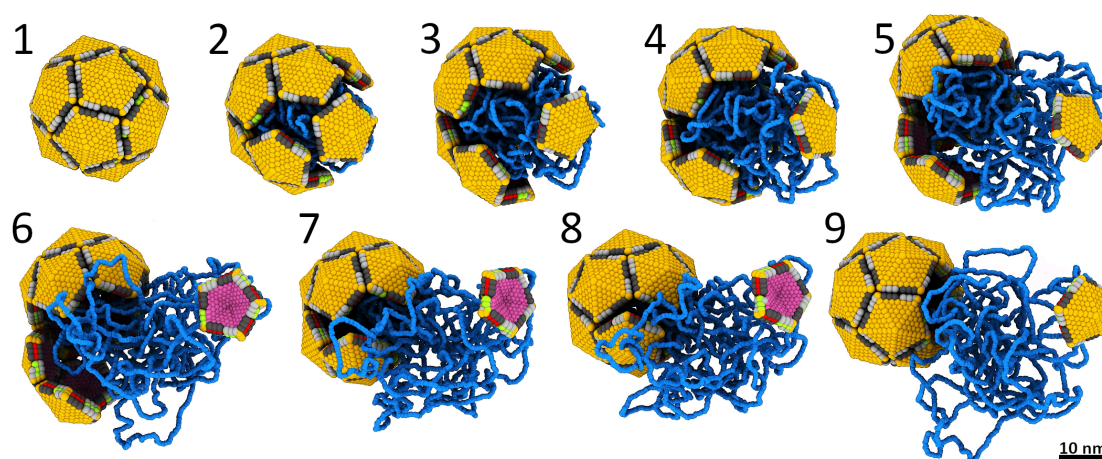


Fig. 10. Molecular dynamics simulation of genome release from enterovirus particles. Nine snapshots from the process are shown. The genome is shown in blue, outer capsid surface in orange, inner capsid surface in purple, beads at pentamer edges are shown in grey, green, and red.

3.4.3 Model of picornavirus genome release (paper XI)

Besides echovirus 18, we also identified open particles in the samples of echovirus 30. Furthermore, Harutyunyan et al. detected particles lacking pentamers in a sample of human rhinovirus 2 with cross-linked RNA genomes exposed to acidic pH (165). Our unpublished results provide evidence that dicistroviruses and iflaviruses also form open particles upon genome release. These observations indicate that viruses from the order *Picornavirales* may release their genomes by the transient opening of particles, resulting in the removal of pentamers of capsid protein protomers from their capsids. In summary, our data show that the genome release of picorna-like viruses requires several consecutive structural changes in a capsid (Fig. 11). Receptor binding or acidic pH induces the transformation of native virions into activated particles with reduced inter-pentamer interfaces (5, 21, 26-28, 30, 161). The weakening of inter-pentamer contacts and changes in the genome structure enable opening of the capsids and release of the RNA genome.

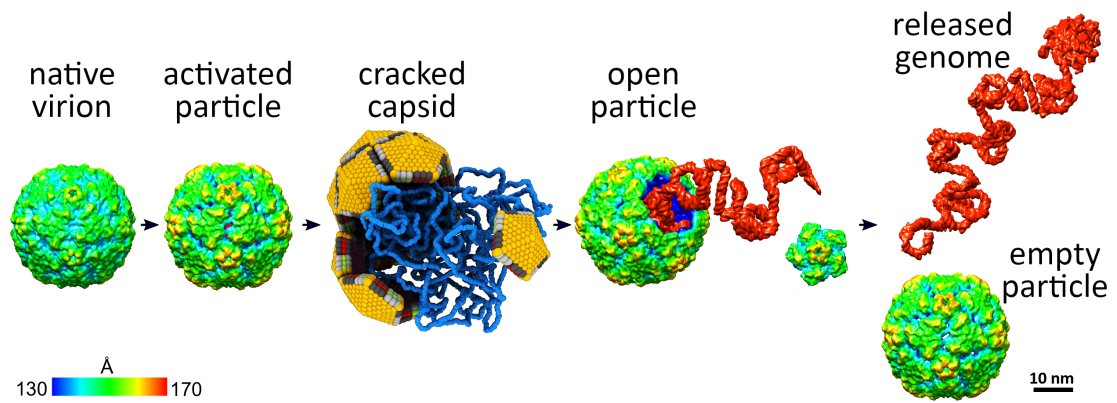


Fig. 11. Model of enterovirus genome release. Exposure to acidic pH in endosomes or binding to receptors induces the formation of activated particles. The reduction of inter-pentamer contacts and structural changes within the virus RNA enable the opening of the capsid, resulting in genome release and the expulsion of pentamers. After the genome release, the pentamers may re-associate with the empty open capsids.

4 SUMMARY AND FUTURE PROSPECTS

Viruses from the order *Picornavirales* are among the smallest self-replicating organisms. Their particles consist of only a single-stranded RNA molecule protected by a protein capsid. Even though individually these viruses are simple, as a group they are diverse. They share the organization of capsids with pseudo T = 3 icosahedral symmetry, but the structural changes in their particles which precede the genome release are distinct. Capsids of picornaviruses and iflaviruses expand after exposure to acidic pH or binding to receptors, whereas those of dicistroviruses do not change in size. We have shown that capsids of viruses from the order *Picornavirales* crack open to release their genomes in microsecond time scales, which decreases the likelihood of the degradation of their genomic RNAs by ribonucleases. Picorna-like viruses differ in the mechanisms that enable passage of their genomes across cell membranes into the cytoplasm. Whereas picornaviruses and dicistroviruses use VP4 subunits for membrane disruption, virions of iflaviruses probably lack VP4 subunits and employ protruding domains of VP3 subunits or minor capsid proteins attached to the particle surface to penetrate membranes.

The delivery of the genome to the cytoplasm of a cell is an essential event in the initiation of virus infection, and provides a potential target for the development of antiviral treatments. *In vivo* experiments identified the mechanisms responsible for the endocytosis of picornavirus particles and localized the uncoating sites within cells. Structural studies enabled the characterization of the changes in virions required for their RNA release *in vitro*. However, there is a disconnect between the *in vivo* and *in vitro* studies. Illuminating results may be obtained with the use of *in situ* cryo-electron tomography techniques that will enable high-resolution observations of interactions of virus particles with cellular structures. The identification of macromolecules based on projection matching or three-dimensional volume comparisons may provide unprecedented insight into macromolecular interactions that are essential for picornavirus infection. The efficiency of the tomographic studies may be increased by the combination of light and electron microscopy, which will enable the targeting of high-resolution studies to the sites of virus infection.

5 REFERENCES

1. A. C. Palmenberg *et al.*, Sequencing and analyses of all known human rhinovirus genomes reveal structure and evolution. *Science* **324**, 55-59 (2009).
2. H. Norder *et al.*, Picornavirus non-structural proteins as targets for new anti-virals with broad activity. *Antiviral research* **89**, 204-218 (2011).
3. A. M. Fendrick, A. S. Monto, B. Nightengale, M. Sarnes, The economic burden of non-influenza-related viral respiratory tract infection in the United States. *Archives of internal medicine* **163**, 487-494 (2003).
4. A. King, *Virus taxonomy: ninth report of the International Committee on Taxonomy of Viruses*. A. King, Ed., (Elsevier, Oxford, 2011).
5. T. J. Tuthill, E. Groppelli, J. M. Hogle, D. J. Rowlands, Picornaviruses. *Curr Top Microbiol Immunol* **343**, 43-89 (2010).
6. A. M. De Palma, I. Vliegen, E. De Clercq, J. Neyts, Selective inhibitors of picornavirus replication. *Med Res Rev* **28**, 823-884 (2008).
7. K. C. Wolthers *et al.*, Human parechoviruses as an important viral cause of sepsislike illness and meningitis in young children. *Clinical infectious diseases : an official publication of the Infectious Diseases Society of America* **47**, 358-363 (2008).
8. N. Jonsson, K. Wahlstrom, L. Svensson, L. Serrander, A. M. Lindberg, Aichi virus infection in elderly people in Sweden. *Archives of virology* **157**, 1365-1369 (2012).
9. X. Q. Dai, X. G. Hua, T. L. Shan, E. Delwart, W. Zhao, Human cosavirus infections in children in China. *Journal of clinical virology : the official publication of the Pan American Society for Clinical Virology* **48**, 228-229 (2010).
10. M. H. Allsopp, W. J. de Lange, R. Veldtman, Valuing insect pollination services with cost of replacement. *PloS one* **3**, e3128 (2008).
11. J. C. Biesmeijer *et al.*, Parallel declines in pollinators and insect-pollinated plants in Britain and the Netherlands. *Science* **313**, 351-354 (2006).
12. D. Vanengelsdorp, M. D. Meixner, A historical review of managed honey bee populations in Europe and the United States and the factors that may affect them. *J Invertebr Pathol* **103 Suppl 1**, S80-95 (2010).
13. S. G. Potts *et al.*, Global pollinator declines: trends, impacts and drivers. *Trends in ecology & evolution* **25**, 345-353 (2010).
14. S. J. Martin *et al.*, Global honey bee viral landscape altered by a parasitic mite. *Science* **336**, 1304-1306 (2012).
15. M. G. Rossmann *et al.*, Structure of a human common cold virus and functional relationship to other picornaviruses. *Nature* **317**, 145-153 (1985).
16. R. R. Rueckert, E. Wimmer, Systematic nomenclature of picornavirus proteins. *J Virol* **50**, 957-959 (1984).
17. J. M. Hogle, M. Chow, D. J. Filman, Three-dimensional structure of poliovirus at 2.9 Å resolution. *Science* **229**, 1358-1365 (1985).
18. P. Plevka *et al.*, Interaction of decay-accelerating factor with echovirus 7. *J Virol* **84**, 12665-12674 (2010).

19. D. M. Belnap *et al.*, Three-dimensional structure of poliovirus receptor bound to poliovirus. *Proceedings of the National Academy of Sciences of the United States of America* **97**, 73-78 (2000).
20. J. Ren *et al.*, Picornavirus uncoating intermediate captured in atomic detail. *Nature communications* **4**, 1929 (2013).
21. H. C. Levy, M. Bostina, D. J. Filman, J. M. Hogle, Catching a virus in the act of RNA release: a novel poliovirus uncoating intermediate characterized by cryo-electron microscopy. *J Virol* **84**, 4426-4441 (2010).
22. D. Garriga *et al.*, Insights into minor group rhinovirus uncoating: the X-ray structure of the HRV2 empty capsid. *PLoS Pathog* **8**, e1002473 (2012).
23. X. Wang *et al.*, A sensor-adaptor mechanism for enterovirus uncoating from structures of EV71. *Nat Struct Mol Biol* **19**, 424-429 (2012).
24. M. G. Rossmann, Viral cell recognition and entry. *Protein Sci* **3**, 1712-1725 (1994).
25. K. L. Shingler *et al.*, The enterovirus 71 A-particle forms a gateway to allow genome release: a cryoEM study of picornavirus uncoating. *PLoS pathogens* **9**, e1003240 (2013).
26. J. J. Seitsonen *et al.*, Structural analysis of coxsackievirus A7 reveals conformational changes associated with uncoating. *J Virol* **86**, 7207-7215 (2012).
27. M. Bostina, H. Levy, D. J. Filman, J. M. Hogle, Poliovirus RNA is released from the capsid near a twofold symmetry axis. *J Virol* **85**, 776-783 (2011).
28. D. M. Belnap *et al.*, Molecular tectonic model of virus structural transitions: the putative cell entry states of poliovirus. *J Virol* **74**, 1342-1354 (2000).
29. A. T. Hadfield *et al.*, The refined structure of human rhinovirus 16 at 2.15 Å resolution: implications for the viral life cycle. *Structure* **5**, 427-441 (1997).
30. E. A. Hewat, E. Neumann, D. Blaas, The concerted conformational changes during human rhinovirus 2 uncoating. *Mol Cell* **10**, 317-326 (2002).
31. H. J. Thibaut, A. M. De Palma, J. Neyts, Combating enterovirus replication: state-of-the-art on antiviral research. *Biochemical pharmacology* **83**, 185-192 (2012).
32. A. V. Paul, A. Schultz, S. E. Pincus, S. Oroszlan, E. Wimmer, Capsid protein VP4 of poliovirus is N-myristoylated. *Proceedings of the National Academy of Sciences of the United States of America* **84**, 7827-7831 (1987).
33. C. E. Fricks, J. M. Hogle, Cell-induced conformational change in poliovirus: externalization of the amino terminus of VP1 is responsible for liposome binding. *J Virol* **64**, 1934-1945 (1990).
34. N. Y. Hsu *et al.*, Viral reorganization of the secretory pathway generates distinct organelles for RNA replication. *Cell* **141**, 799-811 (2010).
35. K. Bienz, D. Egger, M. Troxler, L. Pasamontes, Structural organization of poliovirus RNA replication is mediated by viral proteins of the P2 genomic region. *J Virol* **64**, 1156-1163 (1990).
36. U. Boege, D. S. Ko, D. G. Scraba, Toward an in vitro system for picornavirus assembly: purification of mengovirus 14S capsid precursor particles. *J Virol* **57**, 275-284 (1986).
37. M. F. Jacobson, D. Baltimore, Morphogenesis of poliovirus. I. Association of the viral RNA with coat protein. *Journal of molecular biology* **33**, 369-378 (1968).
38. M. E. Marongiu, A. Pani, M. V. Corrias, M. Sau, P. La Colla, Poliovirus morphogenesis. I. Identification of 80S dissociable particles and evidence for the artifactual production of procapsids. *J Virol* **39**, 341-347 (1981).
39. Z. Feng *et al.*, A pathogenic picornavirus acquires an envelope by hijacking cellular membranes. *Nature* **496**, 367-371 (2013).
40. T. Dokland *et al.*, Structure determination of the phiX174 closed procapsid. *Acta Crystallogr D Biol Crystallogr* **54**, 878-890 (1998).

41. S. Munshi, L. Liljas, J. E. Johnson, Structure determination of Nudaurelia capensis omega virus. *Acta Crystallogr D Biol Crystallogr* **54**, 1295-1305 (1998).
42. M. S. Chapman, J. Tsao, M. G. Rossmann, Ab initio phase determination for spherical viruses: parameter determination for spherical-shell models. *Acta Crystallogr A* **48 (Pt 3)**, 301-312 (1992).
43. M. G. Rossmann, Ab initio phase determination and phase extension using non-crystallographic symmetry. *Curr Opin Struct Biol* **5**, 650-655 (1995).
44. J. Tsao, M. S. Chapman, M. G. Rossmann, Ab initio phase determination for viruses with high symmetry: a feasibility study. *Acta Crystallogr A* **48 (Pt 3)**, 293-301 (1992).
45. G. J. Kleywegt, Use of non-crystallographic symmetry in protein structure refinement. *Acta Crystallogr D Biol Crystallogr* **52**, 842-857 (1996).
46. R. M.G., B. D.M., The detection of sub-units within the crystallographic asymmetric unit. *Acta Cryst.* **15**, 24-31 (1962).
47. M. Buehner, G. C. Ford, K. W. Olsen, D. Moras, M. G. Rossman, Three-dimensional structure of D-glyceraldehyde-3-phosphate dehydrogenase. *Journal of molecular biology* **90**, 25-49 (1974).
48. B. W. Matthews, P. B. Sigler, R. Henderson, D. M. Blow, Three-dimensional structure of tosyl-alpha-chymotrypsin. *Nature* **214**, 652-656 (1967).
49. S. C. Harrison, A. J. Olson, C. E. Schutt, F. K. Winkler, G. Bricogne, Tomato bushy stunt virus at 2.9 Å resolution. *Nature* **276**, 368-373 (1978).
50. M. Adrian, J. Dubochet, J. Lepault, A. W. McDowell, Cryo-electron microscopy of viruses. *Nature* **308**, 32-36 (1984).
51. J. Dubochet *et al.*, Cryo-electron microscopy of vitrified specimens. *Q Rev Biophys* **21**, 129-228 (1988).
52. D. J. De Rosier, A. Klug, Reconstruction of three dimensional structures from electron micrographs. *Nature* **217**, 130-134 (1968).
53. R. G. Hart, Electron microscopy of unstained biological material: the polytropic montage. *Science* **159**, 1464-1467 (1968).
54. W. Hoppe, J. Gassmann, N. Hunsmann, H. J. Schramm, M. Sturm, Three-dimensional reconstruction of individual negatively stained yeast fatty-acid synthetase molecules from tilt series in the electron microscope. *Hoppe Seylers Z Physiol Chem* **355**, 1483-1487 (1974).
55. M. Marko, C. Hsieh, R. Schalek, J. Frank, C. Mannella, Focused-ion-beam thinning of frozen-hydrated biological specimens for cryo-electron microscopy. *Nat Methods* **4**, 215-217 (2007).
56. A. Rigort *et al.*, Micromachining tools and correlative approaches for cellular cryo-electron tomography. *J Struct Biol* **172**, 169-179 (2010).
57. H. R., Cryo-Protection of Protein Crystals against Radiation Damage in Electron and X-Ray Diffraction. *Proc. R. Soc. Lond.* **B**, 6-8 (1990).
58. W. Wan, J. A. Briggs, Cryo-Electron Tomography and Subtomogram Averaging. *Methods Enzymol* **579**, 329-367 (2016).
59. J. A. Briggs, Structural biology in situ--the potential of subtomogram averaging. *Curr Opin Struct Biol* **23**, 261-267 (2013).
60. P. Zhang, Advances in cryo-electron tomography and subtomogram averaging and classification. *Curr Opin Struct Biol*, (2019).
61. F. K. Schur, Toward high-resolution in situ structural biology with cryo-electron tomography and subtomogram averaging. *Curr Opin Struct Biol* **58**, 1-9 (2019).
62. K. E. Leigh *et al.*, Subtomogram averaging from cryo-electron tomograms. *Methods Cell Biol* **152**, 217-259 (2019).

63. T. Yamashita *et al.*, Complete nucleotide sequence and genetic organization of Aichi virus, a distinct member of the Picornaviridae associated with acute gastroenteritis in humans. *J Virol* **72**, 8408-8412 (1998).
64. T. Hyypia *et al.*, A distinct picornavirus group identified by sequence analysis. *Proceedings of the National Academy of Sciences of the United States of America* **89**, 8847-8851 (1992).
65. H. L. Lipton, A. S. Kumar, S. Hertzler, H. V. Reddi, Differential usage of carbohydrate co-receptors influences cellular tropism of Theiler's murine encephalomyelitis virus infection of the central nervous system. *Glycoconj J* **23**, 39-49 (2006).
66. C. Fotiadis, D. R. Kilpatrick, H. L. Lipton, Comparison of the binding characteristics to BHK-21 cells of viruses representing the two Theiler's virus neurovirulence groups. *Virology* **182**, 365-370 (1991).
67. A. H. Shah, H. L. Lipton, Low-neurovirulence Theiler's viruses use sialic acid moieties on N-linked oligosaccharide structures for attachment. *Virology* **304**, 443-450 (2002).
68. S. A. Huber, VCAM-1 is a receptor for encephalomyocarditis virus on murine vascular endothelial cells. *Journal of virology* **68**, 3453-3458 (1994).
69. G. Boivin, Y. Abed, F. D. Boucher, Human parechovirus 3 and neonatal infections. *Emerging infectious diseases* **11**, 103-105 (2005).
70. I. Schuffenecker *et al.*, Human parechovirus infections, Lyon, France, 2008-10: evidence for severe cases. *Journal of clinical virology : the official publication of the Pan American Society for Clinical Virology* **54**, 337-341 (2012).
71. J. G. Wildenbeest, K. C. Wolthers, B. Straver, D. Pajkrt, Successful IVIG treatment of human parechovirus-associated dilated cardiomyopathy in an infant. *Pediatrics* **132**, e243-247 (2013).
72. G. Stanway, P. Joki-Korpela, T. Hyypia, Human parechoviruses--biology and clinical significance. *Reviews in medical virology* **10**, 57-69 (2000).
73. S. Esposito *et al.*, Pediatric parechovirus infections. *Journal of clinical virology : the official publication of the Pan American Society for Clinical Virology* **60**, 84-89 (2014).
74. M. A. Verboon-Macielek *et al.*, Human parechovirus causes encephalitis with white matter injury in neonates. *Annals of neurology* **64**, 266-273 (2008).
75. R. E. Levorson, B. A. Jantusch, B. L. Wiedermann, H. M. Spiegel, J. M. Campos, Human parechovirus-3 infection: emerging pathogen in neonatal sepsis. *The Pediatric infectious disease journal* **28**, 545-547 (2009).
76. R. Wigand, A. B. Sabin, Properties of ECHO types 22, 23 and 24 viruses. *Archiv fur die gesamte Virusforschung* **11**, 224-247 (1961).
77. ENTERIC cytopathogenic human orphan (ECHO) viruses. *Science* **122**, 1187-1188 (1955).
78. G. Stanway *et al.*, Molecular and biological characteristics of echovirus 22, a representative of a new picornavirus group. *Journal of virology* **68**, 8232-8238 (1994).
79. G. Sun *et al.*, Complete genome sequence of a novel type of human parechovirus strain reveals natural recombination events. *Journal of virology* **86**, 8892-8893 (2012).
80. C. H. Williams *et al.*, Evolution and conservation in human parechovirus genomes. *The Journal of general virology* **90**, 1702-1712 (2009).
81. L. Zhu *et al.*, Structure of Ljungan virus provides insight into genome packaging of this picornavirus. *Nat Commun* **6**, 8316 (2015).
82. A. Domanska, J. W. Flatt, J. J. Jukonen, J. A. Geraets, S. J. Butcher, A 2.8-Angstrom-Resolution Cryo-Electron Microscopy Structure of Human Parechovirus 3 in Complex with Fab from a Neutralizing Antibody. *J Virol* **93**, (2019).

83. S. Shakeel *et al.*, Genomic RNA folding mediates assembly of human parechovirus. *Nat Commun* **8**, 5 (2017).
84. J. Seitsonen *et al.*, Interaction of alphaVbeta3 and alphaVbeta6 integrins with human parechovirus 1. *Journal of virology* **84**, 8509-8519 (2010).
85. T. Yamashita *et al.*, Isolation of cytopathic small round viruses with BS-C-1 cells from patients with gastroenteritis. *J Infect Dis* **164**, 954-957 (1991).
86. T. Yamashita *et al.*, Isolation of cytopathic small round virus (Aichi virus) from Pakistani children and Japanese travelers from Southeast Asia. *Microbiol Immunol* **39**, 433-435 (1995).
87. K. Ambert-Balay *et al.*, Prevalence and genetic diversity of Aichi virus strains in stool samples from community and hospitalized patients. *J Clin Microbiol* **46**, 1252-1258 (2008).
88. S. Kaikkonen, S. Rasanen, M. Ramet, T. Vesikari, Aichi virus infection in children with acute gastroenteritis in Finland. *Epidemiol Infect* **138**, 1166-1171 (2010).
89. D. Y. Oh *et al.*, Molecular characterization of the first Aichi viruses isolated in Europe and in South America. *Arch Virol* **151**, 1199-1206 (2006).
90. K. Sdiri-Loulizi *et al.*, Acute infantile gastroenteritis associated with human enteric viruses in Tunisia. *J Clin Microbiol* **46**, 1349-1355 (2008).
91. M. Kitajima, C. P. Gerba, Aichi virus 1: environmental occurrence and behavior. *Pathogens* **4**, 256-268 (2015).
92. T. Yamashita, K. Sakae, Y. Ishihara, S. Isomura, E. Utagawa, Prevalence of newly isolated, cytopathic small round virus (Aichi strain) in Japan. *J Clin Microbiol* **31**, 2938-2943 (1993).
93. K. A. Dryden *et al.*, Immature and mature human astrovirus: structure, conformational changes, and similarities to hepatitis E virus. *J Mol Biol* **422**, 650-658 (2012).
94. L. Zhu *et al.*, Structure of human Aichi virus and implications for receptor binding. *Nat Microbiol* **1**, 16150 (2016).
95. S. Kalynych, L. Palkova, P. Plevka, The Structure of Human Parechovirus 1 Reveals an Association of the RNA Genome with the Capsid. *J Virol* **90**, 1377-1386 (2016).
96. Z. Liang, A. S. Kumar, M. S. Jones, N. J. Knowles, H. L. Lipton, Phylogenetic analysis of the species Theilovirus: emerging murine and human pathogens. *Journal of virology* **82**, 11545-11554 (2008).
97. T. Himeda *et al.*, The preparation of an infectious full-length cDNA clone of Saffold virus. *Virology journal* **8**, 110 (2011).
98. T. Himeda, T. Hosomi, T. Okuwa, Y. Muraki, Y. Ohara, Saffold virus type 3 (SAFV-3) persists in HeLa cells. *PLoS one* **8**, e53194 (2013).
99. T. Himeda, Y. Ohara, Saffold virus, a novel human Cardiovirus with unknown pathogenicity. *Journal of virology* **86**, 1292-1296 (2012).
100. O. Blinkova *et al.*, Cardioviruses are genetically diverse and cause common enteric infections in South Asian children. *Journal of virology* **83**, 4631-4641 (2009).
101. Y. Abed, G. Boivin, New Saffold cardioviruses in 3 children, Canada. *Emerging infectious diseases* **14**, 834-836 (2008).
102. J. F. Drexler *et al.*, Circulation of 3 lineages of a novel Saffold cardiovirus in humans. *Emerging infectious diseases* **14**, 1398-1405 (2008).
103. Z. Q. Xu *et al.*, New Saffold cardiovirus in children, China. *Emerging infectious diseases* **15**, 993-994 (2009).
104. M. Luo *et al.*, The atomic structure of Mengo virus at 3.0 Å resolution. *Science* **235**, 182-191 (1987).

105. R. A. Grant, D. J. Filman, R. S. Fujinami, J. P. Icenogle, J. M. Hogle, Three-dimensional structure of Theiler virus. *Proceedings of the National Academy of Sciences of the United States of America* **89**, 2061-2065 (1992).
106. T. J. Tuthill *et al.*, Equine rhinitis A virus and its low pH empty particle: clues towards an aphthovirus entry mechanism? *PLoS pathogens* **5**, e1000620 (2009).
107. B. Baxt, H. L. Bachrach, Early interactions of foot-and-mouth disease virus with cultured cells. *Virology* **104**, 42-55 (1980).
108. L. Hall, R. R. Rueckert, Infection of mouse fibroblasts by cardioviruses: premature uncoating and its prevention by elevated pH and magnesium chloride. *Virology* **43**, 152-165 (1971).
109. M. G. Rossmann *et al.*, Structure of a Human Common Cold Virus and Functional-Relationship to Other Picornaviruses. *Nature* **317**, 145-153 (1985).
110. E. Mullapudi, A. Pridal, L. Palkova, J. R. de Miranda, P. Plevka, Virion Structure of Israeli Acute Bee Paralysis Virus. *Journal of virology* **90**, 8150-8159 (2016).
111. J. Tate *et al.*, The crystal structure of cricket paralysis virus: the first view of a new virus family. *Nature structural biology* **6**, 765-774 (1999).
112. G. Squires *et al.*, Structure of the Triatoma virus capsid. *Acta crystallographica. Section D, Biological crystallography* **69**, 1026-1037 (2013).
113. A. C. Palmenberg, In vitro synthesis and assembly of picornaviral capsid intermediate structures. *Journal of virology* **44**, 900-906 (1982).
114. J. R. Putnak, B. A. Phillips, Picornaviral structure and assembly. *Microbiol Rev* **45**, 287-315 (1981).
115. B. Rombaut, A. Foriers, A. Boeye, In vitro assembly of poliovirus 14 S subunits: identification of the assembly promoting activity of infected cell extracts. *Virology* **180**, 781-787 (1991).
116. B. Rombaut, R. Vrijssen, A. Boeye, In vitro assembly of poliovirus empty capsids: antigenic consequences and immunological assay of the morphopoietic factor. *Virology* **135**, 546-550 (1984).
117. J. Agirre *et al.*, Capsid protein identification and analysis of mature Triatoma virus (TrV) virions and naturally occurring empty particles. *Virology* **409**, 91-101 (2011).
118. A. J. Fisher, J. E. Johnson, Ordered duplex RNA controls capsid architecture in an icosahedral animal virus. *Nature* **361**, 176-179 (1993).
119. S. Munshi *et al.*, The 2.8 Å structure of a T = 4 animal virus and its implications for membrane translocation of RNA. *Journal of molecular biology* **261**, 1-10 (1996).
120. J. R. de Miranda, G. Cordonis, G. Budge, The Acute bee paralysis virus-Kashmir bee virus-Israeli acute paralysis virus complex. *J Invertebr Pathol* **103 Suppl 1**, S30-47 (2010).
121. E. Maori *et al.*, IAPV, a bee-affecting virus associated with Colony Collapse Disorder can be silenced by dsRNA ingestion. *Insect Mol Biol* **18**, 55-60 (2009).
122. I. A. Berthoud H, Haueter M, Radloff S, Neumann P, Virus infections and winter losses of honey bee colonies (*Apis mellifera*). . *Journal of Apicultural Research*, 60-65 (2010).
123. J. Agirre *et al.*, Cryo-electron microscopy reconstructions of triatoma virus particles: a clue to unravel genome delivery and capsid disassembly. *J Gen Virol* **94**, 1058-1068 (2013).
124. A. Shukla, A. K. Padhi, J. Gomes, M. Banerjee, The VP4 peptide of hepatitis A virus ruptures membranes through formation of discrete pores. *Journal of virology* **88**, 12409-12421 (2014).
125. A. Panjwani *et al.*, Capsid protein VP4 of human rhinovirus induces membrane permeability by the formation of a size-selective multimeric pore. *PLoS pathogens* **10**, e1004294 (2014).

126. J. D. Ellis, Munn, P.A., The worldwide health status of honey bees. *Bee World* **86**, 88–101 (2005).
127. D. Tentcheva *et al.*, Prevalence and seasonal variations of six bee viruses in *Apis mellifera* L. and *Varroa destructor* mite populations in France. *Applied and environmental microbiology* **70**, 7185-7191 (2004).
128. F. Mondet, J. R. de Miranda, A. Kretzschmar, Y. Le Conte, A. R. Mercer, On the front line: quantitative virus dynamics in honeybee (*Apis mellifera* L.) colonies along a new expansion front of the parasite *Varroa destructor*. *PLoS pathogens* **10**, e1004323 (2014).
129. Y. P. Chen, J. S. Pettis, A. Collins, M. F. Feldlaufer, Prevalence and transmission of honeybee viruses. *Applied and environmental microbiology* **72**, 606-611 (2006).
130. W. R. Bailey L, Two more small RNA viruses from honey bees and further observations on sacbrood and acute paralysis viruses. *J. Gen. Virol.* **25**, 175-186 (1977).
131. N. Leat, B. Ball, V. Govan, S. Davison, Analysis of the complete genome sequence of black queen-cell virus, a picorna-like virus of honey bees. *The Journal of general virology* **81**, 2111-2119 (2000).
132. G. DeGrandi-Hoffman, Y. Chen, R. Simonds, The Effects of Pesticides on Queen Rearing and Virus Titers in Honey Bees (*Apis mellifera* L.). *Insects* **4**, 71-89 (2013).
133. Z. Tapasztai *et al.*, Genetic analysis and phylogenetic comparison of Black queen cell virus genotypes. *Vet Microbiol* **139**, 227-234 (2009).
134. D. P. McMahon *et al.*, A sting in the spit: widespread cross-infection of multiple RNA viruses across wild and managed bees. *J Anim Ecol*, (2015).
135. J. Zhang *et al.*, Three-dimensional structure of the Chinese Sacbrood bee virus. *Science in China. Series C, Life sciences / Chinese Academy of Sciences* **44**, 443-448 (2001).
136. G. Lanzi *et al.*, Molecular and biological characterization of deformed wing virus of honeybees (*Apis mellifera* L.). *Journal of virology* **80**, 4998-5009 (2006).
137. J. R. de Miranda *et al.*, Genetic characterization of slow bee paralysis virus of the honeybee (*Apis mellifera* L.). *The Journal of general virology* **91**, 2524-2530 (2010).
138. L. Bailey, R. D. Woods, Three previously undescribed viruses from the honey bee. *J Gen Virol* **25**, 175-186 (1974).
139. B. B. Carreck NL, Wilson JK, Allen MF. , The epodemiology of slow paralysis virus in honey bee colonies infested by *Varroa destructor* in the UK. *Proceedings of XXXIXth International Apicultural Congress, Dublin, Ireland*, 32-33 (2005).
140. M. T. Santillan-Galicia, Ball, B. V., Clark, S. J., Alderson, P. G. , Transmission of deformed wing virus and slow paralysis virus to adult bees (*Apis mellifera* L.) by *Varroa destructor*. *Journal of Apicultural Research* **49**, 141-148 (2010).
141. G. Dodson, A. Wlodawer, Catalytic triads and their relatives. *Trends Biochem Sci* **23**, 347-352 (1998).
142. S. Canaan, A. Roussel, R. Verger, C. Cambillau, Gastric lipase: crystal structure and activity. *Biochim Biophys Acta* **1441**, 197-204 (1999).
143. M. E. Vaquero, J. Barriuso, M. J. Martinez, A. Prieto, Properties, structure, and applications of microbial sterol esterases. *Appl Microbiol Biotechnol* **100**, 2047-2061 (2016).
144. J. R. Ongus *et al.*, Complete sequence of a picorna-like virus of the genus Iflavirus replicating in the mite *Varroa destructor*. *The Journal of general virology* **85**, 3747-3755 (2004).
145. T. Fujiyuki *et al.*, Novel insect picorna-like virus identified in the brains of aggressive worker honeybees. *Journal of virology* **78**, 1093-1100 (2004).

146. J. F. E. Newman, Brown, F., Bailey L., Gibbs, A.J., Some Physico-chemical properties of two Honey-bee Picornaviruses. *Journal of General Virology* **19**, 405-409 (1973).
147. L. Bailey, R. D. Woods, Two More Small RNA Viruses from Honey Bees and Further Observations on Sacbrood and Acute Bee-Paralysis Viruses. *Journal of General Virology* **37**, 175-182 (1977).
148. E. Prchla, E. Kuechler, D. Blaas, R. Fuchs, Uncoating of human rhinovirus serotype 2 from late endosomes. *Journal of virology* **68**, 3713-3723 (1994).
149. R. Fuchs, D. Blaas, Productive entry pathways of human rhinoviruses. *Advances in virology* **2012**, 826301 (2012).
150. P. L. Bowen-Walker, S. J. Martin, A. Gunn, The transmission of deformed wing virus between honeybees (*Apis mellifera* L.) by the ectoparasitic mite *varroa jacobsoni* Oud. *J Invertebr Pathol* **73**, 101-106 (1999).
151. A. C. Highfield *et al.*, Deformed wing virus implicated in overwintering honeybee colony losses. *Appl Environ Microbiol* **75**, 7212-7220 (2009).
152. J. R. de Miranda, L. Gauthier, M. Ribiere, and Y. P. Chen, in *Honey bee colony health: challenges and sustainable solutions*, Y. J. Sammataro D., Ed. (CRC Press, Boca Raton, 2012), pp. 71-102.
153. K. M. Smith *et al.*, Pathogens, pests, and economics: drivers of honey bee colony declines and losses. *Ecohealth* **10**, 434-445 (2013).
154. L. J. Organtini *et al.*, Honey Bee Deformed Wing Virus Structures Reveal that Conformational Changes Accompany Genome Release. *J Virol* **91**, (2017).
155. S. Gisder, E. Genersch, Viruses of commercialized insect pollinators. *J Invertebr Pathol* **147**, 51-59 (2017).
156. M. J. Nicklin, H. G. Krausslich, H. Toyoda, J. J. Dunn, E. Wimmer, Poliovirus polypeptide precursors: expression in vitro and processing by exogenous 3C and 2A proteinases. *Proceedings of the National Academy of Sciences of the United States of America* **84**, 4002-4006 (1987).
157. M. J. Nicklin, K. S. Harris, P. V. Pallai, E. Wimmer, Poliovirus proteinase 3C: large-scale expression, purification, and specific cleavage activity on natural and synthetic substrates in vitro. *J Virol* **62**, 4586-4593 (1988).
158. P. V. Pallai *et al.*, Cleavage of synthetic peptides by purified poliovirus 3C proteinase. *J Biol Chem* **264**, 9738-9741 (1989).
159. E. Groppelli *et al.*, Picornavirus RNA is protected from cleavage by ribonuclease during virion uncoating and transfer across cellular and model membranes. *PLoS Pathog* **13**, e1006197 (2017).
160. A. Rich, D. R. Davies, A NEW TWO STRANDED HELICAL STRUCTURE: POLYADENYLIC ACID AND POLYURIDYLIC ACID. *Journal of the American Chemical Society* **78**, 3548-3549 (1956).
161. E. A. Hewat, D. Blaas, Cryoelectron microscopy analysis of the structural changes associated with human rhinovirus type 14 uncoating. *J Virol* **78**, 2935-2942 (2004).
162. K. M. Reinisch, M. L. Nibert, S. C. Harrison, Structure of the reovirus core at 3.6 Å resolution. *Nature* **404**, 960-967 (2000).
163. H. Naitow, J. Tang, M. Canady, R. B. Wickner, J. E. Johnson, L-A virus at 3.4 Å resolution reveals particle architecture and mRNA decapping mechanism. *Nat Struct Biol* **9**, 725-728 (2002).
164. J. Pelletier, N. Sonenberg, Internal initiation of translation of eukaryotic mRNA directed by a sequence derived from poliovirus RNA. *Nature* **334**, 320-325 (1988).
165. S. Harutyunyan *et al.*, Viral uncoating is directional: exit of the genomic RNA in a common cold virus starts with the poly-(A) tail at the 3'-end. *PLoS Pathog* **9**, e1003270 (2013).

PAPER I



The Structure of Human Parechovirus 1 Reveals an Association of the RNA Genome with the Capsid

Sergei Kalynych, Lenka Pálková, Pavel Plevka

Central European Institute of Technology, Masaryk University, Brno, Czech Republic

ABSTRACT

Parechoviruses are human pathogens that cause diseases ranging from gastrointestinal disorders to encephalitis. Unlike those of most picornaviruses, parechovirus capsids are composed of only three subunits: VP0, VP1, and VP3. Here, we present the structure of a human parechovirus 1 (HPeV-1) virion determined to a resolution of 3.1 Å. We found that interactions among pentamers in the HPeV-1 capsid are mediated by the N termini of VP0s, which correspond to the capsid protein VP4 and the N-terminal part of the capsid protein VP2 of other picornaviruses. In order to facilitate delivery of the virus genome into the cytoplasm, the N termini of VP0s have to be released from contacts between pentamers and exposed at the particle surface, resulting in capsid disruption. A hydrophobic pocket, which can be targeted by capsid-binding antiviral compounds in many other picornaviruses, is not present in HPeV-1. However, we found that interactions between the HPeV-1 single-stranded RNA genome and subunits VP1 and VP3 in the virion impose a partial icosahedral ordering on the genome. The residues involved in RNA binding are conserved among all parechoviruses, suggesting a putative role of the genome in virion stability or assembly. Therefore, putative small molecules that could disrupt HPeV RNA-capsid protein interactions could be developed into antiviral inhibitors.

IMPORTANCE

Human parechoviruses (HPeVs) are pathogens that cause diseases ranging from respiratory and gastrointestinal disorders to encephalitis. Recently, there have been outbreaks of HPeV infections in Western Europe and North America. We present the first atomic structure of parechovirus HPeV-1 determined by X-ray crystallography. The structure explains why HPeVs cannot be targeted by antiviral compounds that are effective against other picornaviruses. Furthermore, we found that the interactions of the HPeV-1 genome with the capsid resulted in a partial icosahedral ordering of the genome. The residues involved in RNA binding are conserved among all parechoviruses, suggesting an evolutionarily fixed role of the genome in virion assembly. Therefore, putative small molecules disrupting HPeV RNA-capsid protein interactions could be developed into antiviral inhibitors.

Human parechoviruses (HPeVs) belong to the family *Picornaviridae*, which contains many vertebrate and human pathogens. Parechoviruses mainly cause mild gastrointestinal diseases in neonates and young children (1–4). Occasionally, however, parechovirus infections progress to serious and debilitating illnesses, including pneumonia, flaccid paralysis, encephalitis, sepsis, and meningitis (5–7). After their discovery (8, 9), HPeVs were placed in the same genus as human enteroviruses, exemplified by polioviruses and rhinoviruses (10). In the early 1990s, a separate genus, *Parechovirus*, was designated, which now includes HPeVs and Ljungan viruses (11). Parechoviruses exhibit high genetic variability, with at least 16 different types (12, 13). HPeV-1, HPeV-3, and HPeV-6 are the most prevalent clinically diagnosed types (14, 15).

HPeVs are small, nonenveloped icosahedral viruses. Their virions have an outer diameter of about 300 Å and contain a positive-sense single-stranded RNA (ssRNA) genome approximately 7,500 nucleotides long (16). HPeV capsids are built out of 60 copies of each of three viral proteins, VP0, VP1, and VP3. These three capsid proteins are co- and posttranslationally cleaved from a single polyprotein and constitute a protomer—the elementary building block of the capsid. In most picornaviruses, the capsid protein VP0 is cleaved into fragments VP2 and VP4 after virion assembly (17). The RNA genome has been proposed to have a role in cleavage (18). However, in parechoviruses, VP0 proteins remain intact, even in the mature virions (11, 19).

A distinctive feature of the capsid surface of many picornavi-

ruses is a depression encircling the icosahedral 5-fold axes, called the “canyon” (20). For many picornaviruses, the canyon is the binding site of receptors with an immunoglobulin fold (21–23). Integrins $\alpha_V\beta_3$ and $\alpha_V\beta_6$ were proposed to be receptors for HPeVs that possess the integrin recognition sequence arginine-glycine-aspartate (RGD) in the C terminus of VP1, including HPeV-1, -2, -4, -5, and -6 (24, 25). The binding of receptors within the canyon induces the release of a pocket factor from a hydrophobic pocket immediately below the surface of the canyon (26). The shape of the electron density and the hydrophobic environment of the pocket suggest that the pocket factor is a lipid (27–30). The expulsion of the pocket factor is associated with a decrease in virion stability and leads to genome release.

Genome release from picornavirus virions requires structural

Received 15 September 2015 Accepted 9 November 2015

Accepted manuscript posted online 18 November 2015

Citation Kalynych S, Pálková L, Plevka P. 2016. The structure of human parechovirus 1 reveals an association of the RNA genome with the capsid. *J Virol* 90:1377–1386. doi:10.1128/JVI.02346-15.

Editor: B. Williams

Address correspondence to Pavel Plevka, pavel.plevka@ceitec.muni.cz.

Supplemental material for this article may be found at <http://dx.doi.org/10.1128/JVI.02346-15>.

Copyright © 2016 Kalynych et al. This is an open-access article distributed under the terms of the [Creative Commons Attribution 4.0 International license](http://creativecommons.org/licenses/by/4.0/).

rearrangements of the capsid (31, 32). In enteroviruses, the capsid proteins change their positions relative to each other, resulting in the opening of pores at icosahedral 2-fold symmetry axes (33–35). VP1 N termini become exposed at the particle surface, and VP4s are released from the virion. Finally, the genomic RNA leaves the empty capsids. The standard *in vitro* procedure to induce the genome release of picornaviruses by heating to 56°C (34) results in disruption of the HPeV-1 virions to pentamers (36). Thus, the *in vitro* experiments provide putative evidence that the genome release mechanism of parechoviruses might be different from that of the other enteroviruses.

Pocket-binding antipicornavirus compounds have been developed that overstabilize the capsids and thus prevent genome release (30, 37–40). The capsid-binding inhibitors targeting rhinoviruses demonstrated a moderate level of success in human clinical trials (41, 42); however, they were not effective against parechovirus infections (43).

Single-particle cryo-electron microscopy reconstructions of HPeV-1 and its complex with the integrin receptor were reported previously at a resolution of 8.5 Å (25). However, despite the impact of HPeVs on human health, the atomic-level structural details of their virions are unknown. Here, we report the crystal structure of the virion of HPeV-1 (strain Harris) determined to a resolution of 3.1 Å. We show that specific interactions of the RNA genome with the capsid proteins result in a partial icosahedral ordering of the genome. This indicates a possible role of the genome in the stability or assembly of the HPeV-1 virion.

MATERIALS AND METHODS

Virus preparation. Human parechovirus (strain Harris; ATCC VR-52) was propagated in A549 human lung carcinoma cells (ATCC CCL-185). For a typical preparation, fifty 140-cm² tissue culture plates were infected with HPeV-1 at a multiplicity of infection (MOI) of 0.1 at 90% confluence, and the infection was allowed to proceed for 72 h at 37°C, at which point 90% of the cells exhibited cytopathic effects. The supernatant was harvested, and any remaining attached cells were removed from the plates using cell scrapers. The supernatant was centrifuged at 7,500 × g for 15 min, and the resulting pellet was resuspended in 10 ml of resuspension buffer (0.25 M HEPES-HCl, pH 7.5, 0.25 M NaCl). This fraction was subjected to three rounds of freeze-thawing by sequential transfer between –80°C and 37°C and homogenized with a Dounce tissue grinder to lyse the remaining cells. Cell debris was separated from the supernatant by low-speed centrifugation at 7,500 × g for 15 min. The resulting supernatant was combined with that obtained during the first low-speed centrifugation step. Viral particles were precipitated by adding polyethylene glycol (PEG) 8000 and NaCl to final concentrations of 15% (wt/vol) and 0.5 M, respectively, and incubating at 4°C with mild shaking (60 rpm) overnight. The following day, the solution was spun down at 10,000 × g for 20 min, and the visible white precipitate was resuspended in 12 ml of the resuspension buffer. MgCl₂ was added to a final concentration of 5 mM, and the sample was subjected to trypsin (80 µg/ml), DNase (10 µg/ml), and RNase (10 µg/ml) treatment for 30 min at 22°C. EDTA (pH 9.5) was added to a final concentration of 15 mM, and a nonionic detergent, Nonidet P-40 (Sigma-Aldrich Inc.), was added to a final concentration of 1%. The solution was incubated for an additional 20 min at 22°C and centrifuged at 3,500 × g, and the supernatant was spun down through a 30% (wt/wt) sucrose cushion in 30 mM Tris-HCl, pH 8.0, 250 mM NaCl at 200,000 × g using a Ti50.2 rotor (Beckman Coulter). The pellet was resuspended in approximately 1 ml of cold resuspension buffer and added to 10 ml of 60% (wt/wt) CsCl solution in an ultracentrifuge tube. Gradient ultracentrifugation was allowed to proceed for at least 12 h at 100,000 × g in a SW40Ti rotor (Beckman Coulter). The opaque virus band was extracted with an 18-gauge needle on a 3-ml disposable syringe. The virus

TABLE 1 Diffraction data and structure quality indicators

| Parameter | Value |
|---|----------------------|
| Space group | P6 ₃ 22 |
| Cell parameters | |
| <i>a</i> , <i>b</i> , <i>c</i> (Å) | 399.5, 399.5, 332.9 |
| α, β, γ (°) | 90, 90, 120 |
| Resolution shell ^a | 65.0–3.1 (3.15–3.10) |
| No. of observations ^a | 1,187,478 (5,621) |
| No. of unique reflections ^a | 233,083 (4,306) |
| Observation multiplicity ^a | 5.4 (1.3) |
| Completeness ^a | 78.2 (31.8) |
| <i>R</i> _{merge} (%) ^{a,b} | 0.354 (0.904) |
| <i>I</i> / <i>σ</i> (<i>I</i>) ^a | 5.0 (0.9) |
| <i>R</i> _{factor} ^a | 0.29 (0.41) |
| No. of protein atoms ^c | 5,283 |
| No. of RNA atoms ^c | 119 |
| Average B factor protein (Å ²) | 50 |
| Average B factor RNA (Å ²) | 71 |
| Ramachandran plot statistics | |
| Preferred regions (%) ^d | 90 |
| Allowed regions (%) ^d | 9.41 |
| Disallowed regions (%) ^d | 0.59 |
| RMSD ^e bond angles (°) | 0.005 |
| RMSD bond lengths (Å) | 1.16 |

^a Statistics for the highest-resolution shell are shown in parentheses.

^b $R_{\text{merge}} = \sum_i \sum_j |I_{ij} - \langle I_i \rangle| / \sum_i \sum_j I_{ij}$.

^c Statistics are given for one icosahedral asymmetric unit.

^d As calculated by Molprobity (79).

^e RMSD, root mean square deviation.

was transferred to the resuspension buffer by multiple rounds of centrifugation using a centrifugal-filter device with a 100-kDa molecular mass cutoff (Centricon, Millipore Inc.). The yield was approximately 100 µg of purified virus.

Crystallization, data collection, and data processing. Purified HPeV-1 at a concentration of 3.5 mg/ml was subjected to sparse-matrix screening using a number of commercially available crystallization screens. The initial hits were obtained at room temperature using 0.1 M Tris-HCl, pH 8.0, 1 M ammonium sulfate in a sitting-drop format. The crystals measured about 30 µm in the largest dimension and diffracted X rays to a resolution of 3.1 Å in the Diamond Light Source beamline I23. In an effort to obtain larger crystals, optimization of the original crystallization conditions centered around testing various salts as precipitants and various divalent cations as additives. The best crystals were obtained in 0.1 M Tris-HCl, pH 8.0, 0.6 M ammonium sulfate, 0.1 M MgCl₂, 5% (wt/vol) glycerol with growth at room temperature for about 3 weeks in a 2.0-µl hanging drop consisting of 0.5 µl reservoir solution and 1.5 µl of purified virus at a concentration of 3.5 mg/ml. Two independent data sets from two different crystals were collected in the Synchrotron Soleil Proxima 1 beamline and processed to a resolution of 3.1 Å using the XDS software package in space group P6₃22 (44). The two data sets were scaled together using the program Aimless from the CCP4 suite (45, 46).

Phasing, model building, and refinement. HPeV-1 crystallized in space group P6₃22. Plots of the 2-fold, 3-fold, and 5-fold self-rotation function calculated using the program GLRF had shown that virions crystallized with one of the icosahedral 3-fold axes aligned with the crystallographic 3-fold axis and icosahedral 2-fold axes aligned with the crystallographic 2-fold axes (47). Reflections between 5 Å and 3.8 Å were used for the calculations. The radius of integration was set to 140 Å. Thus, icosahedral symmetry had to be rotated ($\varphi = 90^\circ$, $\varphi = 90^\circ$, $\kappa = 60^\circ$) according to the XYK polar-angle convention relative to the standard icosahedral orientation as defined by Rossmann and Blow (48). One sixth of a virus particle occupied a crystallographic asymmetric unit. The only possible

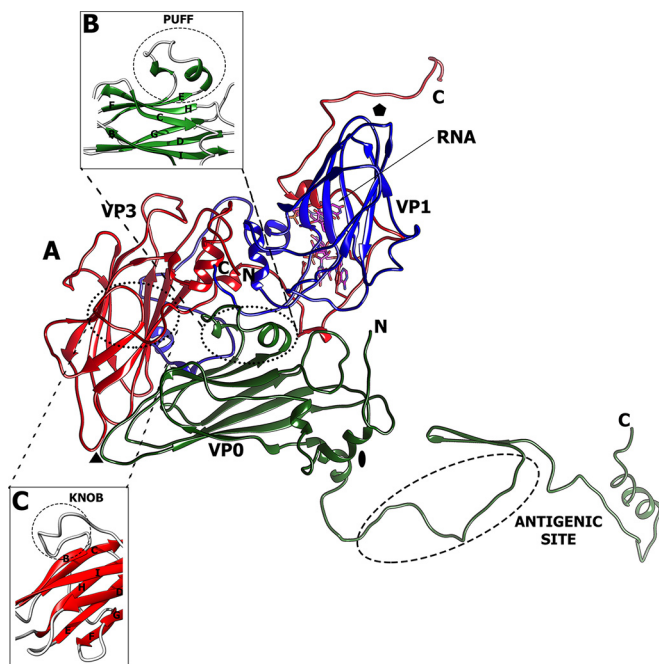


FIG 1 Icosahedral asymmetric unit of HPeV-1. (A) Cartoon representation of major capsid proteins: VP0 (green), VP1 (blue), and VP3 (red). The locations of the 5-fold, 3-fold, and 2-fold symmetry axes are indicated by a pentagon, a triangle, and an oval, respectively. (B and C) The puff (B) and knob (C) loops constituting the major capsid surface features.

way to place the particle center in the crystallographic unit cell was at the intersection of the crystallographic 3-fold and 2-fold axes [$x = a/2$, $y = (atg30^\circ)$, $z = c/4$] (Table 1).

A Protein Data Bank [PDB] model of bovine enterovirus 1 (BeV1) (PDB code 1BEV) converted to polyalanine was used for molecular replacement (28). The model was rotated and positioned in the unit cell and used to calculate the initial phases for reflections up to a resolution of 10 Å in the program CNS (49, 50). The phases were refined by 15 cycles of real-space electron density averaging in the program AVE, using 10-fold noncrystallographic symmetry (NCS) (51). A mask for electron density averaging was generated using the program Mama from the Uppsala Software Factory program package by including all voxels within 5 Å of any atoms of the PDB model of the BeV1 icosahedral asymmetric unit (52). Phase extension was applied in order to obtain phases for higher-resolution reflections (53). The addition of a small fraction of higher-resolution data (one index along the a axis at a time) was followed by three cycles of

averaging. This procedure was repeated until phases were obtained for all the reflections up to a resolution of 3.1 Å. The program SigmaA from the CCP4 package was used to include weights in the electron density calculations (45, 54). Inspection of the resulting electron density map indicated that the molecular-averaging mask was too large. Thus, a new mask was prepared based on a correlation map calculated by comparing electron density distributions among the 10 NCS-related icosahedral asymmetric units. The correlation map was calculated using the program Coma from Uppsala Software Factory (55). A cutoff value of 0.7 was used for the inclusion of voxels in the mask. The phase extension procedure was repeated using the new mask. The resulting map was of sufficient quality to enable model building. The program Buccaneer was used for automated building of the protein part of the model, utilizing the 10-fold NCS present in the crystallographic asymmetric unit (56, 57). The program Nautilus from the CCP4 suite (45) was used for the automated building of RNA chains and was able to build 3 nucleotides, while the remaining 3 nucleotides were built manually using the program Coot (58). The combined protein-RNA model from the automated building was about 80% complete with the assigned amino acid sequence. This initial model was subjected to manual rebuilding using the programs Coot and O (59) and to coordinate and B-factor refinement using the program CNS (49, 50). No water molecules were added, due to the limited resolution of the diffraction data. All the measured reflections were used in the refinement.

Data analysis. The volumes of the particles were calculated using the programs Mama and Voidoo from Uppsala Software Factory (60). Average radii of virions were calculated using the program Moleman2 from Uppsala Software Factory (55). Multiple-sequence alignments were carried out using the ClustalW server (<http://www.ebi.ac.uk/Tools/msa/clustalw2/>) (61). Figures were generated using the programs UCSF Chimera (62), PyMOL (PyMOL Molecular Graphics System, version 1.7.4; Schrödinger, LLC), and RiverM (63). Structure-based pairwise alignments of biological protomers of various picornaviruses were prepared using the program Gr-Align (64). The similarity score provided by Gr-Align was used as an evolutionary distance to construct a nexus format matrix file, which was converted into the phylogenetic tree and visualized with the program SplitsTree (65).

Protein structure accession number. The HPeV-1 model, structure factor amplitudes, and phases derived by phase extension have been deposited in the Protein Data Bank with PDB code 4Z92.

RESULTS AND DISCUSSION

Quality of diffraction data and HPeV-1 structure. The structure of HPeV-1 was determined by X-ray crystallography at a resolution of 3.1 Å. The electron density map resulting from 10-fold NCS averaging enabled the HPeV-1 capsid proteins to be built, except for residues 1 to 31 and 289 of VP0, 1 to 24 and 217 to 235 of VP1, and 1 to 14 of VP3. Identifying the sequences of the indi-

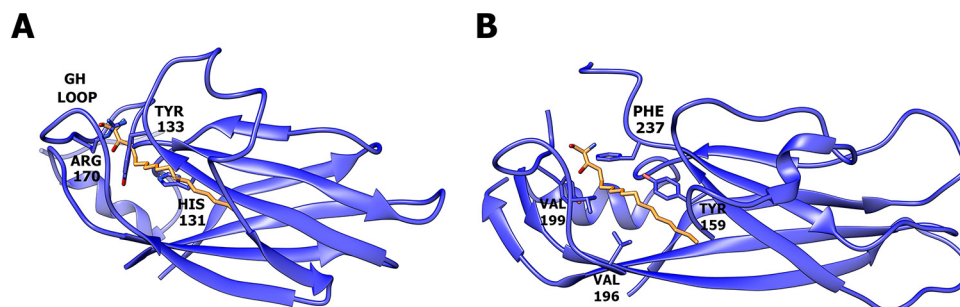


FIG 2 VP1 of HPeV-1 does not contain a hydrophobic pocket. The VP1 proteins of HPeV-1 (A) and poliovirus type 1 (B) are shown as cartoon representations. The pocket factor in poliovirus type 1 is shown as a stick model in orange. The side chains of residues that interact with the pocket factor are also shown as sticks. In panel A, the poliovirus type 1 pocket factor was superimposed onto the HPeV-1 structure. However, the pocket is not formed, and the side chains of several residues clash with the pocket factor.

TABLE 2 Physical parameters of selected picornaviruses

| Virus ^a /PDB code | Diameter (Å) ^b | Virion vol (10 ⁶ Å ³) | Genome size (nucleotides) | RNA density (Å ³ /nucleotide) |
|------------------------------|---------------------------|--|---------------------------|--|
| HPeV-1 | 247 | 6.88 | 7,321 | 10.6 |
| Poliovirus type 1/1ASJ | 256 | 8.70 | 7,433 | 8.6 |
| HRV-16/1AYM | 258 | 8.44 | 7,124 | 8.4 |
| BeV1/1BEV | 259 | 8.14 | 7,414 | 8.0 |
| FMDV/1BTT | 258 | 7.19 | 8,176 | 11.3 |
| HAV/4QPI | 254 | 7.45 | 7,478 | 10.0 |

^a HRV-16, human rhinovirus type 16.

^b Determined as the distance between the center of mass of the capsid protein protomer and the center of the virion.

vidual residues was straightforward, due to the good quality of the electron density map. Six nucleotides corresponding to the RNA genome were modeled per icosahedral asymmetric unit. Water molecules could not be modeled because of the limited resolution of the available diffraction data. If calculated, the R_{free} value would have been very close to the R_{work} value due to the 10-fold NCS (66). Thus, all measured reflections were used in the crystallographic refinement. The basic crystallographic structure quality indicators are listed in Table 1.

Structures of HPeV-1 capsid proteins and virion. The icosahedral asymmetric unit of HPeV-1 consists of subunits VP0, VP1, and VP3 (Fig. 1). The core of each of the capsid proteins is a jelly roll β -sandwich composed of two β -sheets, each containing four antiparallel β -strands. The β -strands are conventionally named B to I, and the two β -sheets contain strands BIDG and CHEF, respectively. The C termini of the capsid proteins are located on the virion surface, while the extended N termini mediate interactions

among the capsid proteins and with the RNA genome on the inner surface of the capsid.

A pocket in the capsid protein VP1, which is present in most picornaviruses, can be targeted by capsid-binding inhibitors. This pocket is not formed in HPeV-1 (Fig. 2). Bulky amino acid side chains of His-131, Tyr-133, and Arg-170 fill the equivalent volume of the cavity, and the mouth of the pocket is occluded by the main-chain atoms of the GH loop (Fig. 2A). This explains the previous findings that the capsid-binding inhibitors that inhibit enteroviruses and rhinoviruses are not effective against parechoviruses (43).

Of the picornaviruses that have been structurally characterized, HPeV-1 has the smallest observed virion, with an average diameter of 247 Å (Table 2). The surface of the HPeV-1 virion is relatively flat in comparison to the other picornaviruses because no canyon is formed (Fig. 3A). This is due to the relative shortening of features on the capsid surface that form the borders of the canyon. The HI loop of VP1, which forms protrusions around a 5-fold axis, is shortened from 12 residues in poliovirus type 1 (PDB code 1ASJ) to 6 residues in HPeV-1, resulting in a decrease in the height of the “northern rim” of the canyon. The “southern rim” of the canyon is mostly formed by two loops called the “puff” and the “knob.” The puff is a loop between β E and β F of VP0/VP2 and in HPeV-1 contains two short 3_{10} helices connected by a 10-residue loop (Fig. 1B). The knob is a loop preceding β B of VP3 and in HPeV-1 contains 10 residues (Fig. 1C). The knob and puff of HPeV-1 are 2 and 65 residues shorter than those found in poliovirus type 1. In addition, the residues forming the puff and knob do not protrude away from the viral surface, as observed in poliovirus type 1 (Fig. 3B).

The availability of the HPeV-1 virion structure enabled the

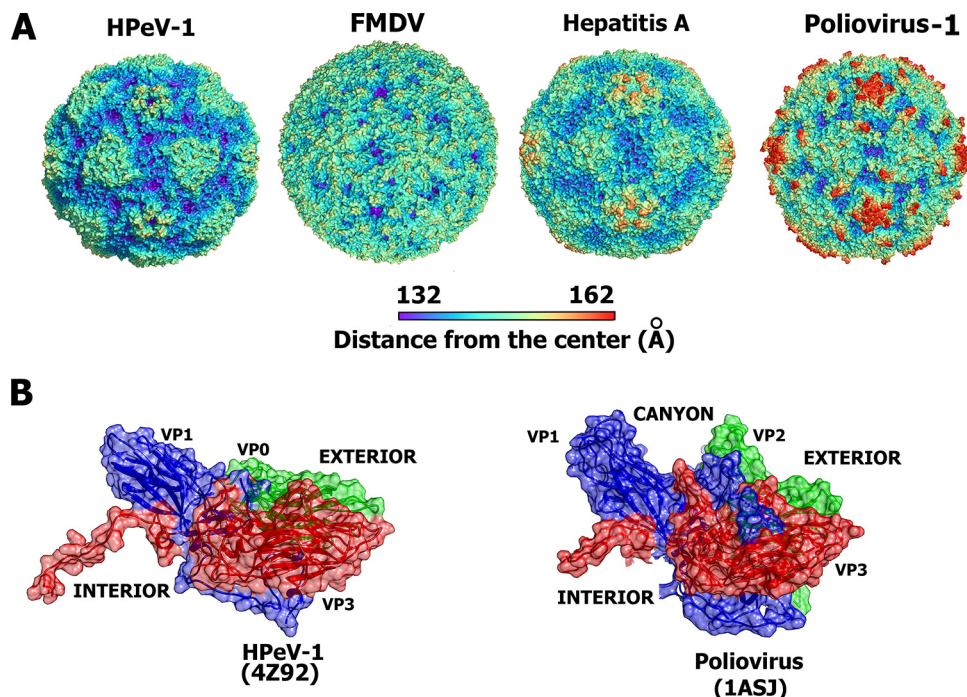


FIG 3 Comparison of virion surface features of selected picornaviruses. (A) Molecular surfaces of selected picornaviruses rainbow colored according to the distance from the particle center. (B) Comparison of side views of biological protomers of HPeV-1 and poliovirus type 1 showing that the canyon is not formed in the HPeV-1 structure. The subunits VP0 and VP2 are shown in green, VP1 in blue, and VP3 in red.

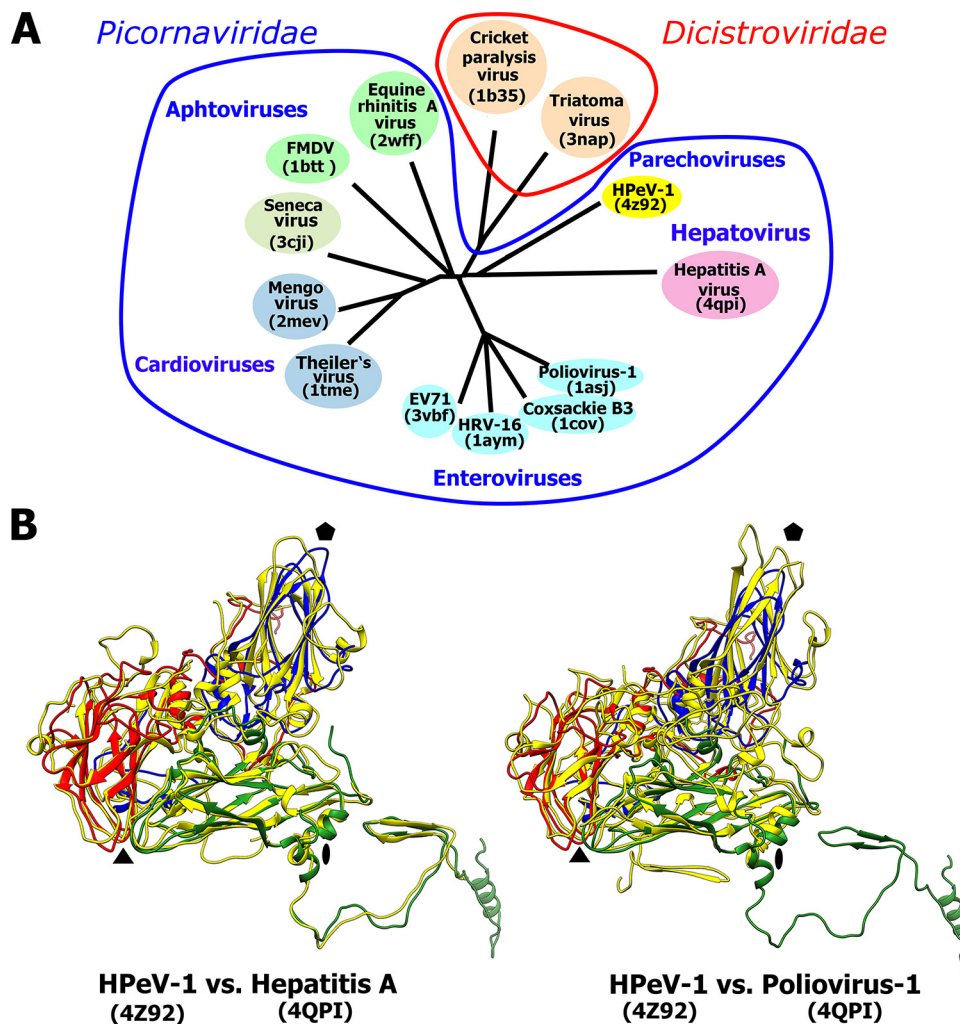


FIG 4 Evolutionary relationship among viruses from the families *Picornaviridae* and *Dicistroviridae* based on structural alignment of capsid proteins. (A) Phylogenetic tree based on structural similarity of icosahedral asymmetric units of the indicated viruses. For details on the construction of the diagram, see Materials and Methods. (B) Icosahedral asymmetric unit of HPeV-1 (VP0, green; VP1, blue; VP3, red) superimposed on those of HAV and poliovirus type 1 (all capsid proteins, yellow). Pentagons, triangles, and ovals indicate the positions of the icosahedral 5-fold, 3-fold, and 2-fold symmetry axes, respectively.

construction of a structure-based phylogenetic tree comparing HPeV-1 to 12 other viruses from the order *Picornavirales* (Fig. 4A). The phylogenetic analysis shows that the HPeV-1 capsid is most similar to that of hepatitis A virus (HAV) from the family *Picornaviridae* and to those of cricket paralysis virus and triatoma virus from the family *Dicistroviridae* (Fig. 4A). The relatively close evolutionary relationship between HPeV-1 and HAV is further indicated by the similar positions of the structured N-terminal arms of HPeV-1 VP0 and of HAV VP2 (Fig. 4B). The structured parts of the N termini of the two viruses mediate interactions among the capsid protein protomers along a line connecting the icosahedral 2-fold and 3-fold axes of the capsid (Fig. 4B). The N-terminal arm of VP2 of poliovirus type 1 has the same function; however, in poliovirus type 1, the structured part of the N-terminal arm of VP2 mediates interactions among protomers different than those in the virions of HPeV-1 and HAV (Fig. 4B). This is an example of domain swapping where part of a protein retains its function; however, its location in the quaternary complex is different. The closer similarity of the HPeV-1 capsid to those of vi-

ruses from the family *Dicistroviridae* than to those of viruses from the family *Picornaviridae*, with the exception of HAV, might be due to the differences in the processing of the polyprotein precursor of capsid proteins. The amino acid sequence of the VP4 subunit is located between VP2 and VP3 in viruses from the family *Dicistroviridae* while it is located before the VP2 sequence in viruses from the family *Picornaviridae*. In contrast, parechovirus capsids do not contain VP4, and this might be reflected in the structural organization of the capsid. Thus, HPeVs might represent an evolutionary link between picornaviruses and other virus families in the order *Picornavirales*, as was previously suggested for HAV (67).

Integrin receptor binding site of HPeV-1. The integrin $\alpha_v\beta_6$ is a cellular receptor for HPeV-1 (24, 25). The integrin binds to an integrin recognition motif, RGD, in the C terminus of VP1. However, the RGD residues are not visible in the HPeV-1 electron density map, probably due to the flexibility of the loop that contains the sequence. The last structured residue of VP1 is Thr-216, which is 6 residues before the integrin-binding sequence (Fig. 5).

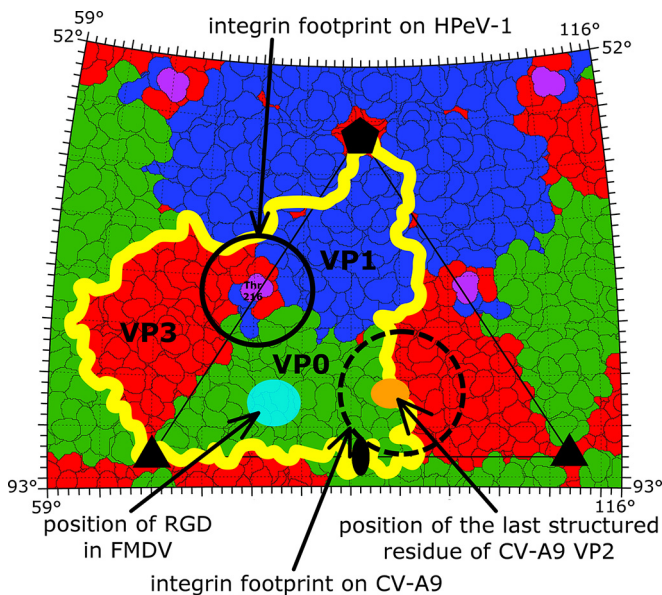


FIG 5 Comparison of $\alpha_v\beta_6$ integrin receptor binding sites of HPeV-1, FMDV, and CV-A9. Shown is a stereographic projection of HPeV-1 surface residues, with subunits VP0, VP1, and VP3 in green, blue, and red, respectively. The yellow line shows the border of a selected protomer. Features of FMDV and CV-A9 were plotted onto the HPeV-1 surface. The last structured C-terminal residue of HPeV-1 VP1 is highlighted in magenta, while that of CV-A9 is shown as an orange oval. The integrin-binding site in HPeV-1 as determined previously by cryo-electron microscopy is encircled by a solid line. The location of the footprint of the integrin receptor on CV-A9 (EMD-5512) is encircled by a dashed line. The conserved RGD motif in FMDV (PDB code 1FOD) is shown as a light-blue oval. The positions of the icosahedral-symmetry axes are indicated by a pentagon (5-fold), triangles (3-fold), and an oval (2-fold).

Seitonen et al. used cryo-electron microscopy to calculate a three-dimensional reconstruction of the HPeV-1–integrin complex (25). Rigid-body fitting of the HPeV-1 virion into the map of the complex enabled us to estimate the location of the RGD motif to be approximately in the middle between the icosahedral 5-fold and 3-fold axes immediately above the last structured residue of VP1 (Fig. 5; see Fig. S1 in the supplemental material). In contrast to HPeV-1, the integrin-binding site in foot and mouth disease virus (FMDV) is located above the core of subunit VP2 in the GH loop of VP1 (Fig. 5) (68). In coxsackievirus A9 (CV-A9), the integrin-binding site is next to the icosahedral 5-fold axis (Fig. 5) (69). Similar to HPeV-1, the RGD residues are not visible in the CV-A9 crystal structure (70). Thus, the location of the RGD sequence in the flexible part of the capsid protein might be required for binding to the integrin receptor. The distinct integrin-binding sites in HPeV-1, FMDV, and CV-A9 indicate a convergent evolution in which the different viruses independently acquired the ability to utilize the integrins as receptors for cell entry.

HPeV-1 virion-antibody interactions. An intravenous immunoglobulin infusion containing large amounts of HPeV-1-neutralizing antibodies proved to be an efficient treatment for parechovirus-induced cardiomyopathy in an infant (3). One of the strongest antigenic sites of HPeV-1 consists of residues 82 to 94 in the N-terminal arm of VP0, which form an extended loop connecting β_3 and α_2 on the inside of the capsid (Fig. 6A) (71, 72). A possible explanation for the high immunogenicity of a sequence

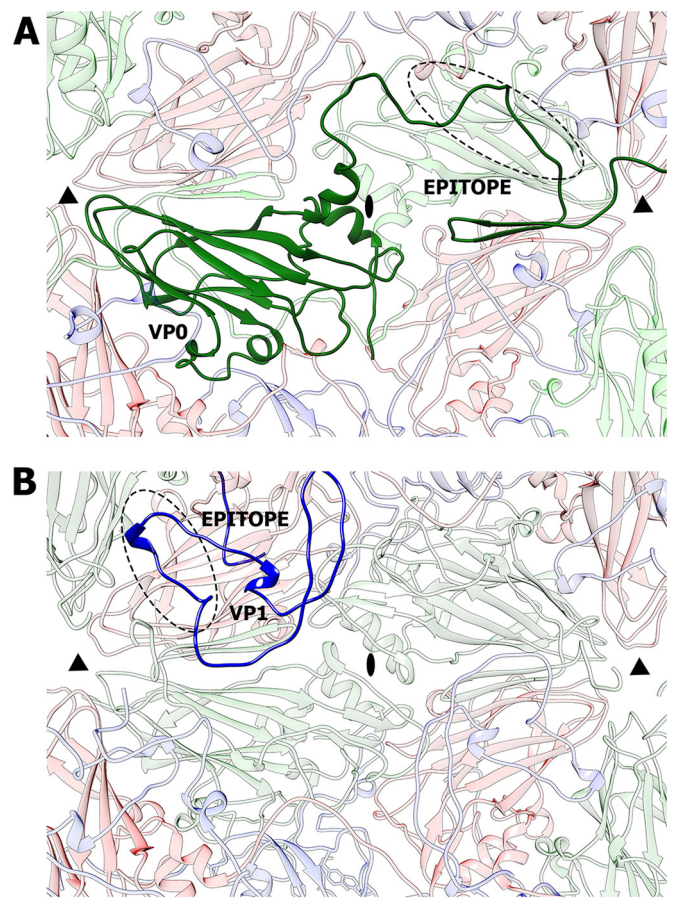


FIG 6 Comparison of internal immunogenic epitopes of HPeV-1 and poliovirus type 1 located at the interpentamer boundary. (A) Interior view of an HPeV-1 particle. A selected VP0 subunit is shown in dark green. Residues 82 to 94, targeted by the neutralizing antibodies, are highlighted with a dashed oval. (B) Interior view of a poliovirus type 1 particle. The N-terminal arm of a selected VP1 subunit is shown in dark blue. The immunogenic epitope, consisting of residues 33 to 54 of VP1, is highlighted with a dashed oval. The positions of the 2-fold and 3-fold icosahedral-symmetry axes are indicated by ovals and triangles, respectively.

that is inside the capsid is the dynamic motions of virions referred to as “capsid breathing.” Even residues that are located on the inside of the capsid can be temporarily exposed on the virion surface and may be accessible to antibodies. Similar targeting of internal peptides by antibodies has been described in other picornaviruses (73, 74). In poliovirus type 1, antibodies can bind to residues 34 to 53 of VP1 located on the interior of the particle (Fig. 6B) (73, 75). The buried antigenic sites of poliovirus type 1 and HPeV-1 are located at the interpentamer boundary (Fig. 6B). The immunological reactivity of the buried epitopes suggests that they might be temporarily exposed on the capsid surface without disrupting the integrity of the virion.

Role of N termini of VP0 subunits in mediating interpentamer contacts within the HPeV-1 capsid. The N-terminal part of HPeV-1 VP0 corresponds to the residues of VP4 and of the N terminus of VP2 in enteroviruses, according to the positions of the amino acids in the polyprotein precursors of the capsid proteins. However, the locations of the structured residues of the N terminus of VP0 in the HPeV-1 capsid are different from those of VP2

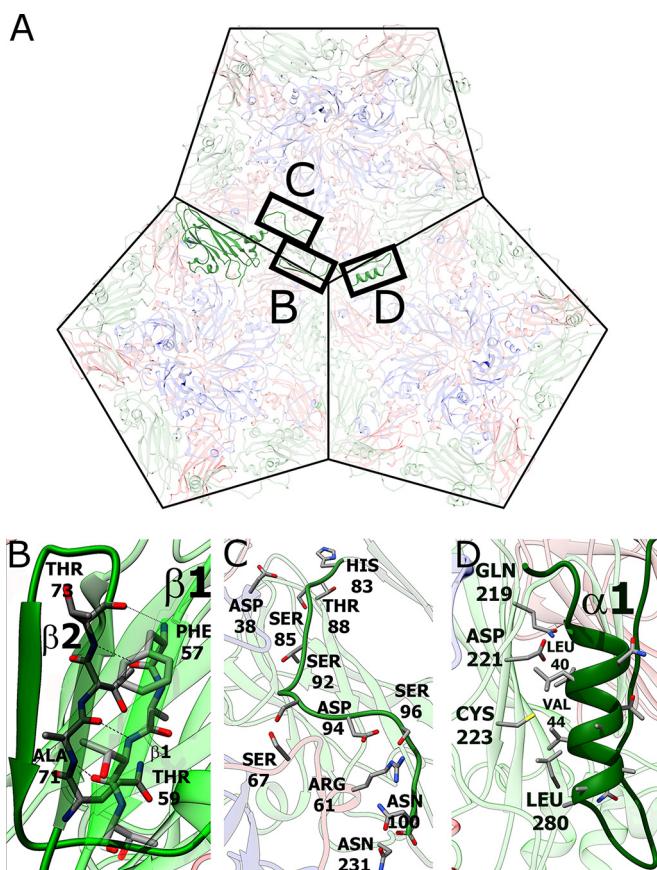


FIG 7 Role of the N-terminal arm of VP0 in interpentamer interactions. (A) The N-terminal arm of VP0 mediates contacts among three pentamers in the HPeV-1 virion. Shown is a view from inside the virion. (B) Interactions between antiparallel β -strands β 1 and β 2 of VP0 proteins from two adjacent pentamers. (C) Residues 83 to 100 of VP1 interact with residues from all three subunits, VP0, VP1, and VP3. (D) Interactions of α 1 with β G of VP0 from another, neighboring pentamer.

and VP4 in poliovirus type 1 and other enteroviruses while they are similar to those of HAV (Fig. 4). In HPeV-1, the structured N-terminal part of VP0 forms a tentacle-like extension that interacts with capsid proteins from two neighboring pentamers (Fig. 7A). Residues from the VP0 N terminus following helix α 1 form stabilizing interactions with other parts of the capsid, including the following: (i) residues between β 3 and α 2 of VP0 form hydrogen bonds to Ser-67 and Arg-71 of VP3 and Asp-38 of VP1 subunits in the neighboring pentamer (Fig. 7B) and (ii) β 1 of VP0 forms a two-stranded antiparallel β -sheet with β 2 of VP0 in another adjacent pentamer (Fig. 7C). The N-terminal part of parechovirus VP0 might be homologous to VP4 of enteroviruses, which has to be released from the virion in order to ensure delivery of the virus genome across the endosomal membrane into the cytoplasm. Therefore, upon cell entry, the N terminus of VP0 might be required for interaction with the host cell membranes. Since the VP0 N termini are involved in interpentamer interactions, alteration of their structure leads to capsid disruption. Thus, the role of the VP0 N-terminal arm in mediating interactions among the pentamers within the HPeV-1 capsid might explain why the parechovirus capsids disassemble into pentamers after genome release *in vitro* (36). The first N-terminal residues of VP0

that are visible in the HPeV-1 electron density map form helix α 1, which contains predominantly hydrophobic amino acids. The side chains of residues from helix α 1 interact with the polar side chains of the residues from β G of subunit VP0 in the adjacent pentamer (Fig. 7D). The unfavorable nature of α 1- β G interactions indicates that they are not required for capsid stability. The average B factor of α 1 atoms is 51 \AA^2 , while it is 40 \AA^2 for the whole capsid. The elevated B factor shows that the helix is more mobile and might be ready for exposure at the virion surface and interaction with membranes. However, it is possible that the part of the VP0 N terminus that is not visible in the structure (the first 30 residues) is responsible for interaction with the host membranes. In that case, the disruption of the HPeV-1 capsids into pentamers would not be required to ensure transfer of the ssRNA genome across the biological membrane.

The putative role of the HPeV-1 genome in HPeV-1 virion stability and assembly. The HPeV-1 virion has an inner volume of $6.9 \times 10^6 \text{ \AA}^3$ (Table 2). This is 20% smaller than the interior particle volumes of both poliovirus type 1 and rhinovirus type 16. However, the size of the genome of HPeV-1 is similar to that of poliovirus type 1, leading to a higher RNA density than in enteroviruses but similar to that in FMDV and HAV (Table 2). Furthermore, the internal surface of the HPeV-1 capsid around the 5-fold axis is more positively charged than the corresponding areas in other picornaviruses (see Fig. S2 in the supplemental material). This is probably required to neutralize the negative charge of the tightly packed RNA.

An electron density corresponding to an RNA hexanucleotide associated with each icosahedral asymmetric unit is located close to the 5-fold icosahedral axis on the inside of the HPeV-1 capsid (Fig. 8). The HPeV-1 genome is a linear RNA molecule that forms unique interactions with the inner surface of the capsid. However, the RNA does not affect the packing of particles within the crystal or the measured diffraction data, and therefore, it contains information about the icosahedrally averaged RNA structure. Thus, the observed RNA density corresponds to an averaged nucleotide sequence. The shapes of the electron densities of the individual bases indicate that the first nucleotide is a purine, while the following 5 nucleotides are pyrimidines. The RNA was modeled as an adenosine followed by five uridines (Fig. 8B). The average B factor of the RNA is 71 \AA^2 , while that of the protein part of the capsid is 40 \AA^2 , indicating higher mobility of the RNA. A crystallographic refinement resulted in 94% occupancy of the RNA, showing that the RNA is bound to nearly all the available positions in the icosahedral capsid. Each hexanucleotide forms extensive interactions with one VP1 and three VP3 subunits belonging to different protomers from one pentamer (Fig. 8). Overall, the 60 copies of the ordered hexanucleotides represent 5% of the 7,500-nucleotide genome.

The HPeV-1 virion contains more ordered RNA than is seen in other picornaviruses, in which only 1 or 2 nucleotides are observed (27, 76, 77). For example, in enteroviruses, a nucleotide base makes stacking interactions with a conserved tryptophan residue of VP1 located close to the icosahedral 2-fold axis (76). However, the partly ordered genomic RNA has been previously observed in a bean pod mottle virus (BPMV) from the family *Secoviridae* of the order *Picornavirales* (78). In BPMV, the RNA interacts with the capsid proteins close to the icosahedral 3-fold axis, while in HPeV-1, the RNA binds close to the 5-fold axis (see Fig. S3 in the supplemental material). The differences in the RNA-

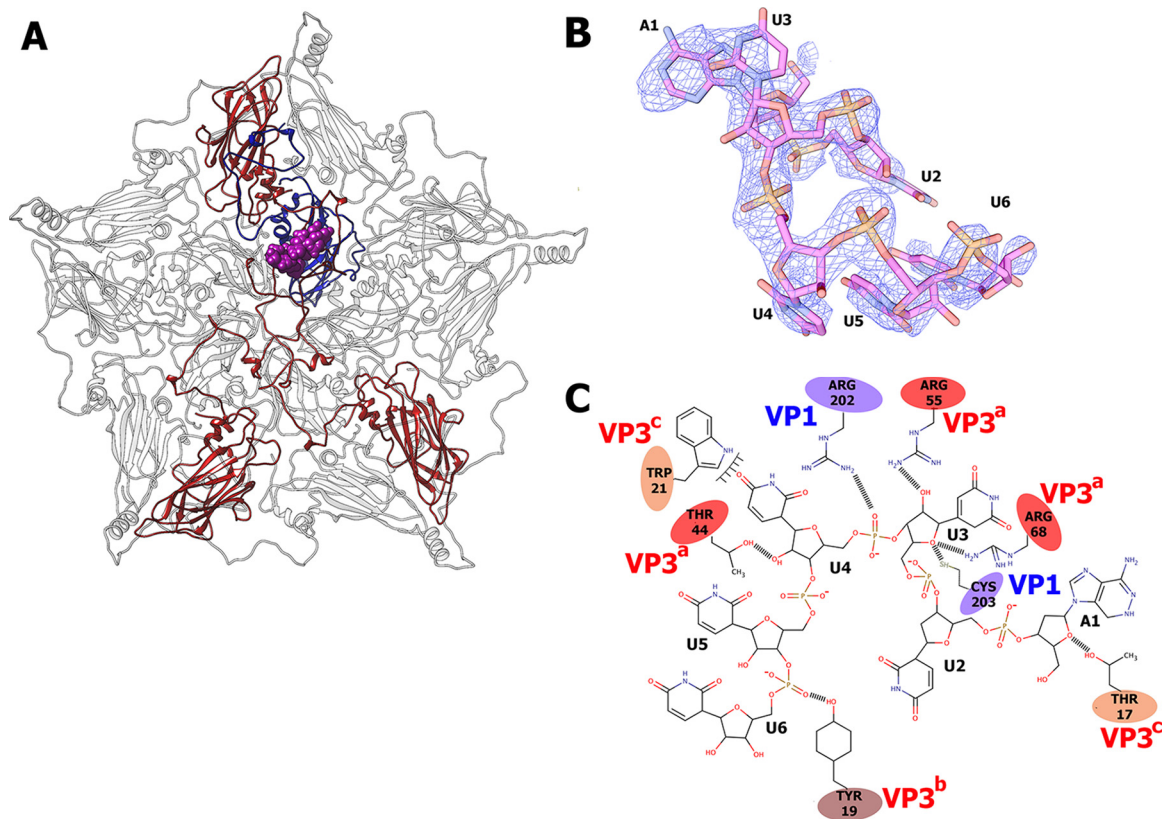


FIG 8 Interactions of HPeV-1 genomic RNA with the capsid. (A) Location of an RNA hexanucleotide (shown as a space-filling model in magenta) within the pentamer of capsid protein protomers as seen from inside the virion. Subunits in contact with RNA are shown in color (VP1, blue, and VP3s, red). (B) Electron density map of RNA hexanucleotide contoured at 2σ . (C) Two-dimensional representation of RNA-protein interactions. Hydrophobic interactions and hydrogen bonds are shown. VP3 subunits from different icosahedral asymmetric units are distinguished by the label colors and superscript a, b, and c.

protein interactions between the two viruses indicate that the two viruses might differ in the structures of their packaged genomes. It is likely that the genome organization in HPeV-1 virions is also different from that in enteroviruses, which may be due to the necessity to package the genome with a higher density. The complete conservation of the RNA binding residues among HPeVs, together with the nearly complete occupancy of the RNA, indicates that the binding might have a role in virion assembly and perhaps also in ensuring the selective packaging of HPeV genomes into capsids. Small molecules that interfere with the genomic-RNA-capsid protein interactions could therefore be developed into antiviral compounds preventing HPeV virion assembly.

ACKNOWLEDGMENTS

We thank Charles Sabin and Synchrotron Soleil Proxima 1/Proxima 2A and beamline scientists Martin Slavko and Beatriz Guimaraes for their help with crystal screening and data collection. We thank the synchrotron Diamond beamline scientists for their help with preliminary crystal screening and data collection. We also thank Noel Malod-Dognin and Daniel Lundin for their help with structure-based phylogenetic analysis.

The research leading to these results received funding from the European Research Council under the European Union's Seventh Framework Programme, (FP/2007-2013)/ERC grant agreement no. 355855', and from EMBO installation grant no. 3041 to Pavel Plevka.

L.P. optimized and conducted large-scale virus purifications. S.K. performed crystallization, model building, refinement, and data analysis and participated in manuscript preparation. P.P. designed the study, per-

formed structure determination, directed and participated in data analysis, and wrote the manuscript.

FUNDING INFORMATION

EC | European Research Council (ERC) provided funding to Pavel Plevka under grant number 335855. European Molecular Biology Organization (EMBO) provided funding to Pavel Plevka under grant number 3041.

REFERENCES

- Boivin G, Abed Y, Boucher FD. 2005. Human parechovirus 3 and neonatal infections. *Emerg Infect Dis* 11:103–105. <http://dx.doi.org/10.3201/eid1101.040606>.
- Schuffenecker I, Javouhey E, Gillet Y, Kugener B, Billaud G, Floret D, Lina B, Morfin F. 2012. Human parechovirus infections, Lyon, France, 2008–10: evidence for severe cases. *J Clin Virol* 54:337–341. <http://dx.doi.org/10.1016/j.jcv.2012.04.016>.
- Wildenbeest JG, Wolthers KC, Straver B, Pajkrt D. 2013. Successful IVIG treatment of human parechovirus-associated dilated cardiomyopathy in an infant. *Pediatrics* 132:e243–e247. <http://dx.doi.org/10.1542/peds.2012-1136>.
- Stanway G, Joki-Korpela P, Hyypia T. 2000. Human parechoviruses—biology and clinical significance. *Rev Med Virol* 10:57–69.
- Esposito S, Rahamat-Langendoen J, Ascolese B, Senatore L, Castellazzi L, Niesters HG. 2014. Pediatric parechovirus infections. *J Clin Virol* 60:84–89. <http://dx.doi.org/10.1016/j.jcv.2014.03.003>.
- Verboon-Macielek MA, Groenendaal F, Hahn CD, Hellmann J, van Loon AM, Boivin G, de Vries LS. 2008. Human parechovirus causes encephalitis with white matter injury in neonates. *Ann Neurol* 64:266–273. <http://dx.doi.org/10.1002/ana.21445>.
- Levorson RE, Jantusch BA, Wiedermann BL, Spiegel HM, Campos JM.

2009. Human parechovirus-3 infection: emerging pathogen in neonatal sepsis. *Pediatr Infect Dis J* 28:545–547. <http://dx.doi.org/10.1097/INF.0b013e318194596a>.
8. Wigand R, Sabin AB. 1961. Properties of ECHO types 22, 23 and 24 viruses. *Arch Gesamte Virusforsch* 11:224–247. <http://dx.doi.org/10.1007/BF01241688>.
 9. Anonymous. 1955. ENTERIC cytopathogenic human orphan (ECHO) viruses. *Science* 122:1187–1188. <http://dx.doi.org/10.1126/science.122.3181.1187>.
 10. King AMQ, Adams MJ, Carstens EB, Lefkowitz EJ (ed). 2012. Virus taxonomy. Ninth report of the International Committee on Taxonomy of Viruses. Elsevier Academic Press, Waltham, MA.
 11. Stanway G, Kalkkinen N, Roivainen M, Ghazi F, Khan M, Smyth M, Meurman O, Hyyppia T. 1994. Molecular and biological characteristics of echovirus 22, a representative of a new picornavirus group. *J Virol* 68:8232–8238.
 12. Sun G, Wang Y, Tao G, Shen Q, Cao W, Chang X, Zhang W, Shao C, Yi M, Shao S, Yang Y. 2012. Complete genome sequence of a novel type of human parechovirus strain reveals natural recombination events. *J Virol* 86:8892–8893. <http://dx.doi.org/10.1128/JVI.01241-12>.
 13. Williams CH, Panayiotou M, Girling GD, Peard CI, Oikarinen S, Hyoty H, Stanway G. 2009. Evolution and conservation in human parechovirus genomes. *J Gen Virol* 90:1702–1712. <http://dx.doi.org/10.1099/vir.0.008813-0>.
 14. Sedmak G, Nix WA, Jentzen J, Haupt TE, Davis JP, Bhattacharyya S, Pallansch MA, Oberste MS. 2010. Infant deaths associated with human parechovirus infection in Wisconsin. *Clin Infect Dis* 50:357–361. <http://dx.doi.org/10.1086/649863>.
 15. Li L, Victoria J, Kapoor A, Naeem A, Shaikat S, Sharif S, Alam MM, Angez M, Zaidi SZ, Delwart E. 2009. Genomic characterization of novel human parechovirus type. *Emerg Infect Dis* 15:288–291. <http://dx.doi.org/10.3201/eid1502.080341>.
 16. Hyyppia T, Horsnell C, Maaronen M, Khan M, Kalkkinen N, Auvinen P, Kinnunen L, Stanway G. 1992. A distinct picornavirus group identified by sequence analysis. *Proc Natl Acad Sci U S A* 89:8847–8851. <http://dx.doi.org/10.1073/pnas.89.18.8847>.
 17. Arnold E, Luo M, Vriend G, Rossmann MG, Palmenberg AC, Parks GD, Nicklin MJ, Wimmer E. 1987. Implications of the picornavirus capsid structure for polyprotein processing. *Proc Natl Acad Sci U S A* 84:21–25. <http://dx.doi.org/10.1073/pnas.84.1.21>.
 18. Basavappa R, Syed R, Flore O, Icenogle JP, Filman DJ, Hogle JM. 1994. Role and mechanism of the maturation cleavage of VP0 in poliovirus assembly: structure of the empty capsid assembly intermediate at 2.9 Å resolution. *Protein Sci* 3:1651–1669. <http://dx.doi.org/10.1002/pro.5560031005>.
 19. Stanway G, Hyyppia T. 1999. Parechoviruses. *J Virol* 73:5249–5254.
 20. Rossmann MG. 1989. The canyon hypothesis. Hiding the host cell receptor attachment site on a viral surface from immune surveillance. *J Biol Chem* 264:14587–14590.
 21. He Y, Chipman PR, Howitt J, Bator CM, Whitt MA, Baker TS, Kuhn RJ, Anderson CW, Freimuth P, Rossmann MG. 2001. Interaction of coxsackievirus B3 with the full length coxsackievirus-adenovirus receptor. *Nat Struct Biol* 8:874–878. <http://dx.doi.org/10.1038/nsb1001-874>.
 22. Xiao C, Bator CM, Bowman VD, Rieder E, He Y, Hebert B, Bella J, Baker TS, Wimmer E, Kuhn RJ, Rossmann MG. 2001. Interaction of coxsackievirus A21 with its cellular receptor, ICAM-1. *J Virol* 75:2444–2451. <http://dx.doi.org/10.1128/JVI.75.5.2444-2451.2001>.
 23. Olson NH, Kolatkar PR, Oliveira MA, Cheng RH, Greve JM, McClelland A, Baker TS, Rossmann MG. 1993. Structure of a human rhinovirus complexed with its receptor molecule. *Proc Natl Acad Sci U S A* 90:507–511. <http://dx.doi.org/10.1073/pnas.90.2.507>.
 24. Boonyakiat Y, Hughes PJ, Ghazi F, Stanway G. 2001. Arginine-glycine-aspartic acid motif is critical for human parechovirus 1 entry. *J Virol* 75:10000–10004. <http://dx.doi.org/10.1128/JVI.75.20.10000-10004.2001>.
 25. Seitsonen J, Susi P, Heikkilä O, Sinkovits RS, Laurinmaki P, Hyyppia T, Butcher SJ. 2010. Interaction of alphaVbeta3 and alphaVbeta6 integrins with human parechovirus 1. *J Virol* 84:8509–8519. <http://dx.doi.org/10.1128/JVI.02176-09>.
 26. Rossmann MG, He Y, Kuhn RJ. 2002. Picornavirus-receptor interactions. *Trends Microbiol* 10:324–331. [http://dx.doi.org/10.1016/S0966-842X\(02\)02383-1](http://dx.doi.org/10.1016/S0966-842X(02)02383-1).
 27. Filman DJ, Syed R, Chow M, Macadam AJ, Minor PD, Hogle JM. 1989. Structural factors that control conformational transitions and serotype specificity in type 3 poliovirus. *EMBO J* 8:1567–1579.
 28. Smyth M, Tate J, Hoey E, Lyons C, Martin S, Stuart D. 1995. Implications for viral uncoating from the structure of bovine enterovirus. *Nat Struct Biol* 2:224–231. <http://dx.doi.org/10.1038/nsb0395-224>.
 29. Smyth M, Pettitt T, Symonds A, Martin J. 2003. Identification of the pocket factors in a picornavirus. *Arch Virol* 148:1225–1233. <http://dx.doi.org/10.1007/s00705-002-0974-4>.
 30. Plevka P, Perera R, Yap ML, Cardosa J, Kuhn RJ, Rossmann MG. 2013. Structure of human enterovirus 71 in complex with a capsid-binding inhibitor. *Proc Natl Acad Sci U S A* 110:5463–5467. <http://dx.doi.org/10.1073/pnas.1222379110>.
 31. Bakker SE, Gropelli E, Pearson AR, Stockley PG, Rowlands DJ, Ranson NA. 2014. Limits of structural plasticity in a picornavirus capsid revealed by a massively expanded equine rhinitis A virus particle. *J Virol* 88:6093–6099. <http://dx.doi.org/10.1128/JVI.01979-13>.
 32. Fuchs R, Blaas D. 2012. Productive entry pathways of human rhinoviruses. *Adv Virol* 2012:826301. <http://dx.doi.org/10.1155/2012/826301>.
 33. Garriga D, Pickl-Herk A, Luque D, Wruss J, Caston JR, Blaas D, Verdagner N. 2012. Insights into minor group rhinovirus uncoating: the X-ray structure of the HRV2 empty capsid. *PLoS Pathog* 8:e1002473. <http://dx.doi.org/10.1371/journal.ppat.1002473>.
 34. Levy HC, Bostina M, Filman DJ, Hogle JM. 2010. Catching a virus in the act of RNA release: a novel poliovirus uncoating intermediate characterized by cryo-electron microscopy. *J Virol* 84:4426–4441. <http://dx.doi.org/10.1128/JVI.02393-09>.
 35. Bostina M, Levy H, Filman DJ, Hogle JM. 2011. Poliovirus RNA is released from the capsid near a twofold symmetry axis. *J Virol* 85:776–783. <http://dx.doi.org/10.1128/JVI.00531-10>.
 36. Shakeel S. 2014. Human picornaviruses: uncoating, assembly and interaction with cellular receptors. University of Helsinki, Helsinki, Finland.
 37. De Palma AM, Vlieghe I, De Clercq E, Neyts J. 2008. Selective inhibitors of picornavirus replication. *Med Res Rev* 28:823–884. <http://dx.doi.org/10.1002/med.20125>.
 38. Thibaut HJ, De Palma AM, Neyts J. 2012. Combating enterovirus replication: state-of-the-art on antiviral research. *Biochem Pharmacol* 83:185–192. <http://dx.doi.org/10.1016/j.bcp.2011.08.016>.
 39. Smith TJ, Kremer MJ, Luo M, Vriend G, Arnold E, Kamer G, Rossmann MG, McKinlay MA, Diana GD, Otto MJ. 1986. The site of attachment in human rhinovirus 14 for antiviral agents that inhibit uncoating. *Science* 233:1286–1293. <http://dx.doi.org/10.1126/science.3018924>.
 40. Grant RA, Hiremath CN, Filman DJ, Syed R, Andries K, Hogle JM. 1994. Structures of poliovirus complexes with anti-viral drugs: implications for viral stability and drug design. *Curr Biol* 4:784–797.
 41. Rotbart HA. 2000. Antiviral therapy for enteroviruses and rhinoviruses. *Antivir Chem Chemother* 11:261–271. <http://dx.doi.org/10.1177/095632020001100402>.
 42. Rotbart HA, Webster AD, Pleconaril Treatment Registry Group. 2001. Treatment of potentially life-threatening enterovirus infections with pleconaril. *Clin Infect Dis* 32:228–235. <http://dx.doi.org/10.1086/318452>.
 43. van de Ven AA, Douma JW, Rademaker C, van Loon AM, Wensing AM, Boelens JJ, Sanders EA, van Montfrans JM. 2011. Pleconaril-resistant chronic parechovirus-associated enteropathy in agammaglobulinemia. *Antivir Ther* 16:611–614. <http://dx.doi.org/10.3851/IMP1792>.
 44. Kabsch W. 2010. Xds. *Acta Crystallogr D Biol Crystallogr* 66:125–132. <http://dx.doi.org/10.1107/S0907444909047337>.
 45. Winn MD, Ballard CC, Cowtan KD, Dodson EJ, Emsley P, Evans PR, Keegan RM, Krissinel EB, Leslie AG, McCoy A, McNicholas SJ, Murshudov GN, Pannu NS, Potterton EA, Powell HR, Read RJ, Vagin A, Wilson KS. 2011. Overview of the CCP4 suite and current developments. *Acta Crystallogr D Biol Crystallogr* 67:235–242. <http://dx.doi.org/10.1107/S0907444910045749>.
 46. Evans P. 2006. Scaling and assessment of data quality. *Acta Crystallogr D Biol Crystallogr* 62:72–82. <http://dx.doi.org/10.1107/S0907444905036693>.
 47. Tong L, Rossmann MG. 1997. Rotation function calculations with GLRF program. *Methods Enzymol* 276:594–611. [http://dx.doi.org/10.1016/S0076-6879\(97\)76080-4](http://dx.doi.org/10.1016/S0076-6879(97)76080-4).
 48. Rossmann MG, Blow DM. 1962. Detection of sub-units within crystallographic asymmetric unit. *Acta Crystallogr* 15:24–31. <http://dx.doi.org/10.1107/S0365110X62000067>.
 49. Brunger AT, Adams PD, Clore GM, DeLano WL, Gros P, Grosse-Kunstleve RW, Jiang JS, Kuszewski J, Nilges M, Pannu NS, Read RJ, Rice LM, Simonson T, Warren GL. 1998. Crystallography and NMR

- system: a new software suite for macromolecular structure determination. *Acta Crystallogr D Biol Crystallogr* 54:905–921.
50. Brunger AT. 2007. Version 1.2 of the crystallography and NMR system. *Nat Protoc* 2:2728–2733. <http://dx.doi.org/10.1038/nprot.2007.406>.
 51. Kleywegt GJ, Read RJ. 1997. Not your average density. *Structure* 5:1557–1569. [http://dx.doi.org/10.1016/S0969-2126\(97\)00305-5](http://dx.doi.org/10.1016/S0969-2126(97)00305-5).
 52. Kleywegt GJ, Jones TA. 1999. Software for handling macromolecular envelopes. *Acta Crystallogr D Biol Crystallogr* 55:941–944. <http://dx.doi.org/10.1107/S0907444999001031>.
 53. Rossmann MG. 1995. Ab initio phase determination and phase extension using non-crystallographic symmetry. *Curr Opin Struct Biol* 5:650–655. [http://dx.doi.org/10.1016/0959-440X\(95\)80058-1](http://dx.doi.org/10.1016/0959-440X(95)80058-1).
 54. Read RJ. 1986. Improved Fourier coefficients for maps using phases from partial structures with errors. *Acta Crystallogr A* 42:140–149. <http://dx.doi.org/10.1107/S0108767386099622>.
 55. Kleywegt GJ. 1999. Experimental assessment of differences between related protein crystal structures. *Acta Crystallogr D Biol Crystallogr* 55:1878–1884. <http://dx.doi.org/10.1107/S0907444999010495>.
 56. Cowtan K. 2006. The Buccaneer software for automated model building. 1. Tracing protein chains. *Acta Crystallogr D Biol Crystallogr* 62:1002–1011. <http://dx.doi.org/10.1107/S0907444906022116>.
 57. Cowtan K. 2008. Fitting molecular fragments into electron density. *Acta Crystallogr D Biol Crystallogr* 64:83–89. <http://dx.doi.org/10.1107/S0907444907033938>.
 58. Emsley P, Cowtan K. 2004. Coot: model-building tools for molecular graphics. *Acta Crystallogr D Biol Crystallogr* 60:2126–2132. <http://dx.doi.org/10.1107/S0907444904019158>.
 59. Jones TA, Zou JY, Cowan SW, Kjeldgaard M. 1991. Improved methods for building protein models in electron density maps and the location of errors in these models. *Acta Crystallogr A* 47:110–119. <http://dx.doi.org/10.1107/S0108767390010224>.
 60. Kleywegt GJ, Jones TA. 1994. Detection, delineation, measurement and display of cavities in macromolecular structures. *Acta Crystallogr D Biol Crystallogr* 50:178–185. <http://dx.doi.org/10.1107/S0907444993011333>.
 61. Chenna R, Sugawara H, Koike T, Lopez R, Gibson TJ, Higgins DG, Thompson JD. 2003. Multiple sequence alignment with the Clustal series of programs. *Nucleic Acids Res* 31:3497–3500. <http://dx.doi.org/10.1093/nar/gkg500>.
 62. Pettersen EF, Goddard TD, Huang CC, Couch GS, Greenblatt DM, Meng EC, Ferrin TE. 2004. UCSF Chimera—a visualization system for exploratory research and analysis. *J Comput Chem* 25:1605–1612. <http://dx.doi.org/10.1002/jcc.20084>.
 63. Xiao C, Rossmann MG. 2007. Interpretation of electron density with stereographic roadmap projections. *J Struct Biol* 158:182–187. <http://dx.doi.org/10.1016/j.jsb.2006.10.013>.
 64. Malod-Dognin N, Przulj N. 2014. GR-Align: fast and flexible alignment of protein 3D structures using graphlet degree similarity. *Bioinformatics* 30:1259–1265. <http://dx.doi.org/10.1093/bioinformatics/btu020>.
 65. Huson DH. 1998. SplitsTree: analyzing and visualizing evolutionary data. *Bioinformatics* 14:68–73. <http://dx.doi.org/10.1093/bioinformatics/14.1.68>.
 66. Kleywegt GJ, Brunger AT. 1996. Checking your imagination: applications of the free R value. *Structure* 4:897–904. [http://dx.doi.org/10.1016/S0969-2126\(96\)00097-4](http://dx.doi.org/10.1016/S0969-2126(96)00097-4).
 67. Wang X, Ren J, Gao Q, Hu Z, Sun Y, Li X, Rowlands DJ, Yin W, Wang J, Stuart DJ, Rao Z, Fry EE. 2015. Hepatitis A virus and the origins of picornaviruses. *Nature* 517:85–88. <http://dx.doi.org/10.1038/nature13806>.
 68. Logan D, Abu-Ghazaleh R, Blakemore W, Curry S, Jackson T, King A, Lea S, Lewis R, Newman J, Parry N, Rowlands D, Stuart D, Fry E. 1993. Structure of a major immunogenic site on foot-and-mouth disease virus. *Nature* 362:566–568. <http://dx.doi.org/10.1038/362566a0>.
 69. Shakeel S, Seitsonen JJ, Kajander T, Laurinmaki P, Hyypia T, Susi P, Butcher SJ. 2013. Structural and functional analysis of coxsackievirus A9 integrin alphavbeta6 binding and uncoating. *J Virol* 87:3943–3951. <http://dx.doi.org/10.1128/JVI.02989-12>.
 70. Hendry E, Hatanaka H, Fry E, Smyth M, Tate J, Stanway G, Santti J, Maaronen M, Hyypia T, Stuart D. 1999. The crystal structure of coxsackievirus A9: new insights into the uncoating mechanisms of enteroviruses. *Structure* 7:1527–1538. [http://dx.doi.org/10.1016/S0969-2126\(00\)88343-4](http://dx.doi.org/10.1016/S0969-2126(00)88343-4).
 71. Joki-Korpela P, Roivainen M, Lankinen H, Poyry T, Hyypia T. 2000. Antigenic properties of human parechovirus 1. *J Gen Virol* 81:1709–1718. <http://dx.doi.org/10.1099/0022-1317-81-7-1709>.
 72. Alho A, Marttila J, Ilonen J, Hyypia T. 2003. Diagnostic potential of parechovirus capsid proteins. *J Clin Microbiol* 41:2294–2299. <http://dx.doi.org/10.1128/JCM.41.6.2294-2299.2003>.
 73. Roivainen M, Piirainen L, Rysa T, Narvanen A, Hovi T. 1993. An immunodominant N-terminal region of VP1 protein of poliovirus that is buried in crystal structure can be exposed in solution. *Virology* 195:762–765. <http://dx.doi.org/10.1006/viro.1993.1427>.
 74. Park KB, Lim BK, Ye MB, Chung SY, Nam JH. 2012. A peptide vaccine based on a B-cell epitope on the VP1 protein of enterovirus 70 induces a strong antibody response. *Acta Virol* 56:337–342. http://dx.doi.org/10.4149/av_2012_04_337.
 75. Lin J, Lee LY, Roivainen M, Filman DJ, Hogle JM, Belnap DM. 2012. Structure of the Fab-labeled “breathing” state of native poliovirus. *J Virol* 86:5959–5962. <http://dx.doi.org/10.1128/JVI.05990-11>.
 76. Hadfield AT, Lee W, Zhao R, Oliveira MA, Minor I, Rueckert RR, Rossmann MG. 1997. The refined structure of human rhinovirus 16 at 2.15 Å resolution: implications for the viral life cycle. *Structure* 5:427–441. [http://dx.doi.org/10.1016/S0969-2126\(97\)00199-8](http://dx.doi.org/10.1016/S0969-2126(97)00199-8).
 77. Arnold E, Rossmann MG. 1990. Analysis of the structure of a common cold virus, human rhinovirus 14, refined at a resolution of 3.0 Å. *J Mol Biol* 211:763–801. [http://dx.doi.org/10.1016/0022-2836\(90\)90076-X](http://dx.doi.org/10.1016/0022-2836(90)90076-X).
 78. Chen ZG, Stauffacher C, Li Y, Schmidt T, Bomu W, Kamer G, Shanks M, Lomonosoff G, Johnson JE. 1989. Protein-RNA interactions in an icosahedral virus at 3.0 Å resolution. *Science* 245:154–159. <http://dx.doi.org/10.1126/science.2749253>.
 79. Davis IW, Leaver-Fay A, Chen VB, Block JN, Kapral GJ, Wang X, Murray LW, Arendall WB III, Snoeyink J, Richardson JS, Richardson DC. 2007. MolProbity: all-atom contacts and structure validation for proteins and nucleic acids. *Nucleic Acids Res* 35:W375–W383. <http://dx.doi.org/10.1093/nar/gkm216>.

PAPER II



Structure of Aichi Virus 1 and Its Empty Particle: Clues to Kobuvirus Genome Release Mechanism

Charles Sabin,^a Tibor Füzik,^a Karel Škubník,^a Lenka Pálková,^a A. Michael Lindberg,^b Pavel Plevka^a

Structural Virology, Central European Institute of Technology, Masaryk University, Brno, Czech Republic^a; Department of Chemistry and Biomedical Sciences, Linnaeus University, Kalmar, Sweden^b

ABSTRACT

Aichi virus 1 (AiV-1) is a human pathogen from the *Kobuvirus* genus of the *Picornaviridae* family. Worldwide, 80 to 95% of adults have antibodies against the virus. AiV-1 infections are associated with nausea, gastroenteritis, and fever. Unlike most picornaviruses, kobuvirus capsids are composed of only three types of subunits: VP0, VP1, and VP3. We present here the structure of the AiV-1 virion determined to a resolution of 2.1 Å using X-ray crystallography. The surface loop puff of VP0 and knob of VP3 in AiV-1 are shorter than those in other picornaviruses. Instead, the 42-residue BC loop of VP0 forms the most prominent surface feature of the AiV-1 virion. We determined the structure of AiV-1 empty particle to a resolution of 4.2 Å using cryo-electron microscopy. The empty capsids are expanded relative to the native virus. The N-terminal arms of capsid proteins VP0, which mediate contacts between the pentamers of capsid protein protomers in the native AiV-1 virion, are disordered in the empty capsid. Nevertheless, the empty particles are stable, at least *in vitro*, and do not contain pores that might serve as channels for genome release. Therefore, extensive and probably reversible local reorganization of AiV-1 capsid is required for its genome release.

IMPORTANCE

Aichi virus 1 (AiV-1) is a human pathogen that can cause diarrhea, abdominal pain, nausea, vomiting, and fever. AiV-1 is identified in environmental screening studies with higher frequency and greater abundance than other human enteric viruses. Accordingly, 80 to 95% of adults worldwide have suffered from AiV-1 infections. We determined the structure of the AiV-1 virion. Based on the structure, we show that antiviral compounds that were developed against related enteroviruses are unlikely to be effective against AiV-1. The surface of the AiV-1 virion has a unique topology distinct from other related viruses from the *Picornaviridae* family. We also determined that AiV-1 capsids form compact shells even after genome release. Therefore, AiV-1 genome release requires large localized and probably reversible reorganization of the capsid.

Aichi virus 1 (AiV-1) is a human pathogen from the genus *Kobuvirus* of the family *Picornaviridae*. The first strain of AiV-1 A846/88 was isolated from a patient with acute gastroenteritis in Japan in 1989 (1). Subsequently, AiV-1 was also identified in other Asian countries (2), Europe (3, 4), America (5), and Africa (6). In environmental survey studies, AiV-1 is detected with higher frequency and greater abundance than other human enteric viruses (7). Accordingly, 80 to 95% of adults worldwide have antibodies against AiV-1 (5, 7, 8). Symptoms associated with AiV-1 include diarrhea, abdominal pain, nausea, gastroenteritis, vomiting, and fever (1, 7). However, the infections can also be asymptomatic or cause only subclinical symptoms.

The AiV-1 genome is an ~8,400-nucleotide, single-stranded, positive-sense RNA that contains one open reading frame encoding a 2,433-residue polyprotein (9). The polyprotein is cotranslationally and posttranslationally cleaved into leader protein (L-protein), viral capsid proteins VP0, VP3, and VP1, and nonstructural proteins that control the replication of AiV-1 in the infected cell (9). The cleavage is performed by virus-encoded proteases. L-protein is an additional N-terminal peptide present in some picornaviruses that can have a protease activity or fulfill another function in the virus life cycle. The capsid proteins originating from one polyprotein precursor constitute a protomer, which is the basic building block of the picornavirus capsid. While details of the assembly of kobuviruses are unknown, the assembly of related enteroviruses has been studied extensively. Initially, the VP0-VP3-VP1 protomers associate into pentamers (10,

11). Subsequently, 12 pentamers self-assemble into empty capsids (12, 13). The mechanism of self-assembly and the function of the empty capsids in the formation of enterovirus virions *in vivo*, however, are not well understood. It was shown that active replication and translation of the poliovirus genome is required for virion formation (14). RNA-containing enterovirus particles mature to virions by the cleavage of VP0 into VP2 and VP4 (15). VP4 subunits are peptides 70 to 80 residues long attached to the inner face of the capsid. Although the virions of mature enteroviruses and many other picornaviruses contain VP2 and VP4, VP0 cleavage does not occur in kobuviruses, which retain intact VP0 in mature particles. Negative-stain electron microscopy showed that AiV-1 virions have an average diameter of 30 nm (1). Furthermore, it was suggested that the AiV-1 capsid proteins form surface protrusions, giving the virus a shape similar to those of astroviruses (1, 16).

Received 12 August 2016 Accepted 16 September 2016

Accepted manuscript posted online 28 September 2016

Citation Sabin C, Füzik T, Škubník K, Pálková L, Lindberg AM, Plevka P. 2016. Structure of Aichi virus 1 and its empty particle: clues to kobuvirus genome release mechanism. *J Virol* 90:10800–10810. doi:10.1128/JVI.01601-16.

Editor: S. López, Instituto de Biotecnología/UNAM

Address correspondence to Pavel Plevka, pavel.plevka@ceitec.muni.cz.

Copyright © 2016 Sabin et al. This is an open-access article distributed under the terms of the [Creative Commons Attribution 4.0 International license](https://creativecommons.org/licenses/by/4.0/).

Details of the mechanism of kobuvirus genome release are not known. However, enteroviruses are also studied as models for genome release and delivery (17–21). The surface of the enterovirus capsid contains circular depressions around icosahedral 5-fold symmetry axes called “canyons.” The canyons of many enteroviruses, including major group HRVs, are the binding sites of receptors from the immunoglobulin superfamily (22–25). Nevertheless, other enteroviruses use different regions of their capsids to recognize their receptors (26). Before genome release, enterovirus virions convert into “altered” (A) particles characterized by radial expansion of the capsid and the formation of pores at the icosahedral 2-fold symmetry axes (18–21, 27–31). This conversion into A particles may be induced by binding to receptors or by exposure to the low pH of late endosomes (17, 28, 32–34). In poliovirus and coxsackievirus-A16 (CVA16), the genome release is accompanied by the exposure of the N-terminal region of VP1 and the release of the myristoylated VP4 (28, 35, 36). The VP4 subunits and N termini of VP1 were proposed to interact with the endosomal membranes and allow delivery of the RNA genome into the cytoplasm (28). Kobuviruses lack the separate capsid protein VP4. However, similar to the VP4 of enteroviruses, the N terminus of AiV-1 VP0 contains a myristoylation signal and might therefore supplement the membrane-disrupting function of VP4 (9). Here, we present a crystal structure of the AiV-1 virion and a cryo-electron microscopy (cryo-EM) reconstruction of an empty AiV-1 particle that show functionally important differences from the previously studied picornaviruses.

MATERIALS AND METHODS

Virus production and purification. African green monkey kidney cells (ATCC CCL-81) grown in 50 150-mm-diameter plates in minimal essential medium (MEM) with 10% fetal bovine serum (FBS) at 37°C in a 5% CO₂ incubator to 80% confluence were used for AiV-1 infection. The medium was aspirated from the plates, and the cells were washed with 5 ml of serum-free MEM. The cells were infected with 2 ml of the virus diluted to obtain a multiplicity of infection (MOI) of 0.2 in serum-free MEM and incubated for 3 h at 37°C in a 5% CO₂ incubator with gentle shaking every 30 min. Subsequently, 18 ml of MEM, supplemented with 10% FBS and 1 mM L-glutamine, was added to each plate, followed by incubation at 37°C. After 72 h, a cytopathic effect was observed, and the cells were pelleted by centrifugation at 9,000 rpm at 4°C for 15 min. The virus was precipitated overnight at 4°C by adding PEG 8000 and NaCl to final concentrations of 10% and 0.5 M, respectively. The solution was centrifuged at 9,000 rpm at 4°C for 10 min, and the supernatant was discarded. The resulting pellet was resuspended in 10 ml of 20 mM HEPES (pH 7.5) and 150 mM NaCl at 4°C and then homogenized with a Dounce tissue grinder. DNase and RNase were added to final concentrations of 10 µg/ml, and the solution was incubated at 37°C for 30 min. Subsequently, trypsin was added to a final concentration of 80 µg/ml, and the solution was incubated at 37°C for an additional 30 min, followed by centrifugation at 4,500 rpm at 10°C for 10 min. The clarified supernatant was layered over a 25% (wt/vol) sucrose cushion and centrifuged in a Beckman Ti 50.2 rotor at 48,000 rpm at 10°C for 2 h. After centrifugation, the supernatant was discarded, the pellet was resuspended in 2 ml of 20 mM HEPES (pH 7.5) and 150 mM NaCl buffer at 4°C, and the virus suspension was layered onto a 10 to 40% potassium tartrate gradient and centrifuged in an SW40 rotor at 36,000 rpm at 10°C for 90 min. The gradient layer containing the virus was collected by piercing the wall of the tube with a syringe and needle. The virus-containing fraction was transferred to 20 mM HEPES (pH 7.5) and 150 mM NaCl buffer using sequential centrifugations, and buffer additions in Vivaspin (Sigma-Aldrich) columns at 4°C.

AiV-1 crystallization, diffraction data collection, and structure determination. AiV-1 crystallization, diffraction data collection, and structure determination were described previously (37).

Preparation of empty AiV-1 particles by heating. The stability of AiV-1 was determined as the temperature at which 50% of its RNA genome was accessible to fluorescent RNA-binding dye Sybr green II. Virions at a concentration of 0.02 mg/ml were incubated with Sybr green II (3,000× diluted from the stock solution according to the manufacturer’s instructions), and the mixture was heated from 25 to 95°C in 1°C increments with a 2-min incubation time at each temperature in a real-time PCR instrument (Roche LightCycler 480). The fluorescence signal increases as the dye interacts with RNA that is released from the thermally destabilized particles, or the dye might be able to enter the particles. The thermal stability of the virus was estimated as the temperature corresponding to an increase in the fluorescence to 50% of the maximal value obtained when all virions were thermally denatured. The measurements were carried out in triplicates.

Single particle data acquisition and image processing. A solution of freshly purified AiV-1 (50 µl at concentration 2 mg/ml) was heated to 53°C for 10 min, and 3.5 µl of this sample was then immediately applied onto holey carbon grids (Quantifoil R2/1, mesh 300; Quantifoil Micro Tools) and vitrified by being plunged into liquid ethane using an FEI Vitrobot Mark IV. Grids with the vitrified sample were transferred to an FEI Titan Krios electron microscope operated at 300 kV aligned for parallel illumination in nanoprobe mode. The column of the microscope was kept at –196°C. Images were recorded with an FEI Falcon II direct electron detection camera under low-dose conditions (20 e[–]/Å²) with under-focus values ranging from 1.0 to 3.0 µm at a nominal magnification of 47,000, resulting in a pixel size of 1.73 Å/pixel. Each image was recorded in movie mode with 1-s total acquisition time and saved as seven separate movie frames. In total, 3,893 micrographs were acquired. The frames from each exposure were aligned to compensate for drift and beam-induced motion during image acquisition using the program SPIDER (38).

Icosahedral reconstruction of the AiV-1 empty particles. Regions comprised of the AiV-1 empty particles (324×324 pixels) were extracted from the micrographs using the program e2boxer.py from the package EMAN2 (39), resulting in 11,606 particles. Contrast transfer function (CTF) parameters of incoherently averaged particles from each micrograph were automatically estimated using the program ctfind4 (40). Subsequently, the particles were separated into two half-data sets for all of the subsequent reconstruction steps to follow the gold standard procedure for resolution determination (41). The structure of AiV-1 determined by X-ray crystallography was used to initiate the reconstruction. The phases of the initial model were randomized beyond a resolution of 40 Å. The images were processed using the package RELION (42). The data set of 11,606 particles was subjected to multiple rounds of two-dimensional (2D) classification and 3D classification, resulting in a near-homogeneous set of empty AiV-1 particles. Subsequent refinement was performed using the 3dautorefine procedure, with the starting model from the previous reconstruction low-pass filtered to a resolution of 60 Å. The reconstruction was followed by another round of 3D classification, where the alignment step was omitted and the estimated orientations and particle center positions from the previous refinement step were used. The resulting map was masked with a threshold mask and B-factor sharpened (43). The resulting resolution was determined at the 0.143 Fourier shell correlation of the two independent reconstructions.

Cryo-EM structure determination and refinement. The initial model, derived from the native AiV-1 structure obtained by X-ray crystallography (44), was fitted into the B-factor-sharpened cryo-EM map and subjected to manual rebuilding using the programs Coot and O, and coordinate and B-factor refinement using the programs CNS and phenix (45–48).

Data analysis. The volumes of the particles were calculated using the programs Mاما and Voidoo of the Uppsala Software Factory (49). Average radii were calculated using the program Moleman2 from the Uppsala Software Factory (50). Figures were generated using the programs UCSF Chimera (51) and PyMOL (The PyMOL Molecular Graphics System, v1.7.4; Schrödinger, LLC). Structure-based alignments of biological

TABLE 1 AiV-1 virion and empty particle structure quality indicators

| Parameter | AiV-1 empty particle cryo-EM structure | AiV-1 virion crystal structure ^b |
|--|--|---|
| Space group | NA ^d | I23 |
| Unit cell dimensions | | |
| <i>a</i> , <i>b</i> , <i>c</i> (Å) | NA | 350.80, 350.80, 350.80 |
| α, β, γ (°) | NA | 90, 90, 90 |
| Resolution (Å) | 4.2 | 72.0–2.3 (2.34–2.30) |
| <i>R</i> _{merge} ^a | NA | 0.15 (0.63) |
| <i>I</i> / <i>σ</i> (<i>I</i>) | NA | 6.0 (1.8) |
| Completeness (%) | NA | 91.0 (94.0) |
| Observation multiplicity | NA | 3.2 (3.0) |
| No. of observations | NA | 902,384 (43,198) |
| No. of unique observations | NA | 282,853 (14,471) |
| <i>R</i> _{work} | 0.34 | 0.33 ^e |
| No. of: | | |
| Protein atoms* | 5,455 | 5,791 |
| Water atoms* | NA | 147 |
| RMSD | | |
| Bond lengths (Å) | 0.016 | 0.013 |
| Bond angles (°) | 1.57 | 1.43 |
| Ramachandran statistics (%) ^c | | |
| Preferred regions | 89.1 | 95.7 |
| Allowed regions | 8.4 | 4.0 |
| Disallowed regions | 2.5 | 0.3 |
| Avg atomic B factor (Å ²) | 127.8 | 22.9 |

^a $R_{\text{merge}} = \sum_h \sum_j |I_{hj} - \langle I_h \rangle| / \sum_h \sum_j I_{hj}$. *, Statistics are given for one icosahedral asymmetric unit.

^b Statistics for the highest-resolution shell are indicated in parentheses.

^c Determined according to the criterion of Molprobity (78).

^d NA, not applicable.

^e All reflections were used in the refinement. The *R*_{free} value, if it were calculated, would be very similar to *R*_{work} because of the 5-fold noncrystallographic symmetry present in the crystal. Therefore, the *R*_{free} would not provide an unbiased measure of model quality in this case (55).

protomers of various picornaviruses were prepared using the Multiseq tool in VMD and the program STAMP (52). The root mean square deviation (RMSD) values provided by STAMP were used to create a nexus-format matrix file, which was converted into a structure-based phylogenetic tree and visualized using the program FigTree (<http://tree.bio.ed.ac.uk/software/figtree/>).

Accession number(s). The Protein Data Bank (PDB) model of native AiV-1, together with structure factor amplitudes and phases derived by phase extension, was deposited under PDB code 5A0O. A cryo-EM reconstruction map of the empty AiV-1 particle was deposited with EMDB under the number EMD-4112, and the fitted coordinates were deposited under PDB code 5LVC.

RESULTS AND DISCUSSION

Structure of AiV-1 virion and capsid proteins. The crystal structure of the AiV-1 virion was determined to a resolution of 2.1 Å using X-ray crystallography. The diffraction data were affected by perfect hemihedral twinning. The structure determination process has been described elsewhere (37), but for completeness of the discussion the basic crystallographic and structure quality indicators are reprinted here (Table 1). The maximum outer diameter of the AiV-1 capsid is 318 Å. The capsid is built from major

capsid proteins VP0, VP1, and VP3 arranged with pseudo-T3 icosahedral symmetry (Fig. 1A). VP1 subunits form pentamers around 5-fold axes, while VP0 and VP3 alternate around the icosahedral 3-fold axes. The three capsid proteins have jellyroll β-sandwich folds with β-strands named according to the picornavirus convention B to I (53). Two antiparallel β-sheets forming the cores of the subunits contain strands BIDG and CHEF, respectively (Fig. 1A). Loops of the capsid proteins are named according to the β-strands they connect. N termini of the major capsid proteins are located on the inside of the capsid, whereas C termini are exposed at the virion surface. A complete model of the AiV-1 icosahedral asymmetric unit could be built apart from residues 1 to 12, 56 to 63, and 76 to 111 of VP0, residues 84 to 87 and 234 to 253 of VP1, and residues 221 to 223 of VP3.

Topology of AiV-1 virion surface is distinct from the previously structurally characterized picornaviruses. While structures of numerous viruses from the *Picornaviridae* and *Dicistroviridae* families have been determined previously, AiV-1 is the first characterized representative of the *Kobuvirus* genus. AiV-1 shares less than 26% sequence identity with poliovirus 1, HRV14, EV71, human parechovirus 1 (HPeV-1), and hepatitis virus A (Table 2) (54–57). Structure-based phylogenetic analysis indicates that AiV-1 is quite distinct from all previously determined structures of picornaviruses and dicistroviruses (Fig. 1D). Most of the differences are located at the capsid surface. Our high-resolution analysis did not confirm the presence of the previously proposed astrovirus-like protrusions in the AiV-1 capsid (1, 16). Instead, the AiV-1 virion is rather spherical in shape with plateaus around 3-fold axes, slight depressions at 2-fold axes, and low protrusions around icosahedral 5-fold axes that are encircled by circular depressions that we, according to the enterovirus convention, call canyons (Fig. 2A and B). However, the AiV-1 canyon is shallower and has a different shape to that of enteroviruses (Fig. 2C). The differences in the capsid topology between AiV-1 and other enteroviruses are due to different lengths of loops of the capsid proteins that form the capsid surface. The central wall of the enterovirus canyon is formed by CD loops of VP1, whereas the outer wall is formed by the EF loop of VP2 called puff and a loop before β-strand B of VP3 called knob, the CD loop of VP3, and the GH loop of VP1 (Fig. 3C, D, G, and H). However, capsid protein VP3 of AiV-1 lacks the knob loop and its VP0 (a homologue of enterovirus VP2) contains only a very small puff, including a single seven-residue α-helix (Fig. 3A, B, E, and F). Interestingly, the puff and knob loops of AiV-1 are shorter than those in HPeV-1, which lacks the canyon altogether (Fig. 3I and J). However, the BC loop of VP0 of AiV-1 is relatively elongated and forms a protrusion on the capsid surface located in the volume occupied by the puff and knob of enteroviruses (Fig. 3E to J). Therefore, the BC loop of AiV-1 VP1 substitutes for the missing knob and small puff of AiV-1 and forms the outer wall of the canyon (Fig. 3A, B, and F). Moreover, the GH loop of AiV-1 VP1 is relatively short and fills the canyon instead of reinforcing its outer wall, as is the case in poliovirus 1 (Fig. 3A and B). The long C-terminal arm of poliovirus 1 VP1, which wraps around a side of the puff, is not structured in AiV-1, resulting in a relative broadening of the canyon (Fig. 3A to D). Furthermore, the depth of the AiV-1 canyon is further diminished by the α3 helix in the CD loop of AiV-1 VP1 that partially fills the volume of the canyon (Fig. 3A and B). In summary, the differences in the surface-exposed loops make

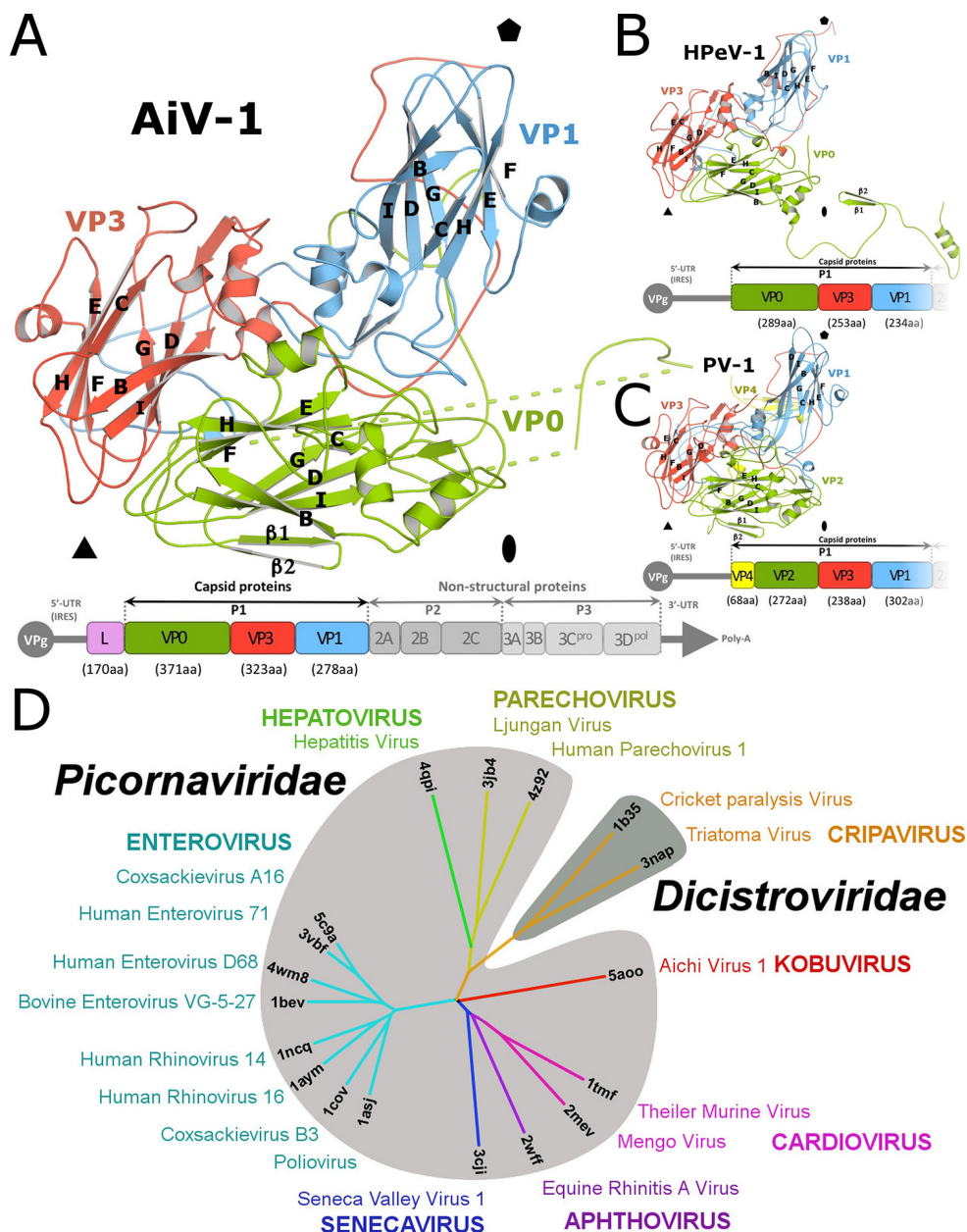


FIG 1 Structure of icosahedral asymmetric unit of AiV-1 and structure-based evolutionary tree of picornaviruses and dicistroviruses. (A to C) Cartoon representations of icosahedral asymmetric units of AiV-1 (A), HPeV-1 (B), and poliovirus 1 (C). VP1 subunits are shown in blue, VP2 and VP0 are shown in green, VP3 is shown in red, and VP4 is shown in yellow. Schematic diagrams of the genome organizations of the viruses are shown below the structure figures. (D) Phylogenetic tree based on the structural similarity of icosahedral asymmetric units of indicated viruses from the *Picornaviridae* and *Dicistroviridae* families. For details on the construction of the diagram, please see Materials and Methods.

AiV-1 unique among picornaviruses and dicistroviruses characterized to date. They are reflected in the isolated position of AiV-1 in the structure-based evolutionary tree (Fig. 1D). The differences in surface topology indicate the possibility of a different type of receptor binding in AiV-1 than is found in enteroviruses.

Absence of hydrophobic pocket in VP1. The genome release of some enteroviruses can be initiated by the interaction of the virus with receptors with an immunoglobulin fold that bind to the canyon (25, 53, 58). At the bottom of the canyons of some enteroviruses is a small aperture leading to a hydrophobic pocket within

the β -barrel core of the VP1 subunit (54, 55). The pocket is filled with a lipid moiety called a “pocket factor,” which was proposed to function in the regulation of virus stability and uncoating (25). Importantly, compounds binding to the VP1 pocket with high affinity have been demonstrated to increase enterovirus stability, block its genome release or receptor binding, and prevent virus infection (59–64). However, in comparison to enteroviruses the β -sandwich core of AiV-1 VP1 is filled with hydrophobic side chains of residues and does not form the pocket (Fig. 3A and C). In this respect, AiV-1 is similar to other picornaviruses such as cardioviruses (65–67), parechoviruses (56, 68), and aphthoviruses

TABLE 2 Sequence and structural similarity of capsid proteins of selected picornaviruses

| Family and genus | Virus | Sequence and structural similarity (% or RMSD) ^a | | | | | | | | | | |
|------------------------|--------|---|------|------|-------|------|-------|------|-------|-----|--------|------|
| | | AiV-1 | TMEV | ERAV | SVV-1 | PV-1 | HRV14 | EV71 | CVA16 | HAV | HPeV-1 | CrPV |
| <i>Picornaviridae</i> | | | | | | | | | | | | |
| <i>Kobuvirus</i> | AiV-1 | | 1.9 | 2.0 | 1.8 | 1.8 | 1.8 | 1.8 | 1.8 | 2.1 | 2.2 | 2.6 |
| <i>Cardiovirus</i> | TMEV | 28 | | 1.9 | 1.4 | 1.5 | 1.5 | 1.7 | 1.6 | 2.0 | 2.1 | 2.8 |
| <i>Aphthovirus</i> | ERAV | 25 | 33 | | 1.9 | 1.8 | 1.7 | 1.7 | 1.7 | 2.4 | 2.6 | 3.0 |
| <i>Senecavirus</i> | SVV-1 | 28 | 38 | 31 | | 2.3 | 1.7 | 1.8 | 1.7 | 2.0 | 2.2 | 3.2 |
| <i>Enterovirus</i> | PV-1 | 24 | 29 | 24 | 29 | | 1.0 | 1.1 | 1.0 | 2.1 | 2.1 | 2.6 |
| | HRV14 | 25 | 26 | 25 | 28 | 49 | | 1.1 | 1.2 | 2.1 | 2.1 | 2.8 |
| | EV71 | 26 | 30 | 23 | 29 | 44 | 44 | | 0.5 | 2.1 | 2.2 | 2.5 |
| | CVA16 | 25 | 30 | 22 | 30 | 47 | 44 | 79 | | 2.1 | 2.2 | 2.6 |
| <i>Hepatovirus</i> | HAV | 17 | 21 | 18 | 20 | 18 | 19 | 17 | 15 | | 2.1 | 2.6 |
| <i>Parechovirus</i> | HPeV-1 | 20 | 20 | 18 | 18 | 17 | 17 | 17 | 15 | 18 | | 2.7 |
| <i>Dicistroviridae</i> | | | | | | | | | | | | |
| <i>Cripavirus</i> | CrPV | 16 | 14 | 17 | 11 | 13 | 11 | 14 | 14 | 16 | 17 | |

^a The top right portion of the table presents the root mean square deviations (Å) of superimposed C α atoms of the respective 3D structures. The distance cutoff for inclusion of residues in the calculation was 3.8 Å. Capsid protein protomers corresponding to icosahedral asymmetric units consisting of subunits VP1 to VP4 were used in the comparisons. The program Coot was used for superposition of the molecules (47). The bottom left portion of the table presents the percent identities between respective virus coat protein sequences. Gaps were ignored in the calculations.

(32, 69). Therefore, capsid-binding inhibitors are unlikely to be effective against AiV-1 and other kobuviruses.

Structural changes of AiV-1 capsid associated with genome release. It has been shown previously that virions of enteroviruses convert to A particles before the genome release (17, 28, 33, 34). The A particles are characterized by an expanded virion diameter and channels in the capsid that were speculated to serve in the release of the RNA genomes. The empty capsid shells produced after the genome release were named B particles, which are structurally similar to the A particles. It was demonstrated that the formation of A particles and the genome release of many picornaviruses might be induced nonphysiologically by heating the virions to 42 to 56°C (21). In order to study the genome release of AiV-1, its virions were gradually heated, and the genome release was monitored (Fig. 2E). AiV-1 virions released their RNA rather abruptly at 53°C. Electron microscopy of AiV-1 virions heated to 53°C for 10 min identified 95% of empty capsids, which were used to reconstruct the empty particle to a resolution of 4.2 Å (Fig. 2G and Table 1). The AiV-1 empty capsid is expanded by 7.6 Å in diameter relative to the native virus (Fig. 2A and B). The volume of the particle increases from $4.8 \times 10^6 \text{ Å}^3$ to $5.5 \times 10^6 \text{ Å}^3$. The structure of the empty particle differs from that of the native virion, mostly in the contacts between the pentamers of capsid protein protomers. In the native AiV-1 virion, the interpentamer contacts are mediated by strand β 2 of VP0, which interacts with β -strand F of VP3 (Fig. 2C and 4A). Strands β 1 and β 2 of VP0 extend the β -sheet CHEF of VP3. However, in the empty particle residues 112 to 139, which form the β 1 and β 2 strands of VP0, are disordered (Fig. 2D and 4B). As a consequence, the interpentamer interface is reduced from 2,750 to 1,400 Å² (see Fig. 5). Furthermore, residues 139 to 144 of VP0 form new interactions with the core of subunit VP3 (Fig. 4B). At the same time, residues 55 to 60 of VP0 became structured in the empty AiV-1 particle and residues 67 to 75 retain the same structure as in the native virions (Fig. 2C and D and Fig. 4A and B). Therefore, the N-terminal arm of AiV-1 VP0 does not appear to be externalized from the empty particle. This is in contrast to the presumption that the N-terminal part of AiV-1 VP0 is functionally homologous to the VP4 of other

picornaviruses and might therefore play a role in the transport of the virus genome across the endosomal membrane into the host cytoplasm. However, it is possible that *in vivo*, because of interactions with an as-yet-unknown receptor, the empty AiV-1 particles dissociate into pentamers and the VP0 N termini could interact with the membranes.

The structure of HPeV-1, which also contains VP0 in mature virions, was recently determined (56). However, in contrast to AiV-1, empty particles of HPeV-1 rapidly dissociate into pentamers after the genome release (56, 70). Major differences between AiV-1 and HPeV-1 are in the interpentamer interactions mediated by the N-terminal arm of VP0 (Fig. 1A and B). While in AiV-1 the β 1 and β 2 strands extend the β -sheet CHEF of VP3 from the icosahedral asymmetric unit from a neighboring pentamer; in HPeV-1 the N-terminal arm forms a loop that stretches around the icosahedral 2-fold axis and the β -strands extend the β -sheet of the VP3 subunit from the same pentamer (Fig. 1A and B). The differences in the positioning of the N-terminal arm of VP0 might influence the stability of the empty capsid, since enteroviruses, which produce empty particles after genome release, have the same type of interpentamer interaction mediated by the N terminus of VP0/VP2 as that of AiV-1 (Fig. 1C).

The N-terminal arm of AiV-1 VP1 undergoes structural reorganization upon the formation of the empty particle. Residues 1 to 30 become disordered, and residues 31 to 35 refold into a new structure with the last resolved residue pointing toward the particle center (Fig. 4A and B and Fig. 2C and D). This is in contrast to the previous observation of the A particle of CVA16, in which the N terminus of VP1 was exposed at the capsid surface (Fig. 4C and D) (29). The N termini of VP1 of enteroviruses were proposed to interact with membranes and facilitate the delivery of the virus genome into the cytoplasm (29, 71). Similar to the N termini of AiV-1 VP0s, the N termini of AiV-1 VP1 subunits might interact with the membrane after particle dissociation.

The structural changes of the AiV-1 capsid linked to the genome release result in a reduction of interpentamer contacts by 49%, whereas the contacts within the protomer and within the pentamer are only reduced by 22 and 10%, respectively (Fig. 5).

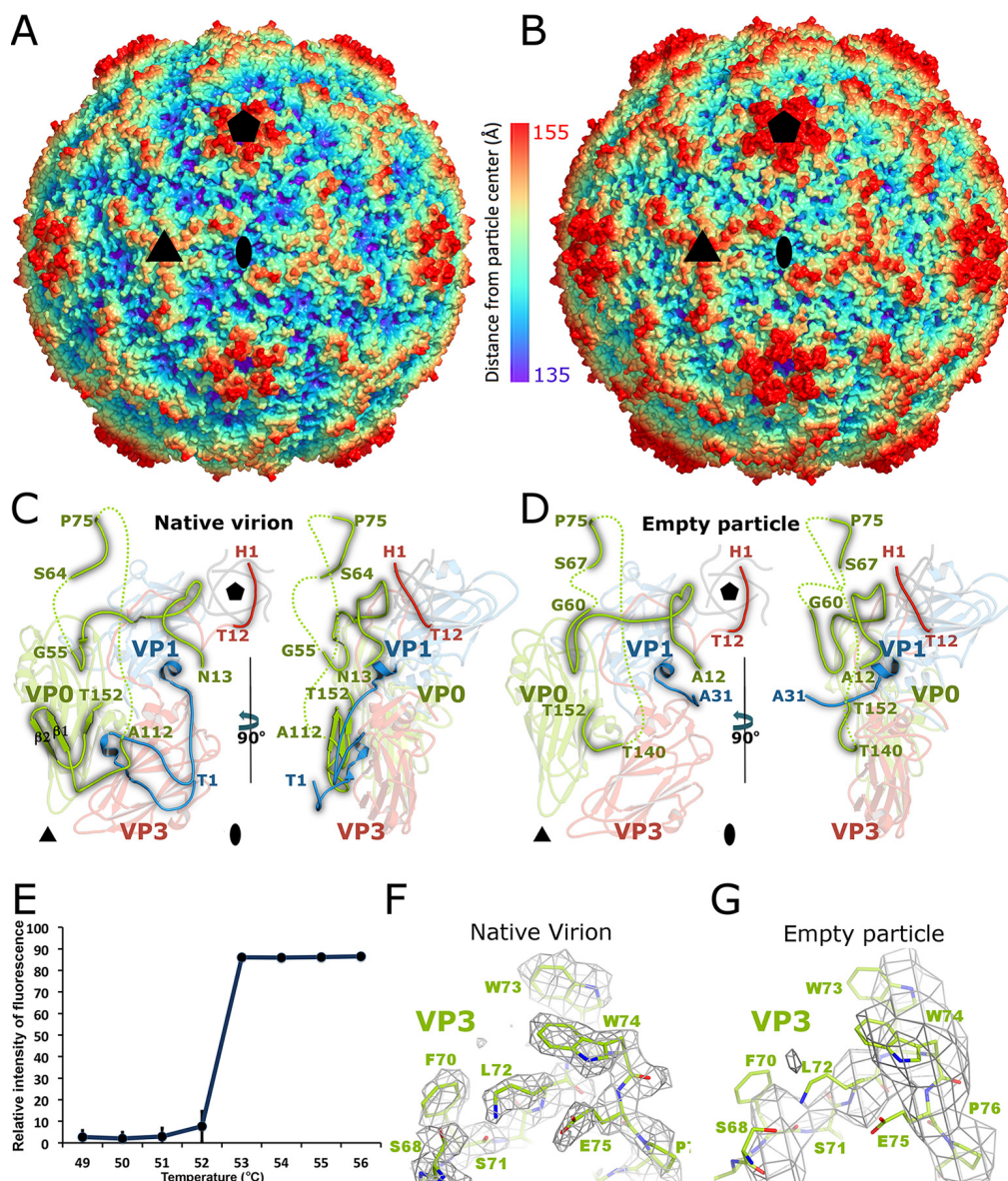


FIG 2 Changes of AiV-1 capsid associated with genome release. (A and B) Surface rendering of AiV-1 virion (A) and empty particle (B) rainbow-colored based on distance from the particle center. The positions of selected 5-fold, 3-fold, and 2-fold icosahedral symmetry axes are indicated with pentagons, triangles, and ovals, respectively. (C and D) Icosahedral asymmetric unit of native AiV-1 virion (C) and the empty particle (D). VP1, VP0, and VP3 are shown in blue, green, and red, respectively. N-terminal arms of the capsid proteins are highlighted in brighter colors. The positions of the 5-fold-symmetry-related N termini of VP3 subunits are shown in gray. Dashed lines indicate the putative positions of the unstructured chains. The positions of 5-fold, 3-fold, and 2-fold icosahedral symmetry axes are indicated with pentagons, triangles, and ovals, respectively. (E) A Sybr green fluorescence assay was performed to measure the stability of AiV-1 virions. AiV-1 virions were mixed with Sybr green dye II and heated to the indicated temperatures (*x* axis). The fluorescence signal increases as the dye binds to RNA that is released from thermally destabilized particles. Error bars indicate the standard deviations of the measurements. Please see Materials and Methods for details. (E and F) Examples of electron densities of AiV-1 virion at a resolution of 2.1 Å (E) and empty particle at the resolution of 4.2 Å (F). The maps are contoured at 1.5 σ .

The reduction in the interface area cannot be directly converted to binding energies, but the reduced interpentamer contacts indicate that the expanded AiV-1 particles might be prone to the formation of capsid pores for genome release or to disassembly into pentamers.

Differences between kobuvirus and enterovirus genome release. The structure of the empty particle of AiV-1 is different from that of empty and A particles of enteroviruses. “A” particles of CVA7, EV71, poliovirus 1, HRV-2, and CVA16 contain two types of pores located at icosahedral 2-fold axes and between ico-

sahedral 2-fold and 5-fold symmetry axes (Fig. 4C and D) (18–21, 27–31). In the CVA16 A particle, the pores at 2-fold axes were proposed to allow externalization of VP1 N termini that then translocate to the channels between 2-fold and 5-fold axes (Fig. 4C and D) (29). In addition, the pores at 2-fold axes were speculated to serve as channels for the release of VP4 subunits and the RNA genome. The borders of the channels located at 2-fold axes in enterovirus particles are formed by helix $\alpha 3$ from the CD loop of VP2 and EF loop of VP3 (29, 72). In contrast to the enterovirus A and empty particles, the empty particle of AiV-1 does not contain

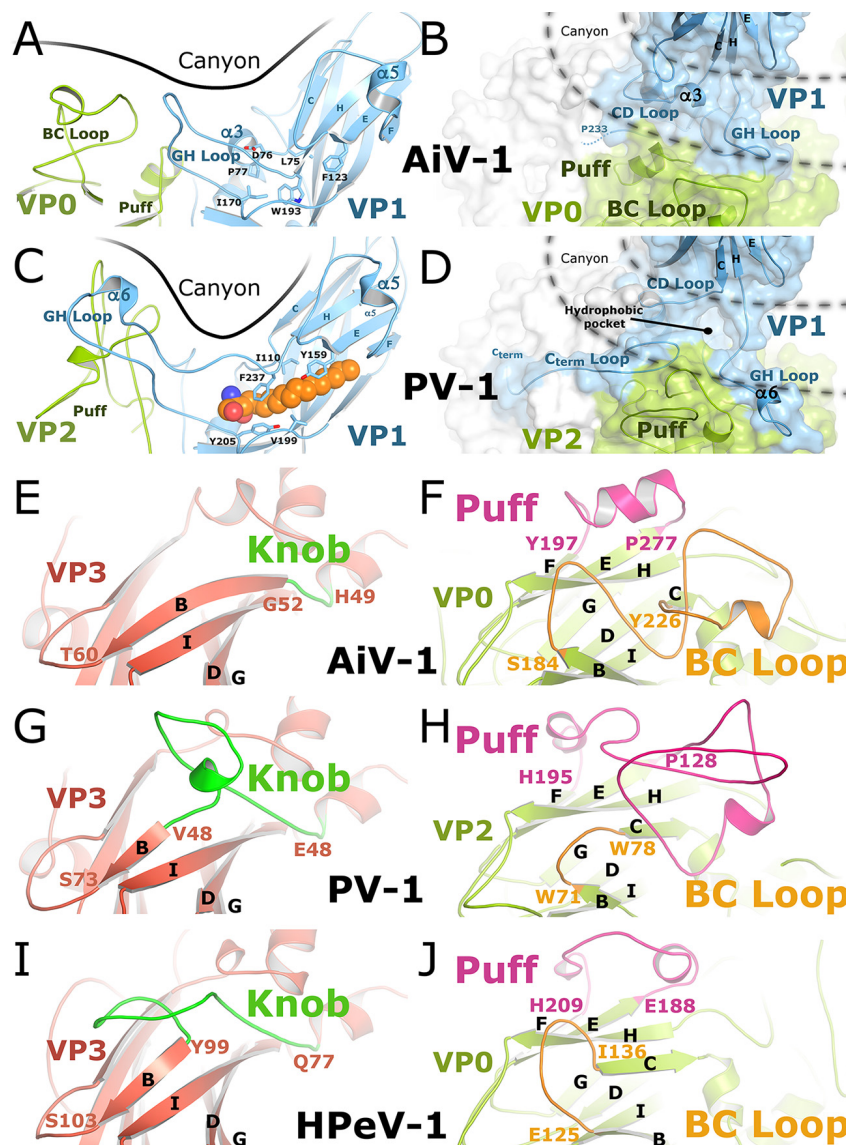


FIG 3 Comparison of capsid surface features of AiV-1, poliovirus 1, and HPeV-1. (A to D) Side and top views of the canyons of AiV-1 (A and B) and poliovirus 1 (C and D). Capsid proteins are shown in a cartoon representation. VP1 is shown in blue, and VP2/VP0 are shown in green. A pocket factor of poliovirus 1 is shown in space-filling representation in orange. Residues that interact with the pocket factor are depicted as sticks. The molecular surface is displayed in panels B and D. (E to J) Comparison of subunits VP0 and VP3 of AiV-1 (E and F), poliovirus 1 (G and H), and HPeV-1 (I and J). VP3 of AiV-1 (E) lacks the loop knob (highlighted in green) that forms a prominent surface feature of poliovirus 1 (G) and HPeV-1 (I). The loop puff (highlighted in magenta) of AiV-1 (F) contains a single 7-residue helix and is shorter than the puffs of poliovirus 1 (H) and HPeV-1 (J). The BC loop (highlighted in orange) of AiV-1 forms a prominent feature in its capsid and is longer than those of poliovirus 1 (H) and HPeV-1 (J). Selected secondary structure elements are labeled.

any pores (Fig. 2B). Aphthovirus equine rhinitis A virus (ERAV) also forms empty particles with compact capsids that do not contain any pores for genome release (32). Nevertheless, the empty particles of ERAV rapidly dissociate into pentamers.

The most likely positions for the formation of channels in the AiV-1 capsid are the borders of the pentamers of capsid protein protomers and specifically areas around the icosahedral symmetry axes. Helices $\alpha 3$ of VP0 subunits related by a 2-fold axis move 1.8 Å away from each other when the AiV-1 virion converts to the empty particle (Fig. 4A and B). Nevertheless, the movement does not result in the formation of a channel around the 2-fold axis (Fig. 2B and 4B). The channels at the 2-fold axes observed in the A and empty particles of enteroviruses are also not of sufficient size

and require expansion in order to allow the genome release (Fig. 2D) (29, 71, 72). It is therefore possible that an opening in the AiV-1 capsid at the 2-fold axis might serve as a channel for genome release; however, more extensive local reorganization of the capsid than in enteroviruses would be required. This possibility is to some extent supported by the presence of residues with neutral and negatively charged side chains in the vicinity of the 2-fold symmetry axis of AiV-1, similar to the situation in enteroviruses (Fig. 6A to C) (73). The negative charge might provide a “slippery” surface facilitating the egress of viral RNA (74).

It was proposed previously that an “iris-like aperture” movement of the N termini of VP3 subunits might result in the opening of 10-Å diameter channels through the rhinovirus capsid, which

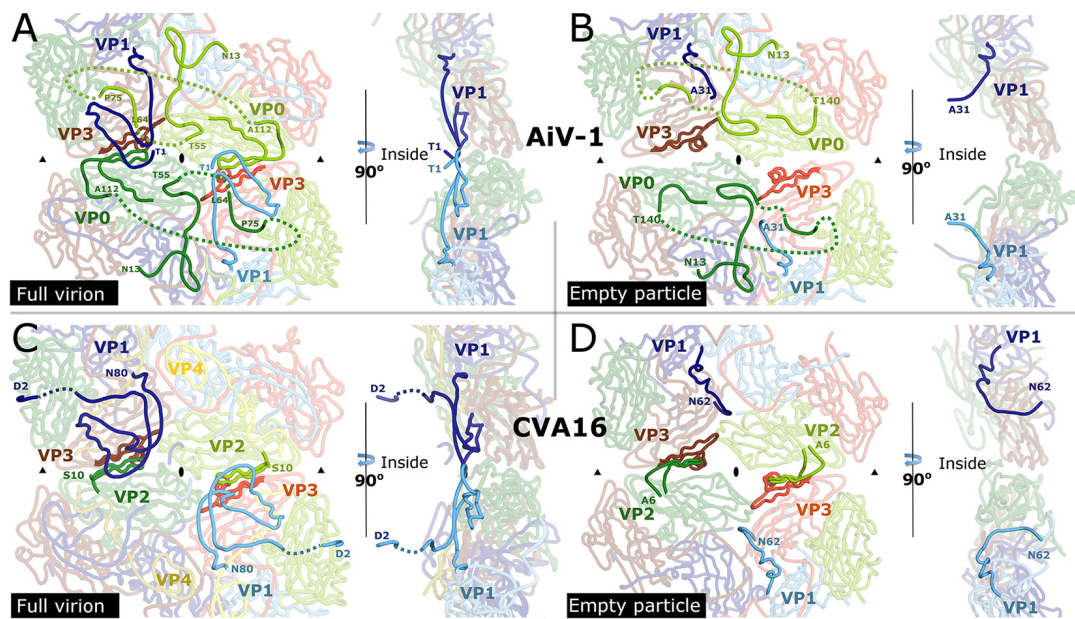


FIG 4 Comparison of interpentamer contacts in virions and expanded particles of CVA16 and AiV-1. (A to D) Structures of AiV-1 virion (A), AiV-1 empty particle (B), CVA16 virion (C), and CVA16 empty particle (D) in the vicinity of the icosahedral 2-fold axes viewed from the particle center (left) and perpendicular to the capsid surface (right). VP1 subunits are shown in blue, VP0/VP2 are shown in green, and VP3 is shown in red. Subunits from different icosahedral asymmetric units are distinguished by color tones. N-terminal arms of VP0 in AiV-1 and VP2 in CVA16 that participate in interpentamer contacts are shown in bright green. Dashed lines indicate the putative positions of unstructured residues. N-terminal residues of VP1 are shown in bright blue. Residues of VP3-forming strands β E and β F that interact with the N termini of VP0/VP2 are shown in bright red. The positions of icosahedral 2-fold and 3-fold symmetry axes are indicated with ovals and triangles, respectively.

might enable the exit of the genomic RNA (75, 76). The narrowest constriction along the AiV-1 5-fold axis is formed by the N-terminal arms of VP3 subunits, which might perform such an “iris-like aperture” movement (Fig. 2C). However, the structures of AiV-1 VP1 and VP3 subunits, which are in contacts around the 5-fold axes, are not affected by the capsid expansion (Fig. 2D), and

the pore along the 5-fold axis is obstructed in both the native and the empty particle structures (Fig. 6A, B, and E). Therefore, the 5-fold axes of the AiV-1 capsid do not seem to be likely portals for the genome release. It is possible that the iris-like aperture movements in the rhinovirus capsids may represent structural rearrangements accompanying the genome release rather than forma-

| A | AiV-1 | | | CVA16 | | |
|----------------|-------------------------------------|--------------|--------------|-------------------------------------|---------------|--------------|
| | (VP _x -VP _y) | Native | Empty | (VP _x -VP _y) | Native | Empty |
| Intra-protomer | VP1a-VP3a | 2 600 | 1 900 | VP1a-VP3a | 3 750 | 3 350 |
| | VP1a-VP0a | 2 150 | 1 500 | VP1a-VP2a | 2 250 | 1 650 |
| | VP0a-VP3a | 2 000 | 1 900 | VP2a-VP3a | 1 550 | 1 500 |
| | | | | VP4a-VP1a | 1 500 | 0 |
| | | | | VP4a-VP3a | 1 000 | 0 |
| | | | VP4a-VP2a | 500 | 0 | |
| | Sum | 6 750 | 5 300 | Sum | 10 550 | 6 500 |
| Intra-pentamer | VP0a-VP3b | 1 400 | 1 300 | VP1a-VP1b | 850 | 1 000 |
| | VP1a-VP3b | 1 300 | 1 300 | VP1a-VP3b | 1 450 | 950 |
| | VP3a-VP3b | 700 | 700 | VP3a-VP3b | 800 | 700 |
| | VP1a-VP1b | 600 | 600 | VP2a-VP3b | 700 | 400 |
| | VP0a-VP1b | 600 | 200 | VP2a-VP1b | 450 | 350 |
| | Other* | 100 | 150 | VP3a-VP1b | 250 | 200 |
| | | | | Other* | 300 | 0 |
| | Sum | 4 700 | 4 250 | Sum | 4 800 | 3 600 |
| Inter-pentamer | VP0a-VP3f | 1 200 | 900 | VP2a-VP3f | 1 300 | 1 200 |
| | VP0a-VP0g | 650 | 450 | VP2a-VP2g | 650 | 50 |
| | VP0a-VP1f | 650 | 0 | VP2a-VP1f | 700 | 0 |
| | VP0a-VP0f | 200 | 0 | Other* | 200 | 100 |
| | Other* | 50 | 50 | | | |
| | Sum | 2 750 | 1 400 | Sum | 2 850 | 1 350 |

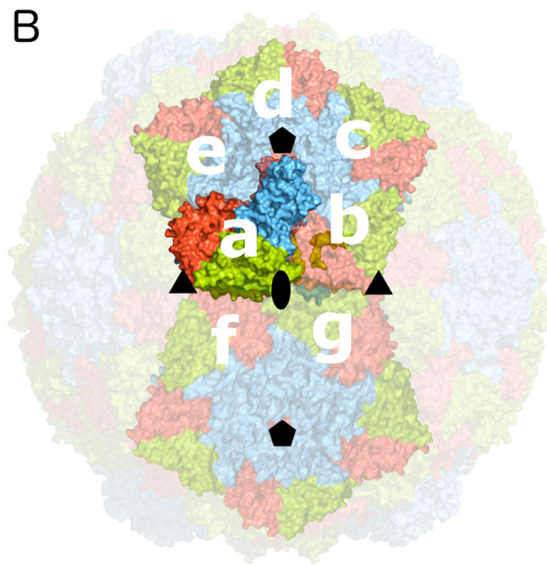


FIG 5 Buried surface areas of interfaces within AiV-1 and CVA16 virions and empty particles. (A) List of buried surface areas. Individual subunits are labeled according to their relative positions shown in panel B. “Other*” indicates the sum of buried surface areas of additional small interfaces. (B) Capsid surface representation of AiV-1 virion with subunits VP0, VP1, and VP3 shown in green, blue, and red, respectively. Icosahedral asymmetric units considered for buried surface calculations are labeled with letters.

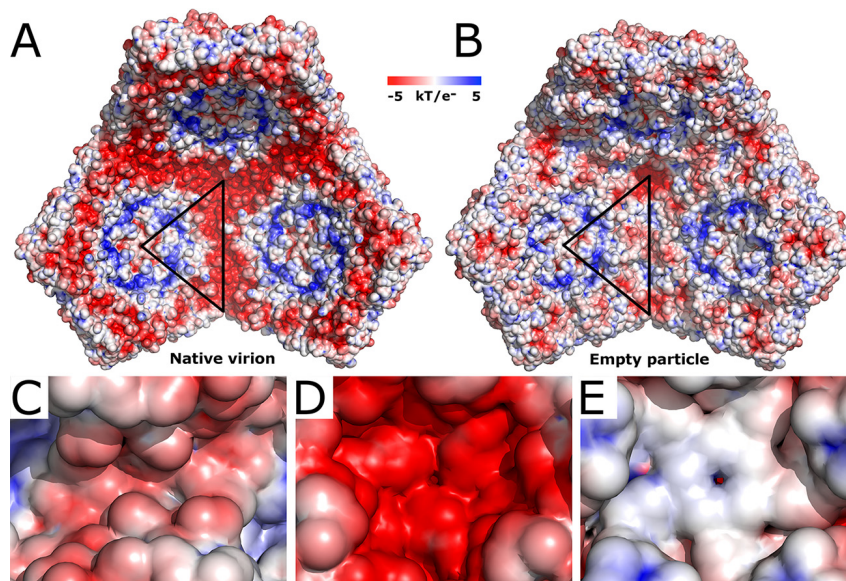


FIG 6 Comparison of charge distribution inside the AiV-1 virion and empty particle. (A and B) Comparison of electrostatic potential distribution inside the native virion (A) and empty particle (B). Three pentamers of capsid protein protomers are displayed. The borders of a selected icosahedral asymmetric unit are highlighted with a black triangle. (C to E) Details of the electrostatic surface of the empty particle around 2-fold (C), 3-fold (D), and 5-fold (E) symmetry axes.

tion of a pore through which the RNA exits the virion. Similarly, the 3-fold axes of the AiV-1 capsid are entirely closed by side chains located in their vicinity, and the internal face of AiV-1 capsid around the 3-fold axes is covered by negatively charged residues (Fig. 6B and D).

Comparison of the native virion and empty particle structures of AiV-1 indicates that the genome release necessitates the formation of a special pore within the capsid shell. However, the possibility of obtaining a 4.2-Å-resolution reconstruction of the empty particle indicates that the pore does not affect the overall icosahedral symmetry of the capsid or that the structural changes required for the genome release are reversible. In that case the empty capsids would not provide information on how the genome was released from the particle. The absence of pores in the AiV-1 capsid presents an obstacle for genome release. It was shown previously that the genome release of HRV2 proceeds in the 3'-to-5' direction (77). Assuming that AiV-1 genome release has the same directionality, it is not clear how the 3' end of the AiV-1 genome might induce the formation of a pore in the capsid or how it finds the special preformed pore within the capsid. The alterations in the structures of the N termini of VP2 and VP1 connected with the formation of the empty AiV-1 particle result in the removal of the negative charge that is located at the edges of the pentamers in the native virion (Fig. 6A and B). This may promote interactions of the genomic RNA with the capsid and its eventual release from the virion.

ACKNOWLEDGMENTS

We thank the synchrotron Diamond beamline I03 scientists and the synchrotron Soleil beamlines Proxima 1 and Proxima 2A scientists for their help with crystal screening and data collection. We thank Sergei Kalynch for his help with refinement of the empty particle structure. We acknowledge the CF Cryo-Electron Microscopy and Tomography, CF X-ray Diffraction and Bio-SAXS, and CF Biomolecular Interactions and Crystallization for their support with obtaining scientific data presented here. Access to computing and storage facilities owned by parties and projects

contributing to the National Grid Infrastructure MetaCentrum, provided under the program Projects of Large Infrastructure for Research, Development, and Innovations (LM2010005), is greatly appreciated.

This study was supported by the IT4Innovations Centre of Excellence (project CZ.1.05/1.1.00/02.0070).

C.S. calculated the single-particle cryo-EM reconstruction, performed crystallization, model building, refinement, and data analysis, and participated in writing the manuscript. L.P. optimized and conducted large-scale virus purifications. K.S. and T.F. participated in single-particle cryo-EM reconstruction. A.M.L. provided material for the study and participated in data analysis. P.P. designed the study, performed AiV-1 crystal structure determination, participated in data analysis, and wrote the manuscript.

FUNDING INFORMATION

This work, including the efforts of Pavel Plevka, was funded by EC | European Research Council (ERC) (355855). This work, including the efforts of Pavel Plevka, was funded by European Molecular Biology Organization (EMBO) (3041). This work, including the efforts of Pavel Plevka, was funded by Ministerstvo Školství, Mládeže a Tělovýchovy (MŠMT) (LQ1601).

The funders had no role in study design, data collection and interpretation, or the decision to submit the work for publication.

REFERENCES

1. Yamashita T, Kobayashi S, Sakae K, Nakata S, Chiba S, Ishihara Y, Isomura S. 1991. Isolation of cytopathic small round viruses with BS-C-1 cells from patients with gastroenteritis. *J Infect Dis* 164:954–957. <http://dx.doi.org/10.1093/infdis/164.5.954>.
2. Yamashita T, Sakae K, Kobayashi S, Ishihara Y, Miyake T, Mubina A, Isomura S. 1995. Isolation of cytopathic small round virus (Aichi virus) from Pakistani children and Japanese travelers from Southeast Asia. *Microbiol Immunol* 39:433–435. <http://dx.doi.org/10.1111/j.1348-0421.1995.tb02225.x>.
3. Ambert-Balay K, Lorrot M, Bon F, Giraudon H, Kaplon J, Wolfer M, Lebon P, Gendrel D, Pothier P. 2008. Prevalence and genetic diversity of Aichi virus strains in stool samples from community and hospitalized patients. *J Clin Microbiol* 46:1252–1258. <http://dx.doi.org/10.1128/JCM.02140-07>.
4. Kaikonen S, Rasanen S, Ramet M, Vesikari T. 2010. Aichi virus infec-

- tion in children with acute gastroenteritis in Finland. *Epidemiol Infect* 138:1166–1171. <http://dx.doi.org/10.1017/S0950268809991300>.
5. Oh DY, Silva PA, Hauroeder B, Diedrich S, Cardoso DD, Schreier E. 2006. Molecular characterization of the first Aichi viruses isolated in Europe and in South America. *Arch Virol* 151:1199–1206. <http://dx.doi.org/10.1007/s00705-005-0706-7>.
 6. Sdiri-Loulizi K, Gharbi-Khelifi H, de Rougemont A, Chouchane S, Sakly N, Ambert-Balay K, Hassine M, Guediche MN, Aouni M, Pothier P. 2008. Acute infantile gastroenteritis associated with human enteric viruses in Tunisia. *J Clin Microbiol* 46:1349–1355. <http://dx.doi.org/10.1128/JCM.02438-07>.
 7. Kitajima M, Gerba CP. 2015. Aichi virus 1: environmental occurrence and behavior. *Pathogens* 4:256–268. <http://dx.doi.org/10.3390/pathogens4020256>.
 8. Yamashita T, Sakae K, Ishihara Y, Isomura S, Utagawa E. 1993. Prevalence of newly isolated, cytopathic small round virus (Aichi strain) in Japan. *J Clin Microbiol* 31:2938–2943.
 9. Yamashita T, Sakae K, Tsuzuki H, Suzuki Y, Ishikawa N, Takeda N, Miyamura T, Yamazaki S. 1998. Complete nucleotide sequence and genetic organization of Aichi virus, a distinct member of the *Picornaviridae* associated with acute gastroenteritis in humans. *J Virol* 72:8408–8412.
 10. Palmenberg AC. 1982. In vitro synthesis and assembly of picornaviral capsid intermediate structures. *J Virol* 44:900–906.
 11. Putnak JR, Phillips BA. 1981. Picornaviral structure and assembly. *Microbiol Rev* 45:287–315.
 12. Rombaut B, Foriers A, Boeye A. 1991. In vitro assembly of poliovirus 14S subunits: identification of the assembly promoting activity of infected cell extracts. *Virology* 180:781–787. [http://dx.doi.org/10.1016/0042-6822\(91\)90091-0](http://dx.doi.org/10.1016/0042-6822(91)90091-0).
 13. Rombaut B, Vrijnsen R, Boeye A. 1984. In vitro assembly of poliovirus empty capsids: antigenic consequences and immunological assay of the morphopoietic factor. *Virology* 135:546–550. [http://dx.doi.org/10.1016/0042-6822\(84\)90209-5](http://dx.doi.org/10.1016/0042-6822(84)90209-5).
 14. Nugent CI, Johnson KL, Sarnow P, Kirkegaard K. 1999. Functional coupling between replication and packaging of poliovirus replicon RNA. *J Virol* 73:427–435.
 15. Jiang P, Liu Y, Ma HC, Paul AV, Wimmer E. 2014. Picornavirus morphogenesis. *Microbiol Mol Biol Rev* 78:418–437. <http://dx.doi.org/10.1128/MMBR.00012-14>.
 16. Dryden KA, Tihova M, Nowotny N, Matsui SM, Mendez E, Yeager M. 2012. Immature and mature human astrovirus: structure, conformational changes, and similarities to hepatitis E virus. *J Mol Biol* 422:650–658. <http://dx.doi.org/10.1016/j.jmb.2012.06.029>.
 17. Tuthill TJ, Gropelli E, Hogle JM, Rowlands DJ. 2010. Picornaviruses. *Curr Top Microbiol Immunol* 343:43–89.
 18. Bostina M, Levy H, Filman DJ, Hogle JM. 2011. Poliovirus RNA is released from the capsid near a twofold symmetry axis. *J Virol* 85:776–783. <http://dx.doi.org/10.1128/JVI.00531-10>.
 19. Lyu K, Ding J, Han JF, Zhang Y, Wu XY, He YL, Qin CF, Chen R. 2014. Human enterovirus 71 uncoating captured at atomic resolution. *J Virol* 88:3114–3126. <http://dx.doi.org/10.1128/JVI.03029-13>.
 20. Wang X, Peng W, Ren J, Hu Z, Xu J, Lou Z, Li X, Yin W, Shen X, Porta C, Walter TS, Evans G, Axford D, Owen R, Rowlands DJ, Wang J, Stuart DI, Fry EE, Rao Z. 2012. A sensor-adaptor mechanism for enterovirus uncoating from structures of EV71. *Nat Struct Mol Biol* 19:424–429. <http://dx.doi.org/10.1038/nsmb.2255>.
 21. Shingler KL, Yoder JL, Carnegie MS, Ashley RE, Makhov AM, Conway JF, Hafenstein S. 2013. The enterovirus 71 A-particle forms a gateway to allow genome release: a cryoEM study of picornavirus uncoating. *PLoS Pathog* 9:e1003240. <http://dx.doi.org/10.1371/journal.ppat.1003240>.
 22. He Y, Chipman PR, Howitt J, Bator CM, Whitt MA, Baker TS, Kuhn RJ, Anderson CW, Freimuth P, Rossmann MG. 2001. Interaction of coxsackievirus B3 with the full-length coxsackievirus-adenovirus receptor. *Nat Struct Biol* 8:874–878. <http://dx.doi.org/10.1038/nsb1001-874>.
 23. Xiao C, Bator CM, Bowman VD, Rieder E, He Y, Hebert B, Bella J, Baker TS, Wimmer E, Kuhn RJ, Rossmann MG. 2001. Interaction of coxsackievirus A21 with its cellular receptor, ICAM-1. *J Virol* 75:2444–2451. <http://dx.doi.org/10.1128/JVI.75.5.2444-2451.2001>.
 24. Olson NH, Kolatkar PR, Oliveira MA, Cheng RH, Greve JM, McClelland A, Baker TS, Rossmann MG. 1993. Structure of a human rhinovirus complexed with its receptor molecule. *Proc Natl Acad Sci U S A* 90:507–511. <http://dx.doi.org/10.1073/pnas.90.2.507>.
 25. Rossmann MG, He Y, Kuhn RJ. 2002. Picornavirus-receptor interactions. *Trends Microbiol* 10:324–331. [http://dx.doi.org/10.1016/S0966-842X\(02\)02383-1](http://dx.doi.org/10.1016/S0966-842X(02)02383-1).
 26. Plevka P, Hafenstein S, Harris KG, Cifuentes JO, Zhang Y, Bowman VD, Chipman PR, Bator CM, Lin F, Medof ME, Rossmann MG. 2010. Interaction of decay-accelerating factor with echovirus 7. *J Virol* 84:12665–12674. <http://dx.doi.org/10.1128/JVI.00837-10>.
 27. Levy HC, Bostina M, Filman DJ, Hogle JM. 2010. Catching a virus in the act of RNA release: a novel poliovirus uncoating intermediate characterized by cryo-electron microscopy. *J Virol* 84:4426–4441. <http://dx.doi.org/10.1128/JVI.02393-09>.
 28. Fricks CE, Hogle JM. 1990. Cell-induced conformational change in poliovirus: externalization of the amino terminus of VP1 is responsible for liposome binding. *J Virol* 64:1934–1945.
 29. Ren J, Wang X, Hu Z, Gao Q, Sun Y, Li X, Porta C, Walter TS, Gilbert RJ, Zhao Y, Axford D, Williams M, McAuley K, Rowlands DJ, Yin W, Wang J, Stuart DI, Rao Z, Fry EE. 2013. Picornavirus uncoating intermediate captured in atomic detail. *Nat Commun* 4:1929.
 30. Seitsonen JJ, Shakeel S, Susi P, Pandurangan AP, Sinkovits RS, Hyvonen H, Laurinmaki P, Yla-Pelto J, Topf M, Hyypia T, Butcher SJ. 2012. Structural analysis of coxsackievirus A7 reveals conformational changes associated with uncoating. *J Virol* 86:7207–7215. <http://dx.doi.org/10.1128/JVI.06425-11>.
 31. Garriga D, Pickl-Herk A, Luque D, Wruss J, Caston JR, Blaas D, Verdagner N. 2012. Insights into minor group rhinovirus uncoating: the X-ray structure of the HRV2 empty capsid. *PLoS Pathog* 8:e1002473. <http://dx.doi.org/10.1371/journal.ppat.1002473>.
 32. Tuthill TJ, Harlos K, Walter TS, Knowles NJ, Gropelli E, Rowlands DJ, Stuart DI, Fry EE. 2009. Equine rhinitis A virus and its low pH empty particle: clues towards an aphthovirus entry mechanism? *PLoS Pathog* 5:e1000620. <http://dx.doi.org/10.1371/journal.ppat.1000620>.
 33. Greve JM, Forte CP, Marlor CW, Meyer AM, Hoover-Litty H, Wunderlich D, McClelland A. 1991. Mechanisms of receptor-mediated rhinovirus neutralization defined by two soluble forms of ICAM-1. *J Virol* 65:6015–6023.
 34. Prchla E, Kuechler E, Blaas D, Fuchs R. 1994. Uncoating of human rhinovirus serotype 2 from late endosomes. *J Virol* 68:3713–3723.
 35. Chow M, Newman JF, Filman D, Hogle JM, Rowlands DJ, Brown F. 1987. Myristylation of picornavirus capsid protein VP4 and its structural significance. *Nature* 327:482–486. <http://dx.doi.org/10.1038/327482a0>.
 36. Lin J, Cheng N, Chow M, Filman DJ, Steven AC, Hogle JM, Belnap DM. 2011. An externalized polypeptide partitions between two distinct sites on genome-released poliovirus particles. *J Virol* 85:9974–9983. <http://dx.doi.org/10.1128/JVI.05013-11>.
 37. Sabin C, Plevka P. 2016. The use of noncrystallographic symmetry averaging to solve structures from data affected by perfect hemihedral twinning. *Acta Crystallogr F Struct Biol Commun* 72:188–197. <http://dx.doi.org/10.1107/S2053230X16000923>.
 38. Shaikh TR, Gao H, Baxter WT, Asturias FJ, Boisset N, Leith A, Frank J. 2008. SPIDER image processing for single-particle reconstruction of biological macromolecules from electron micrographs. *Nat Protoc* 3:1941–1974. <http://dx.doi.org/10.1038/nprot.2008.156>.
 39. Tang G, Peng L, Baldwin PR, Mann DS, Jiang W, Rees I, Ludtke SJ. 2007. EMAN2: an extensible image processing suite for electron microscopy. *J Struct Biol* 157:38–46. <http://dx.doi.org/10.1016/j.jsb.2006.05.009>.
 40. Mindell JA, Grigorieff N. 2003. Accurate determination of local defocus and specimen tilt in electron microscopy. *J Struct Biol* 142:334–347. [http://dx.doi.org/10.1016/S1047-8477\(03\)00069-8](http://dx.doi.org/10.1016/S1047-8477(03)00069-8).
 41. Scheres SH, Chen S. 2012. Prevention of overfitting in cryo-EM structure determination. *Nat Methods* 9:853–854. <http://dx.doi.org/10.1038/nmeth.2115>.
 42. Scheres SH. 2012. RELION: implementation of a Bayesian approach to cryo-EM structure determination. *J Struct Biol* 180:519–530. <http://dx.doi.org/10.1016/j.jsb.2012.09.006>.
 43. Rosenthal PB, Henderson R. 2003. Optimal determination of particle orientation, absolute hand, and contrast loss in single-particle electron cryomicroscopy. *J Mol Biol* 333:721–745. <http://dx.doi.org/10.1016/j.jmb.2003.07.013>.
 44. Tate J, Liljas L, Scotti P, Christian P, Lin T, Johnson JE. 1999. The crystal structure of cricket paralysis virus: the first view of a new virus family. *Nat Struct Biol* 6:765–774. <http://dx.doi.org/10.1038/11543>.

45. Brunger AT. 2007. Version 1.2 of the crystallography and NMR system. *Nat Protoc* 2:2728–2733. <http://dx.doi.org/10.1038/nprot.2007.406>.
46. Jones TA, Zou JY, Cowan SW, Kjeldgaard M. 1991. Improved methods for building protein models in electron density maps and the location of errors in these models. *Acta Crystallogr A* 47(Pt 2):110–119. <http://dx.doi.org/10.1107/S0108767390010224>.
47. Emsley P, Cowtan K. 2004. Coot: model-building tools for molecular graphics. *Acta Crystallogr D Biol Crystallogr* 60:2126–2132. <http://dx.doi.org/10.1107/S0907444904019158>.
48. Afonine PV, Grosse-Kunstleve RW, Echols N, Headd JJ, Moriarty NW, Mustyakimov M, Terwilliger TC, Urzhumtsev A, Zwart PH, Adams PD. 2012. Towards automated crystallographic structure refinement with phenix.refine. *Acta Crystallogr D Biol Crystallogr* 68:352–367. <http://dx.doi.org/10.1107/S0907444912001308>.
49. Kleywegt GJ, Jones TA. 1994. Detection, delineation, measurement, and display of cavities in macromolecular structures. *Acta Crystallogr D Biol Crystallogr* 50:178–185. <http://dx.doi.org/10.1107/S0907444993011333>.
50. Kleywegt GJ. 1999. Experimental assessment of differences between related protein crystal structures. *Acta Crystallogr D Biol Crystallogr* 55:1878–1884. <http://dx.doi.org/10.1107/S0907444999010495>.
51. Pettersen EF, Goddard TD, Huang CC, Couch GS, Greenblatt DM, Meng EC, Ferrin TE. 2004. UCSF Chimera: a visualization system for exploratory research and analysis. *J Comput Chem* 25:1605–1612. <http://dx.doi.org/10.1002/jcc.20084>.
52. Russell RB, Barton GJ. 1992. Multiple protein sequence alignment from tertiary structure comparison: assignment of global and residue confidence levels. *Proteins* 14:309–323. <http://dx.doi.org/10.1002/prot.340140216>.
53. Rossmann MG, Arnold E, Erickson JW, Frankenberger EA, Griffith JP, Hecht HJ, Johnson JE, Kamer G, Luo M, Mosser AG, Rueckert RR, Sherry B, Vriend G. 1985. Structure of a human common cold virus and functional-relationship to other picornaviruses. *Nature* 317:145–153. <http://dx.doi.org/10.1038/317145a0>.
54. Hogle JM, Chow M, Filman DJ. 1985. Three-dimensional structure of poliovirus at 2.9 Å resolution. *Science* 229:1358–1365. <http://dx.doi.org/10.1126/science.2994218>.
55. Plevka P, Perera R, Cardoso J, Kuhn RJ, Rossmann MG. 2012. Crystal structure of human enterovirus 71. *Science* 336:1274. <http://dx.doi.org/10.1126/science.1218713>.
56. Kalynych S, Palkova L, Plevka P. 2016. The structure of human parechovirus 1 reveals an association of the RNA genome with the capsid. *J Virol* 90:1377–1386. <http://dx.doi.org/10.1128/JVI.02346-15>.
57. Wang X, Ren J, Gao Q, Hu Z, Sun Y, Li X, Rowlands DJ, Yin W, Wang J, Stuart DI, Rao Z, Fry EE. 2015. Hepatitis A virus and the origins of picornaviruses. *Nature* 517:85–88. <http://dx.doi.org/10.1038/nature13806>.
58. Zhang P, Mueller S, Morais MC, Bator CM, Bowman VD, Hafenstein S, Wimmer E, Rossmann MG. 2008. Crystal structure of CD155 and electron microscopic studies of its complexes with polioviruses. *Proc Natl Acad Sci U S A* 105:18284–18289. <http://dx.doi.org/10.1073/pnas.0807848105>.
59. Smith TJ, Kremer MJ, Luo M, Vriend G, Arnold E, Kamer G, Rossmann MG, Mckinlay MA, Diana GD, Otto MJ. 1986. The site of attachment in human rhinovirus-14 for antiviral agents that inhibit uncoating. *Science* 233:1286–1293. <http://dx.doi.org/10.1126/science.3018924>.
60. Hadfield AT, Lee W, Zhao R, Oliveira MA, Minor I, Rueckert RR, Rossmann MG. 1997. The refined structure of human rhinovirus 16 at 2.15 Å resolution: implications for the viral life cycle. *Structure* 5:427–441. [http://dx.doi.org/10.1016/S0969-2126\(97\)00199-8](http://dx.doi.org/10.1016/S0969-2126(97)00199-8).
61. Smyth M, Pettitt T, Symonds A, Martin J. 2003. Identification of the pocket factors in a picornavirus. *Arch Virol* 148:1225–1233. <http://dx.doi.org/10.1007/s00705-002-0974-4>.
62. Hadfield AT, Diana GD, Rossmann MG. 1999. Analysis of three structurally related antiviral compounds in complex with human rhinovirus 16. *Proc Natl Acad Sci U S A* 96:14730–14735. <http://dx.doi.org/10.1073/pnas.96.26.14730>.
63. Grant RA, Hiremath CN, Filman DJ, Syed R, Andries K, Hogle JM. 1994. Structures of poliovirus complexes with anti-viral drugs: implications for viral stability and drug design. *Curr Biol* 4:784–797. [http://dx.doi.org/10.1016/S0960-9822\(00\)00176-7](http://dx.doi.org/10.1016/S0960-9822(00)00176-7).
64. Hiremath CN, Grant RA, Filman DJ, Hogle JM. 1995. Binding of the antiviral drug WIN51711 to the Sabin strain of type 3 poliovirus: structural comparison with drug binding in rhinovirus 14. *Acta Crystallogr D Biol Crystallogr* 51:473–489. <http://dx.doi.org/10.1107/S090744499401084X>.
65. Luo M, Vriend G, Kamer G, Minor I, Arnold E, Rossmann MG, Boege U, Scraba DG, Duke GM, Palmenberg AC. 1987. The atomic structure of Mengo virus at 3.0 Å resolution. *Science* 235:182–191. <http://dx.doi.org/10.1126/science.3026048>.
66. Grant RA, Filman DJ, Fujinami RS, Icenogle JP, Hogle JM. 1992. Three-dimensional structure of Theiler virus. *Proc Natl Acad Sci U S A* 89:2061–2065. <http://dx.doi.org/10.1073/pnas.89.6.2061>.
67. Mullapudi E, Novacek J, Palkova L, Kulich P, Lindberg AM, van Kuppeveld FJ, Plevka P. 2016. Structure and genome release mechanism of human cardiovirus Saffold virus-3. *J Virol* 90:7628–7639. <http://dx.doi.org/10.1128/JVI.00746-16>.
68. Zhu L, Wang X, Ren J, Porta C, Wenham H, Ekstrom JO, Panjwani A, Knowles NJ, Kotecha A, Siebert CA, Lindberg AM, Fry EE, Rao Z, Tuthill TJ, Stuart DI. 2015. Structure of Ljungan virus provides insight into genome packaging of this picornavirus. *Nat Commun* 6:8316. <http://dx.doi.org/10.1038/ncomms9316>.
69. Acharya R, Fry E, Stuart D, Fox G, Rowlands D, Brown F. 1989. The three-dimensional structure of foot-and-mouth disease virus at 2.9 Å resolution. *Nature* 337:709–716. <http://dx.doi.org/10.1038/337709a0>.
70. Shakeel S. 2014. Human picornaviruses: uncoating, assembly and interaction with cellular receptors. University of Helsinki, Helsinki, Finland.
71. Smyth MS, Martin JH. 2002. Picornavirus uncoating. *Mol Pathol* 55:214–219. <http://dx.doi.org/10.1136/mp.55.4.214>.
72. Butan C, Filman DJ, Hogle JM. 2014. Cryo-electron microscopy reconstruction shows poliovirus 135S particles poised for membrane interaction and RNA release. *J Virol* 88:1758–1770. <http://dx.doi.org/10.1128/JVI.01949-13>.
73. Belnap DM, Filman DJ, Trus BL, Cheng N, Booy FP, Conway JF, Curry S, Hiremath CN, Tsang SK, Steven AC, Hogle JM. 2000. Molecular tectonic model of virus structural transitions: the putative cell entry states of poliovirus. *J Virol* 74:1342–1354. <http://dx.doi.org/10.1128/JVI.74.3.1342-1354.2000>.
74. Guasch A, Pous J, Ibarra B, Gomis-Ruth FX, Valpuesta JM, Sousa N, Carrascosa JL, Coll M. 2002. Detailed architecture of a DNA translocating machine: the high-resolution structure of the bacteriophage phi29 connector particle. *J Mol Biol* 315:663–676. <http://dx.doi.org/10.1006/jmbi.2001.5278>.
75. Hewat EA, Neumann E, Blaas D. 2002. The concerted conformational changes during human rhinovirus 2 uncoating. *Mol Cell* 10:317–326. [http://dx.doi.org/10.1016/S1097-2765\(02\)00603-2](http://dx.doi.org/10.1016/S1097-2765(02)00603-2).
76. Hewat EA, Blaas D. 2004. Cryoelectron microscopy analysis of the structural changes associated with human rhinovirus type 14 uncoating. *J Virol* 78:2935–2942. <http://dx.doi.org/10.1128/JVI.78.6.2935-2942.2004>.
77. Harutyunyan S, Kumar M, Sedivy A, Subirats X, Kowalski H, Kohler G, Blaas D. 2013. Viral uncoating is directional: exit of the genomic RNA in a common cold virus starts with the poly(A) tail at the 3'-end. *PLoS Pathog* 9:e1003270. <http://dx.doi.org/10.1371/journal.ppat.1003270>.
78. Davis IW, Leaver-Fay A, Chen VB, Block JN, Kapral GJ, Wang X, Murray LW, Arendall WB, III, Snoeyink J, Richardson JS, Richardson DC. 2007. MolProbity: all-atom contacts and structure validation for proteins and nucleic acids. *Nucleic Acids Res* 35:W375–W383. <http://dx.doi.org/10.1093/nar/gkm216>.

PAPER III



Structure and Genome Release Mechanism of the Human Cardiovirus Saffold Virus 3

Edukondalu Mullapudi,^a Jiří Nováček,^a Lenka Pálková,^a Pavel Kulich,^b A. Michael Lindberg,^c Frank J. M. van Kuppeveld,^d Pavel Plevka^a

Central European Institute of Technology, Masaryk University, Brno, Czech Republic^a; Veterinary Research Institute, Brno, Czech Republic^b; Department of Chemistry and Biomedical Sciences, Linnaeus University, Kalmar, Sweden^c; Department of Medical Microbiology, Virology Section, Radboud University Nijmegen Medical Centre, Nijmegen, The Netherlands^d

ABSTRACT

In order to initiate an infection, viruses need to deliver their genomes into cells. This involves uncoating the genome and transporting it to the cytoplasm. The process of genome delivery is not well understood for nonenveloped viruses. We address this gap in our current knowledge by studying the uncoating of the nonenveloped human cardiovirus Saffold virus 3 (SAFV-3) of the family *Picornaviridae*. SAFVs cause diseases ranging from gastrointestinal disorders to meningitis. We present a structure of a native SAFV-3 virion determined to 2.5 Å by X-ray crystallography and an 11-Å-resolution cryo-electron microscopy reconstruction of an “altered” particle that is primed for genome release. The altered particles are expanded relative to the native virus and contain pores in the capsid that might serve as channels for the release of VP4 subunits, N termini of VP1, and the RNA genome. Unlike in the related enteroviruses, pores in SAFV-3 are located roughly between the icosahedral 3- and 5-fold axes at an interface formed by two VP1 and one VP3 subunit. Furthermore, in native conditions many cardioviruses contain a disulfide bond formed by cysteines that are separated by just one residue. The disulfide bond is located in a surface loop of VP3. We determined the structure of the SAFV-3 virion in which the disulfide bonds are reduced. Disruption of the bond had minimal effect on the structure of the loop, but it increased the stability and decreased the infectivity of the virus. Therefore, compounds specifically disrupting or binding to the disulfide bond might limit SAFV infection.

IMPORTANCE

A capsid assembled from viral proteins protects the virus genome during transmission from one cell to another. However, when a virus enters a cell the virus genome has to be released from the capsid in order to initiate infection. This process is not well understood for nonenveloped viruses. We address this gap in our current knowledge by studying the genome release of *Human Saffold virus 3*. Saffold viruses cause diseases ranging from gastrointestinal disorders to meningitis. We show that before the genome is released, the Saffold virus 3 particle expands, and holes form in the previously compact capsid. These holes serve as channels for the release of the genome and small capsid proteins VP4 that in related enteroviruses facilitate subsequent transport of the virus genome into the cell cytoplasm.

Human Saffold virus 3 (SAFV-3) belongs to the species *Theilovirus* in the genus *Cardiovirus* of the family *Picornaviridae* (1, 2). Cardioviruses are pathogens of vertebrates, frequently infecting rodents. The first human cardiovirus, *Vilyuisk virus*, was isolated in 1960 and characterized as a divergent Theiler's virus in 1992 (3). SAFV-1 was identified in a stool sample of an infant with fever (4), and SAFV-3 was isolated from the cerebrospinal fluid of a patient with aseptic meningitis (5, 6). Experimental infections of mice have shown that SAFV-3 replicates primarily in heart tissue and the central nervous system (6, 7). To date, 11 genotypes of SAFV have been identified (8–11).

Cardioviruses have nonenveloped virions with an external diameter of about 30 nm (12, 13). The icosahedral capsid contains a nonsegmented positive-sense single-stranded RNA (ssRNA) genome with a virally encoded protein VPg attached to the 5' end and a poly(A) sequence at the 3' end. The genome contains a single open reading frame flanked by untranslated regions (UTR) at both ends. Both the 5' and 3' UTRs are required for the initiation of replication. Translation of the genome is directed by an internal ribosomal entry site (IRES) within the 5' UTR. The myristylated structural polypeptide P1 of enteroviruses is co- and post-translationally cleaved by the viral proteases 3C and 3CD, re-

sulting in the formation of the VP0-VP3-VP1 heterotrimeric protomer that sediments at 5S (14, 15). It was shown that 5S protomers associate into 14S pentamers and that 12 copies of 14S particles self-assemble into 80S empty capsids (16–18). The mechanism of self-assembly and the function of the empty capsids in the formation of enterovirus virions *in vivo*, however, are not well understood. In addition, active replication and translation of the poliovirus genome is required for virion formation (19). RNA-containing particles mature to virions by the cleavage of VP0 into VP2 and VP4 (20). The capsid proteins VP1, VP2, VP3, and VP4 originating from one polyprotein form a heterotetrameric

Received 21 April 2016 Accepted 31 May 2016

Accepted manuscript posted online 8 June 2016

Citation Mullapudi E, Nováček J, Pálková L, Kulich P, Lindberg AM, van Kuppeveld FJM, Plevka P. 2016. Structure and genome release mechanism of the human cardiovirus Saffold virus 3. *J Virol* 90:7628–7639. doi:10.1128/JVI.00746-16.

Editor: S. López, Instituto de Biotecnología/UNAM

Address correspondence to Pavel Plevka, pavel.plevka@muni.ceitec.cz.

Copyright © 2016 Mullapudi et al. This is an open-access article distributed under the terms of the [Creative Commons Attribution 4.0 International license](https://creativecommons.org/licenses/by/4.0/).

protomer, an elementary building block of the capsid. The major capsid proteins VP1 to VP3 form the capsid shell with pseudo- $T=3$ icosahedral symmetry whereas VP4 subunits are attached to the inner surface of the capsid. VP1 subunits form pentamers around icosahedral 5-fold axes, whereas VP2 and VP3 subunits form heterohexamers positioned on icosahedral 3-fold axes. The major capsid proteins have the jellyroll β -sandwich fold common to many other virus capsid proteins.

Enteroviruses of the family *Picornaviridae*, which are related to cardiociruses, are extensively studied as models for genome delivery (21–26). The surface of the enterovirus capsid contains circular depressions around icosahedral 5-fold symmetry axes called “canyons.” The canyons of many enteroviruses, including major group human rhinoviruses (HRVs), are the binding sites of receptors from the immunoglobulin superfamily (27–30). However, other enteroviruses use different regions of their capsids to recognize their receptors (31, 32). Binding of receptors within the enterovirus canyon induces the release of a “pocket factor” from a hydrophobic pocket immediately below the surface of the canyon (30). Receptors that do not bind to the canyon, including LDL-R and DAF, do not induce release of the pocket factor (30–32). Furthermore, some enteroviruses, including HRV-14, lack the pocket factor even in the native state (33). In these viruses the conversion to the A particles might be induced by exposure to the low pH of the endosome (34–36). Before genome release, enterovirus virions convert into “altered” (A) particles characterized by radial expansion of the capsid and the formation of pores at the icosahedral 2-fold symmetry axes (22–25, 36–40). These changes allow the exposure of the membrane-active peptides from the capsid, which facilitates delivery of the genome into the cytoplasm. In poliovirus and CAV-A16, the genome release is accompanied by the exposure of the N-terminal region of VP1 and the release of the myristoylated VP4 (38, 41, 42).

Cardiociruses differ from enteroviruses in the details of their capsid structures and in the receptor molecules they utilize for cell entry. The structures of Mengo virus (MeV) and Theiler’s murine encephalomyelitis virus (TMEV) have shown that cardiocirus virions lack canyons and pocket factors (12, 13). Some TMEV strains use glycolipids or N- and O-linked carbohydrates containing sialic acid as coreceptors (43–45). Furthermore, the murine vascular cell adhesion molecule-1 is a receptor of the D variant of an encephalomyocarditis virus (46). However, the receptor of SAFV is unknown. Despite the impact of cardiociruses on human health, we do not yet have an atomic-level structural description of SAFV virions, and the mechanism of their genome release is unknown. Here we report a crystal structure of SAFV-3 determined to a 2.5-Å resolution and a cryo-electron microscopy (cryo-EM) reconstruction of an A particle at a 10.6-Å resolution. Comparison of the two structures enabled us to propose a mechanism for the uncoating of the cardiocirus genome.

MATERIALS AND METHODS

SAFV-3 recovery from cDNA. HeLa cells were transfected with the cDNA of SAFV-3 (7) using Fugene 6 according to the manufacturer’s instructions. Briefly, 10 μ g of SAFV-3 cDNA (7) was diluted in 168 μ l of Opti-MEM medium, and 27 μ l of Fugene 6 was added. The cDNA-Fugene 6 mixture was applied to a 50% confluent cell monolayer on a 50-mm-diameter plate. The cells were incubated with the transfection mixture for 2 h. Subsequently, 10 ml of minimal essential medium (MEM) was added, and the cells were grown at 37°C in a 5% CO₂ incubator. After 48 h, a

cytopathic effect (CPE) was observed, and the cells were harvested and freeze-thawed three times (at –80 and 37°C) to release the virions.

Virus production and purification. HeLa cells clone Ohio grown in 50 150-mm-diameter plates to 80% confluence were used for infection. The medium was aspirated from the plates, and the cells were washed with 5 ml of serum-free MEM. Cells were infected with 2 ml of the virus diluted to obtain a multiplicity of infection of 0.2 in serum-free MEM, followed by incubation for 3 h at 37°C in a 5% CO₂ incubator with gentle shaking every 30 min. The virus titer was determined using a plaque assay on HeLa cells. Subsequently, 18 ml of MEM supplemented with 10% fetal bovine serum (FBS) and 0.2 mM L-glutamine were added to each plate, followed by incubation at 37°C. After 48 to 72 h, CPE was observed, and the cells were pelleted by centrifugation at 9,000 rpm in TA-10-250 Beckman Coulter rotor at 4°C for 15 min. After centrifugation, the cell pellet was dissolved in 10 ml of phosphate-buffered saline (PBS) and subjected to three cycles of freeze-thawing at –80 and 37°C. Subsequently, the cell debris was homogenized on ice using a Dounce tissue grinder, followed by centrifugation at 4°C at 5,000 rpm in TA-10-250 Beckman Coulter rotor for 10 min. The supernatant was mixed with the medium collected from the infected cells. The virus was precipitated from the supernatant overnight at 4°C by adding PEG 8000 and NaCl to final concentrations of 10% and 0.5 M, respectively. The solution was centrifuged at 9,000 rpm in TA-10-250 Beckman Coulter rotor at 4°C for 10 min, and the supernatant was discarded. The resulting pellet was resuspended in 10 ml of 20 mM HEPES (pH 7.5) and 150 mM NaCl at 4°C and homogenized with a Dounce tissue grinder. DNase and RNase were added to final concentrations of 10 μ g/ml, and the solution was incubated at 37°C for 30 min. Subsequently, trypsin was added to a final concentration of 80 μ g/ml, and the solution was incubated at 37°C for an additional 30 min, followed by centrifugation at 4,500 rpm in TA-10-250 Beckman Coulter rotor at 10°C for 10 min. The 10°C temperature was used to limit temperature changes when manipulating with the virus. The clarified supernatant was layered over 2 ml of 25% (wt/vol) sucrose cushion and centrifuged in a Beckman Ti 50.2 rotor at 48,000 rpm at 10°C for 2 h. After centrifugation, the supernatant was discarded, the pellet was resuspended in 2 ml of 20 mM HEPES (pH 7.5) and 150 mM NaCl buffer at 4°C, and the virus suspension was layered onto a 10 to 40% (wt/vol) potassium tartrate gradient prepared in the same buffer and centrifuged in an SW40 rotor at 36,000 rpm at 10°C for 90 min. The gradient layer containing the virus was collected by perforating the wall of the tube with a syringe and needle. The virus-containing fraction was transferred to 20 mM HEPES (pH 7.5) and 150 mM NaCl buffer using sequential centrifugations, and buffer additions were made using a 100-kDa cutoff Vivaspin columns (Sigma-Aldrich) at 4°C. Virus purity and concentration was verified by sodium dodecyl sulfate-gel electrophoresis. For long-term storage, the virus at 2 mg/ml was maintained at –80°C.

Negative-stain transmission electron microscopy. Morphology and the size of the virus particles were analyzed by transmission electron microscopy. A total of 5 μ l of purified virus sample at 0.2 mg/ml was applied to a carbon-coated copper grid, allowed to adsorb for 10 min, and stained with 0.5% molybdenum acetate for 30 s. Between each transfer, excess liquid was blotted with filter paper. The grid was thoroughly dried before being mounted on a grid holder. The grids were examined, and images of viruses were captured in a Morgan Philips 201C transmission electron microscope.

SAFV-3 crystallization and diffraction data collection. The purified virus at a concentration of 3 mg/ml was crystallized in 2.8 M sodium acetate buffer (pH 7.0) using the hanging-drop vapor diffusion method. Rhombic crystals (~200 μ m in size) were flash cooled in liquid nitrogen and used to obtain X-ray diffraction data. The crystallization solution served as a sufficient cryoprotectant. Diffraction data were collected using a Swiss Light Source beamline X06SA and a Diamond Light Source beamline I03. Data obtained using the Swiss Light Source beamline were collected from formaldehyde-treated virus crystals.

TABLE 1 Diffraction data and structure quality indicators^a

| Parameter | Native SAFV-3 | DTT-treated SAFV-3 |
|--|---------------------|---------------------|
| Space group | P3 ₂ 21 | P3 ₂ 21 |
| Unit cell dimensions | | |
| <i>a</i> , <i>b</i> , <i>c</i> (Å) | 300.5, 300.5, 722.1 | 299.9, 299.9, 723.4 |
| α , β , γ (°) | 90, 90, 120 | 90, 90, 120 |
| Resolution range (Å) | 70.0–2.5 (2.6–2.5) | 70.0–2.5 (2.6–2.5) |
| No. of observations | 1,540,201 (64,360) | 1,606,180 (141,586) |
| No. of unique reflections | 794,529 (43,288) | 864,367 (93,415) |
| Observation multiplicity | 1.9 (1.5) | 1.9 (1.5) |
| Completeness (%) | 61.9 (33.9) | 67.5 (73.8) |
| R_{merge} (%) ^b | 0.114 (0.505) | 0.123 (0.648) |
| $\langle I \rangle / \langle \sigma I \rangle$ | 6.8 (1.2) | 5.5 (1.0) |
| R_{factor} (%) ^c | 22.7 (38.5) | 21.5 (33.5) |
| No. of ^d : | | |
| Protein atoms | 6,012 | 6,012 |
| Water molecules | 343 | 341 |
| Avg B factor (Å ²) | 32.8 | 27.6 |
| No. of Ramachandran outliers ^e | 2 | 3 |
| RMSD | | |
| Bond angle (°) | 0.005 | 0.022 |
| Bond length (Å) | 1.36 | 1.83 |

^a The statistics for the highest-resolution shell are shown in parentheses.

^b $R_{\text{merge}} = \sum_i \sum_j |I_{ij} - \langle I_i \rangle| / \sum_i \sum_j I_{ij}$.

^c All reflections were used in the refinement. The R_{free} value, if it were calculated, would be very similar to R_{work} because of the 30-fold noncrystallographic symmetry present in the crystal. Therefore, the R_{free} would not provide an unbiased measure of model quality in this case (55). See Materials and Methods for details.

^d That is, in an icosahedral asymmetric unit.

^e According to the Molprobity criterion (75).

Structure determination. Native SAFV-3 crystallized in space group P3₂21. Unit cell parameters (Table 1) and packing considerations indicated that one-half of a virus particle occupied a crystallographic asymmetric unit. Plots of the 2-fold self-rotation function calculated using the program GLRF indicated that the icosahedral 2-fold axis of the virion was positioned on a crystallographic 2-fold axis (47). The locked self-rotation function had shown that the particle is rotated $\phi = 0^\circ$, $\varphi = 90^\circ$, $\kappa = 130.5^\circ$ according to the XYK polar angle convention from the standard icosahedral orientation as defined by Rossmann and Blow (48). Reflections between resolutions of 5.0 and 4.5 Å were used for the calculations. The radius of integration was set to 140 Å. Since the particle was positioned on an icosahedral 2-fold axis, the position of the particle center had to be determined in a one-dimensional search along a line defined by $y = 0$ and $z = 1/6$. The position of the particle center was identified at the fractional coordinate $x = 0.349$ using the program Phaser from the CCP4 suite (49).

A model of the cardiovirus Theiler's murine encephalitis virus (TMEV) PDB entry 1TME converted to polyalanine was used for the molecular replacement. The model was placed into the orientation and position in the unit cell as described above and used to calculate phases for reflections up to a resolution of 10 Å using the program CNS (50). The phases were refined by 25 cycles of 30-fold real-space electron density map averaging using the program AVE (51). Phase extension was applied in order to obtain phases for higher resolution reflections. The addition of a small fraction of higher resolution data (one index at a time) was followed by three cycles of averaging. This procedure was repeated until phases were obtained for all the reflections up to a resolution of 2.5 Å. The model was built using the programs O and Coot (52, 53), starting from the TMEV coordinates where the respective residues were mutated to those of SAFV-3. The model was refined by manual rebuilding, alternating with

coordinate refinement using the program CNS (simulated annealing, gradient minimization, and individual B-factor refinement) (50). Other calculations were carried out using CCP4 (54). All the measured reflections were used in the refinement. If calculated, R_{free} would be very similar to the R value due to the 30-fold noncrystallographic symmetry (NCS) present in the diffraction data (55). Reflections related by the NCS present in the crystal and diffraction data are correlated with each other. This correlation was utilized in the phase extension; however, because of the correlation it was not possible to select reflections in the R_{free} test set that were not correlated with the working set reflections used in the refinement. It was demonstrated previously that in the presence of 30-fold NCS, even the use of thin shells or symmetry-related groups of reflections for the test set is not sufficient (56). Crystals of dithiothreitol (DTT)-treated SAFV-3 were of the same space group as those of the native virus but had slightly different unit cell parameters. The structure was determined in the same manner as the native one; however, the native model of SAFV-3 was used for the molecular replacement.

Induction of SAFV-3 genome release by heating. The stability of SAFV-3 was determined as the temperature at which 50% of its RNA genome was accessible to fluorescent RNA-binding dye Sybr green II. Virions at a concentration of 0.02 mg/ml in 0.25 M HEPES (pH 7.5)–0.25 M NaCl buffer were incubated with Sybr green II (diluted $\times 3,000$ times from the stock solution according to the manufacturer's instructions), and the mixture was heated from 25 to 95°C in 1°C increments with a 2-min incubation time at each temperature in the real-time PCR instrument (Roche LightCycler 480). The fluorescence signal increases as the dye interacts with RNA that is released from the thermally destabilized particles, or the dye might be able to enter the particles. The thermal stability of the virus was estimated at the temperature corresponding to an increase in the fluorescence to 50% of the maximal value obtained when all virions were thermally denatured. The measurements were carried out in triplicate.

Determination of the effect of DTT on SAFV-3 infectivity. The effect of DTT on the infectivity of SAFV-3 was quantified by flow cytometry using propidium iodide dye to stain dead and apoptotic cells. DTT at a final concentration of 10 mM was added to SAFV-3 and EV71 in MEM supplemented with 10% serum and 0.2 mM L-glutamine, followed by incubation for 15 min at room temperature. The DTT was removed from the virus by repeated medium exchange in Vivaspin concentrators by concentrating the virus to 1/10 of the initial volume and diluting the samples three times. The control virus stocks were treated in the same way except for the absence of DTT. Prior to virus infection, HeLa cells grown to 80% confluence grown in a six-well dish were washed with 2 ml of serum-free MEM. The cells were incubated at 37°C for 2 h with 200 μ l of the DTT-treated and control untreated viruses. The medium was removed and 2 ml of fresh MEM supplemented with 10% FBS and 0.2 mM L-glutamine were added to the cells, followed by incubation at 37°C. After 24 h, the cells from one plate were washed with PBS, trypsinized into 0.1 ml of final volume of PBS, and stained with 1 μ l of 1 mg/ml propidium iodide dissolved in water for 5 min. The number of dead cells was determined using a flow cytometer (BD FACSVerser). All experiments were performed in triplicates.

Cryo-EM data collection and structure determination. SAFV-3 solution with a concentration of 2 mg/ml in 20 mM HEPES (pH 7.5) and 150 mM NaCl buffer was heated for 2 min at 42°C to produce A particles, applied to a holey carbon film, blotted, and immediately vitrified by plunging into liquid ethane using Vitrobot Mark 4. The use of a 2-s blotting time with force -2 resulted in optimal ice thickness.

Electron micrographs were recorded with a BM Eagle CCD detector in a FEI TF20 FEG microscope using defocus ranging from -2.33 to -3.95 μ m. The micrographs had a pixel size of 2.22 Å. In total, 17,483 particles were boxed out from the micrographs using the program e2boxer.py, and the defocus of each micrograph was determined using the program e2ctf.py from the EMAN2 suite (57). Particle images were phase corrected for the effect of the contrast transfer function using the program fitctf2.py

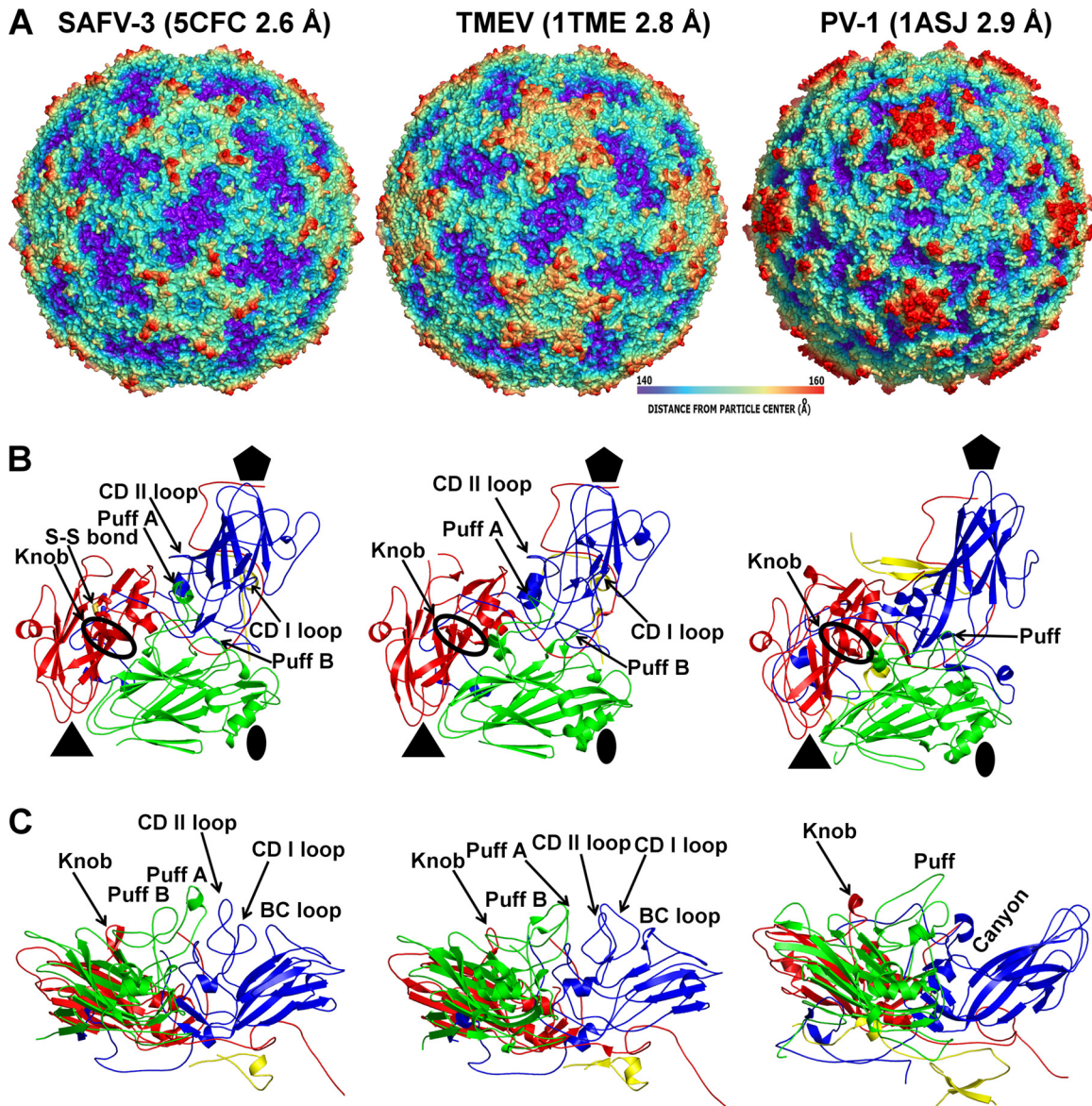


FIG 1 Comparison of SAFV-3, TMEV, and poliovirus 1 capsid protein and virion structures. (A) Surface rendering of virions rainbow-colored based on distance from particle center. (B) Diagrams of icosahedral asymmetric units. VP1 is shown in blue, VP2 is shown in green, VP3 is shown in red, and VP4 is shown in yellow. The positions of the prominent surface features “puff” in VP2 and “knob” in VP3 are indicated. Cys87 and cys89 forming a disulfide bond in SAFV-3 VP3 are shown in stick representation. (C) Side views of icosahedral asymmetric units demonstrating the absence of a canyon in SAFV-3.

(58). Particles were separated into two halves (odd and even image numbers) and treated completely independently in according to the gold standard approach (59). First, nine sets of 400 particles were randomly selected from each half of the data and assigned random orientation parameters for initial reconstruction using the program j3dr (59). Icosahedral symmetry was imposed during the reconstruction. The orientation parameters were then refined using template matching within the icosahedral asymmetric unit in the program jalign (59). Independent initial models were selected for the even and odd data sets, and the phases of these initial models were randomized below a resolution of 40 Å. Multiple independent alignment reconstruction steps were iterated to select bad particles based on their inconsistency in the assignment of orientations. Finally, the orientation parameters for 7,014 selected particles in each half of the data were further refined to produce final reconstructions for the even and odd data sets. The resolution of the resulting map was estimated

as the resolution at which the correlation between the two sets of structure factors derived from the two reconstructions fell below 0.143.

Fitting native SAFV-3 model into cryo-EM reconstruction of empty particle. The electron density map of VP1, VP2, and VP3 derived from the native structure of SAFV-3 was manually positioned into the cryo-EM map of the A particle using the program VMD (60), and its position was refined using the program Chimera (61). A “difference map” was calculated by setting to zero the density values of grid points within 5 Å of any VP1, VP2, or VP3 atoms for all but one of the subunits at a time. The crystal structures of VP1, VP2, and VP3 were consequently fitted into the corresponding difference maps using the multifragment refinement program Collage (62). New difference maps were calculated based on the updated positions of VP1, VP2, and VP3, and the fitting was repeated iteratively. A convergence was reached in four repeats of the fitting. The resulting positions of VP1, VP2, and VP3 determined by multifragment

TABLE 2 Sequence and structural similarities of capsid proteins of selected picornaviruses

| Virus | RMSD (Å) and % identity ^a | | | | | | | | | | |
|-------|--------------------------------------|------|------|-----|-------|-----|-------|------|-----|------|-------|
| | SAFV3 | TMEV | EMCV | PV1 | HRV14 | HAV | HPeV1 | EV71 | EV7 | CVB3 | CVA16 |
| SAFV3 | | 0.8 | 1.1 | 1.5 | 1.5 | 2.0 | 2.1 | 1.5 | 2.7 | 1.6 | 1.6 |
| TMEV | 70 | | 1.0 | 1.5 | 1.5 | 2.0 | 2.1 | 1.7 | 1.5 | 1.5 | 1.6 |
| EMCV | 60 | 64 | | 1.8 | 1.7 | 2.6 | 2.6 | 1.9 | 1.7 | 1.7 | 1.8 |
| PV1 | 29 | 29 | 28 | | 1.0 | 2.1 | 2.1 | 1.1 | 0.9 | 1.0 | 1.0 |
| HRV14 | 25 | 26 | 28 | 49 | | 2.1 | 2.1 | 1.1 | 1.1 | 1.0 | 1.2 |
| HAV | 20 | 21 | 18 | 18 | 19 | | 2.1 | 2.1 | 2.1 | 2.0 | 2.1 |
| HPeV1 | 19 | 20 | 19 | 17 | 17 | 18 | | 2.2 | 2.1 | 3.0 | 2.2 |
| EV71 | 29 | 30 | 29 | 44 | 44 | 17 | 15 | | 1.0 | 1.0 | 0.5 |
| EV7 | 28 | 29 | 27 | 55 | 47 | 19 | 17 | 46 | | 0.7 | 1.0 |
| CVB3 | 28 | 29 | 28 | 54 | 50 | 20 | 10 | 48 | 72 | | 1.0 |
| CVA16 | 30 | 30 | 29 | 47 | 44 | 17 | 15 | 79 | 48 | 49 | |

^aThe top right portion of the table shows the root mean square deviations (RMSD) of superimposed C α atoms of the respective three-dimensional structures. Capsid protein protomers corresponding to icosahedral asymmetric units consisting of subunits VP1 to VP4 were used in the comparisons. The program Coot was used for superposition of the molecules (53). In the bottom left portion of the table are the percent identities between the respective virus coat protein sequences. Gaps were ignored in the calculations.

rigid-body fitting in the program Collage achieved a 5% increase in the correlation coefficient, with 98% of the atoms contained within the map.

Accession number(s). Protein Data Bank (PDB) models of native and DTT-treated SAFV-3, together with structure factor amplitudes and phases derived by phase extension, have been deposited in the PDB under codes 5CFC and 5CFD, respectively. A cryo-EM reconstruction map of the SAFV-3 A particle was deposited with EMDDB under number EMD-3097 (http://emsearch.rutgers.edu/atlas/3097_summary.html), and the fitted coordinates were deposited in the PDB under code 5A8F.

RESULTS AND DISCUSSION

Structure of the SAFV-3 virion and capsid proteins. The crystal structure of the SAFV-3 virion was determined to a resolution of 2.5 Å. Each of the major capsid proteins, VP1, VP2, and VP3, has a β -sandwich fold that consists of eight β -strands, conventionally named B-I, forming the two antiparallel β -sheets containing strands BIDG and CHEF (12, 13, 33, 63). The N termini of the major capsid proteins are located on the inside the capsid, while the C termini are exposed on the particle surface. The electron density map enabled residues 1 to 260 of VP1, 11 to 268 of VP2, and 1 to 232 of VP3 to be built. The VP4 protein of SAFV-3 contains 72 residues; however, only residues 15 to 38 could be built. Crystallographic diffraction data and structure quality indicators are listed in Table 1.

The surface of the SAFV-3 virion is characterized by the presence of star-shaped plateaus around icosahedral 5-fold axes and depressions located around icosahedral 2-fold axes (Fig. 1A). The highest protrusions on the virus surface are formed by the BC and CD loops of VP1 positioned at the border of the arms of the star-shaped plateau and the edges of the 2-fold depressions (Fig. 1). In place of a continuous canyon, as seen in enteroviruses (33, 63), there are five pits around each 5-fold axis in SAFV-3 (Fig. 1A). The CD loop of VP1 fills the volume that corresponds to the canyon in enteroviruses (Fig. 1B and C). The EF loop of VP2 (residues 132 to 195), which is by convention named “puff,” is subdivided into two loops, puff A and B, in the SAFV-3 virion (Fig. 1B and C). Puff B contains a short α helix that has not been observed in other cardioviruses (Fig. 1B and C) (12, 13). Residues from puff B interact with the CD loop of VP1, and the short α helix is located on the surface of the virion (Fig. 1B and C). Structures resembling puff B are not present in enteroviruses (Fig. 1B and C) (33, 63). The most prominent feature on the capsid surface formed by VP3 is a finger-

like protrusion conventionally named a “knob,” which in SAFV-3 contains two β -strands (Fig. 1C). Similar short β -strands have been previously observed in knobs of TMEV and MeV (Fig. 1B and C) (12, 13). In enteroviruses the knob is usually five residues shorter and lacks the β -strands (Fig. 1B and C) (33, 63). However, the knob and puff regions were implicated in the receptor binding of echovirus 7 to its cellular receptor DAF (31). RMSD values comparing the distances between equivalent C α atoms of icosahedral asymmetric units of SAFV-3 with selected picornaviruses are listed in Table 2. Overall, the architecture of SAFV-3 is most similar to that of TMEV (13).

The space between the two β -sheets of VP1, which in some enteroviruses contains a hydrophobic cavity with a pocket factor, is filled by the side chains of residues forming the core of the protein in SAFV-3 (Fig. 2). Thus, it is unlikely that pocket binding inhibitors that can prevent genome release from enteroviruses (64, 65) could be used to inhibit SAFV infections.

The disulfide bond in the surface loop of VP3 and its role in cardiovirus infectivity. SAFV-3 contains a disulfide bond connecting cys87 and cys89 in the CD loop of VP3 (Fig. 3A). Disulfide bonds connecting side chains of cysteines that are separated by a single residue are uncommon, because such links introduce sharp bends in the polypeptide main chain (12, 13). The CD loop of VP3 is located on the surface of the virus close to the knob region (Fig. 1B). The two cysteine residues are conserved among SAFVs, except for SAFV-5 and SAFV-6, and also in homologous positions in the MeV and TMEV capsids. The disulfide bond was observed in

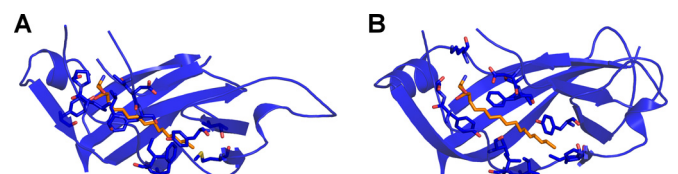


FIG 2 VP1 of SAFV-3 does not contain a hydrophobic pocket. (A and B) Diagrams of VP1 of SAFV-3 (A) and poliovirus 1 (B). The pocket factor in poliovirus 1 is shown as a stick model in orange. Residues that interact with the pocket factor are also shown as sticks. In panel A, the poliovirus pocket factor was superimposed onto the structure of SAFV-3. However, the pocket is not formed in SAFV-3 VP1, and the side chains of several residues clash with the pocket factor.

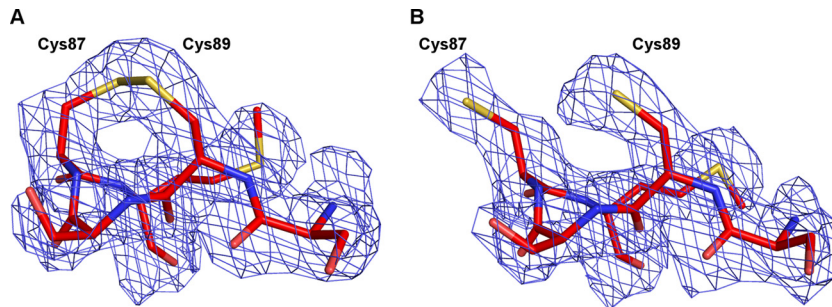


FIG 3 Disruption of VP3 Cys87-Cys89 disulfide bond results in reorientation of cysteine side chains; however, it has limited impact on VP3 structure. (A and B) Detail diagram of the CD loop in VP3 of SAFV-3 in native virus (A) and DTT-treated virus (B). An electron density map contoured at 2σ is shown as a blue mesh.

the MeV (12) but not in TMEV (13). It was suggested by Grant et al. that the disulfide bond in TMEV was disrupted because of covalent modifications of the cysteine side chains that occurred during virus purification or crystallization (13).

In order to investigate the importance of the disulfide bond for maintaining the native structure and infectivity, the SAFV-3 virions were crystallized in reducing conditions containing 10 mM DTT. Crystals of DTT-treated SAFV-3 virions diffracted to a resolution of 2.5 Å. A comparison to the native SAFV-3 virion showed that disruption of the Cys87-Cys89 disulfide bond had minimal effect on the structure of the VP3 CD-loop (Fig. 3) and no effect on the other parts of the virion. The root mean square deviation (RMSD) of equivalent atoms in the two SAFV structures is 0.062 Å. The average crystallographic temperature factors of atoms of residues 86 to 89 of the CD loop of VP3 were 38.1 Å² in the native structure and 40.7 Å² in the structure with the disrupted disulfide bond. Similar values of temperature factors indicate that the disruption of the disulfide bond did not increase the flexibility of the loop. However, disruption of the disulfide bond by DTT increased the stability of the capsid by 2°C, measured as the temperature at which the virions release their RNA genomes (Fig. 4A). A similar increase in temperature stability has been previously reported for enterovirus virions upon binding of WIN compounds (66). This DTT-induced increase in virion stability is not associated with structural changes at 22°C, the temperature at

which the SAFV-3 crystals were grown. However, it is possible that at temperatures in the range of 48 to 52°C, the disruption of the disulfide bond results in an alteration of capsid dynamics, so-called “capsid breathing” (67), that might allow the virions to retain their genomes at higher temperatures. Furthermore, the reduction of the bond resulted in a 70% decrease in the infectivity of SAFV-3 (Fig. 4B). In contrast, a similar decrease in infectivity was not observed for EV71, which does not contain disulfide bonds in the capsid (Fig. 4B). Conservation of the cysteine residues in loops exposed on the cardiovascular virion surface indicates a possible role of the disulfide bond in virus infection. A putative explanation of the reduced infectivity of SAFV-3 virions with the disrupted disulfide bond might be that residues 86 to 89 of the VP3 CD loop play a role in receptor binding. The disulfide bond could be important for retaining the optimal conformation of the loop for binding to the receptor. Alternatively, the increased stability of the virions caused by the disruption of the disulfide bond might decrease the efficiency of genome release from virions (21, 26, 38, 68); however, we did not observe differences in genome release between native and DTT-treated virus (data not shown). Previous work on MeV demonstrated that addition of 0.1% β-mercaptoethanol increased its infectivity by reducing abortive infection of mouse fibroblasts (69). Furthermore, heat stability of many picornaviruses can be increased by interaction with sulfhydryl reduc-

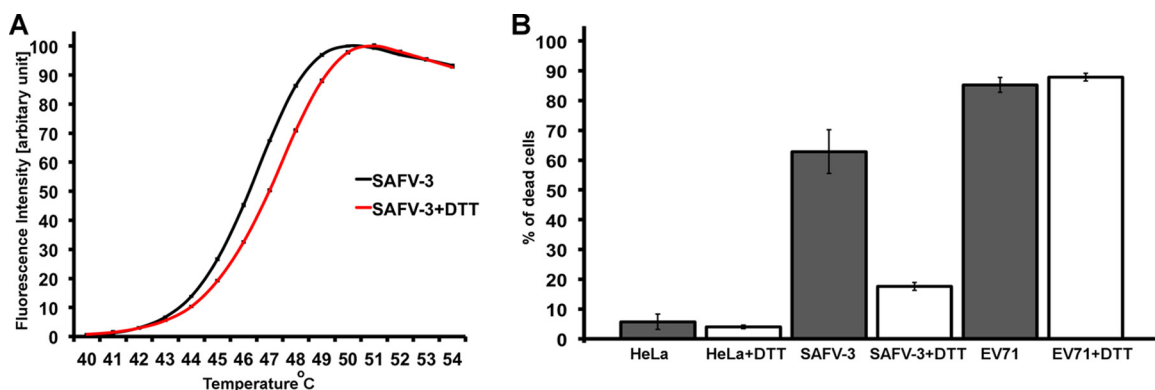


FIG 4 Impact of disruption of the Cys87-Cys89 disulfide bond on stability and infectivity of SAFV-3. (A) A Sybr green fluorescence assay was performed to measure the stability of SAFV-3 particles. SAFV-3 virions were mixed with Sybr green dye II and heated to the indicated temperatures (x axis). The fluorescence signal increases as the dye binds to RNA that is released from thermally destabilized particles. The black line represents native SAFV-3 virions, and the red line represents SAFV-3 treated with 10 mM DTT. Error bars indicate the standard deviations of the measurements. See Materials and Methods for additional details. (B) Effect of DTT treatment on infectivity of SAFV-3 and EV71. Fractions of dead cells were determined based on propidium iodide staining.

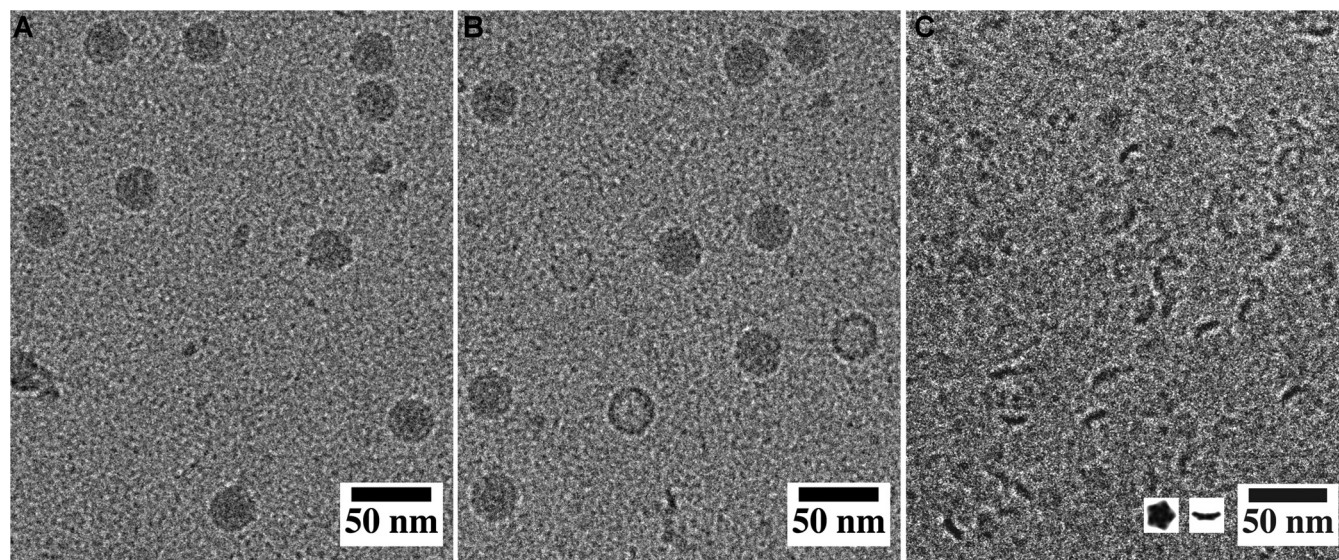


FIG 5 Release of SAFV-3 genome results in the formation of empty particles that disintegrate into pentamers. (A) Cryo-EM images of native virions. (B) SAFV-3 particles heated to 42°C for 2 min. The sample contained A particles and a few empty capsids. (C) Pentamers of capsid protein protomers prepared by incubating SAFV-3 virions at 42°C for 2 min and at 23°C for 5 min. The inset in panel C shows top and side view projections of pentamers of SAFV-3 protomers calculated from the structure of capsid proteins.

ing groups (70). The effects of reducing agents indicate that compounds specifically disrupting or binding to the disulfide Cys87-Cys89 bond might reduce SAFV infectivity.

Cardiovirus genome release results in formation of unstable empty capsids that disassemble into pentamers. In order to initiate infection, virus genomes need to be released from virions and transferred across the biological membrane into the cell cytoplasm. For most eukaryotic nonenveloped viruses, this process is poorly understood. However, enteroviruses from the family *Picornaviridae* have been extensively studied as model organisms for genome delivery into the cytoplasm (21–25, 37, 71). The genome release of enteroviruses is preceded by structural changes to the capsid, leading to the formation of an expanded A particle that is induced by receptor binding and/or by the low pH of late endosomes (21, 26, 38, 68). Similar structural changes to particles can be induced *in vitro* by heating enterovirus virions to nonphysiological temperatures of about 56°C (37, 71). After the genome release, enterovirus capsids remain stable, at least *in vitro*, forming empty “B” particles (72).

The formation of SAFV-3 A particles can be induced by heating the virions to 42°C for 2 min. In addition to A particles, the sample also contained about 1% of empty capsids (Fig. 5B). However, if SAFV-3 virions were left at room temperature for more than 5 min after heating, the sample contained almost exclusively pentamers of capsid protein protomers (Fig. 5C). Native protein electrophoresis combined with mass spectrometry analysis verified that Safv-3 virions disassembled into pentamers after heating to 42°C, followed by cooling to 25°C (data not shown). This corroborates the previous suggestion that cardiovirus virions disassemble upon or shortly after genome release (34, 73). However, RNA uncoating of the related MeV is triggered at 37°C upon cell attachment, possibly leaving behind an unstable empty capsid, which subsequently disintegrates into 14S pentamers (69). We show that *in vitro* after being heated to 42°C, the SAFV-3 virions convert to A

particles and release their genomes, and the resulting empty capsids rapidly dissociate into pentamers.

The SAFV-3 A particle contains pores that enable the externalization of VP1 N termini and of VP4 subunits. The enterovirus A particle represents a virion state that not only is primed for genome release but also facilitates the transport of the genome across a biological membrane. This function is ensured by the release of VP4 subunits that make cellular membranes permeable for viral RNA and by externalization of the N-terminal arms of VP1, which contain hydrophobic residues that, in some viruses, anchor virions to membranes (38). Here, we present a 10.6-Å resolution cryo-EM reconstruction of the SAFV-3 A particle and show that it is expanded 4% in diameter compared to the native virion (Fig. 6A and B). Capsids of SAFV-3 A particles have pores located approximately in the middle between the 5-fold and 3-fold icosahedral symmetry axes (Fig. 6A and C) at the interface between two VP1 subunits related by a 5-fold symmetry axis and a VP3 subunit (Fig. 6E). The pores are circular in shape with a diameter of ~15 Å. Models of the capsid protein subunits determined in the native SAFV-3 structure were fitted as rigid bodies into the native cryo-EM density map of the A particle. The formation of the pore is caused by shifts of the VP1 subunits toward the icosahedral 5-fold axis and of VP3 toward the icosahedral 3-fold axis relative to their positions in the native virus (Fig. 6E and F). The changes in subunit positions are possible due to the radial expansion of the capsid. However, parts of the VP1 and VP3 subunits located close to the pore did not entirely fit into the cryo-EM electron density map (Fig. 6C and E). Low values of density at the border of the pore indicate that the EF loop and C terminus of VP1 and CD, GH loops and C terminus of VP3, which are located in the vicinity of the pore, are flexible.

A difference map calculated by subtracting the electron density map of the SAFV-3 A particle from that of the native virion indicates that VP4 is missing from the A particle (Fig. 7). The last

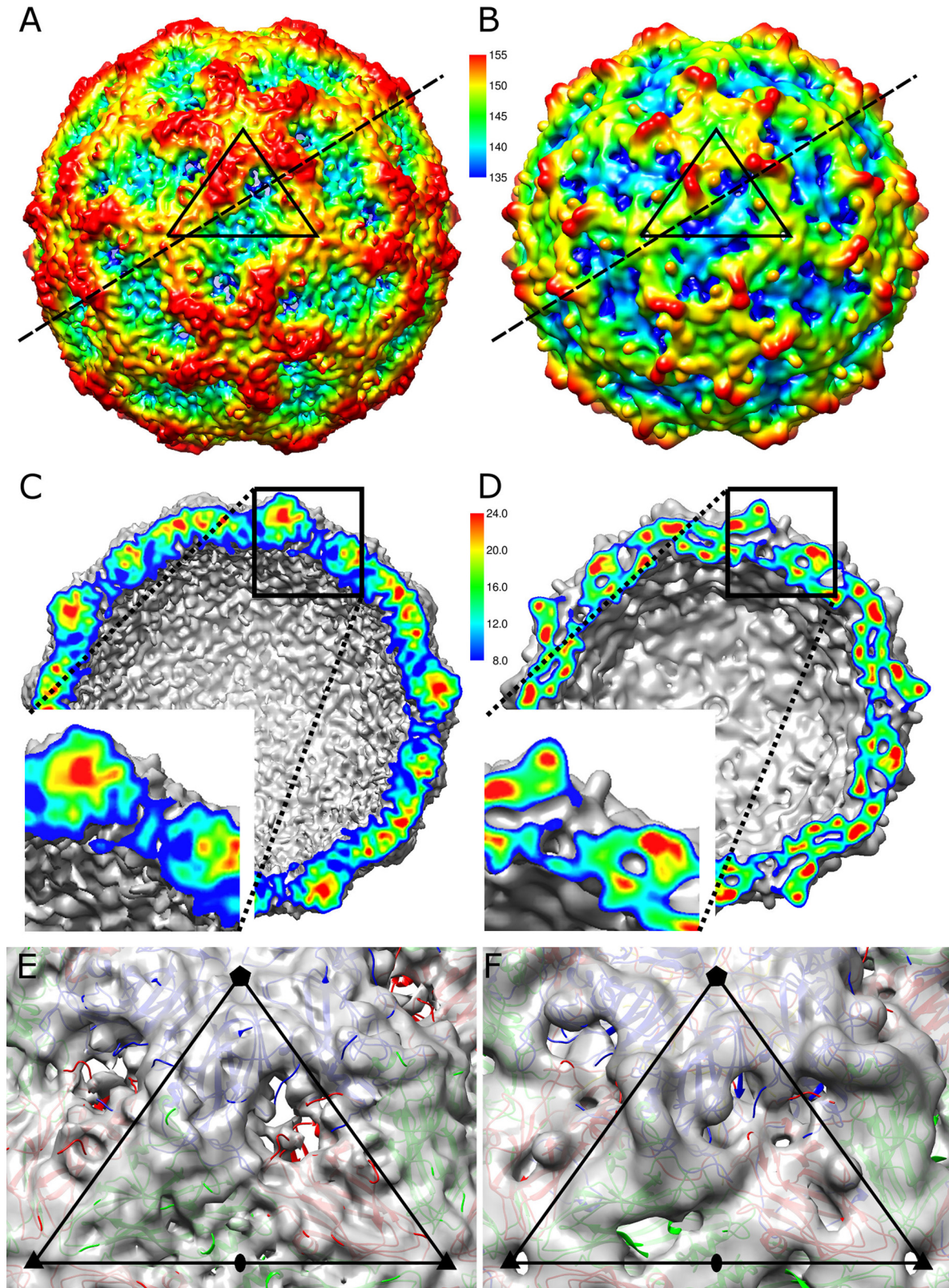


FIG 6 Native SAFV-3 virion has compact capsid, whereas A particle contains pores. (A and B) Surface renderings of SAFV-3 A particle (A) and native virion (B) at a 10.6-Å resolution. The surfaces displayed at 0.5σ are rainbow-colored based on the distance from the particle center, as indicated by the scale bar. Distances are indicated in angstroms. The borders of a selected icosahedral asymmetric unit are indicated with a black triangle. Dashed lines indicate the planes of cross sections through the particles, as displayed in panels C and D. (C and D) Cross-section views of SAFV-3 A particle (C) and native virion (D). The insets show enlarged regions of the cross sections corresponding to the opening in the capsid of the A particle. The cross sections are colored according to electron density, as indicated by the scale bar in arbitrary units. (E and F) Details of icosahedral asymmetric units of A particle (E) and native virus (F). Electron densities displayed at 1σ are shown as semitransparent surfaces. VP1 subunits are shown in blue, VP2 subunits are shown in green, and VP3 subunits are shown in red. The borders of the icosahedral asymmetric unit are highlighted as black triangles, and the positions of 5-fold, 3-fold, and 2-fold icosahedral symmetry axes are indicated by pentagons, triangles, and ovals, respectively.

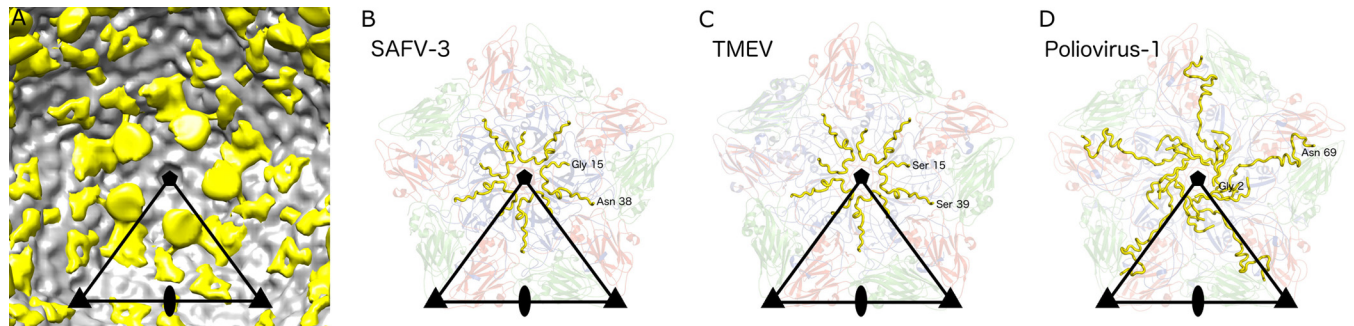


FIG 7 SAFV-3 A particles lack capsid protein VP4. (A) The cryo-EM density of SAFV-3 A particle displayed at 1σ is shown in gray, and a difference map calculated by subtracting the electron density of A particle from that of the native virus is shown in yellow. The yellow difference density displayed at 1σ corresponds to VP4 in the native particle. (B to D) Positions of VP4 subunits in SAFV-3 (B), TMEV (C), and poliovirus 1 (D) virions. The pentamers of capsid protein protomers are shown. VP4 subunits are shown in yellow, VP1 subunits are shown in blue, VP2 subunits are shown in green, and VP3 subunits are shown in red. The labels indicate the type and number of the first and last structured residues of VP4 in the respective models.

ordered residues of the SAFV-3 VP4 are located at contacts between two 5-fold related VP1 subunits and VP3, immediately below the opening of the pore in the A particle (Fig. 7B). In contrast to the HRV-14 and poliovirus virions, the ordered part of SAFV-3 VP4 begins close to a 5-fold axis and ends at a 3-fold axis of the same protomer (Fig. 7D). The flexible part of VP4, not visible in the native SAFV-3 virion, is thus optimally positioned for release from the A particle.

Structural differences between cardiovirus and enterovirus A particles. The structure of the A particle of SAFV-3 is different from that of enteroviruses. “A” particles of EV71, poliovirus, HRV-2, CAV-7, and CAV-16 contain two types of pores located at (i) icosahedral 2-fold axes and (ii) between icosahedral 2-fold axes and 5-fold axes (22–25, 36–40). In the CAV-16 A particle, the pores at the 2-fold axes were proposed to be locations for the externalization of VP1 N termini that are then translocated to the channels between the 2-fold and 5-fold axes (39). In addition, the pores at 2-fold axes were proposed to serve as channels for the release of VP4 subunits and the RNA genome. However, the channels in enterovirus A particles had to expand in order to allow the passage of ssRNA (39, 74). The borders of the channels located at 2-fold axes in enterovirus particles are formed by helix $\alpha 3$ from the CD loop of VP2 and EF loop of VP3 (39, 74). The overall distribution of charges inside the SAFV-3 and enterovirus capsids does not exhibit differences that could explain the different stabilities of their empty capsids (Fig. 8).

SAFV-3 A particles do not contain pores at icosahedral 2-fold symmetry axes (Fig. 6A and E). However, the pores located between the 3-fold and 5-fold axes are larger than either of the pores observed in enterovirus A particles. There is a higher density in the center of the pore in the SAFV-3 A particle that is not connected to the surrounding electron density of the capsid (Fig. 6C). The unconnected density might belong to VP1 N termini passing through the pore from inside the virion to outside the virion. Presumably, VP1 N termini are flexible or adopt various conformations both inside and outside the capsid and therefore are not visible in the cryo-EM reconstruction that corresponds to the average of many particles. However, the movements of the VP1 N-terminal arms are restricted to the pore center, resulting in the observed density (Fig. 6C and E).

Structure of the genome in SAFV-3 virions and A particles. The conversion of SAFV-3 virions to A particles not only affects the

structure of the capsid but also the structure of the RNA genome. In the native virus, the RNA is distributed in two spherical shells of density located 35 and 95 Å from the particle center (Fig. 9A). Parts of the genome located around 5-fold and 2-fold icosahedral axes of the particle appear to be in contact with the capsid. It was previously speculated that the N-terminal parts of major capsid proteins VP1 to VP3 that are not resolved in the structure are in direct contact with the genome. In contrast, in the A particle the RNA density is distributed uniformly at the central part of the virion within a sphere with a radius of 105 Å (Fig. 9B). The RNA does not form any contacts with the capsid of the A particle, unlike in the previously studied A particles of enteroviruses (25, 39). The

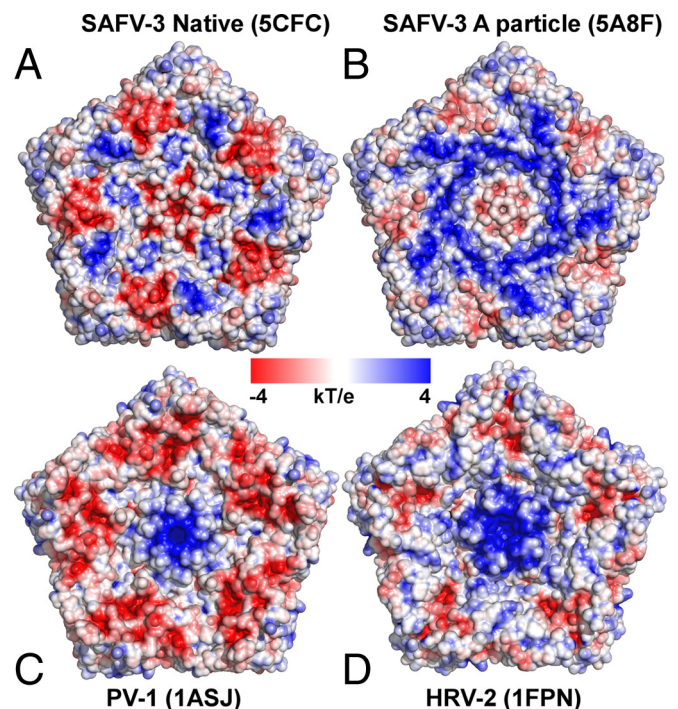


FIG 8 Charge distributions inside picornavirus capsids. (A and B) Charge distributions inside native SAFV-3 virion (A) and A particle (B). (C and D) Charge distributions inside poliovirus 1 (C) and HRV-2 (D). Pentamers of capsid protein protomers are shown.

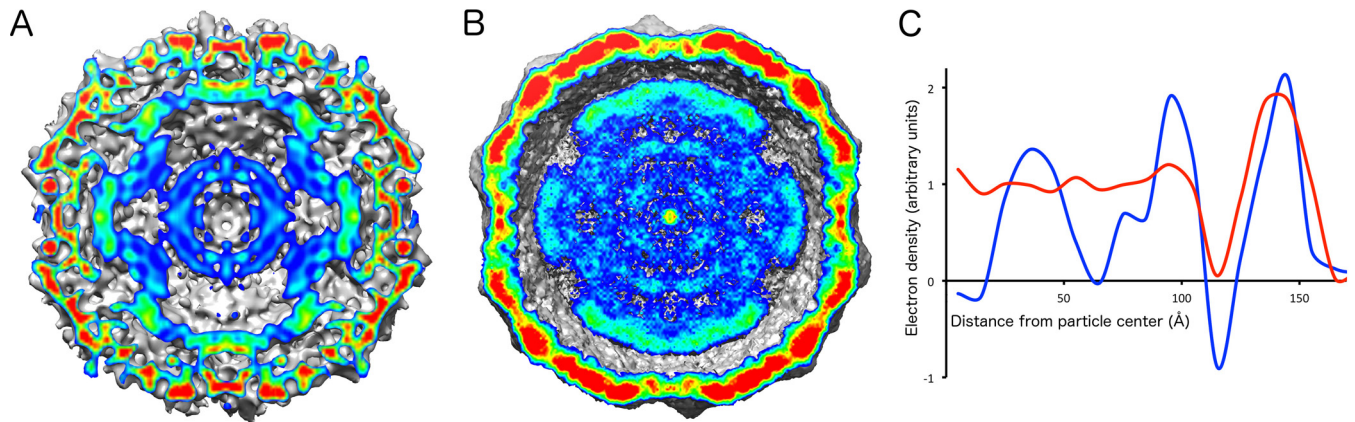


FIG 9 (A and B) Electron density of RNA inside SAFV-3 native virion (A) and A particle (B). The central sections of the particles are shown. The cross sections are colored according to electron density values. (C) Spherically averaged electron density distribution of native SAFV-3 virion (blue) and A particle (red).

disruption of the capsid RNA contacts might be due to the changes in the distribution of charges on the inner face of the capsid associated with the release of VP4 subunits and externalization of VP1 N termini from the particle. However, the overall charge of the inner face of the A particle is more positive than that of the native virion (Fig. 8). The disruption of the interactions of the capsid with the genome upon conversion of the virion to the A particle might facilitate subsequent release of the RNA from the capsid.

Genome release from the SAFV-3 A particle. Expansion of the SAFV-3 capsid upon formation of the A particle results in an increase in the interior volume of the virion from $5.3 \times 10^6 \text{ \AA}^3$ to $6.8 \times 10^6 \text{ \AA}^3$. This expansion might be required to increase the mobility of the genome within the particle, which might be necessary to enable the 3' end of the RNA to find one of the pores within the A particle before it can be released from the capsid (71).

Observations of empty SAFV-3 particles immediately after heating to 42°C (Fig. 5B and C) indicate that the genome is released from A particles that then disassemble into pentamers. The pores in the capsid of the A particles are sufficiently large to allow passage of single-stranded RNA. However, the genome contains RNA sequences that form functional double-stranded regions, which are components of the IRES and stem-loop structures required for picornavirus translation and replication. It is possible that these RNA secondary structure elements are retained when the genome is packaged in the virion. If this was the case, the genome would either have to unwind or the pore serving for genome release would have to be expanded in order to allow passage of the RNA. The flexible nature of the loops surrounding the pore (Fig. 6C) indicates that pore enlargement might be possible. Thus, compounds stabilizing or blocking the pores in the A particle might serve as tools for further study of cardiovascular genome release and might be developed into SAFV inhibitors.

ACKNOWLEDGMENTS

We thank synchrotron Diamond Proxima-1 and Proxima-2A beamline scientists Martin Slavko and Beatriz Guimaraes and the synchrotron SLS beamline scientists Vincent Olieric, Takashi Tomizaki, Justyna Wojdyła, and Meitian Wang for help with the crystal screening and data collection. We thank Jana Moravcová for help with the preparation of the manuscript for submission. Computational resources were provided by the MetaCentrum under the program LM2010005 and the CERIT-SC under the program Centre

CERIT Scientific Cloud, part of the Operational Program Research and Development for Innovations (reg. no. CZ.1.05/3.2.00/08.0144).

E.M. performed large-scale virus purifications, crystallization, model building, refinement, data analysis, and participated in writing the manuscript. J.N. calculated the single-particle cryo-EM reconstruction and participated in data analysis and manuscript preparation. L.P. optimized and conducted large-scale virus purifications. P.K. performed negative-stain electron microscopy of SAFV-3. A.M.L. and F.J.M.V.K. provided material for the study. P.P. designed the study, performed SAFV-3 structure determination, directed and participated in data analysis, and wrote the manuscript.

This research was conducted under the project CEITEC 2020 (LQ1601) with financial support from the Ministry of Education, Youth, and Sports of the Czech Republic under National Sustainability Program II. We acknowledge CF Cryo-Electron Microscopy and Tomography, CF X-Ray Diffraction and Bio-SAXS, and CF Biomolecular Interactions and Crystallization, supported by the Czech Infrastructure for Integrative Structural Biology (CIISB) research infrastructure (LM2015043 funded by MEYS CR), for their support in obtaining scientific data presented in this paper. The research leading to these results received funding from the European Research Council under the European Union's Seventh Framework Program (FP/2007-2013)/ERC grant agreement 355855' and from EMBO installation grant 3041 to Pavel Plevka. The funders had no role in the study's design, data collection and interpretation, or the decision to submit the work for publication.

FUNDING INFORMATION

This work, including the efforts of Pavel Plevka, was funded by EC | European Research Council (ERC) (355855). This work, including the efforts of Pavel Plevka, was funded by European Molecular Biology Organization (EMBO) (3041).

REFERENCES

- Liang Z, Kumar AS, Jones MS, Knowles NJ, Lipton HL. 2008. Phylogenetic analysis of the species theilovirus: emerging murine and human pathogens. *J Virol* 82:11545–11554. <http://dx.doi.org/10.1128/JVI.01160-08>.
- Himeda T, Hosomi T, Asif N, Shimizu H, Okuwa T, Muraki Y, Ohara Y. 2011. The preparation of an infectious full-length cDNA clone of Saffold virus. *Virology* 418:110. <http://dx.doi.org/10.1016/j.virol.2011.07.010>.
- Pritchard AE, Strom T, Lipton HL. 1992. Nucleotide sequence identifies Vilyuisk virus as a divergent Theiler's virus. *Virology* 191:469–472. [http://dx.doi.org/10.1016/0042-6822\(92\)90212-8](http://dx.doi.org/10.1016/0042-6822(92)90212-8).
- Jones MS, Lukashov VV, Ganac RD, Schnurr DP. 2007. Discovery of a novel human picornavirus in a stool sample from a pediatric patient presenting with fever of unknown origin. *J Clin Microbiol* 45:2144–2150. <http://dx.doi.org/10.1128/JCM.00174-07>.

5. Himeda T, Hosomi T, Okuwa T, Muraki Y, Ohara Y. 2013. Saffold virus type 3 (SAFV-3) persists in HeLa cells. *PLoS One* 8:e53194. <http://dx.doi.org/10.1371/journal.pone.0053194>.
6. Himeda T, Ohara Y. 2012. Saffold virus, a novel human cardiomyovirus with unknown pathogenicity. *J Virol* 86:1292–1296. <http://dx.doi.org/10.1128/JVI.06087-11>.
7. Zoll J, Erkens Hulshof S, Lanke K, Verduyn Lunel F, Melchers WJ, Schoondermark-van de Ven E, Roivainen M, Galama JM, van Kuppeveld FJ. 2009. Saffold virus, a human Theiler's-like cardiomyovirus, is ubiquitous and causes infection early in life. *PLoS Pathog* 5:e1000416. <http://dx.doi.org/10.1371/journal.ppat.1000416>.
8. Blinkova O, Kapoor A, Victoria J, Jones M, Wolfe N, Naem A, Shaikat S, Sharif S, Alam MM, Angez M, Zaidi S, Delwart EL. 2009. Cardiomyoviruses are genetically diverse and cause common enteric infections in South Asian children. *J Virol* 83:4631–4641. <http://dx.doi.org/10.1128/JVI.02085-08>.
9. Abed Y, Boivin G. 2008. New Saffold cardiomyoviruses in 3 children, Canada. *Emerg Infect Dis* 14:834–836. <http://dx.doi.org/10.3201/eid1405.071675>.
10. Drexler JF, Luna LK, Stocker A, Almeida PS, Ribeiro TC, Petersen N, Herzog P, Pedroso C, Huppertz HI, Ribeiro Hda C, Jr, Baumgarte S, Drosten C. 2008. Circulation of 3 lineages of a novel Saffold cardiomyovirus in humans. *Emerg Infect Dis* 14:1398–1405. <http://dx.doi.org/10.3201/eid1409.080570>.
11. Xu ZQ, Cheng WX, Qi HM, Cui SX, Jin Y, Duan ZJ. 2009. New Saffold cardiomyovirus in children, China. *Emerg Infect Dis* 15:993–994. <http://dx.doi.org/10.3201/eid1506.090109>.
12. Luo M, Vriend G, Kamer G, Minor I, Arnold E, Rossmann MG, Boege U, Scraba DG, Duke GM, Palmenberg AC. 1987. The atomic structure of Mengo virus at 3.0 Å resolution. *Science* 235:182–191. <http://dx.doi.org/10.1126/science.3026048>.
13. Grant RA, Filman DJ, Fujinami RS, Icenogle JP, Hogle JM. 1992. Three-dimensional structure of Theiler virus. *Proc Natl Acad Sci U S A* 89:2061–2065. <http://dx.doi.org/10.1073/pnas.89.6.2061>.
14. Palmenberg AC. 1982. In vitro synthesis and assembly of picornaviral capsid intermediate structures. *J Virol* 44:900–906.
15. Putnak JR, Phillips BA. 1981. Picornaviral structure and assembly. *Microbiol Rev* 45:287–315.
16. Rombaut B, Foriers A, Boeye A. 1991. In vitro assembly of poliovirus 14S subunits: identification of the assembly promoting activity of infected cell extracts. *Virology* 180:781–787. [http://dx.doi.org/10.1016/0042-6822\(91\)90091-O](http://dx.doi.org/10.1016/0042-6822(91)90091-O).
17. Rombaut B, Vrijnsen R, Boeye A. 1984. In vitro assembly of poliovirus empty capsids: antigenic consequences and immunological assay of the morphopoietic factor. *Virology* 135:546–550. [http://dx.doi.org/10.1016/0042-6822\(84\)90209-5](http://dx.doi.org/10.1016/0042-6822(84)90209-5).
18. Li C, Wang JC, Taylor MW, Zlotnick A. 2012. In vitro assembly of an empty picornavirus capsid follows a dodecahedral path. *J Virol* 86:13062–13069. <http://dx.doi.org/10.1128/JVI.01033-12>.
19. Nugent CI, Johnson KL, Sarnow P, Kirkegaard K. 1999. Functional coupling between replication and packaging of poliovirus replicon RNA. *J Virol* 73:427–435.
20. Jiang P, Liu Y, Ma HC, Paul AV, Wimmer E. 2014. Picornavirus morphogenesis. *Microbiol Mol Biol Rev* 78:418–437. <http://dx.doi.org/10.1128/MMBR.00012-14>.
21. Tuthill TJ, Gropelli E, Hogle JM, Rowlands DJ. 2010. Picornaviruses. *Curr Top Microbiol Immunol* 343:43–89.
22. Bostina M, Levy H, Filman DJ, Hogle JM. 2011. Poliovirus RNA is released from the capsid near a twofold symmetry axis. *J Virol* 85:776–783. <http://dx.doi.org/10.1128/JVI.00531-10>.
23. Lyu K, Ding J, Han JF, Zhang Y, Wu XY, He YL, Qin CF, Chen R. 2014. Human enterovirus 71 uncoating captured at atomic resolution. *J Virol* 88:3114–3126. <http://dx.doi.org/10.1128/JVI.03029-13>.
24. Wang X, Peng W, Ren J, Hu Z, Xu J, Lou Z, Li X, Yin W, Shen X, Porta C, Walter TS, Evans G, Axford D, Owen R, Rowlands DJ, Wang J, Stuart DI, Fry EE, Rao Z. 2012. A sensor-adaptor mechanism for enterovirus uncoating from structures of EV71. *Nat Struct Mol Biol* 19:424–429. <http://dx.doi.org/10.1038/nsmb.2255>.
25. Shingler KL, Yoder JL, Carnegie MS, Ashley RE, Makhov AM, Conway JF, Hafenstein S. 2013. The enterovirus 71 A-particle forms a gateway to allow genome release: a cryoEM study of picornavirus uncoating. *PLoS Pathog* 9:e1003240. <http://dx.doi.org/10.1371/journal.ppat.1003240>.
26. Prchla E, Kuechler E, Blaas D, Fuchs R. 1994. Uncoating of human rhinovirus serotype 2 from late endosomes. *J Virol* 68:3713–3723.
27. He Y, Chipman PR, Howitt J, Bator CM, Whitt MA, Baker TS, Kuhn RJ, Anderson CW, Freimuth P, Rossmann MG. 2001. Interaction of coxsackievirus B3 with the full-length coxsackievirus-adenovirus receptor. *Nat Struct Biol* 8:874–878. <http://dx.doi.org/10.1038/nsb1001-874>.
28. Xiao C, Bator CM, Bowman VD, Rieder E, He Y, Hebert B, Bella J, Baker TS, Wimmer E, Kuhn RJ, Rossmann MG. 2001. Interaction of coxsackievirus A21 with its cellular receptor, ICAM-1. *J Virol* 75:2444–2451. <http://dx.doi.org/10.1128/JVI.75.5.2444-2451.2001>.
29. Olson NH, Kolatkar PR, Oliveira MA, Cheng RH, Greve JM, McClelland A, Baker TS, Rossmann MG. 1993. Structure of a human rhinovirus complexed with its receptor molecule. *Proc Natl Acad Sci U S A* 90:507–511. <http://dx.doi.org/10.1073/pnas.90.2.507>.
30. Rossmann MG, He Y, Kuhn RJ. 2002. Picornavirus-receptor interactions. *Trends Microbiol* 10:324–331. [http://dx.doi.org/10.1016/S0966-842X\(02\)02383-1](http://dx.doi.org/10.1016/S0966-842X(02)02383-1).
31. Plevka P, Hafenstein S, Harris KG, Cifuentes JO, Zhang Y, Bowman VD, Chipman PR, Bator CM, Lin F, Medof ME, Rossmann MG. 2010. Interaction of decay-accelerating factor with echovirus 7. *J Virol* 84:12665–12674. <http://dx.doi.org/10.1128/JVI.00837-10>.
32. Hewat EA, Neumann E, Conway JF, Moser R, Ronacher B, Marlovits TC, Blaas D. 2000. The cellular receptor to human rhinovirus 2 binds around the 5-fold axis and not in the canyon: a structural view. *EMBO J* 19:6317–6325. <http://dx.doi.org/10.1093/emboj/19.23.6317>.
33. Rossmann MG, Arnold E, Erickson JW, Frankenberger EA, Griffith JP, Hecht HJ, Johnson JE, Kamer G, Luo M, Mosser AG, Rueckert RR, Sherry B, Vriend G. 1985. Structure of a human common cold virus and functional relationship to other picornaviruses. *Nature* 317:145–153. <http://dx.doi.org/10.1038/317145a0>.
34. Tuthill TJ, Harlos K, Walter TS, Knowles NJ, Gropelli E, Rowlands DJ, Stuart DI, Fry EE. 2009. Equine rhinitis A virus and its low pH empty particle: clues towards an aphthovirus entry mechanism? *PLoS Pathog* 5:e1000620. <http://dx.doi.org/10.1371/journal.ppat.1000620>.
35. Neubauer C, Frasel L, Kuechler E, Blaas D. 1987. Mechanism of entry of human rhinovirus 2 into HeLa cells. *Virology* 158:255–258. [http://dx.doi.org/10.1016/0042-6822\(87\)90264-9](http://dx.doi.org/10.1016/0042-6822(87)90264-9).
36. Garriga D, Pickl-Herk A, Luque D, Wruss J, Caston JR, Blaas D, Verdaguer N. 2012. Insights into minor group rhinovirus uncoating: the X-ray structure of the HRV2 empty capsid. *PLoS Pathog* 8:e1002473. <http://dx.doi.org/10.1371/journal.ppat.1002473>.
37. Levy HC, Bostina M, Filman DJ, Hogle JM. 2010. Catching a virus in the act of RNA release: a novel poliovirus uncoating intermediate characterized by cryo-electron microscopy. *J Virol* 84:4426–4441. <http://dx.doi.org/10.1128/JVI.02393-09>.
38. Fricks CE, Hogle JM. 1990. Cell-induced conformational change in poliovirus: externalization of the amino terminus of VP1 is responsible for liposome binding. *J Virol* 64:1934–1945.
39. Ren J, Wang X, Hu Z, Gao Q, Sun Y, Li X, Porta C, Walter TS, Gilbert RJ, Zhao Y, Axford D, Williams M, McAuley K, Rowlands DJ, Yin W, Wang J, Stuart DI, Rao Z, Fry EE. 2013. Picornavirus uncoating intermediate captured in atomic detail. *Nat Commun* 4:1929.
40. Seitsonen JJ, Shakeel S, Susi P, Pandurangan AP, Sinkovits RS, Hyvonen H, Laurinmaki P, Yla-Pelto J, Topf M, Hyypia T, Butcher SJ. 2012. Structural analysis of coxsackievirus A7 reveals conformational changes associated with uncoating. *J Virol* 86:7207–7215. <http://dx.doi.org/10.1128/JVI.06425-11>.
41. Chow M, Newman JF, Filman D, Hogle JM, Rowlands DJ, Brown F. 1987. Myristylation of picornavirus capsid protein VP4 and its structural significance. *Nature* 327:482–486. <http://dx.doi.org/10.1038/327482a0>.
42. Lin J, Cheng N, Chow M, Filman DJ, Steven AC, Hogle JM, Belnap DM. 2011. An externalized polypeptide partitions between two distinct sites on genome-released poliovirus particles. *J Virol* 85:9974–9983. <http://dx.doi.org/10.1128/JVI.05013-11>.
43. Lipton HL, Kumar AS, Hertzler S, Reddi HV. 2006. Differential usage of carbohydrate co-receptors influences cellular tropism of Theiler's murine encephalomyelitis virus infection of the central nervous system. *Glycoconj J* 23:39–49. <http://dx.doi.org/10.1007/s10719-006-5436-x>.
44. Fotiadis C, Kilpatrick DR, Lipton HL. 1991. Comparison of the binding characteristics to BHK-21 cells of viruses representing the two Theiler's virus neurovirulence groups. *Virology* 182:365–370. [http://dx.doi.org/10.1016/0042-6822\(91\)90683-3](http://dx.doi.org/10.1016/0042-6822(91)90683-3).
45. Shah AH, Lipton HL. 2002. Low-neurovirulence Theiler's viruses use sialic acid moieties on N-linked oligosaccharide structures for attachment. *Virology* 304:443–450. <http://dx.doi.org/10.1006/viro.2002.1735>.

46. Huber SA. 1994. VCAM-1 is a receptor for encephalomyocarditis virus on murine vascular endothelial cells. *J Virol* 68:3453–3458.
47. Tong L, Rossmann MG. 1997. Rotation function calculations with GLRF program. *Methods Enzymol* 276:594–611. [http://dx.doi.org/10.1016/S0076-6879\(97\)76080-4](http://dx.doi.org/10.1016/S0076-6879(97)76080-4).
48. Rossmann MG, Blow DM. 1962. Detection of sub-units within crystallographic asymmetric unit. *Acta Crystallogr* 15:24. <http://dx.doi.org/10.1107/S0365110X62000067>.
49. McCoy AJ, Grosse-Kunstleve RW, Adams PD, Winn MD, Storoni LC, Read RJ. 2007. Phaser crystallographic software. *J Appl Crystallogr* 40: 658–674. <http://dx.doi.org/10.1107/S0021889807021206>.
50. Brunger AT, Adams PD, Clore GM, DeLano WL, Gros P, Grosse-Kunstleve RW, Jiang JS, Kuszewski J, Nilges M, Pannu NS, Read RJ, Rice LM, Simonson T, Warren GL. 1998. Crystallography and NMR system: a new software suite for macromolecular structure determination. *Acta Crystallogr D Biol Crystallogr* 54:905–921. <http://dx.doi.org/10.1107/S0907444998003254>.
51. Kleywegt GJ, Read RJ. 1997. Not your average density. *Structure* 5:1557–1569. [http://dx.doi.org/10.1016/S0969-2126\(97\)00305-5](http://dx.doi.org/10.1016/S0969-2126(97)00305-5).
52. Jones TA, Zou JY, Cowan SW, Kjeldgaard M. 1991. Improved methods for building protein models in electron density maps and the location of errors in these models. *Acta Crystallogr A* 47(Pt 2):110–119. <http://dx.doi.org/10.1107/S0108767390010224>.
53. Emsley P, Cowtan K. 2004. Coot: model-building tools for molecular graphics. *Acta Crystallogr D Biol Crystallogr* 60:2126–2132. <http://dx.doi.org/10.1107/S0907444904019158>.
54. Collaborative Computational Project N. 1994. The CCP4 suite: programs for protein crystallography. *Acta Crystallogr D Biol Crystallogr* 50: 760–763. <http://dx.doi.org/10.1107/S0907444994003112>.
55. Kleywegt GJ, Brunger AT. 1996. Checking your imagination: applications of the free R value. *Structure* 4:897–904. [http://dx.doi.org/10.1016/S0969-2126\(96\)00097-4](http://dx.doi.org/10.1016/S0969-2126(96)00097-4).
56. Fabiola F, Korostelev A, Chapman MS. 2006. Bias in cross-validated free R factors: mitigation of the effects of non-crystallographic symmetry. *Acta Crystallogr D Biol Crystallogr* 62:227–238. <http://dx.doi.org/10.1107/S0907444905040680>.
57. Tang G, Peng L, Baldwin PR, Mann DS, Jiang W, Rees I, Ludtke SJ. 2007. EMAN2: an extensible image processing suite for electron microscopy. *J Struct Biol* 157:38–46. <http://dx.doi.org/10.1016/j.jsb.2006.05.009>.
58. Jiang W, Guo F, Liu Z. 2012. A graph theory method for determination of cryo-EM image focuses. *J Struct Biol* 180:343–351. <http://dx.doi.org/10.1016/j.jsb.2012.07.005>.
59. Guo F, Jiang W. 2014. Single particle cryo-electron microscopy and 3-D reconstruction of viruses. *Methods Mol Biol* 1117:401–443. http://dx.doi.org/10.1007/978-1-62703-776-1_19.
60. Humphrey W, Dalke A, Schulten K. 1996. VMD: visual molecular dynamics. *J Mol Graph* 14:33–38, 27–38. [http://dx.doi.org/10.1016/0263-7855\(96\)00018-5](http://dx.doi.org/10.1016/0263-7855(96)00018-5).
61. Pettersen EF, Goddard TD, Huang CC, Couch GS, Greenblatt DM, Meng EC, Ferrin TE. 2004. UCSF Chimera: a visualization system for exploratory research and analysis. *J Comput Chem* 25:1605–1612. <http://dx.doi.org/10.1002/jcc.20084>.
62. Birmanns S, Rusu M, Wriggers W. 2011. Using Sculptor and Situs for simultaneous assembly of atomic components into low-resolution shapes. *J Struct Biol* 173:428–435. <http://dx.doi.org/10.1016/j.jsb.2010.11.002>.
63. Hogle JM, Chow M, Filman DJ. 1985. Three-dimensional structure of poliovirus at 2.9 Å resolution. *Science* 229:1358–1365. <http://dx.doi.org/10.1126/science.2994218>.
64. Tsang SK, Danthi P, Chow M, Hogle JM. 2000. Stabilization of poliovirus by capsid-binding antiviral drugs is due to entropic effects. *J Mol Biol* 296:335–340. <http://dx.doi.org/10.1006/jmbi.1999.3483>.
65. Smith TJ, Kremer MJ, Luo M, Vriend G, Arnold E, Kamer G, Rossmann MG, McKinlay MA, Diana GD, Otto MJ. 1986. The site of attachment in human rhinovirus 14 for antiviral agents that inhibit uncoating. *Science* 233:1286–1293. <http://dx.doi.org/10.1126/science.3018924>.
66. Plevka P, Perera R, Yap ML, Cardoso J, Kuhn RJ, Rossmann MG. 2013. Structure of human enterovirus 71 in complex with a capsid-binding inhibitor. *Proc Natl Acad Sci U S A* 110:5463–5467. <http://dx.doi.org/10.1073/pnas.1222379110>.
67. Lewis JK, Bothner B, Smith TJ, Siuzdak G. 1998. Antiviral agent blocks breathing of the common cold virus. *Proc Natl Acad Sci U S A* 95:6774–6778. <http://dx.doi.org/10.1073/pnas.95.12.6774>.
68. Greve JM, Forte CP, Marlor CW, Meyer AM, Hoover-Litty H, Wunderlich D, McClelland A. 1991. Mechanisms of receptor-mediated rhinovirus neutralization defined by two soluble forms of ICAM-1. *J Virol* 65:6015–6023.
69. Hall L, Rueckert RR. 1971. Infection of mouse fibroblasts by cardioviruses: premature uncoating and its prevention by elevated pH and magnesium chloride. *Virology* 43:152–165. [http://dx.doi.org/10.1016/0042-6822\(71\)90233-9](http://dx.doi.org/10.1016/0042-6822(71)90233-9).
70. Halsted CC, Seto DS, Simkins J, Carver DH. 1970. Protection of enteroviruses against heat inactivation by sulfhydryl-reducing substances. *Virology* 40:751–754. [http://dx.doi.org/10.1016/0042-6822\(70\)90221-7](http://dx.doi.org/10.1016/0042-6822(70)90221-7).
71. Harutyunyan S, Kumar M, Sedivy A, Subirats X, Kowalski H, Kohler G, Blaas D. 2013. Viral uncoating is directional: exit of the genomic RNA in a common cold virus starts with the poly-A tail at the 3' end. *PLoS Pathog* 9:e1003270. <http://dx.doi.org/10.1371/journal.ppat.1003270>.
72. Hogle JM. 2002. Poliovirus cell entry: common structural themes in viral cell entry pathways. *Annu Rev Microbiol* 56:677–702. <http://dx.doi.org/10.1146/annurev.micro.56.012302.160757>.
73. Baxt B, Bachrach HL. 1980. Early interactions of foot-and-mouth disease virus with cultured cells. *Virology* 104:42–55. [http://dx.doi.org/10.1016/0042-6822\(80\)90364-5](http://dx.doi.org/10.1016/0042-6822(80)90364-5).
74. Butan C, Filman DJ, Hogle JM. 2014. Cryo-electron microscopy reconstruction shows poliovirus 135S particles poised for membrane interaction and RNA release. *J Virol* 88:1758–1770. <http://dx.doi.org/10.1128/JVI.01949-13>.
75. Davis IW, Leaver-Fay A, Chen VB, Block JN, Kapral GJ, Wang X, Murray LW, Arendall WB, III, Snoeyink J, Richardson JS, Richardson DC. 2007. MolProbity: all-atom contacts and structure validation for proteins and nucleic acids. *Nucleic Acids Res* 35:W375–W383. <http://dx.doi.org/10.1093/nar/gkm216>.

PAPER IV



Virion Structure of Israeli Acute Bee Paralysis Virus

Edukondalu Mullapudi,^a Antonín Přidal,^b Lenka Pálková,^a Joachim R. de Miranda,^c Pavel Plevka^a

Structural Virology, Central European Institute of Technology, Masaryk University, Brno, Czech Republic^a; Department of Zoology, Fishery, Hydrobiology, and Apidology, Faculty of Agronomy, Mendel University in Brno, Brno, Czech Republic^b; Department of Ecology, Swedish University of Agricultural Sciences, Uppsala, Uppsala, Sweden^c

ABSTRACT

The pollination services provided by the western honeybee (*Apis mellifera*) are critical for agricultural production and the diversity of wild flowering plants. However, honeybees suffer from environmental pollution, habitat loss, and pathogens, including viruses that can cause fatal diseases. Israeli acute bee paralysis virus (IAPV), from the family *Dicistroviridae*, has been shown to cause colony collapse disorder in the United States. Here, we present the IAPV virion structure determined to a resolution of 4.0 Å and the structure of a pentamer of capsid protein protomers at a resolution of 2.7 Å. IAPV has major capsid proteins VP1 and VP3 with noncanonical jellyroll β-barrel folds composed of only seven instead of eight β-strands, as is the rule for proteins of other viruses with the same fold. The maturation of dicistroviruses is connected to the cleavage of precursor capsid protein VP0 into subunits VP3 and VP4. We show that a putative catalytic site formed by the residues Asp-Asp-Phe of VP1 is optimally positioned to perform the cleavage. Furthermore, unlike many picornaviruses, IAPV does not contain a hydrophobic pocket in capsid protein VP1 that could be targeted by capsid-binding antiviral compounds.

IMPORTANCE

Honeybee pollination is required for agricultural production and to sustain the biodiversity of wild flora. However, honeybee populations in Europe and North America are under pressure from pathogens, including viruses that cause colony losses. Viruses from the family *Dicistroviridae* can cause honeybee infections that are lethal, not only to individual honeybees, but to whole colonies. Here, we present the virion structure of an *Aparavirus*, Israeli acute bee paralysis virus (IAPV), a member of a complex of closely related viruses that are distributed worldwide. IAPV exhibits unique structural features not observed in other picorna-like viruses. Capsid protein VP1 of IAPV does not contain a hydrophobic pocket, implying that capsid-binding antiviral compounds that can prevent the replication of vertebrate picornaviruses may be ineffective against honeybee virus infections.

The agricultural production of most flowering food crops depends on the pollination services provided by the western honeybee (*Apis mellifera*) (1). Furthermore, honeybee pollination is also critical for maintaining the ecological and genetic diversity of wild plants (2). However, winter honeybee colony mortality has been increasing in North America and Europe over the last 2 decades, leading to a decline in the number of honeybee colonies that is becoming a serious threat to the adequate provision of pollination services and food security (3–5). Honeybees suffer from habitat loss, intensified agricultural management, pesticides, parasites, and pathogens, including numerous viruses that contribute to the collapse of honeybee colonies (6).

The viruses that have the greatest impact on honeybee populations are small icosahedral picorna-like viruses from the families *Dicistroviridae* and *Iflaviridae* (7). Israeli acute paralysis virus (IAPV) is an *Aparavirus* from the family *Dicistroviridae*. IAPV, Kashmir bee virus (KBV), and acute bee paralysis virus (ABPV) constitute a group of closely related viruses that are distributed worldwide, with different members predominating in different geographical regions (8). Infections by IAPV and related viruses decrease the longevity of individual bees and endanger the survival of whole colonies. Furthermore, IAPV infection decreases the homing ability of foraging honeybees, which are not able to find their way back to the hive (9). The spread of the viruses is accelerated by transmission by a parasitic mite, *Varroa destructor* (7, 8, 10). IAPV has been linked with colony collapse disorder in the United States (11), while ABPV has been associated with similar rapid adult bee depopulation phenomena in Europe (8, 12).

Viruses from the family *Dicistroviridae* have nonenveloped

icosahedral virions containing a linear, single-stranded, positive-sense RNA genome 8,500 to 10,200 nucleotides in length (13). The genome of dicistroviruses includes two nonoverlapping open reading frames (ORFs), ORF1 and ORF2, which encode polyproteins containing nonstructural and structural (capsid-forming) proteins, respectively. The polyproteins are cotranslationally and posttranslationally cleaved by viral proteases to produce functional subunits. The capsid proteins originating from a single polyprotein precursor form a protomer—the basic building block of the capsid. Previously, structures of two dicistroviruses from the genus *Cripavirus*, triatoma virus (TrV) and cricket paralysis virus (CrPV), were determined (14–17). Protomers, as well as icosahedral asymmetric units of dicistroviruses, consist of subunits VP1 to -4. The major capsid proteins VP1 to -3 form the capsid shell, with pseudo-T=3 icosahedral symmetry, whereas VP4 is a small protein attached to the inner surface of the capsid. The major capsid proteins have the jellyroll β-sandwich fold common to many other virus capsid proteins. Dicistrovirus virions

Received 2 May 2016 Accepted 24 June 2016

Accepted manuscript posted online 6 July 2016

Citation Mullapudi E, Přidal A, Pálková L, de Miranda JR, Plevka P. 2016. Virion structure of Israeli acute bee paralysis virus. *J Virol* 90:8150–8159. doi:10.1128/JVI.00854-16.

Editor: A. Simon, University of Maryland

Address correspondence to Pavel Plevka, pavel.plevka@ceitec.muni.cz.

Copyright © 2016 Mullapudi et al. This is an open-access article distributed under the terms of the [Creative Commons Attribution 4.0 International license](https://creativecommons.org/licenses/by/4.0/).

assemble as immature particles containing the precursor protein VP0, which is presumed to be cleaved into VP4 and VP3 after the particles are filled with the RNA genome, similar to the situation in picornaviruses (18, 19).

In order to initiate infection, virus genomes need to be released from virions and transferred across the biological membrane into the cell cytoplasm. There is limited information about this process in viruses from the family *Dicistroviridae*. However, related enteroviruses from the family *Picornaviridae* have been extensively studied as model organisms for genome delivery (20–25). The genome release of enteroviruses is preceded by structural changes of the capsid, leading to the formation of an expanded A particle that is induced by receptor binding or by the low pH of late endosomes (20, 26–28). The A particles contain pores at the icosahedral 2-fold symmetry axes (21–26, 29–31) that allow the release of the genome and VP4 subunits and the exposure of the N-terminal region of VP1 subunits on the virion surface (26, 32, 33).

Here, we present the crystal structures of the IAPV virion, the first structurally characterized representative of the genus *Aparavirus*. In addition, we determined the structure of the IAPV pentamer of the capsid protein protomers produced by capsid disassembly after genome release.

MATERIALS AND METHODS

Virus propagation in honeybee pupae. The propagation of IAPV was carried out as described in the COLOSS BeeBook (34). Brood areas with *A. mellifera* white-eyed pupae were identified by the color and structural features of the cell caps. White-eyed pupae were carefully extracted from the brood combs so as not to injure the pupae. The pupae were placed on paper furrows with their ventral side up. In total, 2,262 pupae were used for IAPV propagation. The virus inoculum (1 μ l) was injected into pupae with a Hamilton micropipette with a 30-gauge 22-mm-long needle through the intersegmental cuticle between the 4th and 5th sternites. Pupae that leaked hemolymph after the injection were discarded. The optimal concentration of the virus in the inoculum for virus production was determined experimentally by comparing virus yields when using different virus concentrations in the injection inoculum. Inoculated pupae were placed into petri dishes with paper furrows and incubated at 30°C and 75% humidity for 5 days. Typical IAPV-induced darkening was observed in 80% of the injected pupae (35). After incubation, the pupae were frozen at –20°C. For long-term storage, the pupae were kept at –80°C.

Virus purification. Fifty experimentally infected honeybee pupae were homogenized with a Dounce homogenizer in 30 ml of phosphate-buffered saline (PBS), pH 7.5 (Sigma-Aldrich). The nonionic detergent NP-40 was added to a final concentration of 0.5%, and the homogenate was incubated for 1 h at room temperature. The extract was centrifuged at 8,000 \times g for 30 min. The pellet was discarded, and the supernatant was centrifuged at 150,000 \times g for 3 h in a Ti50.2 fixed-angle rotor (Beckman-Coulter). The resulting pellet was resuspended in PBS to a final volume of 5 ml. MgCl₂ was added to a final concentration of 5 mM, as well as 20 μ g/ml DNase I and 20 μ g/ml RNase. The solution was incubated at room temperature for 30 min and centrifuged at 4,000 \times g for 15 min. The resulting supernatant was loaded onto a CsCl (0.6-g/ml) solution prepared in PBS. The ultracentrifugation proceeded for 16 h to establish the CsCl gradient. Virus bands were collected by gentle piercing of the ultracentrifuge tubes with an 18-gauge needle. The viruses were transferred to PBS by several rounds of concentration and dilution using centrifuge filter units with a 100-kDa molecular mass cutoff. This procedure yielded about 300 μ g of virus with a purity sufficient for crystallization screening. Sample purity with respect to contaminating honeybee viruses was checked by reverse transcription-quantitative PCR (RT-qPCR), using previously reported virus-specific assays (34). In both preparations, the total sum of contaminating viruses was less than 1% of the virus of interest. The nu-

TABLE 1 Crystallographic data collection and refinement statistics

| Crystallization condition | IAPV pentamer ^a | IAPV virion ^b |
|---|---|----------------------------------|
| Space group | P2 ₁ 2 ₁ 2 ₁ | P2 ₁ 2 ₁ 2 |
| Wavelength (Å) | 0.9998 | 0.9998 |
| a, b, c (Å) | 112.2, 274.2, 288.3 | 343.1, 383.3, 329.9 |
| α , β , γ (°) | 90, 90, 90 | 90, 90, 90 |
| Resolution (Å) ^c | 70–2.7 (2.79–2.70) | 70–4.0 (4.07–4.00) |
| R_{merge} ^c | 0.086 (0.51) | 0.21 (0.63) |
| $\langle I \rangle / \langle \sigma I \rangle$ ^c | 13.2 (2.7) | 4.7 (1.5) |
| Completeness (%) ^c | 98.7 (99.5) | 72.7 (54.8) |
| Redundancy | 4.2 | 2.5 |
| No. of reflections | 240,313 | 250,379 |
| $R_{\text{work}}/R_{\text{free}}$ | 24.4/25.1 | 30.6 ^e |
| No. of atoms | 5,617 | 6,116 |
| RMSD ^d bond length (Å) | 0.013 | 0.015 |
| RMSD bond angle (°) | 1.49 | 1.42 |
| Ramachandran favored (%) ^f | 90.0 | 79.1 |
| Ramachandran allowed (%) ^f | 9.3 | 19.1 |
| Ramachandran outliers (%) ^f | 0.7 | 1.8 |
| Poor rotamers (%) ^f | 2.7 | 2.6 |
| C β deviation (%) | 0.9 | 0.1 |

^a 0.1 M cadmium chloride, 0.1 M sodium acetate, pH 4.5, 15% (vol/vol) PEG 400.

^b Twenty percent PEG 10,000, 8% ethylene glycol, 0.1 M HEPES, pH 7.5.

^c Values in parentheses are for the highest resolution shell.

^d RMSD, root mean square deviation.

^e All reflections were used in the refinement. The R_{free} , if it were calculated, would be very similar to R_{work} because of the 30-fold noncrystallographic symmetry present in the crystal. See Materials and methods for details.

^f According to the criterion of MolProbity (59).

cleotide sequences of the virus preparations were determined by sequencing 300 ng of RNA, purified using a Qiagen RNA purification kit, by IonTorrent (Thermo Fisher Scientific) technology and standard protocols for library preparation and sequencing. The IonTorrent reads were mapped to the IAPV GenBank reference sequence [NC_009025](#) using Tmap v4.4.8, included in TorrentSuite 4.4.2, with Life Technologies-recommended parameters. Variability and consensus sequences were created using mpileup from samtools v.0.1.8 and an in-house script.

IAPV crystallization. IAPV crystallization screening was performed at 20°C using the virus dissolved in PBS at a concentration of 3 mg/ml. Approximately 1,800 crystallization conditions were tested by the sitting-drop vapor diffusion method in 96-well plates. Cuboid crystals with a longest dimension of approximately 0.05 mm were obtained in 0.1 M cadmium chloride, 0.1 M Na acetate, pH 4.5, and 15% (vol/vol) polyethylene glycol (PEG) 400. These crystals were flash frozen in liquid nitrogen without additional cryoprotectant and used to collect diffraction data. Crystals of a different type with a rhombic shape and a longest dimension of approximately 0.2 mm were obtained in 20% PEG 10,000, 8% ethylene glycol, 0.1 M HEPES, pH 7.5. These crystals diffracted X rays to a resolution of 2.7 Å. However, subsequent analysis revealed that they were composed of pentamers of IAPV capsid protein protomers.

IAPV structure determination and refinement. IAPV crystallization produced two types of crystals: (i) P2₁2₁2, containing one-half of a virus particle in the crystallographic asymmetric unit, and (ii) the P2₁2₁2₁ crystal form, which did not contain a virus particle. Instead the P2₁2₁2₁ crystallographic asymmetric unit contained two pentamers of capsid protein protomers, whose bases faced each other. The orientations of the virion and of the pentamers in the crystals were determined using the programs GLRF and Phaser (36, 37).

The P2₁2₁2 crystal form was solved initially. Self-rotation function plots and packing considerations indicated that 1/2 of a virus particle occupied a crystallographic asymmetric unit. The IAPV virion was positioned with one of the icosahedral 2-fold axes superimposed on the crystallographic 2-fold axis. The orientation of the virion was determined in a

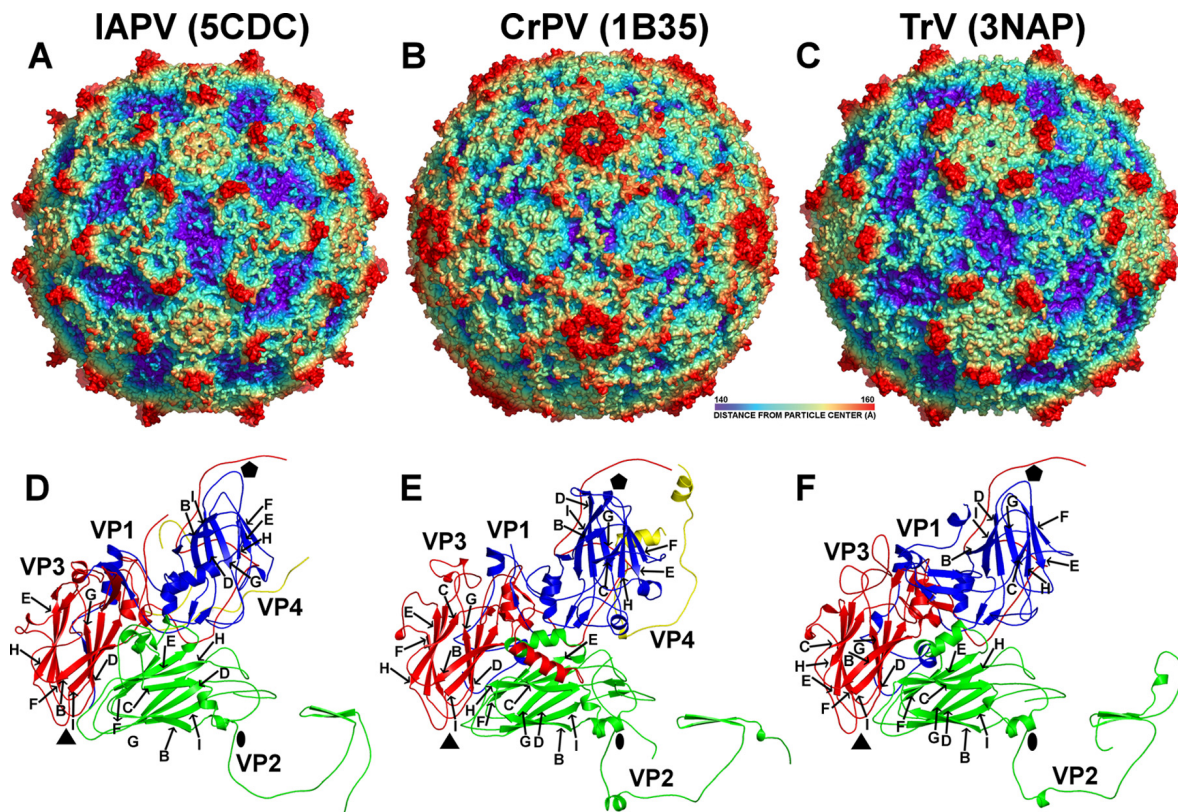


FIG 1 Comparison of virion and capsid protein structures of IAPV, CrPV, and TrV. (A to C) The molecular surfaces of IAPV (A), CrPV (B), and TrV (C) virions are colored based on the distance from the virion center. The depressions are shown in blue and protrusions in red. (D to F) Cartoon representations of the capsid protein protomers of IAPV (D), CrPV (E), and TrV (F). VP1 subunits are shown in blue, VP2 in green, VP3 in red, and VP4 in yellow. The names of β -strands of IAPV capsid proteins are shown. The positions of the 5-fold, 3-fold, and 2-fold icosahedral symmetry axes are indicated by pentagons, triangles, and ovals, respectively.

one-dimensional locked-rotation function search with the icosahedral symmetry in starting orientation, defined as described by Rossmann and Blow, rotated around the y coordinate axis (36, 38). Reflections at between 5.0- and 4.5-Å resolution were used for the calculations. The radius of integration was set to 140 Å. The results suggested that the virion is rotated ($\Phi = 90^\circ$, $\phi = 90^\circ$, and $\kappa = 12.57^\circ$) from the standard icosahedral orientation according to the polar-angle convention. The position of the center of the particle was identified in a one-dimensional translation function search using the program Phaser (37). An appropriately oriented and positioned CrPV model (Protein Data Bank [PDB] code 1B35) was used to calculate phases up to a resolution of 10 Å using the program CNS (39). The phases were refined by 25 cycles of real-space electron density map averaging by the program AVE (40), using the 30-fold noncrystallographic symmetry. Phase extension was applied in order to obtain phases for higher-resolution reflections. Addition of a small fraction of higher-resolution data (one index at a time) was followed by three cycles of averaging. This procedure was repeated until phases were obtained for all the reflections to 4.0-Å resolution.

The electron density map corresponding to an icosahedral asymmetric unit from the $P2_12_12$ crystal (the virion) was used as a molecular replacement model for the phasing of the $P2_12_12$ crystal form (the pentamers). Phase extension was applied in order to obtain phases for reflections in the 4- to 2.7-Å resolution range. The electron density of the capsid protein protomer was then used to phase the $P2_12_12$ (virion) crystal form.

The initial model, derived from the CrPV structure converted to poly-alanine, was subjected to manual rebuilding using the programs Coot and O and to coordinate and B factor refinement using the program CNS (simulated annealing, gradient minimization, and individual B factor refinement) (39, 41, 42). Noncrystallographic symmetry constraints were

enforced during the refinement. The model of the capsid proteins was built in the $P2_12_12$ crystal form, using data to a resolution of 2.7 Å. The model could not be built for residues 1 to 58 and 259 to 318 of VP2, because the corresponding electron density was not resolved in the map. No density corresponding to VP4 could be identified in the $P2_12_12$ crystal form.

The model building for the $P2_12_2$ crystal form that contained the IAPV virion was started from the model built in the $P2_12_12$ crystal form. The main differences between the two crystal forms were in the structure of the N terminus of VP2 and in the electron density for IAPV VP4. The

TABLE 2 Sequence and structural similarity comparison of capsid proteins of IAPV to those of dicistroviruses and picornaviruses

| Virus | Comparison to ^a : | | | | |
|--------------------|------------------------------|--------|--------|-------------------|--------|
| | IAPV | CrPV | TrV | Poliovirus type 1 | HRV14 |
| IAPV | | 2.6/63 | 1.9/80 | 2.6/65 | 2.7/54 |
| CrPV | 23 | | 1.8/82 | 2.6/60 | 2.6/69 |
| TrV | 22 | 29 | | 2.4/64 | 2.3/66 |
| Polio virus type 1 | 11 | 13 | 16 | | 1.0/95 |
| HRV14 | 12 | 13 | 14 | 49 | |

^a Top right: root mean square (RMS) deviations (Å) of superimposed C α atoms of the respective three-dimensional (3D) structures. The second number indicates the percentage of available amino acid residues used for the calculations. The limit for inclusion was set to 3.8 Å. Bottom left: percent identity between the respective virus coat protein sequences. Gaps were ignored in the calculation. The icosahedral asymmetric units consisting of subunits VP1 to -4 were used in the comparison as rigid bodies. HRV14, human rhinovirus 14.

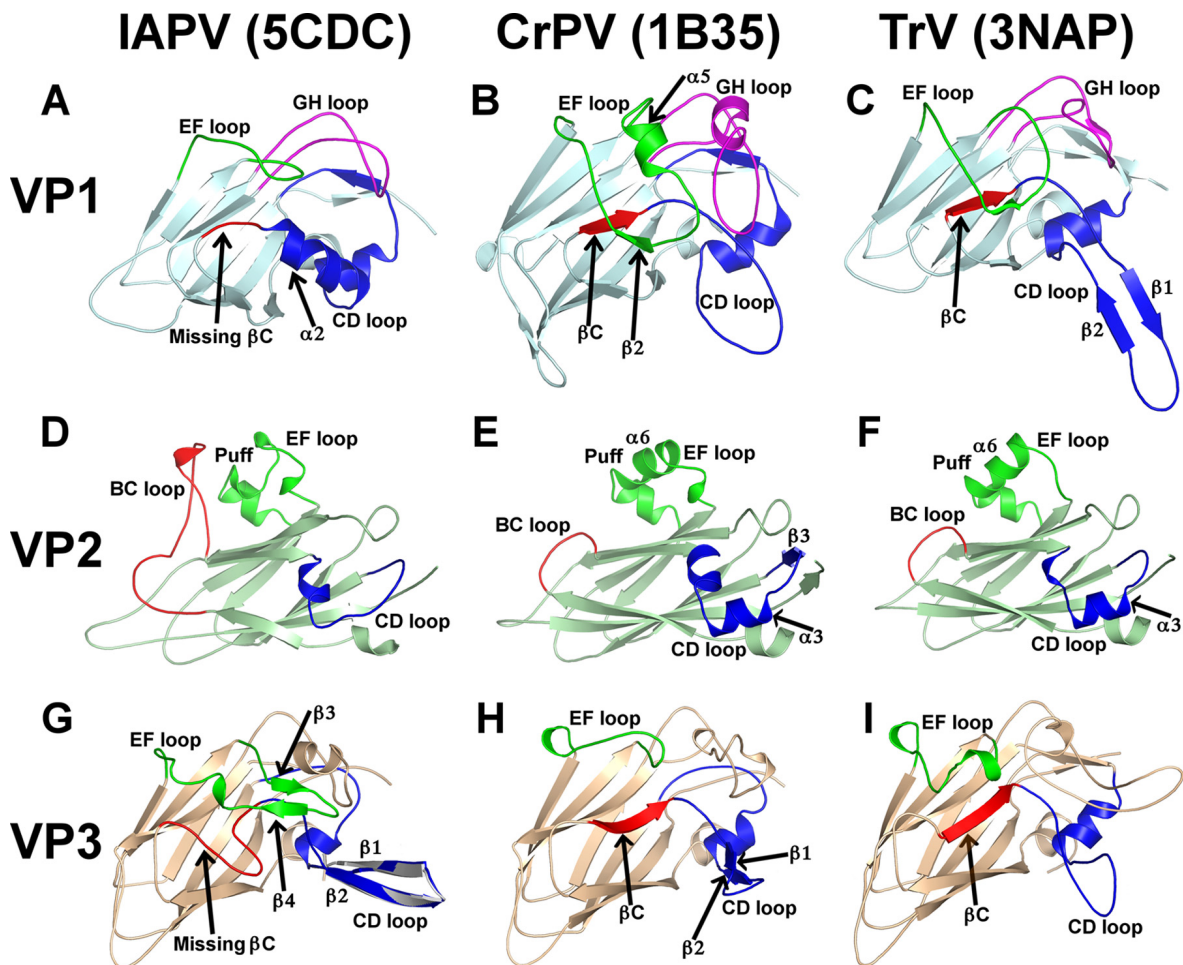


FIG 2 Comparison of capsid proteins of IAPV, CrPV, and TrV. (A to C) VP1 of IAPV contains a loop and α -helix 2, highlighted in red and blue (A), that replace β -strand C in VP1 of CrPV (B) and TrV (C). The EF loop in VP1 of IAPV (A), highlighted in green, is 18 residues shorter than that of CrPV and TrV and lacks α -helix 5 (B and C). The GH loop of IAPV VP1, shown in magenta (A), is 9 and 7 residues shorter than those of CrPV (B) and TrV (C). (D to F) The EF loop, or puff, of IAPV VP2, highlighted in bright green (D), lacks α -helix 6, which is present in CrPV (E) and TrV (F). (D) The BC loop of IAPV VP2 is 15 residues longer than those of CrPV and TrV and interacts with the CD loop. (D and F) The CD loop of IAPV VP2 lacks α -helix 3 and β -strand 3, which are present in CrPV and TrV. (G to I) The VP3 subunit of IAPV lacks β -strand C, which is replaced by a loop, highlighted in red (G); the IAPV VP3 EF loop, shown in green, is 12 residues longer than those in CrPV (H) and TrV (I) and contains two β -strands and a short α -helix. (G) Strands β 1 and β 2 in the CD loop of IAPV VP3, shown in blue, form the most prominent surface feature of the IAPV virion. The structure of the CD loop from the pentamer crystal form (shown in gray) is superimposed on the virion structure.

VP4 model was built as a polyanaline. The P2₁2₁2 model was refined using dynamic energy network (DEN) restraints to the pentamer structure of the P2₁2₁2₁ crystal form. No water molecules were added to the P2₁2₁2 crystal model due to the limited resolution of the diffraction data. All the measured reflections were used in the refinement of the P2₁2₁2 crystal. If calculated, the R_{free} value would be very similar to the R value, due to the 30-fold noncrystallographic symmetry present in the diffraction data (43).

Determination of the effect of IAPV proteins on liposome integrity.

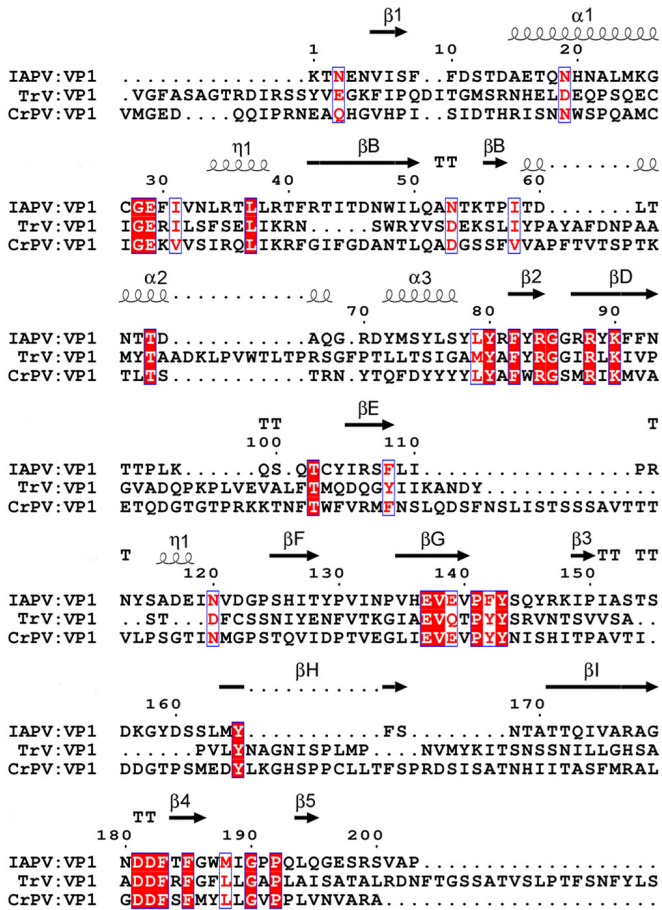
Liposomes composed of phosphatidylcholine, phosphatidylethanolamine, lysophosphatidylcholine, sphingomyelin, phosphatidylserine, and phosphatidylinositol (Avanti Polar Lipids) in molar ratios (43:23:13:9:6:6) filled with the self-quenching fluorescent dye carboxyfluorescein were prepared as described previously (44). The fluorescence quantum yield of the dye encapsulated in liposomes is about 5% of that obtained when the liposomes are disrupted and the dye is released and diluted in the medium. The percentage of dye release induced by addition of detergent or IAPV was determined by measuring fluorescence at an excitation wavelength of 485 nm and an emission wavelength of 520 nm, as described previously (44).

Accession numbers. The atomic coordinates of the IAPV virion, together with the structure factors and phases obtained by phase extension, were deposited in the Protein Data Bank under the code 5CDC. The IAPV pentamer was deposited as 5CDD. The consensus nucleotide sequences of the IAPV preparation were deposited in GenBank under accession number EF219380.

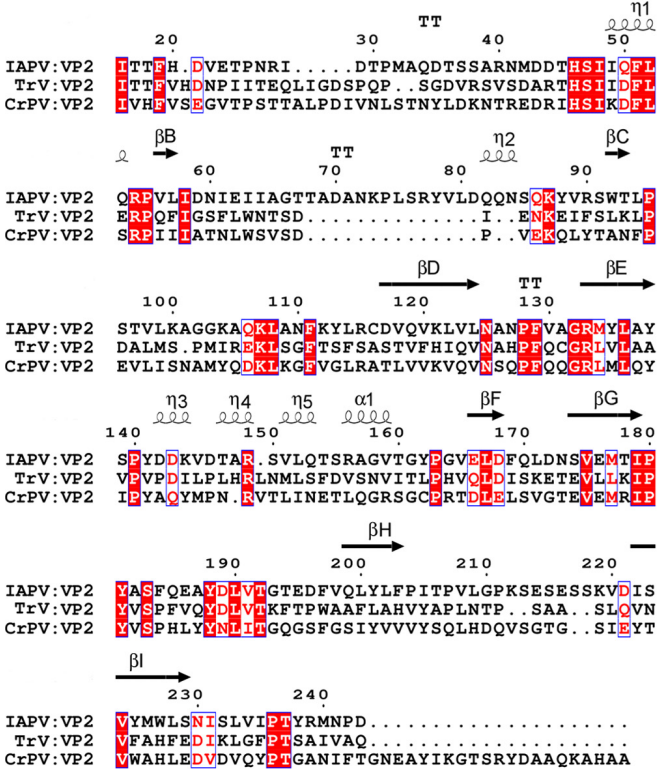
RESULTS AND DISCUSSION

Structures of the IAPV virion and capsid proteins. The crystal structures of the IAPV virion and of the pentamer of capsid protein protomers were determined to resolutions of 4.0 Å and 2.7 Å, respectively (Table 1). The maximum outer diameter of the IAPV virion is 340 Å (Fig. 1A). The IAPV capsid is built from major capsid proteins VP1, VP2, and VP3 arranged in a pseudo-T=3 icosahedral symmetry (Fig. 1D). VP1 subunits form pentamers around 5-fold axes, while VP2 and VP3 subunits constitute alternating heterohexamers around the icosahedral 3-fold axes (Fig. 1D). The three major capsid proteins have jellyroll β -sandwich folds with β -strands named, according to the picornavirus con-

VP1



VP2



VP3

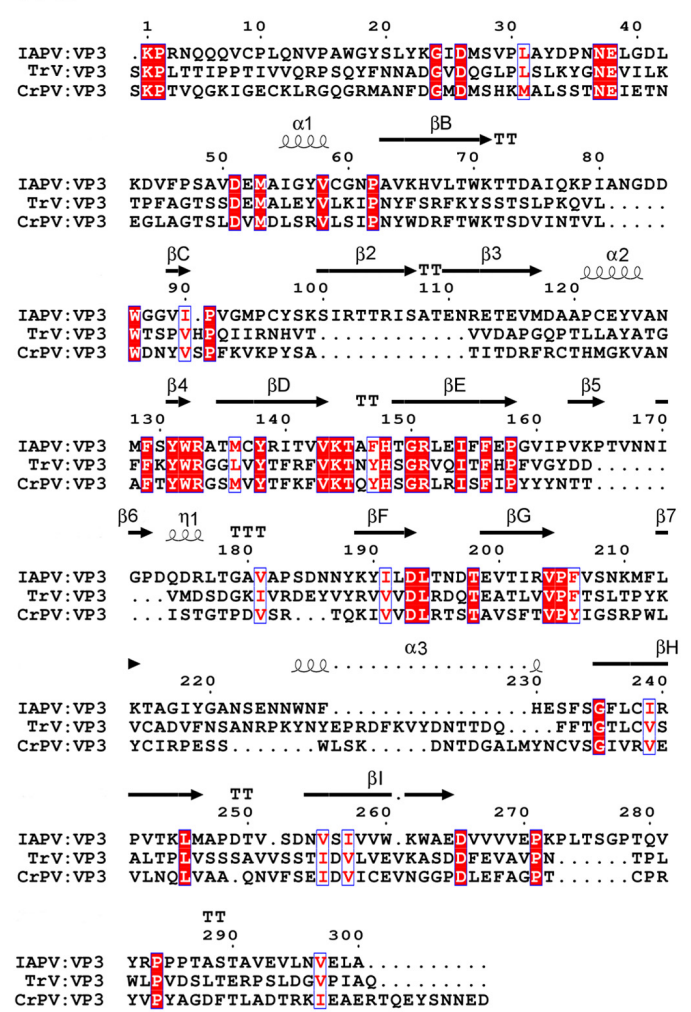


FIG 3 Structure-based alignment of the coat protein sequences of IAPV, CrPV, and TrV. White letters with a red background represent conserved residues, and red letters with a white background represent residues with conserved properties. Secondary-structure elements of IAPV are indicated above the sequence. The arrows represent β -strands, and the spirals represent the α -helices.

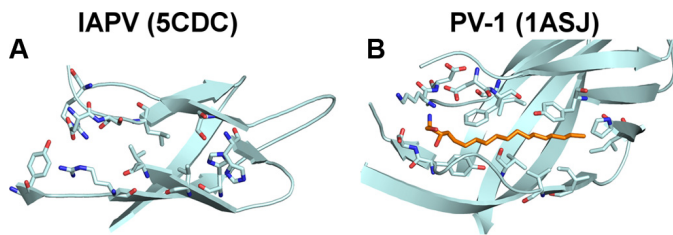


FIG 4 VP1 of IAPV does not contain a hydrophobic pocket. VP1 of IAPV (A) and poliovirus type 1 (B) are shown in cartoon representations. The pocket factor in poliovirus type 1 is shown as a stick model in orange. The residues that form the cores of the subunits and, in the case of poliovirus type 1, interact with the pocket factor are shown as sticks.

vention, B to I (Fig. 1D) (45). Two antiparallel β -sheets forming the cores of the subunits contain strands BIDG and CHEF, respectively. The N termini of the major capsid proteins are located inside the capsid, while the C termini are exposed on the virion surface. The minor capsid protein VP4 is attached to the inner face of the capsid (Fig. 1D). A complete model of the IAPV icosahedral asymmetric unit could be built, except for residues 1 to 5 of VP1, 1 to 15 and 259 to 318 of VP2, and 1 of VP3. The minor capsid protein VP4 has 69 residues; however, due to the lack of features in the corresponding regions of the electron density map, it was modeled as a 45-residue-long polyalanine chain.

Noncanonical jellyroll folds of IAPV VP1 and VP3 subunits and comparison to virions of cricaviruses. While the structures of two dicistroviruses from the genus *Cricavirus*, CrPV and TrV, have been determined previously (14, 15), IAPV represents the first structurally characterized member of the genus *Aparavirus*. IAPV shares less than 25% sequence identity with CrPV and TrV (Table 2) and has a different surface topology (Fig. 1A to C). The IAPV virion is spherical, with plateaus around the icosahedral 5-fold and 3-fold axes. There are depressions on the IAPV capsid surface around the icosahedral 2-fold axes similar to those identified previously in TrV (Fig. 1A and C). However, in CrPV, the depressions are partly filled with residues from the C terminus of VP2 (Fig. 1B and E). The most prominent features of the IAPV virion are spikes located between the icosahedral 5-fold and 3-fold

axes of symmetry that rise about 20 Å above the virion surface (Fig. 1A). The spikes are formed by two antiparallel β -strands from the CD loop of VP3 and a C-terminal β -strand of VP1 (Fig. 1D and 2A and G). The corresponding β -strands in the CD loop of VP3 in CrPV are 9 residues shorter (Fig. 2H), whereas in TrV, the β -strands are not formed at all (Fig. 2I and 3). The CD loops in IAPV have higher temperature factors in both the virion and pentamer crystal forms (127 and 59 Å², respectively) than the rest of the capsid (120 and 39 Å², respectively), indicating their higher flexibility. As the most prominent features of the IAPV virion, the CD loops might function in receptor binding. The structure of the CD loops is the same in the IAPV virions and the pentamer crystal form (Fig. 2G). The most prominent surface feature formed by IAPV subunit VP2 is the EF loop, which is, according to picornavirus convention, named the puff. The puffs of CrPV and TrV contain short α -helices, α 5, α 6, and α 7 (Fig. 2E and F). However, in IAPV, helix α 6 is replaced by a loop (Fig. 2D). The BC loop of IAPV VP2 is 15 residues longer than those in CrPV and TrV and interacts with the CD loop (Fig. 2D to F). Furthermore, the CD loop of IAPV VP2 lacks α -helix 3, which is present in CrPV and TrV VP2 subunits (Fig. 2D to F).

Unlike capsid proteins with the jellyroll fold of other viruses studied so far (14, 15, 45–47), VP1 and VP3 of IAPV exhibit non-canonical jellyroll folds composed of seven instead of the conventional eight antiparallel β -strands (Fig. 2A and G). The absence of the eighth β -strand in IAPV VP1 and VP3 could be observed both in the 2.7-Å-resolution structure of the pentamer and in the 4.0-Å-resolution structure of the entire virion. β -Strand C in subunit VP1 of IAPV is replaced by a loop and an α -helix that extends into the CD loop (Fig. 2A). The corresponding regions of CrPV and TrV VP1 subunits contain β -strand C (β C), which interacts with a short β -strand, β 2, that is part of the EF loop from VP1 (Fig. 2B and C). However, the EF loop of IAPV VP1 is 16 residues shorter than that of CrPV and lacks the β 2 strand and α -helix 5 (Fig. 2A and B). The absence of β -strand 2 and its putative stabilizing interaction with residues that form β C in CrPV might enable the corresponding residues in IAPV to adopt a main-chain conformation that does not resemble the β -strand. The EF loop of TrV VP1 is intermediate in size between those of IAPV and CrPV (Fig. 2C).

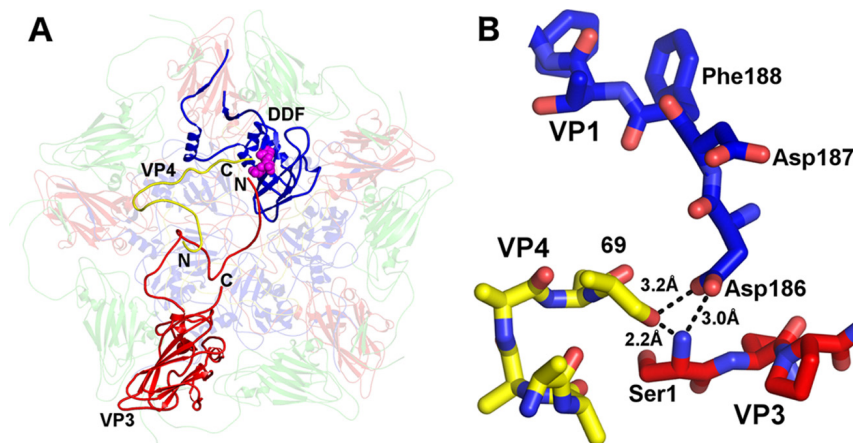


FIG 5 Residues Asp-Asp-Phe of VP1, constituting the putative proteolytic site that might mediate the cleavage of VP0 into VP3 and VP4, are positioned close to the N terminus of VP3 and the C terminus of VP4 from another protomer related by an icosahedral 5-fold axis of symmetry. (A) Cartoon representation of a pentamer of capsid protein protomers viewed from inside the virion. (B) Detail of the putative active site in stick representation. VP1 subunits are shown in blue, VP2 in green, VP3 in red, and VP4 in yellow.

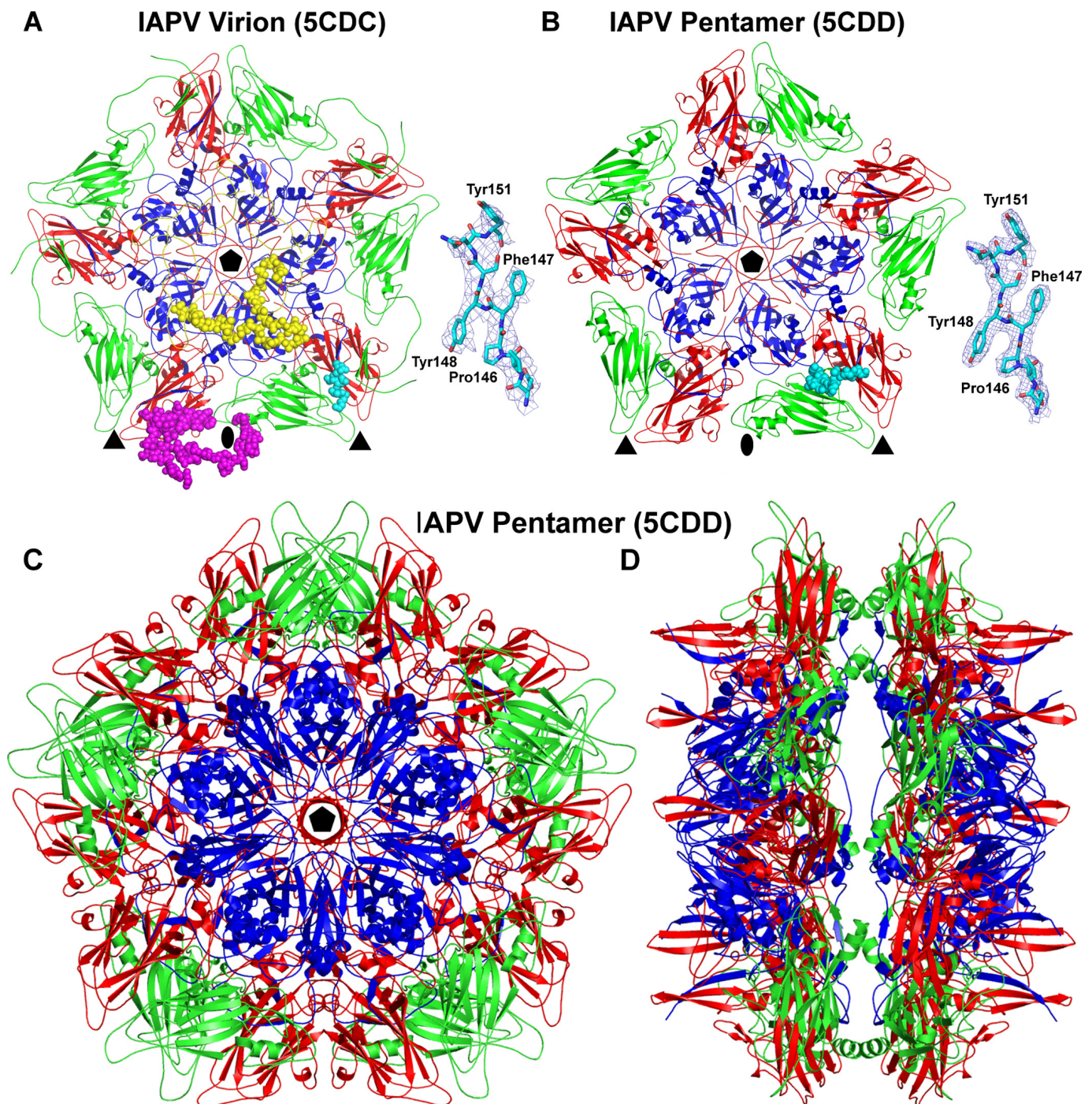


FIG 6 (A and B) Comparison of pentamer structures from the IAPV virion (A) and separately crystallized pentamers of capsid protein protomers (B). VP1 subunits are shown in blue, VP2 in green, VP3 in red, and VP4 in yellow. The differences between the two structures are highlighted in one of the protomers: nine N-terminal residues of VP1 are shown as space-filling spheres in cyan and 64 N-terminal residues of VP2 as space-filling spheres in magenta. (B) VP4, shown in yellow, is missing from the pentamer structure. (A) The N-terminal arms of VP2 subunits mediate interpentamer interactions in the virion. The positions of 5-fold, 3-fold, and 2-fold icosahedral symmetry axes are indicated by pentagons, triangles, and ovals, respectively. The insets show representative electron densities and corresponding models in stick display. (C and D) Top (C) and side (D) views of the decamer assembly of capsid protein protomers from the pentamer crystal form.

In addition, the GH loop of IAPV VP1 is 9 and 7 residues shorter than the GH loops of CrPV and TrV, respectively (Fig. 2A to C). As a consequence of the relatively short loops of IAPV VP1, it contains only 208 residues, whereas VP1 of CrPV consists of 260 residues and that of TrV has 264 residues (Fig. 3).

β -Strand C in IAPV subunit VP3 is replaced by an elongated loop that forms the capsid surface (Fig. 2G). Moreover, the EF loop of IAPV VP3 is 12 residues longer than those of CrPV and TrV and contains two short β -strands, β 3 and β 4, that form an antiparallel β -sheet (Fig. 2G). Residues from the EF loop interact

with the CD loop of IAPV VP3 (Fig. 2G). In contrast, the residues from the shorter EF loops of CrPV and TrV do not interact with residues from β -strand C (Fig. 2H and I). The unique features affecting the fold of IAPV subunits VP1 and VP3 are exposed at the virion surface and might, therefore, represent functional adaptations to the receptor binding.

Dicistroviruses are structurally and genetically related to vertebrate picornaviruses, for which numerous capsid-binding inhibitors have been developed (48). Compounds that bind into a hydrophobic pocket within VP1 can inhibit receptor binding and/or genome release of some picornaviruses (49–52). However, such a hydrophobic pocket is not formed in IAPV VP1 subunits (Fig. 4). Similarly, the hydrophobic pockets were not observed in VP1 subunits of CrPV and TrV (14, 15). This suggests that capsid-binding inhibitors may not be effective as antivirals against honeybee viruses from the genus *Aparavirus*.

Maturation cleavage of VP0 into VP4 and VP3. The maturation of the capsids of many viruses from the order *Picornavirales* is dependent on cleavage of capsid protein VP4 from the N terminus of a precursor subunit, called VP0. In picornaviruses, the VP0 cleavage generates the proteins VP4 and VP2, while in dicistroviruses, the precursor cleavage generates VP4 and VP3 (14, 15). It has been proposed previously that a conserved Asp-Asp-Phe (DDF) motif, which is part of the VP1 subunit that is exposed to the virion cavity, is involved in the VP0 cleavage (14, 15, 17). The cricaviruses CrPV and TrV contain the DDF sequence in a loop immediately following β -strand I of VP1. TrV has an additional, second DDF sequence in a loop following β -strand I of VP3 (14, 15). IAPV has the DDF sequence in VP1, formed by residues 186 to 188, located in a position similar to those in the DDF sequences of TrV and CrPV. Asp186 of the IAPV DDF motif is located close to the N terminus of VP3 and the C terminus of VP4 from the neighboring protomer, indicating that it may catalyze the cleavage (Fig. 5). The conformation of the DDF site is similar to that observed in flockhouse virus, even though it has completely different capsid morphology, in which the Asp residue performs an autocatalytic cleavage that is necessary for capsid maturation (53). The relative positioning of the DDF motif in IAPV and the VP4 C terminus and VP3 N terminus indicates that the formation of pentamers is sufficient to achieve the optimal spatial arrangement of the catalytic center and substrate for the cleavage (Fig. 5A). However, the mechanism that ensures that the VP0 cleavage occurs only in virions containing the RNA genome (14, 53) remains to be determined.

Putative roles of VP4 and the N terminus of VP1 in delivery of the IAPV genome across the biological membrane. The delivery of dicistrovirus genomes into the host cell cytoplasm has not been studied. However, findings from related mammalian picornaviruses showed that VP4 subunits are released together with the genome and that the N termini of VP1 are externalized on the capsid surface at the beginning of the infection. The genome release of many picornaviruses results in the formation of empty capsids, the so-called B particles (54). However, the empty capsids of some picornaviruses and dicistroviruses disassemble into pentamers of capsid protein protomers (55, 56). Furthermore, pentamers of capsid protomers were also shown to be capsid precursors (57, 58). Even though the crystallization of native IAPV virions was attempted, one type of crystal was formed from pentamers of capsid protein protomers (Table 1). Dimers of pentamers of capsid protein protomers very similar to the crystallized

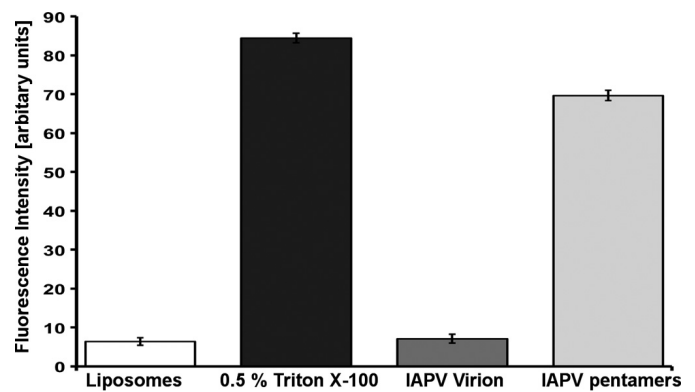


FIG 7 Heat-disrupted IAPV virions induce permeabilization of liposomes. Liposomes filled with self-quenching fluorescent dye were incubated with the detergent Triton X-100, native IAPV virions, and IAPV virions heated to 62°C for 5 min. Permeabilization of the liposomes was detected as an increase in fluorescence. See Materials and Methods for details.

form of IAPV capsid proteins (Fig. 6) were previously observed as disassembly products of TrV (56). The two pentamers are held together by interactions of residue His61 of VP2 with Val11 from the N terminus of VP1 and of Gln65 from VP2 with Asp198 from VP3 (Fig. 6D). It is of particular interest that capsid protein VP4 is missing from the pentamers and that 9 residues from the N-terminal arm of the VP1 subunit have a different structure than in the virion (Fig. 6A and B). It is therefore possible that the extended exposure of IAPV to the crystallization conditions of 0.1 M sodium acetate at pH 4.5 induced the virions to release their genomes and disassemble into pentamers in a process mimicking natural genome release. The detachment of VP4 from the pentamers and changes in the structure of the VP1 N termini indicate that these peptides in IAPV might have functions similar to those in picornaviruses (26, 32, 33). This speculation is reinforced by the observation that, whereas native IAPV virions do not affect the integrity of liposomes *in vitro*, heat-dissociated IAPV particles induce liposome disruption (Fig. 7).

VP2 of IAPV has an elongated N-terminal arm that mediates contacts between the pentamers of the capsid protein protomers (Fig. 6A). The N-terminal arm of the VP2 subunit reaches around an icosahedral 2-fold axis into a neighboring pentamer; approaches a 3-fold axis; and forms two β -strands, β 1 and β 2, that extend the β -sheet HEF of a VP3 subunit from the same pentamer that contains the VP2 subunit (Fig. 6A). The electron density corresponding to residues 1 to 58 from the N terminus of VP2 is not resolved in the pentamer crystal form (Fig. 6B). This verifies that interpentamer contacts are required to maintain the structure of the VP2 N terminus and its stabilizing function within the virion.

ACKNOWLEDGMENTS

We thank Jiří Svoboda for his technical assistance with pupa preparation. We thank the beamline scientists at the SLS and Soleil synchrotrons for their outstanding technical assistance with crystal screening and data collection. We thank Christian Tellgren-Roth from LifeSciLabs at Uppsala University, Uppsala, Sweden, for assembling virus genome sequences and Emilia Semberg at SLU for technical assistance. We acknowledge CF Cryo-Electron Microscopy and Tomography, CF X-ray Diffraction and Bio-SAXS, and CF Biomolecular Interactions and Crystallization, supported by the CIISB research infrastructure (LM2015043, funded by

MEYS CR), for their support with obtaining scientific data presented in this paper.

The mass spectrometry (MS) part of the work was carried out with the support of the Proteomics Core Facility of the CEITEC-Central European Institute of Technology under the CIISB project, ID number LM2015043, funded by the Ministry of Education, Youth and Sports of the Czech Republic. The research was carried out under project CEITEC 2020 (LQ1601) with financial support from the Ministry of Education, Youth and Sports of the Czech Republic under National Sustainability Program II. The research leading to these results received funding from the European Research Council under the European Union's Seventh Framework Program (FP/2007-2013)/ERC through grant agreement 355855 and from EMBO installation grant 3041 to Pavel Plevka.

FUNDING INFORMATION

This work, including the efforts of Pavel Plevka, was funded by EC | European Research Council (ERC) (355855). This work, including the efforts of Pavel Plevka, was funded by European Molecular Biology Organization (EMBO) (3041).

REFERENCES

- Allsopp MH, de Lange WJ, Veldtman R. 2008. Valuing insect pollination services with cost of replacement. *PLoS One* 3:e3128. <http://dx.doi.org/10.1371/journal.pone.0003128>.
- Biesmeijer JC, Roberts SP, Reemer M, Ohlemuller R, Edwards M, Peeters T, Schaffers AP, Potts SG, Kleukers R, Thomas CD, Settele J, Kunin WE. 2006. Parallel declines in pollinators and insect-pollinated plants in Britain and the Netherlands. *Science* 313:351–354. <http://dx.doi.org/10.1126/science.1127863>.
- van Engelsdorp D, Hayes J, Jr, Underwood RM, Pettis J. 2008. A survey of honey bee colony losses in the U.S., fall 2007 to spring 2008. *PLoS One* 3:e4071. <http://dx.doi.org/10.1371/journal.pone.0004071>.
- Dainat B, Vanengelsdorp D, Neumann P. 2012. Colony collapse disorder in Europe. *Environ Microbiol Rep* 4:123–125. <http://dx.doi.org/10.1111/j.1758-2229.2011.00312.x>.
- Smith KM, Loh EH, Rostal MK, Zambrana-Torrel CM, Mendiola L, Daszak P. 2013. Pathogens, pests, and economics: drivers of honey bee colony declines and losses. *Ecohealth* 10:434–445. <http://dx.doi.org/10.1007/s10393-013-0870-2>.
- Vanengelsdorp D, Meixner MD. 2010. A historical review of managed honey bee populations in Europe and the United States and the factors that may affect them. *J Invertebr Pathol* 103(Suppl 1):S80–S95. <http://dx.doi.org/10.1016/j.jip.2009.06.011>.
- Chen YP, Siede R. 2007. Honey bee viruses. *Adv Virus Res* 70:33–80. [http://dx.doi.org/10.1016/S0065-3527\(07\)70002-7](http://dx.doi.org/10.1016/S0065-3527(07)70002-7).
- de Miranda JR, Cordoni G, Budge G. 2010. The acute bee paralysis virus-Kashmir bee virus-Israeli acute paralysis virus complex. *J Invertebr Pathol* 103(Suppl 1):S30–S47. <http://dx.doi.org/10.1016/j.jip.2009.06.014>.
- Li Z, Chen Y, Zhang S, Chen S, Li W, Yan L, Shi L, Wu L, Sohr A, Su S. 2013. Viral infection affects sucrose responsiveness and homing ability of forager honey bees, *Apis mellifera* L. *PLoS One* 8:e77354. <http://dx.doi.org/10.1371/journal.pone.0077354>.
- de Miranda JR, Genersch E. 2010. Deformed wing virus. *J Invertebr Pathol* 103(Suppl 1):S48–S61. <http://dx.doi.org/10.1016/j.jip.2009.06.012>.
- Maori E, Paldi N, Shafir S, Kalev H, Tsur E, Glick E, Sela I. 2009. IAPV, a bee-affecting virus associated with Colony Collapse Disorder can be silenced by dsRNA ingestion. *Insect Mol Biol* 18:55–60. <http://dx.doi.org/10.1111/j.1365-2583.2009.00847.x>.
- Berthoud HIA, Haueter M, Radloff S, Neumann P. 2010. Virus infections and winter losses of honey bee colonies (*Apis mellifera*). *J Apicult Res* 49:60–65.
- Le Gall O, Christian P, Fauquet CM, King AM, Knowles NJ, Nakashima N, Stanway G, Gorbalenya AE. 2008. Picornavirales, a proposed order of positive-sense single-stranded RNA viruses with a pseudo-T=3 virion architecture. *Arch Virol* 153:715–727. <http://dx.doi.org/10.1007/s00705-008-0041-x>.
- Tate J, Liljas L, Scotti P, Christian P, Lin T, Johnson JE. 1999. The crystal structure of cricket paralysis virus: the first view of a new virus family. *Nat Struct Biol* 6:765–774. <http://dx.doi.org/10.1038/11543>.
- Squires G, Pous J, Agirre J, Rozas-Dennis GS, Costabel MD, Marti GA, Navaza J, Bressanelli S, Guerin DM, Rey FA. 2013. Structure of the Triatoma virus capsid. *Acta Crystallogr D Biol Crystallogr* 69:1026–1037. <http://dx.doi.org/10.1107/S0907444913004617>.
- Acharya R, Fry E, Stuart D, Fox G, Rowlands D, Brown F. 1989. The three-dimensional structure of foot-and-mouth disease virus at 2.9 Å resolution. *Nature* 337:709–716. <http://dx.doi.org/10.1038/337709a0>.
- Agirre J, Aloria K, Arizmendi JM, Iloro I, Elortza F, Sanchez-Eugenía R, Marti GA, Neumann E, Rey FA, Guerin DM. 2011. Capsid protein identification and analysis of mature Triatoma virus (TrV) virions and naturally occurring empty particles. *Virology* 409:91–101. <http://dx.doi.org/10.1016/j.virol.2010.09.034>.
- Rombaut B, Foriers A, Boeye A. 1991. In vitro assembly of poliovirus 14 S subunits: identification of the assembly promoting activity of infected cell extracts. *Virology* 180:781–787. [http://dx.doi.org/10.1016/0042-6822\(91\)90091-O](http://dx.doi.org/10.1016/0042-6822(91)90091-O).
- Rombaut B, Vrijnsen R, Boeye A. 1984. In vitro assembly of poliovirus empty capsids: antigenic consequences and immunological assay of the morphopoietic factor. *Virology* 135:546–550. [http://dx.doi.org/10.1016/0042-6822\(84\)90209-5](http://dx.doi.org/10.1016/0042-6822(84)90209-5).
- Tuthill TJ, Gropelli E, Hogle JM, Rowlands DJ. 2010. Picornaviruses. *Curr Top Microbiol Immunol* 343:43–89. http://dx.doi.org/10.1007/82_2010_37.
- Levy HC, Bostina M, Filman DJ, Hogle JM. 2010. Catching a virus in the act of RNA release: a novel poliovirus uncoating intermediate characterized by cryo-electron microscopy. *J Virol* 84:4426–4441. <http://dx.doi.org/10.1128/JVI.02393-09>.
- Lyu K, Ding J, Han JF, Zhang Y, Wu XY, He YL, Qin CF, Chen R. 2014. Human enterovirus 71 uncoating captured at atomic resolution. *J Virol* 88:3114–3126. <http://dx.doi.org/10.1128/JVI.03029-13>.
- Wang X, Peng W, Ren J, Hu Z, Xu J, Lou Z, Li X, Yin W, Shen X, Porta C, Walter TS, Evans G, Axford D, Owen R, Rowlands DJ, Wang J, Stuart DI, Fry EE, Rao Z. 2012. A sensor-adaptor mechanism for enterovirus uncoating from structures of EV71. *Nat Struct Mol Biol* 19:424–429. <http://dx.doi.org/10.1038/nsmb.2255>.
- Shingler KL, Yoder JL, Carnegie MS, Ashley RE, Makhov AM, Conway JF, Hafenstein S. 2013. The enterovirus 71 A-particle forms a gateway to allow genome release: a cryoEM study of picornavirus uncoating. *PLoS Pathog* 9:e1003240. <http://dx.doi.org/10.1371/journal.ppat.1003240>.
- Bostina M, Levy H, Filman DJ, Hogle JM. 2011. Poliovirus RNA is released from the capsid near a twofold symmetry axis. *J Virol* 85:776–783. <http://dx.doi.org/10.1128/JVI.00531-10>.
- Fricks CE, Hogle JM. 1990. Cell-induced conformational change in poliovirus: externalization of the amino terminus of VP1 is responsible for liposome binding. *J Virol* 64:1934–1945.
- Greve JM, Forte CP, Marlor CW, Meyer AM, Hoover-Litty H, Wunderlich D, McClelland A. 1991. Mechanisms of receptor-mediated rhinovirus neutralization defined by two soluble forms of ICAM-1. *J Virol* 65:6015–6023.
- Prchla E, Kuechler E, Blaas D, Fuchs R. 1994. Uncoating of human rhinovirus serotype 2 from late endosomes. *J Virol* 68:3713–3723.
- Ren J, Wang X, Hu Z, Gao Q, Sun Y, Li X, Porta C, Walter TS, Gilbert RJ, Zhao Y, Axford D, Williams M, McAuley K, Rowlands DJ, Yin W, Wang J, Stuart DI, Rao Z, Fry EE. 2013. Picornavirus uncoating intermediate captured in atomic detail. *Nat Commun* 4:1929. <http://dx.doi.org/10.1038/ncomms2889>.
- Seitsonen JJ, Shakeel S, Susi P, Pandurangan AP, Sinkovits RS, Hyvonen H, Laurinmaki P, Yla-Pelto J, Topf M, Hyypia T, Butcher SJ. 2012. Structural analysis of coxsackievirus A7 reveals conformational changes associated with uncoating. *J Virol* 86:7207–7215. <http://dx.doi.org/10.1128/JVI.06425-11>.
- Garriga D, Pickl-Herk A, Luque D, Wruss J, Caston JR, Blaas D, Verdaguer N. 2012. Insights into minor group rhinovirus uncoating: the X-ray structure of the HRV2 empty capsid. *PLoS Pathog* 8:e1002473. <http://dx.doi.org/10.1371/journal.ppat.1002473>.
- Chow M, Newman JF, Filman D, Hogle JM, Rowlands DJ, Brown F. 1987. Myristylation of picornavirus capsid protein VP4 and its structural significance. *Nature* 327:482–486. <http://dx.doi.org/10.1038/327482a0>.
- Lin J, Cheng N, Chow M, Filman DJ, Steven AC, Hogle JM, Belnap DM. 2011. An externalized polypeptide partitions between two distinct sites on genome-released poliovirus particles. *J Virol* 85:9974–9983. <http://dx.doi.org/10.1128/JVI.05013-11>.
- de Miranda JR, Bailey L, Ball BV, Blanchard P, Budge G, Chejanovsky

- N, Chen Y-P, Gauthier L, Genersch E, De Graaf D, Ribière M, Ryabov E, De Smet L, van der Steen JJM. 2013. Standard methods for *Apis mellifera* pest and pathogen research, p 1–55. In Dietemann V, Ellis JD, Neumann P. (ed), The COLOSS beebook, vol II. IBRA, Treforest, United Kingdom.
35. Boncristiani HF, Evans JD, Chen Y, Pettis J, Murphy C, Lopez DL, Simone-Finstrom M, Strand M, Tarpay DR, Rueppell O. 2013. In vitro infection of pupae with Israeli acute paralysis virus suggests disturbance of transcriptional homeostasis in honey bees (*Apis mellifera*). *PLoS One* 8:e73429. <http://dx.doi.org/10.1371/journal.pone.0073429>.
 36. Tong L, Rossmann MG. 1997. Rotation function calculations with GLRF program. *Methods Enzymol* 276:594–611. [http://dx.doi.org/10.1016/S0076-6879\(97\)76080-4](http://dx.doi.org/10.1016/S0076-6879(97)76080-4).
 37. McCoy AJ, Grosse-Kunstleve RW, Adams PD, Winn MD, Storoni LC, Read RJ. 2007. Phaser crystallographic software. *J Appl Crystallogr* 40: 658–674. <http://dx.doi.org/10.1107/S0021889807021206>.
 38. Rossmann MG, Blow DM. 1962. The detection of sub-units within the crystallographic asymmetric unit. *Acta Crystallogr* 15:24–31. <http://dx.doi.org/10.1107/S0365110X62000067>.
 39. Brunger AT. 2007. Version 1.2 of the crystallography and NMR system. *Nat Protoc* 2:2728–2733. <http://dx.doi.org/10.1038/nprot.2007.406>.
 40. Kleywegt GJ, Read RJ. 1997. Not your average density. *Structure* 5:1557–1569. [http://dx.doi.org/10.1016/S0969-2126\(97\)00305-5](http://dx.doi.org/10.1016/S0969-2126(97)00305-5).
 41. Emsley P, Cowtan K. 2004. Coot: model-building tools for molecular graphics. *Acta Crystallogr D Biol Crystallogr* 60:2126–2132. <http://dx.doi.org/10.1107/S0907444904019158>.
 42. Jones TA, Zou JY, Cowan SW, Kjeldgaard M. 1991. Improved methods for building protein models in electron density maps and the location of errors in these models. *Acta Crystallogr A* 47:110–119. <http://dx.doi.org/10.1107/S0108767390010224>.
 43. Kleywegt GJ, Brunger AT. 1996. Checking your imagination: applications of the free R value. *Structure* 4:897–904. [http://dx.doi.org/10.1016/S0969-2126\(96\)00097-4](http://dx.doi.org/10.1016/S0969-2126(96)00097-4).
 44. Blumenthal R, Seth P, Willingham MC, Pastan I. 1986. pH-dependent lysis of liposomes by adenovirus. *Biochemistry* 25:2231–2237. <http://dx.doi.org/10.1021/bi00356a057>.
 45. Rossmann MG, Arnold E, Erickson JW, Frankenberger EA, Griffith JP, Hecht HJ, Johnson JE, Kamer G, Luo M, Mosser AG, Rueckert RR, Sherry B, Vriend G. 1985. Structure of a human common cold virus and functional relationship to other picornaviruses. *Nature* 317:145–153. <http://dx.doi.org/10.1038/317145a0>.
 46. Olson AJ, Bricogne G, Harrison SC. 1983. Structure of tomato bushy stunt virus IV. The virus particle at 2.9 Å resolution. *J Mol Biol* 171:61–93.
 47. Hogle JM, Chow M, Filman DJ. 1985. Three-dimensional structure of poliovirus at 2.9 Å resolution. *Science* 229:1358–1365. <http://dx.doi.org/10.1126/science.2994218>.
 48. Rotbart HA. 2002. Treatment of picornavirus infections. *Antiviral Res* 53:83–98. [http://dx.doi.org/10.1016/S0166-3542\(01\)00206-6](http://dx.doi.org/10.1016/S0166-3542(01)00206-6).
 49. Smith TJ, Kremer MJ, Luo M, Vriend G, Arnold E, Kamer G, Rossmann MG, McKinlay MA, Diana GD, Otto MJ. 1986. The site of attachment in human rhinovirus 14 for antiviral agents that inhibit uncoating. *Science* 233:1286–1293. <http://dx.doi.org/10.1126/science.3018924>.
 50. Hadfield AT, Diana GD, Rossmann MG. 1999. Analysis of three structurally related antiviral compounds in complex with human rhinovirus 16. *Proc Natl Acad Sci U S A* 96:14730–14735. <http://dx.doi.org/10.1073/pnas.96.26.14730>.
 51. Grant RA, Hiremath CN, Filman DJ, Syed R, Andries K, Hogle JM. 1994. Structures of poliovirus complexes with anti-viral drugs: implications for viral stability and drug design. *Curr Biol* 4:784–797.
 52. Hiremath CN, Grant RA, Filman DJ, Hogle JM. 1995. Binding of the antiviral drug WIN51711 to the Sabin strain of type 3 poliovirus: structural comparison with drug binding in rhinovirus 14. *Acta Crystallogr D Biol Crystallogr* 51:473–489.
 53. Zlotnick A, Reddy VS, Dasgupta R, Schneemann A, Ray WJ, Jr, Rueckert RR, Johnson JE. 1994. Capsid assembly in a family of animal viruses primes an autoproteolytic maturation that depends on a single aspartic acid residue. *J Biol Chem* 269:13680–13684.
 54. Hogle JM. 2002. Poliovirus cell entry: common structural themes in viral cell entry pathways. *Annu Rev Microbiol* 56:677–702. <http://dx.doi.org/10.1146/annurev.micro.56.012302.160757>.
 55. Boege U, Ko DS, Scraba DG. 1986. Toward an in vitro system for picornavirus assembly: purification of mengovirus 14S capsid precursor particles. *J Virol* 57:275–284.
 56. Agirre J, Goret G, LeGoff M, Sanchez-Eugenía R, Marti GA, Navaza J, Guerin DM, Neumann E. 2013. Cryo-electron microscopy reconstructions of triatoma virus particles: a clue to unravel genome delivery and capsid disassembly. *J Gen Virol* 94:1058–1068. <http://dx.doi.org/10.1099/vir.0.048553-0>.
 57. Snijder J, Uetrecht C, Rose RJ, Sanchez-Eugenía R, Marti GA, Agirre J, Guerin DM, Wuite GJ, Heck AJ, Roos WH. 2013. Probing the biophysical interplay between a viral genome and its capsid. *Nat Chem* 5:502–509. <http://dx.doi.org/10.1038/nchem.1627>.
 58. Li C, Wang JC, Taylor MW, Zlotnick A. 2012. In vitro assembly of an empty picornavirus capsid follows a dodecahedral path. *J Virol* 86:13062–13069. <http://dx.doi.org/10.1128/JVI.01033-12>.
 59. Chen VB, Arendall WB III, Headd JJ, Keedy DA, Immormino RM, Kapral GJ, Murray LW, Richardson JS, Richardson DC. 2010. MolProbity: all-atom structure validation for macromolecular crystallography. *Acta Crystallogr D Biol Crystallogr* 66:12–21. <http://dx.doi.org/10.1107/S0907444909042073>.

PAPER V





Cryo-electron Microscopy Study of the Genome Release of the Dicistrovirus Israeli Acute Bee Paralysis Virus

Edukondalu Mullapudi,^{a*} Tibor Füzik,^a Antonín Přidal,^b Pavel Plevka^a

Structural Virology, Central European Institute of Technology, Masaryk University, Brno, Czech Republic^a; Department of Zoology, Fishery, Hydrobiology, and Apidology, Faculty of Agronomy, Mendel University in Brno, Brno, Czech Republic^b

ABSTRACT Viruses of the family *Dicistroviridae* can cause substantial economic damage by infecting agriculturally important insects. Israeli acute bee paralysis virus (IAPV) causes honeybee colony collapse disorder in the United States. High-resolution molecular details of the genome delivery mechanism of dicistroviruses are unknown. Here we present a cryo-electron microscopy analysis of IAPV virions induced to release their genomes *in vitro*. We determined structures of full IAPV virions primed to release their genomes to a resolution of 3.3 Å and of empty capsids to a resolution of 3.9 Å. We show that IAPV does not form expanded A particles before genome release as in the case of related enteroviruses of the family *Picornaviridae*. The structural changes observed in the empty IAPV particles include detachment of the VP4 minor capsid proteins from the inner face of the capsid and partial loss of the structure of the N-terminal arms of the VP2 capsid proteins. Unlike the case for many picornaviruses, the empty particles of IAPV are not expanded relative to the native virions and do not contain pores in their capsids that might serve as channels for genome release. Therefore, rearrangement of a unique region of the capsid is probably required for IAPV genome release.

IMPORTANCE Honeybee populations in Europe and North America are declining due to pressure from pathogens, including viruses. Israeli acute bee paralysis virus (IAPV), a member of the family *Dicistroviridae*, causes honeybee colony collapse disorder in the United States. The delivery of virus genomes into host cells is necessary for the initiation of infection. Here we present a structural cryo-electron microscopy analysis of IAPV particles induced to release their genomes. We show that genome release is not preceded by an expansion of IAPV virions as in the case of related picornaviruses that infect vertebrates. Furthermore, minor capsid proteins detach from the capsid upon genome release. The genome leaves behind empty particles that have compact protein shells.

KEYWORDS virus, *Apis mellifera*, honey bee, honeybee, *Picornavirales*, *Dicistroviridae*, *Aparavirus*, virion, structure, cryo, electron microscopy, capsid, genome, release, uncoating, colony collapse disorder, CCD, empty

The productivity of many flowering food plants depends on the pollination provided by the western honeybee (*Apis mellifera*) (1). Honeybees are also critical for maintaining the biodiversity of wild flowering plants (2). Winter honeybee colony mortality has been increasing in North America and Europe over the last couple of decades, leading to a decline in the number of honeybee colonies (3–5). Virus infections are a major factor in the winter honeybee colony losses (6, 7). Generally, honeybee viruses cause latent asymptomatic infections; however, they can occasionally lead to outbreaks characterized by high virus titers. For some of these viruses, such outbreaks are connected with increased virulence, resulting in the deaths of individual workers as well

Received 17 October 2016 Accepted 21 November 2016

Accepted manuscript posted online 7 December 2016

Citation Mullapudi E, Füzik T, Přidal A, Plevka P. 2017. Cryo-electron microscopy study of the genome release of the dicistrovirus Israeli acute bee paralysis virus. *J Virol* 91:e02060-16. <https://doi.org/10.1128/JVI.02060-16>.

Editor Susana López, Instituto de Biotecnología/UNAM

Copyright © 2017 Mullapudi et al. This is an open-access article distributed under the terms of the Creative Commons Attribution 4.0 International license.

Address correspondence to Pavel Plevka, pavel.plevka@ceitec.muni.cz.

* Present address: Edukondalu Mullapudi, Center for Structural Systems Biology, Department for Structural Infection Biology, Hamburg & Helmholtz Center for Infection Research, Braunschweig, Germany.

E.M. and T.F. contributed equally to this article.

as of whole colonies (6). Israeli acute bee paralysis virus (IAPV) is a member of the *Aparavirus* genus of the family *Dicistroviridae* (8–10). IAPV, Kashmir bee virus, and acute bee paralysis virus constitute a cluster of closely related viruses that are distributed worldwide (11). The spread of these viruses is accelerated by transmission by the parasitic mite *Varroa destructor* (6, 11–13). IAPV has been linked to colony collapse disorder (CCD), still a largely unexplained rapid loss of adult bees from colonies in the United States (14–17), while acute bee paralysis virus has been associated with a similar rapid adult bee mortality in Europe (11, 18). Other dicistroviruses are pathogens of economically important arthropods, including crickets and shrimps (19).

Viruses of the family *Dicistroviridae* have nonenveloped icosahedral capsids protecting linear, single-stranded, positive-sense RNA genomes of 8,500 to 10,200 nucleotides (20). The genomes of dicistroviruses include two nonoverlapping open reading frames, ORF1 and ORF2, which encode polyproteins containing nonstructural and structural (capsid-forming) proteins, respectively. The polyproteins are cotranslationally and post-translationally cleaved by viral proteases to produce functional subunits. The major capsid proteins VP1 to VP3 of IAPV form the capsid shell with pseudo-T=3 icosahedral symmetry, whereas VP4 is a small protein attached to the inner surface of the capsid (21). The major capsid proteins of IAPV have a jelly roll β -sandwich fold common to many other virus capsid proteins (21). The maturation of the capsids of viruses of the order *Picornavirales* depends on the cleavage of the capsid protein VP4 from the N terminus of a precursor subunit, VP0. In dicistroviruses, the precursor cleavage generates VP4 and VP3 subunits (19, 22). It was proposed previously that a conserved Asp-Asp-Phe (DDF) motif, which is a part of the VP1 subunit that is exposed inwards toward the virion cavity, is involved in VP0 cleavage (19, 22, 23).

In order to initiate infection, virus genomes need to be released from capsids and transferred across the biological membrane into the cell cytoplasm. Previously, the genome release of another dicistrovirus, triatoma virus (TrV), was analyzed by cryo-electron microscopy (cryo-EM) of full and empty TrV particles to resolutions of 15 to 22 Å (24). TrV RNA release led to empty capsids that had a size similar to that of the native virions. A tectonic model of subunit movements was described, according to which the individual capsid proteins rotated within the capsid (24). Subsequently, the empty capsids of TrV disassembled into small, symmetrical, lip-shaped particles that were probably dimers of pentamers of capsid protein protomers (21, 24). It was proposed that capsid cracking or dismantling was associated with the RNA externalization process of TrV (24).

Genome release and delivery have been studied more extensively for viruses of the family *Picornaviridae*, and for enteroviruses in particular (25–30). The genome release of enteroviruses is preceded by structural changes of the capsid leading to the formation of an expanded A particle that is induced by receptor binding or by the low pH of late endosomes (25, 31–33). The A particles of enteroviruses contain pores at icosahedral 2-fold symmetry axes (26–31, 34–36) that were speculated to allow the release of the genome and of VP4 subunits. Another type of pores, located between 2-fold and 5-fold symmetry axes, serve for the externalization of N-terminal arms of VP1 subunits (28, 34).

Here we present a high-resolution cryo-EM analysis of IAPV virions induced to release their genomes *in vitro*. We show that IAPV genome release is not preceded by the formation of A particles. Furthermore, IAPV empty capsids are compact and do not contain pores that might serve as channels for genome release.

RESULTS AND DISCUSSION

***In vitro* induction of IAPV genome release.** The mechanism of dicistrovirus genome release *in vivo* has not been studied. However, the genome release of related picornaviruses is induced by receptor binding or by the low pH in endosomes (25, 31–33, 37). Furthermore, it was shown that elevated temperatures trigger conformational changes to the capsids of many picornaviruses that lead to genome release *in vitro* (29). Therefore, we used an RNA-binding fluorescent-dye assay to measure the stability of IAPV virions at increasing temperatures (Fig. 1A). The exposure of IAPV to 63°C allowed 50% of the RNA

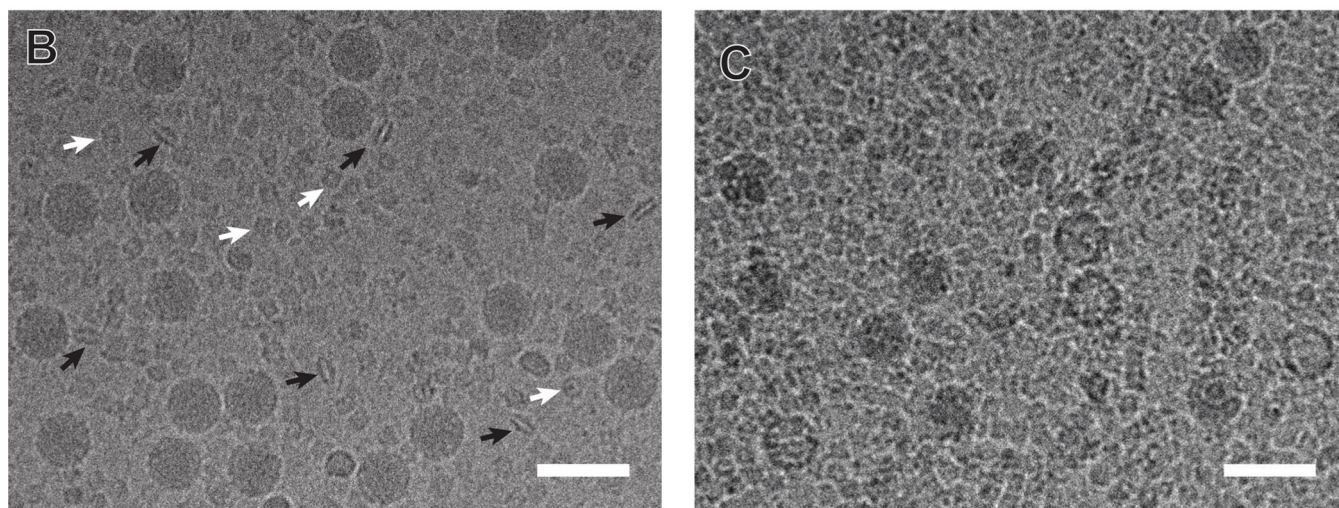
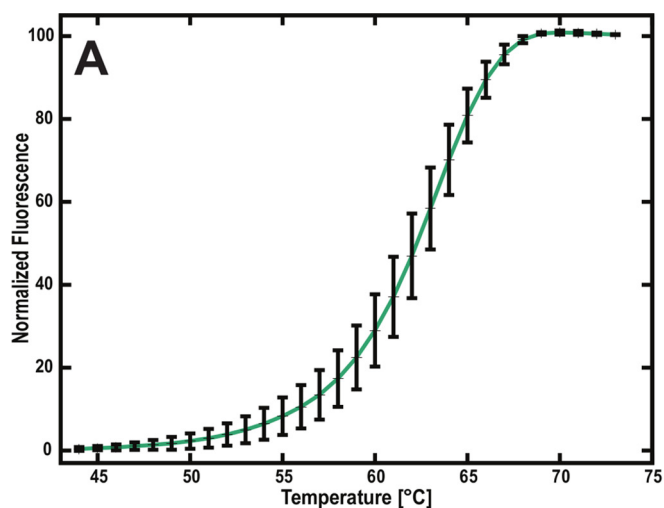


FIG 1 Increased temperature triggers genome release of IAPV. (A) Thermal stability of IAPV virions. IAPV virions were mixed with Sybr green II dye and heated to the indicated temperatures (x axis). The fluorescence signal increased as the dye bound to RNA. Error bars indicate standard deviations of the means ($n = 3$). See Materials and Methods for details. Cryo-electron micrographs show native IAPV virions at room temperature (B) and empty IAPV particles (C), induced by incubating the virus at 63°C for 10 min. The black arrows in panel B indicate “lip-shaped” particles formed by IAPV capsid proteins. The white arrows indicate complexes of the honeybee protein hexamerin that contaminated the virus purification. Bars, 50 nm.

genome to interact with the fluorescent dye (Fig. 1A). It is possible that the increased temperature induced the release of the RNA genome from IAPV virions or that the RNA-binding fluorescent dye could enter the virus particles. Furthermore, cryo-EM images show that IAPV virions heated to 63°C for 10 min contained 8% empty particles (Fig. 1B and C). A similar temperature-induced genome release was described previously for TrV (24). The temperature required to induce the release of the IAPV genome is higher than those required for the genome release of vertebrate picornaviruses, which are in the range of 42 to 56°C (29). This higher stability might be an adaptation of IAPV virions to remain intact in plant nectar with high ionic strength (38).

Comparison of structures of native and heated IAPV virions. The genome release of nonenveloped viruses requires capsid disassembly or the formation of pores of sufficient size to allow passage of the genome across the capsid. The incubation of IAPV virions at 63°C resulted in a mixed population of full and empty particles (Fig. 1C). Cryo-EM images of the full particles were used to calculate a single-particle reconstruction to a resolution of 3.3 Å (Table 1; Fig. 2B and E). The structure of the full virion could be built except for residues 1 to 10 and 258 to 318 of VP2 (Fig. 3A). The structure of the minor capsid protein VP4 was better resolved than that in the 4.0-Å-resolution crystal

TABLE 1 Cryo-EM structure quality indicators for full and empty IAPV particles

| Parameter | Value or description for IAPV heated at 63°C | |
|--------------------------------------|--|-----------------|
| | Full virions | Empty particles |
| EMDB/PDB codes | EMD-4114/5LWG | EMD-4115/5LWI |
| Resolution (Å) | 3.26 | 3.85 |
| R_{work} | 0.314 | 0.366 |
| No. of atoms ^a | 6,373 | 5,876 |
| RMSD | | |
| Bond length (Å) | 0.007 | 0.006 |
| Bond angle (°) | 1.28 | 1.22 |
| Ramachandran region (%) | | |
| Favored ^b | 89.18 | 89.02 |
| Allowed ^b | 10.32 | 10.44 |
| Outliers ^b | 0.50 | 0.54 |
| % poor rotamers ^b | 0.84 | 0.45 |
| Clashscore (percentile) ^b | 3.09 (100) | 3.96 (100) |
| MolProbity score (percentile) | 1.67 (100) | 1.76 (100) |
| C-β deviation (%) ^b | 0.26 | 0.14 |
| Average atomic B factor | 52.2 | 68.4 |

^aFor one icosahedral asymmetric unit.

^bAccording to the criteria of MolProbity (62).

structure of the native virus that was described previously (Fig. 2D and E) (21). Residues 13 to 69 of VP4, among the 69 residues in the polypeptide, could be modeled in the cryo-EM map (Fig. 3A). The positioning of residue 69 from the C terminus of VP4 close to residues Asp186-Asp187-Phe188 of VP1 verifies the previous speculation that these

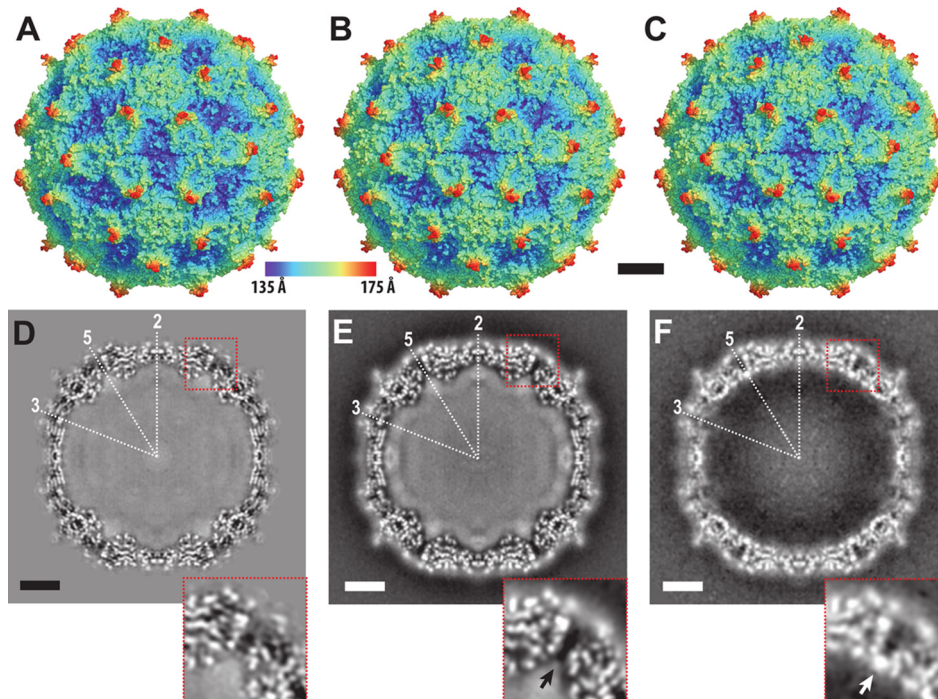


FIG 2 Structures of native IAPV and full and empty particles heated to 63°C. An X-ray structure of a native virion of IAPV (A) and cryo-EM structures of full virions heated to 63°C (B) and of empty particles prepared by heating virions to 63°C (C) are shown. The solvent-accessible surfaces are rainbow colored based on their distances from the particle center. Central slices of electron density maps of native virions (D), full virions heated to 63°C (E), and empty particles heated to 63°C (F) are shown in the bottom row. White areas indicate areas with high electron density values. The positions of selected icosahedral symmetry axes are labeled. The insets in panels D to F show details of electron density distributions near the 5-fold axes. The white arrow in the inset of panel F indicates a position of high electron density formed by putative ions. A corresponding density is not present in the virion structure, as indicated by a black arrow in the inset of panel E. Bars, 50 Å.

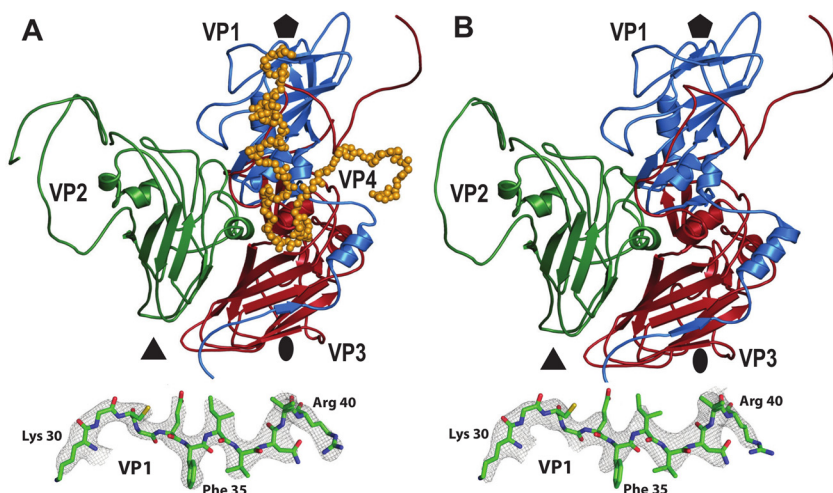


FIG 3 Comparison of icosahedral asymmetric units of IAPV virions and empty particles. Icosahedral asymmetric units of an IAPV virion heated to 63°C (A) and an empty particle (B) are shown as viewed from the particle center. VP1, VP2, VP3, and VP4 are shown in blue, green, red, and orange, respectively. The positions of 5-fold, 3-fold, and 2-fold icosahedral symmetry axes are indicated with pentagons, triangles, and ovals, respectively. The insets at bottom show representative electron densities of the IAPV virion and empty particle at resolutions of 3.26 Å and 3.85 Å, respectively. The maps are contoured at 4σ .

residues form a putative catalytic site responsible for the cleavage of dicistrovirus VP0 into VP4 and VP3 subunits (21).

The structure of the heated IAPV virion is nearly identical to that of the native virus (Fig. 2A, B, D, and E), with a root mean square deviation (RMSD) of C- α atoms from the icosahedral asymmetric units of 0.76 Å (Table 2). Accordingly, the internal volumes of the virion cavities are 6.2×10^6 Å³ and 6.3×10^6 Å³, respectively. This structural similarity indicates that IAPV does not form A particles before genome release. These results are similar to the previous observation that TrV virions do not expand before genome release (24). In contrast, the genome release of enteroviruses is preceded by the formation of A particles that are characterized by a 5% increase in virion diameter and by the formation of channels in the capsid (25, 31–33).

Comparison of RNA distributions in native and heated IAPV virions. Whereas the capsid structures of the native and heated (63°C) IAPV virions were almost identical, there were differences in the distribution of the genomic RNA inside the particles (Fig. 2). The genome of IAPV is a 9,500-nucleotide single-stranded RNA (ssRNA) molecule which is packed inside the icosahedral capsid (9). The RNA molecule cannot entirely follow the icosahedral symmetry of the capsid. Both the X-ray crystallography and single-particle reconstruction methods used for IAPV structure determination employ icosahedral symmetry to calculate the three-dimensional (3D) electron density maps. Therefore, both of the methods used to determine IAPV structures provide electron density maps that contain information about the icosahedrally symmetrized distribution of the genome. In the native virus, the RNA uniformly fills the virion cavity in an approximate sphere with a radius of 110 Å (Fig. 2D). Although direct interactions of the RNA with capsid proteins were not observed, it might be possible that the genome interacts with N-terminal parts of the capsid proteins VP1 and VP2 that are not resolved

TABLE 2 Structural comparison of icosahedral asymmetric units of IAPV in different assembly forms

| IAPV form | RMSD for indicated form | | |
|----------------|-------------------------|----------------|---------------|
| | Pentamer | Empty particle | Heated virion |
| Native virion | 1.09 | 0.93 | 0.80 |
| Heated virion | 0.87 | 0.68 | |
| Empty particle | 0.87 | | |

| A | Interface | Buried surface area (\AA^2) | | | |
|----------------|------------|--|----------------|----------------|--------------|
| | | Native virion* | Heated virion* | Empty particle | Pentamer |
| Intra-protomer | VP1a-VP2a | 1000 | 1050 | 1050 | 1200 |
| | VP1a-VP3a | 4250 | 4350 | 4450 | 4300 |
| | VP1a-VP4a | 100 | 200 | | |
| | VP3a-VP2a | 1500 | 1500 | 1500 | 1500 |
| | VP3a-VP4a | 550 | 850 | | |
| | Sum | 7 400 | 7 950 | 7 000 | 7 000 |
| Intra-pentamer | VP1a-VP1b | 800 | 750 | 750 | 800 |
| | VP1a-VP3b | 1350 | 1350 | 1350 | 1300 |
| | VP1a-VP3d | 150 | 200 | 200 | 200 |
| | VP1a-VP2e | 150 | 300 | 300 | 50 |
| | VP1a-VP3e | 400 | 400 | 400 | 400 |
| | VP1a-VP4e | 250 | 550 | | |
| | VP3a-VP3b | 800 | 850 | 850 | 850 |
| | VP3a-VP3c | | | | 700 |
| | VP3a-VP4b | 150 | 200 | | |
| | VP3a-VP3d | 600 | 700 | 700 | |
| | VP3a-VP4d | 150 | 200 | | |
| | VP3a-VP2e | 1000 | 1050 | 1050 | 650 |
| | VP3a-VP4e | 100 | 150 | | |
| VP4a-VP4b | 300 | 800 | | | |
| | Sum | 6 200 | 7 500 | 5 600 | 4 950 |
| Inter-pentamer | VP1a-VP1f | | 100 | 150 | |
| | VP1a-VP2f | 200 | 300 | 294 | |
| | VP1a-VP2g | 250 | 200 | 50 | |
| | VP2a-VP2g | 3100 | 3500 | 3100 | |
| | VP2a-VP4g | 100 | 200 | | |
| | VP2a-VP3f | 950 | 1050 | 1000 | |
| | VP3a-VP2g | 600 | 650 | 300 | |
| | Sum | 5 200 | 5 900 | 4 744 | |

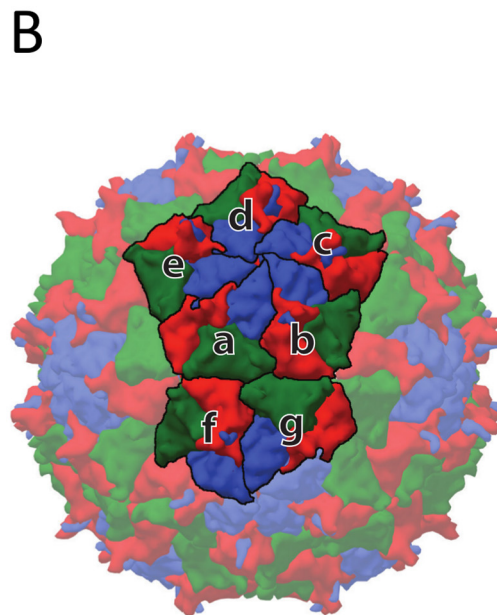


FIG 4 Buried surface areas of interfaces within IAPV virions at different temperatures, within empty particles, and within pentamers. (A) Buried surface areas. Individual subunits are labeled according to their relative positions as shown in panel B. (B) Capsid surface representation of an IAPV virion, with VP1, VP2, and VP3 subunits shown in blue, green, and red, respectively. Icosahedral asymmetric units considered for buried surface calculations are labeled with letters. The buried surface areas were calculated using the PISA server (61). *, note that the differences in buried surface areas between the native and heated virions are due to the extra residues and side chains of VP4 that could be built into the heated virion structure. The differences do not correspond to major conformational changes.

in the virion structure, as previously speculated for picornaviruses (28, 39). In parechoviruses of the family *Picornaviridae*, portions of the RNA interact specifically with the capsid and are therefore resolved in electron density maps calculated with icosahedral symmetry (40–42). However, the current structures show that the IAPV genome is folded in the capsid cavity, without any icosahedral ordering imposed by the surrounding capsid proteins (Fig. 2D and E).

In heated IAPV virions, the RNA forms a 20- \AA -thick shell with a higher density that tightly follows the inner face of the capsid and a sphere in the center of the virion with a radius of 80 \AA (Fig. 2E). These two volumes are separated by a spherical shell of lower RNA density with a diameter of 80 to 90 \AA . The genome in the heated IAPV virions did not form specific contacts with the capsid, similar to what was previously shown for A particles of enteroviruses (29, 34). The changes in the distribution of RNA may facilitate the subsequent release of the genome from the IAPV virion.

Genome release of IAPV is connected to detachment of VP4 subunits from the capsid. Genome release from IAPV virions results in the formation of empty capsids that are the same size as native virions (Fig. 2). The structure of the empty capsid could be built except for residues 1 to 21 and 258 to 318 of VP2 (Fig. 3B). There were no changes in the positions of subunits VP1 to VP3 relative to those in the native virus, and the structures of the icosahedral asymmetric units had a C- α atom RMSD of 0.98 \AA . However, whole VP4 subunits and residues 1 to 21 of the N terminus of VP2 were not resolved for the empty capsids (Fig. 3B). As a consequence, the volume of the capsid cavity increased to $7.0 \times 10^6 \text{\AA}^3$. Furthermore, the loss of the structure of the VP2 N terminus resulted in a reduction in intrapentamer interfaces, from 5,900 \AA^2 to 5,150 \AA^2 (Fig. 4). It is not likely that this limited reduction of protein contacts causes a biologically important reduction in capsid stability. However, the loss of the structure of the VP2 N terminus and of VP4 (Fig. 5A and B) resulted in changes of the distribution of charges inside the capsids (Fig. 5D and E). It is interesting that the empty capsid does not contain any pores that might serve for the release of the genome and the VP4 subunits. It

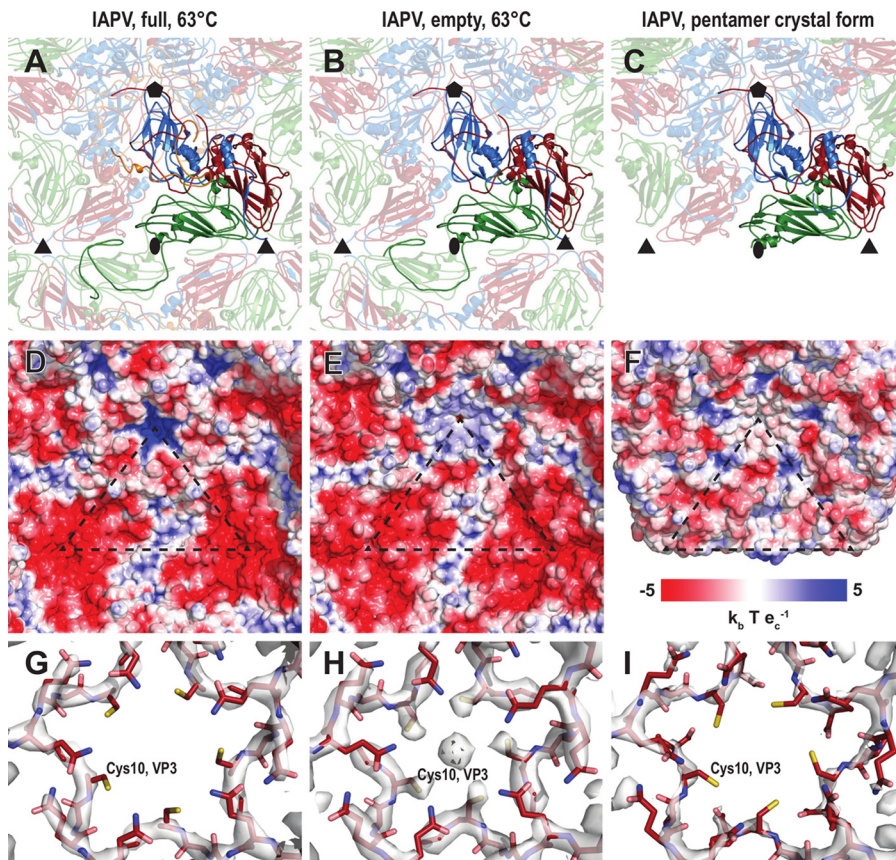


FIG 5 Comparison of intersubunit interactions and charge distributions in IAPV virions, empty particles, and pentamers. Cartoon representations of an IAPV virion heated to 63°C (A), an empty particle (B), and a pentamer (C) are shown as viewed from the particle center. VP1 subunits are shown in blue, VP2 in green, VP3 in red, and VP4 in orange. Selected subunits are shown in bright colors. The positions of 5-fold, 3-fold, and 2-fold icosahedral symmetry axes are indicated with pentagons, triangles, and ovals, respectively. (D to F) Molecular surface of the capsid interior, colored according to the charge distribution. (G to I) Distributions of electron density close to the 5-fold axis. The maps are contoured at 4σ .

is possible that the pores are transitory and close after the genome and VP4 subunits are released. Furthermore, the imposition of icosahedral symmetry during calculations for cryo-EM reconstruction may obscure a unique pore found in the capsid. In contrast, the empty capsids produced after enterovirus genome release, which were named B particles, are similar in structure to A particles and contain two types of pores in their capsid walls (29).

The previously determined structure of the TrV virion lacked a resolved electron density for VP4 subunits (22). However, it was shown that TrV virions contain VP4 peptides, and dissolved TrV crystals could be used to infect triatoma beetles (22–24). It was therefore speculated that VP4 peptides are unstructured components of TrV virions. In contrast, electron density maps enabled the building of the structure of VP4 in cricket paralysis virus (CrPV) (19). It was proposed that viruses closely related to TrV might form a separate genus within the family *Dicistroviridae*, characterized by the absence of structured VP4 subunits (22). Our results show that IAPV virions and empty particles are distinguished by the presence of structured VP4 subunits and 11 residues from the N terminus of VP2.

Putative mechanism ensuring the inclusion of VP4 in dicistrovirus virions. It was shown previously that empty TrV capsids disassemble into pentamers of capsid protein protomers composed of VP1, VP2, and VP3 that subsequently assemble into lip-shaped particles formed by two pentamers of capsid protein protomers facing each other with their bases (24). Our previous crystallographic analysis of IAPV identified conditions that gave rise to crystals containing a similar lip-shaped assembly of IAPV

capsid proteins (21). Furthermore, lip-shaped particles also copurified with native IAPV virions (Fig. 1B). The crystallized IAPV lip-shaped particles lacked a resolved density for VP4 and residues 1 to 58 of the N terminus of VP2 (Fig. 5C). These changes in the pentamer structure resulted in removal of the strong negative charge that was distributed in areas around the 3-fold icosahedral symmetry axes in the full and empty IAPV virions (Fig. 5D to F). The overall structure of the protomer remained very similar to the one observed for the native virus (Table 2). The tendency of capsid proteins to form these lip-shaped particles may interfere with capsid formation. However, it was speculated that during virus assembly, the formation of the lip-shaped particles is prevented by the presence of VP4 residues that are at the time part of VP0 (24). It is unlikely to be a coincidence that the capsid proteins of two different viruses that share only 22% sequence identity are capable of forming similar lip-shaped particles unless it boosts virus fitness. We therefore speculate that the formation of the lip-shaped particles may be a mechanism preventing the assembly of aberrant capsids lacking VP4. It was speculated previously that the cleavage of VP0 into VP4 and VP3 is catalyzed by a DDF sequence that is exposed on the inside of the capsid. Such cleavage might occur in pentamers, and it is possible that the VP4 peptide would then dissociate from the complex. The resulting aberrant pentamers might be incorporated into virions that would then lack VP4 subunits. However, if the VP4-lacking pentamers formed lip-shaped particles, then they could not interfere with virus assembly.

Cations positioned inside empty IAPV particles at 5-fold axes. Cryo-EM reconstruction of the empty IAPV capsid shows a strong electron density located on 5-fold axes close to the inner surface of the capsid, whereas the volume is occupied by VP4 subunits in the virions (Fig. 2D to F). The intensity of this density is similar to that of the surrounding capsid proteins (Fig. 2E); however, it becomes weaker and less resolved after B-factor sharpening (Fig. 5H). The density is located in the vicinity of side chains of five symmetry-related Cys10 residues of VP3 subunits (Fig. 5H). Similar density could not be observed in the full virions (Fig. 5G). The inner surface of the capsid is positively charged in the virions, whereas due to the conformational changes of the VP1 and VP4 subunits, there are negatively charged pockets at the 5-fold axes in the empty IAPV capsid (Fig. 5D and E). We therefore speculate that the extra density belongs to positively charged ions, such as Ca^{2+} or Mg^{2+} . The side chains of the five cysteines do not provide optimal coordination for cations that are not positioned exactly on the 5-fold axis (Fig. 5H). The icosahedrally averaged map therefore contains a somewhat smeared density of the ions (Fig. 2E). The density of the putative cations was not observed in the pentamers (Fig. 5I).

Comparison to genome release and delivery of TrV and enteroviruses. Current knowledge of the genome release processes of small nonenveloped viruses, particularly those of the order *Picornavirales*, is based predominantly on structural analyses of conformational changes of their capsids before and after genome release. Most studies have focused on human enteroviruses, since the genus includes important human pathogens, such as poliovirus, rhinoviruses, and enterovirus 71 (EV71) (36, 43–45). Pores positioned around the 5-fold and 2-fold axes of the icosahedral symmetry of the capsids were speculated to be the channels for genome release (46, 47). Nevertheless, the observed pores were never of a sufficient size to allow passage of the genome, and additional structural changes to the capsid would be required for genome release. Furthermore, a study of an asymmetric interaction of coxsackievirus B3 with a receptor inserted into a nanodisc showed limited particle expansion and indicated that the genome might be released through a specific pore formed along the 2-fold or 3-fold axis of symmetry of the capsid (48). Previous studies of dicistrovirus genome release were limited to the analysis of empty TrV particles at a resolution of 20 Å (24).

It was previously indicated that the genome release of TrV was connected to changes in the orientations of capsid proteins that were proposed to move as rigid blocks in so-called “tectonic movements” in the RMSD ranges of 2.5 to 11.4 Å (22, 24). Furthermore, it was postulated that a partial capsid cracking or disassembly is required for TrV RNA

externalization because there are no obvious pores for RNA egress and empty TrV capsids disassemble upon or after genome release (24). In contrast, the structures and positions of the major capsid proteins VP1, VP2, and VP3 in IAPV virions and empty particles are almost identical (Fig. 3). Furthermore, the structures of empty TrV particles were interpreted as containing narrower channels along 5-fold axes of icosahedral symmetry than is the case in the native virus (24). However, IAPV particles do not contain holes in the capsids, irrespective of whether they are empty or full (Fig. 2 and 5).

The reconstructions of full and empty TrV capsids differed in a “blob” of electron density located on the outside of the capsid, on the 2-fold axes (24). This density was interpreted as a trace of the RNA genome in the process of release from the particle (24). Therefore, a putative channel located at the 2-fold axis of the capsid was speculated to be the place for TrV genome egress. This indicated that TrV genome release is similar to that of enteroviruses (24). The formation of enterovirus A particles is characterized by movements of $\alpha 3$ helices from VP2 subunits away from the icosahedral 2-fold axis, which results in the formation of a 10- by 5-Å pore that was speculated to be utilized for genome release (36, 43–45). However, empty IAPV particles have compact capsids, and the $\alpha 3$ helices remain in the same position in the empty capsid as in the native virus (Fig. 5A and B). There is no evidence that the area around the 2-fold axis should serve as a channel for IAPV genome release. However, it is possible that asymmetric rearrangements of IAPV capsids were averaged out in the icosahedral reconstruction or that short-lived capsid conformations with pores could not be captured by the use of heat to trigger genome release.

Enterovirus A particles contain pores in their capsids, have N termini of VP1 subunits exposed at the virion surface, and release VP4 subunits (46, 47). Residues from N-terminal regions of VP1 subunits were shown to form amphipathic helices, which disrupt endosomal membranes and together with VP4 subunits allow the transport of enterovirus genomes to the cell cytoplasm (31, 49, 50). For the native virions of IAPV, all the residues from the N terminus of VP1 are resolved in the electron density maps. Furthermore, the structure of the N terminus of VP1 of IAPV remains the same in the empty capsid (Fig. 3A and B and 5A and B). Thus, the N terminus of VP1 of IAPV cannot interact with a lipid bilayer. Moreover, a pore at the base of the canyon, which was shown to be the site of externalization of VP1 subunits for coxsackievirus 16 (29, 36), is not present in the empty particles of IAPV. The compact structure of empty IAPV particles together with the previously published negative results for IAPV pentamer-induced liposome lysis (21) indicates that the N termini of IAPV VP1 subunits are unlikely to interact with membranes. The mechanism by which IAPV delivers its genome across the biological membrane requires further study.

The structures of heat-treated full and empty particles indicate that the RNA release mechanism of IAPV is different from that of enteroviruses, such as coxsackievirus 16, human rhinovirus 2, and poliovirus 1 (36, 43–45). Dicroviruses do not form A particles, and the genome is probably released through a transiently formed pore in the capsid wall that closes after genome egress.

MATERIALS AND METHODS

Virus propagation. The propagation of IAPV in honeybee pupae and subsequent purification were carried out as described previously (21).

Preparation of IAPV A particles by heating. Virions at a concentration of 0.02 mg/ml in 0.25 M HEPES, pH 7.5, 0.25 M NaCl buffer were incubated with Sybr green II (diluted 3,000 times from the stock solution according to the manufacturer's instructions), and the mixture was heated from 25 to 95°C in 1°C increments, with a 2-min incubation time at each temperature, in a real-time PCR instrument (Roche LightCycler 480). The fluorescence signal increases as the dye interacts with RNA that is released from thermally destabilized particles, or the dye might be able to enter the particles. The thermal stability of the virus was estimated as the temperature corresponding to an increase in fluorescence to 50% of the maximal value obtained when all virions were thermally denatured. The measurements were carried out in triplicate.

Cryo-electron microscopy of IAPV particles. A solution of freshly purified IAPV (3.5 μ l at 2 mg/ml) was heated to 63°C for 10 min in a thermocycler and stored on ice until it was applied to holey carbon grids (Quantifoil R2/1, 300 mesh; Quantifoil Micro Tools) and plunge frozen using an FEI Vitrobot Mark IV machine, set to a 2-s blotting time and a –2 blot force. The Vitrobot sample application chamber was held at 25°C and 100% humidity during the whole vitrification process. Grids with the vitrified sample

were transferred to an FEI Titan Krios electron microscope operated at 300 kV and aligned for parallel illumination in nanoprobe mode. Images were recorded with an FEI Falcon II direct electron detection camera under low-dose conditions ($20 \text{ e}^-/\text{\AA}^2$), with underfocus values ranging from 1.0 to $3.0 \mu\text{m}$ at a nominal magnification of $\times 75,000$, resulting in a pixel size of $1.07 \text{ \AA}/\text{pixel}$. Each image was recorded in movie mode with 0.5 s of total acquisition time and saved as seven separate movie frames. In total, 1,381 micrographs were acquired.

Icosahedral reconstruction of full and empty particles of IAPV. The reconstructions of full and empty IAPV particles were calculated independently according to the pipeline described below. The movie frames from each exposure were aligned to compensate for drift and beam-induced motion during image acquisition by using the program SPIDER (51). Regions with IAPV particles (450×450 pixels) were manually picked and extracted from the micrographs by using the program e2boxer.py from the package EMAN2 (52), resulting in 2,386 empty-particle and 25,176 full-particle images. Subsequently, the particles were separated into two half-data sets for all of the subsequent reconstruction steps to follow the “gold standard” procedure for resolution determination (53). The contrast transfer function (CTF) parameters of each micrograph were automatically estimated using the program ctfind4 (54). The images were processed using the package RELION 1.4 (55). The particles were subjected to multiple rounds of two-dimensional (2D) classification and 3D classification, resulting in a nearly homogeneous set of IAPV particles. A low-pass-filtered (60 \AA) structure of the native IAPV virion determined by X-ray crystallography was used as an initial model for 3D classification and for subsequent refinement, which was performed using the RELION 3dautorefine procedure. To further homogenize the data set, particles were subjected to another round of 3D classification, omitting the alignment step and using the particle shifts and orientations estimated in the previous refinement step. This classification assumes that the shifts and orientations of the particles were accurately estimated during the refinement step and that the particles are distributed solely among the classes depending on their unique features. This usually helps to discard particles that do not contribute high-resolution information to the particle reconstruction. Final reconstruction, performed according to the gold standard (53), was calculated with RELION 3dautorefine (55). The resulting map was masked with a threshold mask and B-factor sharpened using the RELION postprocess procedure (56). The B factors applied for sharpening were -102.9 \AA^2 and -107.1 \AA^2 for the full- and empty-particle IAPV reconstructions, respectively. The resulting resolutions were estimated to be 3.26 and 3.85 \AA for the full and empty IAPV particles, respectively, at the 0.143 Fourier shell correlation (FSC) cutoff.

Cryo-EM structure determination and refinement. The initial model, derived from the native IAPV virion structure (19), was fitted into the B-factor-sharpened cryo-EM map and subjected to manual rebuilding using the programs Coot and O and to coordinate and B-factor refinement using the programs Refmac5 and Phenix (57–60).

Accession number(s). Cryo-EM electron density maps of the IAPV virion and empty particle were deposited with the Electron Microscopy Data Bank (EMDB) under accession numbers EMD-4114 and EMD-4115, respectively, and the fitted coordinates were deposited in the Protein Data Bank (PDB) under accession codes 5LWG and 5LWI, respectively.

ACKNOWLEDGMENTS

We thank the CEITEC cryo-EM core facility staff members Jiří Nováček and Miroslav Peterek.

This research was carried out under project CEITEC 2020 (LQ1601), with financial support from the Ministry of Education, Youth and Sports of the Czech Republic under the National Sustainability Program II. CIISB research infrastructure project LM2015043, funded by MEYS CR, is gratefully acknowledged for financial support for the measurements at the Cryo-electron Microscopy and Tomography Core Facility, CEITEC, Masaryk University. Access to computing and storage facilities owned by parties and projects contributing to the National Grid Infrastructure MetaCentrum, provided under the program “Projects of Large Infrastructure for Research, Development, and Innovations” (project LM2010005), is greatly appreciated. This work was supported by the IT4Innovations Centre of Excellence project (grant CZ.1.05/1.1.00/02.0070), funded by the European Regional Development Fund and the national budget of the Czech Republic via the Research and Development for Innovations Operational Program, as well as the Czech Ministry of Education, Youth and Sports via the program “Projects of Large Infrastructure for Research, Development, and Innovations” (project LM2011033). The research leading to these results received funding from the European Research Council under the European Union’s Seventh Framework Program (FP/2007-2013)/ERC through grant agreement 355855 and from EMBO installation grant 3041 to P.P.

E.M. performed virus purification, single-particle cryo-EM reconstructions, model building, and refinement. T.F. performed single-particle cryo-EM reconstructions, model building, and refinement and participated in data analysis and manuscript preparation. A.P. conducted large-scale pupa infections. P.P. designed the study, performed cryo-EM data collection, participated in data analysis, and wrote the manuscript.

REFERENCES

- Allsopp MH, de Lange WJ, Veldtman R. 2008. Valuing insect pollination services with cost of replacement. *PLoS One* 3:e3128. <https://doi.org/10.1371/journal.pone.0003128>.
- Biesmeijer JC, Roberts SP, Reemer M, Ohlemuller R, Edwards M, Peeters T, Schaffers AP, Potts SG, Kleukers R, Thomas CD, Settele J, Kunin WE. 2006. Parallel declines in pollinators and insect-pollinated plants in Britain and the Netherlands. *Science* 313:351–354. <https://doi.org/10.1126/science.1127863>.
- van Engelsdorp D, Hayes J, Jr, Underwood RM, Pettis J. 2008. A survey of honey bee colony losses in the U.S., fall 2007 to spring 2008. *PLoS One* 3:e4071. <https://doi.org/10.1371/journal.pone.0004071>.
- Dainat B, Vanengelsdorp D, Neumann P. 2012. Colony collapse disorder in Europe. *Environ Microbiol Rep* 4:123–125. <https://doi.org/10.1111/j.1758-2229.2011.00312.x>.
- Smith KM, Loh EH, Rostal MK, Zambrana-Torrel CM, Mendiola L, Daszak P. 2013. Pathogens, pests, and economics: drivers of honey bee colony declines and losses. *Ecohealth* 10:434–445. <https://doi.org/10.1007/s10393-013-0870-2>.
- Chen YP, Siede R. 2007. Honey bee viruses. *Adv Virus Res* 70:33–80. [https://doi.org/10.1016/S0065-3527\(07\)70002-7](https://doi.org/10.1016/S0065-3527(07)70002-7).
- Genersh E, von der Ohe W, Kaatz H, Schroeder A, Otten C, Buchler R, Berg S, Ritter W, Muhlen W, Gisder S, Meixner M, Leibig G, Rosenkranz P. 2010. The German bee monitoring project: a long term study to understand periodically high winter losses of honey bee colonies. *Apidologie* 41:332–352. <https://doi.org/10.1051/apido/2010014>.
- Govan VA, Leat N, Allsopp M, Davison S. 2000. Analysis of the complete genome sequence of acute bee paralysis virus shows that it belongs to the novel group of insect-infecting RNA viruses. *Virology* 277:457–463. <https://doi.org/10.1006/viro.2000.0616>.
- Maori E, Lavi S, Mozes-Koch R, Gantman Y, Peretz Y, Edelbaum O, Tanne E, Sela I. 2007. Isolation and characterization of Israeli acute paralysis virus, a dicistrovirus affecting honeybees in Israel: evidence for diversity due to intra- and inter-species recombination. *J Gen Virol* 88:3428–3438. <https://doi.org/10.1099/vir.0.83284-0>.
- Chen YP, Pettis JS, Corona M, Chen WP, Li CJ, Spivak M, Visscher PK, DeGrandi-Hoffman G, Boncristiani F, Zhao Y, vanEngelsdorp D, Delaplane K, Solter L, Drummond F, Kramer M, Lipkin WI, Palacios G, Hamilton MC, Smith B, Huang SK, Zheng HQ, Li JL, Zhang X, Zhou AF, Wu LY, Zhou JZ, Lee ML, Teixeira EW, Li ZG, Evans JD. 2014. Israeli acute paralysis virus: epidemiology, pathogenesis and implications for honey bee health. *PLoS Pathog* 10:e1004261. <https://doi.org/10.1371/journal.ppat.1004261>.
- de Miranda JR, Cordoni G, Budge G. 2010. The acute bee paralysis virus-Kashmir bee virus-Israeli acute paralysis virus complex. *J Invertebr Pathol* 103(Suppl 1):S30–S47. <https://doi.org/10.1016/j.jip.2009.06.014>.
- de Miranda JR, Genersch E. 2010. Deformed wing virus. *J Invertebr Pathol* 103(Suppl 1):S48–S61. <https://doi.org/10.1016/j.jip.2009.06.012>.
- Di Prisco G, Pennacchio F, Caprio E, Boncristiani HF, Jr, Evans JD, Chen Y. 2011. Varroa destructor is an effective vector of Israeli acute paralysis virus in the honeybee, *Apis mellifera*. *J Gen Virol* 92:151–155. <https://doi.org/10.1099/vir.0.023853-0>.
- Maori E, Paldi N, Shafrir S, Kalev H, Tsur E, Glick E, Sela I. 2009. IAPV, a bee-affecting virus associated with colony collapse disorder can be silenced by dsRNA ingestion. *Insect Mol Biol* 18:55–60. <https://doi.org/10.1111/j.1365-2583.2009.00847.x>.
- Vanengelsdorp D, Evans JD, Saegerman C, Mullin C, Haubruge E, Nguyen BK, Frazier M, Frazier J, Cox-Foster D, Chen Y, Underwood R, Tarry DR, Pettis JS. 2009. Colony collapse disorder: a descriptive study. *PLoS One* 4:e46481. <https://doi.org/10.1371/journal.pone.0006481>.
- Williams GR, Tarry DR, vanEngelsdorp D, Chauzat MP, Cox-Foster DL, Delaplane KS, Neumann P, Pettis JS, Rogers RE, Shutler D. 2010. Colony collapse disorder in context. *Bioessays* 32:845–846. <https://doi.org/10.1002/bies.201000075>.
- Cox-Foster DL, Conlan S, Holmes EC, Palacios G, Evans JD, Moran NA, Quan PL, Briese T, Hornig M, Geiser DM, Martinson V, vanEngelsdorp D, Kalkstein AL, Drysdale A, Hui J, Zhai J, Cui L, Hutchison SK, Simons JF, Egholm M, Pettis JS, Lipkin WI. 2007. A metagenomic survey of microbes in honey bee colony collapse disorder. *Science* 318:283–287. <https://doi.org/10.1126/science.1146498>.
- Berthoud H, Imdorf A, Haueter M, Radloff S, Neumann P. 2010. Virus infections and winter losses of honey bee colonies (*Apis mellifera*). *J Apicultur Res* 49:60–65. <https://doi.org/10.3896/IBRA.1.49.1.08>.
- Tate J, Liljas L, Scotti P, Christian P, Lin T, Johnson JE. 1999. The crystal structure of cricket paralysis virus: the first view of a new virus family. *Nat Struct Biol* 6:765–774. <https://doi.org/10.1038/11543>.
- Le Gall O, Christian P, Fauquet CM, King AM, Knowles NJ, Nakashima N, Stanway G, Gorbalenya AE. 2008. Picornavirales, a proposed order of positive-sense single-stranded RNA viruses with a pseudo-T=3 virion architecture. *Arch Virol* 153:715–727. <https://doi.org/10.1007/s00705-008-0041-x>.
- Mullapudi E, Pridal A, Palkova L, de Miranda JR, Plevka P. 2016. Virion structure of Israeli acute bee paralysis virus. *J Virol* 90:8150–8159. <https://doi.org/10.1128/JVI.00854-16>.
- Squires G, Pous J, Agirre J, Rozas-Dennis GS, Costabel MD, Marti GA, Navaza J, Bressanelli S, Guerin DM, Rey FA. 2013. Structure of the triatoma virus capsid. *Acta Crystallogr D Biol Crystallogr* 69:1026–1037. <https://doi.org/10.1107/S0907444913004617>.
- Agirre J, Aloria K, Arizmendi JM, Iloro I, Elortza F, Sanchez-Eugenia R, Marti GA, Neumann E, Rey FA, Guerin DM. 2011. Capsid protein identification and analysis of mature triatoma virus (TrV) virions and naturally occurring empty particles. *Virology* 409:91–101. <https://doi.org/10.1016/j.virol.2010.09.034>.
- Agirre J, Goret G, LeGoff M, Sanchez-Eugenia R, Marti GA, Navaza J, Guerin DM, Neumann E. 2013. Cryo-electron microscopy reconstructions of triatoma virus particles: a clue to unravel genome delivery and capsid disassembly. *J Gen Virol* 94:1058–1068. <https://doi.org/10.1099/vir.0.048553-0>.
- Tuthill TJ, Groppelli E, Hogle JM, Rowlands DJ. 2010. Picornaviruses. *Curr Top Microbiol Immunol* 343:43–89. https://doi.org/10.1007/82_2010_37.
- Levy HC, Bostina M, Filman DJ, Hogle JM. 2010. Catching a virus in the act of RNA release: a novel poliovirus uncoating intermediate characterized by cryo-electron microscopy. *J Virol* 84:4426–4441. <https://doi.org/10.1128/JVI.02393-09>.
- Lyu K, Ding J, Han JF, Zhang Y, Wu XY, He YL, Qin CF, Chen R. 2014. Human enterovirus 71 uncoating captured at atomic resolution. *J Virol* 88:3114–3126. <https://doi.org/10.1128/JVI.03029-13>.
- Wang X, Peng W, Ren J, Hu Z, Xu J, Lou Z, Li X, Yin W, Shen X, Porta C, Walter TS, Evans G, Axford D, Owen R, Rowlands DJ, Wang J, Stuart DI, Fry EE, Rao Z. 2012. A sensor-adaptor mechanism for enterovirus uncoating from structures of EV71. *Nat Struct Mol Biol* 19:424–429. <https://doi.org/10.1038/nsmb.2255>.
- Shingler KL, Yoder JL, Carnegie MS, Ashley RE, Makhov AM, Conway JF, Hafenstein S. 2013. The enterovirus 71 A-particle forms a gateway to allow genome release: a cryoEM study of picornavirus uncoating. *PLoS Pathog* 9:e1003240. <https://doi.org/10.1371/journal.ppat.1003240>.
- Bostina M, Levy H, Filman DJ, Hogle JM. 2011. Poliovirus RNA is released from the capsid near a twofold symmetry axis. *J Virol* 85:776–783. <https://doi.org/10.1128/JVI.00531-10>.
- Fricks CE, Hogle JM. 1990. Cell-induced conformational change in poliovirus: externalization of the amino terminus of VP1 is responsible for liposome binding. *J Virol* 64:1934–1945.
- Greve JM, Forte CP, Marlor CW, Meyer AM, Hoover-Litty H, Wunderlich D, McClelland A. 1991. Mechanisms of receptor-mediated rhinovirus neutralization defined by two soluble forms of ICAM-1. *J Virol* 65:6015–6023.
- Prchla E, Kuechler E, Blaas D, Fuchs R. 1994. Uncoating of human rhinovirus serotype 2 from late endosomes. *J Virol* 68:3713–3723.
- Ren J, Wang X, Hu Z, Gao Q, Sun Y, Li X, Porta C, Walter TS, Gilbert RJ, Zhao Y, Axford D, Williams M, McAuley K, Rowlands DJ, Yin W, Wang J, Stuart DI, Rao Z, Fry EE. 2013. Picornavirus uncoating intermediate captured in atomic detail. *Nat Commun* 4:1929. <https://doi.org/10.1038/ncomms2889>.
- Seitsonen JJ, Shakeel S, Susi P, Pandurangan AP, Sinkovits RS, Hyvonen H, Laurinmaki P, Yla-Pelto J, Topf M, Hyypia T, Butcher SJ. 2012. Structural analysis of coxsackievirus A7 reveals conformational changes associated with uncoating. *J Virol* 86:7207–7215. <https://doi.org/10.1128/JVI.06425-11>.
- Garriga D, Pickl-Herk A, Luque D, Wruss J, Caston JR, Blaas D, Verdaguer N. 2012. Insights into minor group rhinovirus uncoating: the X-ray structure of the HRV2 empty capsid. *PLoS Pathog* 8:e1002473. <https://doi.org/10.1371/journal.ppat.1002473>.
- Tuthill TJ, Harlos K, Walter TS, Knowles NJ, Groppelli E, Rowlands DJ, Stuart DI, Fry EE. 2009. Equine rhinitis A virus and its low pH empty particle: clues towards an aphthovirus entry mechanism? *PLoS Pathog* 5:e1000620. <https://doi.org/10.1371/journal.ppat.1000620>.
- Chalcoff VR, Aizen MA, Galetto L. 2006. Nectar concentration and com-

- position of 26 species from the temperate forest of South America. *Ann Bot* 97:413–421.
39. Pickl-Herk A, Luque D, Vives-Adrian L, Querol-Audi J, Garriga D, Trus BL, Verdaguer N, Blaas D, Caston JR. 2013. Uncoating of common cold virus is preceded by RNA switching as determined by X-ray and cryo-EM analyses of the subviral A-particle. *Proc Natl Acad Sci U S A* 110:20063–20068. <https://doi.org/10.1073/pnas.1312128110>.
 40. Kalynych S, Palkova L, Plevka P. 2016. The structure of human parechovirus 1 reveals an association of the RNA genome with the capsid. *J Virol* 90:1377–1386. <https://doi.org/10.1128/JVI.02346-15>.
 41. Shakeel S, Westerhuis BM, Ora A, Koen G, Bakker AQ, Claassen Y, Wagner K, Beaumont T, Wolthers KC, Butcher SJ. 2015. Structural basis of human parechovirus neutralization by human monoclonal antibodies. *J Virol* 89:9571–9580. <https://doi.org/10.1128/JVI.01429-15>.
 42. Zhu L, Wang X, Ren J, Porta C, Wenham H, Ekstrom JO, Panjwani A, Knowles NJ, Kotecha A, Siebert CA, Lindberg AM, Fry EE, Rao Z, Tuthill TJ, Stuart DI. 2015. Structure of Ljungan virus provides insight into genome packaging of this picornavirus. *Nat Commun* 6:8316. <https://doi.org/10.1038/ncomms9316>.
 43. Hewat EA, Neumann E, Blaas D. 2002. The concerted conformational changes during human rhinovirus 2 uncoating. *Mol Cell* 10:317–326. [https://doi.org/10.1016/S1097-2765\(02\)00603-2](https://doi.org/10.1016/S1097-2765(02)00603-2).
 44. Belnap DM, Filman DJ, Trus BL, Cheng N, Booy FP, Conway JF, Curry S, Hiremath CN, Tsang SK, Steven AC, Hogle JM. 2000. Molecular tectonic model of virus structural transitions: the putative cell entry states of poliovirus. *J Virol* 74:1342–1354. <https://doi.org/10.1128/JVI.74.3.1342-1354.2000>.
 45. Belnap DM, McDermott BM, Jr, Filman DJ, Cheng N, Trus BL, Zuccola HJ, Racaniello VR, Hogle JM, Steven AC. 2000. Three-dimensional structure of poliovirus receptor bound to poliovirus. *Proc Natl Acad Sci U S A* 97:73–78. <https://doi.org/10.1073/pnas.97.1.73>.
 46. Wien MW, Curry S, Filman DJ, Hogle JM. 1997. Structural studies of poliovirus mutants that overcome receptor defects. *Nat Struct Biol* 4:666–674. <https://doi.org/10.1038/nsb0897-666>.
 47. Liu Y, Sheng J, Fokine A, Meng G, Shin WH, Long F, Kuhn RJ, Kihara D, Rossmann MG. 2015. Structure and inhibition of EV-D68, a virus that causes respiratory illness in children. *Science* 347:71–74. <https://doi.org/10.1126/science.1261962>.
 48. Lee H, Shingler KL, Organtini LJ, Ashley RE, Makhov AM, Conway JF, Hafenstein S. 2016. The novel asymmetric entry intermediate of a picornavirus captured with nanodiscs. *Sci Adv* 2:e1501929. <https://doi.org/10.1126/sciadv.1501929>.
 49. Shukla A, Padhi AK, Gomes J, Banerjee M. 2014. The VP4 peptide of hepatitis A virus ruptures membranes through formation of discrete pores. *J Virol* 88:12409–12421. <https://doi.org/10.1128/JVI.01896-14>.
 50. Panjwani A, Strauss M, Gold S, Wenham H, Jackson T, Chou JJ, Rowlands DJ, Stonehouse NJ, Hogle JM, Tuthill TJ. 2014. Capsid protein VP4 of human rhinovirus induces membrane permeability by the formation of a size-selective multimeric pore. *PLoS Pathog* 10:e1004294. <https://doi.org/10.1371/journal.ppat.1004294>.
 51. Shaikh TR, Gao H, Baxter WT, Asturias FJ, Boisset N, Leith A, Frank J. 2008. SPIDER image processing for single-particle reconstruction of biological macromolecules from electron micrographs. *Nat Protoc* 3:1941–1974. <https://doi.org/10.1038/nprot.2008.156>.
 52. Tang G, Peng L, Baldwin PR, Mann DS, Jiang W, Rees I, Ludtke SJ. 2007. EMAN2: an extensible image processing suite for electron microscopy. *J Struct Biol* 157:38–46. <https://doi.org/10.1016/j.jsb.2006.05.009>.
 53. Scheres SH, Chen S. 2012. Prevention of overfitting in cryo-EM structure determination. *Nat Methods* 9:853–854. <https://doi.org/10.1038/nmeth.2115>.
 54. Mindell JA, Grigorieff N. 2003. Accurate determination of local defocus and specimen tilt in electron microscopy. *J Struct Biol* 142:334–347. [https://doi.org/10.1016/S1047-8477\(03\)00069-8](https://doi.org/10.1016/S1047-8477(03)00069-8).
 55. Scheres SH. 2012. RELION: implementation of a Bayesian approach to cryo-EM structure determination. *J Struct Biol* 180:519–530. <https://doi.org/10.1016/j.jsb.2012.09.006>.
 56. Rosenthal PB, Henderson R. 2003. Optimal determination of particle orientation, absolute hand, and contrast loss in single-particle electron cryomicroscopy. *J Mol Biol* 333:721–745. <https://doi.org/10.1016/j.jmb.2003.07.013>.
 57. Jones TA, Zou JY, Cowan SW, Kjeldgaard M. 1991. Improved methods for building protein models in electron density maps and the location of errors in these models. *Acta Crystallogr A* 47:110–119. <https://doi.org/10.1107/S0108767390010224>.
 58. Emsley P, Cowtan K. 2004. Coot: model-building tools for molecular graphics. *Acta Crystallogr D Biol Crystallogr* 60:2126–2132. <https://doi.org/10.1107/S0907444904019158>.
 59. Afonine PV, Grosse-Kunstleve RW, Echols N, Headd JJ, Moriarty NW, Mustyakimov M, Terwilliger TC, Urzhumtsev A, Zwart PH, Adams PD. 2012. Towards automated crystallographic structure refinement with phenix.refine. *Acta Crystallogr D Biol Crystallogr* 68:352–367. <https://doi.org/10.1107/S0907444912001308>.
 60. Vagin AA, Steiner RA, Lebedev AA, Pottert L, McNicholas S, Long F, Murshudov GN. 2004. REFMAC5 dictionary: organization of prior chemical knowledge and guidelines for its use. *Acta Crystallogr D Biol Crystallogr* 60:2184–2195. <https://doi.org/10.1107/S0907444904023510>.
 61. Krissinel E, Henrick K. 2007. Inference of macromolecular assemblies from crystalline state. *J Mol Biol* 372:774–797. <https://doi.org/10.1016/j.jmb.2007.05.022>.
 62. Davis IW, Leaver-Fay A, Chen VB, Block JN, Kapral GJ, Wang X, Murray LW, Arendall WB, III, Snoeyink J, Richardson JS, Richardson DC. 2007. MolProbity: all-atom contacts and structure validation for proteins and nucleic acids. *Nucleic Acids Res* 35:W375–W383. <https://doi.org/10.1093/nar/gkm216>.

PAPER VI





Virion Structure of Black Queen Cell Virus, a Common Honeybee Pathogen

Radovan Spurny,^a Antonín Přidal,^b Lenka Pálková,^a Hoa Khanh Tran Kiem,^{a*} Joachim R. de Miranda,^c Pavel Plevka^a

Structural Virology, Central European Institute of Technology, Masaryk University, Brno, Czech Republic^a; Department of Zoology, Fishery, Hydrobiology, and Apidology, Faculty of Agronomy, Mendel University in Brno, Brno, Czech Republic^b; Department of Ecology, Swedish University of Agricultural Sciences, Uppsala, Sweden^c

ABSTRACT Viral diseases are a major threat to honeybee (*Apis mellifera*) populations worldwide and therefore an important factor in reliable crop pollination and food security. Black queen cell virus (BQCV) is the etiological agent of a fatal disease of honeybee queen larvae and pupae. The virus belongs to the genus *Triatovirus* from the family *Dicistroviridae*, which is part of the order *Picornavirales*. Here we present a crystal structure of BQCV determined to a resolution of 3.4 Å. The virion is formed by 60 copies of each of the major capsid proteins VP1, VP2, and VP3; however, there is no density corresponding to a 75-residue-long minor capsid protein VP4 encoded by the BQCV genome. We show that the VP4 subunits are present in the crystallized virions that are infectious. This aspect of the BQCV virion is similar to that of the previously characterized triatoma virus and supports the recent establishment of the separate genus *Triatovirus* within the family *Dicistroviridae*. The C terminus of VP1 and CD loops of capsid proteins VP1 and VP3 of BQCV form 34-Å-tall finger-like protrusions at the virion surface. The protrusions are larger than those of related dicistroviruses.

IMPORTANCE The western honeybee is the most important pollinator of all, and it is required to sustain the agricultural production and biodiversity of wild flowering plants. However, honeybee populations worldwide are suffering from virus infections that cause colony losses. One of the most common, and least known, honeybee pathogens is black queen cell virus (BQCV), which at high titers causes queen larvae and pupae to turn black and die. Here we present the three-dimensional virion structure of BQCV, determined by X-ray crystallography. The structure of BQCV reveals large protrusions on the virion surface. Capsid protein VP1 of BQCV does not contain a hydrophobic pocket. Therefore, the BQCV virion structure provides evidence that capsid-binding antiviral compounds that can prevent the replication of vertebrate picornaviruses may be ineffective against honeybee virus infections.

KEYWORDS virus, *Apis mellifera*, honey bee, honeybee, *Picornavirales*, *Dicistroviridae*, *Cripavirus*, *Triatovirus*, virion, structure, X ray, crystallography, capsid, insect disease, X-ray crystallography

The honeybee (*Apis mellifera*) is found all over the world and plays a vital role in the agricultural industry by providing pollination services for food crops. About 10% of the total economic value of agricultural production depends on insect pollination (1). In addition, it has been shown that the abundance and diversity of wild insect-pollinated plant species declines in areas with reduced populations of honeybees (2, 3). However, the bees suffer from a combination of factors such as environmental stress, parasites, and pathogens, including numerous viruses that result in colony losses (4, 5).

One of the most common and least understood honeybee viruses is black queen cell virus (BQCV). BQCV was first isolated from dead queen larvae and prepupae sealed in

Received 10 October 2016 Accepted 21 December 2016

Accepted manuscript posted online 11 January 2017

Citation Spurny R, Přidal A, Pálková L, Kiem HKT, de Miranda JR, Plevka P. 2017. Virion structure of black queen cell virus, a common honeybee pathogen. *J Virol* 91:e02100-16. <https://doi.org/10.1128/JVI.02100-16>.

Editor Bryan R. G. Williams, Hudson Institute of Medical Research

Copyright © 2017 Spurny et al. This is an open-access article distributed under the terms of the [Creative Commons Attribution 4.0 International license](https://creativecommons.org/licenses/by/4.0/).

Address correspondence to Pavel Plevka, pavel.plevka@ceitec.muni.cz.

* Present address: Hoa Khanh Tran Kiem, Department of Biology, Faculty of Medicine, Masaryk University, Brno, Czech Republic.

queen cells with blackened walls (6, 7). BQCV is one of the most common and abundant honeybee viruses worldwide (8–10). It persists chronically and mostly asymptotically in bee colonies through social transmission among adults and through vertical transmission from the queen to her offspring and from adults to larvae through glandular secretions, e.g., royal jelly (11). However, at elevated titers, BQCV kills developing queen larvae, whose necrotic remains stain their pupal cells black. The disease is of concern for the honeybee queen-rearing industry, but it only rarely has impact outside this context (12, 13). The incidence of BQCV in Europe and Asia peaks during the swarming season, when queens and drones are reared (14–16). There is evidence that the coinfection of BQCV with *Nosema*, a fungal intestinal parasite of honeybees, results in increased mortality caused by the virus (17). In addition, sublethal doses of pesticides result in increased BQCV titers and mortality (12, 18). BQCV belongs to the family *Dicistroviridae*, nonenveloped RNA viruses that infect insects (19). The BQCV host range includes many *Apis* species, as well as several bumblebee species (20). Several other dicistroviruses infect honeybees and bumblebees, whereas others cause diseases in ants, crickets, flies, and aphids.

The structures of Israeli acute bee paralysis virus (IAPV), triatoma virus (TrV), and cricket paralysis virus (CrPV) from the family *Dicistroviridae* have been determined previously (21–23). IAPV belongs to the genus *Aparavirus* and CrPV is part of the genus *Cripavirus*, whereas TrV and BQCV belong to the recently established genus *Triatovirus*. Viruses from the family *Dicistroviridae* have nonenveloped icosahedral capsids that protect linear single-stranded positive-sense RNA genomes 8,500 to 10,200 nucleotides in length (24). The genomes of dicistroviruses include two nonoverlapping open reading frames (ORFs), ORF1 and ORF2, which encode polyproteins containing non-structural and structural (capsid-forming) subunits, respectively. The polyproteins include proteases that cotranslationally and posttranslationally autocleave the polyproteins to produce functional subunits. The major capsid proteins VP1 to VP3 of dicistroviruses have a jelly roll β -sandwich fold common to capsid proteins of many other viruses and form the capsid shell with pseudo-T=3 icosahedral symmetry (21–23, 25). Capsid proteins originating from one polyprotein precursor fold into a protomer that contains subunits VP0, VP1, and VP2. By analogy with human picornaviruses, it is assumed that the protomers assemble into pentamers and subsequently together with the RNA genome form immature virions (26–29). The cleavage of VP0, which produces subunits VP4 and VP3, is required for the maturation of infectious virions (22, 23). It has been proposed previously that a conserved Asp-Asp-Phe (DDF) motif, which is part of the VP1 subunit and conserved among dicistroviruses, is involved in the VP0 cleavage (22, 23, 30–32). The VP4 subunits of dicistroviruses are peptides 51 to 75 residues long (21–23). CrPV and IAPV virions contain structured VP4 subunits attached to the inner faces of their capsids (21, 22). In contrast, it has been shown that TrV virions contain VP4 subunits, but the TrV crystal structure did not reveal a resolved electron density belonging to VP4 (23). The release of VP4 subunits from virions has been shown to be associated with genome release in the related picornaviruses (33–37). The VP4 subunits disrupt cellular membranes and thus enable the delivery of picornavirus genomes into the cytoplasm (38).

Here we present the structure of the BQCV virion and show that it contains large finger-like surface protrusions formed by capsid proteins VP1 and VP3. Furthermore, as in TrV, the VP4 subunits are not structured in BQCV virions.

RESULTS AND DISCUSSION

Structure of BQCV virion and capsid proteins. The crystal structure of the BQCV virion was determined to a resolution of 3.4 Å (Table 1). The maximum outer diameter of the BQCV capsid is 353 Å (Fig. 1A). The particles of BQCV are bigger than those of other dicistroviruses and most picornaviruses (maximum radii of about of 320 Å) because of the finger-like protrusions located in between the 5-fold and 3-fold axes of the icosahedral symmetry of the BQCV capsid (Fig. 1). The virion has pseudo-T=3 icosahedral symmetry with 60 copies of each of the viral structural proteins VP1, VP2,

TABLE 1 BQCV virion structure quality indicators

| Parameter | Value ^a |
|---------------------------------------|------------------------|
| Space group | I222 |
| Cell parameters | |
| <i>a</i> , <i>b</i> , <i>c</i> (Å) | 332.86, 350.60, 362.61 |
| α , β , γ (°) | 90.0, 90.0, 90.0 |
| Resolution (Å) | 40.00–3.40 (3.59–3.40) |
| R_{merge}^b | 0.208 (0.633) |
| $I/\sigma(I)$ | 3.7 (1.0) |
| Completeness (%) | 68.1 (63.3) |
| Multiplicity | 1.9 (1.7) |
| No. of observations | 359,305 (44,199) |
| No. of unique reflections | 193,433 (26,184) |
| R_{work}^d | 0.247 |
| Avg atomic B factor (Å ²) | 46.4 |
| RMSD bond angles (°) | 0.848 |
| RMSD bond lengths (Å) | 0.007 |
| Ramachandran statistics ^c | |
| Favored (%) | 92.2 |
| Outliers (%) | 0.7 |
| Molprobrity score | 9.75 (73rd percentile) |

^aStatistics for the highest-resolution shell are shown in parentheses.

^b $R_{\text{merge}} = \frac{\sum_h \sum_j |I_{hj} - \langle I_h \rangle|}{\sum_h \sum_j I_{hj}}$.

^cAccording to the criterion of Molprobrity (76).

^dAll reflections were used in the refinement. The R_{free} if it were calculated, would be very similar to R_{work} because of the 15-fold noncrystallographic symmetry present in the crystal. Therefore, the R_{free} would not provide an unbiased measure of model quality in this case (71).

and VP3. VP1 subunits form pentamers around the 5-fold axes, whereas VP2 and VP3 subunits constitute alternating heterohexamers around the icosahedral 3-fold axes (Fig. 2). The major capsid proteins have β -sandwich “jelly roll” folds. The β -strands forming the cores of the subunits are named according to the virus jelly roll convention B to I (25). The two antiparallel β -sheets contain strands BIDG and CHEF, respectively (Fig. 2A). The N termini of the major capsid proteins are located on the inside of the capsid,

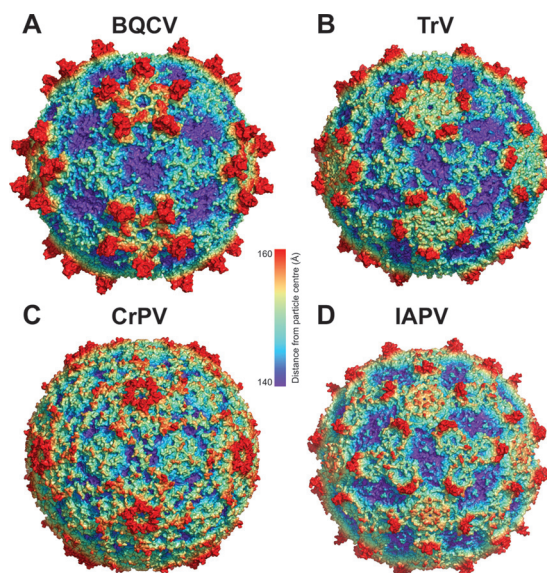


FIG 1 Comparison of virion structures of BQCV, TrV, CrPV, and IAPV. Molecular surfaces of BQCV (A), TrV (B), CrPV (C), and IAPV (D) virions are rainbow-colored based on their distance from the virion center. Depressions are shown in blue and protrusions in red.

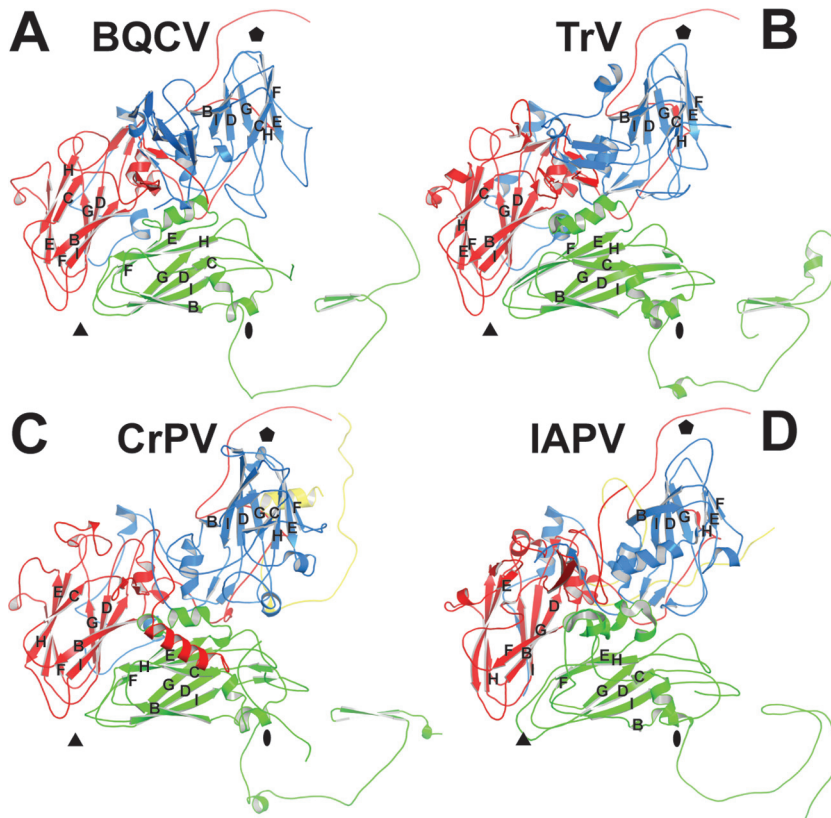


FIG 2 Comparison of structures of icosahedral asymmetric units of BQCV, TrV, CrPV, and IAPV. Shown are cartoon representations of the capsid protein protomers of BQCV (A), TrV (B), CrPV (C), and IAPV (D). VP1 subunits are shown in blue, VP2 in green, VP3 in red, and VP4 (if present) in yellow. Names of the β -strands of the capsid proteins are shown. The positions of the 5-fold, 3-fold, and 2-fold icosahedral symmetry axes are indicated with pentagons, triangles, and ovals, respectively.

whereas the C termini are exposed at the virion surface. A complete model of the major capsid proteins of BQCV could be built except for seven C-terminal residues of VP3. BQCV encodes the 75-residue-long capsid protein VP4. However, no density corresponding to VP4 could be identified in the virion structure. The consequences of the missing VP4 structure for BQCV infectivity are discussed below.

Comparison of BQCV capsid structures to those of other dicistroviruses. BQCV represents the first structurally characterized virus from the genus *Cripavirus* infecting honeybees. It shares less than 35% sequence identity with CrPV, TrV, and IAPV (Table 2) (21–23) and has a rather unique surface topology characterized by the large finger-like protrusions (Fig. 1A and 3A). There are plateaus around the icosahedral 3-fold axes and broad depressions on the BQCV virion surface around the icosahedral 2-fold axes (Fig. 1A). BQCV is structurally the closest to TrV, with a root mean square deviation (RMSD) of 1.9 Å for the C α atoms of residues from icosahedral asymmetric units (Table 2) (23). The two viruses have similar surface features; however, the “fingers” of TrV are less prominent (Fig. 3A). In contrast, the virion surface of CrPV is almost flat (Fig. 3A) (22).

The finger-like protrusions of BQCV reach 34 Å above the virion surface (Fig. 1A and 3A). Each of the protrusions is formed by the C terminus of VP1 and CD loops of VP1 and VP3 (Fig. 3B). The C terminus of VP1 of BQCV is 21 residues longer than that of TrV (23). The 47-residue-long C terminus of BQCV VP1 contains α -helix 6 followed by β -strands 3, 4, and 5 and α -helix 7 (Fig. 3B). The CD loop of VP1 of BQCV is four residues longer than that of TrV. In BQCV the loop contains a four-residue-long α -helix 4 followed by β -strands 1 and 2 and an eight-residue-long α -helix 5 (Fig. 3B). The CD loop of VP3 of BQCV is seven residues longer than those of TrV and CrPV (Fig. 3C) (22, 23).

TABLE 2 Sequence and structural similarity of capsid proteins of selected dicistroviruses, iflaviruses, and picornaviruses

| Family | Genus | Virus | RMSD (Å) of superimposed Ca atoms of the respective 3D structures (top) or % identity between the respective virus coat protein sequences (bottom) ^a | | | | | | | | | | | | | | | | | |
|-----------------|--------------|-----------|---|-----|------|------|-----|------|------|-------|------|------|------|-----|------|-----|-----|--------|------|--|
| | | | BQCV | TrV | CrPV | IAPV | PV1 | CVB3 | EV71 | HRV16 | FMDV | ERAV | TMEV | MEV | SVV1 | AiV | HAV | HPeV-1 | SBPV | |
| Dicistroviridae | Cripavirus | BQCV | | 1.9 | 1.8 | 2.4 | 2.6 | 2.6 | 2.6 | 2.6 | 2.6 | 2.7 | 2.8 | 2.6 | 2.8 | 2.6 | 2.5 | 2.6 | 2.1 | |
| | | TrV | 33 | | 1.9 | 2.0 | 2.3 | 2.3 | 2.4 | 2.8 | 2.5 | 2.5 | 2.4 | 2.7 | 2.5 | 2.2 | 2.4 | 2.0 | | |
| | | CrPV | 29 | 29 | | 2.1 | 2.6 | 2.5 | 2.7 | 2.5 | 2.7 | 3.0 | 2.8 | 2.7 | 3.2 | 2.6 | 2.6 | 2.7 | 2.2 | |
| | Aparavirus | IAPV | 24 | 23 | 24 | | 2.6 | 2.6 | 2.6 | 2.8 | 3.0 | 2.5 | 2.6 | 3.0 | 2.5 | 2.6 | 2.2 | 2.4 | 2.1 | |
| Picornaviridae | Enterovirus | PV1 | 14 | 16 | 13 | 11 | | 1.0 | 1.1 | 1.0 | 1.7 | 1.8 | 1.5 | 1.5 | 2.3 | 2.6 | 2.1 | 2.1 | 2.3 | |
| | | CVB3 | 14 | 16 | 13 | 11 | 56 | | 1.1 | 0.9 | 1.9 | 1.8 | 1.6 | 1.6 | 1.9 | 1.9 | 2.1 | 2.4 | 2.5 | |
| | | EV71 | 13 | 16 | 13 | 12 | 45 | 48 | | 1.1 | 1.9 | 1.7 | 1.7 | 1.7 | 1.8 | 2.5 | 2.1 | 2.2 | 2.2 | |
| | | HRV16 | 14 | 15 | 14 | 9 | 49 | 49 | 45 | | 2.1 | 2.0 | 1.6 | 1.6 | 2.0 | 2.1 | 2.0 | 2.3 | 2.3 | |
| | Aphthovirus | FMDV | 13 | 15 | 13 | 12 | 26 | 26 | 27 | 23 | | 1.6 | 1.6 | 1.5 | 1.6 | 1.9 | 2.1 | 2.7 | 2.6 | |
| | | ERAV | 17 | 18 | 17 | 11 | 24 | 26 | 23 | 26 | 36 | | 1.9 | 1.6 | 1.9 | 2.0 | 2.4 | 2.6 | 2.8 | |
| | Cardiovirus | TMEV | 19 | 15 | 14 | 13 | 29 | 29 | 30 | 27 | 31 | 33 | | 0.9 | 1.4 | 1.9 | 2.0 | 2.1 | 2.3 | |
| | | MEV | 18 | 16 | 15 | 12 | 29 | 29 | 30 | 30 | 30 | 35 | 65 | | 1.3 | 1.7 | 2.1 | 2.1 | 2.3 | |
| | Senecavirus | SVV1 | 15 | 12 | 11 | 14 | 29 | 25 | 29 | 25 | 30 | 31 | 38 | 40 | | 1.8 | 2.0 | 2.2 | 2.4 | |
| | Kobuvirus | AiV | 16 | 14 | 16 | 16 | 24 | 21 | 26 | 24 | 19 | 25 | 28 | 27 | 28 | | 2.1 | 2.2 | 2.3 | |
| | Hepatovirus | HAV | 17 | 21 | 16 | 14 | 18 | 19 | 17 | 19 | 17 | 18 | 21 | 19 | 20 | 17 | | 2.1 | 2.1 | |
| | Parechovirus | HPeV-1 | 16 | 16 | 17 | 15 | 17 | 13 | 17 | 11 | 17 | 18 | 20 | 21 | 18 | 20 | 18 | | 2.2 | |
| | Iflaviridae | Iflavirus | SBPV | 17 | 21 | 19 | 19 | 16 | 15 | 14 | 14 | 15 | 16 | 16 | 16 | 14 | 21 | 18 | 17 | |

^aFor RMSD, the distance cutoff for inclusion of residues in the calculation was 3.8 Å. Capsid protein protomers corresponding to icosahedral asymmetric units consisting of subunits VP1 to VP4 were used in the comparisons. The program Coot was used for superposition of the molecules (69). For percent identity between the respective virus coat protein sequences, gaps were ignored in the calculations. Abbreviations: poliovirus 1 (PV1), coxsackievirus B3 (CVB3), human rhinovirus 16 (HRV16), foot-and-mouth disease virus (FMDV), equine rhinitis A virus (ERAV), Theiler's encephalomyelitis virus (TMEV), mouse encephalomyelitis virus (MEV), Seneca Valley virus (SVV1), Aichi virus (AiV), hepatitis A virus (HAV), and human parechovirus 1 (HPeV-1).

The CD loop of VP3 of IAPV is similar in size to that of BQCV (21). The CD loop of BQCV VP3 contains three β -strands and an α -helix (Fig. 3C). The smaller finger-like protrusions of TrV and IAPV are formed by the C terminus and CD loop of VP1 but not by the CD loop of VP3 (Fig. 3B) (21, 23). There are no finger-like protrusions in CrPV (Fig. 3A) (22). Previously, the finger-like protrusions of TrV were speculated to play a role in the interactions of the virus with its host, in particular to be involved in binding to the entry receptor (23).

The EF loop of VP1 of BQCV is 13 residues shorter than that of CrPV, 2 residues shorter than that of TrV, but 5 residues longer than that of IAPV (Fig. 3B) (21–23). In BQCV the loop does not contain any secondary-structure elements. In contrast, the EF loop of CrPV VP1 contains an α -helix and β -strand (22). The most prominent surface feature formed by subunit VP2 of BQCV is the EF loop, which is, according to the picornavirus convention, named the “puff.” The puff regions of the dicistroviruses are similar (Fig. 2).

The GH loop of VP3 of BQCV is the shortest among the structurally characterized dicistroviruses and lacks the α -helix and β -strand that are present in the GH loops of TrV, CrPV, and IAPV (Fig. 3C) (21–23). The GH loop of VP3 in TrV is the longest of the compared viruses. In contrast, the GH loop of VP3 of CrPV contains two short α -helices (Fig. 3C). The EF loop of VP3 in BQCV is the shortest of all the compared viruses and contains only one short α -helix (Fig. 3C). The longest EF loop of VP3 can be found in IAPV, in which it is formed by two β -strands followed by an α -helix (Fig. 3C) (21).

The capsid of BQCV contains a spherical electron density positioned on a 5-fold axis in the vicinity of the Ile 164 residues of symmetry-related VP1 subunits (Fig. 4). A similar density has been previously observed in the capsid of TrV, where it was attributed to an ion (23). In contrast, no density was observed in the same region of virions of CrPV and IAPV (Fig. 4) (21, 22). It has been speculated previously that the ions may contribute to the capsid stability of viruses, and they might have similar functions in BQCV and TrV.

The BQCV capsid lacks resolved density for minor capsid protein VP4. Virions of many viruses from the order *Picornavirales* assemble as immature particles that contain the precursor subunit VP0 (39). Formation of the mature infectious virions is, in such cases, dependent on the cleavage of capsid protein VP4 from the N terminus of the VP0 precursor. In picornaviruses, the VP0 cleavage generates the proteins VP4 and VP2,

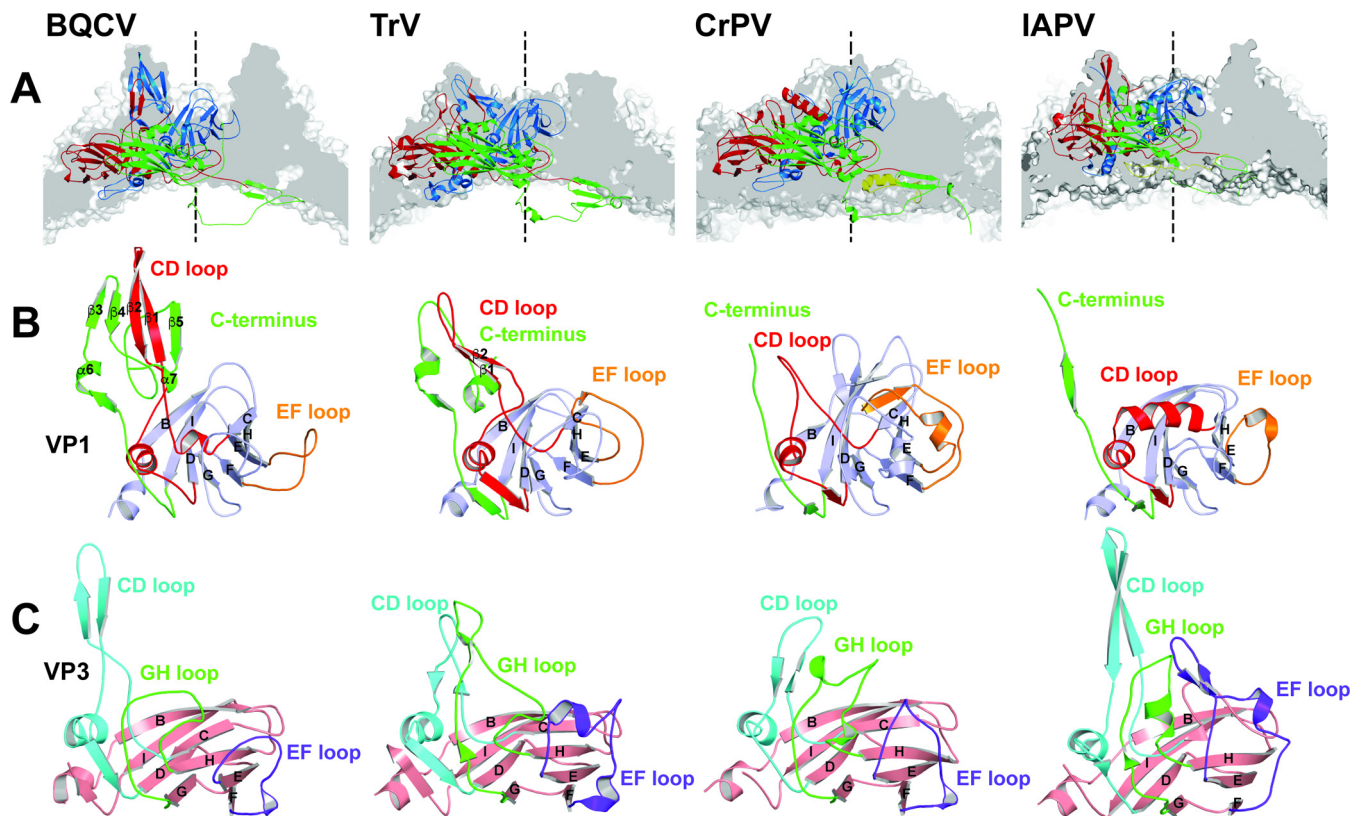


FIG 3 Comparison of prominent virion surface features of BQCV, TrV, CrPV, and IAPV. (A) Cross section of capsids close to 5-fold icosahedral axes are shown in gray. Cartoon representations of capsid proteins from a selected icosahedral asymmetric unit are shown in blue for VP1, green for VP2, red for VP3, and yellow for VP4. Finger-like protrusions of BQCV formed by the C terminus of VP1 and CD loops of VP1 and VP3 are larger than those of TrV, CrPV, and IAPV. The positions of the 5-fold icosahedral symmetry axes are indicated with dashed lines. (B) Comparison of VP1 subunits is shown. The CD loops are highlighted in red, the EF loops in orange, and the C termini in green. Names of the secondary structure elements are indicated. (C) Comparison of VP3 subunits. The CD loops of VP3 are highlighted in cyan, the GH loops in green, and the EF loops in magenta.

whereas in dicistroviruses the precursor cleavage results in the formation of VP4 and VP3 (22, 23). Infections of some picornaviruses produce not only genome-containing virions but also empty particles that have VP0 subunits. However, the purification of BQCV in a CsCl density gradient resulted in the formation of one band, which contained only full virions (Fig. 5). It has been speculated previously that a conserved Asp-Asp-Phe (DDF) motif, which is part of the VP1 subunit, is involved in the VP0 cleavage of dicistroviruses (22, 23, 30). IAPV, CrPV, and TrV contain the DDF motif in a loop immediately following β -strand I of VP1 positioned on the inside of the capsid. Furthermore, TrV and IAPV have additional DDF sequences, in a loop following β -strand I of VP3 (22, 23). The VP1 subunit of BQCV contains an alternative sequence, DDM, at residues 218 to 220, located in a position similar to those of the DDF sequences of TrV, CrPV, and IAPV (Fig. 6). Cleavage of the VP0 precursor generates a new N terminus of VP3, which starts with Ser1 (Fig. 6A to C). With IAPV, the N-terminal serine was not resolved in the electron density map and the structure starts from Lys2 (Fig. 6D). Asp218 of the BQCV DDM motif is located close to the N terminus of VP3 (Fig. 6A). Their relative positioning indicates that the formation of pentamers is sufficient to achieve an optimal spatial arrangement of the putative autocatalytic center formed by residues of VP1 for the cleavage of VP0. The mechanism that ensures that the VP0 cleavage occurs only in dicistrovirus virions containing the RNA genome (22, 40) remains to be determined.

As with BQCV, the previously determined structure of the TrV virion lacked a resolved electron density for the VP4 subunits (23). However, it was shown that TrV virions contain VP4 peptides and that dissolved TrV crystals could be used to infect triatoma insects. Therefore, VP4 peptides are unstructured components of TrV virions

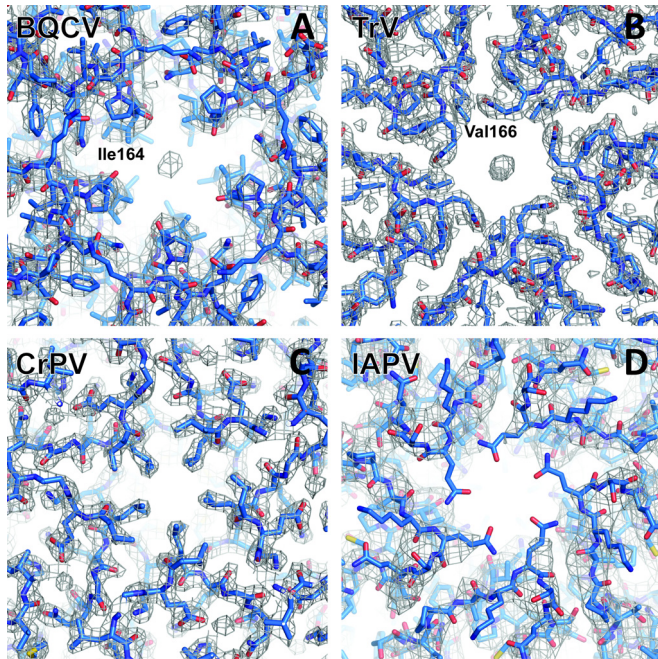


FIG 4 Maps of electron densities of capsids of dicistroviruses close to icosahedral 5-fold axes. Electron densities attributed to putative ions are present on 5-fold axes of BQCV (A) and TrV (B). In contrast, the density is absent in CrPV (C) and IAPV (D). The density maps are shown as gray meshes contoured at 1.8 σ . VP1 subunits are shown in stick representation with carbon atoms in blue. The names of residues of BQCV and TrV closest to the putative ion densities are shown.

(23). In contrast, electron density maps enabled the VP4 structures in CrPV and IAPV to be built (21, 22). It was proposed that one characteristic of viruses from the genus *Triatovirus* within the family *Dicistroviridae* is the absence of structured VP4 subunits (23, 30). SDS gel electrophoresis and mass spectrometry analysis showed that VP4 subunits are present in both native and crystallized BQCV virions (Fig. 7A; see also Fig. S1 in the supplemental material). Furthermore, BQCV genomes could be detected in pupae injected both with the native virus and with particles dissolved from crystals (Fig. 7B). Honeybee pupae injected with BQCV dissolved from crystals stopped their development, similar to those injected with the native virus (Fig. 7C to H). The results show that BQCV virions are infectious even without the structured VP4 subunits, similar to what was shown for TrV (23). However, because the VP4 cleavage is probably required

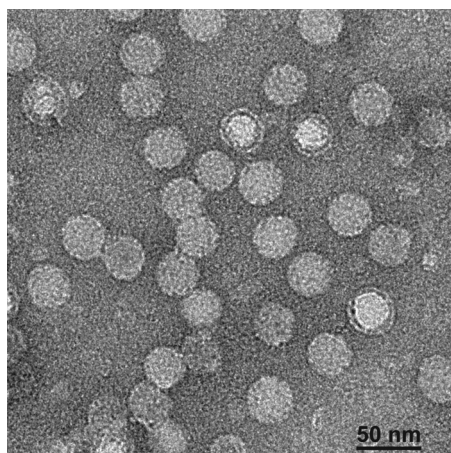


FIG 5 Negative-stain electron microscopy picture of BQCV after purification on CsCl gradient. See Materials and Methods for details on the purification procedure.

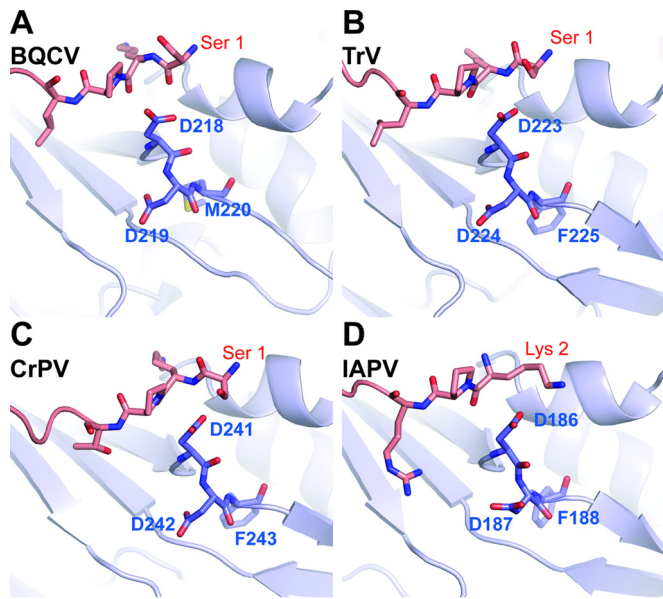


FIG 6 Putative proteolytic site in VP1 subunits of dicistroviruses. The residues Asp-Asp-Phe/Met of VP1 that were speculated to mediate the cleavage of VP0 into VP3 and VP4 are positioned close to the N terminus of VP3 and C terminus of VP4 from another protomer related by an icosahedral 5-fold axis of symmetry. The residues constituting the putative active site are shown in stick representation. VP1 subunits are shown in blue and VP3 in red.

for BQCV maturation, it is likely that at least before maturation the residues corresponding to VP4 are ordered in the capsid. It is also possible that some of the crystallized virions could have lost VP4 by externalization in an aborted entry reaction during *in vitro* handling of the virus, leaving insufficient capsid-associated material to provide a resolved density for VP4.

Absence of hydrophobic pocket in VP1 of BQCV. Dicistroviruses are related to vertebrate picornaviruses, for which numerous capsid-binding inhibitors have been developed (41). The VP1 subunits of some enteroviruses, including human enterovirus 71 (EV71), contain a hydrophobic pocket that can be targeted by small compounds which inhibit the virus-receptor binding and/or genome release (42–45). However, BQCV does not harbor such a hydrophobic pocket in the β -barrel of VP1 (Fig. 8A). The β -barrel of BQCV VP1 is compressed compared to that of EV71, and the remaining space is taken up by hydrophobic side chains of amino acids forming the core of the protein (Fig. 8). In addition, the residues Asn71 from β -strand C and Tyr116 from the CD loop of VP1 occupy the volume of the putative entrance to the pocket (Fig. 8A). Previous structural analyses of CrPV, TrV, and IAPV have shown that these viruses also lack pocket factors (21–23). Therefore, it is likely that pocket binding inhibitors may not be effective as antivirals against honeybee viruses from the family *Dicistroviridae*.

Evolutionary relationship to dicistroviruses, iflaviruses, and picornaviruses. A structure-based evolutionary tree derived from a comparison of icosahedral asymmetric units clearly separates the families *Dicistroviridae*, *Iflaviridae*, and *Picornaviridae* (Fig. 9A). The structural comparison indicates that dicistroviruses are most similar to iflaviruses, which also infect insects (21–23). The viruses closest to BQCV from the *Picornaviridae* family are hepatitis A virus and human parechovirus 1, which were previously suggested to form evolutionary intermediates between human and insect viruses (Fig. 9A) (46, 47).

In order to expand our analysis to viruses with unknown structures, we calculated an evolutionary tree of viruses from the family *Dicistroviridae* based on the amino acid sequences of their ORF2 encoding the capsid proteins (Fig. 9B). The tree separates the viruses into three groups. One of them corresponds to the genus *Aparavirus*, which includes IAPV, acute bee paralysis virus (ABPV), Kashmir bee virus (KBV), taura syndrome

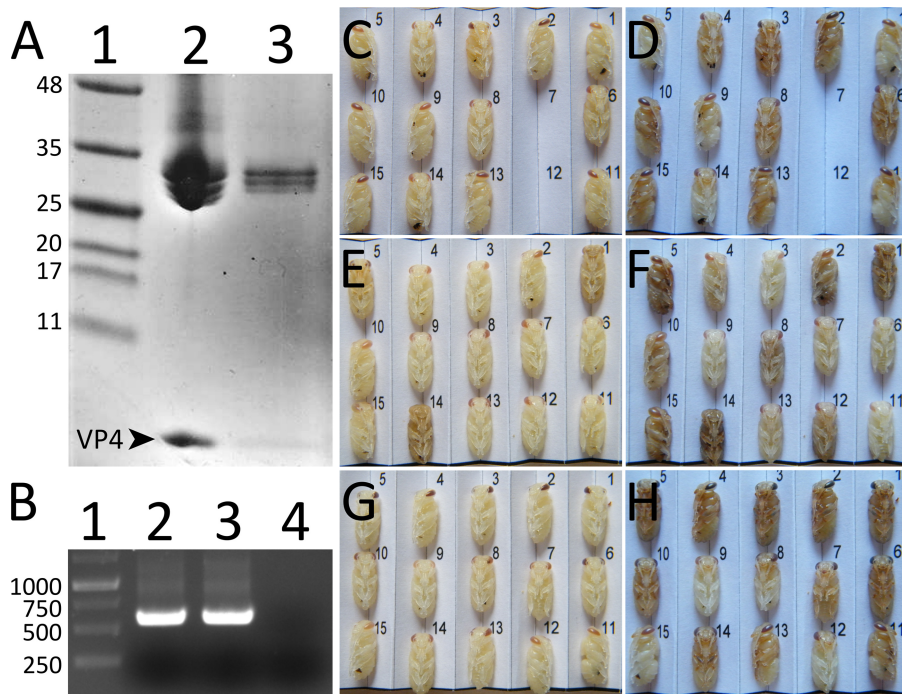


FIG 7 BQCV crystals contain VP4 subunits and the crystallized virus is infectious. (A) Polyacrylamide gel electrophoresis of capsid proteins of BQCV. Lane 1, marker; lane 2, purified BQCV; lane 3, BQCV dissolved from crystals. Arrowhead and VP4 label indicate the position of capsid protein VP4 (8.1 kDa). Capsid proteins VP1, VP2, and VP3 of BQCV have molecular masses in the 25- to 35-kDa range. (B) Agarose gel electrophoresis of PCR fragments obtained from reverse-transcribed RNA isolated from pupae injected with native BQCV (lane 2), BQCV dissolved from crystals (lane 3), and mock-infected with PBS (lane 4). Please see Materials and Methods for details. Lane 1, DNA ladder. (C to H) Images of pupae injected with BQCV dissolved from crystals (C and D) or native virus (E and F) or mock infected with PBS (G and H). The pupae were imaged 1 day (C, E, and G) and 5 days (D, F, and H) after the injection. The pupae injected with virus (C to F) developed slower than the mock-injected pupae (G and H), as shown by the delay in color development of the eyes and the darkening of the body 5 days postinfection. Two pupae missing in the panels (C and D) were accidentally destroyed during imaging.

virus, and *Solenopsis invicta* virus (48–52). Another genus is *Cripavirus*, structurally represented by CrPV and including *Drosophila* C virus, aphid lethal paralysis virus, and *Rhopalosiphum padi* virus (53–56). The remaining group is the recently formed genus *Triatovirus*, which is structurally represented by TrV and BQCV and also includes the *Plautia stali* intestine virus, *Homalodisca coagulata* virus, and himetobi P virus (Fig. 9B) (57–60). A difference that separates triatoviruses from cripaviruses, obvious only in the structural analysis, is the absence of ordered VP4 subunits in the virions of both BQCV

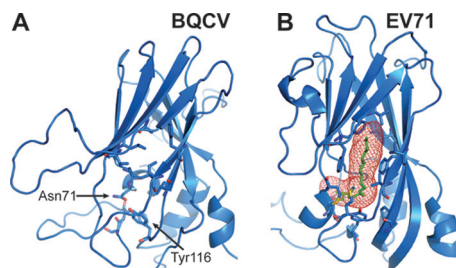


FIG 8 VP1 of BQCV does not contain a hydrophobic pocket. VP1 of BQCV (A) and human enterovirus 71 (EV71) (B) are shown in cartoon representations. The pocket factor of human enterovirus 71 is shown as a stick model in green. The volume of the pocket calculated with the program Cover is shown in panel B. In addition, the side chains of residues that interact with the pocket factor are shown as sticks. In BQCV, the core of the VP1 subunits is filled by side chains of residues forming the β -sheet BIDG and CHEF. The residues Asn71 and Tyr116 in BQCV obscure the volume that corresponds to the opening of the pocket at the capsid surface in EV71.

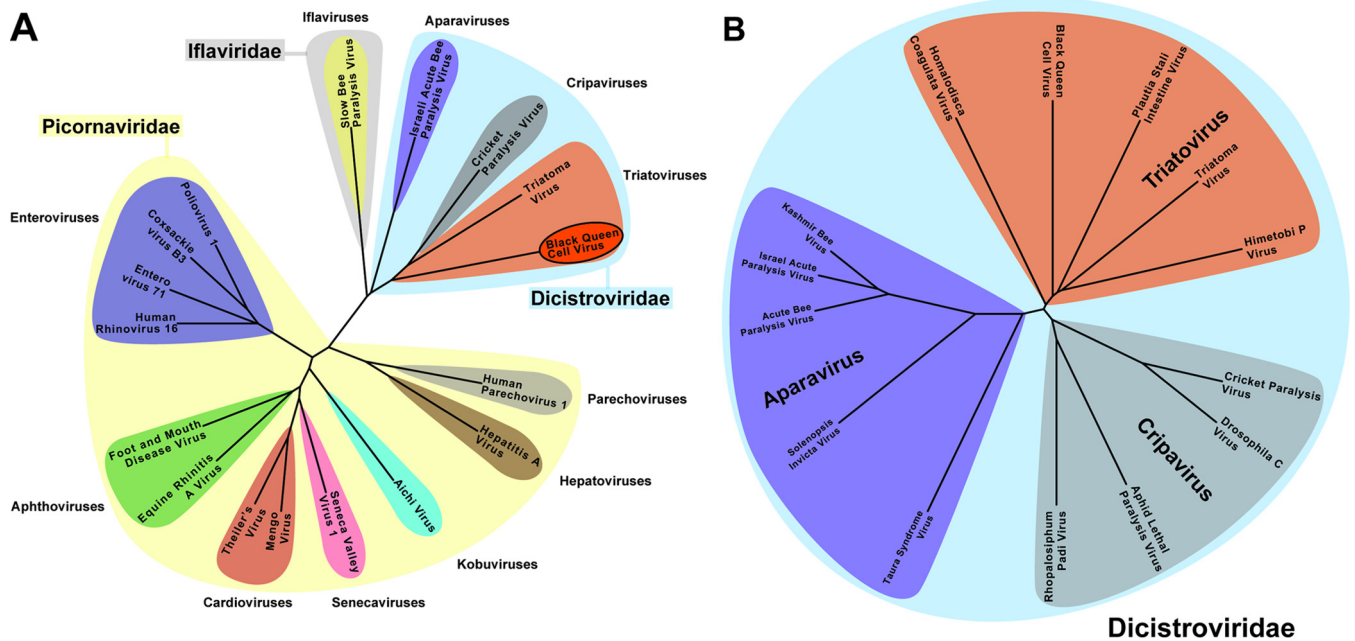


FIG 9 Evolutionary relationship among viruses from the *Dicistroviridae*, *Picornaviridae*, and *Iflaviridae* families based on structural alignment of capsid proteins. (A) Phylogenetic tree based on structural similarity of icosahedral asymmetric units of indicated viruses. (B) Evolutionary tree of dicistroviruses based on alignments of ORF2 sequences verifies division of dicistroviruses into genera *Aparavirus*, *Cripavirus*, and *Triatovirus*. For details on the construction of the diagram, please see Materials and Methods.

and TrV. An additional distinction between cripaviruses and triatoviruses, which can be identified both in structures and in sequences, are the finger-like projections at the virion surface formed by the CD loop of VP1, which are present only in triatoviruses (Fig. 3B). Therefore, the structure of BQCV, which shares some of its unique features with TrV, reinforces the reasons for establishing the genus *Triatovirus*.

MATERIALS AND METHODS

Virus propagation in honeybee pupae. The propagation of BQCV was carried out as described in the COLOSS BEEBOOK (61). Brood areas with *Apis mellifera* white-eyed pupae were identified by the color and structural features of the cell caps. White-eyed pupae were carefully extracted from the brood combs, so as not to injure the pupae. The pupae were placed on paper furrows with their ventral side up. In total 504 pupae were used for the BQCV propagation. The virus inoculum (1 μl) was injected into pupae with a Hamilton micropipette with a 30-gauge 22-mm-long needle through the intersegmental cuticle between the 4th and 5th sternites. Pupae that leaked hemolymph after the injection were discarded. The optimal concentration of the virus in the inoculum for virus production was determined experimentally, by comparing virus yields when using different virus concentrations in the injection inoculum. Inoculated pupae were placed into petri dishes with the paper furrows and incubated at 30°C and 75% humidity for 5 days. After incubation, the pupae were frozen at -20°C. For long-term storage, the pupae were kept at -80°C.

Virus purification. Fifty experimentally infected honeybee pupae were homogenized with a Dounce homogenizer in 30 ml of phosphate-buffered saline (PBS), pH 7.5 (Sigma-Aldrich). The nonionic detergent NP-40 was added to a final concentration of 0.5%, and the homogenate was incubated for 1 h at room temperature. The extract was centrifuged at 8,000 × g for 30 min. The pellet was discarded and the supernatant was centrifuged at 150,000 × g for 3 h in a Ti50.2 fixed-angle rotor (Beckman Coulter). The resulting pellet was resuspended in PBS to a final volume of 5 ml. MgCl₂ was added to a final concentration of 5 mM; 20 μg/ml of DNase I and 20 μg/ml of RNase were added as well. The solution was incubated at room temperature for 30 min and centrifuged at 4,000 × g for 15 min. The resulting supernatant was loaded into a CsCl (0.6 g/ml) solution prepared in PBS. The ultracentrifugation at 220,000 × g proceeded for 16 h to establish the CsCl gradient. BQCV formed a single band in the CsCl gradient. The virus band was collected by gentle piercing of the ultracentrifuge tubes with an 18-gauge needle. The viruses were transferred to PBS by several rounds of concentration and dilution using centrifuge filter units with a 100-kDa molecular mass cutoff. This procedure yielded about 300 μg of virus with purity sufficient for screening. The nucleotide sequences of the virus preparations were determined by sequencing the RNA region encoding the capsid proteins. RNA was extracted from 10 infected honeybee pupae using TRIzol reagent. Viral RNA was reverse transcribed into cDNA using oligo(T) primers, which was used for commercial sequencing. The identical approach was used to prepare cDNA for detection of virus replication in pupae injected with BQCV from dissolved crystals. The primers used

for subsequent PCR were 2F, with the sequence ACTCAAAGGATTTCTTCTT, and 4R, with the sequence AAATAGGCTCATGATTTCA. The resulting product was 599 bp in length.

BQCV genome sequence and virus purity. RNA was extracted from purified BQCV virions using a Qiagen RNEasy kit and the protocol for RNA cleanup. The RNA extracted from the BQCV virions was checked for the presence of other honeybee picorna-like viruses, a common problem of virus propagation in honeybee pupae (61), using previously reported virus-specific quantitative reverse transcription-PCR (RT-qPCR) assays for acute bee paralysis virus (ABPV), IAPV, KBV, deformed wing virus (DWV), BQCV, sacbrood virus (SBV), and slow bee paralysis virus (SBPV) (61). Only SBV and DWV were detected together with the purified BQCV virions. The total sum of SBV and DWV was less than 0.0001% (10^{-6}) of the amount of BQCV. The full BQCV genomic sequence was determined by sequencing 300 ng of RNA using IonTorrent technology and standard protocols for library preparation and sequencing. The IonTorrent reads were mapped to the BQCV GenBank reference sequence (GenBank accession no. [AF183905](https://www.ncbi.nlm.nih.gov/nuccore/AF183905)) using Tmap v4.4.8, included in TorrentSuite 4.4.2, with the parameters recommended by Life Technologies. Variability and consensus sequences were created using mpileup from samtools v.0.1.8 and an in-house script.

BQCV crystallization and data collection. The BQCV crystallization screening was performed at 20°C using the virus dissolved in PBS at a concentration of 3.4 mg/ml. Approximately 500 crystallization conditions were tested with the sitting-drop vapor diffusion method in 96-well plates. Initial conditions that produced crystals were optimized by using hanging drops in 24-well plates. Diamond-shaped crystals with a longest dimension of approximately 0.2 mm were obtained in 0.2 M ammonium acetate, 0.1 M bis-Tris (pH 7.5), and 35% 2-methyl-2,4-pentanediol (MPD). These crystals were flash frozen in liquid nitrogen without additional cryoprotectant and used to collect diffraction data at the PROXIMA-1 beamline of the Soleil synchrotron. The parameters used for data collection were as follows: crystal-to-detector distance, 623.7 mm; oscillation angle, 0.1°; exposure time, 0.1 s; X-ray wavelength, 0.97857 Å.

BQCV structure determination and refinement. BQCV diffraction data were indexed and integrated using the software package XDS (62). The BQCV crystal was of space group I222 (Table 1). Particle packing considerations indicated that the virus particle is positioned at the origin with a subset of icosahedral 2-fold axes aligned with the 222 symmetry axes of the crystal. Therefore, one-quarter of a virion occupied a crystallographic asymmetric unit. There were two alternative orientations of the icosahedral symmetry that could be superimposed with the 222 symmetry of the crystal. The orientation of the particle was determined from a plot of a 5-fold self-rotation function calculated using the program GLRF (63). Reflections with resolutions between 7 and 4 Å were used for the calculations. The radius of integration was set to 280 Å. The particle is rotated 90° about the Z-axis relative to the standard icosahedral orientation, as described by Rossmann and Blow (64).

The model of triatoma virus (TrV) (PDB entry 3nap) was used for the molecular replacement (23). The model was placed into the appropriate orientation and position in the unit cell and used to calculate phases to a resolution of 10 Å in CNS (65). The phases were refined by 25 cycles of averaging with the program AVE (66), using the 15-fold noncrystallographic symmetry. Other calculations, including map calculations from diffraction data and conversion of the averaged map into structure factor amplitudes and phases, were done using programs from the package CCP4 (67). The resulting map was used to recalculate the shape of the averaging mask based on a correlation map calculated using the program coma (68). Phase extension was applied in order to obtain phases for higher-resolution reflections according to the following procedure: the addition of a small fraction of higher-resolution data (one index at a time) was followed by three cycles of averaging. This procedure was repeated until phases were obtained for all the reflections to a resolution of 3.4 Å.

The structure was built manually from the TrV structure converted to polyaniline using the programs Coot and O and coordinate and B-factor refinement using the program CNS (65, 69, 70). Noncrystallographic symmetry constraints were applied during refinement. No water molecules were added to the crystal model due to the limited resolution of the diffraction data. All the measured reflections were used in the refinement. If calculated, the R_{free} value would be very similar to the R value, due to the 15-fold noncrystallographic symmetry present in the diffraction data (71).

Structure and sequence analysis. Multiple sequence alignments were carried out using ClustalW server (<http://www.ebi.ac.uk/Tools/msa/clustalw2/>) (72). Figures were generated using the programs UCSF Chimera (73) and PyMOL (PyMOL molecular graphics system, version 1.7.4; Schrödinger, LLC). Structure-based pairwise alignments of biological protomers of various picornaviruses were prepared using the program VMD (74). The similarity score provided by VMD was used as an evolutionary distance to construct a nexus-format matrix file, which was converted into the phylogenetic tree and visualized with the program SplitsTree (75).

Mass spectrometry analysis. The protein band corresponding to VP4 of BQCV was manually excised from SDS-PAGE gel. After destaining and washing, it was incubated with trypsin (sequencing grade; Promega). Matrix-assisted laser desorption ionization mass spectrometry (MALDI-MS) and tandem mass spectrometry (MS/MS) analyses of tryptic digests were performed on an Ultraflexxtreme mass spectrometer (Bruker Daltonics, Bremen, Germany). The FlexAnalysis 3.4 and MS BioTools 3.2 (Bruker Daltonics) software were used for data processing. Exported MS/MS spectra were searched with in-house Mascot (Matrixscience, London, UK; version 2.4.1) against the NCBI database (no taxonomy restriction) and a local database supplied with the expected sequence. Mass tolerances of peptides and MS/MS fragments for MS/MS ion searches were 50 ppm and 0.5 Da, respectively. Oxidation of methionine and propionylation of cysteine as optional modifications and one enzyme miscleavage were set for all searches. Peptides with a statistically significant peptide score ($P < 0.05$) were considered.

Accession number(s). Atomic coordinates of the BQCV virion at 3.4-Å resolution, together with the structure factors, were deposited in the Protein Data Bank under code [5MQC](#). The consensus nucleotide sequence of the BQCV capsid proteins and of the whole genome were deposited in GenBank under accession numbers [KY363519](#) and [KY243932](#), respectively.

SUPPLEMENTAL MATERIAL

Supplemental material for this article may be found at <https://doi.org/10.1128/JVI.02100-16>.

TEXT S1, PDF file, 1.0 MB.

ACKNOWLEDGMENTS

We thank synchrotron Soleil Proxima-1 and beamline scientists for help with X-ray data collection, Christian Tellgren-Roth of the Science for Life Laboratories consortium at Uppsala University for assembling the IonTorrent sequences, and Emilia Semberg at SLU for technical assistance. Access to computing and storage facilities owned by parties and projects contributing to the National Grid Infrastructure MetaCentrum, provided under the program Projects of Large Infrastructure for Research, Development, and Innovations (LM2010005), is greatly appreciated. Access to the National Genomics Infrastructure (NGI) for sequencing services and the Uppsala Multidisciplinary Center for Advanced Computational Science (UPPMAX) for bioinformatic and computing resources in Sweden is greatly appreciated. We acknowledge the core facilities Biomolecular Interactions and Crystallization and X-ray Diffraction and Bio-SAXS, supported by the Czech Infrastructure for Integrative Structural Biology research infrastructure (LM2015043, funded by MEYS CR), for their support with obtaining scientific data presented in this paper.

This research was carried out under the project Central European Institute of Technology 2020 (LQ1601). The research leading to these results received funding from the European Research Council under the European Union's Seventh Framework Program (FP/2007-2013)/ERC through grant 355855 and from European Molecular Biology Organization installation grant 3041 (to P.P.). Financial support was also received from the IT4Innovations Centre of Excellence project (CZ.1.05/1.1.00/02.0070), funded by the European Regional Development Fund and the national budget of the Czech Republic via the Research and Development for Innovations Operational Program, as well as the Czech Ministry of Education, Youth and Sports via the project Large Research, Development and Innovations Infrastructures (LM2011033).

REFERENCES

- Gallai N, Salles JM, Settele J, Vaissière BE. 2009. Economic valuation of the vulnerability of world agriculture confronted with pollinator decline. *Ecol Econ* 68:810–821. <https://doi.org/10.1016/j.ecolecon.2008.06.014>.
- Potts SG, Biesmeijer JC, Kremen C, Neumann P, Schweiger O, Kunin WE. 2010. Global pollinator declines: trends, impacts and drivers. *Trends Ecol Evol* 25:345–353. <https://doi.org/10.1016/j.tree.2010.01.007>.
- Biesmeijer JC, Roberts SP, Reemer M, Ohlemüller R, Edwards M, Peeters T, Schaffers AP, Potts SG, Kleukers R, Thomas CD, Settele J, Kunin WE. 2006. Parallel declines in pollinators and insect-pollinated plants in Britain and the Netherlands. *Science* 313:351–354. <https://doi.org/10.1126/science.1127863>.
- Vanengelsdorp D, Meixner MD. 2010. A historical review of managed honey bee populations in Europe and the United States and the factors that may affect them. *J Invertebr Pathol* 103(Suppl 1):S80–S95. <https://doi.org/10.1016/j.jip.2009.06.011>.
- Genersh E, von der Ohe W, Kaatz H, Schroeder A, Otten C, Buchler R, Berg S, Ritter W, Muhlen W, Gisder S, Meixner M, Leibig G, Rosenkranz P. 2010. The German bee monitoring project: a long term study to understand periodically high winter losses of honey bee colonies. *Adipologie* 41: 332–352.
- Bailey L, Woods RD. 1977. Two more small RNA viruses from honey bees and further observations on sacbrood and acute bee-paralysis viruses. *J Gen Virol* 37:175–182.
- Leat N, Ball B, Govan V, Davison S. 2000. Analysis of the complete genome sequence of black queen-cell virus, a picorna-like virus of honey bees. *J Gen Virol* 81:2111–2119. <https://doi.org/10.1099/0022-1317-81-8-2111>.
- Ellis JD, Munn PA. 2005. The worldwide health status of honey bees. *Bee World* 86:88–101. <https://doi.org/10.1080/0005772X.2005.11417323>.
- Tentcheva D, Gauthier L, Zappulla N, Dainat B, Cousserans F, Colin ME, Bergoin M. 2004. Prevalence and seasonal variations of six bee viruses in *Apis mellifera* L. and *Varroa destructor* mite populations in France. *Appl Environ Microbiol* 70:7185–7191. <https://doi.org/10.1128/AEM.70.12.7185-7191.2004>.
- Mondet F, de Miranda JR, Kretzschmar A, Le Conte Y, Mercer AR. 2014. On the front line: quantitative virus dynamics in honeybee (*Apis mellifera* L.) colonies along a new expansion front of the parasite *Varroa destructor*. *PLoS Pathog* 10:e1004323. <https://doi.org/10.1371/journal.ppat.1004323>.
- Chen YP, Pettis JS, Collins A, Feldlaufer MF. 2006. Prevalence and transmission of honeybee viruses. *Appl Environ Microbiol* 72:606–611. <https://doi.org/10.1128/AEM.72.1.606-611.2006>.
- DeGrandi-Hoffman G, Chen Y, Simonds R. 2013. The effects of pesticides on queen rearing and virus titers in honey bees (*Apis mellifera* L.). *Insects* 4:71–89. <https://doi.org/10.3390/insects4010071>.
- Tapasztó Z, Forgách P, Kovágo C, Topolska G, Nowotny N, Rusvai M, Bakonyi T. 2009. Genetic analysis and phylogenetic comparison of Black

- queen cell virus genotypes. *Vet Microbiol* 139:227–234. <https://doi.org/10.1016/j.vetmic.2009.06.002>.
14. Noh JH, Reddy KE, Choe SE, Yoo MS, Doan HT, Kweon CH, Ramya M, Yoon BS, Nguyen LT, Nguyen TT, Van Quyen D, Jung SC, Chang KY, Kang SW. 2013. Phylogenetic analysis of black queen cell virus genotypes in South Korea. *Virus Genes* 46:362–368. <https://doi.org/10.1007/s11262-012-0859-x>.
 15. Yang B, Peng G, Li T, Kadowaki T. 2013. Molecular and phylogenetic characterization of honey bee viruses, Nosema microsporidia, protozoan parasites, and parasitic mites in China. *Ecol Evol* 3:298–311. <https://doi.org/10.1002/ece3.464>.
 16. Berényi O, Bakonyi T, Derakhshifar I, Koglbberger H, Nowotny N. 2006. Occurrence of six honeybee viruses in diseased Austrian apiaries. *Appl Environ Microbiol* 72:2414–2420. <https://doi.org/10.1128/AEM.72.4.2414-2420.2006>.
 17. Bailey L, Ball BV, Perry JN. 1983. Association of viruses with two protozoal pathogens of the honey bee. *Ann Appl Biol* 103:13–20. <https://doi.org/10.1111/j.1744-7348.1983.tb02735.x>.
 18. Doublet V, Labarussias M, de Miranda JR, Moritz RF, Paxton RJ. 2015. Bees under stress: sublethal doses of a neonicotinoid pesticide and pathogens interact to elevate honey bee mortality across the life cycle. *Environ Microbiol* 17:969–983. <https://doi.org/10.1111/1462-2920.12426>.
 19. Mayo MA. 2002. Virus taxonomy—Houston 2002. *Arch Virol* 147:1071–1076. <https://doi.org/10.1007/s007050200036>.
 20. McMahon DP, Furst MA, Caspar J, Theodorou P, Brown MJ, Paxton RJ. 3 March 2015. A sting in the spit: widespread cross-infection of multiple RNA viruses across wild and managed bees. *J Anim Ecol* <https://doi.org/10.1111/1365-2656.12345>.
 21. Mullapudi E, Pridal A, Palkova L, de Miranda JR, Plevka P. 2016. Virion structure of Israeli acute bee paralysis virus. *J Virol* 90:8150–8159. <https://doi.org/10.1128/JVI.00854-16>.
 22. Tate J, Liljas L, Scotti P, Christian P, Lin T, Johnson JE. 1999. The crystal structure of cricket paralysis virus: the first view of a new virus family. *Nat Struct Biol* 6:765–774. <https://doi.org/10.1038/11543>.
 23. Squires G, Pous J, Agirre J, Rozas-Dennis GS, Costabel MD, Marti GA, Navaza J, Bressanelli S, Guerin DM, Rey FA. 2013. Structure of the *Triatoma* virus capsid. *Acta Crystallogr D Biol Crystallogr* 69:1026–1037. <https://doi.org/10.1107/S0907444913004617>.
 24. Le Gall O, Christian P, Fauquet CM, King AM, Knowles NJ, Nakashima N, Stanway G, Gorbalenya AE. 2008. Picornavirales, a proposed order of positive-sense single-stranded RNA viruses with a pseudo-T=3 virion architecture. *Arch Virol* 153:715–727. <https://doi.org/10.1007/s00705-008-0041-x>.
 25. Rossmann MG, Arnold E, Erickson JW, Frankenberger EA, Griffith JP, Hecht HJ, Johnson JE, Kamer G, Luo M, Mosser AG, Rueckert RR, Shery B, Vriend G. 1985. Structure of a human common cold virus and functional relationship to other picornaviruses. *Nature* 317:145–153. <https://doi.org/10.1038/317145a0>.
 26. Palmenberg AC. 1982. In vitro synthesis and assembly of picornaviral capsid intermediate structures. *J Virol* 44:900–906.
 27. Putnak JR, Phillips BA. 1981. Picornaviral structure and assembly. *Microbiol Rev* 45:287–315.
 28. Rombaut B, Foriers A, Boeye A. 1991. In vitro assembly of poliovirus 14 S subunits: identification of the assembly promoting activity of infected cell extracts. *Virology* 180:781–787. [https://doi.org/10.1016/0042-6822\(91\)90091-O](https://doi.org/10.1016/0042-6822(91)90091-O).
 29. Rombaut B, Vrijsen R, Boeye A. 1984. In vitro assembly of poliovirus empty capsids: antigenic consequences and immunological assay of the morphopoietic factor. *Virology* 135:546–550. [https://doi.org/10.1016/0042-6822\(84\)90209-5](https://doi.org/10.1016/0042-6822(84)90209-5).
 30. Agirre J, Aloria K, Arizmendi JM, Iloro I, Elortza F, Sanchez-Eugenia R, Marti GA, Neumann E, Rey FA, Guerin DM. 2011. Capsid protein identification and analysis of mature *Triatoma* virus (TrV) virions and naturally occurring empty particles. *Virology* 409:91–101. <https://doi.org/10.1016/j.virol.2010.09.034>.
 31. Fisher AJ, Johnson JE. 1993. Ordered duplex RNA controls capsid architecture in an icosahedral animal virus. *Nature* 361:176–179. <https://doi.org/10.1038/361176a0>.
 32. Munshi S, Liljas L, Cavarelli J, Bomu W, McKinney B, Reddy V, Johnson JE. 1996. The 2.8 Å structure of a T=4 animal virus and its implications for membrane translocation of RNA. *J Mol Biol* 261:1–10. <https://doi.org/10.1006/jmbi.1996.0437>.
 33. Tuthill TJ, Groppelli E, Hogle JM, Rowlands DJ. 2010. Picornaviruses. *Curr Top Microbiol Immunol* 343:43–89.
 34. Bostina M, Levy H, Filman DJ, Hogle JM. 2011. Poliovirus RNA is released from the capsid near a twofold symmetry axis. *J Virol* 85:776–783. <https://doi.org/10.1128/JVI.00531-10>.
 35. Lyu K, Ding J, Han JF, Zhang Y, Wu XY, He YL, Qin CF, Chen R. 2014. Human enterovirus 71 uncoating captured at atomic resolution. *J Virol* 88:3114–3126. <https://doi.org/10.1128/JVI.03029-13>.
 36. Wang X, Peng W, Ren J, Hu Z, Xu J, Lou Z, Li X, Yin W, Shen X, Porta C, Walter TS, Evans G, Axford D, Owen R, Rowlands DJ, Wang J, Stuart DI, Fry EE, Rao Z. 2012. A sensor-adaptor mechanism for enterovirus uncoating from structures of EV71. *Nat Struct Mol Biol* 19:424–429. <https://doi.org/10.1038/nsmb.2255>.
 37. Shingler KL, Yoder JL, Carnegie MS, Ashley RE, Makhov AM, Conway JF, Hafenstein S. 2013. The enterovirus 71 A-particle forms a gateway to allow genome release: a cryoEM study of picornavirus uncoating. *PLoS Pathog* 9:e1003240. <https://doi.org/10.1371/journal.ppat.1003240>.
 38. Fricks CE, Hogle JM. 1990. Cell-induced conformational change in poliovirus: externalization of the amino terminus of VP1 is responsible for liposome binding. *J Virol* 64:1934–1945.
 39. Jiang P, Liu Y, Ma HC, Paul AV, Wimmer E. 2014. Picornavirus morphogenesis. *Microbiol Mol Biol Rev* 78:418–437. <https://doi.org/10.1128/MMBR.00012-14>.
 40. Zlotnick A, Reddy VS, Dasgupta R, Schneemann A, Ray WJ, Jr, Rueckert RR, Johnson JE. 1994. Capsid assembly in a family of animal viruses primes an autoproteolytic maturation that depends on a single aspartic acid residue. *J Biol Chem* 269:13680–13684.
 41. Rotbart HA. 2002. Treatment of picornavirus infections. *Antiviral Res* 53:83–98. [https://doi.org/10.1016/S0166-3542\(01\)00206-6](https://doi.org/10.1016/S0166-3542(01)00206-6).
 42. Smith TJ, Kremer MJ, Luo M, Vriend G, Arnold E, Kamer G, Rossmann MG, McKinlay MA, Diana GD, Otto MJ. 1986. The site of attachment in human rhinovirus 14 for antiviral agents that inhibit uncoating. *Science* 233:1286–1293. <https://doi.org/10.1126/science.3018924>.
 43. Hadfield AT, Diana GD, Rossmann MG. 1999. Analysis of three structurally related antiviral compounds in complex with human rhinovirus 14. *Proc Natl Acad Sci U S A* 96:14730–14735. <https://doi.org/10.1073/pnas.96.26.14730>.
 44. Grant RA, Hiremath CN, Filman DJ, Syed R, Andries K, Hogle JM. 1994. Structures of poliovirus complexes with anti-viral drugs: implications for viral stability and drug design. *Curr Biol* 4:784–797.
 45. Hiremath CN, Grant RA, Filman DJ, Hogle JM. 1995. Binding of the antiviral drug WIN51711 to the sabin strain of type 3 poliovirus: structural comparison with drug binding in rhinovirus 14. *Acta Crystallogr D Biol Crystallogr* 51:473–489.
 46. Kalynych S, Palkova L, Plevka P. 2016. The structure of human parechovirus 1 reveals an association of the RNA genome with the capsid. *J Virol* 90:1377–1386. <https://doi.org/10.1128/JVI.02346-15>.
 47. Wang X, Ren J, Gao Q, Hu Z, Sun Y, Li X, Rowlands DJ, Yin W, Wang J, Stuart DI, Rao Z, Fry EE. 2015. Hepatitis A virus and the origins of picornaviruses. *Nature* 517:85–88.
 48. Maori E, Lavi S, Mozes-Koch R, Gantman Y, Peretz Y, Edelbaum O, Tanne E, Sela I. 2007. Isolation and characterization of Israeli acute paralysis virus, a dicistrovirus affecting honeybees in Israel: evidence for diversity due to intra- and inter-species recombination. *J Gen Virol* 88:3428–3438. <https://doi.org/10.1099/vir.0.83284-0>.
 49. Govan VA, Leat N, Allsopp M, Davison S. 2000. Analysis of the complete genome sequence of acute bee paralysis virus shows that it belongs to the novel group of insect-infecting RNA viruses. *Virology* 277:457–463. <https://doi.org/10.1006/viro.2000.0616>.
 50. de Miranda JR, Drebot M, Tyler S, Shen M, Cameron CE, Stoltz DB, Camazine SM. 2004. Complete nucleotide sequence of Kashmir bee virus and comparison with acute bee paralysis virus. *J Gen Virol* 85:2263–2270. <https://doi.org/10.1099/vir.0.79990-0>.
 51. Mari J, Poulos BT, Lightner DV, Bonami JR. 2002. Shrimp Taura syndrome virus: genomic characterization and similarity with members of the genus Cricket paralysis-like viruses. *J Gen Virol* 83:915–926. <https://doi.org/10.1099/0022-1317-83-4-915>.
 52. Valles SM, Strong CA, Dang PM, Hunter WB, Pereira RM, Oi DH, Shapiro AM, Williams DF. 2004. A picorna-like virus from the red imported fire ant, *Solenopsis invicta*: initial discovery, genome sequence, and characterization. *Virology* 328:151–157. <https://doi.org/10.1016/j.virol.2004.07.016>.
 53. Wilson JE, Powell MJ, Hoover SE, Sarnow P. 2000. Naturally occurring dicistronic cricket paralysis virus RNA is regulated by two internal ribo-

- some entry sites. *Mol Cell Biol* 20:4990–4999. <https://doi.org/10.1128/MCB.20.14.4990-4999.2000>.
54. Johnson KN, Christian PD. 1998. The novel genome organization of the insect picorna-like virus *Drosophila C virus* suggests this virus belongs to a previously undescribed virus family. *J Gen Virol* 79(Part 1):191–203.
 55. Van Munster M, Dulleman AM, Verbeek M, Van Den Heuvel JF, Clerivet A, Van Der Wilk F. 2002. Sequence analysis and genomic organization of *Aphid lethal paralysis virus*: a new member of the family *Dicistroviridae*. *J Gen Virol* 83:3131–3138. <https://doi.org/10.1099/0022-1317-83-12-3131>.
 56. Moon JS, Domier LL, McCoppin NK, D'Arcy CJ, Jin H. 1998. Nucleotide sequence analysis shows that *Rhopalosiphum padi virus* is a member of a novel group of insect-infecting RNA viruses. *Virology* 243:54–65. <https://doi.org/10.1006/viro.1998.9043>.
 57. Czibener C, La Torre JL, Muscio OA, Ugalde RA, Scodeller EA. 2000. Nucleotide sequence analysis of *Triatoma virus* shows that it is a member of a novel group of insect RNA viruses. *J Gen Virol* 81:1149–1154. <https://doi.org/10.1099/0022-1317-81-4-1149>.
 58. Hunnicutt LE, Hunter WB, Cave RD, Powell CA, Mozoruk JJ. 2006. Genome sequence and molecular characterization of *Homalodisca coagulata virus-1*, a novel virus discovered in the glassy-winged sharpshooter (Hemiptera: Cicadellidae). *Virology* 350:67–78. <https://doi.org/10.1016/j.virol.2006.02.034>.
 59. Nakashima N, Sasaki J, Toriyama S. 1999. Determining the nucleotide sequence and capsid-coding region of *himetobi P virus*: a member of a novel group of RNA viruses that infect insects. *Arch Virol* 144:2051–2058. <https://doi.org/10.1007/s007050050726>.
 60. Sasaki J, Nakashima N, Saito H, Noda H. 1998. An insect picorna-like virus, *Plautia stali intestine virus*, has genes of capsid proteins in the 3' part of the genome. *Virology* 244:50–58. <https://doi.org/10.1006/viro.1998.9094>.
 61. de Miranda JR, Bailey L, Ball BV, Blanchard P, Budge G, Chejanovsky N, Chen Y-P, Gauthier L, Genersch E, De Graaf D, Ribière M, Ryabov E, De Smet L, van der Steen JJM. 2013. Standard methods for virus research in *Apis mellifera*, p 1–55. In Dietemann V, Ellis JD, Neumann P (ed), *The COLOSS BEEBOOK*, vol II. Standard methods for *Apis mellifera* pest and pathogen research. IBRA, Treforest, UK.
 62. Kabsch W. 2010. XDS. *Acta Crystallogr D Biol Crystallogr* 66:125–132. <https://doi.org/10.1107/S0907444909047337>.
 63. Tong L, Rossmann MG. 1997. Rotation function calculations with GLRF program. *Methods Enzymol* 276:594–611. [https://doi.org/10.1016/S0076-6879\(97\)76080-4](https://doi.org/10.1016/S0076-6879(97)76080-4).
 64. Rossmann MG, Blow DM. 1962. The detection of sub-units within the crystallographic asymmetric unit. *Acta Cryst* 15:24–31. <https://doi.org/10.1107/S0365110X62000067>.
 65. Brunger AT. 2007. Version 1.2 of the Crystallography and NMR system. *Nat Protoc* 2:2728–2733. <https://doi.org/10.1038/nprot.2007.406>.
 66. Kleywegt GJ, Read RJ. 1997. Not your average density. *Structure* 5:1557–1569. [https://doi.org/10.1016/S0969-2126\(97\)00305-5](https://doi.org/10.1016/S0969-2126(97)00305-5).
 67. Winn MD, Ballard CC, Cowtan KD, Dodson EJ, Emsley P, Evans PR, Keegan RM, Krissinel EB, Leslie AG, McCoy A, McNicholas SJ, Murshudov GN, Pannu NS, Potterton EA, Powell HR, Read RJ, Vagin A, Wilson KS. 2011. Overview of the CCP4 suite and current developments. *Acta Crystallogr D Biol Crystallogr* 67:235–242. <https://doi.org/10.1107/S0907444910045749>.
 68. Kleywegt GJ, Jones TA. 1999. Software for handling macromolecular envelopes. *Acta Crystallogr D Biol Crystallogr* 55:941–944. <https://doi.org/10.1107/S0907444999001031>.
 69. Emsley P, Cowtan K. 2004. Coot: model-building tools for molecular graphics. *Acta Crystallogr D Biol Crystallogr* 60:2126–2132. <https://doi.org/10.1107/S0907444904019158>.
 70. Jones TA, Zou JY, Cowan SW, Kjeldgaard M. 1991. Improved methods for building protein models in electron density maps and the location of errors in these models. *Acta Crystallogr A* 47(Part 2):110–119.
 71. Kleywegt GJ, Brunger AT. 1996. Checking your imagination: applications of the free R value. *Structure* 4:897–904. [https://doi.org/10.1016/S0969-2126\(96\)00097-4](https://doi.org/10.1016/S0969-2126(96)00097-4).
 72. Chenna R, Sugawara H, Koike T, Lopez R, Gibson TJ, Higgins DG, Thompson JD. 2003. Multiple sequence alignment with the Clustal series of programs. *Nucleic Acids Res* 31:3497–3500. <https://doi.org/10.1093/nar/gkg500>.
 73. Pettersen EF, Goddard TD, Huang CC, Couch GS, Greenblatt DM, Meng EC, Ferrin TE. 2004. UCSF Chimera—a visualization system for exploratory research and analysis. *J Comput Chem* 25:1605–1612. <https://doi.org/10.1002/jcc.20084>.
 74. Humphrey W, Dalke A, Schulten K. 1996. VMD: visual molecular dynamics. *J Mol Graph* 14:33–38, 27–38.
 75. Huson DH. 1998. SplitsTree: analyzing and visualizing evolutionary data. *Bioinformatics* 14:68–73. <https://doi.org/10.1093/bioinformatics/14.1.68>.
 76. Davis IW, Leaver-Fay A, Chen VB, Block JN, Kapral GJ, Wang X, Murray LW, Arendall WB, III, Snoeyink J, Richardson JS, Richardson DC. 2007. MolProbity: all-atom contacts and structure validation for proteins and nucleic acids. *Nucleic Acids Res* 35:W375–W383. <https://doi.org/10.1093/nar/gkm216>.

PAPER VII



Virion Structure of Iflavirus Slow Bee Paralysis Virus at 2.6-Angstrom Resolution

Sergei Kalynych,^a Antonín Přidal,^b Lenka Pálková,^a Yevgen Levdansky,^a Joachim R. de Miranda,^c Pavel Plevka^a

Structural Virology, Central European Institute of Technology, Masaryk University, Brno, Czech Republic^a; Department of Zoology, Fishery, Hydrobiology, and Apidology, Faculty of Agronomy, Mendel University in Brno, Brno, Czech Republic^b; Department of Ecology, Swedish University of Agricultural Sciences, Uppsala, Uppsala, Sweden^c

ABSTRACT

The western honeybee (*Apis mellifera*) is the most important commercial insect pollinator. However, bees are under pressure from habitat loss, environmental stress, and pathogens, including viruses that can cause lethal epidemics. Slow bee paralysis virus (SBPV) belongs to the *Iflaviridae* family of nonenveloped single-stranded RNA viruses. Here we present the structure of the SBPV virion determined from two crystal forms to resolutions of 3.4 Å and 2.6 Å. The overall structure of the virion resembles that of picornaviruses, with the three major capsid proteins VP1 to 3 organized into a pseudo-T3 icosahedral capsid. However, the SBPV capsid protein VP3 contains a C-terminal globular domain that has not been observed in other viruses from the order *Picornavirales*. The protruding (P) domains form “crowns” on the virion surface around each 5-fold axis in one of the crystal forms. However, the P domains are shifted 36 Å toward the 3-fold axis in the other crystal form. Furthermore, the P domain contains the Ser-His-Asp triad within a surface patch of eight conserved residues that constitutes a putative catalytic or receptor-binding site. The movements of the domain might be required for efficient substrate cleavage or receptor binding during virus cell entry. In addition, capsid protein VP2 contains an RGD sequence that is exposed on the virion surface, indicating that integrins might be cellular receptors of SBPV.

IMPORTANCE

Pollination by honeybees is needed to sustain agricultural productivity as well as the biodiversity of wild flora. However, honeybee populations in Europe and North America have been declining since the 1950s. Honeybee viruses from the *Iflaviridae* family are among the major causes of honeybee colony mortality. We determined the virion structure of an *Iflavirus*, slow bee paralysis virus (SBPV). SBPV exhibits unique structural features not observed in other picorna-like viruses. The SBPV capsid protein VP3 has a large C-terminal domain, five of which form highly prominent protruding “crowns” on the virion surface. However, the domains can change their positions depending on the conditions of the environment. The domain includes a putative catalytic or receptor binding site that might be important for SBPV cell entry.

The western honeybee *Apis mellifera* plays a vital role in agriculture by providing pollination services for numerous food crops, especially those with high nutritional and economic value (1). Honeybees are also critical for maintaining the ecological and genetic diversity of wild flowering plants (2). In addition, bumblebees and several other solitary bee species are becoming increasingly important commercial pollinators of specific crops (3). However, bees and the pollination services they provide are under increasing stress due to habitat loss, intensified agricultural management, pesticides, parasites, and pathogens, including numerous viruses (3). Annual honeybee colony mortality has been increasing in North America and Europe over the last couple of decades (4), which, coupled with a long-term decline in beekeeping, has become a serious threat to the adequate provision of pollination services and food security (4–6).

Honeybees are hosts to a large number of viruses, most of which persist covertly within the honeybee population interrupted by occasional outbreaks. Such outbreaks of some of the viruses can have fatal consequences for individual workers and whole colonies (7). Colony collapse disorder (CCD), a still largely unexplained rapid loss of adult bees from colonies, has been linked to virus infections (8, 9). Much of winter honeybee colony mortality is also associated with viruses (10, 11). The viruses that have the greatest impact on honeybee populations are small icosahedral picorna-like viruses from the families *Dicistroviridae* and

Iflaviridae, including slow bee paralysis virus (SBPV), sacbrood virus (SBV), deformed wing virus (DWV), and varroa destructor virus 1 (VDV-1) (7). SBPV was discovered in 1974 (12) and was linked to honeybee colony mortality in the United Kingdom in the 1980s (13). Despite its efficient transmission by *Varroa destructor* (14), SBP is a rare disease of honeybees (15). However, it is common in bumblebees (16, 17), and therefore, honeybees may be an incidental, secondary host.

Viruses from the order *Picornavirales* have nonenveloped icosahedral virions containing a single-stranded positive-sense RNA genome about 10,000 nucleotides long (18). Picornavirus genomes are translated into polyproteins that are co- and post-translationally cleaved by viral proteases to produce structural (capsid-forming) and nonstructural proteins. The capsid pro-

Received 10 April 2016 Accepted 27 May 2016

Accepted manuscript posted online 8 June 2016

Citation Kalynych S, Přidal A, Pálková L, Levdansky Y, de Miranda JR, Plevka P. 2016. Virion structure of iflavirus slow bee paralysis virus at 2.6-angstrom resolution. *J Virol* 90:7444–7455. doi:10.1128/JVI.00680-16.

Editor: B. Williams, Hudson Institute of Medical Research

Address correspondence to Pavel Plevka, pavel.plevka@ceitec.muni.cz.

Copyright © 2016 Kalynych et al. This is an open-access article distributed under the terms of the [Creative Commons Attribution 4.0 International license](https://creativecommons.org/licenses/by/4.0/).

teins originating from a single polyprotein form a protomer—the basic building block of the capsid. The entire capsid consists of 60 such protomers, arranged in 12 pentamer units of five protomers each. The major capsid proteins VP1 to VP3 are arranged in a pseudo-T3 icosahedral capsid.

The only structural information available on *Iflaviridae* family members is the 25-Å resolution cryo-electron microscopy structure of the Chinese sacbrood virus (19). The structure confirmed the pseudo-T3 icosahedral symmetry of the capsid and revealed a smooth outer surface of the virion. Iflaviruses were proposed to harbor short VP4 subunits consisting of only about 20 residues (15, 20). However, because of the low molecular weight of the peptides, the existence of VP4 subunits has not been unequivocally established (15, 20). Previous genetic and proteomic analyses of iflaviruses revealed a C-terminal extension of about 160 residues in length of one of the capsid proteins (15, 20, 21). Here we present the structure of SBPV determined from two crystal forms to resolutions of 3.4 Å and 2.6 Å. The structures offer the first high-resolution snapshots of a virus from the family *Iflaviridae* and of a viral pathogen of the honeybee.

MATERIALS AND METHODS

Virus propagation in honeybee pupae. Propagations of SBPV were carried out as described in the COLOSS BEEBOOK (22). Brood areas with *Apis mellifera* white-eyed pupae were identified by color and structural features of the cell caps. White-eyed pupae were carefully extracted from the brood combs, so as not to injure the pupae. The pupae were placed on paper furrows with their ventral side up. In total, 544 pupae were used for the SBPV propagation. A virus inoculum (1 µl) was injected into pupae with a Hamilton micropipette with a 30-gauge 22-mm-long needle through the intersegmental cuticle between the 4th and 5th sternites. Pupae that leaked hemolymph after the injection were discarded. The optimal concentration of the virus in the inoculum for virus production was determined experimentally by comparing virus yields when using different virus concentrations in the injection inoculum. Inoculated pupae were placed into petri dishes with the paper furrows and incubated at 30°C and 75% humidity for 5 days. After incubation, the pupae were frozen at –20°C. For long-term storage, the pupae were kept at –80°C.

Virus purification. Fifty to 70 experimentally infected honeybee pupae were homogenized with a Dounce homogenizer in 30 ml of phosphate-buffered saline (PBS), pH 7.5 (Sigma-Aldrich). The nonionic detergent NP-40 was added to a final concentration of 0.5%, and the homogenate was incubated for 1 h at room temperature. The extract was centrifuged at $8,000 \times g$ for 30 min. The pellet was discarded and the supernatant was centrifuged at $150,000 \times g$ for 3 h in a Ti50.2 fixed-angle rotor (Beckman-Coulter). The resulting pellet was resuspended in PBS to a final volume of 5 ml. $MgCl_2$ was added to a final concentration of 5 mM, along with 20 µg/ml of DNase I and 20 µg/ml of RNase. The solution was incubated at room temperature for 30 min and centrifuged at $4,000 \times g$ for 15 min. The resulting supernatant was loaded onto a CsCl (0.6-g/ml) solution prepared in PBS. The ultracentrifugation proceeded for 16 h to establish the CsCl gradient. Virus bands were collected by gentle piercing of the ultracentrifuge tubes with an 18-gauge needle. The viruses were transferred to PBS by several rounds of concentration and dilution using centrifuge filter units with a 100-kDa-molecular-mass cutoff. This procedure yielded about 300 µg of virus with a purity sufficient for sparse-matrix crystallization screening experiments. Sample purity with respect to contaminating honeybee viruses was checked by reverse transcription-quantitative PCR (RT-qPCR) using previously reported virus-specific assays (22). In both preparations, the total sum of contaminating viruses was less than 1% of the virus of interest. The nucleotide sequences of the virus preparations were determined by sequencing 300 ng of RNA, purified using a Qiagen RNA purification kit, by IonTorrent technology and standard protocols for library preparation and sequencing. The IonTorrent reads

were mapped to the SBPV GenBank reference sequence [EU035616](#) (SBPV) using Tmap v4.4.8, included in TorrentSuite 4.4.2, with Life Technologies-recommended parameters. Variability and consensus sequences were created using mpileup from samtools v.0.1.8 and an in-house script.

SBPV crystallization. SBPV crystallization screening was conducted at 4°C and 20°C with virus concentrations of 5 mg/ml and 10 mg/ml. In total, 2,100 conditions were tested in a 96-well, sitting-drop vapor diffusion format. The initial crystals that formed in 0.1 M sodium citrate (pH 6.5)–5% (wt/vol) polyethylene glycol 4000 (PEG 4000) after 7 days of incubation at 20°C were spherical, with diameters of less than 0.03 µm. The crystallization conditions were optimized by using a 96-well additive screen (Hampton Research Inc.). Optimized crystals with cubic morphology grew under the starting conditions with extra 0.2 M NDSB-221 (non-detergent sulfobetaine) and could be reproduced in a hanging-drop format by mixing 1.5 µl of 10-mg/ml purified virus solution with 0.5 µl of the reservoir solution. The optimized crystals were cubic and required 3 weeks to reach their final size of about 0.1 µm. The best diffraction was obtained when crystals were transferred to a reservoir solution containing 10% ethylene glycol prior to flash-freezing in liquid nitrogen. Out of approximately 200 crystals tested, two crystals diffracted X rays to a resolution of 3.4 Å.

Another crystal form was discovered at 4°C in 0.1 M sodium acetate (pH 4.5)–5% PEG 10000 and contained rectangular crystals of about 0.1 mm. The crystals could be reproduced in a hanging-drop format, with some crystals reaching a length of 0.3 mm. The crystals were subjected to dehydration by gradually transferring the coverslip containing the hanging drop to the reservoir solution containing increasing concentrations of sodium acetate (pH 4.5) and of PEG 10000 as described previously (23). At 20% PEG 10000, crystals were harvested, cryoprotected in mother liquor solution containing 20% glycerol, and flash-frozen in liquid nitrogen. Out of 50 crystals screened, two crystals diffracted X rays to a resolution of 2.6 Å.

SBPV structure determination and refinement. Diffraction data from SBPV crystal form 1 were collected at the Swiss Light Source X06SA beamline equipped with Pilatus-6M detector at the wavelength of 1.00003 Å at 100 K using a 0.1° rotation per image. The crystals were of space group I23. Unit cell size and packing considerations indicated that one pentamer of capsid protein protomers occupied a crystallographic asymmetric unit. There are two possibilities for superimposing icosahedral 532 symmetry with the 23 symmetry of the crystal, which are perpendicular to each other. The orientation of the virion was determined from a plot of the 5-fold rotation function, calculated with the program GLRF (24). Reflections between 5.0-Å and 4.5-Å resolutions were used for the calculations. Because of the superposition of the icosahedral and crystallographic symmetry, the center of the particle had to be positioned at the intersection of the 2-fold and 3-fold symmetry axes of the crystal. The triatoma virus (TrV) structure (PDB code 3NAP), converted to polyalanine, was used as a molecular replacement model. The model was placed into the orientation and position in the unit cell as described above and used to calculate phases for reflections at up to a 10-Å resolution, using the program CNS (25). The model-derived phases were refined by 25 cycles of 5-fold real-space electron density map averaging using the program ave (26). The mask for electron density averaging was generated by including all voxels within 5 Å of any atom of the TrV model, using the program mama from the package USF (27). Phase extension was applied in order to obtain phases for higher-resolution reflections. The addition of a small fraction of higher-resolution data (one index at a time) was followed by three cycles of averaging. This procedure was repeated until phases were obtained for all the reflections, up to a resolution of 3.4 Å. Inspection of the map showed that the mask used for electron density averaging cut the electron density of the capsid in an area around the icosahedral 5-fold axis. Thus, a new mask was prepared based on a correlation map calculated by comparing the electron density distributions among the five noncrystallographic symmetry (NCS)-related icosahedral asymmetric units. The

TABLE 1 Crystallographic data collection and refinement statistics

| Parameter | Crystal form 1 | Crystal form 2 |
|---|--|---|
| Crystallization conditions | Sodium citrate (pH 6.5), 5% (vol/vol) PEG 4000, 0.2 M NDSB-221 | Sodium acetate (pH 4.5), 5% (vol/vol) PEG 10000 |
| Space group | I23 | I222 |
| a, b, c (Å) | 360.7, 360.7, 360.7 | 340.0, 396.8, 431.7 |
| α , β , γ (°) | 90, 90, 90 | 90, 90, 90 |
| Resolution (Å) ^a | 70.7–3.41 (3.45–3.41) | 49.5–2.6 (2.64–2.60) |
| R_{merge} ^a | 0.31 (1.26) | 0.20 (0.98) |
| $\langle I \rangle / \langle \sigma I \rangle$ ^a | 5.6 (0.4) | 6.0 (0.9) |
| Completeness (%) ^a | 87.4 (43.7) | 88.3 (69.3) |
| Redundancy | 6.0 | 6.8 |
| No. of reflections | 92,015 | 780,730 |
| R_{work} ^b | 0.339 | 0.274 |
| No. of atoms ^c | | |
| Protein | 7,029 | 7,369 |
| Water | 0 | 75 |
| Average B factors | | |
| Protein | 73 | 32 |
| Water | NA ^d | 30 |
| RMSD | | |
| Bond lengths (Å) | 1.04 | 1.10 |
| Bond angles (°) | 0.004 | 0.004 |
| Ramachandran ^e | | |
| Favored (%) | 94.37 | 94.47 |
| Allowed (%) | 5.40 | 5.19 |
| Outliers (%) | 0.23 | 0.11 |
| Poor rotamers (%) ^e | 1.59 | 0.74 |
| C β deviations (%) ^e | 0 | 0 |
| Clash score ^e | 11.57 | 10.47 |
| Molprobity score ^e | 2.11 (100th percentile) | 1.92 (98th percentile) |

^a The values in parentheses are for the highest-resolution shell.

^b If calculated, the R_{free} value would have been very close to the R_{work} value due to the 5- and 15-fold NCS (79). Thus, all measured reflections were used in the crystallographic refinement.

^c The values are for the icosahedral asymmetric unit.

^d NA, not applicable.

^e According to the criterion of Molprobity (80).

correlation map was calculated using the program coma from Uppsala Software Factory (USF) (28). A cutoff value of 0.5 was used for the inclusion of voxels into the mask. The surface of the correlation mask was smoothed using the program mama (28). The phase extension procedure was repeated using the new mask. The resulting map was of sufficient quality to allow model building.

The program Buccaneer was used for automated model building, utilizing the 5-fold NCS present in the crystal (29, 30). The model from the automated building was about 50% complete, with assigned amino acid sequences. The initial model was subjected to iterative manual rebuilding using the programs Coot and O (31, 32) and coordinate and B-factor refinement using the programs CNS (25) and Phenix (33). No water molecules were added due to the limited resolution of the diffraction data.

Diffraction data from SBPV crystal form 2 crystals were collected at the synchrotron Soleil Proxima-1 beamline equipped with the Pilatus-6M detector at a wavelength of 0.97857 Å at 100 K using a 0.1° rotation per image. The crystals were of space group I222. The unit cell dimensions and the virus packaging considerations indicated that the crystallographic asymmetric unit consists of three pentamers of capsid protein protomers. Initially, a pentamer corresponding to the entire atomic model of crystal form I was used as a molecular replacement model to find the orientation and translation of the three pentamers in the crystallographic asymmetric

unit using the program Phaser (34). The initial electron density map was subjected to 30 cycles of noncrystallographic symmetry averaging using the program AVE (26) and employing the mask based on the model from crystal form I. The averaged map lacked the electron density corresponding to the protruding domain altogether, which suggested that the molecular mask did not cover the correct part of the map. Therefore, a correlation map was calculated, as described for crystal form I, and the mask based on the correlation map was used for averaging. This map was used for the automated model building in the program Buccaneer (29) from the CCP4i software suite (35). The geometry of the model was adjusted manually using the program Coot (32). The coordinate and B-factor refinement were carried out using the program CNS (25) employing strict NCS constraints.

In order to improve the structure of the P domain in crystal form I, the P domain determined from crystal form II was positioned in crystal I using the program Phaser (34). The model of the icosahedral asymmetric unit with the properly positioned P domain was then used to generate a new mask for real-space electron density averaging in the program mama (27). Thirty cycles of real-space electron density averaging were carried out using the program AVE (26). P domain residues with no corresponding density in the averaged map were manually removed using the program Coot (32). The model was subjected to coordinate and B-factor

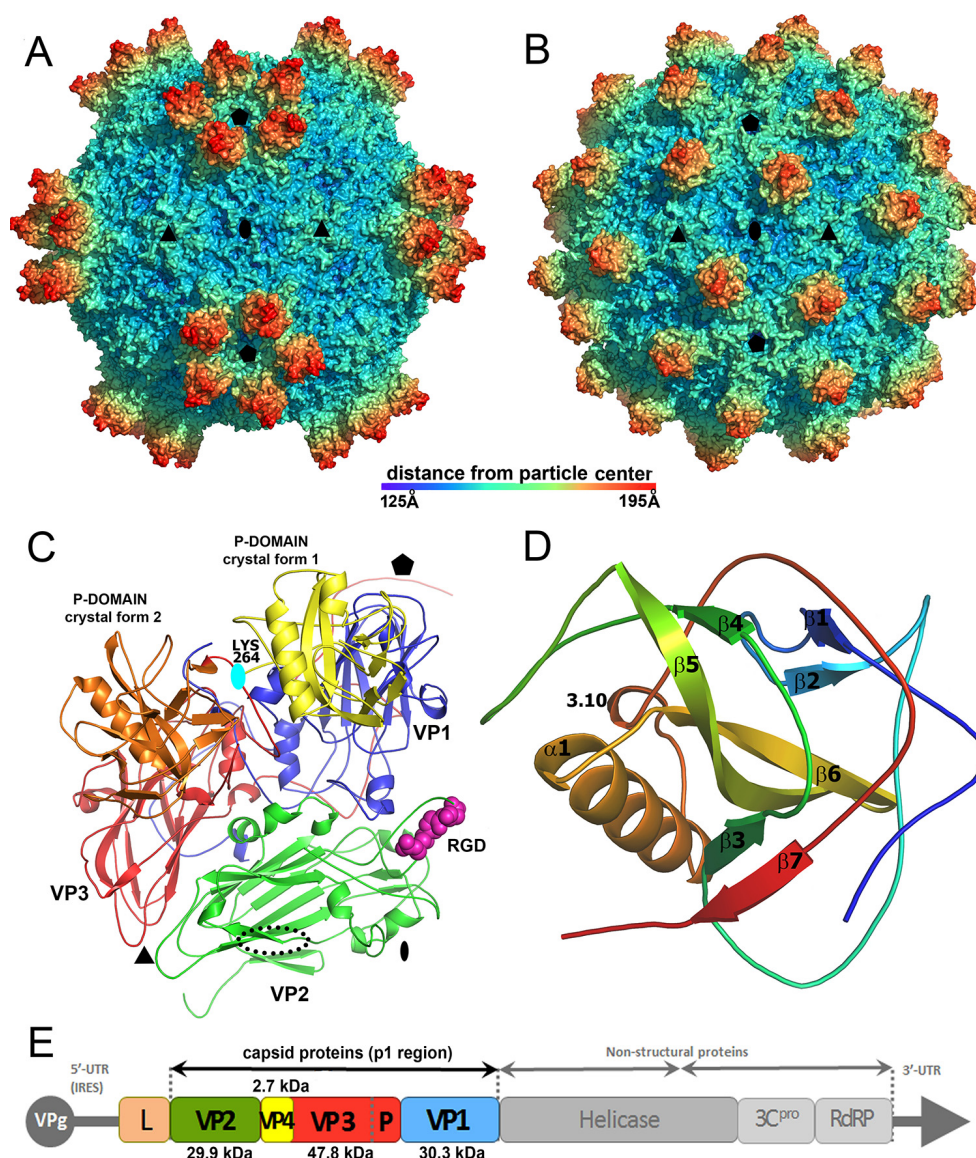


FIG 1 Structure of SBPV virion and icosahedral asymmetric unit. Surface representations of SBPV virions determined in crystal form 1 (A) and crystal form 2 (B) show differences in the positioning of the P domains. The surfaces of the particles are rainbow-colored based on the distance from the particle center. Depressions are shown in blue and peaks in red. (C) Cartoon representation of SBPV icosahedral asymmetric unit. VP1 is shown in blue, VP2 in green, and VP3 in red. The P domain positioned as in crystal form 1 is shown in yellow and in crystal form 2 in orange. Locations of 5-fold, 3-fold, and 2-fold icosahedral symmetry axes are indicated by a pentagon, triangle, and oval, respectively. The RGD motif found in the GH loop of VP2 subunit is shown as space-filling model in magenta. The position of the RGD motif in FMDV is indicated with a dotted black oval. The cyan oval indicates the position of rotation axis relating the two P domain positions. (D) Cartoon representation of P domain rainbow colored from the N terminus in blue to the C terminus in red. Names of secondary structure elements are indicated. (E) Diagram of SBPV genome organization. Capsid proteins VP1, VP2, and VP3 were identified based on their location in the capsid according to the picornavirus convention. Predicted molecular masses of capsid proteins are specified. The location of the P domain of VP3 is indicated. VPg, viral protein, genome linked; L, leader peptide; IRES, internal ribosome entry site; UTR, untranslated region; 3C^{PRO}, 3C protease; RdRP, RNA-dependent RNA polymerase.

DEN-assisted refinement using the atomic model of crystal form 2 as a reference structure using the software package CNS (25, 36).

Protein structure accession numbers. The atomic coordinates of the SBPV virion in crystal forms 1 and 2, together with the structure factors and phases obtained by phase extension, were deposited into the Protein Data Bank under codes 5J96 and 5J98, respectively.

RESULTS AND DISCUSSION

Structure of SBPV virion and capsid proteins. The structure of SBPV was determined from two crystal forms to resolutions of 3.4

Å and 2.6 Å (Table 1). The two structures are similar, with a C α -atom root mean square deviation (RMSD) of 0.27 Å; however, they differ in the positions of protruding (P) domains of the VP3 subunits on the virion surface (Fig. 1A and B). The maximum outer diameter of the virion is 388 Å. The virion is bigger than those of other picornaviruses because of the P domains. The organization of capsid proteins within the SBPV virion is similar to that of other viruses from the order *Picornavirales* (Fig. 1C). The capsid is built from major capsid proteins VP1 to 3 arranged in

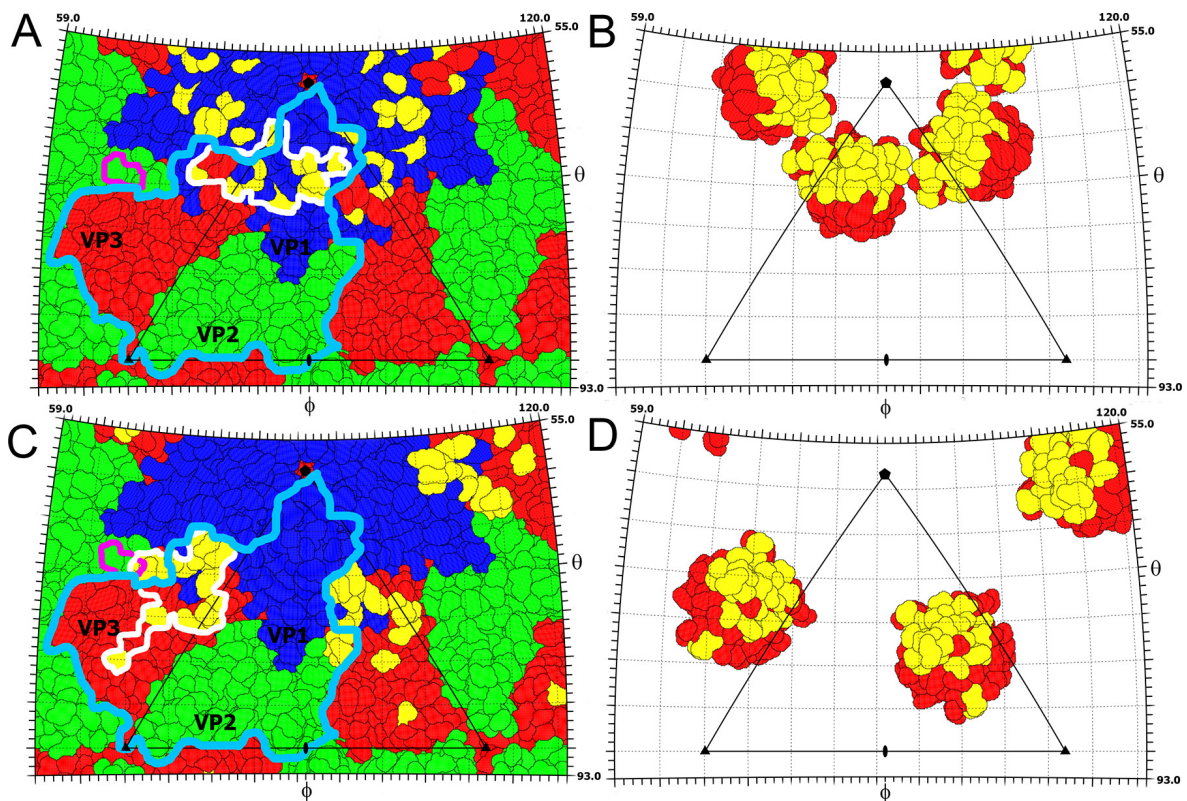


FIG 2 Interactions of P domain with the core of the SBPV capsid. (A and B) P domain footprints on the SBPV surface in crystal forms 1 (A) and 2 (B). The images show two-dimensional projections of the SBPV virion surface without the P domains. Residues of capsid proteins VP1, VP2, and VP3 are outlined in blue, green, and red, respectively. Residues involved in interaction with the P domain are shown in yellow. The P domain footprints are outlined by white lines. The border of one VP2-VP3-VP1 protomer is indicated by a light blue line. RGD residues of VP2 are indicated by a magenta line. (C and D) Inner surfaces of P domains in crystal forms 1 (C) and 2 (D), viewed from inside the particle. Residues interacting with the core of the capsid are shown in yellow and the remaining residues in red. Positions of 2-fold, 3-fold, and 5-fold icosahedral symmetry axes are shown as ovals, triangles, and pentagons, respectively. One icosahedral asymmetric unit is outlined by a triangle.

pseudo-T3 icosahedral symmetry (Fig. 1). The major capsid proteins have jellyroll β -sandwich folds with β -strands named according to the picornavirus convention B to I (37). The two antiparallel β -sheets forming the β -sandwich fold contain the strands BIDG and CHEF, respectively. The structures of the major capsid proteins could be built except for residues 253 to 266 of VP1, 92 to 100 and 261 of VP2, and 418 to 430 of VP3. The electron density corresponding to VP4 could not be identified in either of the two structures.

Structure of the VP3 P domain. The SBPV virion represents the first atomic structure of a virus from the family *Iflaviridae*. Unlike in the previously structurally characterized viruses from the order *Picornavirales*, the SBPV capsid protein VP3 contains a C-terminal extension of residues 267 to 430 (15) that fold into the globular P domain positioned on the capsid surface (Fig. 1C and D). The domain consists of a central twisted antiparallel β -sheet formed from strands β_4 , β_5 , and β_6 surrounded by the 14-residue-long α -helix α_1 , 3-residue-long 3.10 helix, and two shorter β -sheets containing strands β_1 and β_2 and β_3 to β_7 (Fig. 1D). The β -strands are connected by loops that vary in length between 6 and 23 residues. In both of the crystal forms, the residues of the P domain have higher average B factors (crystal 1 $B = 110 \text{ \AA}^2$; crystal 2 $B = 57 \text{ \AA}^2$) than the average B factors of the rest of the capsid (crystal 1 $B = 57 \text{ \AA}^2$; crystal 2 $B = 16 \text{ \AA}^2$), indicating a higher

mobility of the P domain. The P domains in the two crystal forms are similar, with an RMSD of 0.32 \AA for 144 $C\alpha$ atoms.

The P domains are positioned in different locations on the virion surface in the two crystal forms (Fig. 1 and 2). It is important to note that the domains are not held in position by crystal contact in either of the crystal forms. In crystal form 1, five P domains related by one icosahedral 5-fold axis form a “crown” on the virion surface (Fig. 1A and 3A). The crowns have a diameter of 90 \AA and protrude 50 \AA above the capsid surface, giving the SBPV virion its characteristic shape (Fig. 1A). Residues from loop β_2 - β_3 as well as the N- and C-terminal loops and β_2 of the P domain interact with the BC, CD, and EF loops of VP1, forming an interface with a buried surface area of 850 \AA^2 (Fig. 2A and B). P domains within the same crown do not interact with each other (Fig. 1A and 3A). In crystal form 1, the electron density map corresponding to the P domains is less well ordered than that of the rest of the SBPV virion, indicating an increased mobility of the crown.

In crystal form 2, the P domain is positioned approximately equal distances from the icosahedral 5-fold, 3-fold, and 2-fold axes (Fig. 1B and 3B). Residues from α_1 , β_3 , β_5 , β_7 , and loops β_2 - β_3 , β_3 - β_4 , and β_4 - β_5 of the P domain interact with the CD and GH loops of VP3, the C terminus of VP1, and the GH loop of VP2, forming an interface with a buried surface area of $1,150 \text{ \AA}^2$ (Fig. 2C and D). The density of the P domain is better resolved

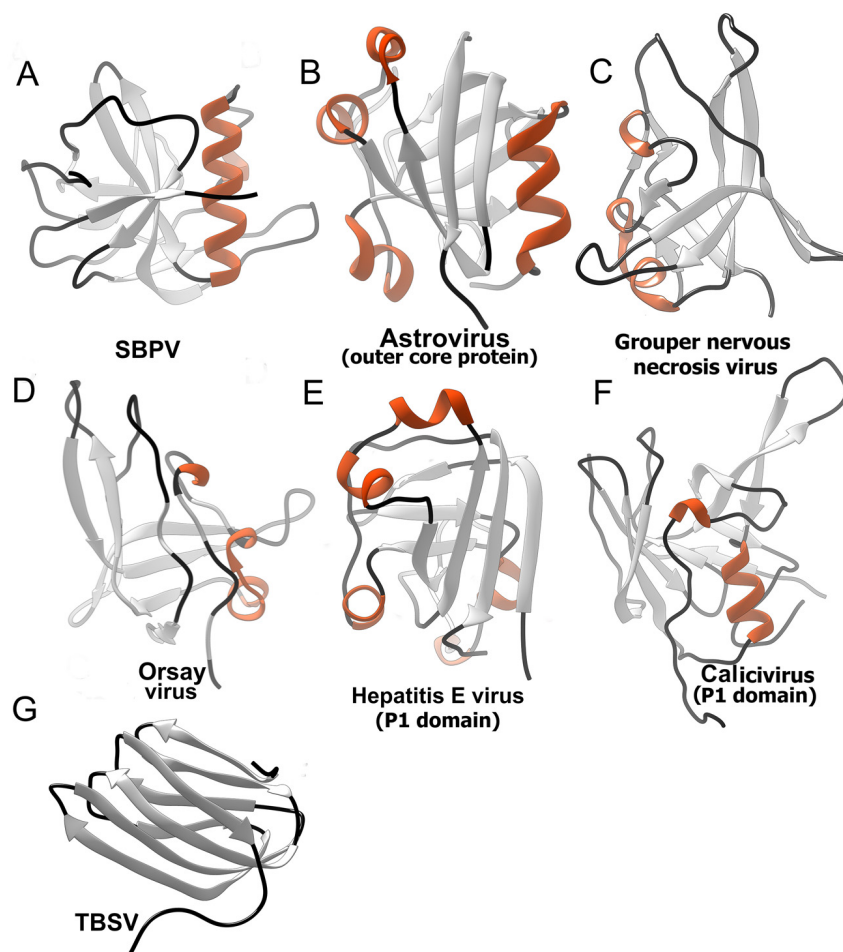


FIG 4 Protruding domains of viruses identified in a DALI search based on similarity to SBPV P domain. (A) SBPV; (B) human astrovirus outer coat protein (5EWN) (55); (C) grouper nervous necrosis virus (4RFU) (56); (D) orsay virus (4NWW) (57); (E) P1 domain of human hepatitis E virus (3HAG) (76); (F) P1 domain of human calicivirus (2GH8) (77). Protruding domain of tomato bushy stunt virus (2TBV) (78) is shown for comparison, however, it was not identified in the DALI server search. β -Strands are shown in light gray, helices in orange, and loops in black.

facilitate virus-receptor interactions (38–40). The cell entry of iflaviruses has not been studied, but it is likely to involve receptor-mediated endocytosis as has been described for mammalian picornaviruses (41, 42). The endosomal entry involves exposure of the virions to low pH that could trigger movements of the P domain that might be required for cleavage of substrate by the putative catalytic triad within the P domain as described below.

The P domain contains a putative receptor-binding or catalytic site. Residues Ser284, His283, and Asp300 from the P do-

main of VP3 are located close to each other, indicating the presence of a putative catalytic triad (43) that might be involved in the cleavage of an as-yet-unknown substrate. These residues face the interior of the crown in crystal form 1; however, they constitute the apex of the P domain in crystal form 2 (Fig. 3A and B). The distances between the side chains of the putative reactive site are larger than ideal for catalyzing the hydrolytic reaction (Fig. 3C) (43). Nevertheless, it is possible that the optimal configuration of the active site might be achieved upon binding the unknown substrate to the P domain. This type of catalytic triad has been previously identified in proteases, lipases, and esterases (43–45). The residues constituting the putative active site are conserved among other iflaviruses that have P domains, including DWV, VDV-1, and Kakugo virus (20, 46, 47). However, the iflaviruses Sacbrood and *Perina nuda* virus lack P domains altogether (48, 49). Catalytic activity of the putative active site might be required for the virions to escape from endosomes in a manner analogous to the lipase activity present in the N-terminal domain of capsid proteins of parvoviruses (50). There are five additional conserved residues located in the vicinity of the putative active site in strand β 1 and loops connecting strands β 1- β 2 and β 2- β 3 (Fig. 3C). This is in contrast to the overall 12% sequence identity

TABLE 3 Comparison of size and volume of SBPV particles determined in crystal forms 1 and 2

| Crystal form | Mean virion radius (\AA) ^a | Virion vol (\AA^3) ^b |
|--------------|--|--|
| 1 | 140 | 6.385×10^6 |
| 2 | 139 | 6.386×10^6 |

^a Determined as distance of the center of mass of the icosahedral asymmetric unit from the particle center.

^b Volume of virion cavity calculated based on virion structures. The space occupied by the unstructured parts of the capsid proteins located on the inside of the capsid was calculated based on average amino acid volumes and subtracted from the cavity volume.

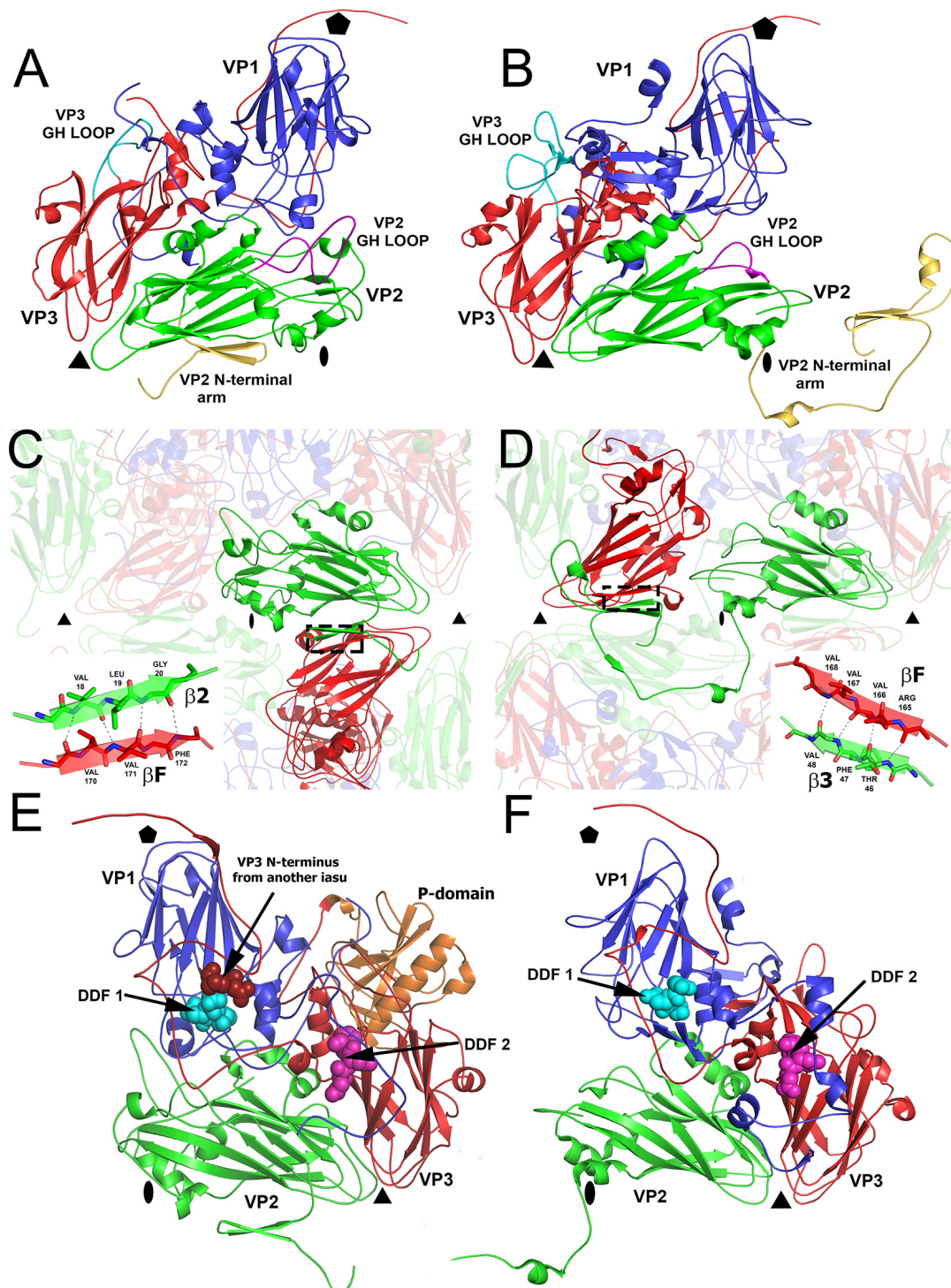


FIG 5 Comparison of SBPV structure to that of dicistrovirus TrV. (A and B) Cartoon representations of icosahedral asymmetric units of SBPV (A) and TrV (B). VP1 subunits are shown in blue, VP2 in green, and VP3 in red. The GH loop of VP2 is highlighted in magenta, the GH loop of VP3 is in cyan, and the N-terminal arms of VP2 are in yellow. (C and D) Domain swapping between SBPV (C) and TrV (D) N-terminal arms of VP2 subunits that mediate interpentamer interactions. The insets show details of hydrogen bonds between $\beta 2$ of VP2 and βF of VP3. (E and F) Location of DDF sequences, which might be involved in the cleavage of VP0 to VP4 and VP3, on the inside of the capsid of SBPV (E) and TrV (F).

of the P domains. The conservation of the residues reinforces the possibility that they may constitute a receptor or substrate-binding site. Furthermore, a similar conserved patch of residues in P domains of noroviruses was shown to bind glycans (51, 52). Additional experiments are required to identify the putative receptor of SBPV and to determine whether the catalytic triad cleaves it.

The DALI server was used to identify structures similar to the P domain (Table 2) (53). Most of the top hits were domains of virus capsid proteins that are exposed on the virion surface and therefore might be involved in receptor binding or cell entry. A common feature of these domains is a core formed of β -strands that is in some cases complemented by one or more short α -helices located at the periphery of the domain (Fig. 4). Furthermore, the P domains were also found in plant picorna-like viruses from the family *Tombusviridae* (54). In these species, however, the protrusions exhibit a β -jellyroll fold. Even though the surface domains could be identified in the DALI search, the structures of the domains are quite different and cannot be meaningfully superimposed. The surface domains were identified in viruses from the families *Tombusviridae*, *Nodaviridae*, *Hepeviridae*, and *Astroviridae* (54–57). All these viruses have positive-sense single-stranded RNA (ssRNA) genomes and similar overall virion architectures. It is therefore possible that a common ancestor of these viruses contained the P domain. However, the P domains were retained in the evolution of only some of the viruses.

Putative SBPV integrin receptor binding site. Currently there is no information about the cell entry of honeybee viruses, and the putative receptors remain to be identified. However, the VP2 subunit of SBPV contains the integrin recognition motif Arg-Gly-Asp (RGD) in the GH loop (Fig. 1C). The GH loop is exposed on the virion surface in crystal form 1 but is partly covered by the P domain in crystal form 2 (Fig. 2A and B). Integrins serve as cell entry receptors for numerous viruses, including human picornaviruses such as the foot-and-mouth disease virus (FMDV) and several parechoviruses (58–60). The RGD motif within FMDV is located in the VP2 subunit, similar to the case with SBPV, although closer to the icosahedral 2-fold axis (Fig. 1C). The RGD motif is not conserved across different iflaviruses and may confer specific tissue tropism to SBPV. Even though honeybees encode a number of integrins (61), their involvement in virus cell entry has not been demonstrated so far.

Decreased pH does not induce formation of SBPV A particles. Picornaviruses enter cells through receptor-mediated endocytosis. The receptor binding and low pH of endosomes were shown to trigger the formation of expanded A particles and the subsequent genome release of many picornaviruses (62). The A particles are characterized by a 5 to 10% increase in virion radius and the formation of holes in the capsid (42, 63–66). However, the SBPV virion structures determined at pH 6.5 and 4.5 are nearly identical in size (Table 3). Therefore, it appears that the pH (4.5) of the crystallization condition was not sufficient to induce formation of the SBPV A particles. The induction of SBPV genome release might require binding to a receptor, or iflaviruses might use an entirely different mechanism for genome release.

Comparison to virion structures of dicistroviruses. The most notable difference between SBPV and structurally characterized dicistroviruses, besides the P domain, is in the positioning of the N-terminal arm of the VP2 protein, which contributes to the interpentamer contacts within the capsid (Fig. 5A to D). In SBPV, two β -strands from the N-terminal arm of VP2 extend the β -sheet

CHEF of a VP3 from the neighboring pentamer (Fig. 5C). In contrast, in dicistroviruses represented by TrV and cricket paralysis virus (CrPV), the N-terminal arm of the VP2 subunit reaches around an icosahedral 2-fold axis into the neighboring pentamer, approaches a 3-fold axis, and forms two β -strands that extend the β -sheet CHEF of a VP3 subunit from the same pentamer (Fig. 5D) (67, 68). Thus, the VP2 N-terminal arms of SBPV and dicistroviruses mediate interactions between VP2 and VP3 subunits in different relative positions within their virions. However, the type of interaction, i.e., extension of the β -sheet CHEF of VP3, is the same for both the viruses, representing domain swapping of the VP2 N-terminal arms. It was speculated previously that the observation of domain swapping among homologous complexes is indicative of hinge movements of structural units connected by the swapped domains. The alternative placements of the N-terminal arms of VP2 subunits therefore indicate that pentamers of capsid proteins could move relative to each other.

Additional differences between SBPV and dicistroviruses can be found on the capsid surface. The RGD containing the GH loop of the SBPV VP2 subunit contains 30 residues, while in TrV and CrPV it is only 17 residues long (Fig. 5A and B) (67, 68). The SBPV loop therefore elevates higher above the surface of the virion, which might be required for binding to the putative integrin receptor (Fig. 1C). On the other hand, the GH loop of the VP3 subunit is longer in TrV, containing 36 residues in comparison to 24 in SBPV (Fig. 5A and B) (68).

The maturation of capsids of viruses from the order *Picornavirales* is connected to a cleavage of capsid protein VP4 from the N terminus of a precursor subunit, called VP0. In picornaviruses, VP0 cleavage generates the proteins VP4 and VP2, while it was suggested that in iflaviruses the precursor cleavage produces VP4 and VP3 (67, 68). It has been proposed that a conserved Asp-Asp-Phe (DDF) motif, present in parts of capsid proteins that are exposed to the virion cavity, is involved in the VP0 cleavage (67–69). The dicistroviruses CrPV and TrV contain the DDF sequence in a loop immediately following β -strand I of VP1, while TrV has an additional DDF sequence, in a loop following β -strand I of VP3 (Fig. 5F) (67, 68). SBPV also has two DDF sequences. One is in VP1, residues 226 to 228, and the second one is formed by residues 239 to 241 of VP3 (Fig. 5E). Therefore, the locations of the DDF sequences in SBPV are similar to those in TrV (Fig. 5E and F). The DDF site in VP1 subunit of SBPV is located within 4 Å of the N terminus of VP3 subunit from a neighboring protomer, suggesting that it might mediate the VP0 maturation cleavage (Fig. 5E).

Absence of a hydrophobic pocket in VP1. The VP1 subunits of enteroviruses and several other vertebrate picornaviruses were indicated to contain a hydrophobic pocket that might bind a putative lipid-like molecule called the “pocket factor” (70, 71). Pocket factor mimetics that bind into the VP1 pocket with high affinity were shown to inhibit the infection of some picornaviruses (72–75). However, such a hydrophobic pocket is not formed within the VP1 subunits of SBPV. This suggests that capsid binding inhibitors may not be effective as antivirals against honeybee viruses. However, compounds targeting the putative His-Ser-Asp catalytic or receptor binding site in the P domain may prevent the infection of iflaviruses containing P domains.

ACKNOWLEDGMENTS

We thank Jiří Svoboda for technical assistance with pupa preparation. We thank the beamline scientists at SLS and Soleil synchrotrons for their outstanding technical assistance with crystal screening and data collection. We thank Christian Tellgren-Roth from LifeSciLabs at Uppsala University, Sweden, for assembling virus genome sequences and Emilia Semberg at SLU for technical assistance. We thank Jana Moravcová for her help with the preparation of the manuscript for submission. We thank Charles Sabin for his help with preparation of the figure depicting the genome of SBPV.

This research was carried out under the project CEITEC 2020 (LQ1601) with financial support from the Ministry of Education, Youth and Sports of the Czech Republic under National Sustainability Program II. We acknowledge the CF Cryo-Electron Microscopy and Tomography, CF X-ray Diffraction and Bio-SAXS, and CF Biomolecular Interactions and Crystallization supported by the CIISB research infrastructure (LM2015043 funded by MEYS CR) for their support with obtaining scientific data presented in this paper. The research leading to these results received funding from the European Research Council under the European Union's Seventh Framework Program (FP/2007-2013)/ERC Grant Agreement no. 355855' and from EMBO installation grant no. 3041 to Pavel Plevka.

FUNDING INFORMATION

This work, including the efforts of Pavel Plevka, was funded by EC | European Research Council (ERC) (355855). This work, including the efforts of Pavel Plevka, was funded by European Molecular Biology Organization (EMBO) (3041).

REFERENCES

- Allsopp MH, de Lange WJ, Veldtman R. 2008. Valuing insect pollination services with cost of replacement. *PLoS One* 3:e3128. <http://dx.doi.org/10.1371/journal.pone.0003128>.
- Biesmeijer JC, Roberts SP, Reemer M, Ohlemuller R, Edwards M, Peeters T, Schaffers AP, Potts SG, Kleukers R, Thomas CD, Settele J, Kunin WE. 2006. Parallel declines in pollinators and insect-pollinated plants in Britain and the Netherlands. *Science* 313:351–354. <http://dx.doi.org/10.1126/science.1127863>.
- Vanengelsdorp D, Meixner MD. 2010. A historical review of managed honey bee populations in Europe and the United States and the factors that may affect them. *J Invertebr Pathol* 103(Suppl 1):S80–S95.
- Dainat B, Vanengelsdorp D, Neumann P. 2012. Colony collapse disorder in Europe. *Environ Microbiol Rep* 4:123–125. <http://dx.doi.org/10.1111/j.1758-2229.2011.00312.x>.
- van Engelsdorp D, Hayes J, Jr, Underwood RM, Pettis J. 2008. A survey of honey bee colony losses in the U.S., fall 2007 to spring 2008. *PLoS One* 3:e4071. <http://dx.doi.org/10.1371/journal.pone.0004071>.
- Smith KM, Loh EH, Rostal MK, Zambrana-Torrel CM, Mendiola L, Daszak P. 2013. Pathogens, pests, and economics: drivers of honey bee colony declines and losses. *Ecohealth* 10:434–445. <http://dx.doi.org/10.1007/s10393-013-0870-2>.
- Chen YP, Siede R. 2007. Honey bee viruses. *Adv Virus Res* 70:33–80. [http://dx.doi.org/10.1016/S0065-3527\(07\)70002-7](http://dx.doi.org/10.1016/S0065-3527(07)70002-7).
- Vanengelsdorp D, Evans JD, Saegerman C, Mullin C, Haubruge E, Nguyen BK, Frazier M, Frazier J, Cox-Foster D, Chen Y, Underwood R, Tarpy DR, Pettis JS. 2009. Colony collapse disorder: a descriptive study. *PLoS One* 4:e6481. <http://dx.doi.org/10.1371/journal.pone.0006481>.
- Williams GR, Tarpy DR, vanEngelsdorp D, Chauzat MP, Cox-Foster DL, Delaplane KS, Neumann P, Pettis JS, Rogers RE, Shutler D. 2010. Colony collapse disorder in context. *Bioessays* 32:845–846. <http://dx.doi.org/10.1002/bies.201000075>.
- Berthoud HIA, Haueter M, Radloff S, Neumann P. 2010. Virus infections and winter losses of honey bee colonies (*Apis mellifera*). *J Apic Res* 49:60–65. <http://dx.doi.org/10.3896/IBRA.1.49.1.08>.
- Genersh EviD, W, Kaatz H, Schroeder A, Otten C, Buchler R, Berg S, Ritter W, Muhlen W, Gisder S, Meixner M, Leibig G, Rosenkranz P. 2010. The German bee monitoring project: a long term study to understand periodically high winter losses of honey bee colonies. *Adipologie* 41:332–352.
- Bailey L, Woods RD. 1974. Three previously undescribed viruses from the honey bee. *J Gen Virol* 25:175–186. <http://dx.doi.org/10.1099/0022-1317-25-2-175>.
- Carreck NL BB, Wilson JK, Allen MF. 2005. The epidemiology of slow paralysis virus in honey bee colonies infested by *Varroa destructor* in the UK, p 32–33. Proceedings of XXXIXth International Apicultural Congress, Dublin, Ireland.
- Santillan-Galicia MT, Ball BV, Clark SJ, Alderson PG. 2010. Transmission of deformed wing virus and slow paralysis virus to adult bees (*Apis mellifera* L.) by *Varroa destructor*. *J Apic Res* 49:141–148. <http://dx.doi.org/10.3896/IBRA.1.49.2.01>.
- de Miranda JR, Dainat B, Locke B, Cordoni G, Berthoud H, Gauthier L, Neumann P, Budge GE, Ball BV, Stoltz DB. 2010. Genetic characterization of slow bee paralysis virus of the honeybee (*Apis mellifera* L.). *J Gen Virol* 91:2524–2530. <http://dx.doi.org/10.1099/vir.0.022434-0>.
- Fürst MA, McMahon DP, Osborne JL, Paxton RJ, Brown MJ. 2014. Disease associations between honeybees and bumblebees as a threat to wild pollinators. *Nature* 506:364–366. <http://dx.doi.org/10.1038/nature12977>.
- McMahon DP, Fürst MA, Caspar J, Theodorou P, Brown MJ, Paxton RJ. 3 March 2015. A sting in the spit: widespread cross-infection of multiple RNA viruses across wild and managed bees. *J Anim Ecol* <http://dx.doi.org/10.1111/1365-2656.12345>.
- Le Gall O, Christian P, Fauquet CM, King AM, Knowles NJ, Nakashima N, Stanway G, Gorbalenya AE. 2008. Picornavirales, a proposed order of positive-sense single-stranded RNA viruses with a pseudo-T = 3 virion architecture. *Arch Virol* 153:715–727. <http://dx.doi.org/10.1007/s00705-008-0041-x>.
- Zhang J, Feng J, Liang Y, Chen D, Zhou ZH, Zhang Q, Lu X. 2001. Three-dimensional structure of the Chinese Sacbrood bee virus. *Sci China C Life Sci* 44:443–448. <http://dx.doi.org/10.1007/BF02879612>.
- Lanzi G, de Miranda JR, Boniotti MB, Cameron CE, Lavazza A, Capucci L, Camazine SM, Rossi C. 2006. Molecular and biological characterization of deformed wing virus of honeybees (*Apis mellifera* L.). *J Virol* 80:4998–5009. <http://dx.doi.org/10.1128/JVI.80.10.4998-5009.2006>.
- Geng P, Li W, Lin L, de Miranda JR, Emrich S, An L, Terenius O. 2014. Genetic characterization of a novel iflavivirus associated with vomiting disease in the Chinese oak silkworm *Antheraea pernyi*. *PLoS One* 9:e92107. <http://dx.doi.org/10.1371/journal.pone.0092107>.
- de Miranda JR, Bailey L, Ball BV, Blanchard P, Budge G, Chejanovsky N, Chen Y-P, Gauthier L, Genersch E, De Graaf D, Ribière M, Ryabov E, De Smet L, van der Steen JJM. 2013. Standard methods for *Apis mellifera* pest and pathogen research. In Dietemann V, Ellis JD, Neumann P (ed), *The COLOSS BEEBOOK*, vol II. IBRA, Treforest, United Kingdom.
- Newman J. 2006. A review of techniques for maximizing diffraction from a protein crystal in stilla. *Acta Crystallogr D Biol Crystallogr* 62:27–31. <http://dx.doi.org/10.1107/S0907444905032130>.
- Tong L, Rossmann MG. 1997. Rotation function calculations with GLRF program. *Methods Enzymol* 276:594–611. [http://dx.doi.org/10.1016/S0076-6879\(97\)76080-4](http://dx.doi.org/10.1016/S0076-6879(97)76080-4).
- Brunger AT. 2007. Version 1.2 of the Crystallography and NMR system. *Nat Protoc* 2:2728–2733. <http://dx.doi.org/10.1038/nprot.2007.406>.
- Kleywegt GJ, Read RJ. 1997. Not your average density. *Structure* 5:1557–1569. [http://dx.doi.org/10.1016/S0969-2126\(97\)00305-5](http://dx.doi.org/10.1016/S0969-2126(97)00305-5).
- Kleywegt GJ, Jones TA. 1999. Software for handling macromolecular envelopes. *Acta Crystallogr D Biol Crystallogr* 55:941–944. <http://dx.doi.org/10.1107/S0907444999001031>.
- Kleywegt GJ. 1999. Experimental assessment of differences between related protein crystal structures. *Acta Crystallogr D Biol Crystallogr* 55:1878–1884. <http://dx.doi.org/10.1107/S0907444999010495>.
- Cowtan K. 2006. The Buccaneer software for automated model building. 1. Tracing protein chains. *Acta Crystallogr D Biol Crystallogr* 62:1002–1011. <http://dx.doi.org/10.1107/S0907444906022116>.
- Cowtan K. 2008. Fitting molecular fragments into electron density. *Acta Crystallogr D Biol Crystallogr* 64:83–89. <http://dx.doi.org/10.1107/S0907444907033938>.
- Jones TA, Zou JY, Cowan SW, Kjeldgaard M. 1991. Improved methods for building protein models in electron density maps and the location of errors in these models. *Acta Crystallogr A* 47(Part 2):110–119.
- Emsley P, Cowtan K. 2004. Coot: model-building tools for molecular graphics. *Acta Crystallogr D Biol Crystallogr* 60:2126–2132. <http://dx.doi.org/10.1107/S0907444904019158>.
- Afonine PV, Grosse-Kunstleve RW, Echols N, Headd JJ, Moriarty NW,

- Mustyakimov M, Terwilliger TC, Urzhumtsev A, Zwart PH, Adams PD. 2012. Towards automated crystallographic structure refinement with phenix.refine. *Acta Crystallogr D Biol Crystallogr* 68:352–367. <http://dx.doi.org/10.1107/S0907444912001308>.
34. McCoy AJ, Grosse-Kunstleve RW, Adams PD, Winn MD, Storoni LC, Read RJ. 2007. Phaser crystallographic software. *J Appl Crystallogr* 40: 658–674. <http://dx.doi.org/10.1107/S0021889807021206>.
35. Winn MD, Ballard CC, Cowtan KD, Dodson EJ, Emsley P, Evans PR, Keegan RM, Krissinel EB, Leslie AG, McCoy A, McNicholas SJ, Murshudov GN, Pannu NS, Pottertton EA, Powell HR, Read RJ, Vagin A, Wilson KS. 2011. Overview of the CCP4 suite and current developments. *Acta Crystallogr D Biol Crystallogr* 67:235–242. <http://dx.doi.org/10.1107/S0907444910045749>.
36. Brunger AT, Adams PD, Clore GM, DeLano WL, Gros P, Grosse-Kunstleve RW, Jiang JS, Kuszewski J, Nilges M, Pannu NS, Read RJ, Rice LM, Simonson T, Warren GL. 1998. Crystallography & NMR system: a new software suite for macromolecular structure determination. *Acta Crystallogr D Biol Crystallogr* 54:905–921.
37. Rossmann MG, Arnold E, Erickson JW, Frankenberger EA, Griffith JP, Hecht HJ, Johnson JE, Kamer G, Luo M, Mosser AG, Rueckert RR, Sherry B, Vriend G. 1985. Structure of a human common cold virus and functional relationship to other picornaviruses. *Nature* 317:145–153. <http://dx.doi.org/10.1038/317145a0>.
38. Katpally U, Voss NR, Cavazza T, Taube S, Rubin JR, Young VL, Stuckey J, Ward VK, Virgin HW, IV, Wobus CE, Smith TJ. 2010. High-resolution cryo-electron microscopy structures of murine norovirus 1 and rabbit hemorrhagic disease virus reveal marked flexibility in the receptor binding domains. *J Virol* 84:5836–5841. <http://dx.doi.org/10.1128/JVI.00314-10>.
39. Taube S, Rubin JR, Katpally U, Smith TJ, Kendall A, Stuckey JA, Wobus CE. 2010. High-resolution x-ray structure and functional analysis of the murine norovirus 1 capsid protein protruding domain. *J Virol* 84: 5695–5705. <http://dx.doi.org/10.1128/JVI.00316-10>.
40. Prasad BV, Hardy ME, Dokland T, Bella J, Rossmann MG, Estes MK. 1999. X-ray crystallographic structure of the Norwalk virus capsid. *Science* 286:287–290. <http://dx.doi.org/10.1126/science.286.5438.287>.
41. Bergelson JM, Coyne CB. 2013. Picornavirus entry. *Adv Exp Med Biol* 790:24–41. http://dx.doi.org/10.1007/978-1-4614-7651-1_2.
42. Fuchs R, Blaas, D. 2012. Productive entry pathways of human rhinoviruses. *Adv Virol* 2012:826301.
43. Dodson G, Wlodawer A. 1998. Catalytic triads and their relatives. *Trends Biochem Sci* 23:347–352. [http://dx.doi.org/10.1016/S0968-0004\(98\)01254-7](http://dx.doi.org/10.1016/S0968-0004(98)01254-7).
44. Canaan S, Roussel A, Verger R, Cambillau C. 1999. Gastric lipase: crystal structure and activity. *Biochim Biophys Acta* 1441:197–204. [http://dx.doi.org/10.1016/S1388-1981\(99\)00160-2](http://dx.doi.org/10.1016/S1388-1981(99)00160-2).
45. Vaquero ME, Barriuso J, Martinez MJ, Prieto A. 2016. Properties, structure, and applications of microbial sterol esterases. *Appl Microbiol Biotechnol* 100: 2047–2061. <http://dx.doi.org/10.1007/s00253-015-7258-x>.
46. Ongus JR, Peters D, Bonmatin JM, Bengsch E, Vlask JM, van Oers MM. 2004. Complete sequence of a picorna-like virus of the genus Iflavirus replicating in the mite Varroa destructor. *J Gen Virol* 85:3747–3755. <http://dx.doi.org/10.1099/vir.0.80470-0>.
47. Fujiyuki T, Takeuchi H, Ono M, Ohka S, Sasaki T, Nomoto A, Kubo T. 2004. Novel insect picorna-like virus identified in the brains of aggressive worker honeybees. *J Virol* 78:1093–1100. <http://dx.doi.org/10.1128/JVI.78.3.1093-1100.2004>.
48. Bailey L, Gibbs AJ, Woods RD. 1964. Sacbrood virus of the larval honey bee (*Apis Mellifera* Linnaeus). *Virology* 23:425–429. [http://dx.doi.org/10.1016/0042-6822\(64\)90266-1](http://dx.doi.org/10.1016/0042-6822(64)90266-1).
49. Wu CY, Lo CF, Huang CJ, Yu HT, Wang CH. 2002. The complete genome sequence of Perina nuda picorna-like virus, an insect-infecting RNA virus with a genome organization similar to that of the mammalian picornaviruses. *Virology* 294:312–323. <http://dx.doi.org/10.1006/viro.2001.1344>.
50. Farr GA, Zhang LG, Tattersall P. 2005. Parvoviral virions deploy a capsid-tethered lipolytic enzyme to breach the endosomal membrane during cell entry. *Proc Natl Acad Sci U S A* 102:17148–17153. <http://dx.doi.org/10.1073/pnas.0508477102>.
51. Cao S, Lou Z, Tan M, Chen Y, Liu Y, Zhang Z, Zhang XC, Jiang X, Li X, Rao Z. 2007. Structural basis for the recognition of blood group trisaccharides by norovirus. *J Virol* 81:5949–5957. <http://dx.doi.org/10.1128/JVI.00219-07>.
52. Hansman GS, Shahzad-Ul-Hussan S, McLellan JS, Chuang GY, Georgiev I, Shimoike T, Katayama K, Bewley CA, Kwong PD. 2012. Structural basis for norovirus inhibition and fucose mimicry by citrate. *J Virol* 86:284–292. <http://dx.doi.org/10.1128/JVI.05909-11>.
53. Holm L, Rosenstrom P. 2010. Dali server: conservation mapping in 3D. *Nucleic Acids Res* 38:W545–W549. <http://dx.doi.org/10.1093/nar/gkq366>.
54. Morgunova E, Dauter Z, Fry E, Stuart DI, Stel'mashchuk V, Mikhailov AM, Wilson KS, Vainshtein BK. 1994. The atomic structure of carnation mottle virus capsid protein. *FEBS Lett* 338:267–271. [http://dx.doi.org/10.1016/0014-5793\(94\)80281-5](http://dx.doi.org/10.1016/0014-5793(94)80281-5).
55. York RL, Yousefi PA, Bogdanoff W, Haile S, Tripathi S, DuBois RM. 2015. Structural, mechanistic, and antigenic characterization of the human astrovirus capsid. *J Virol* 90:2254–2263.
56. Chen NC, Yoshimura M, Guan HH, Wang TY, Misumi Y, Lin CC, Chuankhayan P, Nakagawa A, Chan SI, Tsukihara T, Chen TY, Chen CJ. 2015. Crystal structures of a piscine betanodavirus: mechanisms of capsid assembly and viral infection. *PLoS Pathog* 11:e1005203. <http://dx.doi.org/10.1371/journal.ppat.1005203>.
57. Guo YR, Hryc CF, Jakana J, Jiang H, Wang D, Chiu W, Zhong W, Tao YJ. 2014. Crystal structure of a nematode-infecting virus. *Proc Natl Acad Sci U S A* 111:12781–12786. <http://dx.doi.org/10.1073/pnas.1407122111>.
58. Jackson T, Mould AP, Sheppard D, King AM. 2002. Integrin alpha-beta1 is a receptor for foot-and-mouth disease virus. *J Virol* 76:935–941. <http://dx.doi.org/10.1128/JVI.76.3.935-941.2002>.
59. Boonyakiat Y, Hughes PJ, Ghazi F, Stanway G. 2001. Arginine-glycine-aspartic acid motif is critical for human parechovirus 1 entry. *J Virol* 75:10000–10004. <http://dx.doi.org/10.1128/JVI.75.20.10000-10004.2001>.
60. Kalynych S, Palkova L, Plevka P. 2016. The structure of human parechovirus 1 reveals an association of the RNA genome with the capsid. *J Virol* 90:1377–1386. <http://dx.doi.org/10.1128/JVI.02346-15>.
61. Weinstock GM et al. 2006. Insights into social insects from the genome of the honeybee *Apis mellifera*. *Nature* 443:931–949. <http://dx.doi.org/10.1038/nature05260>.
62. Groppelli E, Tuthill TJ, Rowlands DJ. 2010. Cell entry of the aphthovirus equine rhinitis A virus is dependent on endosome acidification. *J Virol* 84:6235–6240. <http://dx.doi.org/10.1128/JVI.02375-09>.
63. Bakker SE, Groppelli E, Pearson AR, Stockley PG, Rowlands DJ, Ranson NA. 2014. Limits of structural plasticity in a picornavirus capsid revealed by a massively expanded equine rhinitis A virus particle. *J Virol* 88:6093–6099. <http://dx.doi.org/10.1128/JVI.01979-13>.
64. Garriga D, Pickl-Herk A, Luque D, Wruss J, Caston JR, Blaas D, Verdaguer N. 2012. Insights into minor group rhinovirus uncoating: the X-ray structure of the HRV2 empty capsid. *PLoS Pathog* 8:e1002473. <http://dx.doi.org/10.1371/journal.ppat.1002473>.
65. Levy HC, Bostina M, Filman DJ, Hogle JM. 2010. Catching a virus in the act of RNA release: a novel poliovirus uncoating intermediate characterized by cryo-electron microscopy. *J Virol* 84:4426–4441. <http://dx.doi.org/10.1128/JVI.02393-09>.
66. Bostina M, Levy H, Filman DJ, Hogle JM. 2011. Poliovirus RNA is released from the capsid near a twofold symmetry axis. *J Virol* 85:776–783. <http://dx.doi.org/10.1128/JVI.00531-10>.
67. Tate J, Liljas L, Scotti P, Christian P, Lin T, Johnson JE. 1999. The crystal structure of cricket paralysis virus: the first view of a new virus family. *Nat Struct Biol* 6:765–774. <http://dx.doi.org/10.1038/11543>.
68. Squires G, Pous J, Agirre J, Rozas-Dennis GS, Costabel MD, Marti GA, Navaza J, Bressanelli S, Guerin DM, Rey FA. 2013. Structure of the Triatoma virus capsid. *Acta Crystallogr D Biol Crystallogr* 69:1026–1037. <http://dx.doi.org/10.1107/S0907444913004617>.
69. Agirre J, Aloria K, Arizmendi JM, Iloro I, Elortza F, Sanchez-Eugenía R, Marti GA, Neumann E, Rey FA, Guerin DM. 2011. Capsid protein identification and analysis of mature Triatoma virus (TrV) virions and naturally occurring empty particles. *Virology* 409:91–101. <http://dx.doi.org/10.1016/j.virol.2010.09.034>.
70. Smyth M, Pettitt T, Symonds A, Martin J. 2003. Identification of the pocket factors in a picornavirus. *Arch Virol* 148:1225–1233. <http://dx.doi.org/10.1007/s00705-002-0974-4>.
71. Hadfield AT, Lee W, Zhao R, Oliveira MA, Minor I, Rueckert RR, Rossmann MG. 1997. The refined structure of human rhinovirus 16 at 2.15 Å resolution: implications for the viral life cycle. *Structure* 5:427–441. [http://dx.doi.org/10.1016/S0969-2126\(97\)00199-8](http://dx.doi.org/10.1016/S0969-2126(97)00199-8).
72. Smith TJ, Kremer MJ, Luo M, Vriend G, Arnold E, Kamer G, Rossmann MG, McKinlay MA, Diana GD, Otto MJ. 1986. The site of attachment in human rhinovirus 14 for antiviral agents that inhibit uncoating. *Science* 233:1286–1293. <http://dx.doi.org/10.1126/science.3018924>.

73. Hadfield AT, Diana GD, Rossmann MG. 1999. Analysis of three structurally related antiviral compounds in complex with human rhinovirus 16. *Proc Natl Acad Sci U S A* **96**:14730–14735. <http://dx.doi.org/10.1073/pnas.96.26.14730>.
74. Grant RA, Hiremath CN, Filman DJ, Syed R, Andries K, Hogle JM. 1994. Structures of poliovirus complexes with anti-viral drugs: implications for viral stability and drug design. *Curr Biol* **4**:784–797.
75. Hiremath CN, Grant RA, Filman DJ, Hogle JM. 1995. Binding of the antiviral drug WIN51711 to the sabin strain of type 3 poliovirus: structural comparison with drug binding in rhinovirus 14. *Acta Crystallogr D Biol Crystallogr* **51**:473–489.
76. Guu TS, Liu Z, Ye Q, Mata DA, Li K, Yin C, Zhang J, Tao YJ. 2009. Structure of the hepatitis E virus-like particle suggests mechanisms for virus assembly and receptor binding. *Proc Natl Acad Sci U S A* **106**:12992–12997. <http://dx.doi.org/10.1073/pnas.0904848106>.
77. Chen R, Neill JD, Estes MK, Prasad BV. 2006. X-ray structure of a native calicivirus: structural insights into antigenic diversity and host specificity. *Proc Natl Acad Sci U S A* **103**:8048–8053. <http://dx.doi.org/10.1073/pnas.0600421103>.
78. Hopper P, Harrison SC, Sauer RT. 1984. Structure of tomato bushy stunt virus. V. Coat protein sequence determination and its structural implications. *J Mol Biol* **177**:701–713.
79. Kleywegt GJ, Brunger AT. 1996. Checking your imagination: applications of the free R value. *Structure* **4**:897–904. [http://dx.doi.org/10.1016/S0969-2126\(96\)00097-4](http://dx.doi.org/10.1016/S0969-2126(96)00097-4).
80. O’Flaherty S, Coffey A, Edwards R, Meaney W, Fitzgerald GF, Ross RP. 2004. Genome of staphylococcal phage K: a new lineage of Myoviridae infecting gram-positive bacteria with a low G+C content. *J Bacteriol* **186**:2862–2871. <http://dx.doi.org/10.1128/JB.186.9.2862-2871.2004>.

PAPER VIII



Cryo-EM study of slow bee paralysis virus at low pH reveals iflavirus genome release mechanism

Sergei Kalynych^a, Tibor Füzik^a, Antonín Přidal^b, Joachim de Miranda^c, and Pavel Plevka^{a,1}

^aStructural Virology, Central European Institute of Technology, Masaryk University, 62500 Brno, Czech Republic; ^bDepartment of Zoology, Fishery, Hydrobiology, and Apidology, Faculty of Agronomy, Mendel University in Brno, 61300 Brno, Czech Republic; and ^cDepartment of Ecology, Swedish University of Agricultural Sciences, 75651 Uppsala, Sweden

Edited by Michael G. Rossmann, Purdue University, West Lafayette, IN, and approved December 7, 2016 (received for review October 6, 2016)

Viruses from the family *Iflaviridae* are insect pathogens. Many of them, including slow bee paralysis virus (SBPV), cause lethal diseases in honeybees and bumblebees, resulting in agricultural losses. Iflaviruses have nonenveloped icosahedral virions containing single-stranded RNA genomes. However, their genome release mechanism is unknown. Here, we show that low pH promotes SBPV genome release, indicating that the virus may use endosomes to enter host cells. We used cryo-EM to study a heterogeneous population of SBPV virions at pH 5.5. We determined the structures of SBPV particles before and after genome release to resolutions of 3.3 and 3.4 Å, respectively. The capsids of SBPV virions in low pH are not expanded. Thus, SBPV does not appear to form “altered” particles with pores in their capsids before genome release, as is the case in many related picornaviruses. The egress of the genome from SBPV virions is associated with a loss of interpentamer contacts mediated by N-terminal arms of VP2 capsid proteins, which result in the expansion of the capsid. Pores that are 7 Å in diameter form around icosahedral threefold symmetry axes. We speculate that they serve as channels for the genome release. Our findings provide an atomic-level characterization of the genome release mechanism of iflaviruses.

electron microscopy | uncoating | honeybee | structure | virus

The family *Iflaviridae* includes arthropod pathogens, some of which infect economically important insects such as western honeybees (*Apis mellifera*), bumblebees, and silkworms (1). The iflavirus slow bee paralysis virus (SBPV) was identified in 1974 in the United Kingdom as a causative agent of honeybee colony mortality (2, 3). The related iflaviruses deformed wing virus and varroa destructor virus are found worldwide and, in combination with the ectoparasitic mite *Varroa destructor*, cause collapses of honeybee colonies (4). Despite the efficient transmission of SBPV by *Varroa destructor* (5), it only rarely causes disease in honeybees. However, it is common in bumblebees and solitary bees, whereas honeybees are probably an accidental secondary host (6). Honeybees are vital for agricultural productivity (7) and for maintaining the biodiversity of wild flowering plants (8). Furthermore, bumblebees and solitary bees are also important pollinators of specific commercial crops (3).

The family *Iflaviridae* belongs, together with *Dicistroviridae* and *Picornaviridae*, to the order *Picornavirales* of small non-enveloped viruses. The viruses from the family *Iflaviridae* have icosahedral capsids containing positive-sense ssRNA genomes about 9,500 nt long (9). These genomes encode a single polyprotein that is cotranslationally and posttranslationally cleaved into functional subunits. The capsid proteins originating from one polyprotein form a protomer—the basic building block of the capsid. The entire capsid consists of 60 such protomers, each of them composed of capsid proteins VP1–3, arranged in 12 pentamers (10). VP1 subunits are clustered around fivefold axes, and VP2 and VP3 form hetero-hexamers around icosahedral threefold axes. Unlike in the related picornaviruses and dicistroviruses, capsid protein VP3 of SBPV contains a C-terminal extension that folds into a globular protruding (P) domain

positioned at the virion surface (10–13). At neutral pH, the P domains form “crowns” on the virion surface around each fivefold axis of the virus. However, the P domains can shift 36 Å toward the threefold axes in a different solution composition. The P domain consists of a central twisted antiparallel β-sheet surrounded by shorter β-sheets and α-helix. The P domain contains an Asp–His–Ser catalytic triad that is, together with the four surrounding residues, conserved among iflaviruses. These residues may participate in receptor binding or provide the protease, lipase, or esterase activity required for the entry of the virus into the host cell (10).

Virus capsids have to be stable and compact to protect the virus RNA genome in the extracellular environment. However, the capsids also need to allow genome release at the appropriate moment after the contact of the virus with its host cell. Whereas there is limited information about the cell entry of iflaviruses, the related picornaviruses that infect vertebrates have been extensively studied as models for nonenveloped virus genome delivery. Picornaviruses usually enter the host cells by receptor-mediated endocytosis (14). The acidic environment of the endosomes triggers the uncoating of some picornaviruses, including minor group rhinoviruses (15, 16). In contrast, major group rhinoviruses, which use receptors from the Ig superfamily, are stable at low pH and their genome release requires receptor binding (17, 18). Regardless of the trigger mechanism, enterovirus genome release is preceded by the formation of an uncoating intermediate called the altered (A) particle that has an expanded capsid with pores, N termini of VP1 subunits exposed at the

Significance

Here, we present a structural analysis of the genome delivery of slow bee paralysis virus (SBPV) that can cause lethal infections of honeybees and bumblebees. The possibility of blocking virus genome delivery would provide a tool to prevent the spread of this viral pathogen. We describe the three-dimensional structures of SBPV particles in a low-pH buffer, which imitates the conditions that the virus is likely to encounter after cell entry. The low pH induces a reduction in the contacts between capsid proteins and a formation of pores within the capsid that may serve as channels for the genome release. Our work provides a structural characterization of iflavirus genome release.

Author contributions: P.P. designed research; S.K. and A.P. performed research; J.d.M. contributed new reagents/analytic tools; S.K., T.F., and P.P. analyzed data; and S.K. and P.P. wrote the paper.

The authors declare no conflict of interest.

This article is a PNAS Direct Submission.

Freely available online through the PNAS open access option.

Data deposition: Cryo-EM electron density maps of the low-pH SBPV virion and empty particle have been deposited in the Electron Microscopy Data Bank, <https://www.ebi.ac.uk/pdbe/emdb/> (accession numbers EMD-4063 and EMD-4064), and the fitted coordinates have been deposited in the Protein Data Bank, www.pdb.org (PDB ID codes 5LK7 and 5LK8, respectively).

¹To whom correspondence should be addressed. Email: pavel.plevka@ceitec.muni.cz.

This article contains supporting information online at www.pnas.org/lookup/suppl/doi:10.1073/pnas.1616562114/-DCSupplemental.

particle surface, and released VP4 subunits (19–24). Amphipathic sequences from the N termini of VP1 and myristoylated VP4 subunits interact with endosome membranes and enable the delivery of enterovirus genomes into the cell cytoplasm (25–27). It has been previously proposed that the enterovirus genome leaves the capsid via a pore located at a twofold icosahedral axis (19–21). The resulting empty capsids are conventionally referred to as B particles (19). Acidic pH in the endosomes also induces the genome release of the aphthoviruses foot and mouth disease virus (FMDV) and equine rhinitis A virus (ERAV) (28–30). However, aphthovirus genome release is not connected to capsid expansion or the formation of stable openings in the capsid. Furthermore, FMDV and ERAV empty capsids rapidly dissociate into pentamers after the genome release (28–30).

Genome release has also been studied for a triatoma virus (TrV), a member of the insect virus family *Dicistroviridae*. Cryo-EM reconstructions of genome-containing and empty TrV particles determined to resolutions of 15–22 Å demonstrated that the TrV empty particles are very similar to the native virions. After the genome release, the empty TrV capsids rapidly disassemble into pentamers (13).

Delivery of the genome into the cell cytoplasm constitutes a critical step in the life cycle of positive-sense ssRNA viruses. However, molecular details underlying the uncoating of iflaviruses are currently unknown. To describe the genome release mechanism of SBPV, we used cryo-EM to determine the structures of SBPV particles in a low-pH buffer mimicking conditions that the virus is likely to encounter during cell entry. By comparing the structures of full and empty particles, we determined that iflaviruses use an uncoating mechanism distinct from that of picornaviruses and dicistroviruses.

Results and Discussion

Low pH Induces SBPV Genome Release. The exposure of SBPV to pH 5.5 or lower induces a gradual release of the RNA genome from the virions (Fig. 1). Similar effects were previously described for the iflavirus sacbrood virus and several picornaviruses (31–33). The induction of genome release under acidic conditions implies that SBPV uses endosomes for cell entry (14). Alternatively, SBPV virions might be endocytosed, escape the endosomes, and subsequently uncoat in the cytoplasm. The nonphysiological pH 3.5 induced precipitation of SBPV particles that subsequently could not be observed in the cryo-EM images (Fig. 1A). Only 30–50% of SBPV virions released their genomes in the *in vitro* low-pH

conditions (Fig. 1B). It is possible that the binding of SBPV to currently unknown receptors *in vivo* might increase the efficiency of the genome release. The effect of the low pH on SBPV genome release was further verified by the observation that SBPV virions in a buffer with pH 5.5 release their genomes at 52.5 °C, whereas those in buffer with neutral pH at 54.2 °C (Fig. 1C). Thus, the stability of SBPV virions is similar to that of previously studied vertebrate picornaviruses (19, 22, 34).

SBPV Does Not Form A Particles Before Genome Release. The exposure of SBPV to pH 5.5 for 18 h resulted in a mixed population of full virions and empty particles (Fig. 1A). Reconstructions of the two forms were determined independently to resolutions of 3.3 and 3.4 Å, respectively (Fig. 2 and Table S1). The quality of the cryo-EM map was sufficient to enable the virion structure to be built, except for residues 1–12, 181–193, and 246–266 of VP1; 1–35, 191–201, and 261 of VP2; and 1, 73–75, 218–221, and 267–431 of VP3. The structure of the low-pH genome-containing virion is nearly identical to that of the neutral pH SBPV virion, which was characterized previously by X-ray crystallography (Fig. 2C and D) (10). The rmsd of the corresponding C α atoms of the two structures is 0.67 Å. The major capsid proteins VP1–3 have jellyroll β -sandwich folds with β -strands named according to the picornavirus convention B to I (Fig. 2H, Fig. S1, and Movie S1) (35). The two antiparallel β -sheets forming the β -sandwich fold contain the strands BIDG and CHEF. The loops are named according to the secondary structure elements they connect. The differences between the native and low-pH virion structures are restricted to the loops of the capsid proteins exposed at the particle surface, some of which are not resolved in the cryo-EM map of the low-pH virus (Fig. 2H). Subunit VP3 of SBPV has a C-terminal extension that forms a globular P domain (Figs. 2A, B, and H, and 3). It was shown previously that the P domains can occupy different locations at the virion surface (10). In agreement with one of the SBPV structures determined previously by X-ray crystallography, the P domains in the cryo-EM reconstruction are located close to the fivefold axes and form “crowns” at the virion surface (Fig. 2A–E). However, the volumes of the cryo-EM electron density map corresponding to the P domains lack high-resolution details, most likely because the P domains can attach to different positions at the capsid surface. This results in a smearing of the high-resolution details of the map (Fig. 2D and E), because the reconstruction process depends on an averaging of the images of many particles.

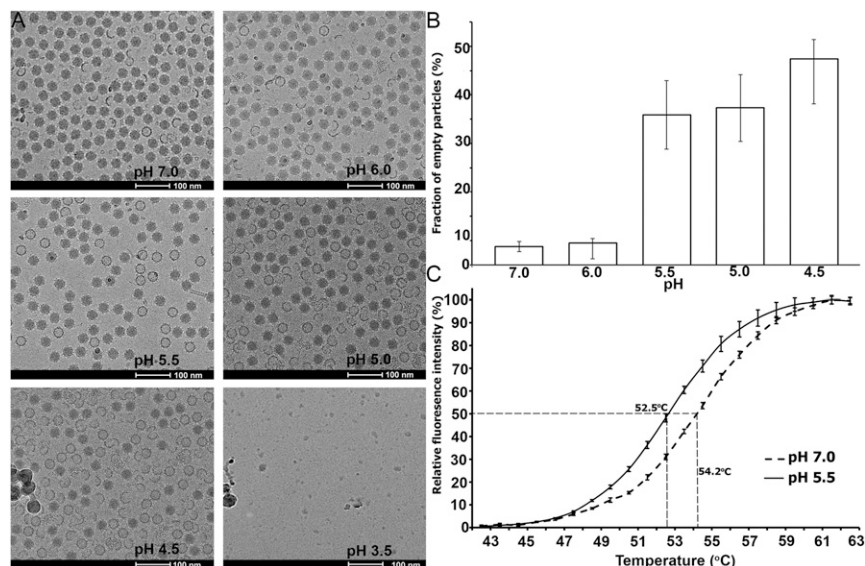


Fig. 1. Low pH triggers genome release of SBPV. (A) Cryo-electron micrographs of SBPV virions show increasing number of empty particles with decreasing pH. (B) Graph showing dependence of the fraction of empty particles on pH of the buffer. (C) Stability of SBPV virions at different pH values. SBPV virions were mixed with Sybr Green dye II and heated to indicated temperatures (*x* axis). The fluorescence signal increases as the dye binds to RNA that is released from thermally destabilized particles. The dashed line represents SBPV at neutral pH, and the full line represents SBPV at pH 5.5. Error bars indicate SDs of the measurements ($n = 3$). Please see *Materials and Methods* for details.

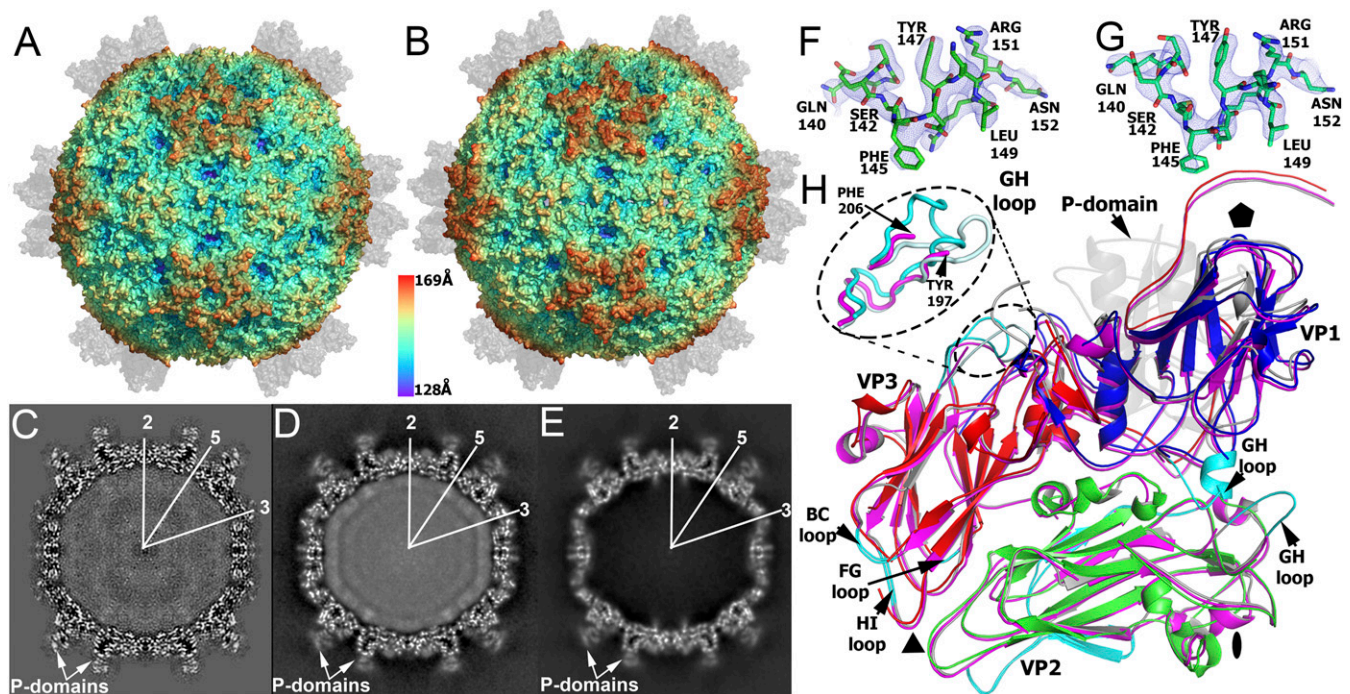


Fig. 2. Cryo-EM structures of full virions and empty SBPV particles at pH 5.5. Structures of SBPV at pH 5.5 before (A) and after genome release (B). The solvent-accessible surfaces are rainbow-colored based on their distance from the particle center. The positions of P domains that are not well resolved in the cryo-EM maps are indicated as gray transparent surfaces. Central slices of electron density maps are shown for SBPV virions at pH 6.5 (C), virions at pH 5.5 (D), and empty particle at pH 5.5 (E). White indicates high values of electron density. The positions of selected icosahedral symmetry axes are labeled. F and G show representative electron densities of SBPV virion and empty particle at resolutions of 3.3 and 3.4 Å, respectively. The maps are contoured at 2.0 σ . (H) Superposition of cartoon representations of icosahedral asymmetric units of native SBPV virion with VP1 shown in blue, VP2 in green, and VP3 in red. The structure of the P domain is shown in semitransparent gray. The structure of SBPV virion at pH 5.5 is shown in magenta, and that of the empty particle at pH 5.5 is in gray. Parts of the capsid proteins with the largest structural differences among the three structures are highlighted in the native virion in cyan.

Three-dimensional classification of images of full SBPV virions at pH 5.5 did not identify a subclass of particles with expanded capsids. Therefore, unlike in many picornaviruses (16, 24), the exposure of SBPV virions to pH 5.5 did not induce the transition of the virions to the A form.

The GH loop of SBPV subunit VP2, which harbors an RGD motif, is disordered in the low-pH virion structure (Fig. 2H). The RGD sequence enables proteins to bind to integrins (36), which are used as receptors by several viruses (37, 38). We previously speculated that SBPV may use integrins to infect honeybee cells (10). The low-pH-induced flexibility of the GH loop might enable the virus to detach from the integrin receptor after it enters the endosome. This could be required for subsequent interaction of the virion with the membrane of the endosome and delivery of the virus genome into the cell cytoplasm. Other parts of capsid proteins that contain residues that are not resolved in the low-pH virion structure are the BC, GH, and HI loops of VP3 and the N terminus and GH loop of VP1 (Fig. 2H).

Structure of the Genome in SBPV Virions at Neutral and Low pH. Although structures of the SBPV capsids at pH 6.5, determined by X-ray crystallography (10), and 5.5, determined by cryo-EM, are similar, there are differences in the distribution of the genomic RNA inside the particles (Fig. 2C and D). The genome of SBPV is a 9,500-nt-long ssRNA molecule that cannot entirely obey the icosahedral symmetry of the capsid. However, both X-ray crystallography and single-particle reconstruction used for SBPV structure determination use the icosahedral symmetry of the capsid that provides the dominant signal in the experimental data. Therefore, both the cryo-EM and crystallographic electron density maps contain information about the icosahedrally symmetrized distribution of the genome. In the neutral-pH SBPV

structure, the RNA is distributed uniformly within the capsid cavity (Fig. 2C). It was previously speculated that the disordered N-terminal parts of major capsid proteins VP1–3 of picornaviruses, which carry positively charged residues, are in direct contact with the genome (20). However, the N termini of the capsid proteins are fully determined in the crystal structure of SBPV (10), whereas the details of the RNA structure are not even partially resolved (Fig. 2C). Therefore, the SBPV genome appears to be folded in the lumen of the capsid without specific interactions with the surrounding capsid proteins. In contrast, in the low-pH SBPV virion structure, the RNA density is accumulated in a spherical shell with a radius of 110–90 Å and in a central part of the virion within a sphere with a radius of 80 Å (Fig. 2D). These two regions are separated by a spherical shell 90–80 Å in diameter with a lower RNA density. The SBPV RNA does not appear to form specific contacts with the capsid, similar to the previously studied A particles of enteroviruses (22, 39). No particles in the process of RNA release were observed in the cryo-micrographs of low-pH SBPV. Therefore, we speculate that the genome release from SBPV virion is stochastic and rapid with only short-lived genome release intermediates. The conformational changes of the capsid associated with the genome release (Fig. 3), described in detail below, result in alterations in the distribution of charge on the inside of the capsid (Fig. 4). Whereas the areas around the icosahedral threefold axes on the inside of the capsid are strongly negatively charged in the genome-containing virions, they become neutral in the empty particle (Fig. 4). The changes in the distribution of the RNA induced by the low pH and the alteration of charge distribution within the capsid might facilitate the release of the genome from the SBPV virion.

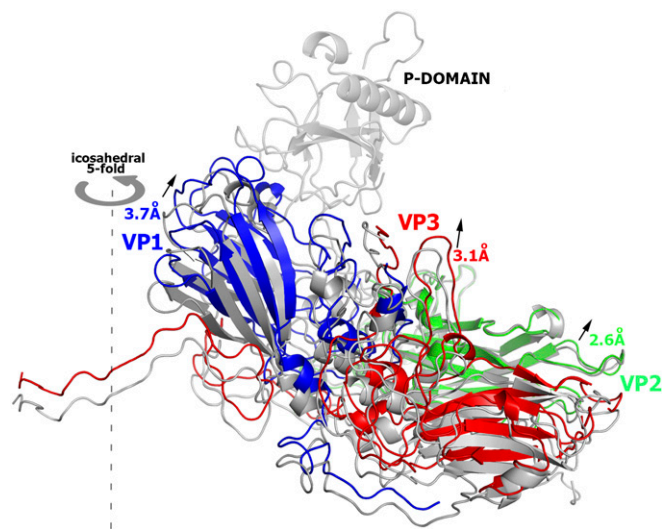


Fig. 3. Movements of capsid proteins associated with SBPV genome release. Capsid protein subunits of the empty SBPV particle are shown in blue, green, and red for VP1, VP2, and VP3, respectively. The P domain of VP3 from the empty capsid is not shown. Relative positions of the capsid proteins in the native SBPV virion are shown in gray. Shifts between the positions of the individual capsid proteins subunits in the two structures are indicated. The position of an icosahedral fivefold symmetry axis is shown as a dashed line.

Genome Release Is Associated with Formation of Pores at Threefold Axes of SBPV Capsid. The genome release of SBPV results in the formation of empty particles that are expanded compared with the native virions (Figs. 2 *A* and *B*, and 3). The radius of the particle, measured as the distance of the center of mass of a protomer from the particle center, changes from 133 Å in the native virus to 136 Å in the empty low-pH particle. Accordingly, the volume of the capsid increases from 6.4×10^6 to 7.2×10^6 Å³. The expansion of the capsid is achieved by movements of the capsid proteins VP1, VP2, and VP3 3.7, 2.6, and 3.1 Å away from the particle center, respectively (Fig. 3). In addition, the subunits VP1, VP2, and VP3 rotate 3.1°, 1.7°, and 1.9°, respectively. These shifts and rotations are approximately one-half of those previously reported for the conversion of enteroviruses to A particles (19, 20). The rotations together with small conformational changes to residues located at the periphery of the pentamers allow the capsid proteins to remain in contact after the expansion of the capsid.

The expansion of the SBPV capsid is connected to a loss of structure of the first 35 residues from the N terminus of VP2 (Fig. 5 *A* and *B*). The strands β 1 and β 2 of VP2, which in the native virion mediate contacts between pentamers of capsid protein protomers by extending the β -sheet CHEF of VP3 from the neighboring pentamer, are not resolved in the empty SBPV particle (Fig. 5 *A* and *C*). Furthermore, residues 218–221 of VP3 that form part of the interpentamer interface in the native virus are not structured in the empty particle (Fig. 5*B*). The conformational changes of the SBPV capsid linked to the genome release result in a reduction of the interpentamer contacts from 2,800 to 1,200 Å², which corresponds to a 68% decrease in the buried surface area (Fig. S2). The loss of the structure of the N-terminal arm of VP2 accounts for the removal of 800 Å² of the buried surface area of the interface. In contrast, the contacts within the protomer and within the pentamer are only reduced by 25 and 14%, respectively (Fig. S2). The reduction in the interface areas cannot be directly converted to binding energies, but the restricted interpentamer contacts indicate that the expanded SBPV particles are less stable than the native virions.

The movements of the capsid proteins away from the particle center and reduction in the interpentamer interfaces result in

the formation of pores around icosahedral threefold axes of the SBPV capsid (Figs. 4 and 5 *E* and *F*). Besides the subunit movements, the pores are enlarged by conformational changes of residues 126–129 from the DE loop and 221–224 from the HI loop of VP2 and 136–141 from the DE loop and 223–225 from the HI loop of VP3 that are located around the threefold axis (Fig. 5 *E* and *F*). Upon particle expansion, the loops move away from the threefold axis, giving rise to a 7-Å-diameter pore (Fig. 5*F*). The size of the pore is not sufficient to allow the release of ssRNA, which would require an aperture about 10 Å in diameter. However, the loops of capsid proteins located around the threefold axis are more flexible (average temperature factor, 70 Å²) than the rest of the capsid (average temperature factors, 50 Å²). Therefore, the loops at the border of the channels located at threefold axes might fold back and expand the pore as necessary for the release of the genome. Two additional small openings 1–2 Å in width are formed at the interface between the pentamers (Fig. 5*H*). In contrast, there are no pores in genome-containing SBPV virions both under neutral- and low-pH conditions (Fig. 5*G*). Because of their small size, the pores at the interface between the pentamers are unlikely to be channels for RNA egress. In addition, in some parts of the capsid the pores might be obscured by the N termini of VP2 subunits, which are not visible in the averaged cryo-EM reconstructions of the empty SBPV particles.

The strand β 3 that extends the β -sheet BIDG of the VP2 subunit is not structured in the empty particle, whereas it interacts with Glu-2 and Arg-3 from the N terminus of VP1 in the virions (Fig. 5*D*). The loss of the structure of the VP2 β 3 strand might contribute to alterations in the structure of the N terminus of VP1 as discussed below.

Several surface loops are not resolved in the cryo-EM electron density map of the empty particles, similar to the structure of full SBPV virions at pH 5.5 (Fig. 2*H*). However, the GH loop of VP3 (residues 185–210) has a different conformation in the empty particle than in the native virion, whereas it is partially disordered in the low-pH virion structure (Fig. 2*H*). The neutral-pH structure of the loop is stabilized by interactions with the C terminus and EF loop of VP1 and the GH loop from VP2 subunits from the neighboring icosahedral asymmetric unit. Residues 198–205 of the loop are disordered in the low-pH virion structure (Fig. 2*H*). However, in the empty particle, the GH loop is structured and interacts with the CD loop and α 2 from the same VP3 subunit and with DE and FG loops of VP1 from the neighboring icosahedral asymmetric unit. Therefore, the GH loop might stabilize interactions within the pentamer of capsid protein protomers. Similar to the low-pH SBPV virion structure, the high-resolution details are not resolved in the P-domain region of the cryo-EM map of the empty particle (Fig. 2 *D* and *E*).

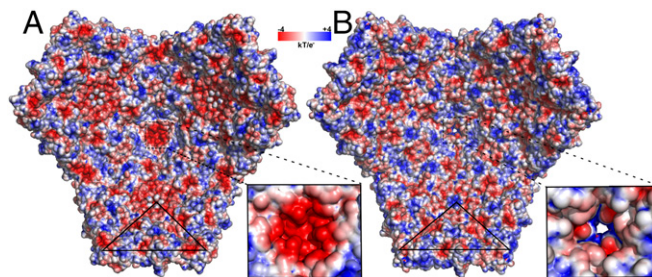


Fig. 4. Comparison of charge distribution on the inside of SBPV virion and empty particle. Comparison of electrostatic potential distribution on the inside of the native virion (*A*) and empty particle (*B*). Three pentamers of capsid protein protomers are displayed. The borders of a selected icosahedral asymmetric unit are highlighted with a black triangle. The *insets* show details of the electrostatic potential distribution around threefold symmetry axes.

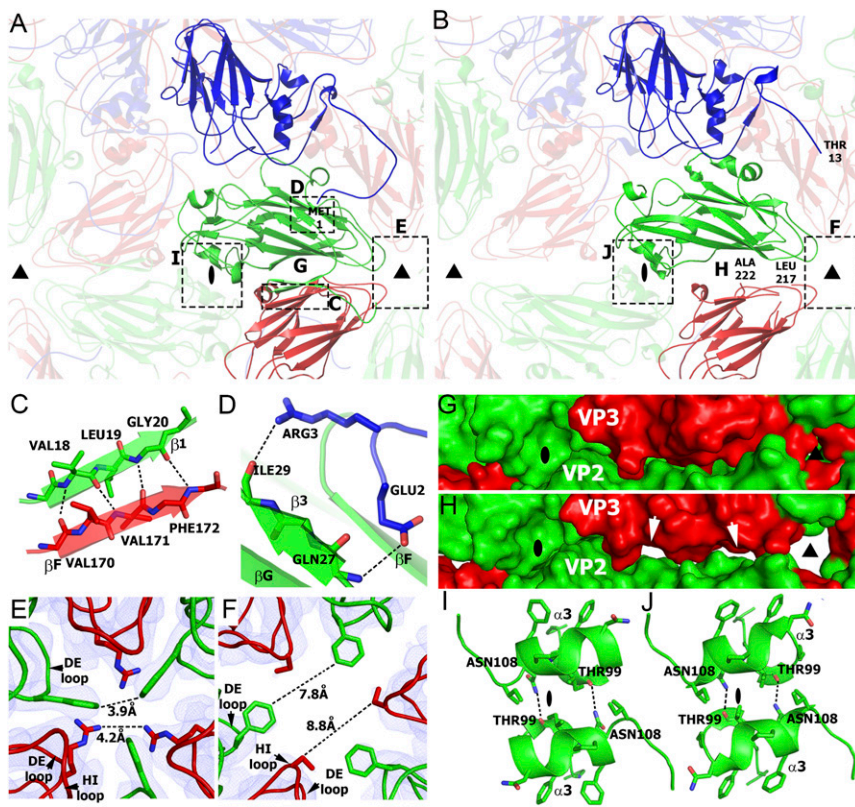


Fig. 5. Changes to the SBPV capsid structure associated with genome release. Cartoon representation of capsid of SBPV virion at neutral pH (A) and empty particle at pH 5.5 (B) viewed from the particle inside. VP1 subunits are shown in blue, VP2 in green, and VP3 in red. Selected subunits are shown in bright colors. Positions of icosahedral twofold and threefold axes are indicated by ovals and triangles, respectively. Dashed boxes outline areas displayed in higher details in indicated panels. (C) Interaction of $\beta 2$ of VP2 with βF of VP3 from neighboring pentamer in SBPV virions. Hydrogen bonds are shown as dashed black lines. The interaction is not present in the empty SBPV particle. (D) Interaction of N terminus of VP1 with $\beta 3$ of VP2 present only in native and low-pH SBPV virions. Comparison of interactions of residues around threefold symmetry axis of the capsid in native SBPV (E) and empty low-pH particle (F). Electron density map is contoured at 1.5 σ . Comparison of interface between pentamers of capsid protein protomers in SBPV virion (G) and empty particle (H). Interactions between $\alpha 3$ helices of VP2 subunits related by icosahedral twofold axis in SBPV virion (I) and empty particle (J).

SBPV Virions Do Not Have Liposome-Disrupting Activity. During cell entry, nonenveloped viruses have to breach a biological membrane to deliver their genomes to the cell cytoplasm. Previously, it has been shown that both myristoylated and unmodified VP4 minor capsid proteins (which are 60–80 residues long) of several picornaviruses and dicistroviruses can induce the lysis of liposomes (26, 40, 41). In contrast, the VP4 subunits of SBPV have been predicted to be only 20 residues long, and lack the myristoylation signal sequence (42). In silico analysis predicts that residues 4–21 of VP4 of SBPV form an amphipathic α -helix in which the polar and hydrophobic residues are segregated to the opposite sides (Fig. S3A) (43, 44). Helices with this type of charge distribution have been shown to interact with membranes (45). Nevertheless, electron density corresponding to the VP4 subunits could not be identified in the SBPV virion structures (10). Furthermore, mass spectrometry analysis [liquid chromatography–tandem mass spectrometry (LC-MS/MS)] shows that the SBPV virions contain at least some subunits in which VP4 was not cleaved from the N terminus of VP3 (Fig. S4). Therefore, it is not clear whether the VP4 peptides contribute to the delivery of the SBPV genome across the biological membrane.

We suggested previously that the P domains of SBPV and several other flaviviruses contain a putative catalytic triad Asp300–His283–Ser284 that might have esterase, protease, glycosidase, or lipase activity (10). However, in this study, the membrane lytic activity of SBPV could not be detected under neutral- or low-pH conditions on liposomes composed of phosphatidylcholine, phosphatidyl-ethanolamine, lysophosphatidylcholine, sphingomyelin, phosphatidyl-serine, and phosphatidyl-inositol (Fig. S3B). Thus, we can now exclude the possibility that the putative active site in the P domain cleaves the abovementioned lipids.

Comparison of Genome Release of I flaviviruses, Picornaviruses, and Dicistroviruses. Conformational changes of capsids associated with genome release were previously studied for viruses from the

families *Picornaviridae* and *Dicistroviridae* (13, 19–21, 30, 39). There are functionally important differences between the two families as well as with the genome release mechanism of SBPV described here. The uncoating of enteroviruses from the family *Picornaviridae* is preceded by the formation of expanded A particles (19–21, 23). The A particles contain two types of pores located at twofold and between twofold and fivefold symmetry axes of the capsids, have N termini of VP1 subunits exposed at the virion surface, and spontaneously release VP4 subunits (46, 47). The formation of enterovirus A particles is characterized by the movement of $\alpha 3$ helices from the VP2 subunits away from the icosahedral twofold axis, which results in the formation of a 9×20 -Å pore (22, 39). In contrast, the $\alpha 3$ helices of VP2 subunits remain tightly associated in the SBPV empty capsid (Fig. 5 I and J). The buried surface area between the two SBPV helices $\alpha 3$ is 800 \AA^2 in the native virus and 600 \AA^2 in the empty particle.

The N-terminal regions of VP1 subunits of enteroviruses contain sequences, which were proposed to form amphipathic α -helices that disrupt endosome membranes, and together with VP4 subunits enable translocation of the virus genome to the cytoplasm (26, 27, 41). Twelve residues from the N terminus of SBPV VP1 become disordered upon genome release (Fig. 5 A and B). However, the disordered peptide is not sufficiently long to reach the surface of the capsid or to interact with a lipid bilayer (48). In contrast, the disordered N termini of VP1 subunits of enteroviruses are about 60 residues long (19, 20). Moreover, a pore at the base of the canyon, which was shown to be the site of the externalization of the N termini of VP1 subunits in coxsackievirus A16 (19, 22), is not present in the empty particle of SBPV. Therefore, the structure of the SBPV empty particle together with the negative results of the liposome lysis experiment described above indicate that the N terminus of SBPV VP1 is unlikely to interact with membranes. The genome release of TrV from the family *Dicistroviridae* does not involve structural changes to the capsid before the genome release (13). However, the empty

capsids of TrV are compact and do not contain any pores that might serve as channels for genome release.

The conformational changes of iflavivirus capsid associated with genome release are distinct from those of both picornaviruses and dicistroviruses. Specific features of SBPV genome release are the loss of structure of the N termini of VP2 subunits and the formation of pores around the threefold icosahedral axes of symmetry of the capsid. Unlike in enteroviruses, the contacts between VP2 capsid proteins close to the icosahedral twofold axes are retained in the empty SBPV particle. SBPV virions do not form A particles, and the genome appears to be released through pores located at the threefold axes.

Materials and Methods

The propagation of SBPV in honeybee pupae and subsequent purification were carried out as described previously (10). Images were recorded in a FEI Titan Krios electron microscope operated at 300 kV with an FEI Falcon II camera. The particles were separated into two half-datasets for all of the

subsequent reconstruction steps to follow the “gold-standard” procedure for resolution determination (49). Three-dimensional refinement was carried out using the 3dautorefine procedure of RELION (50).

ACKNOWLEDGMENTS. We thank the Core Facility (CF) Cryo-Electron Microscopy and Tomography and CF Proteomics supported by the Czech Infrastructure for Integrative Structural Biology research infrastructure (LM2015043 funded by Ministry of Education, Youth and Sport of the Czech Republic) for their assistance in obtaining the scientific data presented in this paper. This research was carried out under the project Central European Institute of Technology 2020 (LQ1601). Access to computing and storage facilities owned by parties and projects contributing to the National Grid Infrastructure MetaCentrum, provided under the program “Projects of Large Infrastructure for Research, Development, and Innovations” (LM2010005), is greatly appreciated. Computational resources were provided by the IT4Innovations Centre of Excellence project (CZ.1.05/1.1.00/02.0070; LM2011033). The research leading to these results received funding from the European Research Council under the European Union’s Seventh Framework Program (FP/2007-2013)/ERC through Grant 355855 and from European Molecular Biology Organization installation Grant 3041 (to P.P.).

- Chen YP, Pettis JS, Collins A, Feldlaufer MF (2006) Prevalence and transmission of honeybee viruses. *Appl Environ Microbiol* 72(1):606–611.
- Bailey L, Woods RD (1974) Three previously undescribed viruses from the honey bee. *J Gen Virol* 25(2):175–186.
- Carreck NLBB, Wilson JK, Allen MF (2005) The epidemiology of slow paralysis virus in honey bee colonies infested by Varroa destructor in the UK. *Proceedings of XXXIXth International Apicultural Congress* (Document Transformation Technologies, Dublin), pp 32–33.
- Wilfert L, et al. (2016) Deformed wing virus is a recent global epidemic in honeybees driven by Varroa mites. *Science* 351(6273):594–597.
- Santillan-Galicia MT, Ball BV, Clark SJ, Alderson PG (2010) Transmission of deformed wing virus and slow paralysis virus to adult bees (*Apis mellifera* L.) by Varroa destructor. *J Apic Res* 49(2):141–148.
- Fürst MA, McMahon DP, Osborne JL, Paxton RJ, Brown MJ (2014) Disease associations between honeybees and bumblebees as a threat to wild pollinators. *Nature* 506(7488):364–366.
- Allsopp MH, de Lange WJ, Veldtman R (2008) Valuing insect pollination services with cost of replacement. *PLoS One* 3(9):e3128.
- Biesmeijer JC, et al. (2006) Parallel declines in pollinators and insect-pollinated plants in Britain and the Netherlands. *Science* 313(5785):351–354.
- Van Regenmortel MHV, Fauquet CM, Bishop DHL (1999) *Virus Taxonomy: Seventh Report of the International Committee on Taxonomy of Viruses* (Academic, San Diego).
- Kalynych S, et al. (2016) Virion structure of iflavivirus slow bee paralysis virus at 2.6-angstrom resolution. *J Virol* 90(16):7444–7455.
- Jiang P, Liu Y, Ma HC, Paul AV, Wimmer E (2014) Picornavirus morphogenesis. *Microbiol Mol Biol Rev* 78(3):418–437.
- Tate J, et al. (1999) The crystal structure of cricket paralysis virus: The first view of a new virus family. *Nat Struct Biol* 6(8):765–774.
- Squires G, et al. (2013) Structure of the Triatoma virus capsid. *Acta Crystallogr D Biol Crystallogr* 69(Pt 6):1026–1037.
- Fuchs R, Blaas D (2012) Productive entry pathways of human rhinoviruses. *Adv Virol* 2012:826301.
- Vázquez-Calvo A, Saiz JC, McCullough KC, Sobrino F, Martín-Acebes MA (2012) Acid-dependent viral entry. *Virus Res* 167(2):125–137.
- Neubauer C, Frasel L, Kuechler E, Blaas D (1987) Mechanism of entry of human rhinovirus 2 into HeLa cells. *Virology* 158(1):255–258.
- Hogle JM (2002) Poliovirus cell entry: Common structural themes in viral cell entry pathways. *Annu Rev Microbiol* 56:677–702.
- Tuthill TJ, Bubeck D, Rowlands DJ, Hogle JM (2006) Characterization of early steps in the poliovirus infection process: Receptor-decorated liposomes induce conversion of the virus to membrane-anchored entry-intermediate particles. *J Virol* 80(1):172–180.
- Garriga D, et al. (2012) Insights into minor group rhinovirus uncoating: The X-ray structure of the HRV2 empty capsid. *PLoS Pathog* 8(1):e1002473.
- Wang X, et al. (2012) A sensor-adaptor mechanism for enterovirus uncoating from structures of EV71. *Nat Struct Mol Biol* 19(4):424–429.
- Bostina M, Levy H, Filman DJ, Hogle JM (2011) Poliovirus RNA is released from the capsid near a twofold symmetry axis. *J Virol* 85(2):776–783.
- Shingler KL, et al. (2013) The enterovirus 71 A-particle forms a gateway to allow genome release: A cryoEM study of picornavirus uncoating. *PLoS Pathog* 9(3):e1003240.
- Huang Y, Hogle JM, Chow M (2000) Is the 135S poliovirus particle an intermediate during cell entry? *J Virol* 74(18):8757–8761.
- Lonberg-Holm K, Gosser LB, Kauer JC (1975) Early alteration of poliovirus in infected cells and its specific inhibition. *J Gen Virol* 27(3):329–342.
- Davis MP, et al. (2008) Recombinant VP4 of human rhinovirus induces permeability in model membranes. *J Virol* 82(8):4169–4174.
- Panjwani A, et al. (2014) Capsid protein VP4 of human rhinovirus induces membrane permeability by the formation of a size-selective multimeric pore. *PLoS Pathog* 10(8):e1004294.
- Fricks CE, Hogle JM (1990) Cell-induced conformational change in poliovirus: Externalization of the amino terminus of VP1 is responsible for liposome binding. *J Virol* 64(5):1934–1945.
- Baxt B, Bachrach HL (1980) Early interactions of foot-and-mouth disease virus with cultured cells. *Virology* 104(1):42–55.
- Curry S, et al. (1995) Viral RNA modulates the acid sensitivity of foot-and-mouth disease virus capsids. *J Virol* 69(1):430–438.
- Tuthill TJ, et al. (2009) Equine rhinitis A virus and its low pH empty particle: Clues towards an aphthovirus entry mechanism? *PLoS Pathog* 5(10):e1000620.
- Newman JFE, Brown F, Bailey L, Gibbs AJ (1973) Some physico-chemical properties of two honey-bee picornaviruses. *J Gen Virol* 19:405–409.
- Bailey L, Woods RD (1977) Two more small RNA viruses from honey bees and further observations on Sacbrood and acute bee-paralysis viruses. *J Gen Virol* 37:175–182.
- Prchla E, Kuechler E, Blaas D, Fuchs R (1994) Uncoating of human rhinovirus serotype 2 from late endosomes. *J Virol* 68(6):3713–3723.
- Levy HC, Bostina M, Filman DJ, Hogle JM (2010) Catching a virus in the act of RNA release: A novel poliovirus uncoating intermediate characterized by cryo-electron microscopy. *J Virol* 84(9):4426–4441.
- Rossmann MG, et al. (1985) Structure of a human common cold virus and functional relationship to other picornaviruses. *Nature* 317(6033):145–153.
- Barczyk M, Carracedo S, Gullberg D (2010) Integrins. *Cell Tissue Res* 339(1):269–280.
- Jackson T, Mould AP, Sheppard D, King AM (2002) Integrin alphabeta1 is a receptor for foot-and-mouth disease virus. *J Virol* 76(3):935–941.
- Shakeel S, et al. (2013) Structural and functional analysis of coxsackievirus A9 integrin $\alpha\beta 6$ binding and uncoating. *J Virol* 87(7):3943–3951.
- Ren J, et al. (2013) Picornavirus uncoating intermediate captured in atomic detail. *Nat Commun* 4:1929.
- Prchla E, Plank C, Wagner E, Blaas D, Fuchs R (1995) Virus-mediated release of endosomal content in vitro: Different behavior of adenovirus and rhinovirus serotype 2. *J Cell Biol* 131(1):111–123.
- Shukla A, Padhi AK, Gomes J, Banerjee M (2014) The VP4 peptide of hepatitis A virus ruptures membranes through formation of discrete pores. *J Virol* 88(21):12409–12421.
- Marc D, Drugeon G, Haenni AL, Girard M, van der Werf S (1989) Role of myristoylation of poliovirus capsid protein VP4 as determined by site-directed mutagenesis of its N-terminal sequence. *EMBO J* 8(9):2661–2668.
- Gautier R, Dougout D, Antony B, Drin G (2008) HELIQUEST: A web server to screen sequences with specific alpha-helical properties. *Bioinformatics* 24(18):2101–2102.
- Sharadadevi A, Sivakamasundari C, Nagaraj R (2005) Amphipathic alpha-helices in proteins: Results from analysis of protein structures. *Proteins* 59(4):791–801.
- Segrest JP, Jackson RL, Morrisett JD, Gotto AM, Jr (1974) A molecular theory of lipid-protein interactions in the plasma lipoproteins. *FEBS Lett* 38(3):247–258.
- Wien MW, Curry S, Filman DJ, Hogle JM (1997) Structural studies of poliovirus mutants that overcome receptor defects. *Nat Struct Biol* 4(8):666–674.
- Liu Y, et al. (2015) Structure and inhibition of EV-D68, a virus that causes respiratory illness in children. *Science* 347(6217):71–74.
- Sharpe HJ, Stevens TJ, Munro S (2010) A comprehensive comparison of transmembrane domains reveals organelle-specific properties. *Cell* 142(1):158–169.
- Scheres SH, Chen S (2012) Prevention of overfitting in cryo-EM structure determination. *Nat Methods* 9(9):853–854.
- Scheres SH (2012) A Bayesian view on cryo-EM structure determination. *J Mol Biol* 415(2):406–418.
- Shaikh TR, et al. (2008) SPIDER image processing for single-particle reconstruction of biological macromolecules from electron micrographs. *Nat Protoc* 3(12):1941–1974.
- Tang G, et al. (2007) EMAN2: An extensible image processing suite for electron microscopy. *J Struct Biol* 157(1):38–46.
- Rohou A, Grigorieff N (2015) CTFIND4: Fast and accurate defocus estimation from electron micrographs. *J Struct Biol* 192(2):216–221.
- Pettersen EF, et al. (2004) UCSF Chimera—a visualization system for exploratory research and analysis. *J Comput Chem* 25(13):1605–1612.
- Emsley P, Cowtan K (2004) Coot: Model-building tools for molecular graphics. *Acta Crystallogr D Biol Crystallogr* 60(Pt 12 Pt 1):2126–2132.
- Afonine PV, et al. (2012) Towards automated crystallographic structure refinement with phenix.refine. *Acta Crystallogr D Biol Crystallogr* 68(Pt 4):352–367.
- Kleywegt GJ, Jones TA (1994) Detection, delineation, measurement and display of cavities in macromolecular structures. *Acta Crystallogr D Biol Crystallogr* 50(Pt 2):178–185.

PAPER IX



Structure of deformed wing virus, a major honey bee pathogen

Karel Škubník^a, Jiří Nováček^a, Tibor Füzik^a, Antonín Přidal^b, Robert J. Paxton^c, and Pavel Plevka^{a,1}

^aStructural Virology, Central European Institute of Technology, Masaryk University, 62500 Brno, Czech Republic; ^bDepartment of Zoology, Fishery, Hydrobiology, and Apidology, Faculty of Agronomy, Mendel University in Brno, 613 00 Brno, Czech Republic; and ^cInstitute of Biology/Zoology, Martin Luther University Halle-Wittenberg, 06120 Halle, Germany

Edited by Wolfgang Baumeister, Max Planck Institute of Chemistry, Martinsried, Germany, and approved February 10, 2017 (received for review September 20, 2016)

The worldwide population of western honey bees (*Apis mellifera*) is under pressure from habitat loss, environmental stress, and pathogens, particularly viruses that cause lethal epidemics. Deformed wing virus (DWV) from the family *Iflaviridae*, together with its vector, the mite *Varroa destructor*, is likely the major threat to the world's honey bees. However, lack of knowledge of the atomic structures of iflaviruses has hindered the development of effective treatments against them. Here, we present the virion structures of DWV determined to a resolution of 3.1 Å using cryo-electron microscopy and 3.8 Å by X-ray crystallography. The C-terminal extension of capsid protein VP3 folds into a globular protruding (P) domain, exposed on the virion surface. The P domain contains an Asp-His-Ser catalytic triad that is, together with five residues that are spatially close, conserved among iflaviruses. These residues may participate in receptor binding or provide the protease, lipase, or esterase activity required for entry of the virus into a host cell. Furthermore, nucleotides of the DWV RNA genome interact with VP3 subunits. The capsid protein residues involved in the RNA binding are conserved among honey bee iflaviruses, suggesting a putative role of the genome in stabilizing the virion or facilitating capsid assembly. Identifying the RNA-binding and putative catalytic sites within the DWV virion structure enables future analyses of how DWV and other iflaviruses infect insect cells and also opens up possibilities for the development of antiviral treatments.

colony collapse disorder | virus | structure | *Apis mellifera* | honey bee

The western honey bee (*Apis mellifera*) plays a vital role in world agriculture by providing pollination services to diverse commercial crops, a service valued at US\$ 215 billion annually (1). In addition, honey bees pollinate numerous wild flowering plants, thereby supporting biodiversity (2, 3). However, over the past two decades, honey bees have suffered from elevated mortality in North America and Europe (4, 5). Colony losses have been associated with the exotic ectoparasitic mite *Varroa destructor*, which feeds on honey bee hemolymph, thereby vectoring numerous honey bee viral pathogens, in particular the iflavirus deformed wing virus (DWV). In the absence of varroa, DWV levels are low, and the virus causes asymptomatic infections. Varroa-infested colonies show elevated levels of DWV (6, 7). Symptoms associated with acute DWV infections include the death of pupae, as well as deformed wings, shortened abdomen, and cuticle discoloration of adult bees that die soon after pupation, causing colony collapse (6, 8). Indeed, winter colony mortality is strongly correlated with the presence of DWV, irrespective of the levels of varroa infestation (8, 9). DWV-induced loss of honey bees, coupled with a long-term decline in beekeeping, has become a serious threat to adequate provision of pollination services, threatening food security and ecosystem stability (1).

Viruses from the order *Picornavirales*, including the family *Iflaviridae*, have nonenveloped icosahedral virions that are about 30 nm in diameter (10). Iflavirus capsids protect 10,000-nt-long ssRNA genomes, which are translated into polyproteins that are cotranslationally and posttranslationally cleaved by viral proteases

to produce structural (capsid-forming) and nonstructural proteins (11). The major capsid proteins VP1, VP2, and VP3 originating from a single polyprotein form a protomer, the basic building block of the pseudo-T3 icosahedral capsid. The entire capsid consists of 60 such protomers, arranged in 12 pentamer units of 5 protomers each.

Previously, the structure of the iflavirus Chinese sacbrood virus was characterized to a resolution of 25 Å by cryo-electron microscopy. The structure confirmed the pseudo-T3 icosahedral symmetry of its capsid and a smooth outer surface of the virion (12). Recently, we determined the structure of the iflavirus slow bee paralysis virus (SBPV) to a resolution of 2.6 Å by X-ray crystallography (13). Despite its efficient transmission by *V. destructor*, SBPV infection is a rare disease of honey bees (14). The structure revealed that the C-terminal extension of capsid protein VP3 of SBPV forms a globular protruding (P) domain positioned at the virion surface. The P domain is anchored to the core of the VP3 subunit by a 23-residue-long flexible linker that allows the P domain to attach to different areas of the capsid (13). In addition, the P domain contains the putative active site Asp-His-Ser, which is conserved among several iflaviruses (13). Iflaviruses were also proposed to harbor short VP4 subunits consisting of only about 20 residues (11, 14); however, electron density

Significance

Honey bee populations in Europe and North America have been decreasing since the 1950s. Deformed wing virus (DWV), which is undergoing a worldwide epidemic, causes the deaths of individual honey bees and collapse of whole colonies. We determined three-dimensional structures of DWV at different conditions and show that the virus surface is decorated with protruding globular extensions of capsid proteins. The protruding domains contain a putative catalytic site that is probably required for the entry of the virus into the host cell. In addition, parts of the DWV RNA genome interact with the inside of the virus capsid. Identifying the RNA binding and catalytic sites within the DWV virion offers prospects for the development of antiviral treatments.

Author contributions: P.P. designed research; K.Š. and A.P. performed research; R.J.P. contributed new reagents/analytic tools; K.Š., J.N., T.F., and P.P. analyzed data; and K.Š., R.J.P., and P.P. wrote the paper.

The authors declare no conflict of interest.

This article is a PNAS Direct Submission.

Freely available online through the PNAS open access option.

Data deposition: Cryo-EM maps of the DWV virions from different conditions have been deposited in the Electron Microscopy Data Bank (EMDB) (accession nos. EMD-4014, EMD-3574, EMD-3570, and EMD-3575); the corresponding coordinates and structure factors have been deposited in the Protein Data Bank (PDB), www.pdb.org (PDB ID codes 5L8Q, 5MV5, 5MUP, and 5MV6). The crystal structures of the DWV virion and P domain have been deposited under PDB ID codes 5G52 and 5G51.

¹To whom correspondence should be addressed. Email: pavel.plevka@ceitec.muni.cz.

This article contains supporting information online at www.pnas.org/lookup/suppl/doi:10.1073/pnas.1615695114/-DCSupplemental.

corresponding to SBPV VP4 was not identified in the SBPV virion structure (13).

Here, we present the structure of the DWV virion and show that, similar to SBPV, it contains a C-terminal extension of capsid protein VP3 that forms a globular domain with a putative receptor-binding site located at the virion surface. We show that, unlike SBPV, DWV's putative active site not only is flexible but also adopts two alternative conformations. Furthermore, bases from the RNA genome interact with the DWV capsid close to the fivefold axes. These structural details provide potential targets for development of antiviral compounds.

Results and Discussion

Structure of DWV Virion and Capsid Proteins. The structure of the DWV virion was determined to a resolution of 3.5 Å using cryo-electron microscopy and to 3.8 Å using X-ray crystallography (Table S1 and Fig. S1). The DWV virion is built from subunits VP1, VP2, and VP3 arranged in a capsid with pseudo-T3 icosahedral symmetry (Fig. 1). The major capsid proteins have jellyroll β -sandwich folds with β -strands named according to the virus jellyroll fold convention B to I (Fig. 1A) (15, 16). The complete structures of the major capsid proteins could be built except for residues 1 and 254 to 258 out of the 258 residues of VP1, 251 to 254 out of the 254 residues of VP2, and 1 and 416 out of the 416 residues of VP3. I flaviruses were suggested to harbor short VP4 subunits consisting of about 20 residues (11, 14). Nevertheless, the electron density corresponding to VP4 could not be identified in either of the two DWV virion structures.

Subunit VP3 of DWV contains a C-terminal extension that forms a P domain positioned on the virion surface (Fig. 1). Because of the P domains, the maximum diameter of the DWV virion (397 Å) is similar to that of SBPV (398 Å) and bigger than those of other picornaviruses and dicistroviruses (about 300 Å). The cryo-EM and X-ray structures of the capsid shell of DWV are similar, with an rmsd of C α -atoms of 0.77 Å; however, the positioning of the P domains on the surface of the virions is different (Fig. 1B and C). The location of the P domains in the crystal structure is not affected by crystal contacts, indicating that it depends on the composition of the solution surrounding the virus. The cryo-EM images were collected on virions in PBS (137 mM NaCl, 2.7 mM KCl, 10 mM Na₂HPO₄, 2 mM KH₂PO₄, pH 7.4) whereas the crystallization conditions contained 0.8 M

KH₂PO₄, 0.8 M NaH₂PO₄, and 0.1 M sodium Hepes, pH 7.5. The movement of the P domain between the two alternative attachment sites at the virion surface involves a 39-Å shift of its center of mass and 145° rotation. This change in position is possible due to a 20-residue-long linker that connects the P domain to the core of the VP3 subunit.

Host cell entry of flaviruses has not been studied, but it probably includes receptor-mediated endocytosis, as has been demonstrated for some picornaviruses (17, 18). Endosomal entry involves exposure of the virions to a solution differing in composition (e.g., low pH), which could trigger detachment of the P domain from the virion surface. It is possible that, during cell entry, the P domain functions without being fixed to a specific position at the virion surface. Instead, it may be anchored by its polypeptide linker to the core of the VP3 subunit. Similar, alternative attachment sites of the P domain at the virion surface have been observed previously for SBPV, reinforcing the possibility that movement of the P domains might be required for their biological function (13). It was speculated previously that the movements of the SBPV P domains were induced by differences in pH. In contrast, the DWV structures were determined at similar pH; however, the crystallization solution was of high ionic strength (0.8 M KH₂PO₄, 0.8 M NaH₂PO₄). It is therefore possible that the movements of the P domain of DWV that we observed were induced by these high, nonphysiological ion concentrations.

Structure of the P Domain. The P domain of the VP3 subunit of DWV is globular, with a diameter of 30 Å (Fig. 1). In both cryo-EM and X-ray structures of the DWV virion, the residues of the P domain have higher average temperature factors than residues from the remainder of the capsid, indicating a higher mobility of the P domain. As a result, electron density maps of the P domains are less well-resolved than other parts of the capsid. We therefore used X-ray crystallography to determine the structure of the isolated P domain to a resolution of 1.45 Å (Table S1). In addition to the globular core, the P domain of DWV contains a finger-shaped loop with four-residue-long antiparallel β -strands β 8 and β 9 (Fig. 2A). The core of the P domain consists of a central antiparallel β -sheet formed from strands β 5 and β 6 surrounded by the 11-residue-long α -helix α 1, the 5-residue long α 2, and two β -sheets containing strands β 1 and β 2 and β 3 to β 7 (Fig. 2A). The β -strands are connected by loops that vary in length between

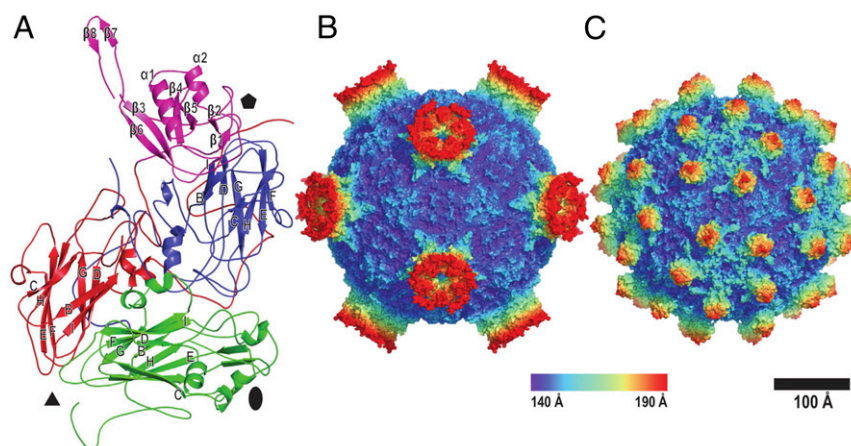


Fig. 1. Structures of the icosahedral asymmetric unit of DWV and its virions in alternative conformations. Icosahedral asymmetric unit of DWV in schematic representation (A) with major capsid protein VP1 colored in blue, VP2 in green, and VP3 in red. The P domain, which is part of VP3, is highlighted in magenta. Selected secondary structure elements are labeled. The locations of the fivefold, threefold, and twofold symmetry axes are denoted by a pentagon, triangle, and oval, respectively. Molecular surfaces of DWV virions determined by (B) cryo-EM and (C) X-ray crystallography. The virion surfaces are rainbow-colored according to their distance from the particle center. (Scale bar: 100 Å.)

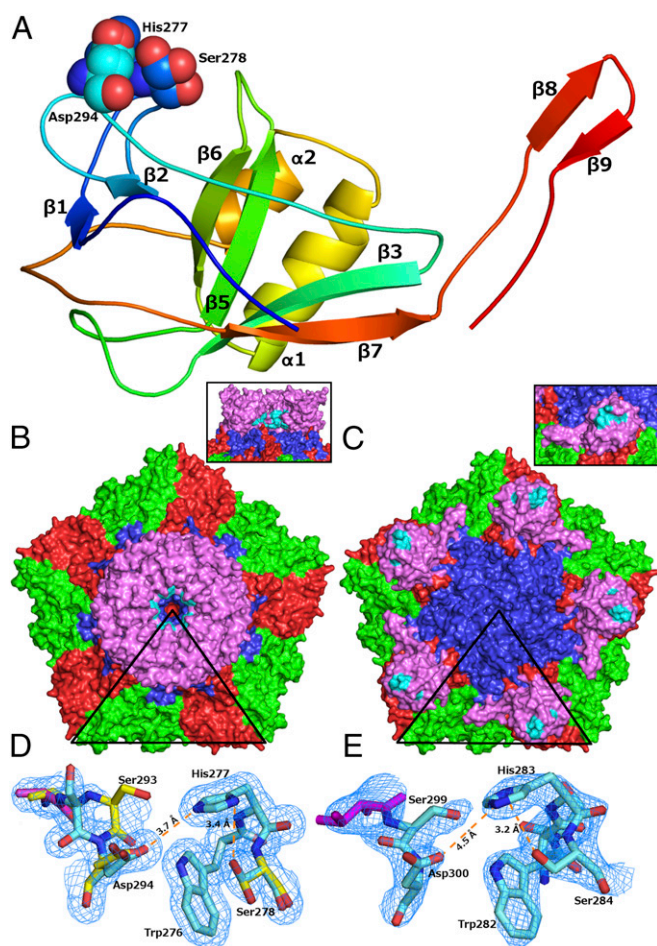


Fig. 2. Structure of the DWV P domain, its localization on the virion surface, and details of the putative catalytic or receptor-binding site. Schematic representation of the crystal structure of the P domain (A), rainbow-colored from residue 260 in blue to 416 in red. Atoms of residues forming the putative active site Asp294, His277, and Ser278 are shown as spheres. Please note that β -strand 4, which is present in the P domain of SBPV, is missing in the DWV structure. Surface representation of pentamers of capsid protein protomers of (B) native cryo-EM structure and (C) X-ray structure of DWV virions. VP1 subunits are shown in blue, VP2 in green, VP3 in red, and the P domain in magenta. Positions of the conserved residues that form a putative active or receptor-binding site of DWV are highlighted in cyan. The borders of one icosahedral asymmetric unit are highlighted with a black triangle. (Insets) Detailed views of the conserved residues forming a compact patch at the P domain surface. In the Inset of B, one of the P domains was removed to allow a view of the inside of the crown formed by the P domains. The P domains of DWV (D) and SBPV (E) contain putative Ser-His-Asp active sites, which are parts of groups of seven residues that are conserved among iflaviruses. The residues are displayed in stick representation. The conserved residues are shown with carbon atoms in cyan. Residues that are not conserved are shown with carbon atoms in magenta. Residues Ser278, Ala292, Ser293, and Asp294 of DWV adopt alternative conformations that are shown with carbon atoms in yellow. Distances between the side chains constituting the putative catalytic triad are shown as orange dashed lines. The electron density maps are contoured at 1σ .

6 and 45 residues. The high-resolution structure of the P domain was fitted into the corresponding regions of the cryo-EM and crystallographic electron density maps of the DWV virion and refined against the experimental data. The resulting P domain structures are similar, with an rmsd in atom positions smaller than 0.50 \AA . However, residues 399 to 416 forming the P domain “finger” were not resolved in either of the virion electron density maps, probably due to the flexibility of the loop.

Comparison of DWV and SBPV Virion Structures. DWV shares 32% sequence identity in capsid proteins with SBPV (13). The two viruses have similar surface topologies with capsids decorated with P domains. The differences between the SBPV and DWV capsids are predominantly in the loops of the major capsid proteins exposed at the outer virion surface. Capsid protein VP1 of DWV has a GH loop that is five residues shorter than that of SBPV and lacks an α -helix $\alpha 6$ (Fig. S2A and B). The GH loop of the VP2 subunit of SBPV contains the integrin-recognition motif Arg192-Gly193-Asp194 (RGD) and is four residues longer than that of DWV (Fig. S2C and D). Integrins serve as cell entry receptors for numerous viruses, including the foot and mouth disease virus and several parechoviruses (19–21). However, the RGD motif is not present in DWV and other iflaviruses. Differences in the structure of the GH loop between DWV and SBPV might reflect different functions of the loops in receptor recognition.

DWV and SBPV differ in the structures of both the core and P domains of their VP3 subunits (Fig. S2E and F). The β -sandwich cores of VP3 subunits of DWV and SBPV can be superimposed with an rmsd of 1.35 \AA for 94% of the residues whereas the P domains have an rmsd of 1.69 \AA for 80% of the residues. The P domain of DWV contains 18 structured residues at the C terminus that form a finger with a 4-residue-long anti-parallel beta sheet (Fig. 2A and Fig. S2G). Notably, these residues are not resolved in the crystal structures of SBPV virions (Fig. S2H). The sequence identity within the P domains of the two viruses is 17% whereas it is 33% for the remaining parts of the capsid proteins. Thus, it seems that the P domain is more tolerant to mutations than the parts of the virus proteins forming the capsid shell. Nevertheless, the P domains of DWV and SBPV contain 8 conserved residues that are also shared with several other iflaviruses and that might form a catalytic or receptor-binding site as discussed below.

Comparison of the P Domain with Other Proteins. A search for structures similar to the DWV P domain (22) identified a globular surface domain of a virus from the *Astroviridae*, an additional family of nonenveloped viruses like the picornaviruses and caliciviruses, all of which possess a single-stranded positive sense RNA genome (Table S2) (23). The domain is similar to the P domain of DWV in terms of having a core formed by β -strands that are complemented by short α -helices located at the periphery of the domain. Nevertheless, the two domains are quite different and could not be meaningfully superimposed. Several additional proteins could be detected, but their structural similarities to the DWV P domain were low and the alignments always included only a small fraction of the structures (Table S2). Therefore, it seems that the P domains of iflaviruses might have evolved de novo as C-terminal extensions of the capsid proteins and therefore have a unique fold.

Position of the P Domain at the Virion Surface. In the cryo-EM structure of DWV, the P domains related by one icosahedral fivefold axis form a crown-like arrangement at the virion surface (Figs. 1B and 2B). The crowns have a diameter of 80 \AA and protrude 40 \AA above the capsid surface. The P domains within the same crown contact each other with a buried surface area of 380 \AA^2 , and each of them binds to the capsid through a $430\text{-}\text{\AA}^2$ interface located next to the fivefold axis. In contrast, the P domains of native SBPV, which also forms crowns, are not in contact with each other (Fig. S3). In the crystal structure of DWV, the P domains are positioned approximately in between the icosahedral fivefold, threefold, and twofold axes and interact with the capsid through a $1,000\text{-}\text{\AA}^2$ interface (Fig. 2C). The P domains in this structure do not interact with each other, and, therefore, we refer to them as being in “centered” arrangement. The movements of the P domains between the two positions

seem to be accomplished by “rolling” over the virion surface (Fig. 2*B* and *C* and *Movies S1* and *S2*). The residues forming the 430 Å² of the VP1 surface that became exposed after the P domain movements do not contain any specific motives to indicate their function in receptor binding. Similar movements of the P domains have been observed previously in SBPV crystallized in low pH conditions (13). Unlike in the case of SPBV, movements of the DWV P domain could not be induced by exposing DWV to pH 5.0 (Fig. *S4 A* and *B*). However, the structures of the P domains determined by cryo-EM of DWV at low pH are less resolved and therefore more mobile than those of the virus in neutral pH (Fig. *S5 A* and *B*). To determine whether the movements of the P domains are reversible, we exposed DWV virions to the crystallization condition and subsequently dialyzed them back against PBS. Cryo-EM reconstruction of these particles determined to a resolution of 3.8 Å showed P domains in the crown arrangement similar to native virions (Figs. *S4C* and *S5C*). It was not possible to calculate cryo-EM reconstruction of the DWV virions in the crystallization buffer because the 1.6-M phosphate salts prevent preparation of grids with vitreous ice of sufficient quality for cryo-EM data collection. In an attempt to directly observe the virus with P domains in the centered arrangement, DWV virions were exposed to the crystallization condition and cross-linked by addition of 1% glutaraldehyde. The particles were then dialyzed against PBS and used for cryo-EM reconstruction that was determined to a resolution of 3.1 Å. These particles had P domains in the crown arrangement (Figs. *S4D* and *S5D*). Three-dimensional classification using the program RELION did not identify a subclass of particles with P domains in the centered arrangement. Thus, the cryo-EM analysis did not confirm the positioning of P domains in the centered arrangement observed in the crystal structure (Fig. 1*C*). The differences in the virion structures obtained by the two types of structural analysis could be caused by low-efficiency of cross-linking of the P domains. Furthermore, it is likely that the movements of P domains within a single virus particle are not synchronized with each other. Cryo-EM analysis, even in combination with 3D classification, may therefore not allow detection of a subset of the P domains in the centered arrangement. In contrast, crystallization, which required 5 months, probably specifically selected for particles with a centered P domain arrangement.

P domains of DWV virions that were exposed to high salt or low pH became more mobile than those of native virions or viruses cross-linked by 1% glutaraldehyde (Fig. *S5*). We speculate that it is the mobility of the P domains rather than their precise positioning that is important for DWV cell entry, during which the virus is likely to encounter low pH. Our results provide evidence of the possible extent of movements of the P domains.

Putative Role of the P Domain in Cell Entry. The P domain of DWV contains residues Asp294, His277, and Ser278 located close to each other, and the arrangement of their side chains indicates that they constitute a catalytic triad (Fig. 2*A* and *D*) (24). The distances between the side chains of the residues are larger than ideal for catalyzing a hydrolytic reaction (Fig. 2*D*) (24). However, the 1.45-Å-resolution structure of the DWV P domain shows that residues Ser278, Ala292, Ser293, and Asp294 adopt alternative conformations (Fig. 2*D*), indicating local flexibility of the structure. It is therefore possible that the optimal configuration of the active site might be achieved upon binding the as-yet-unknown substrate. This type of catalytic triad has been previously identified in proteases, lipases, and esterases (24–26). Therefore, DWV may use the putative catalytic activity of its P domains in cell entry. The P domains might bind to virus receptors or disrupt membranes and thus allow the virus to deliver its genome into the cell cytoplasm.

The putative catalytic triad and five additional residues, which form a compact patch on the P domain surface, are conserved

among iflaviruses containing P domains (Figs. 2*B* and *C* and 3*A*) (11, 27–29), which is in contrast to the limited 3% overall sequence identity of the remaining residues of the P domains. Conservation of these residues indicates that they constitute a functionally important receptor-binding or substrate-binding site. The Asp294-His277-Ser278 catalytic triad of SBPV also has a 3D arrangement indicative of an active site (Fig. 2*E*) (13). A similar group of residues in the P domains of noroviruses was shown to bind glycans (30, 31). Alternatively, the putative catalytic site may facilitate the escape of DWV virions from endosomes in a manner analogous to the lipase activity present in the N-terminal domain of the capsid protein VP1 from parvoviruses (32).

The conserved residues in the iflavivirus P domain provide a potential target for antiviral compounds. The putative active site faces the interior of the crown in the native virus; however, it is exposed at the apex of the P domain in the virion structure with the centered arrangement of the P domains (Fig. 2*B* and *C*). The exposure of the active site after the P domain rotation reinforces the possibility that movements of the P domain might be required for efficient DWV infection.

Evolutionary Relationship to Other Viruses from the Order Picornvirales. The availability of the DWV and SBPV virion structures enabled the construction of a structure-based phylogenetic tree comparing the iflaviruses to other viruses from the families *Dicistroviridae* and *Iflaviridae* (Fig. 4). The structural comparison shows that iflaviruses are most similar to the insect-infecting dicistroviruses Israeli acute bee paralysis virus, cricket paralysis virus, and triatoma virus (33–35). The viruses most similar to DWV and SBPV from the *Picornaviridae* family are hepatitis A virus and human parechovirus 1 (HPEV-1), which were previously suggested to form evolutionary intermediates between human and insect viruses (21, 36) (Fig. 4). The closer structural similarity of DWV and SBPV capsid to the viruses from the *Dicistroviridae* family than to viruses from the *Picornaviridae* family might be because of similarities in the processing of the polyprotein precursor of capsid proteins. The amino acid sequence of the VP4 subunit is located in front of the N terminus of VP3 in viruses from the family *Dicistroviridae* whereas it is located in front of the VP2 sequence in viruses of the family *Picornaviridae*. The VP4 sequences of iflaviruses were predicted to be located in front of VP3 in the polyprotein (11, 14). Even though the VP4 subunits of DWV and SBPV are not resolved in the virion structures, the similar cleavage pattern of the capsid

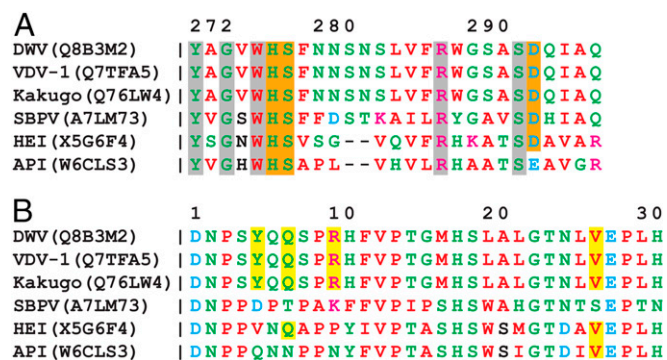


Fig. 3. Sequence alignment of residues of iflavivirus VP3 subunits. API, *Antheraea pernyi* iflavivirus; HEI, *Heliconius erato* iflavivirus. UniProt accession numbers of the sequences used in the alignment are provided. (A) Conserved residues constituting the putative catalytic triad Asp-His-Ser are highlighted with an orange background; other conserved residues located in the structure close to the putative active site are highlighted with a gray background. (B) Conserved residues involved in the interaction with genomic RNA are highlighted with a yellow background.

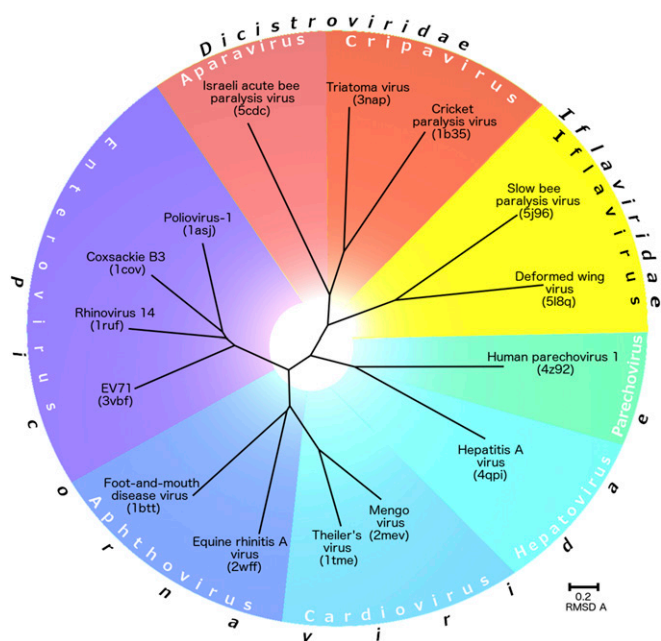


Fig. 4. Evolutionary relationship among viruses from the families *Iflaviridae*, *Picornaviridae*, and *Dicistroviridae* based on structural alignment of their capsid proteins. Phylogenetic tree based on structural similarity of icosahedral asymmetric units of indicated viruses. For details on the construction of the diagram, please see *Materials and Methods*.

protein subunits from the precursor polyprotein P1 might impose constraints on the organization of the capsid, resulting in the closer similarity of iflaviruses to dicistroviruses.

Iflaviruses are structurally and genetically related to vertebrate picornaviruses, for which numerous capsid-binding inhibitors have been developed. Compounds that bind into a hydrophobic pocket within VP1 can inhibit receptor binding and/or genome release of some picornaviruses (37–39). However, such a hydrophobic pocket is not formed in DWV VP1 subunits. Similarly, the hydrophobic pocket was not observed in VP1 of SBPV (13), which suggests that capsid binding inhibitors that intercalate into VP1 subunits may not be effective as antivirals against honey bee viruses of the family *Iflaviridae*.

Capsid–RNA Interactions. The DWV genome is a 10,140-nt-long linear RNA molecule (11) that forms unique interactions with the inner surface of the icosahedral capsid. The virus RNA does not affect the packing of particles within the crystal or the determination of particle orientations performed in the course of the cryo-EM reconstruction. Therefore, both X-ray and cryo-EM maps contain information about the icosahedrally averaged RNA structure.

Clearly defined electron density corresponding to an RNA nucleotide is associated with each VP3 subunit of DWV close to the fivefold icosahedral axis (Fig. 5*A*). The shape of the density indicates that the base of the nucleotide is a pyrimidine, and it was therefore modeled as a uridine (Fig. 5*B*). The nucleotide has 90% occupancy, showing that the genome binds to nearly all of the 60 available positions within the virion. Each nucleotide interacts with residues from three VP3 subunits belonging to different protomers within one pentamer (Fig. 5*B*). The residues that bind the RNA are conserved among several honey bee iflaviruses (Fig. 3*B*). However, the structured RNA was not observed in the SBPV virion, which does not have the conserved RNA-binding residues (Fig. 3*B*) (40). Reminiscent of the RNA–protein interactions in DWV are structured RNA oligonucleotides that have been recently described in the parechoviruses HPeV-1, HPeV-3, and Ljungan virus, where they also mediate

contacts among capsid proteins from different protomers (21, 41, 42). The conservation of the RNA-binding residues among some of the honey bee iflaviruses, together with the near-complete occupancy of the RNA, indicates that the RNA–capsid binding might play a role in virion stability. In addition, RNA–capsid interactions may play a role in DWV virion assembly, as was previously suggested for related picornaviruses (43). Therefore, future mutational analyses of the residues involved in the RNA binding may lead to determination of the mechanism that ensures packaging of the DWV genome into newly forming particles, and which may offer alternative targets for antiviral compounds.

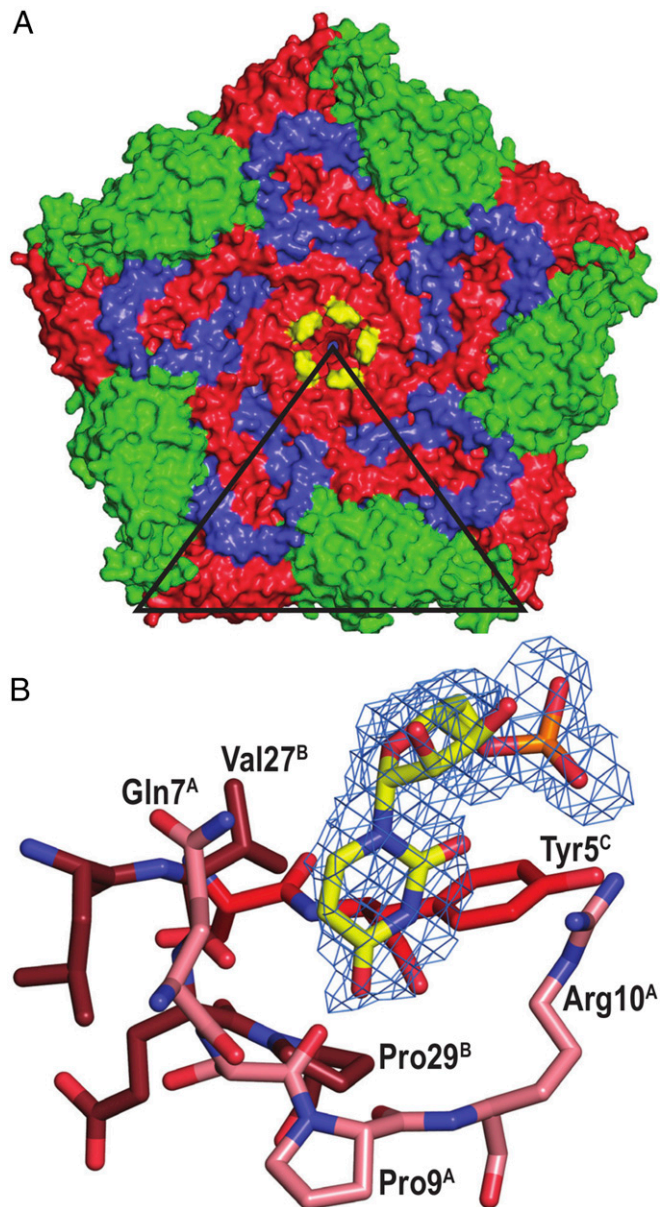


Fig. 5. Interactions of DWV genomic RNA with capsid. Location of RNA nucleotides displayed in yellow within the pentamer of capsid protein protomers as seen from the inside of the virion (*A*). VP1 subunits are shown in blue, VP2 in green, and VP3 in red. The borders of one icosahedral asymmetric unit are highlighted with a triangle. (*B*) Detail of the interaction of viral RNA with the VP3 subunits. The electron density map of the nucleotide is contoured at 1σ . VP3 subunits from different icosahedral asymmetric units are distinguished by color shades and superscripts “A,” “B,” and “C.”

Materials and Methods

The propagation of DWV was carried out as described in the COLOSS BeeBook (44). A suspension of DWV was applied onto holey carbon grids and vitrified by plunging into liquid ethane. Images were recorded with an FEI Falcon II camera in an FEI Titan Krios electron microscope. The images were processed using the package RELION (45). The P domain was expressed in *Escherichia coli* BL21(DE3). Crystals of the DWV P domain were obtained using the sitting-drop technique with a bottom solution containing 4.3 M sodium chloride and 0.1 M Hepes, pH 7.5.

ACKNOWLEDGMENTS. We thank synchrotron “Soleil” Proxima-1 and beamline scientist Dr. Pierre Legrand for help with X-ray data collection and processing. This research was carried out under the project CEITEC 2020 (LQ1601), with financial support from the Ministry of Education, Youth

and Sports of the Czech Republic under National Sustainability Program II. Access to computing and storage facilities owned by parties and projects contributing to the National Grid Infrastructure MetaCentrum, provided under the program “Projects of Large Infrastructure for Research, Development, and Innovations” Grant (LM2010005), is greatly appreciated. This work was supported by the IT4Innovations Centre of Excellence project Grant (CZ.1.05/1.1.00/02.0070), funded by the European Regional Development Fund and the national budget of the Czech Republic via the Research and Development for Innovations Operational Program, as well as the Czech Ministry of Education, Youth and Sports via the project Large Research, Development and Innovations Infrastructures Grant (LM2011033). The research leading to these results received funding from the European Research Council under the European Union’s Seventh Framework Program Grant (FP2007-2013)/ERC Grant Agreement 355855 and from EMBO Grant Agreement European Molecular Biology Organization (EMBO)-IG 3041 (to P.P.).

- Smith KM, et al. (2013) Pathogens, pests, and economics: Drivers of honey bee colony declines and losses. *EcoHealth* 10(4):434–445.
- Allsopp MH, de Lange WJ, Veldtman R (2008) Valuing insect pollination services with cost of replacement. *PLoS One* 3(9):e3128.
- Biesmeijer JC, et al. (2006) Parallel declines in pollinators and insect-pollinated plants in Britain and the Netherlands. *Science* 313(5785):351–354.
- Dainat B, Vanengelsdorp D, Neumann P (2012) Colony collapse disorder in Europe. *Environ Microbiol Rep* 4(1):123–125.
- van Engelsdorp D, Hayes J, Jr, Underwood RM, Pettis J (2008) A survey of honey bee colony losses in the U.S., fall 2007 to spring 2008. *PLoS One* 3(12):e4071.
- Bowen-Walker PL, Martin SJ, Gunn A (1999) The transmission of deformed wing virus between honeybees (*Apis mellifera* L.) by the ectoparasitic mite varroa jacobsoni Oud. *J Invertebr Pathol* 73(1):101–106.
- Shen M, Yang X, Cox-Foster D, Cui L (2005) The role of varroa mites in infections of Kashmir bee virus (KBV) and deformed wing virus (DWV) in honey bees. *Virology* 342(1):141–149.
- Highfield AC, et al. (2009) Deformed wing virus implicated in overwintering honeybee colony losses. *Appl Environ Microbiol* 75(22):7212–7220.
- de Miranda JR, Gauthier L, Ribiere M, Chen YP (2012) Honey bee viruses and their effect on bee and colony health. *Honey Bee Colony Health: Challenges and Sustainable Solutions*, ed Samataro DYJ (CRC Press, Boca Raton, FL), pp 71–102.
- Le Gall O, et al. (2008) Picornavirales, a proposed order of positive-sense single-stranded RNA viruses with a pseudo-T = 3 virion architecture. *Arch Virol* 153(4):715–727.
- Lanzi G, et al. (2006) Molecular and biological characterization of deformed wing virus of honeybees (*Apis mellifera* L.). *J Virol* 80(10):4998–5009.
- Zhang J, et al. (2001) Three-dimensional structure of the Chinese Sacbrood bee virus. *Sci China C Life Sci* 44(4):443–448.
- Kalynych S, et al. (2016) Virion structure of iflavirus slow bee paralysis virus at 2.6-angstrom resolution. *J Virol* 90(16):7444–7455.
- de Miranda JR, et al. (2010) Genetic characterization of slow bee paralysis virus of the honeybee (*Apis mellifera* L.). *J Gen Virol* 91(Pt 10):2524–2530.
- Rossmann MG, et al. (1985) Structure of a human common cold virus and functional relationship to other picornaviruses. *Nature* 317(6033):145–153.
- Harrison SC, Olson AJ, Schutt CE, Winkler FK, Bricogne G (1978) Tomato bushy stunt virus at 2.9 Å resolution. *Nature* 276(5686):368–373.
- Bergelson JM, Coyne CB (2013) Picornavirus entry. *Adv Exp Med Biol* 790:24–41.
- Fuchs R, Blaas D (2012) Productive entry pathways of human rhinoviruses. *Adv Virol* 2012:826301.
- Jackson T, Mould AP, Sheppard D, King AM (2002) Integrin alphavbeta1 is a receptor for foot-and-mouth disease virus. *J Virol* 76(3):935–941.
- Boonyakiat Y, Hughes PJ, Ghazi F, Stanway G (2001) Arginine-glycine-aspartic acid motif is critical for human parechovirus 1 entry. *J Virol* 75(20):10000–10004.
- Kalynych S, Pálková L, Plevka P (2015) The structure of human parechovirus 1 reveals an association of the RNA genome with the capsid. *J Virol* 90(3):1377–1386.
- Holm L, Rosenstrom P (2010) Dali server: Conservation mapping in 3D. *Nucleic Acids Res* 38(Web Server issue):W545–W549.
- York RL, et al. (2015) Structural, mechanistic, and antigenic characterization of the human astrovirus capsid. *J Virol* 90(5):2254–2263.
- Dodson G, Wlodawer A (1998) Catalytic triads and their relatives. *Trends Biochem Sci* 23(9):347–352.
- Canaan S, Roussel A, Verger R, Cambillau C (1999) Gastric lipase: Crystal structure and activity. *Biochim Biophys Acta* 1441(2-3):197–204.
- Vaquero ME, Barriuso J, Martínez MJ, Prieto A (2016) Properties, structure, and applications of microbial sterol esterases. *Appl Microbiol Biotechnol* 100(5):2047–2061.
- Ongus JR, et al. (2004) Complete sequence of a picorna-like virus of the genus Iflavirus replicating in the mite Varroa destructor. *J Gen Virol* 85(Pt 12):3747–3755.
- Fujiyuki T, et al. (2004) Novel insect picorna-like virus identified in the brains of aggressive worker honeybees. *J Virol* 78(3):1093–1100.
- Bailey L, Woods RD (1974) Three previously undescribed viruses from the honey bee. *J Gen Virol* 25(2):175–186.
- Cao S, et al. (2007) Structural basis for the recognition of blood group trisaccharides by norovirus. *J Virol* 81(11):5949–5957.
- Hansman GS, et al. (2012) Structural basis for norovirus inhibition and fucose mimicry by citrate. *J Virol* 86(1):284–292.
- Farr GA, Zhang LG, Tattersall P (2005) Parvoviral virions deploy a capsid-tethered lipolytic enzyme to breach the endosomal membrane during cell entry. *Proc Natl Acad Sci USA* 102(47):17148–17153.
- Mullapudi E, Pridal A, Pálková L, de Miranda JR, Plevka P (2016) Virion structure of Israeli acute bee paralysis virus. *J Virol* 90(18):8150–8159.
- Tate J, et al. (1999) The crystal structure of cricket paralysis virus: The first view of a new virus family. *Nat Struct Biol* 6(8):765–774.
- Squires G, et al. (2013) Structure of the triatoma virus capsid. *Acta Crystallogr D Biol Crystallogr* 69(Pt 6):1026–1037.
- Wang X, et al. (2015) Hepatitis A virus and the origins of picornaviruses. *Nature* 517(7532):85–88.
- Smith TJ, et al. (1986) The site of attachment in human rhinovirus 14 for antiviral agents that inhibit uncoating. *Science* 233(4770):1286–1293.
- Hadfield AT, Diana GD, Rossmann MG (1999) Analysis of three structurally related antiviral compounds in complex with human rhinovirus 16. *Proc Natl Acad Sci USA* 96(26):14730–14735.
- Grant RA, et al. (1994) Structures of poliovirus complexes with anti-viral drugs: Implications for viral stability and drug design. *Curr Biol* 4(9):784–797.
- Morgunova EYu, et al. (1994) The atomic structure of carnation mottle virus capsid protein. *FEBS Lett* 338(3):267–271.
- Zhu L, et al. (2015) Structure of Ljungan virus provides insight into genome packaging of this picornavirus. *Nat Commun* 6:8316.
- Shakeel S, et al. (2016) Multiple capsid-stabilizing interactions revealed in a high-resolution structure of an emerging picornavirus causing neonatal sepsis. *Nat Commun* 7:11387.
- Nugent CI, Kirkegaard K (1995) RNA binding properties of poliovirus subviral particles. *J Virol* 69(1):13–22.
- de Miranda JR, et al. (2013) Standard methods for *Apis mellifera* pest and pathogen research. *The COLOSS BEEBOOK*, eds Diatemann V, Ellis JD, Neumann P (IBRA, Treforest, UK), Vol II.
- Scheres SH (2012) RELION: Implementation of a Bayesian approach to cryo-EM structure determination. *J Struct Biol* 180(3):519–530.
- Davis IW, et al. (2007) MolProbity: All-atom contacts and structure validation for proteins and nucleic acids. *Nucleic Acids Res* 35(Web Server issue):W375–W383.
- Shaikh TR, et al. (2008) SPIDER image processing for single-particle reconstruction of biological macromolecules from electron micrographs. *Nat Protoc* 3(12):1941–1974.
- Tang G, et al. (2007) EMAN2: An extensible image processing suite for electron microscopy. *J Struct Biol* 157(1):38–46.
- Mindell JA, Grigorieff N (2003) Accurate determination of local defocus and specimen tilt in electron microscopy. *J Struct Biol* 142(3):334–347.
- Scheres SH, Chen S (2012) Prevention of overfitting in cryo-EM structure determination. *Nat Methods* 9(9):853–854.
- Chen S, et al. (2013) High-resolution noise substitution to measure overfitting and validate resolution in 3D structure determination by single particle electron cryomicroscopy. *Ultramicroscopy* 135:24–35.
- Emsley P, Cowtan K (2004) Coot: Model-building tools for molecular graphics. *Acta Crystallogr D Biol Crystallogr* 60(Pt 12):2126–2132.
- Afonine PV, et al. (2012) Towards automated crystallographic structure refinement with phenix.refine. *Acta Crystallogr D Biol Crystallogr* 68(Pt 4):352–367.
- Kabsch W (2010) Integration, scaling, space-group assignment and post-refinement. *Acta Crystallogr D Biol Crystallogr* 66(Pt 2):133–144.
- Tong L, Rossmann MG (1997) Rotation function calculations with GLRF program. *Methods Enzymol* 276:594–611.
- McCoy AJ, et al. (2007) Phaser crystallographic software. *J Appl Cryst* 40(Pt 4):658–674.
- Kleywegt GJ, Read RJ (1997) Not your average density. *Structure* 5(12):1557–1569.
- Winn MD, et al. (2011) Overview of the CCP4 suite and current developments. *Acta Crystallogr D Biol Crystallogr* 67(Pt 4):235–242.
- Studier FW (2005) Protein production by auto-induction in high density shaking cultures. *Protein Expr Purif* 41(1):207–234.
- Vagin AA, et al. (2004) REFMACS dictionary: Organization of prior chemical knowledge and guidelines for its use. *Acta Crystallogr D Biol Crystallogr* 60(Pt 12 Pt 1):2184–2195.
- Langer G, Cohen SX, Lamzin VS, Perrakis A (2008) Automated macromolecular model building for X-ray crystallography using ARP/wARP version 7. *Nat Protoc* 3(7):1171–1179.
- Chenna R, et al. (2003) Multiple sequence alignment with the Clustal series of programs. *Nucleic Acids Res* 31(13):3497–3500.
- Petersen EF, et al. (2004) UCSF Chimera: A visualization system for exploratory research and analysis. *J Comput Chem* 25(13):1605–1612.
- Humphrey W, Dalke A, Schulten K (1996) VMD: Visual molecular dynamics. *J Mol Graph* 14(1):33–38.
- Huson DH (1998) SplitsTree: Analyzing and visualizing evolutionary data. *Bioinformatics* 14(1):68–73.

PAPER X





Virion structure and genome delivery mechanism of sacbrood honeybee virus

Michaela Procházková^a, Tibor Füzik^a, Karel Škubník^a, Jana Moravcová^a, Zorica Ubiparip^a, Antonín Přidal^b, and Pavel Plevka^{a,1}

^aCentral European Institute of Technology, Masaryk University, 625 00 Brno, Czech Republic; and ^bFaculty of Agronomy, Mendel University, 613 00 Brno, Czech Republic

Edited by Wolfgang Baumeister, Max Planck Institute of Biochemistry, Martinsried, Germany, and approved June 14, 2018 (received for review December 22, 2017)

Infection by sacbrood virus (SBV) from the family Iflaviridae is lethal to honey bee larvae but only rarely causes the collapse of honey bee colonies. Despite the negative effect of SBV on honey bees, the structure of its particles and mechanism of its genome delivery are unknown. Here we present the crystal structure of SBV virion and show that it contains 60 copies of a minor capsid protein (MiCP) attached to the virion surface. No similar MiCPs have been previously reported in any of the related viruses from the order Picornavirales. The location of the MiCP coding sequence within the SBV genome indicates that the MiCP evolved from a C-terminal extension of a major capsid protein by the introduction of a cleavage site for a virus protease. The exposure of SBV to acidic pH, which the virus likely encounters during cell entry, induces the formation of pores at threefold and fivefold axes of the capsid that are 7 Å and 12 Å in diameter, respectively. This is in contrast to vertebrate picornaviruses, in which the pores along twofold icosahedral symmetry axes are currently considered the most likely sites for genome release. SBV virions lack VP4 subunits that facilitate the genome delivery of many related dicistroviruses and picornaviruses. MiCP subunits induce liposome disruption *in vitro*, indicating that they are functional analogs of VP4 subunits and enable the virus genome to escape across the endosome membrane into the cell cytoplasm.

honeybee | virus | structure | genome | release

The pollination services provided by the western honey bee (*Apis mellifera*) are required for agricultural production and to maintain the diversity of wild flowering plants (1). Over the last few decades, the combination of environmental pollution, habitat loss, and pathogens has resulted in a decrease in honey bee populations in North America and Europe (2, 3). Symptoms of the sacbrood virus (SBV) infection of pupae include the accumulation of ecdysial fluid, cuticle discoloration, and death, resulting in a typical gondola-shaped dry cadaver. Although SBV is lethal for infected larvae, infected colonies rarely collapse, and thus SBV poses only a limited threat to managed honey bees (3). SBV is distributed worldwide, with specific strains also infecting *Apis cerana* (4).

SBV has a positive-sense single-stranded RNA genome that is 8,832 nt long and contains an additional poly-A sequence at its 3' end (5). The genome encodes a single 2,858-aa-long polyprotein that is cotranslationally and posttranslationally cleaved by virus proteases into functional protein subunits. The capsid proteins VP1, VP2, and VP3 from one polyprotein precursor form a protomer, an elementary building block of the virus capsid. Based on homology with vertebrate picornaviruses, SBV protomers are expected to assemble into pentamers, and, subsequently, 12 pentamers associate with the genome to form a virion (6). The capsid proteins of iflaviruses have jelly roll β -sandwich folds shared by all picornaviruses and numerous other viruses from other families (7–10). To date, three iflaviruses have been structurally characterized: slow bee paralysis virus (SBPV), deformed wing virus (DWV), and Chinese SBV (CSBV) (8, 11, 12).

Here we present the structure of the SBV virion and show that it contains 60 copies of a minor capsid protein (MiCP) attached

at the virion surface. No similar proteins have been observed in any virus from the order Picornavirales. A comparison of the structure of SBV with the structures of other iflaviruses indicates that the protein evolved from an ancestral C-terminal extension of the VP3 subunit through the introduction of a cleavage site for virus-encoded protease. In addition, we show that the MiCP induces the disruption of liposome membranes and thus may facilitate delivery of the SBV genome into the cytoplasm.

Results and Discussion

SBV Virion Structure and Its Comparison with Iflaviruses Containing P-Domains. The virion structure of SBV has been determined to a resolution of 2.1 Å using X-ray crystallography (*SI Appendix, Table S1*). The maximum diameter of the SBV virion is 312 Å, which is 90 Å less than the maximum diameters of related iflaviruses DWV and SBPV (7, 8, 13). The virions of DWV and SBPV are larger because their VP3 subunits contain 160-residue-long C-terminal extensions, which fold into globular P-domains positioned at the virion surface (Figs. 1 and 2). The capsid of SBV is of spherical shape, with plateaus around icosahedral fivefold symmetry axes and shallow depressions at twofold

Significance

Honey bee pollination is required to sustain the biodiversity of wild flora and for agricultural production; however, honey bee populations in Europe and North America are declining due to virus infections. Sacbrood virus (SBV) infection is lethal to honey bee larvae and decreases the fitness of honey bee colonies. Here we present the structure of the SBV particle and show that it contains 60 copies of a minor capsid protein attached to its surface. No similar minor capsid proteins have been previously observed in any of the related viruses. We also present a structural analysis of the genome release of SBV. The possibility of blocking virus genome delivery may provide a tool to prevent the spread of this honey bee pathogen.

Author contributions: M.P. and P.P. designed research; M.P., T.F., J.M., Z.U., and A.P. performed research; M.P., T.F., K.S., and P.P. analyzed data; and M.P., T.F., and P.P. wrote the paper.

The authors declare no conflict of interest.

This article is a PNAS Direct Submission.

This open access article is distributed under [Creative Commons Attribution-NonCommercial-NoDerivatives License 4.0 \(CC BY-NC-ND\)](https://creativecommons.org/licenses/by-nc-nd/4.0/).

Data deposition: Cryo-EM maps of the SBV virions from the different conditions have been deposited in the Electron Microscopy Data Bank [accession nos. 3863 (native virion, pH 7.4); 3881 (empty particle, pH 7.4); 3865 (virion, pH 5.8); 3866 (empty particle, pH 5.8, expansion state I); and 3867 (empty particle, pH 5.8, expansion state II)], and the corresponding coordinates have been deposited in the Protein Data Bank [PDB ID codes 5OYP (native virion, pH 7.4); 6EIW (empty particle, pH 7.4); 6EGV (virion, pH 5.8); 6EGX (empty particle, pH 5.8, expansion state I); and 6EH1 (empty particle, pH 5.8, expansion state II)]. The crystal structure of the SBV virion also has been deposited in the Protein Data Bank (PDB ID code 5LSF). The consensus nucleotide sequence of the SBV capsid proteins has been deposited in GenBank (accession no. KY617033).

¹To whom correspondence should be addressed. Email: pavel.plevka@ceitec.muni.cz.

This article contains supporting information online at www.pnas.org/lookup/suppl/doi:10.1073/pnas.1722018115/-DCSupplemental.

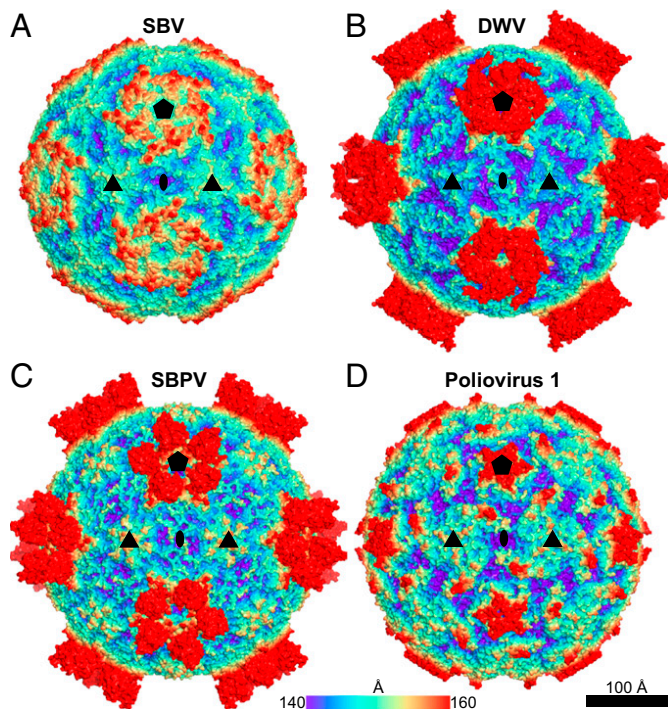


Fig. 1. Virion structures of SBV (PDB ID code 5LSF) (A), DWV (PDB ID code 5L7Q) (B), SBPV (PDB ID code 5J96) (C), and poliovirus 1 (PDB ID code 1ASJ) (D). The molecular surfaces of the respective virions are rainbow-colored according to their distance from the center. The locations of the selected symmetry axes are denoted by pentagons for fivefold, triangles for threefold, and ellipses for twofold.

symmetry axes (Fig. 1A). SBV lacks the typical canyon depressions that are dominant surface features of the virions of enteroviruses and some other picornaviruses (Fig. 1D) (9).

There are two alternative conventions for naming the capsid proteins of picorna-like viruses. In some previous annotations of the iflavirus genomes and in the structural characterization of DWV by Organtini et al. (13), the virus proteins were named according to a molecular weight convention from the largest subunit, VP1, to the smallest, VP4. An alternative approach is to label the capsid proteins according to their homology with picornavirus proteins (14). The homology-based convention was used in the previous structural studies of SBPV and DWV (7, 8, 15). Application of the molecular weight convention results in different gene orders of SBV, DWV, and SBPV. Therefore, to simplify the structural comparison of SBV, DWV, and SBPV with one another and to picornaviruses, we use the homology-

based convention. The order of the major capsid proteins in the P1 polyprotein is VP2, VP3, and VP1 (Fig. 2). The capsid proteins labeled according to the picornavirus convention occupy homologous positions in the virus capsid (Fig. 3).

The SBV capsid is built from the major capsid proteins VP1, VP2, and VP3 organized with pseudo-T3 icosahedral symmetry (Fig. 3A). The VP1 subunits form pentamers around fivefold axes, whereas the VP2 and VP3 subunits constitute heterohexamers positioned at the icosahedral threefold axes. The major capsid proteins have jelly roll β -sandwich folds with β -strands named according to the virus capsid protein convention B-I (6). The two antiparallel β -sheets forming the core of each of the capsid proteins contain the strands BIDG and CHEF, respectively (Fig. 3A). The N termini of the capsid proteins are located on the inside of the capsid, whereas their C termini are exposed at the virion surface. The crystallographic electron density map of the SBV virion enabled the building of residues 1–243 out of 247 residues of VP1; residues 3–241 out of 242 residues of VP2; and residues 1–272 out of 280 residues of VP3. SBV encodes a 36-residue-long VP4 subunit (Fig. 2); however, the electron density map of SBV virion does not contain resolved features that could be interpreted as residues of VP4.

In contrast to all other viruses from the order Picornavirales that have been structurally characterized at high resolution so far (32 picornaviruses, 4 dicistroviruses, and 2 iflaviruses), the SBV virion contains a short protein attached to the capsid surface (Fig. 3A). We termed the peptide the MiCP. The structure of the MiCP could be built for residues 22–47 out of 48 residues. The amino acid sequence of the MiCP is located between the C terminus of VP3 and the N terminus of VP1 in the P1 polypeptide of SBV (Fig. 2). LC-MS-MS was used to verify the protein cleavage sites that separate the MiCP from VP3 and VP1 (SI Appendix, Fig. S1). The identified cleavage site, Ser⁷⁰⁸/Arg⁷⁰⁹Arg⁷¹⁰, is in agreement with the previously characterized target sequences of picornavirus-like proteases (16, 17).

VP1 subunits of enteroviruses have been shown to form hydrophobic pockets that can be targeted by artificial compounds that prevent virus–receptor interaction or genome release (18–20). Similar to SBPV and DWV (7, 8), the VP1 of SBV does not contain such a pocket, and it is unlikely that the virus could be inhibited by capsid-binding inhibitors targeting the hydrophobic core of VP1.

SBV Virions Do Not Contain VP4 Subunits. The formation of mature infectious virions of most picorna-like viruses requires the cleavage of VP4 subunits from the N terminus of their VP0 precursors that is not performed by the virus proteases (21–23). It has been speculated that the proteolysis of the VP4 subunits of picornaviruses is catalyzed by the RNA genome (24, 25). In dicistroviruses, a conserved motif, Asp-Asp-Phe (DDF), in VP1 was suggested to catalyze the VP4 cleavage (22). *Triatoma* virus and black queen cell virus, from the family Dicistroviridae, do

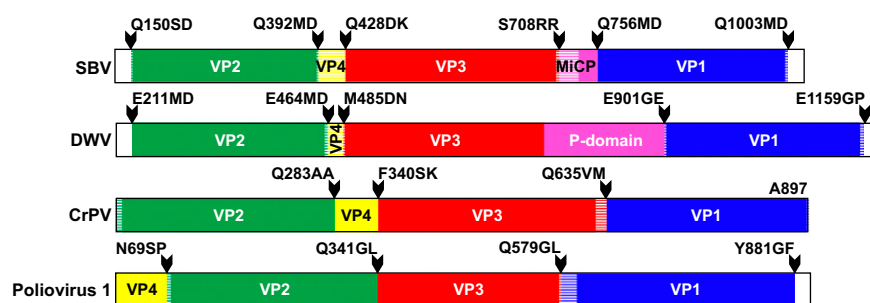


Fig. 2. Organization of P1 polyproteins of iflaviruses SBV and DWV, dicistrovirus cricket paralysis virus, and picornavirus poliovirus-1. Capsid proteins within P1 are labeled and colored according to the picornavirus convention: VP1 in blue, VP2 in green, VP3 in red, and VP4 in yellow. The MiCP of SBV and P-domain of DWV are highlighted in magenta. Note that translation of the P1 sequence of CrPV is initiated from an independent internal ribosomal entry site located after the coding sequence for the virus polymerase. Arrowheads indicate positions of protease cleavage sites, and the target cleavage sequences are shown. Parts of the proteins resolved in experimentally determined structures are shown in bright colors; the parts highlighted with hatching are not structured.

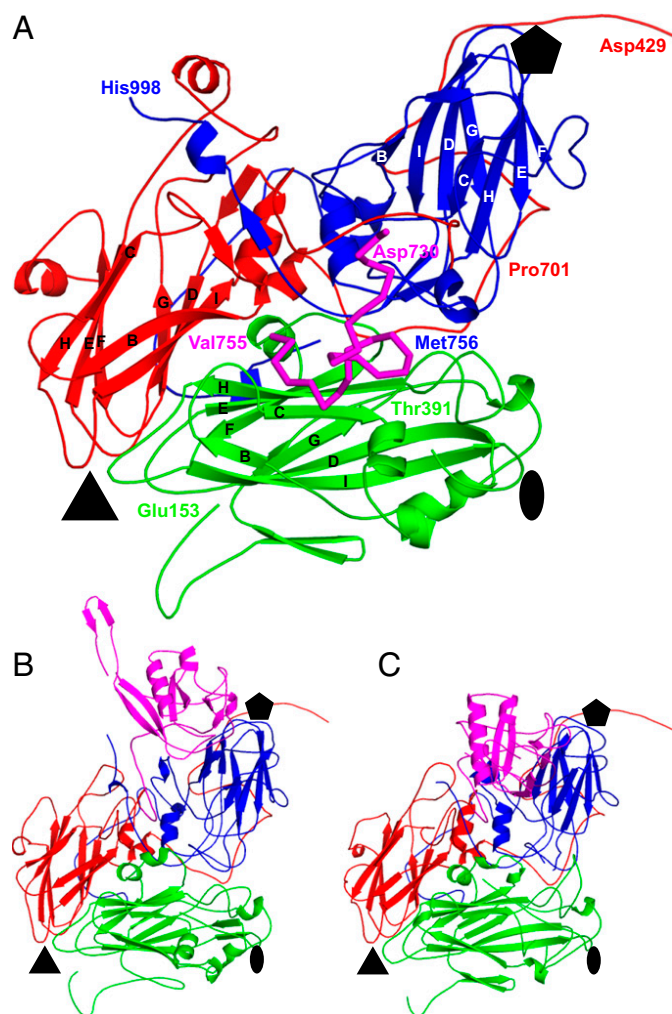


Fig. 3. Comparison of icosahedral asymmetric units of SBV, DWV, and SBPV. Icosahedral asymmetric unit of SBV (A), DWV (B), and SBPV (C) in cartoon representation with major capsid protein VP1 in blue, VP2 in green, and VP3 in red. The MiCP of SBV is highlighted as a magenta ribbon (A). β -strands of the major capsid proteins are labeled. P-domains of VP3 subunits of DWV and SBPV are highlighted in magenta (B and C). The locations of the fivefold, threefold, and twofold symmetry axes are denoted by pentagons, triangles, and ovals, respectively.

not contain structured VP4 subunits (26, 27), but the VP4 peptides are present in the virions and likely function in the transport of the genome across the endosome membrane into the cell cytoplasm (27). Some iflaviruses, including SBV and SBPV, also

contain the DDF motif in their VP1 subunits (7, 8). The DDF motif of VP1 of SBV is located at the inner face of the SBV virion next to the N terminus of the VP3 subunit of another protomer from the same pentamer (*SI Appendix, Fig. S2*). Therefore, the DDF motif might function in the cleavage of VP0 subunits of SBV. Nevertheless, VP4 subunits are not resolved in the electron density maps of SBV virions and could not be detected in the particles by MS analysis (*SI Appendix, Fig. S1*). Similarly, VP4 subunits were not resolved in the structures of SBPV and DWV (7, 8), and they likely were not present in the virions. It is possible that the short 38-residue VP4 subunits of SBV diffuse from the virions after the maturation cleavage of VP0. Iflaviruses lacking the VP4 subunits need to use a different mechanism to penetrate the host membrane than that used by the previously studied picornaviruses and dicistroviruses.

Structure and Putative Receptor-Binding Function of the MiCP. The MiCP is a 48-aa-long protein with a molecular weight of 5.4 kDa. Residues 1–21 of the MiCP, which are not resolved in the SBV virion structure, are more varied among the different SBV isolates than residues 22–47, which form the structured part of the peptide (*SI Appendix, Fig. S3*). The higher tolerance of the flexible part of the MiCP to mutations indicates that its biological function might not depend on a specific structure. In contrast, the structured part is more conserved, as it is required for binding to the virion surface. The structured 26 residues of the MiCP form a loop that turns 360° on itself (Fig. 3A). The MiCP is positioned above the core of subunit VP2 almost equidistant from the icosahedral twofold, threefold, and fivefold symmetry axes of the capsid (Fig. 3A). The N-terminal arm of the MiCP extends toward the icosahedral fivefold axis and interacts with subunits VP1 and VP3. The MiCP binds to the capsid through an interface area of 1,100 Å² formed by 24 residues of VP2, 7 residues of VP1, and 6 residues of VP3 (Fig. 4A). An occupancy refinement showed that MiCP peptides are present in all 60 positions at the virion surface (Table 1).

The volume at the surface of the SBV virion occupied by the MiCP is taken up by the EF loop known as the “puff” loop from the VP2 subunit in enteroviruses (Fig. 4B and C) (9, 28). In poliovirus 1, the 65-residue-long puff loop forms the outer rim of the canyon (Fig. 4C) (28). In contrast, the puff loop of SBV is only 18 residues long (Fig. 4B). In addition, subunit VP3 of SBV lacks a loop known as a “knob” formed by residues before the β -strand B of enteroviruses (Fig. 4D and E). It has been shown that residues from the puff and knob of many enteroviruses participate in receptor binding (29). Therefore, because of its location at the virion surface, it is possible that the MiCP is involved in SBV receptor recognition.

Evolutionary Relationships Within the Family Iflaviridae. There are no structural or sequence similarities between the 48-residue-long MiCP of SBV and the 160-residue-long P-domains of SBPV

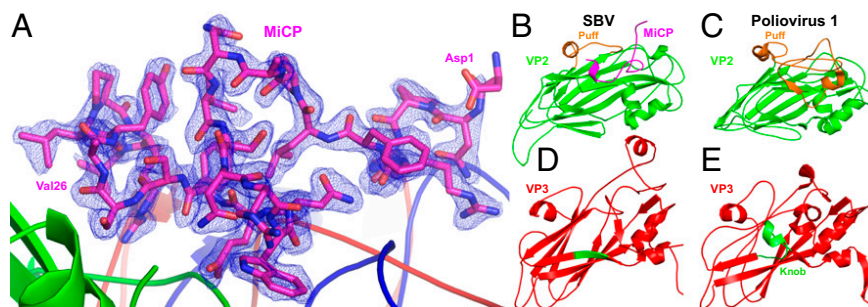


Fig. 4. Structure of the MiCP and its interaction with other capsid proteins. (A) Structure of the MiCP shown in stick representation with carbon atoms in magenta. The first and last structured residues of MiCP are labeled. The electron density map of the MiCP contoured at 2 σ is shown as a blue mesh. Major capsid proteins are shown in cartoon representation with VP1 in blue, VP2 in green, and VP3 in red. (B and C) Comparison of capsid proteins VP2 of SBV (B) and poliovirus 1 (C). The MiCP of SBV, which is highlighted in magenta (B), occupies the volume of the puff loop in VP2 of poliovirus 1, highlighted in orange (C). (D and E) The VP3 subunit of SBV (D) lacks the knob loop present in poliovirus 1 (E), highlighted in green.

Table 1. Comparison of SBV structures under various pH and expansion states

| Parameter | Crystal structure | Virion, pH 7.4 | Empty particle, pH 7.4 | Virion, pH 5.8 | Empty particle, pH 5.8, expansion state I | Empty particle, pH 5.8, expansion state II |
|--|-------------------|----------------|------------------------|----------------|---|--|
| Resolution, Å | 2.10 | 3.22 | 3.87 | 3.18 | 4.06 | 7.25 |
| MiCP occupancy | 1.02 | 0.86 | 0.77 | 0.94 | 0.93 | 0.79 |
| Particle radius,* Å | 136.4 | 136.1 | 137.4 | 136.1 | 137.9 | 139.8 |
| Pentamer distance, [†] Å | 135.8 | 134.4 | 135.7 | 134.4 | 136.2 | 138.4 |
| Pentamer contacts, Å ² | 4,250 | 4,550 | 1,750 | 4,450 | 1,750 | 700 |
| Average B-factor, Å ² | 25 | 39 | 88 | 43 | 118 | 200 |
| Diameter of pore on threefold axis, Å | 4.4 | 3.6 | 4.4 | 3.6 | 5.0 | 7.4 |
| Average B-factor of residues close to threefold axis, Å ² | 23 | 35 | 104 | 40 | 143 | 200 |
| Diameter of pore on fivefold axis, Å | 5.2 | 5.2 | 5.6 | 5.6 | 5.0 | 12.0 |
| Average B-factor of residues close to fivefold axis, Å ² | 19 | 36 | 102 | 41 | 137 | 200 |
| Diameter of pore on twofold axis, Å | 2.6 | 2.6 | 2.8 | 2.4 | 3.0 | 2.8 |
| Average B-factor of residues close to twofold axis, Å ² | 21 | 35 | 55 | 37 | 73 | 200 |

*Particle radius is defined as the distance of the center of mass of the icosahedral asymmetric unit from the particle center.

[†]Pentamer distance is defined as the distance of the centers of mass of two neighboring pentamers.

and DWV. Nevertheless, the locations of the sequences coding the MiCP and P-domains in Iflavirus genomes show that both the MiCP and P-domains evolved as C-terminal extensions of VP3 subunits (Fig. 2). The evolution of the MiCP required the introduction of a cleavage site for virus protease 3C. The phylogenetic tree based on a comparison of the P1 sequences of iflaviruses shows that the family can be divided into two groups: viruses that lack P-domains and viruses with P-domains (Fig. 5A and *SI Appendix*, Fig. S4). The P-domain appears to be a filial feature. Based

on sequence analysis, it is not clear whether all the iflaviruses that lack the P-domains contain MiCPs. A structure-based phylogenetic tree shows branching inside the Iflaviridae family of viruses with and without P-domains (Fig. 5B), corroborating the sequence-based separation of P-domain-containing iflaviruses into a subgroup within the family Iflaviridae.

Genome Release Mechanism of SBV. The cell entry mechanism of iflaviruses is unknown, but the process likely involves receptor-mediated

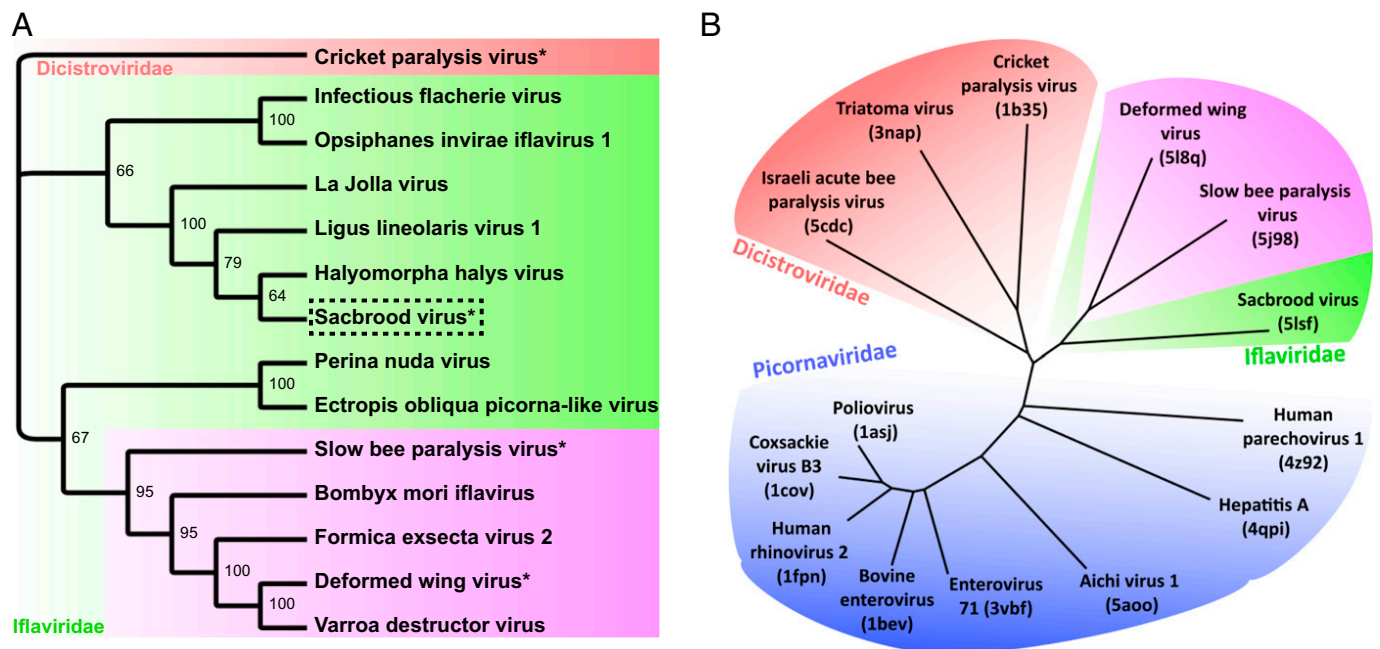


Fig. 5. Phylogenetic analyses of viruses from the families Iflaviridae, Dicistroviridae, and Picornaviridae. (A) Maximum likelihood tree constructed from whole polyprotein sequences of selected iflaviruses with cricket paralysis virus as an outgroup (highlighted in red). Iflaviruses with P-domain are highlighted in the magenta box. The dashed box indicates viruses with observed MiCP; the asterisk indicates viruses with an experimentally determined virion structure. Values at nodes represent thorough bootstrap support. **(B)** Structure-based neighbor-joining phylogeny tree with picornaviruses highlighted in blue, dicistroviruses in red, and iflaviruses in green. The subgroup of iflaviruses with P-domains is highlighted in magenta.

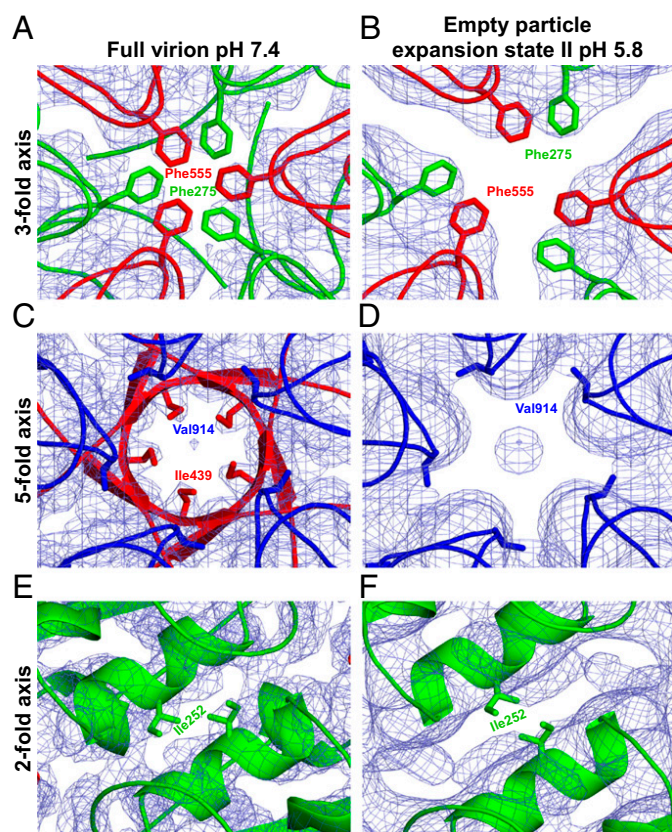


Fig. 6. Comparison of capsid protein conformations close to the threefold, fivefold, and twofold axes of SBV virions and empty particles. The capsid protein loops that form contacts in the vicinity of rotation axes of the capsid are shown in cartoon representation. VP1, VP2, and VP3 are shown in blue, green, and red, respectively. Side chains of residues closest to the rotation axes are shown as sticks; the density map is depicted as a blue mesh. Details of native virion at pH 7.4 (A, C, and E) and the more expanded empty particle at pH 5.8 (B, D, and F) are shown.

endocytosis, as is the case for related picornaviruses (29). Endosomal entry involves exposure of the virions to an environment with acidic pH (30, 31). In picornaviruses, the acidic pH triggers the formation of activated (A)-particles that are expanded, contain pores in capsids, and spontaneously release their genomes (29, 31–33). Freshly purified samples of SBV contain 5% empty particles (*SI Appendix*, Fig. S5A). We used cryo-EM to determine the structures of the full virions and empty particles to resolutions of 3.2 Å and 3.8 Å, respectively (*SI Appendix*, Figs. S6 and S7 and Table S1). The structure of the full virion is nearly identical to that determined by X-ray crystallography, with an rmsd of the corresponding C α atoms of the two structures of 0.44 Å (*SI Appendix*, Table S2). The empty particle is expanded 1.2 Å in radius relative to the genome-containing virion (Table 1). The capsid enlargement is accompanied by movements of pentamers of capsid protein protomers away from one another (Table 1) and by a reduction in interpentamer contacts, as residues 1–14 of VP1 and residues 1–40 of VP2 are not resolved in the empty particles.

The sample of SBV incubated in PBS with pH 5.8, which mimics the environment in endosomes (34), contained 80% empty particles (*SI Appendix*, Fig. S5B). The structure of the full virions at acidic pH, which was determined to a resolution of 3.2 Å (*SI Appendix*, Figs. S6 and S7 and Table S1), is similar to that of the virus at neutral pH, as determined by both X-ray crystallography and cryo-EM (rmsd of 0.32 Å and 0.27 Å, respectively) (*SI Appendix*, Table S2). The structural similarity of the virions, together with the observation that empty SBV particles are expanded, as discussed below, suggests that the SBV RNA genome

contributes to the stability of the virion; however, direct protein–RNA interactions are not resolved in the electron density maps.

Classification of the empty particles from the acidic pH sample identified two capsid expansion intermediates. The smaller of the two capsids was radially expanded by 1.5 Å relative to the native virions, and determined to a resolution of 4.1 Å, whereas the larger one was radially expanded by 3.4 Å and determined to a resolution of 7.3 Å (*SI Appendix*, Figs. S6 and S7 and Table S1). The smaller particle contains pores 5.0 Å in diameter located at the icosahedral threefold axes, whereas the pores in the more expanded particle are 7.4 Å in diameter (Fig. 6A and B, Table 1, and *SI Appendix*, Fig. S8). These pores are not of sufficient size to allow passage of the single-stranded SBV RNA genome. However, amino acids that form the loops of capsid proteins adjacent to the pores have higher temperature factors than the rest of the structure (Table 1). This indicates that the loops are flexible. Furthermore, the presence of two expansion intermediates suggests that the empty SBV capsids are dynamic. The possible role of pores at threefold axes of SBV capsids as channels for genome release is consistent with our previous study of the genome release of SBPV (15). In contrast, Organtini et al. (13) speculated that the genome of DWV may escape from particles through a channel in a fivefold vertex of its capsid. In native SBV virions, the N termini of VP3 subunits form a 5.2-Å narrow iris-like constriction of the channel along the fivefold axis (Fig. 6C, Table 1, and *SI Appendix*, Fig. S8). However, in the more expanded acidic pH empty capsid of SBV, residues 1–48 of VP3 are not structured (Fig. 6D and *SI Appendix*, Fig. S8). Thus, the more expanded empty SBV particles also contain 12-Å-diameter pores along the fivefold axes (Fig. 6D, Table 1, and *SI Appendix*, Fig. S8). The putative release of the SBV genome through pores along threefold or fivefold symmetry axes differs from the currently accepted genome release mechanism of picornaviruses, in which the pores along twofold icosahedral symmetry axes have been implicated (35–37). Pores along the twofold axes of SBV particles are not expanded after genome release, as is the case in enteroviruses (Fig. 6E and F, Table 1, and *SI Appendix*, Fig. S8).

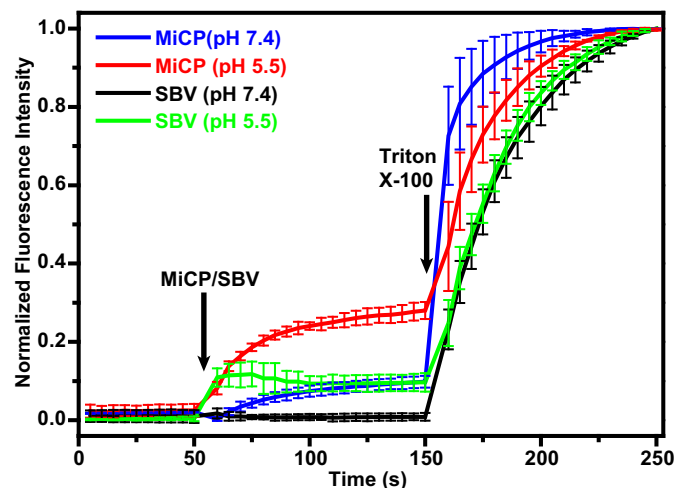


Fig. 7. The MiCP induces disruption of liposomes at pH 5.5. Liposomes containing carboxyfluorescein were mixed with MiCP at a final concentration of 2 μ M in a solution at pH 7.4 (blue line) at the 50-s time point (MiCP/SBV arrow). Liposomes were mixed with SBV virions at a final concentration of 2 nM, corresponding to an MiCP concentration of 120 nM in a solution at pH 7.4 (black line). Liposomes were mixed with MiCP at a final concentration of 2 μ M in a solution at pH 5.5 (red line). Liposomes were mixed with SBV virions at a final concentration of 2 nM in a solution at pH 5.5 (green line). The liposomes were disrupted with 1% Triton X-100 at the 150-s time point (arrow). The fluorescence of carboxyfluorescein was increased due to the dequenching effect of fluorophore dilution after the liposomes dissolved. Measured arbitrary fluorescence values were normalized and plotted as an average of three independent experiments with SDs.

The MiCP May Facilitate Delivery of SBV Genome into Cytoplasm.

MiCP subunits are tightly associated with the native virions of SBV (Table 1). In contrast, in empty SBV particles, particularly those exposed to acidic pH, the electron density corresponding to the MiCP is visible only at lower contour levels than the rest of the capsid. The occupancy refinement indicates that some of the MiCP subunits detach from empty SBV particles at pH 5.8 (Table 1). The dissociation of MiCPs from the SBV capsid occurs in similar conditions as the release of VP4 subunits from the virions of dicistroviruses and picornaviruses before genome egress (29, 31–33). Furthermore, the hydrophobicity profile of the MiCP is similar to that of the VP4 of HRV16 (*SI Appendix, Fig. S3B*). The MiCP with an N-terminal His₆-SUMO tag is expressed as soluble protein in *Escherichia coli* and remains soluble after cleavage of the tag (*SI Appendix, Fig. S9*). However, MiCP expression blocks growth of the bacterial culture at 1 h after induction (*SI Appendix, Fig. S9*). In buffer with pH 5.5, MiCP subunits at micromolar concentrations induce the disruption of liposomes with phospholipid content mimicking that of endosomes (Fig. 7 and *SI Appendix, Fig. S10*) (38). The effect of SBV virions on liposomes in the same conditions is limited (Fig. 7 and *SI Appendix, Fig. S10*); however, in native conditions, receptor binding might contribute to more efficient release of MiCP subunits from virions and thus allow the protein to disrupt the endosome membranes. The biological function of the MiCP may be similar to that of the VP4 of picornaviruses, to facilitate transport of the virus genome across the endosome membrane into the cell cytoplasm (39, 40).

In summary, our results show that SBV virions are structurally distinct from virions of DWV and SBPV. We demonstrate that acidic pH triggers expansion of SBV capsids, genome release, and the partial dissociation of MiCP subunits from the virion

surface. Subsequently, the MiCP subunits may disrupt the endosome membrane to allow the virus genome to reach the cell cytoplasm and initiate infection.

Methods

The propagation of SBV in honey bee larvae was performed as described in The COLOSS *BEEBOOK* (41). Purified SBV was applied onto holey carbon grids and vitrified by plunge-freezing in liquid ethane. Micrographs were recorded with a Falcon II camera in a Titan Krios transmission electron microscope (Thermo Fisher Scientific). Acquired data were processed using the RELION package (42). Crystals of SBV were obtained from the identical material with the hanging-drop technique in crystallization conditions containing 0.05 M magnesium chloride, 0.1 M MES, 8% isopropanol, and 4% PEG 4000. The MiCP was expressed in *E. coli*, purified with Ni-NTA chromatography, and diluted in two types of buffer (pH 8.0 and pH 5.5). A suspension of liposomes filled with carboxyfluorescein dye was distributed to a 96-well plate, and the MiCP was added to wells with respective buffer conditions. Resulting changes in fluorescence levels were recorded before and after the addition of 1% Triton X-100. The methodology is described in detail in *SI Appendix, Methods*.

ACKNOWLEDGMENTS. X-ray data were collected at Soleil Synchrotron, beamline Proxima 1. We acknowledge the Central European Institute of Technology (CEITEC) Core Facilities Cryo-Electron Microscopy and Tomography, Proteomics, and Biomolecular Interactions, supported by Czech Infrastructure for Integrative Structural Biology Project LM2015043, funded by the Ministry of Education, Youth, and Sports (MEYS) of the Czech Republic. This research was carried out under the project CEITEC 2020 (LQ1601), with financial support from the MEYS under National Sustainability Program II. This work was supported by the IT4I Project (CZ.1.05/1.1.00/02.0070), funded by the European Regional Development Fund and the national budget of the Czech Republic via the Research and Development for Innovations Operational Program, as well as the MEYS via Grant LM2011033. The research leading to these results received funding from the European Research Council under Grant Agreement 335855 (to P.P.) and EMBO Grant Agreement IG3041 (to P.P.).

- Ellis JD, Munn PA (2005) The worldwide health status of honey bees. *Bee World* 86:88–101.
- Breeze TD, Bailey AP, Balcombe KG, Potts SG (2011) Pollination services in the UK: How important are honeybees? *Agric Ecosyst Environ* 142:137–143.
- Gisder S, Gensch E (2017) Viruses of commercialized insect pollinators. *J Invertebr Pathol* 147:51–59.
- Choe S-E, et al. (2012) Genetic and phylogenetic analysis of South Korean sacbrood virus isolates from infected honey bees (*Apis cerana*). *Vet Microbiol* 157:32–40.
- Ghosh RC, Ball BV, Willcocks MM, Carter MJ (1999) The nucleotide sequence of sacbrood virus of the honey bee: An insect picorna-like virus. *J Gen Virol* 80:1541–1549.
- Rossmann MG, Johnson JE (1989) Icosahedral RNA virus structure. *Annu Rev Biochem* 58:533–573.
- Kalynych S, et al. (2016) Virion structure of iflavirus slow bee paralysis virus at 2.6-Ångstrom resolution. *J Virol* 90:7444–7455.
- Škubník K, et al. (2017) Structure of deformed wing virus, a major honey bee pathogen. *Proc Natl Acad Sci USA* 114:3210–3215.
- Rossmann MG, et al. (1985) Structure of a human common cold virus and functional relationship to other picornaviruses. *Nature* 317:145–153.
- Harrison SC, Olson AJ, Schutt CE, Winkler FK, Bricogne G (1978) Tomato bushy stunt virus at 2.9-Å resolution. *Nature* 276:368–373.
- de Miranda JR, et al. (2010) Genetic characterization of slow bee paralysis virus of the honeybee (*Apis mellifera* L.). *J Gen Virol* 91:2524–2530.
- Zhang J, et al. (2001) Three-dimensional structure of the Chinese sacbrood bee virus. *Sci China C Life Sci* 44:443–448.
- Organtini LJ, et al. (2017) Honey bee deformed wing virus structures reveal that conformational changes accompany genome release. *J Virol* 91:e01795-16.
- Rueckert RR, Wimmer E (1984) Systematic nomenclature of picornavirus proteins. *J Virol* 50:957–959.
- Kalynych S, Füzik T, Prídál A, de Miranda J, Plevka P (2017) Cryo-EM study of slow bee paralysis virus at low pH reveals iflavirus genome release mechanism. *Proc Natl Acad Sci USA* 114:598–603.
- Nicklin MJ, Kräusslich HG, Toyoda H, Dunn JJ, Wimmer E (1987) Poliovirus polypeptide precursors: Expression in vitro and processing by exogenous 3C and 2A proteinases. *Proc Natl Acad Sci USA* 84:4002–4006.
- Pallai PV, et al. (1989) Cleavage of synthetic peptides by purified poliovirus 3C proteinase. *J Biol Chem* 264:9738–9741.
- Plevka P, et al. (2013) Structure of human enterovirus 71 in complex with a capsid-binding inhibitor. *Proc Natl Acad Sci USA* 110:5463–5467.
- Smith TJ, et al. (1986) The site of attachment in human rhinovirus 14 for antiviral agents that inhibit uncoating. *Science* 233:1286–1293.
- Badger J, et al. (1988) Structural analysis of a series of antiviral agents complexed with human rhinovirus 14. *Proc Natl Acad Sci USA* 85:3304–3308.
- van Oers MM (2010) Genomics and biology of iflaviruses. *Insect Virology*, eds Johnson K, Agari S (Caister Academic Press, Poole, UK), pp 231–250.
- Tate J, et al. (1999) The crystal structure of cricket paralysis virus: The first view of a new virus family. *Nat Struct Biol* 6:765–774.
- Agirre J, et al. (2011) Capsid protein identification and analysis of mature Triatoma virus (TrV) virions and naturally occurring empty particles. *Virology* 409:91–101.
- Arnold E, et al. (1987) Implications of the picornavirus capsid structure for polyprotein processing. *Proc Natl Acad Sci USA* 84:21–25.
- Harber JJ, Bradley J, Anderson CW, Wimmer E (1991) Catalysis of poliovirus VP0 maturation cleavage is not mediated by serine 10 of VP2. *J Virol* 65:326–334.
- Spurny R, et al. (2017) Virion structure of black queen cell virus, a common honeybee pathogen. *J Virol* 91:e02100–e02116.
- Squires G, et al. (2013) Structure of the Triatoma virus capsid. *Acta Crystallogr D Biol Crystallogr* 69:1026–1037.
- Hogle JM, Chow M, Filman DJ (1985) Three-dimensional structure of poliovirus at 2.9-Å resolution. *Science* 229:1358–1365.
- Rossmann MG (1994) Viral cell recognition and entry. *Protein Sci* 3:1712–1725.
- Fuchs R, Blaas D (2010) Uncoating of human rhinoviruses. *Rev Med Virol* 20:281–297.
- Neubauer C, Frasel L, Kuechler E, Blaas D (1987) Mechanism of entry of human rhinovirus 2 into HeLa cells. *Virology* 158:255–258.
- Garriga D, et al. (2012) Insights into minor group rhinovirus uncoating: The X-ray structure of the HRV2 empty capsid. *PLoS Pathog* 8:e1002473.
- Wang X, et al. (2012) A sensor-adaptor mechanism for enterovirus uncoating from structures of EV71. *Nat Struct Mol Biol* 19:424–429.
- Geisow MJ, Evans WH (1984) pH in the endosome: Measurements during pinocytosis and receptor-mediated endocytosis. *Exp Cell Res* 150:36–46.
- Shingler KL, et al. (2013) The enterovirus 71 a-particle forms a gateway to allow genome release: A cryoEM study of picornavirus uncoating. *PLoS Pathog* 9:e1003240.
- Lyu K, et al. (2014) Human enterovirus 71 uncoating captured at atomic resolution. *J Virol* 88:3114–3126.
- Bostina M, Levy H, Filman DJ, Hogle JM (2011) Poliovirus RNA is released from the capsid near a twofold symmetry axis. *J Virol* 85:776–783.
- van Meer G, Voelker DR, Feigenson GW (2008) Membrane lipids: Where they are and how they behave. *Nat Rev Mol Cell Biol* 9:112–124.
- Panjwani A, et al. (2014) Capsid protein VP4 of human rhinovirus induces membrane permeability by the formation of a size-selective multimeric pore. *PLoS Pathog* 10:e1004294.
- Danthi P, Tosteson M, Li Q-H, Chow M (2003) Genome delivery and ion channel properties are altered in VP4 mutants of poliovirus. *J Virol* 77:5266–5274.
- de Miranda JR, et al. (2013) *The COLLOS BEEBOOK: Standard Methods for Apis mellifera Pest and Pathogen Research* (IBRA, Treforest, UK).
- Scheres SHW (2012) RELION: Implementation of a Bayesian approach to cryo-EM structure determination. *J Struct Biol* 180:519–530.

PAPER XI



ARTICLE

<https://doi.org/10.1038/s41467-019-09132-x>

OPEN

Enterovirus particles expel capsid pentamers to enable genome release

David Buchta¹, Tibor Füzik¹, Dominik Hřebík¹, Yevgen Levdansky^{1,3}, Lukáš Sukeník^{1,2}, Liya Mukhamedova¹, Jana Moravcová¹, Robert Vácha^{1,2} & Pavel Plevka¹

Viruses from the genus *Enterovirus* are important human pathogens. Receptor binding or exposure to acidic pH in endosomes converts enterovirus particles to an activated state that is required for genome release. However, the mechanism of enterovirus uncoating is not well understood. Here, we use cryo-electron microscopy to visualize virions of human echovirus 18 in the process of genome release. We discover that the exit of the RNA from the particle of echovirus 18 results in a loss of one, two, or three adjacent capsid-protein pentamers. The opening in the capsid, which is more than 120 Å in diameter, enables the release of the genome without the need to unwind its putative double-stranded RNA segments. We also detect capsids lacking pentamers during genome release from echovirus 30. Thus, our findings uncover a mechanism of enterovirus genome release that could become target for antiviral drugs.

¹Central European Institute of Technology, Masaryk University, Kamenice 5, Brno 625 00, Czech Republic. ²Faculty of Science, Masaryk University, Kamenice 5, Brno 625 00, Czech Republic. ³Present address: Max Planck Institute for Developmental Biology, Max-Planck-Ring 5, 72076 Tübingen, Germany. Correspondence and requests for materials should be addressed to P.P. (email: pavel.plevka@ceitec.muni.cz)

Viruses from the family *Picornaviridae* form non-enveloped icosahedral virions that are about 30 nm in diameter. Picornavirus capsids protect 8000-nucleotide-long single-stranded RNA genomes, which are translated into polyproteins that are co-translationally and post-translationally cleaved by viral proteases to produce structural (capsid-forming) and non-structural proteins¹. The capsid proteins VP1, VP2, VP3, and VP4 originating from a single polyprotein form a protomer, the basic building block of the icosahedral capsid. The entire capsid consists of 60 such protomers, arranged in 12 pentamer units.

The interactions of enteroviruses with receptors or exposure to acidic pH in endosomes induce conformational changes in virions into an activated state characterized by increased particle diameter, reduced contact areas between pentamers of capsid protein protomers, release of VP4 subunits from particles, and externalization of the N termini of VP1 subunits^{1–5}. The activated particles of numerous enteroviruses were shown to contain openings along two-fold ($5 \times 10 \text{ \AA}$) or five-fold (diameters of up to 8 \AA) axes of icosahedral symmetry of their capsids^{2–6}. It has been speculated that these pores serve for the release of enterovirus genomes^{3,6–10}. However, capsids of viruses from the families *Reoviridae* and *Totiviridae* that release single-stranded RNAs as part of their replication cycles contain circular pores larger than 15 \AA in diameter^{11,12}. The size of the pores in enterovirus capsids is not sufficient for the passage of single-stranded RNA^{2–6,13–15}. Furthermore, enterovirus genomes contain sequences that form double-stranded RNA segments, which fold into three-dimensional (3D) structures, such as the internal ribosomal entry site required to initiate translation of viral RNA¹⁶. If these double-stranded RNA segments were present inside enterovirus particles, then the genome release would require either the opening of pores larger than 40 \AA in diameter, or a mechanism to unwind the double-stranded RNA. However, there is no evidence of an association between enzymes with RNA helicase activity and enterovirus virions^{1,17}. The structures of enterovirus particles before and after genome release have been characterized at high resolution^{3,6–10}. Most of these cryo-electron microscopy (cryo-EM) and X-ray crystallography studies imposed icosahedral symmetry during the structure determination process and were not aimed at identifying the unique site of genome exit^{3–7,9}. Asymmetric single-particle reconstruction and sub-tomogram averaging studies, at a resolution of 50 \AA , were used to indicate that RNA exits poliovirus particles close to a two-fold axis⁸. The end stage of the enterovirus genome release are the empty capsids, the structures of which were determined for several enteroviruses^{4,5}.

Here we show that the exit of the RNA from the particles of echoviruses 18 and 30 requires capsid opening and results in a loss of up to three adjacent capsid protein pentamers. The large openings in the capsid enable the release of the genomes without uncoiling their double-stranded RNA segments.

Results and Discussion

Opening of particles enables genome release of echovirus 18. We imaged enterovirus particles in the process of genome release by cryo-EM. Specifically, we performed cryo-EM of echovirus 18 virions exposed to pH 6.0 for 10 min, mimicking the acidic environment that the virus encounters in endosomes (Fig. 1a, Supplementary Fig. 1). Reference-free two-dimensional (2D) class averages show that the particles releasing genomes lack parts of their capsids (Fig. 1b). Asymmetric reconstruction combined with 3D classification identified subpopulations of echovirus 18 particles that lacked up to three pentamers of capsid protein protomers (Fig. 2a–c, Supplementary Fig. 2a). The missing pentamers always formed a single compact opening through the

capsid (Fig. 2a–c). We call the particles lacking one or several pentamers open particles. The remaining particles with complete capsids were either activated particles or empty capsids (Supplementary Fig. 2a). We did not detect native echovirus 18 virions that lacked pentamers at neutral pH. The asymmetric reconstructions of the open particles were determined to resolutions better than 9 \AA (Supplementary Table 1, Supplementary Figs 3–5). The absence of one pentamer of capsid protein protomers creates a 120 \AA -diameter pore in the capsid (Fig. 2a). The openings formed by the removal of one or more pentamers are sufficiently large to allow release of the viral RNA, even if the genome contains double-stranded RNA segments. Individual micrographs of the open particles frequently show multiple strands of RNA passing through the pore (Fig. 1b). In the 3D reconstructions, the capsid openings contain featureless electron densities with average values two times lower than those of the protein capsid (Fig. 2d–i). This diffuse electron density corresponds to an average of the RNA genomes escaping from the virions, which have unique conformations in each of the particles included in the reconstructions (Fig. 1b). In contrast to the formation of the open particles of echovirus 18, complete capsids were observed in the cryo-EM study of the genome release of poliovirus⁸. However, the poliovirus uncoating was induced by the exposure of particles to $56 \text{ }^\circ\text{C}$, which may have affected the secondary structure of the genome and the mechanism of its release. A comparison of the distribution of charges and hydrophobic areas at the inter-pentamer contacts (Supplementary Fig. 6) and a comparison of the inter-pentamer buried surface areas (Supplementary Table 2) of enteroviruses do not provide evidence why distinct enteroviruses should employ different genome release mechanisms.

High-resolution structures of open particles of echovirus 18.

Reconstructions of the open particles missing one, two, or three pentamers with imposed five-fold, two-fold, and three-fold symmetries, respectively, were determined to resolutions of 3.8 , 4.1 , and 3.7 \AA , which allowed their molecular structures to be built (Fig. 3, Supplementary Fig. 4, Supplementary Table 1). Except for the missing pentamers, the open particles are similar in structure to that of the activated echovirus 18 particle: increased diameter relative to the native virus, reduced inter-pentamer contacts, absence of VP4 subunits, and holes along icosahedral two-fold symmetry axes (Fig. 3, Supplementary Fig. 7)^{2–5,14,15}. The capsid proteins next to the missing pentamers are more mobile than the rest of the capsid, as indicated by the three times higher temperature factors than the remainder of the capsid. Residues 1–42 from the N termini of VP1 subunits, which were previously shown to interact with membranes and facilitate enterovirus genome delivery into the cytoplasm^{1,18,19}, are not resolved in the electron density map, indicating that their structures differ among particles. The N-termini of some of the VP1 subunits could reach out of the capsid through the openings formed by the missing pentamers. It has been shown that the RNA genome of poliovirus is protected against RNase A degradation during uncoating and transfer across the membrane²⁰. It may seem that opening the particles of echovirus 18 exposes their genomes for degradation. Nevertheless, in silico simulations (Fig. 4, Supplementary Movie 1) and considerations of genome diffusion from the capsid (for details, see Methods) show that the large capsid opening results in a microsecond release time of the genome. The short time required for genome release limits the potential for its degradation. The externalized VP4 subunits and N termini of VP1 were shown to be required for the subsequent transport of enterovirus genomes across the endosome membranes^{18,21–24}.

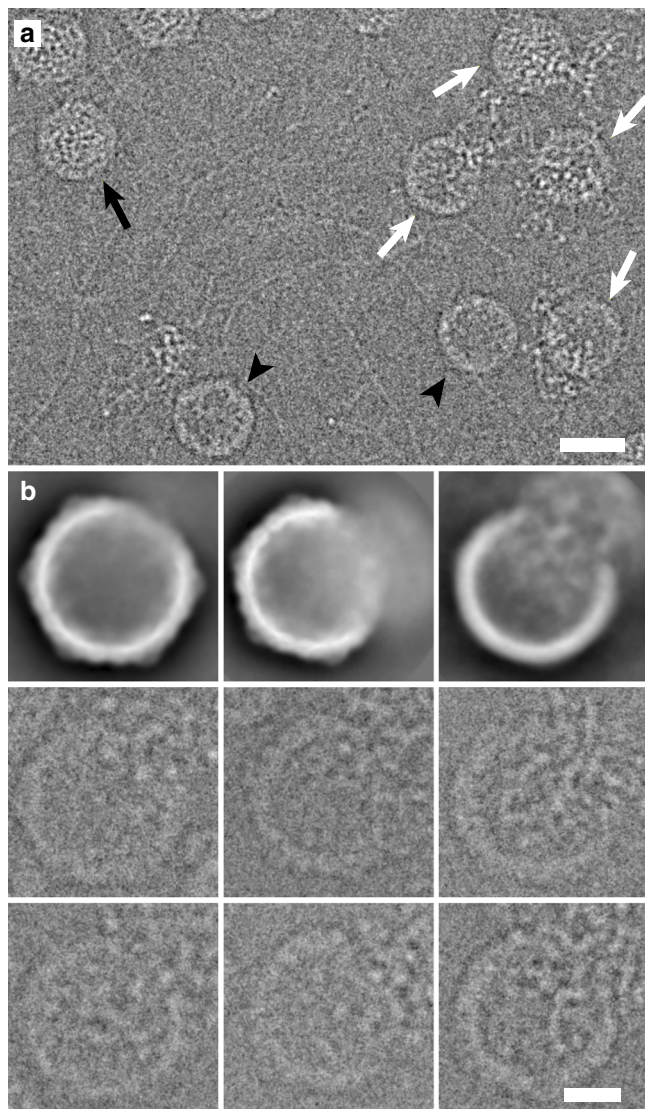


Fig. 1 Particles of echovirus 18 in the process of genome release lack parts of their capsids. **a** Cryo-electron micrograph of echovirus 18 particles captured in the process of genome release after incubation at acidic pH. Black arrow indicates activated particle, white arrows particles in the process of genome release, and black arrowheads empty particles. Scale bar represents 25 nm. **b** Reference-free two-dimensional class averages showing echovirus 18 particles in the process of RNA release lacking parts of their capsids. Two representative electron micrographs of particles are shown for each class average. Scale bar represents 10 nm

Re-structuring of echovirus 18 genome enables capsid opening.

Empty particles of echovirus 18 formed after genome release, induced by exposure to acidic pH for 2 h, were used to calculate their icosahedral reconstruction to a resolution of 3.2 Å (Supplementary Table 1, Supplementary Figs 4, 7). This is consistent with previous experiments, which show that empty capsids of enteroviruses are stable in vivo and in vitro^{1–5,20}. Because the empty capsids of echovirus 18 are stable under the experimental conditions, the discharged pentamers can bind back to the capsid openings after the genome release²⁵. It is likely that the re-assembly of the empty particles was favored by the high (0.5 mg/mL) concentration of echovirus 18 particles in samples that were prepared for cryo-EM observations. Nevertheless, the fate of the empty capsids after genome delivery is unimportant for the infection process in vivo.

The stability of echovirus 18 empty capsids under the conditions promoting genome release provides evidence that the force for the expulsion of pentamers from the activated particles is provided by the RNA genome. Comparing the cryo-EM images of native virions with activated particles of echovirus 18 (Fig. 5), as well as other enteroviruses^{3,26,27}, reveals that their genomic RNAs undergo conformational changes upon exposure to acidic pH. The conversion of echovirus 18 virions to activated particles occurred in <3 min after exposure to acidic pH at 37 °C, however some of the particles also released their RNA and aggregated (Supplementary Fig. 8). This rapid conversion to activated particles and genome release are consistent with previous experiments showing that human rhinovirus 2 delivers its genome into the cell cytoplasm within 2 min²⁸. The electron density of the genomes is distributed uniformly in echovirus 18 virions at neutral pH, but transforms to a grainy appearance in activated particles at acidic pH (Fig. 5). During the shift from neutral to acidic pH, the side chains of histidines of capsid proteins (Supplementary Fig. 9), and probably also parts of the genomic RNA, become protonated, and thus acquire more positive charge. The reduction in the negative charge may disrupt interactions between the RNA and positively charged polyamines present within the virions^{17,29,30}. The changes in the charge distribution and putative release of the polyamines from virions may result in the observed changes in the genome structure and increased pressure on the capsid from the inside. The inter-pentamer contacts of 11,000 Å² in native echovirus 18 virion are reduced to 5400 Å² in the activated particles. Correspondingly, the interaction between two pentamers in an activated particle of echovirus 18 is 25% weaker than that in a native virion (Supplementary Fig. 10). The weakening of the inter-pentamer contacts together with the changes in the genome organization, probably enable the opening of the activated particles for genome release.

Molecular dynamics simulation of genome release.

The dynamics of the capsid opening and genome release were investigated using in silico simulations of a simplified model of the picornavirus capsid with its genome (Fig. 4). Using certain parameters in the model (for details, see Methods), we observed genome release after which a pentamer was separated from a capsid (Fig. 4, Supplementary Movie 1). In the simulations, the capsid first cracked open to allow the release of part of the genome. During this process, one or a few pentamers separated from the rest of the capsid. Subsequently, the two fragments of the capsid closed, resulting in an open capsid missing one or a few pentamers (Fig. 4). The pressure from the inside of the particle required to crack open the capsid is two-thirds of that required to expel a pentamer (for details, see Methods). Consequently, enterovirus capsids are more likely to rupture into two halves than to expel a single pentamer. After capsid rupture the genome pressure decreases, so that the two halves of the capsid may not separate completely and can quickly reassemble. The escaping genome can break off some pentamers, as observed in our cryo-EM experiments and simulations.

Open particles were also observed for other enteroviruses.

Open particles are also present in the samples of echovirus 30 (Fig. 6). Furthermore, Harutyunyan et al. detected particles lacking pentamers in a sample of human rhinovirus 2 with crosslinked RNA genomes exposed to acidic pH²⁶. These observations indicate that enteroviruses may release their genomes through openings formed by the removal of pentamers of capsid protein protomers from their capsids. Numerous capsid-binding antiviral compounds inhibit the genome release of

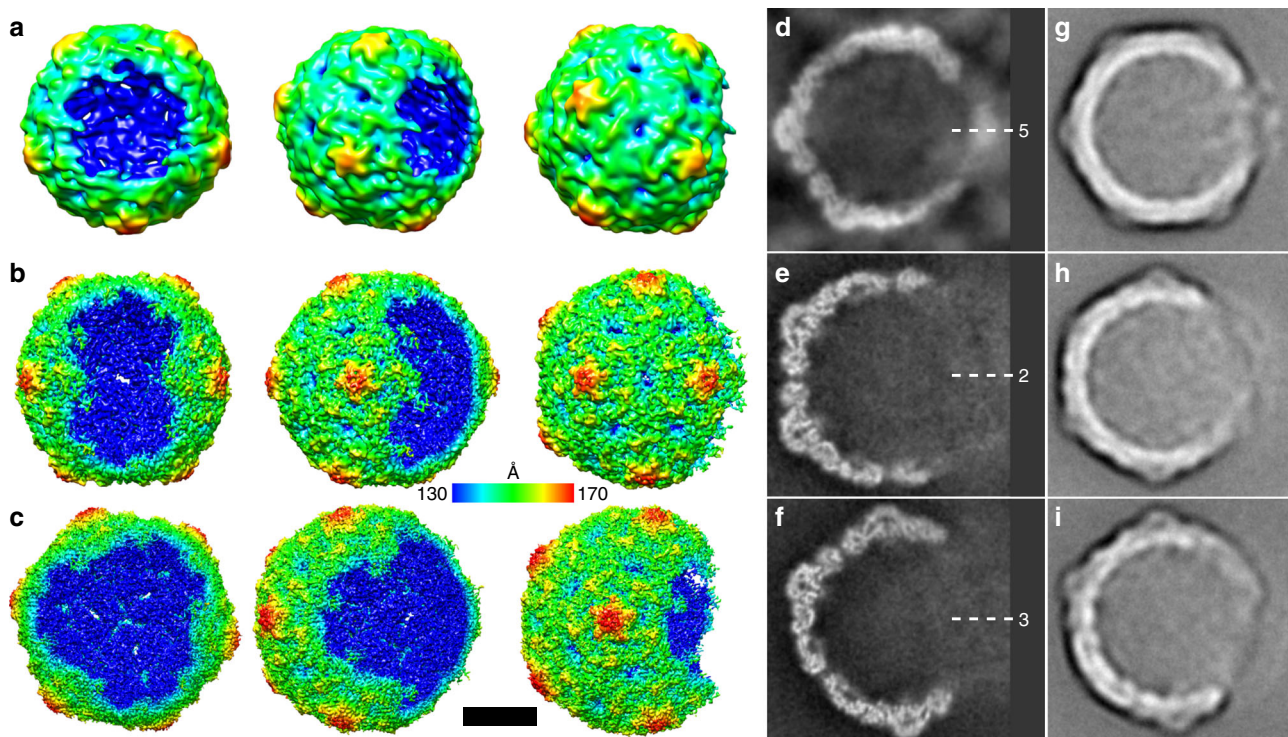


Fig. 2 Open particles of echovirus 18 lacking one, two, or three adjacent pentamers. **a–c** Asymmetric three-dimensional reconstructions of open particles lacking one (**a**), two (**b**), or three (**c**) pentamers. The electron density maps are rainbow colored based on the distance of the electron density surface from the particle center. **d–f** Electron density distributions in central sections of asymmetric reconstruction of open particles missing one (**d**), two (**e**), or three (**f**) pentamers. The directions of five-fold, two-fold, and three-fold symmetry axes are indicated. Diffuse density in the areas of the missing pentamers probably belong to the average of the RNA molecules escaping from the particles. Example reference-free two-dimensional class averages of final three-dimensional refinement with C1 symmetry of open particles missing one (**g**), two (**h**), or three (**i**) pentamers. Scale bar represents 10 nm

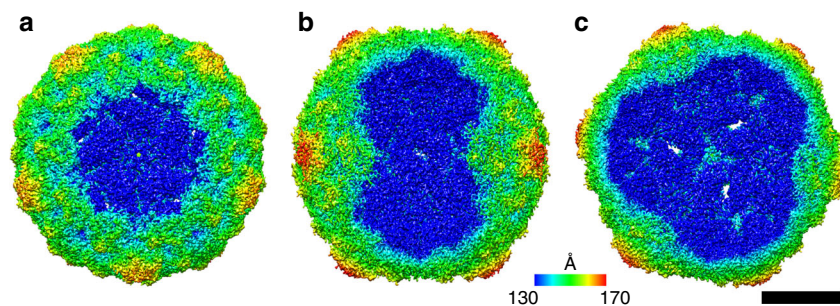


Fig. 3 Symmetrized three-dimensional reconstructions of open particles. Echovirus 18 particles lacking one (**a**), two (**b**), or three (**c**) pentamers. Five-fold (**a**), two-fold (**b**), and three-fold (**c**) symmetries were employed during the reconstructions. The electron density maps are rainbow colored based on the distance of the electron density surface from the particle center. Scale bar represents 10 nm

enteroviruses^{31–34} and an improved understanding of the process may facilitate drug development. In summary, our data show that enterovirus genome release requires several consecutive structural changes in a capsid (Fig. 7). Receptor binding or exposure to acidic pH induces the transformation of native virions into activated particles with reduced inter-pentamer interfaces^{1,3,7–9,14,15}. The weakening of inter-pentamer contacts and changes in the genome structure enable opening of the capsids and release of the RNA genome.

Methods

Production and purification of echovirus 18. Echovirus 18 (strain METCALF, ATCC-VR-852TM) was propagated in immortalized African green monkey kidney (GMK, 84113001 Sigma) cells cultivated in Dulbecco's modified Eagle's medium

enriched with 10% fetal bovine serum. For virus preparation, 50 tissue culture dishes with a diameter of 150 mm of GMK cells grown to 100% confluence were infected with echovirus 18 with a multiplicity of infection of 0.01. The infection was allowed to proceed for 5–7 days, at which point more than 90% of the cells exhibited the cytopathic effect. The cell media were harvested and any remaining attached cells were removed from the dishes using cell scrapers. The cell suspension was centrifuged at $15,000 \times g$ in a Beckman Coulter Allegra 25R centrifuge, rotor A-10 at 10 °C for 30 min. The resulting pellet was re-suspended in 10 mL of phosphate-buffered saline (PBS) (10 mM Na₂HPO₄, 1.8 mM KH₂PO₄, 137 mM NaCl, and 2.7 mM KCl, pH 7.4). The solution was subjected to three rounds of freeze-thawing by transfer between –80 and 37 °C, and homogenized using a Dounce tissue grinder. Cell debris was separated from the supernatant by centrifugation at $3100 \times g$ in a Beckman Coulter Allegra 25R centrifuge, rotor A-10 at 10 °C for 30 min. The resulting supernatant was combined with media from the infected cells. Virus particles were precipitated by the addition of PEG-8000 and NaCl to final concentrations of 12.5% (w/v) and 0.6 M, respectively. The precipitation was allowed to proceed overnight at 10 °C and with mild shaking. The

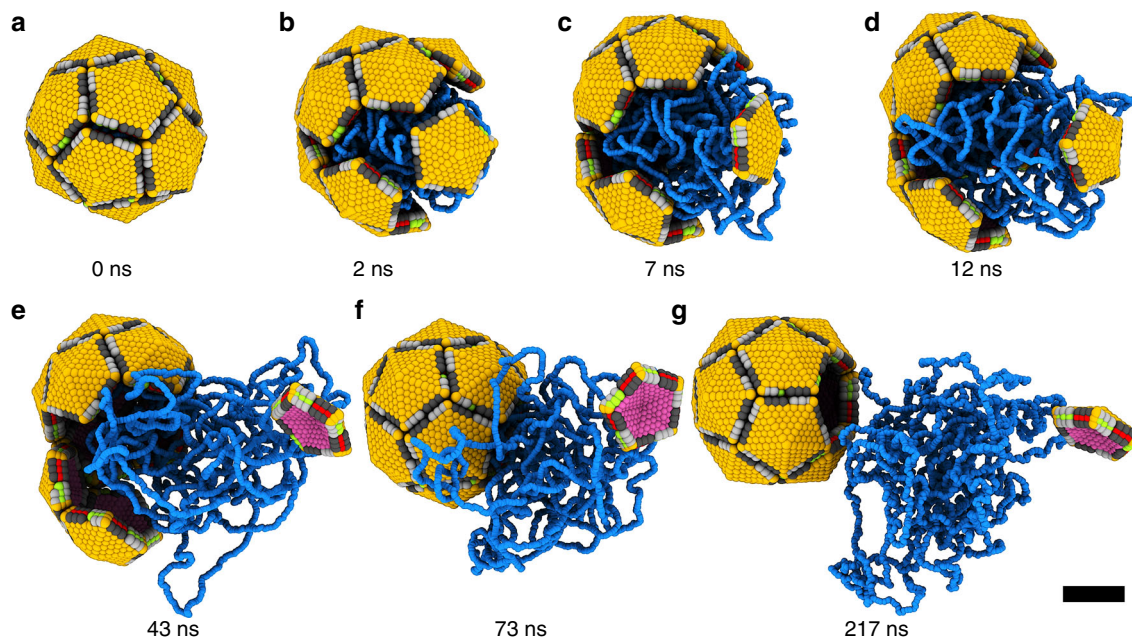


Fig. 4 Molecular dynamics simulation of echovirus 18 genome release. Seven snapshots from the process were selected. **a** Compact capsid just before opening. **b** Initial cracking of the particle with one pentamer separated from the rest of the capsid. **c–e** Continued release of the genome. **f** Re-assembly of the capsid missing one pentamer. **g** Remainder of the genome diffuses from the open capsid. Genome is shown in blue, outer capsid surface in orange, inner capsid surface in purple, beads at pentamer edges shown in dark and light gray, green, and red represent attractive inter-pentamer interfaces. Scale bar represents 10 nm

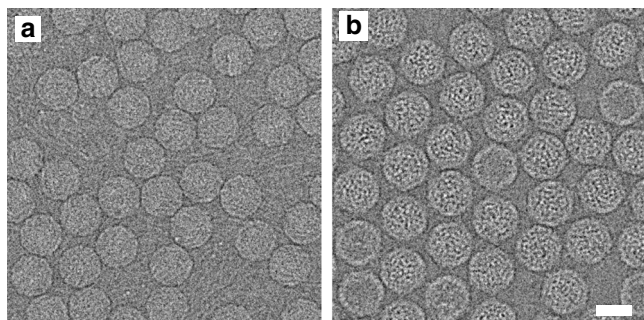


Fig. 5 Exposure to acidic pH for 3 min at 4 °C induces conformational changes in echovirus 18 genome. **a** Electron micrograph of native echovirus 18 virions with uniformly distributed density of RNA genome. **b** Electron micrograph of echovirus 18 activated particles with grainy distribution of electron density belonging to RNA genome. Scale bar represents 25 nm

following day, the precipitate was centrifuged at 15,000 × *g* in a Beckman Coulter Allegra 25R centrifuge, rotor A-10 at 10 °C for 30 min. The pelleted white precipitate was re-suspended in 12 mL of PBS. MgCl₂ was added to a final concentration of 5 mM, and the sample was subjected to DNase (10 μg/mL final concentration) and RNase (10 μg/mL final concentration) treatment for 30 min at ambient temperature. Subsequently, trypsin was added to a final concentration of 0.5 μg/mL and the mixture was incubated at 37 °C for 10 min. EDTA at pH 9.5 was added to a final concentration of 15 mM and non-ionic detergent, NP-40™ (Sigma Aldrich Inc.), was added to a final concentration of 1%. The virus particles were pelleted through a 30% (w/v) sucrose cushion in re-suspension buffer (0.25 M HEPES, pH = 7.5, and 0.25 M NaCl) by centrifugation at 210,000 × *g* in an Optima X80 ultracentrifuge using a Beckman Coulter™ Ti50.2 rotor at 10 °C for 2 h. The pellet was re-suspended in 1.5 mL of PBS and loaded onto 60% (w/w) CsCl solution in PBS. The CsCl gradient was established by ultracentrifugation at 160,000 × *g* in an Optima X80 ultracentrifuge using a Beckman Coulter™ SW41Ti rotor at 10 °C for 18 h. The opaque bands containing the virus was extracted with a 20-gauge needle mounted on a 5 mL disposable syringe. The virus was transferred into 10 mM Tris, pH = 7.4, and 0.1 M NaCl by multiple rounds of buffer exchange using a centrifugal filter device with a 100-kDa molecular weight cutoff.

Cryo-EM sample preparation and data acquisition. For cryo-EM, 3.5 μL of echovirus 18 solution (2 mg/mL) were blotted and vitrified using a Vitrobot Mark IV on Quantifoil R2/1300 mesh holey carbon grids (vitrobot settings blot-force 2, blotting time 2 s). To observe echovirus 18 particles in the process of genome release, 5 μL of virus solution at a concentration of 2 mg/mL in 10 mM Tris, pH = 7.4, and 0.1 M NaCl was diluted in 15 μL of 50 mM Mes, pH 6.0. To obtain samples for single-particle analysis, the virus was incubated in acidic pH for 10 min at 4 °C. To measure the speed of formation of activated particles, the sample was incubated at 37 °C. Electron micrographs of virus particles were collected using an FEI Titan Krios transmission electron microscope operated at 300 kV. The sample in the column of the microscope was kept at –196 °C. Images were recorded with an FEI Falcon III direct electron detection camera under low-dose conditions (22.6 e[–]/Å²) with defocus values ranging from –1.0 to –3.0 μm at a nominal magnification of ×75,000, resulting in a pixel size of 1.061 Å/px. Each 1 s of exposure was recorded in movie mode and saved as 39 separate movie frames. The frames from each exposure were aligned to compensate for drift and beam-induced motion during image acquisition using the program motioncor2³⁵. The resulting dose-weighted sum of aligned frames was used in the subsequent image processing steps, except for estimating contrast transfer function (CTF) parameters, which were determined from non-dose-weighted micrographs using the program gCTF³⁶.

Single-particle reconstructions of echovirus 18. Particles of echovirus 18 (512 × 512 pixels) were automatically selected from micrographs by Gautomatch. The images were processed using the package RELION 2.1³⁷. The dataset of autopicked particles of echovirus 18 was subjected to 2D classification. Classes containing full and empty particles were selected for processing in parallel. Classes containing full particles were 3D-classified to obtain sets of native particles and activated particles. Echovirus 7 [PDB ID: 2X5I] served as the initial model for these classifications³⁸. Similarly, classes containing empty particles were subjected to 3D classification to obtain a homogeneous set of empty particles. Finally, refinement of the selected particles was performed for native, activated particles and empty particles, using the RELION 3dautorefine procedure³⁷. Icosahedral symmetry was imposed on the volumes during the refinement process.

3D reconstructions of open particles. Schemes of the image processing, classification and reconstruction of echovirus 18 and echovirus 30 are shown in Supplementary Fig. 2. Particles of echovirus 18 (512 × 512 pixels) were automatically selected by Gautomatch. Particles of echovirus 30 in the process of genome release (512 × 512 pixels) were manually boxed using the program e2boxer.py from EMAN2³⁹. The images were processed using RELION 2.1³⁷. The dataset of autopicked echovirus 18 articles was subjected to 2D classification. Classes containing particles releasing their genomes were selected for further 3D classification.

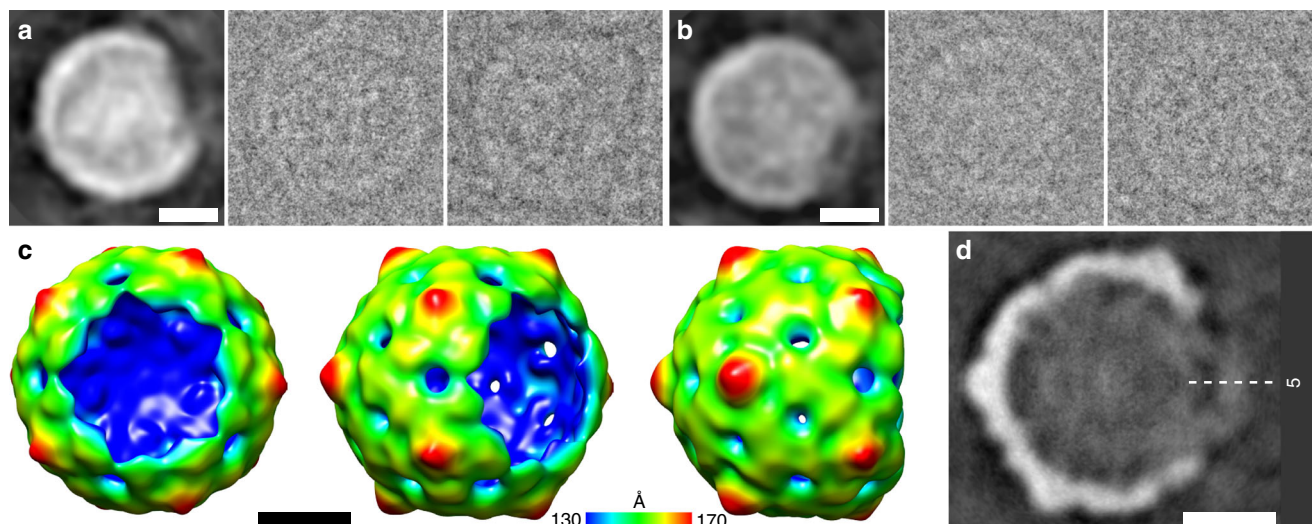


Fig. 6 Open particle of echovirus 30. **a, b** Reference-free two-dimensional class averages showing echovirus 30 particles lacking parts of their capsids. For each class, average images of two representative particles are shown. **c** Three-dimensional reconstruction of open particle of echovirus 30 lacking one pentamer with imposed five-fold symmetry. The electron density map is rainbow colored based on the distance from the particle center. **d** Electron density distribution in central section of reconstruction of open particle. The diffuse density in the pore formed by the missing pentamer probably belongs to the average of RNA molecules escaping from the particles. Scale bars represent 10 nm

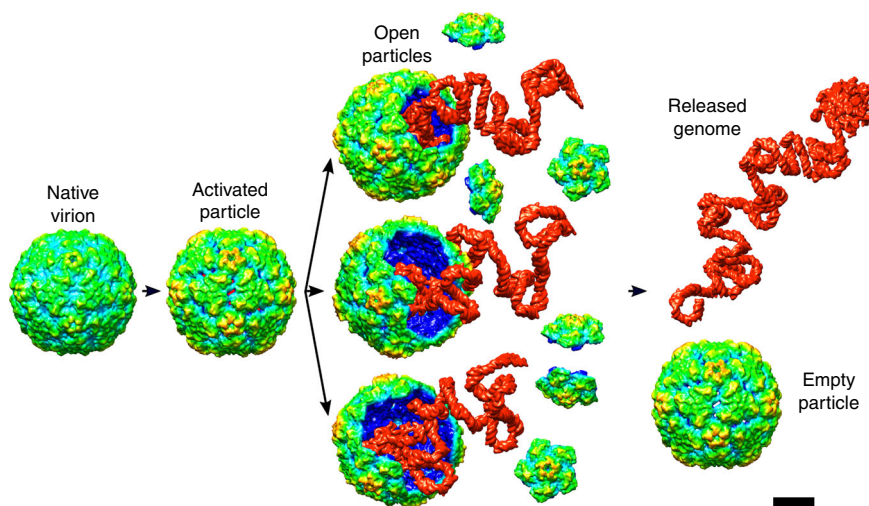


Fig. 7 Scheme of enterovirus genome release. Binding to receptors or exposure to acidic pH in endosomes induces conformational transition of virions to activated particles. The structural changes within the capsid and virus RNA enable the expulsion of pentamers from the capsid, resulting in the formation of open particles. The RNA genomes are released from the open particles. After the genome release, the pentamers may re-associate with the open capsids. Scale bar represents 10 nm

The structure of the echovirus 18 or echovirus 30 “A” particle, low-pass filtered to a resolution of 50 Å, was used to initiate asymmetrical 3D classification of echovirus 18 and echovirus 30, respectively. Classes with particles exhibiting defects corresponding to missing one, two, or three pentamers were selected for further 3D classification. In these classification steps and in the final refinement step, the previous 3D class reconstructions served as the initial models. These reconstructions were rotated so that the symmetry axes of the open particles were aligned with the *z*-axis. The resulting 3D classes with homogenous particles missing one, two, or three pentamers were independently refined using the RELION 3dauto-refine procedure as asymmetric reconstructions or by imposing the appropriate symmetries.

Post-processing of the refined maps. The volumes resulting from the 3D refinement were threshold masked, detector modulation transfer function corrected and B-factor sharpened using the RELION postprocess procedure. To avoid over-masking, the masked maps were visually inspected to exclude the possibility

of the clipping of electron densities belonging to the virus capsid. Additionally, the occurrence of over-masking was monitored by inspecting the shapes of Fourier shell correlation (FSC) curves. Furthermore, the shapes of the FSC curves of phase-randomized half-datasets with the applied mask were checked. The resulting resolutions of the reconstructions were estimated as the values at which the FSC curves fell to 0.143.

Structure determination of open particles of echovirus 18. The initial model, the activated particle of echovirus 18, was rigid-body fitted into the B-factor-sharpened cryo-EM map of echovirus 18 open particles and subjected to manual rebuilding using Coot⁴⁰, and coordinate and B-factor refinement using Phenix⁴¹.

Charge calculation - Monte Carlo simulations. We performed Metropolis Monte Carlo (MC) simulations using the Faunus framework⁴². The spherical cell with a radius of 45 nm contained one copy of the capsid described with an implicit-solvent coarse-grained model, where every residue was treated as a spherical bead

(located at the center of mass of the residue) with a radius derived from the amino acid molecular weight and the common density of 0.9 g/mL. The N- and C termini of both proteins were represented as separate residues. The solvent was treated as a dielectric continuum using the Debye–Hückel approximation with a relative permittivity of 78.7 for the interaction of charged residues^{43,44}. The capsid was placed in the middle of the simulation sphere with all degrees of motion frozen. Each amino acid was allowed to change its protonation state by titration move, where protons are allowed to move between the bead and solution. The energy associated with the exchange is determined by the change in local electrostatic energy $\pm (pH - pK_0)\ln 10$, where pK_0 is the dissociation constant of the isolated amino acid, and pH is that of the system⁴⁵. The plus and minus in the equation is associated with protonation and de-protonation, respectively. Titratable residues with their pK_a values are: C terminus (2.6), Asp (4.0), Glu (4.4), His (6.3), N-terminus (7.5), Tyr (9.6), Lys (10.4), Cys (10.8), and Arg (12.0). The total number of moves, in which there are attempts to protonate/deprotonate residues, was at least 1000 per each residue in all simulations. The temperature of our NVT ensemble was set to 298 K. We performed calculations of capsids of both native virions and activated particles with structures determined from cryo-EM. The average charges of amino acids were determined for $pH = 7.4$ and 6.0 , and monovalent salt solutions of concentrations 150 and 40 mM.

Comparison of forces required to open a capsid. The reason why the capsids are more likely to initially crack open rather than directly expel pentamers can be shown by a comparison of the forces holding the capsids together to the force exerted by the genome, which acts to rupture the capsid from the inside. Assuming that the inside pressure generated by the genome is homogeneous, the force acting on each pentamer is proportional to its area of $1/12$ of the sphere surface:

$$f_{\text{pentamer}} = \pi r^2 p/3,$$

where r is the capsid radius and p is the excess pressure from inside to outside. Each pentamer in the capsid interacts with five others, generating a force of 5 F that holds the pentamer in the capsid. Therefore, the pressure of the genome required to break a pentamer away is $p = 15 F/(\pi r^2)$. However, the pressure to separate two halves of a capsid is only $p = 10 F/(\pi r^2)$, because two half-capsids interact with each other through 10 inter-pentamer interfaces, resulting in a holding force of 10 F and the pressure force exerted by the genome is $f_{\text{half}} = \pi r^2 p$ due to the half-capsid projection in the direction of the force.

Molecular dynamics simulations. All-atom molecular dynamics simulations were performed using GROMACS version 2016.4^{46,47}. The initial structure from cryo-EM was minimized and equilibrated for 10 ns using the all-atom Amber99SB-ILDN force field⁴⁸. During the all-atom equilibration, the system was kept in an isothermal-isobaric ensemble using position restraints on backbone atoms. The spring constant of the position restraints was 1000 kJ/mol/nm². Temperature was held at 300 K with a velocity-rescaling thermostat⁴⁹. The time constant for temperature coupling was set to 0.1 ps. We employed an isotropic Berendsen barostat⁵⁰ set to 1 bar using a 1 ps coupling constant. Lennard-Jones forces were calculated with a cutoff radius of 1.1 nm. The same cutoff was applied for real-space electrostatic interactions, while the long-range contribution was evaluated with particle mesh Ewald⁵¹. All bonds were constrained using the LINCS algorithm⁵², apart from TIP3P water, for which analytical SETTLE was used⁵³. A 2-fs time step was used for the production run. The system consisted of four echovirus 18 protomers in aqueous solution (of roughly 200,000 water molecules) with added NaCl ions at a concentration of 150 mM. We simulated capsids of both native virions and activated particles in a rectangular box of $16 \times 16 \times 21$ and $17 \times 17 \times 25$ nm, respectively. Periodic boundary conditions were applied.

For the binding free energy calculations between two pentamers, we used a computationally efficient, coarse-grained MARTINI 2.2 force field^{54–56}. The resulting structure from all-atom equilibration was converted into a MARTINI model using the *martinize.py* script. As a consequence of coarse-graining, the MARTINI model does not explicitly describe backbone hydrogen bonds. Thus, the secondary structure has to be imposed on the peptides and maintained throughout the simulation. The assignment of secondary structure for both native virion and activated particle echovirus 18 was done with the program DSSP⁵⁷. To help preserve the higher-order structure, an elastic network was added to the standard MARTINI topology. Harmonic bonds were generated between backbone beads by the *martinize.py* script using the option *-elastic*. The elastic bond force constant was set to 500 kJ/mol/nm² (*-ef 500*), and the lower and upper elastic bond cutoff radius to 0.5 and 0.9 nm (*-el 0.5* and *-eu 0.9*), respectively, and the elastic bond decay factor and decay power both to 0 (*-ea 0* and *-ep 0*). Furthermore, elastic bonds were deleted for residues exhibiting a high degree of flexibility in the electron density map (Supplementary Table 3). Additionally, the mapping of histidines with an average charge over 0.4 e, determined from MC simulations, were changed from the uncharged to charged form. The simulation time step was set to 30 fs. A velocity-rescaling thermostat with a coupling constant of 1.0 ps was employed to maintain the temperature at 310 K⁴⁹. Protein and solvent beads were coupled to separate baths to ensure the correct temperature distribution. The pressure was kept at 1 bar with a Parrinello-Rahman barostat with an isotropic coupling scheme with a coupling constant of 12 ps⁵⁸. All non-bonded interactions were cutoff at 1.1 nm and the van der Waals potential was shifted to zero. The relative dielectric constant was set to 15. Periodic boundary conditions were employed, yielding a rectangular box of dimensions $17.7 \times 17.7 \times 28.5$ nm for the activated particle and

$17.7 \times 17.7 \times 31.4$ nm for the native virion. The system consisted of 4 protomers of capsid proteins of echovirus 18 in water with added NaCl ions at a concentration of 150 mM.

The umbrella sampling method was employed to determine the free energy of binding between two pentamers. We defined the reaction coordinate as the z -distance between the centers of mass of protomers 1–2 and 3–4 (Supplementary Fig. 11). We restrained the position of protomers 1–2 through the use of harmonic potentials on backbone beads, excluding the flexible residues from Supplementary Table 3. Cylindrical flat-bottomed position restraints were applied to the backbone beads of protomers 3–4, excluding the residues from Supplementary Table 3, to keep the protomers from tilting and moving in the XY plane. The cylinders were parallel to the z -axis. The force constant was set to 1000 kJ/mol/nm² and the radius of all cylinders was 0.3 nm. The reference configuration for the cylindrical flat-bottomed position restraint was selected from a 1000-ns equilibration run. For the last 500 ns of the equilibration run, the structure of protomers 3–4 was averaged. The reference configuration was selected from the trajectory based on the lowest root mean squared deviation toward the averaged structure. For the native virion, 74 umbrella windows were simulated for 2000 ns each, which was necessary to get a convergence (Supplementary Fig. 12). The spring constant of the umbrella harmonic potential was set to 50,000 kJ/mol/nm² for the first 40 windows, with a spacing of 0.02 nm. The next 34 windows were spaced by 0.025 nm and the spring constant was set to 10,000 kJ/mol/nm². For the activated particle of enterovirus 18, 149 umbrella windows were simulated for 1000 ns each. The first 34 windows were spaced by 0.02 nm and a harmonic spring of 50,000 kJ/mol/nm² was applied. The next 115 windows had the spring constant set to 10,000 kJ/mol/nm² with a spacing of 0.025 nm. To analyze the probability distributions of states from each window, iterative WHAM was used, implemented in the GROMACS tool *gmx wham*^{59,60}.

Phenomenological model. We developed a phenomenological coarse-grained model of a *Picornavirus* family based on human echovirus 18 (Supplementary Fig. 13). The capsid was a regular dodecahedron comprised of 12 pentagonal subunits. Each subunit assumes the role of a stable pentameric intermediate. The pentamers were made of beads (pseudoatoms) organized in three layers.

The outer circumscribed sphere of the capsid had a radius of 16 nm and the inner was 14 nm. Each pentamer was composed of 317 beads connected with 1311 harmonic bonds keeping the structure. The spring constant of the harmonic potential was 250 kJ/mol. Beads within the capsids were only interacting via harmonic bonds. There were six types of beads (Supplementary Fig. 14), all of which were interacting with Weeks-Chandler-Anderson repulsive potential with an epsilon set to 1.0 [<https://doi.org/10.1063/1.1674820>]. In addition, beads at the pentamer edges had an attractive interaction range of 0.3 to 2.0 nm based on the free energy calculation with the Martini model. The interaction decreased to zero with a \cos^2 dependence. The attraction strength was weak, 0.5 kJ/mol, for the inner and outer layer, while the middle layer had stronger attraction strength that varied from 2 to 20 kJ/mol. The attraction only acts between the types, which are in contact in the assembled capsid structure. These interactions represent specific contacts between the protomers in the capsid (Supplementary Fig. 11).

To investigate RNA genome release from the capsid, we modeled the RNA as a chain of repulsive beads. A single bead represented two nucleotides with a radius of 0.6 nm connected by a 1.1-nm-long harmonic bond, which is about twice the distance between phosphates of adjacent nucleotides. All beads were interacting with a shifted truncated Lennard-Jones potential, i.e. Weeks-Chandler-Anderson potential with an epsilon set to 1.0⁶¹.

Simulations were performed in LAMMPS⁶², with the use of a Langevin thermostat^{63–65}. Center of mass motion of the entire system caused by the thermostat was eliminated using the option “zero yes”. Additionally, the “gjf yes” option was turned on, applying Gronbech-Jensen/Farago time-discretization for the Langevin model to enable longer time steps, while still producing the correct Boltzmann distribution of atom positions⁶⁵. The viscous damping term was set to 10,000 time steps. The reduced temperature in our simulations was $T^* = 1 k_B T$. The box size $150 \times 150 \times 150$ nm was constant and the same for all simulations.

The simulation protocol was as follows. First the capsid was generated from pentamers, and then the chain representing the genome was generated within the capsid using a random walk. The equilibration started with the chain equilibration alone, which was simulated with Langevin dynamics for 10^8 steps, while the capsid shell was motionless. The second step was the equilibration of both the capsid and genome. The attraction between pair B-C begun at 35 kJ/mol and was gradually decreased by a rate of 0.25 kJ/mol every 200,000 time steps. The production genome release simulations were repeated 10 times, with different conditions, for each set of parameters (attraction strength, attraction range, flexibility of the capsid, and the size of the genome beads) each of which were concluded at 10^9 time steps or sooner if the release had occurred.

To estimate the timescale of the simulations, we performed 50 independent simulations of the full virus capsid starting from different conditions. Each simulation was performed for 10^8 steps. The parameters for the capsid were chosen to prevent the genome release within the duration of the simulation. We analyzed the averaged square displacement of the full capsid center of mass. Using Fick’s second law, we calculated the diffusion coefficient of the capsid to be $1.37 \times 10^{-4} \pm 2.0 \times 10^{-8} \text{Å}^2/\text{step}$ (Supplementary Fig. 15). We also estimated the diffusion coefficient using the Stokes-Einstein relation, with a capsid radius of 16.5 nm, the

diffusion coefficient is $15 \mu\text{m}^2/\text{s}$. Comparing the estimated coefficient with the simulation one, the simulation time step corresponded to 92 fs (there were $10,901 \pm 1$ steps in a ns).

Timescale of genome release. To estimate the timescale of genome release from the virus capsid, we analyzed the average times of this process in our simulations. The genome was released from the capsid in the order of 10^6 simulation steps corresponding to 100 ns. Another approach is to estimate the time required for the genome to diffuse freely from an open capsid. Using Einstein-Stokes relation, we determined that the genome diffuses 50 nm in microsecond timescale, which makes the observation of the genome release experimentally challenging.

Reporting summary. Further information on experimental design is available in the Nature Research Reporting Summary linked to this article.

Data availability

Cryo-EM electron density maps have been deposited in the Electron Microscopy Data Bank, <https://www.ebi.ac.uk/pdbe/emdb/> (accession numbers EMD-0181, EMD-0182, EMD-0183, EMD-0184, EMD-0185, EMD-0186, EMD-0187, EMD-0188, EMD-0189, and EMD-0217), and the fitted coordinates have been deposited in the Protein Data Bank, www.pdb.org (PDB ID codes 6HBG, 6HHB, 6HBJ, 6HBK, 6HBL, and 6HHT). The authors declare that all other data supporting the findings of this study are available within the article and its Supplementary Information files, or are available from the authors upon request.

Received: 30 August 2018 Accepted: 17 February 2019

Published online: 08 March 2019

References

- Tuthill, T. J., Groppelli, E., Hogle, J. M. & Rowlands, D. J. Picornaviruses. *Curr. Top. Microbiol. Immunol.* **343**, 43–89 (2010).
- Ren, J. et al. Picornavirus uncoating intermediate captured in atomic detail. *Nat. Commun.* **4**, 1929 (2013).
- Levy, H. C., Bostina, M., Filman, D. J. & Hogle, J. M. Catching a virus in the act of RNA release: a novel poliovirus uncoating intermediate characterized by cryo-electron microscopy. *J. Virol.* **84**, 4426–4441 (2010).
- Garriga, D. et al. Insights into minor group rhinovirus uncoating: the X-ray structure of the HRV2 empty capsid. *PLoS Pathog.* **8**, e1002473 (2012).
- Wang, X. et al. A sensor-adaptor mechanism for enterovirus uncoating from structures of EV71. *Nat. Struct. Mol. Biol.* **19**, 424–429 (2012).
- Shingler, K. L. et al. The enterovirus 71 A-particle forms a gateway to allow genome release: a cryoEM study of picornavirus uncoating. *PLoS Pathog.* **9**, e1003240 (2013).
- Seitonen, J. J. et al. Structural analysis of coxsackievirus A7 reveals conformational changes associated with uncoating. *J. Virol.* **86**, 7207–7215 (2012).
- Bostina, M., Levy, H., Filman, D. J. & Hogle, J. M. Poliovirus RNA is released from the capsid near a twofold symmetry axis. *J. Virol.* **85**, 776–783 (2011).
- Belnap, D. M. et al. Molecular tectonic model of virus structural transitions: the putative cell entry states of poliovirus. *J. Virol.* **74**, 1342–1354 (2000).
- Hadfield, A. T. et al. The refined structure of human rhinovirus 16 at 2.15 Å resolution: implications for the viral life cycle. *Structure* **5**, 427–441 (1997).
- Reinisch, K. M., Nibert, M. L. & Harrison, S. C. Structure of the reovirus core at 3.6 Å resolution. *Nature* **404**, 960–967 (2000).
- Naitow, H., Tang, J., Canady, M., Wickner, R. B. & Johnson, J. E. L-A virus at 3.4 Å resolution reveals particle architecture and mRNA decapping mechanism. *Nat. Struct. Mol. Biol.* **9**, 725–728 (2002).
- Rich, A. & Davies, D. R. A new two stranded helical structure: polyadenylic acid and polyuridylic acid. *J. Am. Chem. Soc.* **78**, 3548–3549 (1956).
- Hewat, E. A., Neumann, E. & Blaas, D. The concerted conformational changes during human rhinovirus 2 uncoating. *Mol. Cell* **10**, 317–326 (2002).
- Hewat, E. A. & Blaas, D. Cryoelectron microscopy analysis of the structural changes associated with human rhinovirus type 14 uncoating. *J. Virol.* **78**, 2935–2942 (2004).
- Pelletier, J. & Sonenberg, N. Internal initiation of translation of eukaryotic mRNA directed by a sequence derived from poliovirus RNA. *Nature* **334**, 320–325 (1988).
- Jiang, P., Liu, Y., Ma, H. C., Paul, A. V. & Wimmer, E. Picornavirus morphogenesis. *Microbiol. Mol. Biol. Rev.* **78**, 418–437 (2014).
- Fricks, C. E. & Hogle, J. M. Cell-induced conformational change in poliovirus: externalization of the amino terminus of VP1 is responsible for liposome binding. *J. Virol.* **64**, 1934–1945 (1990).
- Tuthill, T. J., Bubeck, D., Rowlands, D. J. & Hogle, J. M. Characterization of early steps in the poliovirus infection process: receptor-decorated liposomes induce conversion of the virus to membrane-anchored entry-intermediate particles. *J. Virol.* **80**, 172–180 (2006).
- Groppelli, E. et al. Picornavirus RNA is protected from cleavage by ribonuclease during virion uncoating and transfer across cellular and model membranes. *PLoS Pathog.* **13**, e1006197 (2017).
- Chow, M. et al. Myristylation of picornavirus capsid protein VP4 and its structural significance. *Nature* **327**, 482–486 (1987).
- Kirkegaard, K. Mutations in VP1 of poliovirus specifically affect both encapsidation and release of viral RNA. *J. Virol.* **64**, 195–206 (1990).
- Krausslich, H. G., Holscher, C., Reuer, Q., Harber, J. & Wimmer, E. Myristoylation of the poliovirus polyprotein is required for proteolytic processing of the capsid and for viral infectivity. *J. Virol.* **64**, 2433–2436 (1990).
- Moscufo, N., Yafal, A. G., Rogove, A., Hogle, J. & Chow, M. A mutation in VP4 defines a new step in the late stages of cell entry by poliovirus. *J. Virol.* **67**, 5075–5078 (1993).
- Rapaport, D. C. Role of reversibility in viral capsid growth: a paradigm for self-assembly. *Phys. Rev. Lett.* **101**, 186101 (2008).
- Harutyunyan, S. et al. Viral uncoating is directional: exit of the genomic RNA in a common cold virus starts with the poly-(A) tail at the 3'-end. *PLoS Pathog.* **9**, e1003270 (2013).
- Pickl-Herk, A. et al. Uncoating of common cold virus is preceded by RNA switching as determined by X-ray and cryo-EM analyses of the subviral A-particle. *Proc. Natl Acad. Sci. USA* **110**, 20063–20068 (2013).
- Harutyunyan, S., Kowalski, H. & Blaas, D. The Rhinovirus subviral a-particle exposes 3'-terminal sequences of its genomic RNA. *J. Virol.* **88**, 6307–6317 (2014).
- Fout, G. S., Medappa, K. C., Mapoles, J. E. & Rueckert, R. R. Radiochemical determination of polyamines in poliovirus and human rhinovirus 14. *J. Biol. Chem.* **259**, 3639–3643 (1984).
- Mounce, B. C., Olsen, M. E., Vignuzzi, M. & Connor, J. H. Polyamines and their role in virus infection. *Microbiol. Mol. Biol. Rev.* **81**, e00029-17 (2017).
- Rossmann, M. G. Viral cell recognition and entry. *Protein Sci.* **3**, 1712–1725 (1994).
- Grant, R. A. et al. Structures of poliovirus complexes with anti-viral drugs: implications for viral stability and drug design. *Curr. Biol.* **4**, 784–797 (1994).
- Smith, T. J. et al. The site of attachment in human rhinovirus 14 for antiviral agents that inhibit uncoating. *Science* **233**, 1286–1293 (1986).
- Shih, S. R. et al. Selective human enterovirus and rhinovirus inhibitors: An overview of capsid-binding and protease-inhibiting molecules. *Med. Res. Rev.* **24**, 449–474 (2004).
- Zheng, S. Q. et al. MotionCor2: anisotropic correction of beam-induced motion for improved cryo-electron microscopy. *Nat. Methods* **14**, 331–332 (2017).
- Zhang, K. Gctf: real-time CTF determination and correction. *J. Struct. Biol.* **193**, 1–12 (2016).
- Scheres, S. H. RELION: implementation of a Bayesian approach to cryo-EM structure determination. *J. Struct. Biol.* **180**, 519–530 (2012).
- Plevka, P. et al. Interaction of decay-accelerating factor with echovirus 7. *J. Virol.* **84**, 12665–12674 (2010).
- Tang, G. et al. EMAN2: an extensible image processing suite for electron microscopy. *J. Struct. Biol.* **157**, 38–46 (2007).
- Emsley, P., Lohkamp, B., Scott, W. G. & Cowtan, K. Features and development of Coot. *Acta Crystallogr. D Biol. Crystallogr.* **66**, 486–501 (2010).
- Adams, P. D. et al. PHENIX: a comprehensive Python-based system for macromolecular structure solution. *Acta Crystallogr. D Biol. Crystallogr.* **66**, 213–221 (2010).
- Stenqvist, B., Thuresson, A., Kurut, A., Vácha, R. & Lund, M. Faunus—a flexible framework for Monte Carlo simulation. *Mol. Simul.* **39**, 1233–1239 (2013).
- Israelachvili, J. N. *Intermolecular and Surface Forces* (Academic Press, 2011) <https://www.elsevier.com/books/intermolecular-and-surface-forces/israelachvili/978-0-12-391927-4>.
- Bagotsky, V. S. *Fundamentals of Electrochemistry* (John Wiley & Sons, Hoboken, 2005).
- Lund, M., Åkesson, T. & Jönsson, B. Enhanced protein adsorption due to charge regulation. *Langmuir* **21**, 8385–8388 (2005).
- Páll, S., Abraham, M. J., Kutzner, C., Hess, B. & Lindahl, E. Tackling exascale software challenges in molecular dynamics simulations with GROMACS. In *Solving Software Challenges for Exascale*, Vol. 8759 (eds Markidis, S. & Laure, E.) 3–27 (Springer, Switzerland London, 2015).
- Abraham, M. J. et al. GROMACS: high performance molecular simulations through multi-level parallelism from laptops to supercomputers. *SoftwareX* **1–2**, 19–25 (2015).
- Lindorff-Larsen, K. et al. Improved side-chain torsion potentials for the Amber ff99SB protein force field. *Proteins* **78**, 1950–1958 (2010).
- Bussi, G., Donadio, D. & Parrinello, M. Canonical sampling through velocity rescaling. *J. Chem. Phys.* **126**, 014101 (2007).

50. Berendsen, H. J. C., Postma, J. P. M., van Gunsteren, W. F., DiNola, A. & Haak, J. R. Molecular dynamics with coupling to an external bath. *J. Chem. Phys.* **81**, 3684–3690 (1984).
51. Darden, T., York, D. & Pedersen, L. Particle mesh Ewald: an N-log(N) method for Ewald sums in large systems. *J. Chem. Phys.* **98**, 10089–10092 (1993).
52. Hess, B., Bekker, H., Berendsen, H. J. C. & Fraaije, J. G. E. M. LINCS: a linear constraint solver for molecular simulations. *J. Comput. Chem.* **18**, 1463–1472 (1997).
53. Miyamoto, S. & Kollman, P. A. Settle: an analytical version of the SHAKE and RATTLE algorithm for rigid water models. *J. Comput. Chem.* **13**, 952–962 (1992).
54. Marrink, S. J., Risselada, H. J., Yefimov, S., Tieleman, D. P. & de Vries, A. H. The MARTINI force field: coarse grained model for biomolecular simulations. *J. Phys. Chem. B* **111**, 7812–7824 (2007).
55. Monticelli, L. et al. The MARTINI coarse-grained force field: extension to proteins. *J. Chem. Theory Comput.* **4**, 819–834 (2008).
56. de Jong, D. H. et al. Improved parameters for the martini coarse-grained protein force field. *J. Chem. Theory Comput.* **9**, 687–697 (2013).
57. Kabsch, W. & Sander, C. Dictionary of protein secondary structure: pattern recognition of hydrogen-bonded and geometrical features. *Biopolymers* **22**, 2577–2637 (1983).
58. Parrinello, M. & Rahman, A. Polymorphic transitions in single crystals: a new molecular dynamics method. *J. Appl. Phys.* **52**, 7182–7190 (1981).
59. Kumar, S., Rosenberg, J. M., Bouzida, D., Swendsen, R. H. & Kollman, P. A. The weighted histogram analysis method for free-energy calculations on biomolecules. I. The method. *J. Comput. Chem.* **13**, 1011–1021 (1992).
60. Zhang, C., Lai, C. L. & Pettitt, B. M. Accelerating the weighted histogram analysis method by direct inversion in the iterative subspace. *Mol. Simul.* **42**, 1079–1089 (2016).
61. Weeks, J. D., Chandler, D. & Andersen, H. C. Role of repulsive forces in determining the equilibrium structure of simple liquids. *J. Chem. Phys.* **54**, 5237–5247 (1971).
62. Plimpton, S. Fast parallel algorithms for short-range molecular dynamics. *J. Comput. Phys.* **117**, 1–19 (1995).
63. DÜNweg, B. & Paul, W. Brownian dynamics simulations without Gaussian random numbers. *Int. J. Mod. Phys. C* **02**, 817–827 (1991).
64. Schneider, T. & Stoll, E. Molecular-dynamics study of a three-dimensional one-component model for distortive phase transitions. *Phys. Rev. B* **17**, 1302–1322 (1978).
65. Grønbech-Jensen, N., Hayre, N. R. & Farago, O. Application of the G-JF discrete-time thermostat for fast and accurate molecular simulations. *Comput. Phys. Commun.* **185**, 524–527 (2014).
66. Stenqvist, B., Thuresson, A., Kurut, A., Vácha, R. & Lund, M. Faunus—a flexible framework for Monte Carlo simulation. *Mol. Simul.* **39**, 1233–1239 (2013).

Acknowledgements

We wish to thank the Central European Institute of Technology Core Facilities of Cryo-Electron Microscopy and Tomography and of Proteomics, supported by the Czech Infrastructure for Integrative Structural Biology (LM2015043 funded by the Ministry of Education, Youth and Sports of the Czech Republic) for their assistance in obtaining the scientific data presented in this paper. This research was carried out under the project CEITEC 2020

(LQ1601), with financial support from the Ministry of Education, Youth and Sports of the Czech Republic under National Sustainability Program II. This work was supported by The Ministry of Education, Youth and Sports from the Large Infrastructures for Research, Experimental Development and Innovations project "IT4Innovations National Supercomputing Center – LM2015070". Computational resources were provided by CESNET LM2015042, and the CERIT Scientific Cloud LM2015085 provided under the program Projects of Large Research, Development, and Innovations Infrastructures of The Ministry of Education, Youth and Sports. The Titan Xp used for this research was donated by the NVIDIA Corporation. The research leading to these results received funding from the European Research Council under the European Union's Seventh Framework Program Grant (FP7/2007-2013)/ERC Grant Agreement 335855 (to PP), Czech Science Foundation Grant Agreement GX19-25982X (to P.P.), and EMBO Grant Agreement IG 3041 (to P.P.).

Author contributions

P.P. and R.V. designed research; D.B., T.F., D.H., Y.L., L.S., L.M. and J.M. performed research; D.B., T.F., D.H., L.S., R.V. and P.P. analyzed data; and D.B., T.F., L.S., R.V. and P.P. wrote the paper.

Additional information

Supplementary Information accompanies this paper at <https://doi.org/10.1038/s41467-019-09132-x>.

Competing interests: The authors declare no competing interests.

Reprints and permission information is available online at <http://npg.nature.com/reprintsandpermissions/>

Journal peer review information: *Nature Communications* thanks David Rowlands and the other anonymous reviewers for their contribution to the peer review of this work. Peer reviewer reports are available.

Publisher's note: Springer Nature remains neutral with regard to jurisdictional claims in published maps and institutional affiliations.



Open Access This article is licensed under a Creative Commons Attribution 4.0 International License, which permits use, sharing, adaptation, distribution and reproduction in any medium or format, as long as you give appropriate credit to the original author(s) and the source, provide a link to the Creative Commons license, and indicate if changes were made. The images or other third party material in this article are included in the article's Creative Commons license, unless indicated otherwise in a credit line to the material. If material is not included in the article's Creative Commons license and your intended use is not permitted by statutory regulation or exceeds the permitted use, you will need to obtain permission directly from the copyright holder. To view a copy of this license, visit <http://creativecommons.org/licenses/by/4.0/>.

© The Author(s) 2019